High Energy Transients Powered by Black Holes

Thesis by

Yuhan Yao

In Partial Fulfillment of the Requirements for the

Degree of

Doctor of Philosophy

CALIFORNIA INSTITUTE OF TECHNOLOGY

Pasadena, California

2023

Defended May 22, 2023

© 2023

Yuhan Yao
ORCID: 0000-0001-6747-8509

All rights reserved

ACKNOWLEDGEMENTS

This thesis could not have been possible without the time and energy of many people to whom I am deeply grateful:

First and foremost, my advisors Shri Kulkarni and Fiona Harrison, whose guidance has been instrumental in shaping me into the scientist I am today. Shri introduced me to the captivating realm of time domain astronomy, nurtured my approach to scientific challenges, and steered me through periods of desperation when the road ahead was not clear. Apart from sharing with me his broad expertise in astronomy, he also often reminds me to spend time reading broadly and exercising. I will always remember the many sunny afternoons in his backyard, where he offers fresh orange juice and comments on my work with honest critique. Fiona taught me the skills to convey complex physical concepts with simple words and the strategies to deliver speeches with confidence. She created a welcoming and collaborative environment for the high energy research group at Caltech with her remarkable leadership. Despite her busy schedule, she always makes time to provide career development suggestions, leave detailed comments on my manuscripts, and help me set priorities when I tend to procrastinate. Both Shri and Fiona promoted my growth as an independent researcher by providing professional networking resources and giving me the freedom to pursue my own project ideas. I am honored to have been their student and could not have asked for better advisors.

My mentors throughout the years. Adam Miller, mentor of my first-year project, was incredibly selfless in devoting time towards teaching me software skills and supernova classification schemes. I sincerely appreciate his thoughtfulness, elegant scientific aesthetics, and witty jokes. Anna Ho, my peer mentor, has been a good friend and a career role model ever since day one. Her advice has helped me adjust to a new culture, maintain a healthy work-life balance, and advance as a scholar. Wenbin Lu, the incredibly knowledgeable theorist, patiently taught me black hole physics, sharply pointed out the missing pieces in existing studies, and related to my frustration during the final stages of some projects. Suvi Gezari, my guide in exploring tidal disruption events and related nuclear transients. I have had a constant source of inspiration from her keen insights, creativity, and passions.

Caltech faculty members. I would like to express my gratitude to Vikram Ravi for his support in securing telescope time, his service as my committee chair, and the

numerous enlightening discussions over the years. I would also like to credit Mansi Kasliwal for her encouragement throughout my progress, Jim Fuller for discussions on supernova mass-loss and stellar evolution, Lynne Hillenbrand for her supervision of graduate students as the option representative, Sterl Phinney for his stimulating lectures and problem sets in the "radiative transfer" course, and Chris Martin for his constructive questions during my candidacy and PhD exams.

The ZTF and *NuSTAR* groups. Staff members at every single observatory that I have benefited from in this thesis. Collaborators with whom I have had the privilege to engage in a joint effort. While this is by no means an exhaustive list, I would like to thank the contributions from Dan Perley, Brad Cenko, Sjoert van Velzen, Igor Andreoni, Michael Coughlin, Javier García, Murray Brightman, Karl Forster, Brian Grefenstette, Keith Gendreau, Marat Gilfanov, and Rashid Sunyaev.

My undergraduate research advisors. I need to recognize Richard de Grijs and Licai Deng, who welcomed me as a group member, cultivated my interests in astronomy, and broadened my horizons. I am lucky to have worked with Michael Meyer at the University of Michigan, who guided me with meticulousness and clarity. I am indebted to Chao Liu and Hua Feng, who taught me so many things about Galactic astronomy and high-energy astrophysics, respectively. Both of them are talented educators who gave me hands-on instructions and inspired me to pursue a PhD in Astrophysics.

My friends. I would like to thank (among others) Kevin Burdge, Ilaria Caiazzo, Kishalay De, Dillon Dong, Yuping Huang, Suoqing Ji, Xiaolei Meng, Jean Somalwar, Yashvi Sharma, Shangjia Zhang, and Zhuyun Zhuang, who shared passions and made my PhD journey a more enjoyable experience. Special thanks to Yuan Song and Hao Zhang, who have been my steadfast companions ever since childhood.

Finally, my family, to which I would like to dedicate this thesis and my entire PhD. This is to my parents Yang Li (李洋) and Fushan Yao (姚福山), who instill in me a sense of security, encourage me to dream big, and equip me with the abilities to have a happy and fulfilling life. This is to my grandmother Hongjuan Wang (王洪娟), who possesses an incredible amount of energy and never ceases to learn. This is to my husband Ding Zhong, who has been my confidante through thick and thin. I cannot thank any of you enough for your unwavering support.

ABSTRACT

The accretion of matter onto black holes heats the surrounding materials to extremely high temperatures and drives outflows, producing a sudden and intense emission of light. Some of the most well-known examples include gamma-ray bursts, X-ray binaries (XRBs), and tidal disruption events (TDEs). In recent years, modern wide-field time domain sky surveys, such as the optical Zwicky Transient Facility (ZTF) and the *Spektrum-Roentgen-Gamma* (*SRG*) X-ray satellite, have opened up the discovery space of fast-evolving transients and enabled population analysis. In this thesis, I conducted a series of observational studies to understand the inner workings, environments, and demographics of high-energy transients powered by black holes.

The first part of my thesis presents detailed studies on AT2019wey and AT2020mrf — two transients discovered by *SRG*. First, I established that AT2019wey is a Galactic XRB with a low-mass companion star, and provided evidence that its central compact object is a black hole. Next, I demonstrated that AT2020mrf is a massive star explosion likely powered by fall-back accretion onto a newly formed black hole (with a rapidly spinning magnetar as an alternative power source). My work supports the idea that luminous fast blue optical transients form a rare class of engine-driven stellar explosions.

The second part of my thesis concerns TDEs. I contributed to the discovery of two X-ray bright TDEs (AT2021ehb and AT2022cmc) and led comprehensive follow-up campaigns to track their long-term evolution. In both objects, using the *NuSTAR* and *NICER* X-ray telescopes, I identified novel TDE spectral features, which probe massive black hole accretion and jet launching. Additionally, using ZTF, I constructed the largest flux-limited sample of 33 TDEs, which enabled robust estimates of the optical TDE luminosity functions, host galaxy preference, and the black hole mass function. The emerging functional forms resulting from the large sample size represent significant advancements. My work lays a foundation for both TDE population studies with future sky surveys and theoretical inquiries.

PUBLISHED CONTENT AND CONTRIBUTIONS

Yao, Y., V. Ravi, et al. (Mar. 2023). In: *arXiv e-prints*, arXiv:2303.06523, arXiv:2303.06523. DOI: 10.48550/arXiv.2303.06523.
Y.Y. conceived the project, acquired most of the follow-up observations, performed the analysis, and wrote the manuscript.

Yao, Y., A. Y. Q. Ho, et al. (Aug. 2022). In: *ApJ* 934.2, 104, p. 104. DOI: 10.3847/1538-4357/ac7a41.
Y.Y. participated in the discovery of the event, acquired the optical and X-ray follow-up observations, performed the analysis, and wrote the manuscript.

Yao, Y., W. Lu, et al. (Sept. 2022). In: *ApJ* 937.1, 8, p. 8. DOI: 10.3847/1538-4357/ac898a.
Y.Y. led to the discovery of the event, acquired most of the follow-up observations, performed the analysis, and wrote the manuscript.

Yao, Y., S. R. Kulkarni, K. B. Burdge, et al. (Oct. 2021). In: *ApJ* 920.2, 120, p. 120. DOI: 10.3847/1538-4357/ac15f9.
Y.Y. acquired the follow-up observations, performed the analysis, and wrote the manuscript.

Yao, Y., S. R. Kulkarni, K. C. Gendreau, et al. (Oct. 2021). In: *ApJ* 920.2, 121, p. 121. DOI: 10.3847/1538-4357/ac15f8.
Y.Y. helped acquire the follow-up observations, performed part of the analysis, and wrote most of the manuscript.

TABLE OF CONTENTS

LIST OF ILLUSTRATIONS

LIST OF TABLES

NOMENCLATURE

ADAF. Advection-Dominated Accretion Flow.

AGN. Active Galactic Nucleus.

BH. Black Hole.

BHMF. Black Hole Mass Function.

Crab. A unit of X-ray flux, defined as the intensity of the Crab Nebula at the corresponding X-ray photon energy. For reference, 1 Crab (2–10 keV) = 2.3×10^{-8} erg s^{-1} cm^{-2}.

CSM. Circumstellar Medium.

FBOT. Fast Blue Optical Transient.

GRB. Gamma Ray Burst.

HIMS. Hard-intermediate State.

HMXB. High-mass X-ray Binary.

IMBH. Intermediate-mass Black Hole.

ISCO. Innermost Stable Circular Orbit.

LHS. Low-hard State.

LMXB. Low-mass X-ray Binary.

NS. Neutron Star.

SED. Spectral Energy Distribution.

SN/SNe. Supernova/Supernovae.

TDE. Tidal Disruption Event.

ZTF. Zwicky Transient Facility.

Chapter 1

INTRODUCTION AND OUTLINE

1.1 Black Holes in the Universe

Black holes are among the most fascinating objects in the universe. Astrophysical black holes can be described by two parameters: the mass ($M_{\rm BH}$) and spin ($a_* \equiv Jc/GM_{\rm BH}^2$, where J is the angular momentum). Figure 1.1 shows recognized black holes across the mass scale, color-coded by their different system types (see Corral-Santana, Casares, Muñoz-Darias, Bauer, et al. 2016; El-Badry et al. 2023; Mróz, Udalski, and Gould 2022; Abbott et al. 2023; Event Horizon Telescope Collaboration, Akiyama, Alberdi, Alef, Algaba, et al. 2022; Kormendy and Ho 2013; Yao, Ravi, et al. 2023, and references therein).

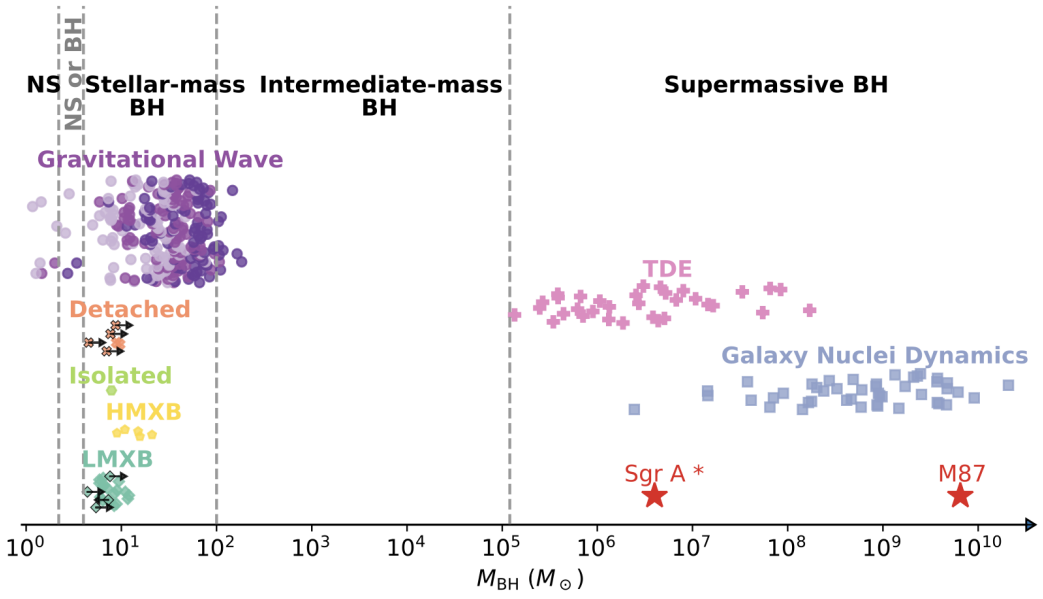

Figure 1.1: Astrophysical black holes across the mass scale.

The conventional approach for determining $M_{\rm BH}$ is through the study of gravity exerted on nearby stars and gas. Astronomers have inferred the existence of stellar-mass black holes in Galactic binaries by tracking the motions of their companion stars, while the presence of a supermassive black hole weighing $4 \times 10^6\ M_\odot$ in the center of our own Galaxy (i.e., Sgr A*) has been confirmed by observing the orbits of stars in its vicinity. Moreover, dynamical modeling of spatially resolved kinematics

in nearby galaxies have measured supermassive black holes withe masses between $\sim 10^6\,M_\odot$ and few $\times\, 10^{10}\,M_\odot$ (Kormendy and Ho, 2013).

Since 2015, the Laser Interferometer Gravitational Wave Observatory (LIGO) and Virgo experiment have detected gravitational wave (GW) signals from compact binary mergers. The GW signals carry information about $M_{\rm BH}$, a_*, as well as the distance and direction of the sources. By the end of the third LIGO/Virgo observation run (O3), 90 compact binary mergers were reported (Abbott et al., 2023), most of which are binary black hole mergers.

General relativity (GR) predicts that light will be bent around black holes, creating a shadow surrounded by a photon ring (Falcke, Melia, and Agol, 2000). Even in the closest supermassive black hole, Sgr A* at the center of the Milky Way, such a photon ring can only be resolved at an angular resolution of $< 10\,\mu$arcsec. Thanks to the technological development in very long baseline interferometry, by combining a global network of radio antennas, the Event Horizon Telescope (EHT) have obtained the shadow images of two supermassive black holes in the centers of the M87 galaxy (Event Horizon Telescope Collaboration, Akiyama, Alberdi, Alef, Asada, et al., 2019) and Sgr A* (Event Horizon Telescope Collaboration, Akiyama, Alberdi, Alef, Algaba, et al., 2022).

Stellar mass black holes come from the death of massive stars with initial masses above $\sim 25\,M_\odot$. They may form either by direct collapse or by fallback accretion onto the nascent neutron star (Heger et al., 2003). Stars with initial masses between $\sim 140\,M_\odot$ and $\sim 260\,M_\odot$ are expected to produce pair instability supernovae (SNe) and leave no remnant behind (Woosley, Heger, and Weaver, 2002). Main uncertainties include the amount of natal kick and mass ejection at the moment of BH formation.

The genesis of supermassive black holes is also an active area of ongoing investigations. Popular "seeding" scenarios include the direct collapse of massive clouds of gas (i.e., heavy seeds, $M_{\rm BH} \sim 10^5\,M_\odot$), gravitational runaway in dense star clusters (i.e., intermediate-mass seeds, $M_{\rm BH} \sim 10^3$–$10^4\,M_\odot$), and Population III stars (i.e., light seeds, $M_{\rm BH} \sim 10^2\,M_\odot$) in the early Universe. These black holes seeds then grow over cosmic time via merger and accretion (Inayoshi, Visbal, and Haiman, 2020).

While the existence and demographics of IMBHs ($10^2\,M_\odot \lesssim M_{\rm BH} \lesssim 10^5\,M_\odot$) provides a sensitive diagnostic for distinguishing between different scenarios of primordial black hole assembly, there is currently a dearth of confirmed IMBHs.

Nevertheless, IMBHs are expected to be probed by a wealth of next-generation facilities, such as next-generation GW detectors, high angular resolution UVOIR telescopes (resolve sphere of influence), sensitive radio/X-ray observatories (detect accretion signatures), and future time domain surveys (rare TDEs, see Chapter 8).

1.2 Black Holes as the Central Engine

The Eddington Limit

The Eddington luminosity is the maximum luminosity an astrophysical source can achieve when there is balance between the force of radiation acting outward and the gravitational force acting inward.

$$L_{\rm Edd} \equiv \frac{4\pi G M c}{\kappa_{\rm es}} = 1.25 \times 10^{38} (M/M_\odot)\,{\rm erg\,s^{-1}}, \tag{1.1}$$

where $\kappa_{\rm es} = 0.4\,{\rm cm^2\,g^{-1}}$ is the opacity of ionized hydrogen to electron scattering. The Eddington accretion rate is the critical rate at which accretion onto a BH produces this luminosity ($\eta \dot{M}_{\rm Edd} c^2 \equiv L_{\rm Edd}$), which gives

$$\dot{M}_{\rm Edd} = 1.4 \times 10^{18} \left(\frac{M_{\rm BH}}{M_\odot}\right) {\rm g\,s^{-1}} = 2.2 \times 10^{-8} \left(\frac{M_{\rm BH}}{M_\odot}\right) M_\odot\,{\rm yr^{-1}}, \tag{1.2}$$

where we have adopted the fiducial radiative efficiency of $\eta = 0.1$.

Accretion in Different Regimes

Although black holes do not themselves emit light, they can exert strong gravity onto the surrounding materials, which attract nearby stellar materials and gas to move closer, and to fall into the black hole's event horizon where the escape velocity exceeds the speed of light. As the material spirals down into the black hole, angular momentum is gradually removed by viscous friction, converting the gravitational energy into heat. The added heat can subsequently be converted into radiation and gas outflows.

In astrophysical accretion disks, the viscous stresses come from turbulence driven by the magneto-rotational instability (MRI; Balbus and Hawley 1991). For an analytical approach, a reasonable model is the α prescription (Shakura and Sunyaev, 1973), which assumes that the shear stress is proportional to pressure: $t_{\phi r} = \alpha P$.

(1) The Standard Thin Disk

In the standard Shakura-Sunyaev model, the infalling materials are organized into an optically thick, geometrically thin disk. Each annulus of the disk surface radiates

roughly as a blackbody with a temperature determined by equating the viscous dissipation rate (i.e., the added heat $Q^{+}_{\rm vis}$) to the blackbody flux ($Q^{-}_{\rm rad}$):

$$\sigma_{\rm sb} T(R)^4 = \frac{3GM_{\rm BH}\dot{M}}{8\pi R^3}\left[1-\left(\frac{R_{\rm in}}{R}\right)^{1/2}\right] \tag{1.3}$$

$$\Rightarrow T(R) = 1.6\times10^7\,{\rm K}\left(\frac{M_{\rm BH}}{M_\odot}\right)^{-1/4}\left(\frac{\dot{M}}{\dot{M}_{\rm Edd}}\right)^{1/4}\left(\frac{R}{6R_g}\right)^{-3/4}\left[1-\left(\frac{R_{\rm in}}{R}\right)^{1/2}\right]^{1/4}, \tag{1.4}$$

where $R_g \equiv 2GM_{\rm BH}/c^2$ is the gravitational radius.

Depending on the dominant sources of opacity and pressure, the entire disk has three distinct regions: (1) the unstable inner region: $P \sim P_{\rm rad}$, $\kappa \sim \kappa_{\rm es}$; (2) the middle region: $P \sim P_{\rm gas}$, $\kappa \sim \kappa_{\rm es}$; (3) the outer region: $P \sim P_{\rm gas}$, $\kappa \sim \kappa_{\rm ff}$.

Adopting $R_{\rm in} = R_{\rm isco} = 6R_g$ and $\dot{M} = 0.1\dot{M}_{\rm Edd}$ in Eq. (1.4), we have the maximum disk temperature at $R = (49/6)R_g$. This successfully explains why the thermal disk emission of "soft-state" accreting X-ray binaries (XRBs, $M_{\rm BH} \sim 10\,M_\odot$) peaks in the soft X-ray band ($\gtrsim 10^6$ K), while the "big blue bump" in luminous AGN ($10^6\,M_\odot \lesssim M_{\rm BH} \lesssim 10^{10}\,M_\odot$) peaks in the ultraviolet and optical bands ($\sim 10^4$–10^5 K). However, in such systems, there is another faint power-law component observed in the hard X-ray band, which has been explained by inverse Compton scattering of thermal seed photons in a region of hot ($\sim 10^9$ K) magnetized corona (in analogy to the observed structure of the solar corona) above (or interior to) the cold thin disk (Galeev, Rosner, and Vaiana, 1979). The coronal flow is believed to be similar to an ADAF-like component (see below) with vertical heat conduction and inverse Compton scattering of disk photons.

At high ($\dot{M} \gtrsim 0.4\dot{M}_{\rm Edd}$) or low ($\dot{M} \lesssim 0.06\dot{M}_{\rm Edd}$) accretion rates, the disk thickness over radius (H/R) is not negligibly small, advective heat transport becomes important ($Q^{-}_{\rm adv} \gtrsim Q^{-}_{\rm rad}$), and other disk solutions come in (Narayan and Quataert, 2005; Abramowicz and Fragile, 2013; Lasota, 2016).

(2) Sub-Eddington Regime: Advection-Dominated Accretion Flow (ADAF)
At low accretion rates, the disk becomes optically thin and geometrically thick (gas-pressure dominated). This accretion regime is often referred as the advection-dominated accretion flow (ADAF; Narayan and Yi 1994; Narayan and Yi 1995a; Narayan and Yi 1995b; Abramowicz, Chen, et al. 1995, see Yuan and Narayan 2014 for a review). In an ADAF, the gas close to the BH is a two-temperature

plasma — the ion temperature ($T_{\rm i} \sim 10^{12}(R/R_{\rm in})^{-1}$ K) is close to virial and the electron temperature is lower ($T_{\rm e} \sim 10^9$–10^{11} K). A fraction of heat goes to electrons, which cools radiatively by bremsstrahlung and synchrotron (enhanced by Compton processes), while the remaining heat goes to ions and is advected towards the BH. Main properties of the ADAF have been confirmed by recent EHT observations (Narayan and Quataert, 2023).

In low-luminosity AGN and BH XRBs in the hard and quiescent states, ADAFs are believed to be present at smaller radii, with the standard thin disk solution restricted to large radii (Remillard and McClintock, 2006; Ho, 2008).

(3) Super-Eddington Regime: Slim Disk and Supercritical Flow

At high accretion rates, the scattering optical depth is so large that radiation is trapped and advected inward with the accretion flow (Begelman and Meier, 1982). The advection of photon thermal energy towards the black hole dominates over radiative loss, rendering a lower η. Such a system is often described by a slim (i.e., moderately thick) disk model (Abramowicz, Czerny, et al., 1988).

Another solution assumes that instead of spending most the extra heat to increase the gas entropy, the dissipated energy can be spent to eject the excess mass (e.g., through disk wind; Shakura and Sunyaev 1973; Poutanen, Lipunova, et al. 2007; King 2008). The disk starts "feeling" that it is supercritical within the so-called "spherization" radius of $R_{\rm sph} = (\dot{M}/\dot{M}_{\rm Edd})R_{\rm in}$, where mass ejection occurs at at rate of $\dot{M}_{\rm out} = \dot{M} - \dot{M}_{\rm Edd}$.

Examples of BH-powered objects in the super-Eddington accretion regime include high-redshift AGN (Pezzulli, Valiante, and Schneider, 2016), some narrow-line Seyfert 1 galaxies (NLSy1s; Collin and Kawaguchi 2004), ultraluminous X-ray sources, and TDEs during their early-time ($\lesssim 2$ yr) evolution (see §1.3).

(4) Hyper-Eddington Regime: Neutrino-dominated Accretion Flow (NDAF)

If a GRB is powered by accretion onto a stellar-mass black hole[1], an extremely high rate of accretion ($\sim 1\ M_\odot\ {\rm s}^{-1}$) is required. This results in such a high temperature that $e^\pm$ capture processes ($e^- + p \rightarrow n + \nu_e$, $e^+ + n \rightarrow p + \bar{\nu}_e$) become dominant. Copious neutrinos are generated, which escape and efficiently cool the disk via neutrino emission (see Liu, Gu, and Zhang 2017 for a review).

[1] An alternative GRB central engine is a millisecond magnetar, which is a neutron star with very high magnetic field at its polar-cap surface ($B_p \gtrsim 10^{14}$ G).

Jets and Winds

Besides the internal stresses within the disk, jets/winds can also remove angular momentum and alter the disk structure. Here I use "jets" to describe highly collimated bipolar plasma moving at relativistic speeds, and "winds" to depict outflows at sub-relativistic speeds that occupy a much larger solid angle, although the exact difference between the two terms are somewhat ambiguous.

Black hole accretion can launch jets by converting the BH rotational energy into Poynting flux (Blandford and Znajek, 1977). The Blandford–Znajek (BZ) mechanism describes this process with magnetic fields threading the black hole, which are twisted by BH spin and exert a torque on the BH to slow it down. The jet power is proportional to the magnetic flux and BH spin $P_{\rm jet} \approx \Phi_{\rm BH}^2 a_*^2$ (Semenov, Dyadechkin, and Punsly, 2004; Tchekhovskoy, Narayan, and McKinney, 2010).

Given enough poloidal magnetic flux, a magnetically arrested disk (MAD) can form (Narayan, Igumenshchev, and Abramowicz, 2003). While accretion inflows generally have modest efficiencies ($\eta \lesssim 0.1$), MHD simulations have shown that the jet efficiency in a MAD around a rapidly spinning BH can achieve much higher efficiencies ($\eta_{\rm jet} \gtrsim 0.2$–$1$) for almost all types of disks: sub-Eddington thick disks (Tchekhovskoy, Narayan, and McKinney, 2011; McKinney, Tchekhovskoy, and Blandford, 2012), super-Eddington thick disks (Dai, McKinney, Roth, et al., 2018; Curd and Narayan, 2019), thin disks (Liska et al., 2019), and GRB disks (Christie et al., 2019).

Moreover, in the super-Eddington regime, the large radiation pressure usually gives rise to an optically thick and nearly spherical wind (Ohsuga and Mineshige, 2011; Sądowski and Narayan, 2016; Jiang, Stone, and Davis, 2019). In the sub-Eddington regime, strong wind can also be launched by the combination of gas/magnetic pressure gradient and centrifugal forces (Yuan, Gan, et al., 2015).

1.3 Transients Powered by Black Holes

Black Hole Binaries

The vast majority of known Galactic stellar mass black holes are in accreting binaries (see Figure 1.1). HMXBs consist of a high-mass ($\gtrsim 2\,M_\odot$) star and a compact object (a NS or a BH), where accretion occurs mainly through stellar winds. LMXBs consist of a low-mass ($\lesssim 2\,M_\odot$) star and a compact object, with accretion occurring through stable Roche Lobe overflow. Most BH HMXBs are persistent X-ray sources, while BH LMXBs are transients with dramatic outbursts.

Outbursts in BH LMXBs are triggered by thermal–viscous instability. The disk instability model was first developed to explain dwarf novae outbursts in accreting white dwarfs (Osaki, 1996), and later applied to XRBs, where inner disk truncation/evaporation and irradiation at the outer disk were found to be important (Lasota, 2001; Dubus, Hameury, and Lasota, 2001; Hameury, 2020).

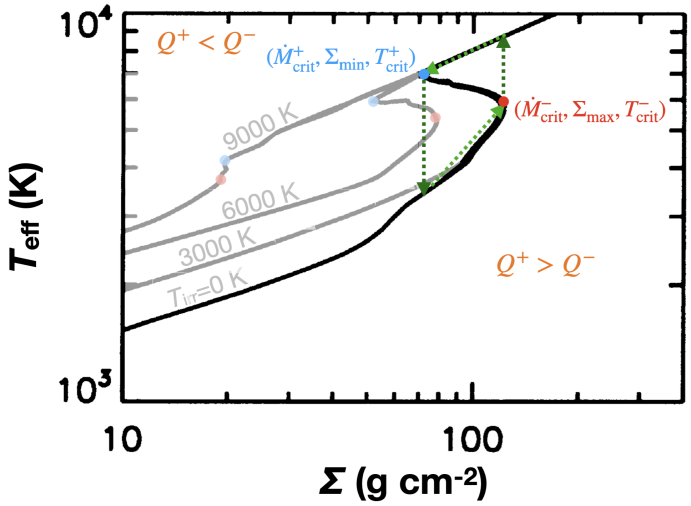

Figure 1.2: Thermal equilibrium S-curves in a typical low-temperature ($\sim 10^4$ K) standard disk. The dotted green lines mark a local thermal limit cycle.

The thermal instability comes from a rapid change of the Rosseland mean opacity around the hydrogen ionization temperature of ~ 6500 K (Frank, King, and Raine, 2002; Kato, Fukue, and Mineshige, 2008). At fixed values of R, α, and $M_{\rm BH}$, one can obtain a family of solutions of disk surface density (Σ) by changing $\dot{M}$ (or $T_{\rm eff}$). Figure 1.2 shows an example S-shaped curve modified from Fig. 5 of Dubus, Lasota, et al. 1999, where $R = 3 \times 10^{10}$ cm, $M = 10\,M_\odot$, and $\alpha = 0.1$. Hydrogen is fully ionized in the stable upper branch, partially ionized in the unstable middle branch, and neutral in the stable lower branch. Here $T_{\rm irr} \equiv (F_{\rm irr}/\sigma_{\rm SB})^{1/4}$ is the irradiation temperature. Using the usual notation of $Q_n = Q/10^n$, the critical mass accretion rates that correspond to the critical densities in the upper and lower branches are (Lasota, 2016):

$$\dot{M}^+_{\rm crit}(R) = 8.07 \times 10^{15} \alpha_{0.1}^{-0.01} R_{10}^{2.64} M_1^{-0.89}\ {\rm g\,s^{-1}}, \tag{1.5}$$

$$\dot{M}^-_{\rm crit}(R) = 2.64 \times 10^{15} \alpha_{0.1}^{+0.01} R_{10}^{2.58} M_1^{-0.85}\ {\rm g\,s^{-1}}, \tag{1.6}$$

which can be modified by irradiation. If $\dot{M} < \dot{M}^+_{\rm crit}$, the disk annulus at ~ 6000 K will be subject to a local thermal limit cycle. The lower $\rightarrow$ upper transition propagates a

heating front, leading to a global increase of accretion rates, temperature, pressure, and viscosity. The disk stays in the upper branch for a viscous timescale ($\sim$ 1 month):

$$t_{\rm vis} = \frac{1}{\alpha}(H/R)^{-2}\left(\frac{GM_{\rm BH}}{R^3}\right)^{-1/2}, \tag{1.7}$$

while self-irradiation can prolong the outburst duration. As the disk is drained by accretion over time, hydrogen in the the outer disk annulus recombines, which triggers a cooling front propagating inward and the outburst switches off on the thermal timescale. Various hard and soft states in LMXBs correspond to accretion at different regimes (see §1.2), and the transitions are likely caused by gas evaporation (Liu and Qiao, 2022; Cho and Narayan, 2022).

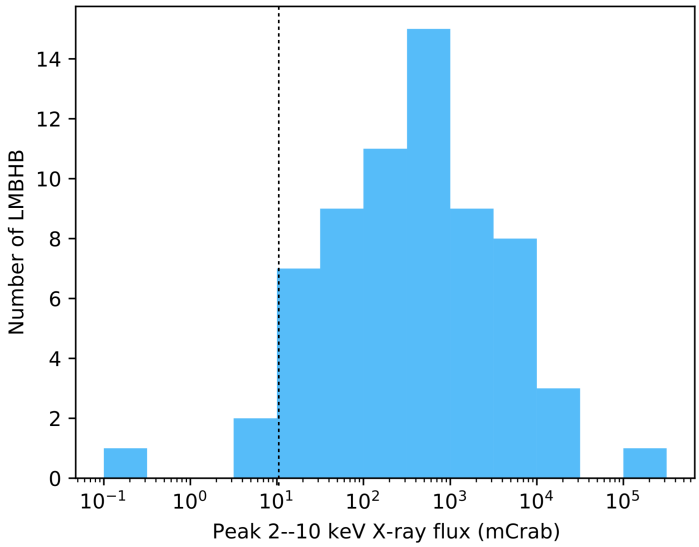

Figure 1.3: The distribution of peak X-ray flux of 66 known BH LMXBs by the end of 2019. The dotted vertical line mark the typical sensitivity of ASMs.

Most BH LMXBs were discovered by all-sky X-ray monitors (ASMs). The most sensitive hard X-ray (*Swift*/BAT) and soft X-ray (*MAXI*) ASMs have sensitivities of $\sim$ 16 mCrab and $\sim$ 10 mCrab, respectively. Before the launch of the *SRG* X-ray satellite, 66 Galactic BH LMXBs were known, and the this population is biased towards those with intrinsically bright peak fluxes/luminosities (see Figure 1.3). The few faint X-ray outbursts were found by dedicated monitoring of the Galactic center. A systematic analysis has shown that 40% of the recorded outbursts remain only in the hard states (Tetarenko, Sivakoff, Heinke, et al., 2016). These "hard-only" outbursts generally exhibit lower peak luminosities, lower mass accretion rates, and shorter orbital periods. They might constitute the bulk of the BH LMXB phenomena,

but have been severely selected against. *SRG*/eROSITA, with an unprecedented survey sensitivity of $\lesssim 1\,\mu$Crab and a survey cadence of 6 months, opens up the discovery space of subluminous BH outbursts (see an example in Chapters 2–3), detailed studies of which will help us understand the formation channel of the Galactic binary BH population (Bahramian and Degenaar, 2022).

lGRBs and Related Transients

During the explosion of a massive star, the stellar core collapses into a compact object (a NS or a BH), and the outer layers are ejected, giving rise to a core-collapse supernova powered by radioactive heating and recombination. In a normal stellar death, the compact object stays mostly inactive, but in the so-called "engine-driven" explosions, the compact object consumes stellar materials, generates heat, and ejects outflows. For a collimated relativistic outflow pointing towards the observer, internal energy dissipation with the jet gives rise to a long-duration GRB (lGRB), known as the prompt emission. The jet also excites external shocks into the surrounding medium, where electrons are accelerated to give rise to long-lasting synchrotron emission from X-ray to the radio, known as the afterglow (see a thorough textbook of GRBs by Zhang 2018).

A few nearby lGRBs have been observed to be associated with type Ic SNe. In high-luminosity lGRBs (HL-GRBs), the central engine releases ultra-relativistic bipolar jets with initial Lorentz factor of $\Gamma_{\rm init} > 100$ and isotropic luminosity of $L_{\rm iso} > 10^{49}\,{\rm erg\,s^{-1}}$. Their high Lorenz factor requires that the jet must contain a small baryon contamination. Separately, the population of low-luminosity lGRBs (LL-GRBs), with $L_{\rm iso} = 10^{46}$–$10^{48}\,{\rm erg\,s^{-1}}$, are thought to be caused by either a choked/mass-loaded jet or an early cessation of the engine activity.

Some recent developments of relativistic transients associated with stellar death is summarized in Ho (2020). It was pointed out in the subsequent studies of ZTF fast blue optical transients (FBOTs) that the population of luminous FBOTs (LFBOTs, also termed as "multi-wavelength FBOTs" or "AT2018cow-like events" in the literature) may represent a new type of engine-driven stellar explosions (Ho, Perley, Gal-Yam, et al., 2021). As implied by the name, LFBOTs rise faster than ordinary supernovae (rise time $\lesssim 5$ days) and are also brighter ($-20 \lesssim M_V < -22$, peak). The earliest studies were stymied by discovery of FBOTs in archival data. This lacuna has been cured by cadenced wide-field optical sky surveys (e.g., ATLAS, ZTF) which enable real-time discovery.

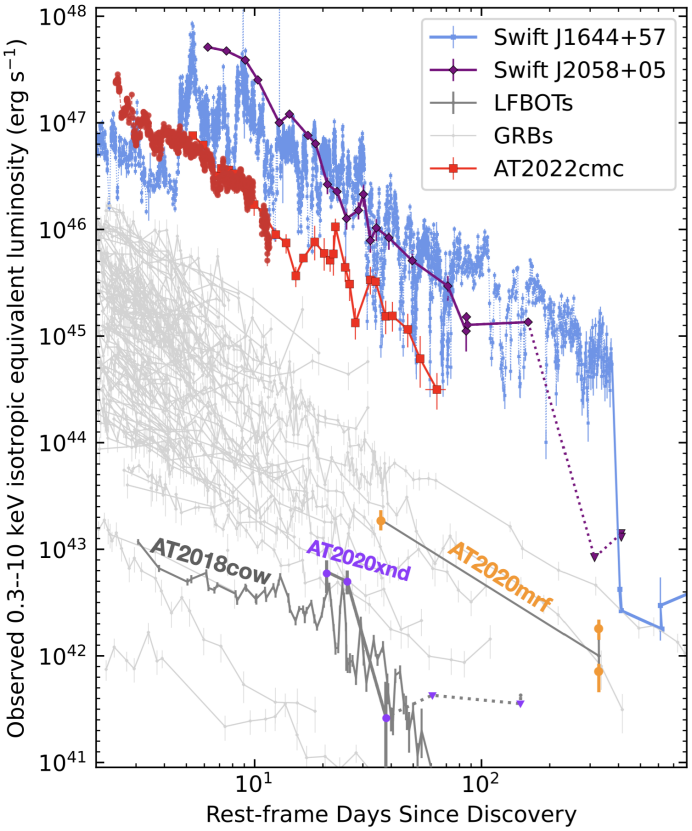

Figure 1.4: X-ray light curves of lGRB afterglows, jetted TDEs (Swift J1644+57, Swift J2058+05, and AT2022cmc), and LFBOTs (AT2018cow, AT2020xnd, and AT2020mrf).

The strongest evidence for the existence of a central engine in LFBOTs comes from the extremely luminous and rapidly variable X-ray emission from the prototype AT2018cow (see Figure 1.4) and AT2020mrf (see Chapter 4), although the nature of the central engine (whether a magnetar or a stellar mass black hole) remains an open question. Another suite of models argue that the central engine in LFBOTs is not born during a stellar explosion. Instead, it might be a compact object brought in close to a massive star by common envelope evolution (Metzger, 2022b), an intermediate-mass black hole at the outskirts of galaxies (Kuin et al., 2019; Perley, Mazzali, et al., 2019), or a stellar-mass black hole in dense stellar environment (Kremer et al., 2021).

Tidal Disruption Events

Since five decades ago, there have been theoretical expectations that the strong tidal forces of a supermassive black hole could cause a passing star to become disrupted

(Frank and Rees, 1976). This happens around the tidal radius $R_{\rm T}$:

$$R_{\rm T} = R_* \left(\frac{M_{\rm BH}}{M_*}\right)^{1/3} \approx 7 \times 10^{12}\,{\rm cm}\, r_* M_6^{1/3} m_*^{-1/3}, \tag{1.8}$$

where $m_* \equiv M_*/M_\odot$, $r_* \equiv R_*/R_\odot$. The tidal radius must be greater than the ISCO of a black hole to power a luminous transient, otherwise the star will be directly captured. Denoting $R_{\rm ISCO} = \lambda R_g$, this requires the BH mass to be less than

$$M_{\rm max} = 3.2 \times 10^8\, M_\odot \left(\frac{\rho_*}{\rho_\odot}\right)^{-1/2} \lambda^{-3/2}, \tag{1.9}$$

where $\rho_\odot = 1.41\,{\rm g\,cm^{-3}}$ is the mean density of the Sun. Eq 1.9 implies that a greater value of $M_{\rm max}$ can be achieved with either a high BH spin (i.e., a small value of λ, see Fig. 1 of Reynolds 2021) or a low stellar density.

Assuming a flat distribution of the specific orbital energy (Evans and Kochanek, 1989), half of the stellar debris is bound to the BH. The fall-back time of the most bound debris is:

$$t_{\rm min} = 41\,{\rm d}\, M_6^{1/2} m_*^{-1} r_*^{3/2}. \tag{1.10}$$

At late time, the debris fall-back rate declines as (Rees, 1988; Phinney, 1989):

$$\dot{M}_{\rm fb} = \frac{M_*}{3t_{\rm min}} \left(\frac{t}{t_{\rm min}}\right)^{-5/3}. \tag{1.11}$$

The peak fall-back rate is

$$\frac{\dot{M}_{\rm peak}}{\dot{M}_{\rm Edd}} = 135\,\eta_{-1} m_*^2 r_*^{-3/2} M_6^{-3/2}. \tag{1.12}$$

The fall-back rate will decline below the Eddington limit at a time

$$t_{\rm Edd} = 2.1\,{\rm yr}\, \eta_{-1}^{3/5} M_6^{-2/5} m_*^{1/5} r_*^{3/5}. \tag{1.13}$$

Over the past three decades, tidal disruption events (TDEs) have gone from theoretical curiosities to established transient phenomena. In recent years, thanks to the advent of time domain sky surveys such as the optical ZTF and the *SRG* X-ray satellite, the TDE discovery rate has increased by more than an order of magnitude to 20–30 $\rm yr^{-1}$ (see Figure 1.5). As of early 2023, $\sim$ 150 TDEs have been reported. Among them, four objects are associated with on-axis relativistic jets, manifested by their extremely bright early-time isotropic equivalent peak X-ray ($\gtrsim 10^{47}\,{\rm erg\,s^{-1}}$;

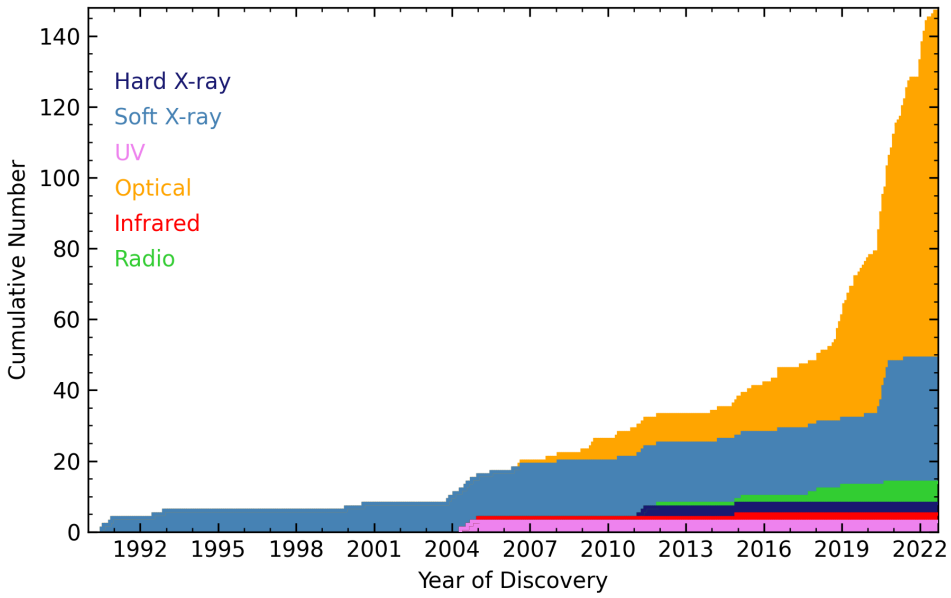

Figure 1.5: Cumulative histogram of TDEs reported in the literature, color-coded by the wavelength in which they were first discovered.

see Figure 1.4 and Chapter 6) and radio ($\gtrsim 10^{41}\,\mathrm{erg\,s^{-1}}$) luminosities. They are often referred as "jetted TDEs."

The remaining objects are sometimes referred as "non-jetted TDEs" or "thermal TDEs." However, note that we cannot completely rule out the existence of off-axis relativistic jets. Moreover, some of these "thermal TDEs" do exhibit non-thermal emission components, such as inverse Compton scattering in a newly-formed corona (see Saxton et al. 2020 and Chapter 5) or synchrotron emission produced by a sub relativistic outflow interacting with the circumnuclear environment (Alexander, van Velzen, et al., 2020).

Ulmer (1999) point out that as the mass fall-back rate declines, a TDE may naturally go through the thick $\rightarrow$ slim $\rightarrow$ thin $\rightarrow$ ADAF disk evolutionary sequence (see §1.2). As such TDEs provide ideal laboratories to study the real-time formation of an accretion disk, and the subsequent interplay between the inflow and outflow/jet.

A natural prediction is that the disk may undergo an instability caused by the change in advective heat transport and radiation pressure (see Figure 1.6), since the middle branch of the S-curve is thermally unstable. Note that the cause of this instability is different from the dwarf-nova type of instability shown in Figure 1.2. Such a thick/slim $\rightarrow$ thin state transition has indeed been invoked to explain the drastic X-ray decrease seen in jetted TDEs around rest-frame one year after discovery (see

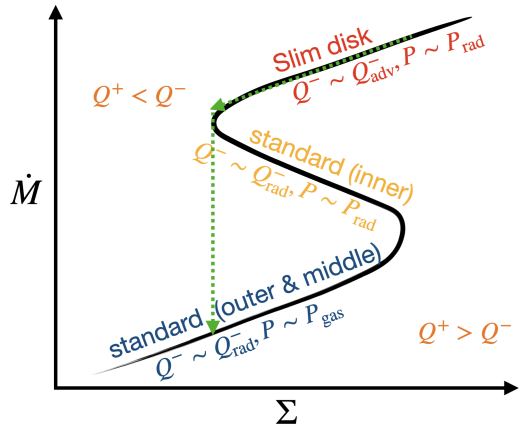

Figure 1.6: A schematic S-curve of a high-temperature ($\sim 10^7$ K) disk. The dotted green line mark a possible state transition in a TDE disk.

Figure 1.4). Here as $\dot{M}_{\rm fb}$ drops from super-Eddington to sub-Eddington, the disk transitions from a $P_{\rm rad}$-dominated state to a $P_{\rm gas}$-dominated state, leading to a much thinner disk that shuts of the jet (Shen and Matzner, 2014; Tchekhovskoy, Metzger, et al., 2014). A similar state transition might has also been observed in non-jetted TDEs (see Chapter 5 and Lu 2022 for a recent review).

The simple 1D diffusion model described above assumes that a significant portion of the fallback debris can rapidly make its way to form the inner nascent accretion flow, resulting in soft X-ray emission. However, the disk formation and evolution processes are extremely hard to computationally simulate given the large dynamic range of lengthscale and GR effects such as relativistic apsidal precession and spin-induced nodal precession (see Dai, Lodato, and Cheng 2021; Bonnerot and Stone 2021 for reviews). Several realistic simulations have recently become available (Bonnerot, Lu, and Hopkins, 2021; Andalman et al., 2022; Steinberg and Stone, 2022), showing that runaway debris circularization happens rapidly via energy dissipation in shocks. Such circularization processes are also efficient at unbounding materials into an outflow, which serves as a reprocessing layer that absorbs high-energy photons (from either accretion or shocks) and re-emits in the UV/optical band. This remains a leading theory to explain the observed TDE UV/optical emission around peak.

Other Common Types of BH-powered Transients

Active Galactic Nuclei (AGN) — While supermassive black holes exist ubiquitously in the centers of medium to large-mass galaxies, only a minority of these black holes

actively accrete from their nearby gas-rich environment to appear as active galactic nulei. Such AGN have either jet mode ($10^{-5} \lesssim L_{\rm AGN}/L_{\rm Edd} \lesssim 10^{-2}$) or radiative mode ($L_{\rm AGN}/L_{\rm Edd} \gtrsim 10^{-2}$) central engines. Their radiation and energy/particle ejection regulate the growth of the host galaxies via the "feedback" mechanisms and shape the cosmic galaxy-BH co-evolution (Fabian, 2012). AGN outbursts are believed to be triggered by galaxy mergers and secular processes (Heckman and Best, 2014). Compared with BHBs, a simple linear scaling with $M_{\rm BH}$ suggests AGN may exhibit state transition on the timescale of ~Myr.

While AGN typically exhibit stochastic variability, some of them show dramatic transient phenomena. These include changing-obscuration AGN which (driven by the variable line-of-sight absorption from clouds orbiting the massive BHs), and changing-state AGN (triggered by the changes in mass accretion rate; see Ricci and Trakhtenbrot 2022 for a review).

Ultraluminous X-ray Sources (ULXs) — ULXs are off-nuclear accreting X-ray sources in nearby galaxies with bolometric luminosities ($L_{\rm bol}$) in excess of the Eddington limit for several tens of solar masses, assuming isotropic emission (Feng and Soria, 2011; Kaaret, Feng, and Roberts, 2017). Their high $L_{\rm bol}$ suggest that the nature of the central accretor could be: (1) an IMBH exhibiting sub-Eddington accretion (Miller and Colbert, 2004); (2) a stellar-mass remnant (NS or BH) exhibiting beamed emission (King et al., 2001) or accretion above the Eddington limit, i.e., $\dot{M} \gg \dot{M}_{\rm Edd}$ (Poutanen, Lipunova, et al., 2007; Yao and Feng, 2019). The latter scenario gained more popularity in recent years. While most ULXs are persistent sources, some exhibit flux variation exceeding a factor of 10. Such transients, if powered by BHs, might be caused by micro-TDEs[2] or the dwarf-nova type thermal–viscous disk instability (Hameury and Lasota, 2020).

Compact Object Mergers and Related Transients — The inspiral and merging of two compact objects greatly alter the second time derivative of the quadrupole moment of the binary system, making them important gravitational wave sources (see Figure 1.1). A BH+BH merger is not expected to shine with any light waves. However, a NS+NS merger and a BH-NS merger are expected to drive both subrelativistic ejecta and relativistic jets. The former produces the so-called "kilonova" and is powered by the radioactive decay of species synthesized via the r-process. The latter can be detected as a short-duration GRB (sGRB) and is powered by the central

[2]Micro-TDEs refer to the disruption of stars by stellar mass black holes, see (Brightman, Earnshaw, et al., 2020).

merging product (a BH or a magnetar; see Nakar 2020 for a review). Similar to lGRBs, afterglow emission has been detected in sGRBs. As has been demonstrated in the famous electromagnetic counterpart of GW170817 (Margutti and Chornock, 2021), the formation and structure of relativistic jets can be uniquely studied with future GW-triggered off-axis events.

1.4 Thesis Outline

The chapters of my thesis cover the different topics broadly outlined in §1.3. The first part focuses on the X-ray (Chapter 2) and multi-wavelength (Chapter 3) properties of the candidate BHB AT2019wey. The second part presents observations of AT2020mrf, the the most X-ray luminous LFBOT to date (Chapter 4) . The third part concerns TDEs, including detailed X-ray monitoring observations and novel results in the non-jetted TDE AT2021ehb (Chapter 5) and the jetted-TDE AT2022cmc (Chapter 6), as well as a thorough study on TDE demographics with ZTF (Chapter 7). Finally, in Chapter 8, I summarize my main results and discuss possible future directions, with a focus on using BH-powered transients as a unique black hole census.

Chapter 2

A COMPREHENSIVE X-RAY REPORT ON AT2019WEY

Yao, Y. et al. (Oct. 2021). In: *ApJ* 920.2, 121, p. 121. DOI: 10.3847/1538-4357/ac15f8.

Yuhan Yao[1], S. R. Kulkarni[1], Keith C. Gendreau[2], Gaurava K. Jaisawal[3], Teruaki Enoto[4], Brian W. Grefenstette[1], Herman L. Marshall[5], Javier A. García[1,6], R. M. Ludlam[1], Sean N. Pike[1], Mason Ng[5], Liang Zhang[7], Diego Altamirano[7], Amruta Jaodand[1], S. Bradley Cenko[8], Ronald A. Remillard[5], James F. Steiner[9], Hitoshi Negoro[10], Murray Brightman[11], Amy Lien[11,12], Michael T. Wolff[13], Paul S. Ray[13], Koji Mukai[12,14], Zorawar Wadiasingh[8,15], Zaven Arzoumanian[8], Nobuyki Kawai[16], Tatehiro Mihara[17], and Tod E. Strohmayer[8]

[1] Cahill Center for Astronomy and Astrophysics, California Institute of Technology, Pasadena, CA 91125, USA
[2] Mail Code 662.1, Goddard Space Flight Center, Greenbelt, MD 20771, USA
[3] National Space Institute, Technical University of Denmark, Elektrovej 327-328, DK-2800 Lyngby, Denmark
[4] Extreme Natural Phenomena RIKEN Hakubi Research Team, Cluster for Pioneering Research, RIKEN, 2-1 Hirosawa, Wako, Saitama 351-0198, Japan
[5] MIT Kavli Institute for Astrophysics and Space Research, 70 Vassar Street, Cambridge, MA 02139, USA
[6] Dr. Karl Remeis-Observatory and Erlangen Centre for Astroparticle Physics, Sternwartstr. 7, D-96049 Bamberg, Germany
[7] Department of Physics and Astronomy, University of Southampton, Southampton, SO17 1BJ, UK
[8] Astrophysics Science Division, NASA Goddard Space Flight Center, Greenbelt, MD 20771, USA
[9] Harvard-Smithsonian Center for Astrophysics, 60 Garden Street, Cambridge, MA 02138, USA
[10] Department of Physics, Nihon University, 1-8, Kanda-Surugadai, Chiyoda-ku, Tokyo 101-8308, Japan
[11] Center for Research and Exploration in Space Science and Technology (CRESST) and NASA Goddard Space Flight Center, Greenbelt, MD 20771, USA
[12] Department of Physics, University of Maryland, Baltimore County, 1000 Hilltop Circle, Baltimore, MD 21250, USA
[13] Space Science Division, U.S. Naval Research Laboratory, Washington, DC 20375, USA
[14] CRESST II and X-ray Astrophysics Laboratory, NASA/GSFC, Greenbelt, MD 20771, USA
[15] Universities Space Research Association (USRA), Columbia, MD 21046, USA
[16] Department of Physics, Tokyo Institute of Technology, 2-12-1 Ookayama, Meguro-ku, Tokyo 152-8551, Japan
[17] Cosmic Radiation Laboratory, RIKEN, 2-1 Hirosawa, Wako, Saitama 351198, Japan

Abstract

Here, we present *MAXI*, *Swift*, *NICER*, *NuSTAR* and *Chandra* observations of the X-ray transient AT2019wey (SRGA J043520.9+552226, SRGE J043523.3+552234). From spectral and timing analyses we classify it as a Galactic low-mass X-ray

binary (LMXB) with a black hole (BH) or neutron star (NS) accretor. AT2019wey stayed in the low/hard state (LHS) from 2019 December to 2020 August 21, and the hard-intermediate state (HIMS) from 2020 August 21 to 2020 November. For the first six months of the LHS, AT2019wey had a flux of ~ 1 mCrab, and displayed a power-law X-ray spectrum with photon index $\Gamma = 1.8$. From 2020 June to August, it brightened to ~ 20 mCrab. Spectral features characteristic of relativistic reflection became prominent. On 2020 August 21, the source left the "hard line" on the rms–intensity diagram, and transitioned from LHS to HIMS. The thermal disk component became comparable to the power-law component. A low-frequency quasi-periodic oscillation (QPO) was observed. The QPO central frequency increased as the spectrum softened. No evidence of pulsation was detected. We are not able to decisively determine the nature of the accretor (BH or NS). However, the BH option is favored by the position of this source on the Γ–$L_{\rm X}$, $L_{\rm radio}$–$L_{\rm X}$, and $L_{\rm opt}$–$L_{\rm X}$ diagrams. We find the BH candidate XTE J1752−223 to be an analog of AT2019wey. Both systems display outbursts with long plateau phases in the hard states. We conclude by noting the potential of *SRG* in finding new members of this emerging class of low luminosity and long-duration LMXB outbursts.

2.1 Introduction

Low-mass X-ray binaries (LMXBs) contain a neutron star (NS) or black hole (BH) accretor and a low-mass ($\lesssim 2\,M_\odot$) companion star. To first order, LMXBs with higher mass transfer rates ($\dot{M}$) can keep the accretion disks fully ionized, and are observed as persistent sources. Systems with lower $\dot{M}$ exhibit prolific outbursts, which are popularly attributed to the thermal-viscous instability (see §1.3; Tanaka and Shibazaki 1996; Done, Gierliński, and Kubota 2007; Coriat, Fender, and Dubus 2012).

Transient BH LMXBs have been observed in several distinct X-ray states, including the steep power-law (SPL) state (also known as the very high state), the high/soft state (HSS; also known as the thermal state), the intermediate state (IMS), the low/hard state (LHS), and the quiescent state (Fender, Belloni, and Gallo, 2004; Remillard and McClintock, 2006; McClintock and Remillard, 2006; Belloni, 2010; Gilfanov, 2010; Zhang, 2013). This classification scheme relies primarily on the shape of the 1–20 keV energy spectrum, the spectral hardness (defined as the ratio of count rates in the hard and soft energy bands), the fractional rms variability integrated over a range of frequencies, and the presence of quasi-periodic oscillation (QPO) in the power density spectrum (PDS).

The evolution of a BH outburst is traditionally described as a counterclockwise q-shaped track in the hardness–intensity diagram (HID; Homan and Belloni 2005), following the sequence of quiescence → LHS → IMS → HSS → IMS → LHS → quiescence. In the LHS, the X-ray spectrum is dominated by a non-thermal power-law component with a photon index (Γ) of of 1.5–2.0. This state is commonly accompanied by strong aperiodic variability and low-frequency QPO (LFQPO; 0.1–30 Hz), with fractional rms of $\sim$ 30%. In the IMS, a thermal disk component with a color temperature of 0.1–1 keV appears and Γ softens to 2.0–2.5. The IMS can be further separated into the hard-intermediate state (HIMS), where the fractional rms is $\sim$ 10–20%, and the soft-intermediate state (SIMS), where the fractional rms is a few percent (Belloni, 2010). In the HSS, the thermal accretion disk becomes the dominant component in the X-ray spectrum. Meanwhile, QPOs are absent or very weak, and the fractional rms drops to $\sim$ 1%. Occasionally, the outburst goes into the SPL state as it approaches the Eddington luminosity $L_{\rm Edd}$. Here, the spectrum is dominated by a power-law spectral component with a photon index of $\Gamma \sim 2.5$.

Although a good number of BH LMXB outbursts follow the hysteresis loop of state transition, some remain in the LHS throughout the entire outburst (Belloni, Colombo, et al., 2002; Brocksopp, Bandyopadhyay, and Fender, 2004; Sidoli et al., 2011), and some only transition between the LHS and the HIMS (Ferrigno et al., 2012; Soleri et al., 2013; Capitanio, Belloni, et al., 2009). By analyzing the BH outbursts between 1996 and 2015, Tetarenko, Sivakoff, Heinke, et al. (2016) show that $\sim$ 40% of them only stay in the LHS or HIMS. These "hard-only" outbursts (also termed as failed outbursts) are generally associated with lower peak luminosities.

NS LMXBs can be broadly classified into Z sources and atoll sources, named after the tracks they trace out in the HID and X-ray color-color diagram (Hasinger and van der Klis, 1989; van der Klis, 2006). Z sources are generally bright ($L_{\rm X} \gtrsim 0.5 L_{\rm Edd}$). Atoll sources are further divided into bright atoll sources (BA; $L_{\rm X} \sim 0.3$–$0.5 L_{\rm Edd}$) and ordinary atoll sources ($L_{\rm X} \sim 0.01$–$0.3 L_{\rm Edd}$). The X-ray spectra of Z and BA sources remain very soft, while ordinary atolls mostly follow the hysteresis pattern of state transition observed in BH LMXBs (Muñoz-Darias, Fender, et al., 2014).

BHs can be identified via dynamical measurements of the mass of the compact object. NS LMXBs can be selected by the existence of thermonuclear X-ray bursts from nuclear burning of the accreted material on the NS surface, or coherent pulsations caused by the magnetic field and NS rotation (Lewin, van Paradijs, and Taam, 1993; Done, Gierliński, and Kubota, 2007; Bhattacharyya, 2009).

Kilo-hertz QPOs have only been observed in NS systems (van Doesburgh, van der Klis, and Morsink, 2018). Furthermore, in the hard state, NSs have systematically lower values of Compton y-parameter and electron temperature (Banerjee et al., 2020), as well as higher values of Γ (Wijnands et al., 2015). Compared with BH LMXBs, the PDS of NS systems can show broad-band noise at frequencies up to 500 Hz (Sunyaev and Revnivtsev, 2000). In the soft state, the spectra of NS LMXBs are harder than those of BH systems due to an additional thermal emission from the boundary layer with a blackbody temperature of ~ 2.4 keV (Done and Gierliński, 2003; Gilfanov, Revnivtsev, and Molkov, 2003).

The Discovery of AT2019wey

AT2019wey was discovered as an optical transient by the ATLAS optical survey in 2019 December (Tonry, Denneau, Heinze, Weiland, et al., 2019). It rose to prominence in 2020 March with the discovery of X-ray emission by the eROSITA (Predehl, Andritschke, et al., 2021) and the Mikhail Pavlinsky ART-XC (Pavlinsky et al., 2021) telescopes on board the *Spektrum-Roentgen-Gamma* (*SRG*) satellite (Sunyaev, Arefiev, et al., 2021). Upon detection, the X-ray flux was 0.36 mCrab in the 0.3–8 keV band and 0.6 mCrab in the 4–12 keV band (Mereminskiy et al., 2020). We note that there is no point source detected at the position of AT2019wey in the 2nd *ROSAT* All-Sky Survey Point Source Catalog (2RXS; Boller et al. 2016), providing a historical upper limit of $\sim 10\,\mu$Crab in 0.1–2.4 keV.

Initially AT2019wey was thought to be a supernova (Mereminskiy et al., 2020) and subsequently proposed to be a BL Lac object (Lyapin et al., 2020). Yao, Enoto, et al. (2020) reported the detection of hydrogen lines at redshift $z = 0$, and proposed AT2019wey to be a Galactic accreting binary.

Here, we report comprehensive X-ray observations from the beginning of 2019 January to the end of 2020 November. We find that AT2019wey is consistent with the spectral and timing behavior expected from a LMXB harbouring a BH or NS accretor. Elsewhere we report the multi-wavelength observations of this source (Yao, Kulkarni, Burdge, et al., 2021).

This paper is organized as follows. In §2.2 we describe the X-ray observations and data reduction. We present the analysis of light curves in §2.3, including the evolution of hardness (§2.3) and the timing properties (§2.3). The spectral analysis including multi-mission joint analysis can be found in §2.4. In §2.5 we present the inferences from the X-ray analysis. We are not able to decisively identify the nature

of the accretor (BH or NS). However, we find the best analog to AT2019wey is a candidate BH LMXB system. We conclude in §2.6.[1]

2.2 Observations and Data Reduction

The data shown here were obtained using the Neutron Star Interior Composition Explorer (*NICER*; Gendreau et al. 2016), the Nuclear Spectroscopic Telescope ARray (*NuSTAR*; Harrison et al. 2013), the *Chandra* X-ray Observatory (Wilkes and Tucker, 2019), the *Neil Gehrels Swift Observatory* (Gehrels et al., 2004), and the Monitor of All-sky X-ray Image (*MAXI*) mission (Matsuoka et al., 2009). As of the time of submission of the paper (2020 November), the source was still active.

NICER

AT2019wey was observed by the X-ray Timing Instrument (XTI) on board *NICER* over the period from 2020 August 4 to 2020 September 30 (PI: K. Gendreau). *NICER* is a soft X-ray telescope on board the International Space Station (ISS). *NICER* is comprised of 56 co-aligned concentrator X-ray optics, each paired with a single-pixel silicon drift detector. Presently, 52 detectors are active with a net peak effective area of $\sim 1900\,\mathrm{cm}^2$ at 1.5 keV, and 50 of these were selected (excluding modules 14 and 34) to make the light curves reported in this paper. The *NICER* observations were processed using `HEASoft` version 6.27 and the *NICER* Data Analysis Software (`nicerdas`) version 7.0 (2020-04-23_V007a).

To generate a background-subtracted light curve, we first defined good time intervals (GTIs) with as much data as possible. Then we computed the background using the `nibackgen3C50` tool (Remillard, Loewenstein, et al., 2022). For each GTI, we explicitly subtracted the background-predicted spectrum from the raw extraction to get the source net spectrum. We also removed GTIs with $|hbg|^2 > 0.07$, to exclude GTIs with less accurate background subtraction. Finally, we computed count rate in five energy bands: 0.4–1.0 keV, 1–2 keV, 2–4 keV, 4–12 keV, and 0.4–12 keV.

To generate spectral files, we used `nimaketime` to select GTIs that occurred when the particle background was low (KP<5 and COR_SAX>4). We removed times of extreme optical light loading and low Sun angle. Using `niextract-events`, the GTIs were applied to the data by selecting EVENT_FLAGS=bxxx1x000 and PI energy channels between 25 and 1200, inclusive. For more information on the

[1] UT time is used throughout the paper.

[2] hbg is the count rate in the 13–15 keV band, which is beyond the effective area of the concentrator optics, as defined in Remillard, Loewenstein, et al. (2022).

NICER screening flags, see Bogdanov et al. (2019). The resulting event files were loaded into `xselect` to extract a combined spectrum after filtering. Systematic errors of 1% in the 2–10 keV band and 5% in the 0.8–2 keV band were added via `grppha`. A background spectrum was generated using the `nibackgen3C50` tool for each cleaned event file and ufa event file pair. These were then combined into a single background spectrum that was weighted by the duration of each observation. Each spectrum was grouped into channels by considering a minimum of 32 counts per channel bin.

NuSTAR

We obtained three epochs of Target of Opportunity (ToO) observations using the hard X-ray telescope *NuSTAR* (PI: Y. Yao, Table 2.7). In this paper, we report the analysis for the first two sequences (sequence IDs 90601315002 and 90601315004, hereafter 002 and 004, respectively). The third sequence was carried out jointly with the Hard X-ray Modulation Telescope (HXMT; Zhang, Li, et al. 2020), and will be reported in Tao et al. in prep.

The focal plane of *NuSTAR* consists of two photon counting detector modules (FPMA and FPMB). The data were processed using the *NuSTAR* Data Analysis Software (`nustardas`) v2.0.0 along with the 2020423 *NuSTAR* CALDB using the default data processing parameters. Cleaned event files were produced with `nupipeline`. The event files were then barycentered and corrected for clock offset using `barycorr` (see Bachetti, Markwardt, et al. 2021 for a description of the clockfile generation).

To generate *NuSTAR* light curves, we filtered the events using source regions with radii of 60″ and 90″ for 002 and 004, respectively. We chose to use a larger source region for observation 004 due to its higher count rate. We only retained events with a photon energy between 3 and 78 keV. For each observation, we were thus left with two lists of filtered and barycenter-corrected events — one for FPMA and one for FPMB. Using `Stingray` (Huppenkothen et al., 2019), we produced light curves for each of these event lists. We binned the light curves with a time resolution of ≈ 2 ms. `Stingray` automatically applied the GTIs recorded by the instrument.

To generate the spectra for FPMA and FPMB, source photons were extracted from a circular region with a radius of 60″ centered on the apparent position of the source in both FPMA and FPMB. For 002 the background was extracted from a 100″ region located on the same detector; For 004 the source was bright enough that a smaller portion of the field-of-view could be used to estimate the background, so

the background was extracted from a 60″ region.

Chandra

We requested and were granted 25 ks of *Chandra* director's discretionary time (PI: S. R. Kulkarni; OBSID = 24651) to obtain a high-energy transmission grating spectrometer (HETGS; Markert et al. 1994; Canizares et al. 2005) spectrum using the Advanced CCD Imaging Spectrometer (ACIS; Garmire et al. 2003). The HETGS is composed of two sets of gratings (see, e.g., Chapter 2 of Wilkes and Tucker 2019): the medium-energy gratings (MEGs) cover the 0.4–7 keV energy band, and the high-energy gratings (HEGs) cover the 0.8–10.0 keV band. The observation was carried out in the timed event (TE) mode around the maximum soft X-ray luminosity of AT2019wey. During the exposure (from 2020 September 20 17:43 to 2020 September 21 01:12), the source count rate varied between 23.1 count s^{-1} to 24.5 count s^{-1}.

To generate spectral files for the source and the background, we extracted the plus and minus first-order ($m = \pm 1$) MEG and HEG data from the -1 and the $+1$ arms of the MEG and HEG gratings. We used the `CIAO` tool `tgextract`. `CIAO` version 4.12.1 and the associated CALDB version 4.9.3 were used in the data reduction. Spectral redistribution matrix files and effective area files were generated with `mkgrmf` and `mkgarf`.

MAXI

MAXI was installed on the Japanese Experiment Module Exposed Facility on the ISS in July 2009. Since August 2009, the *MAXI* Gas Slit Cameras (GSCs; Mihara et al. 2011; Sugizaki et al. 2011) have been observing the source region of AT2019wey in the 2–20 keV band every 92 min synchronized with the ISS orbital period. Owing to the ISS orbit precession of about 72 days, the source region, due to the interference of some structure of the detectors, has been regularly unobservable for about 12 days. Furthermore, in recent years, the source has only been observed with the degraded cameras for $\sim$ 28 days in each precession period. We did not use these data. As a result, there are two data gaps every 72 days.

The 1-day average *MAXI* light curves were generated by the point-spread-function fit method (Morii et al., 2016) to obtain the most reliable curves in the 2–4 keV and 4–10 keV bands. Furthermore, we excluded data with 1σ uncertainties 2.5 times larger than the average uncertainties in the 2–4 and 4–10 keV bands, respectively. We rebinned the data into 4-day bins to improve the statistics.

Swift

AT2019wey was observed by the X-Ray Telescope (XRT; Burrows, Hill, et al. 2005) on board *Swift* in 2020 April (4 epochs), August (5 epochs), and September (4 epochs). We generated the X-ray light curve for AT2019wey using an automated online tool[3] (Evans, Beardmore, Page, Osborne, et al., 2009). The first 9 epochs were obtained in Photon Counting (PC) mode, and thus suffer from "pile-up" at the high observed count rates. Standard corrections (Evans, Beardmore, Page, Tyler, et al., 2007) were applied to the observations taken in 2020 April. The observations from 2020 August were sufficiently piled up that no reliable count rates could be obtained. Beginning in 2020 September, XRT observations were obtained in Window Timing (WT) mode, where larger count rates can still be reliably measured. The observation log and the count rate measurements are shown in Table 2.8.

To generate XRT spectra for the 4 epochs obtained in 2020 April, we processed the data using `xrtproducts`. We extracted source and background photons from circular regions with radii of 50″ and 100″, respectively.

Since 2004 November, the source region of AT2019wey has been observed by the Burst Alert Telescope (BAT; Krimm, Holland, et al. 2013) on board *Swift*. The 15–50 keV BAT light curve is provided by the "scaled map" data product[4]. To generate a light curve with better statistics, we rebinned the light curve into 4-day bins, and excluded data with 1σ uncertainties 3 times larger than the median uncertainties.

2.3 Analysis of Light Curves

The *MAXI*, *NICER*, and *Swift*/BAT light curves of AT2019wey are shown in Figure 2.1. The dashed vertical lines in the three panels mark the epoch of first optical detection on 2019 December 2 (Yao, Kulkarni, Burdge, et al., 2021). From 2019 January 1 to December 2, the *MAXI*/GSC and *Swift*/BAT data show no significant count excess. We refer to Hori et al. (2018) for *MAXI*/GSC detection upper limits during the period from 2009 August 13 to 2016 July 31. From the 2019 December 2 to the *SRG* discovery epoch (2020 March 18), *MAXI*/GSC detected a significant 2–10 keV flux excess of 1.7 ± 0.4 mCrab (see Negoro, Nakajima, Aoki, et al. 2020), and BAT detected a significant 15–50 keV flux excess of 3.7 ± 0.7 mCrab.

As can be seen from the *MAXI* and BAT light curves, the source started to significantly brighten from the beginning of 2020 June to the middle of 2020 August. Since

[3] `https://www.swift.ac.uk/user_objects`

[4] Available at `https://swift.gsfc.nasa.gov/results/transients/weak/AT2019wey/`.

Figure 2.1: *NICER*, *MAXI*, and *Swift*/BAT light curves of AT2019wey. The dashed vertical line marks the optical first detection epoch.

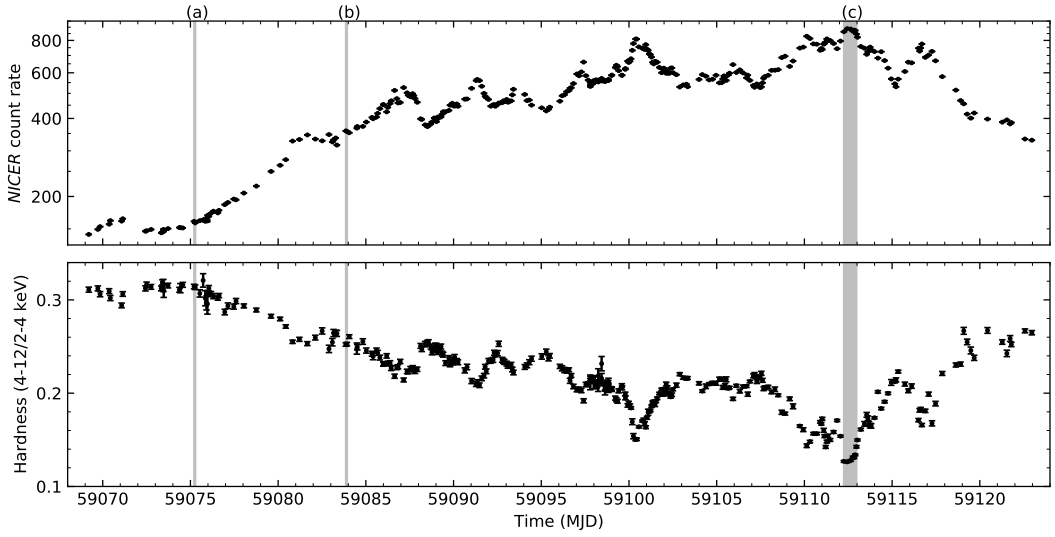

Figure 2.2: *NICER* light curve and hardness of AT2019wey. The vertical grey regions mark epochs where detailed timing analysis are performed.

then, the source has stayed at a relatively high level of flux. From 2020 September 2 to 2020 November 30, the median *MAXI* 2–10 keV flux is 17.7 mCrab and the median BAT 15–50 keV flux is 28.1 mCrab. The *NICER* light curve is presented in the upper panel of Figure 2.2. It clearly shows that after the X-ray brightening, AT2019wey underwent a few week-long mini-outbursts in the 0.4–12 keV band.

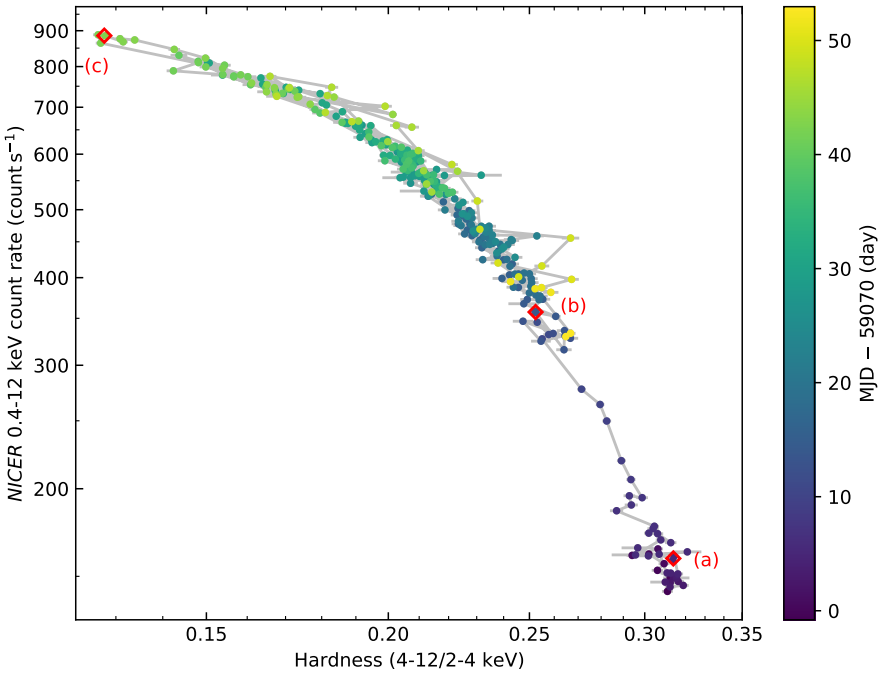

Figure 2.3: The *NICER* HID of AT2019wey.

Hardness Evolution

We define the X-ray hardness (or X-ray color) using the ratio of count rates in the *NICER* 4–12 keV and 2–4 keV bands. The evolution of hardness is shown in the bottom panel of Figure 2.2. Figure 2.3 presents the *NICER* HID of AT2019wey. At the beginning, the source was faint and hard. As it got brighter, the X-ray color became softer. The count rate (hardness) reached the maximum (minimum) value at 59112 MJD, after which the count rate decreased and the X-ray color hardened. The evolution of AT2019wey roughly follows a single line on the HID, i.e., each hardness value corresponds to a single value of count rate. This is very different from the hysteresis pattern generally observed in LMXBs.

Timing Properties

The typical event timestamps for *NICER*/XTI and *NuSTAR* are accurate to ~ 100 ns (Prigozhin et al., 2016) and $\sim 100\,\mu$s (Bachetti, Markwardt, et al., 2021), respec-

tively. The high timing precision makes the two instruments ideal to study fast X-ray variability. We searched for coherent pulsation signals in the *NICER* and *NuSTAR* data and found no viable pulse search candidates to 3σ level despite pulsation searches extending to 100 ns (see §2.7 for details). Here, we present aperiodic analysis of *NICER* and *NuSTAR* observations.

***NICER* Aperiodic Analysis** — We produced an average PDS in the 0.5–12 keV energy band for each *NICER* GTI. We used 16-s long intervals and ≈ 0.12 ms time resolution. The average PDS was rms-normalized (Belloni and Hasinger, 1990) and the contribution due to the photon counting noise was subtracted. We calculated the integrated fractional rms in the 0.1–64 Hz frequency range. We also calculated the absolute rms by multiplying the fractional rms by the net count rate (Muñoz-Darias, Motta, and Belloni, 2011).

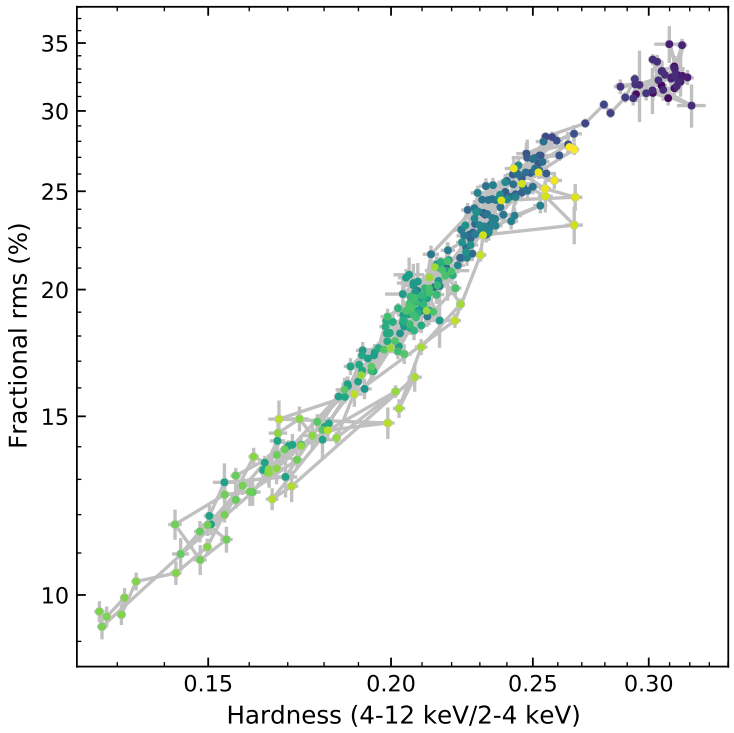

Figure 2.4: The *NICER* HRD of AT2019wey.

In Figure 2.4 we show the hardness–fractional rms diagram (HRD), which is usually used to study the outburst evolution of transient BH LMXBs (Belloni, Homan, et al., 2005). The data is color-coded by time following the scale shown in Figure 2.3. The integrated fractional rms decreased from ~30% to ~10% as the X-ray color softened, and increased back to ~25% as the color hardened again.

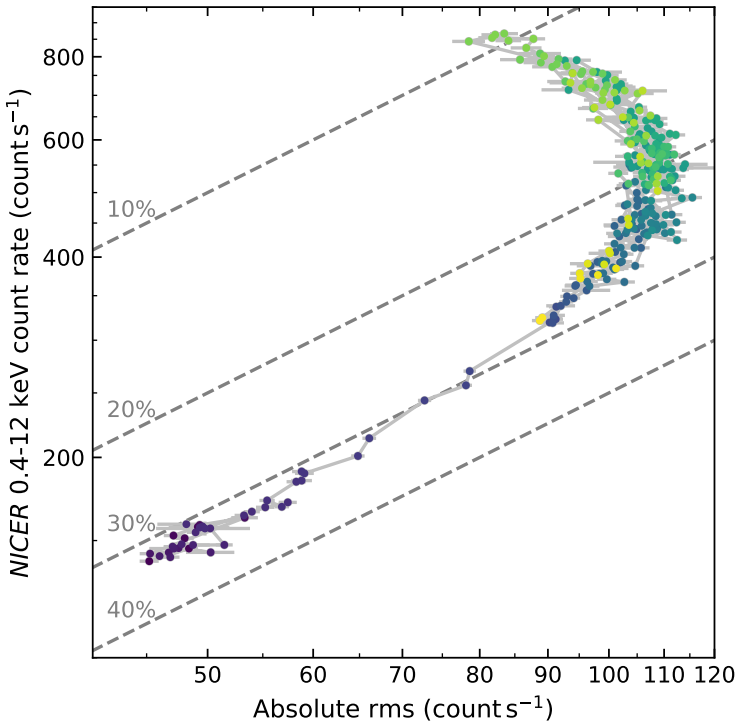

Figure 2.5: The *NICER* RID of AT2019wey.

In Figure 2.5 we show the absolute rms–intensity diagram (RID). The gray dotted lines represent the 10, 20, 30 and 40 percent fractional rms levels. The data is color-coded by time following the scale shown in Figure 2.3. At the beginning of the X-ray brightening, we found that the absolute rms increased with the count rate. This linear trend has been observed in many BH binaries, and is commonly known as the "hard line" (HL; Muñoz-Darias, Motta, and Belloni 2011). Starting from ~59082 MJD, the source left the HL and moved upwards. During the light curve bumps observed between ~59085 MJD and ~59123 MJD, the source moved to the left as the count rate increased, and then went back as the count rate decreased.

During the period we analyzed, the PDS can be well fitted with two or three Lorentzian functions following the prescription laid out by Belloni, Psaltis, and van der Klis (2002). In Figure 2.6 we show three representative PDS averaged from different phases of the outburst (marked as grey regions in Figure 2.2 and red diamonds in Figure 2.3). The power spectra were calculated in the 0.5–12 keV energy band.

The PDS is fitted with a combination of two or three Lorentzian functions, as shown

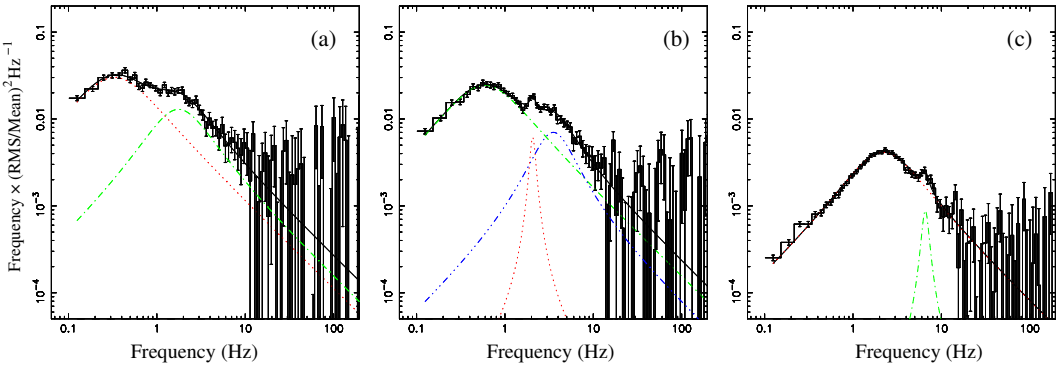

Figure 2.6: Representative *NICER* power spectra of AT2019wey.

Table 2.1: *NICER* power spectral components of AT2019wey.

TIME (MJD)		$\nu_{\max}$ (Hz)	Q	rms (%)
59075.20–59075.29	L_1	0.33 ± 0.02	0.25 ± 0.08	27.57 ± 1.12
	L_2	1.76 ± 0.14	0.44 ± 0.12	16.33 ± 1.62
59083.85–59083.94	L_1	0.59 ± 0.02	0.26 ± 0.04	24.62 ± 0.34
	L_2	2.06 ± 0.03	6 (fixed)	3.95 ± 0.41
	L_3	3.53 ± 0.16	0.81 ± 0.14	10.17 ± 0.69
59112.24–59112.98	L_1	2.21 ± 0.03	0.34 ± 0.02	9.72 ± 0.07
	L_2	6.58 ± 0.21	4.99 ± 1.97	1.64 ± 0.26

by the colored components in each panel. The main properties of the PDS are listed in Table 2.1. At the beginning of the outburst, the PDS were dominated by strong band-limited noise without showing any significant QPOs. The average PDS can be fitted with two broad Lorentzians (Figure 2.6 (a)). Starting from ~59083 MJD, a weak QPO was sometimes observed in the PDS. The characteristic frequency of the QPO increased from ~2 Hz to ~6.5 Hz as the spectra softened. Figure 2.6 (b)–(c) show the PDS of the QPO with the lowest and highest frequency, respectively. Based on the properties of the QPO and noise, this QPO is similar to the type-C QPO (e.g. Casella, Belloni, and Stella, 2005; Motta et al., 2011; Ingram and Motta, 2019; Zhang, Altamirano, et al., 2020) commonly observed in BH and NS binaries (see, e.g., Klein-Wolt and van der Klis, 2008).

***NuSTAR* Aperiodic Analysis** — Rather than summing the FPMA and FPMB light curves and producing PDS for each observation, we chose to analyze the Cross Power Density Spectrum (CPDS; Bachetti, Harrison, et al. 2015). The CPDS taken between FPMA and FPMB is given by

$$C(\nu) = \mathcal{F}_{\rm A}^{*}(\nu)\mathcal{F}_{\rm B}(\nu) \tag{2.1}$$

where $\mathcal{F}_{\rm A}^{*}(\nu)$ is the complex conjugate of the Fourier transform of the light curve observed by FPMA and $\mathcal{F}_{\rm B}(\nu)$ is the Fourier transform corresponding to FPMB. The real part of the CPDS, called the cospectrum, represents only the power of the signals which are in phase between the two light curves, and its imaginary part gives the power of those signals which are in quadrature. The CPDS can therefore be used to calculate time lags and correlations between two light curves.

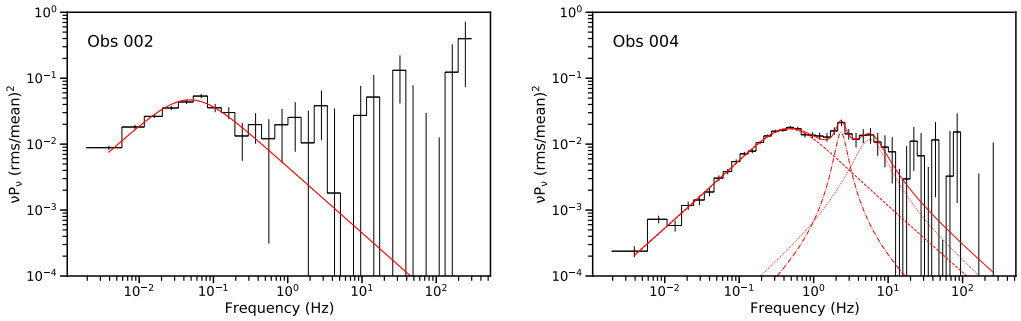

Figure 2.7: The averaged rms-normalized cospectra for *NuSTAR* observations of AT2019wey.

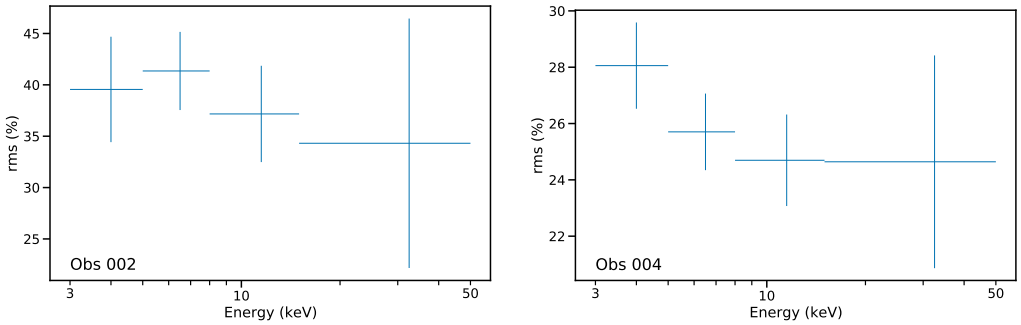

Figure 2.8: The observed variability as measured by the fractional rms as a function of photon energy for *NuSTAR* observations of AT2019wey.

In order to produce a cospectrum for each observation, we split the light curves observed by each FPM into intervals of 256 s each, resulting in 150 intervals for observation 002 and 173 intervals for observation 004. For each of these intervals, we produced a cospectrum, and then averaged these cospectra together. The frequencies sampled are limited to the range 4 mHz $< \nu <$ 256 Hz. The low end of this range is determined by the interval length, and the high end is determined by the sampling rate of the light curves. The resulting averaged, rms-normalized cospectra

for observations 002 and 004 are shown in black in Figure 2.7, where they have been rebinned for clarity. All errors quoted are 1-σ.

Similar to our *NICER* timing analysis, we fit the *NuSTAR* vcospectra with a model consisting of a sum of Lorentzian functions following Belloni, Psaltis, and van der Klis (2002). We used an automated modeling algorithm that fits a cospectrum to composite Lorentzian models with progressively more components, halting when the addition of a component no longer results in the reduction of the χ^2 fit statistic. We chose the model with the minimum number of components which still resulted in a significant improvement to the fit ($|\Delta\chi^2| > 10$), and discarded more complex models with only marginally better fit statistics. For observation 002, this resulted in a single-component model containing only one broad Lorentzian with unconstrained ν_0 and Q. For observation 004, we obtained a model with two broad components centered at considerably higher frequencies than that of the component obtained for observation 002. Following the notation of Klein-Wolt and van der Klis (2008), we dub the lowest frequency broad components L_b, and the higher frequency broad component observed in observation 004 L_h.

Table 2.2: *NuSTAR* power spectral components of AT2019wey.

OBSID	Component	$\nu_{\max}$ (Hz)	Q	rms (%)
90601315002	L_b	0.05 †	3×10^{-4} †	54 ± 5
90601315004	L_b	0.5 ± 0.1	0.15 ± 0.03	28 ± 1
	L_h	5.7 ± 1.4	0.9 ± 0.6	14 ± 3
	$L_{\rm LF}$	2.3 ± 0.1	2.6 ± 1.0	9.5 ± 1.9

† The characteristic frequency and quality factor are not constrained for observation 002, therefore errors are not shown for these quantities.

Following the detection of the two broad components in observation 004 using our fitting algorithm, visual inspection suggested the presence of an additional component at ~ 2 Hz. We therefore added a third QPO-like component to the model and saw a small but significant improvement to the fit of $\Delta\chi^2 = -30$. We label this narrower QPO-like component $L_{\rm LF}$. Defining the QPO significance as the ratio of the integrated power of the component to its error, A/σ_A, the significance of $L_{\rm LF}$ was calculated to be 2.5σ. Note that this component lines up with the QPO seen in the *NICER* PDS (Figure 2.6 (b)), and it is therefore still significant. All of the components observed in each observation as well as their fitted parameters are listed in Table 2.2. The components and the resulting composite models are shown in red in Figure 2.7.

Finally, in order to better understand the physical origins of the source variability, we computed the variability as a function of photon energy for each observation. We produced cospectra in four energy ranges, and determined the fractional rms by integrating the cospectra. Due to the limited frequency range for which significant power was detected, we did not integrate over the entire available frequency range. Rather, for observation 002, we integrated the power between 4 mHz and 1 Hz, while for observation 004, we integrated the power between 4 mHz and 10 Hz. The resulting rms-energy relations are shown in Figure 2.8. Observation 002 is consistent with a flat rms-energy relation, whereas observation 004 may exhibit decreasing variability with increasing photon energy.

2.4 Spectral Analysis

In this section, we examine the spectral evolution of AT2019wey. For this analysis we use `xspec` version 12.11.0 (Arnaud, 1996). Uncertainties of model parameters are represented by the 90% confidence intervals, which are estimated by the `error` command in `xspec`. Below we present joint analysis (i.e., analysis of contemporaneous datasets obtained from several missions) and also specific data sets.

First, we perform joint spectral analyses of three sets of observations obtained in 2020 April, August, and September. In the April 2020 epoch, the *NuSTAR* 002 spectra for FPMA and FPMB were fitted with data from four *Swift*/XRT observations obtained in April 2020 (Table 2.8). In the August 2020 epoch, the *NuSTAR* 004 spectra for FPMA and FPMB were fitted with two *NICER* observations bracketing the *NuSTAR* observation (obsID 3201710112 and 3201710113). In the September 2020 epoch, the *Chandra* spectra were fitted with two *NICER* observations bracketing the *Chandra* observation (obsID 3201710147 and 3201710148). Finally, we analyze the *NICER* spectra for each obsID between 3201710105 and 3201710157.

Joint Analysis, 2020 April

The upper panel of Figure 2.9 shows the *NuSTAR* 002 and *Swift*/XRT spectra in April 2020, which appears relatively featureless. We therefore modeled the data with an absorbed power-law (`tbabs*powerlaw`, in `xspec`, Wilms, Allen, and McCray 2000). We also included a leading cross-calibration term (`constant`; Madsen et al. 2017) between the two *NuSTAR* telescopes (with $C_{\rm FPMA}$ defined to be 1) and a single term used for all four *Swift*/XRT observations.

The four XRT spectra were grouped with `grppha` to have at least one count per bin. The *NuSTAR* FPMA and FPMB spectra were grouped with `ftgrouppha` using the

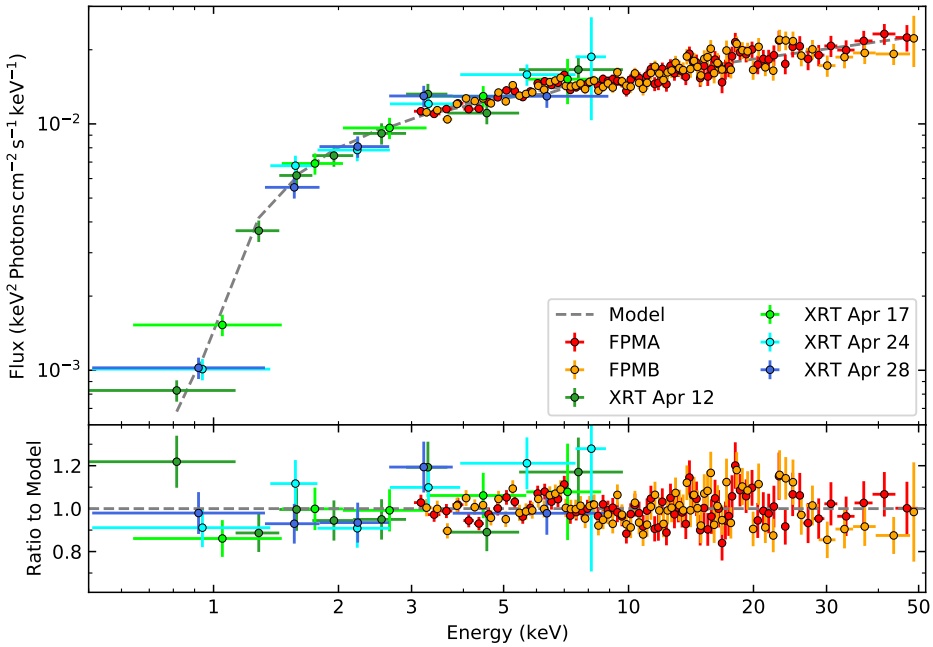

Figure 2.9: The April 2020 *NuSTAR* and *Swift*/XRT spectra of AT2019wey.

optimal binning scheme developed by Kaastra and Bleeker (2016). All data were fitted using C-statistics via `cstat` (Cash, 1979). For *NuSTAR* we fitted the data over the 3–50 keV range as the source spectrum becomes comparable to the background at higher energies, while for *Swift* we fitted from 0.5 to 10 keV.

The best-fit model for *NuSTAR*-FPMA is shown in Figure 2.9. To account for the cross-normalization terms (see Table 2.3), the FPMB and XRT data are divided by 1.037 and 0.796, respectively. The model parameters are given in Table 2.3. We note that the $C_{\rm XRT}$ is lower than we would typically expect. A probable explanation is that the pile-up resulted in an observed flux lower than expected, as the source count rate is relatively high for the XRT PC mode (see Table 2.8).

The unabsorbed flux in the 0.3–100 keV band for FPMA is 1.4×10^{-10} erg cm^{-2} s^{-1}. Yao, Kulkarni, Burdge, et al. (2021) constrains the distance of AT2019wey to be $1 \lesssim D \lesssim 10$ kpc. At distances of [1, 3, 5, 10] kpc, this corresponds to a luminosity of [0.16, 1.5, 4.1, 16.3]$\times10^{35}$ erg s^{-1}. The Eddington luminosity is $L_{\rm Edd} = 1.46\times10^{38}(M/M_\odot)$ erg s^{-1} (assuming solar hydrogen mass fraction $X = 0.71$). Therefore, the X-ray luminosity in 2020 April is $10^{-5} \lesssim L_{\rm X}/L_{\rm Edd} \lesssim 10^{-3}$ for a $\approx10\,M_\odot$ compact object.

Table 2.3: Best-fit model parameters of the 2020 April joint observations.

Parameter	90% Interval
`constant`	
$C_{\rm FPMA}$	1 (frozen)
$C_{\rm FPMB}$	1.037 ± 0.014
$C_{\rm XRT}$	$0.796^{+0.039}_{-0.038}$
`tbabs`	
$N_{\rm H}$ (10^{22} cm^{-2})	$0.609^{+0.049}_{-0.045}$
`powerlaw`	
Γ	1.765 ± 0.013
`norm` †	$9.06^{+0.27}_{-0.26}$
`C-stat / d.o.f.`	1292.70/1541

† Normalization at 1 keV in units of 10^{-3} ph keV^{-1} cm^{-2}.

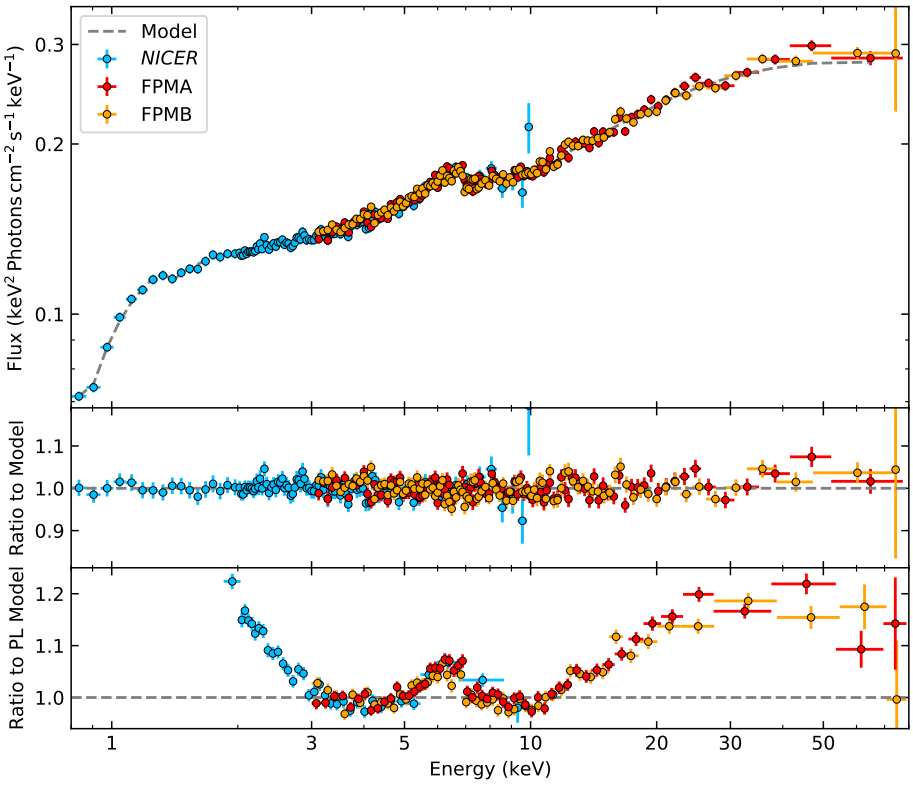

Figure 2.10: The August 2020 *NuSTAR* and *NICER* spectra of AT2019wey.

Joint Analysis, 2020 August 16

The upper panel of Figure 2.10 shows the *NuSTAR* 004 and simultaneous *NICER* spectra, and the bottom panel presents the ratio of data to an absorbed power-law model (`tbabs*powerlaw`) fitted only to the 3–4 keV and 10–12 keV energy bands ($\Gamma \sim 1.8$). As reported by Yao, Garcia, et al. (2020), we clearly detected the broadened Fe Kα line and Compton hump, characteristic of the relativistic reflection spectrum commonly seen in accreting X-ray binaries (García, Kallman, and Mushotzky, 2011).

We modeled the spectrum by a combination of disk blackbody and relativistic reflection from an accretion disk (`tbfeo*edge*(simplcutx*diskbb+relxillCp)`, in `xspec`). In this model, the continuum is assumed to be produced by Comptonization of the disk photons (`simplcut*diskbb`, Steiner, García, et al. 2017; Mitsuda et al. 1984), and the reflection is fitted with a `relxill` model (García, Dauser, et al., 2014; Dauser, García, Parker, et al., 2014) that incorporates such continuum (`relxillCp`). A photoelectric absorption (`edge`) was added to account for instrumental uncertainties within the spectrum where *NICER*'s calibration is still ongoing (see, e.g., Ludlam, Cackett, García, Miller, Bult, et al. 2020).

All data were fitted using *C*-statistics. For *NuSTAR* we fitted the data over the 3–79 keV range, while for *NICER* we fitted from 0.8 to 10 keV. The *NuSTAR* data were grouped to have signal-to-noise ratio of 6 and oversampling factor of 3. Details of the model fitting are presented in §2.7. The best-fit model for *NuSTAR*-FPMA is shown in Figure 2.10. To account for the cross-normalization terms (see Table 2.4), the FPMB and *NICER* data are divided by 1.051 and 1.035, respectively. The model parameters are given in Table 2.4.

The best-fit reflection spectrum is analogous to those observed in other black hole binaries, such as GX 339−4 (Wang-Ji et al., 2018) or XTE J1550−564 (Connors et al., 2020). The unabsorbed flux in the 0.3–100 keV band for FPMA is 1.8×10^{-9} erg cm^{-2} s^{-1}. At distances of [1, 3, 5, 10] kpc, this corresponds to a luminosity of [0.21, 1.9, 5.3, 21.1]$\times 10^{36}$ erg s^{-1}. Therefore, the X-ray luminosity on 2020 August 16 is $1.4 \times 10^{-4} \lesssim L_{\rm X}/L_{\rm Edd} \lesssim 1.4 \times 10^{-2}$ for a 10 $M_\odot$ compact object.

Joint Analysis, 2020 September 20

The upper panel of Figure 2.11 shows the simultaneous *Chandra* and *NICER* observations. No strong narrow emission or absorption lines were detected in the HETGS spectrum. To model the continuum, we adopted the `constant*tbabs*(simpl*`

Table 2.4: Best-fit model parameters of the 2020 August 16 joint observations.

Parameter	90% Interval
`constant`	
$C_{\rm FPMA}$	1 (frozen)
$C_{\rm FPMB}$	1.051 ± 0.003
C_{NICER}	1.035 ± 0.002
`tbfeo`	
$N_{\rm H}$ (10^{22} cm^{-2})	0.513 ± 0.003
O	< 0.020
Fe	< 0.0528
z	0 (frozen)
`simplcutx`	
Γ	1.786 ± 0.001
$f_{\rm sc}$	0.746 ± 0.005
$R_{\rm F}$	1 (frozen)
kT_e (keV)	1000 (frozen)
`diskbb`	
$T_{\rm disk}$ (keV)	0.3542 ± 0.0001
$\rm R^*_{in}$ †	40.58 ± 0.03
`relxillCp`	
q	3 (frozen)
a	0 (frozen)
i (deg)	$27.0^{+0.8}_{-1.2}$
$R_{\rm in}$ ($R_{\rm isco}$)	< 1.05
$R_{\rm out}$ ($R_{\rm g}$)	400 (frozen)
logξ	$3.0121^{+0.0016}_{-0.0020}$
$A_{\rm Fe}$	$2.86^{+0.10}_{-0.09}$
kT_e (keV)	1000 (frozen)
$R_{\rm F}$	1 (frozen)
$\rm Norm_{rel}$ (10^{-4})	2.96 ± 0.03
`edge`	
$E_{\rm c}$ (keV)	$1.369^{+0.017}_{-0.016}$
D	$0.071^{+0.005}_{-0.005}$
`C-stat / d.o.f.`	2006.52 (1769)

† Normalization $(R_{\rm in}/D_{10})\sqrt{\cos i}$, where $R_{\rm in}$ is the inner disk radius in the unit of km, and D_{10} is distance to the source in units of 10 kpc.

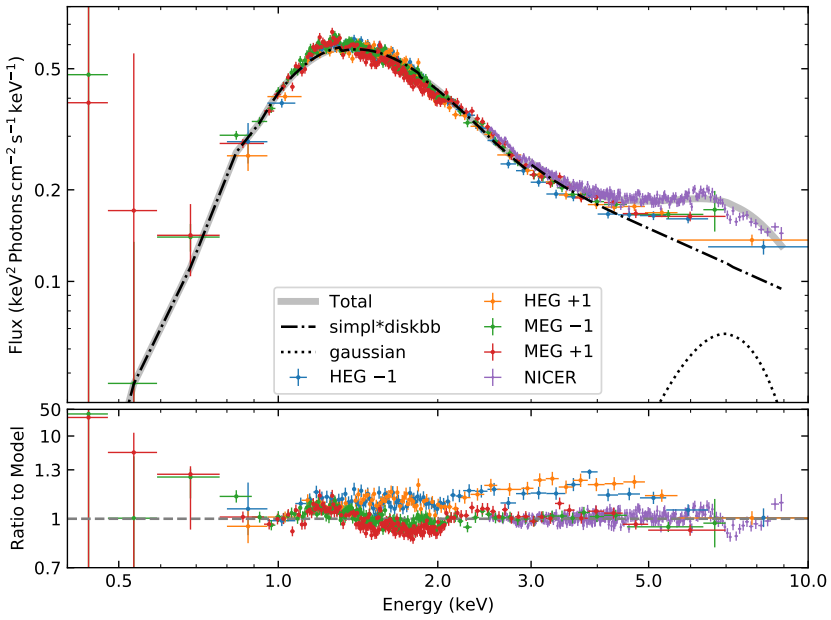

Figure 2.11: The September 2020 *Chandra* and *NICER* spectra of AT2019wey.

`diskbb+gaussian`) model, where `simpl` is a Comptonization model that generates the power-law component via Compton scattering of a fraction ($f_{\rm sc}$) of input seed photons from the disk (Steiner, Narayan, et al., 2009). The flag $R_{\rm up}$ was set to 1 to only include upscattering. The `gaussian` component was added to account for the existence of a relativistic broadened iron line, and we fixed the line center ($E_{\rm line}$) at 6.4 keV. We fitted the *NICER* data over the 2.5–9.0 keV range. For HEG and MEG, we included the 0.8–10 keV and 0.4–7.0 keV bands, respectively. All data were fitted using χ^2-statistics. In Figure 2.11, we show the best-fit model for *NICER* above 4.0 keV, and the best-fit model for MEG −1 below 4.0 keV. To account for the cross-normalization terms (see Table 2.5), the *NICER* data are divided by 0.901. The model parameters are given in Table 2.5.

As can be seen from the bottom panel of Figure 2.11, the model underpredicts the MEG data below $\sim$ 0.8 keV. The MEG effective area below 1 keV is sensitive to the correction for contamination, which currently undercorrects for the increasing depth of the contaminant. The magnitude of the effect is estimated to be about 20% at 0.65 keV and 10% at 0.8 keV, in the sense that estimated MEG fluxes should be even larger than shown in Figure 2.11.

The HETGS data can be used to constrain $N_{\rm H}$. By fitting a simple model to a limited wavelength range, the Mg I and Ne I edges due to the ISM can be determined directly.

Table 2.5: Best-fit model parameters of the 2020 September 20 joint observations.

Parameter	90% Interval
`constant`	
$C_{\rm HETG}$	1 (frozen)
C_{NICER}	0.901 ± 0.007
`tbabs`	
$N_{\rm H}$ (10^{22} cm^{-2})	$0.417^{+0.014}_{-0.013}$
`simpl`	
Γ	2.80 ± 0.05
$f_{\rm sc}$	0.176 ± 0.007
$R_{\rm up}$	1 (fixed)
`diskbb`	
$T_{\rm disk}$ (keV)	$0.315^{+0.004}_{-0.005}$
$R^{*}_{\rm in}$ †	136 ± 6
`gaussian`	
$E_{\rm line}$ (keV)	6.4 (fixed)
$\sigma_{\rm line}$ (keV)	1.84 ± 0.09
$\rm Norm_{line}$ ‡	0.0074 ± 0.0007
χ^2 / `d.o.f.`	12095.94 (23735)

† $R^{*}_{\rm in}$ has the same meaning as that in Table 2.4.

‡ Normalization of the Gaussian in photon cm^{-2} s^{-1}.

The continuum model in this case is empirical, a log-parabolic shape, and the edge is modeled in `isis` (Houck and Denicola, 2000) using the `edge` model, which has no structure at the edge but has the appropriate asymptotic behavior for the ISM edge. Fitting the 11–17 Å (0.73–1.13 keV) region, we find that the Ne I edge optical depth is $0.170^{+0.06}_{-0.07}$, giving an estimate of $N_{\rm H} = 2.2^{+0.7}_{-0.9} \times 10^{21}$ cm^{-2} (Wilms, Allen, and McCray, 2000). An optical depth at the Ne I edge of 0.33 is expected when $N_{\rm H} = 4.2 \times 10^{21}$ cm^{-2}, which is ruled out at the 4.3σ level. An independent measurement from fitting the Mg I line in the 8–11 Å (1.13–1.55 keV) region gives an optical depth of $0.043^{+0.021}_{-0.014}$, and $N_{\rm H} = 3.1^{+1.5}_{-1.0} \times 10^{21}$ cm^{-2}.

Yao, Kulkarni, Burdge, et al. (2021) measured the equivalent width (EW) of Na I D line and diffuse interstellar bands (DIBs) from a summed optical spectrum, and constrained the line-of-sight extinction to be $0.8 \lesssim E(B-V) \lesssim 1.2$. Using the calibration of $N_{\rm H} = 5.55 \times 10^{21} \times E(B-V)$ (Predehl and Schmitt, 1995), the line-of-sight column density can be inferred to be $4.4 < N_{\rm H}/(10^{21}\,{\rm cm}^{-2} < 6.7$. This is consistent with the $N_{\rm H}$ derived from the continuum fit. Therefore, in the

NICER-only spectral analysis (§2.4), we adopt $N_{\rm H} = 5 \times 10^{21}$ cm^{-2}.

NICER-only Spectral Analysis

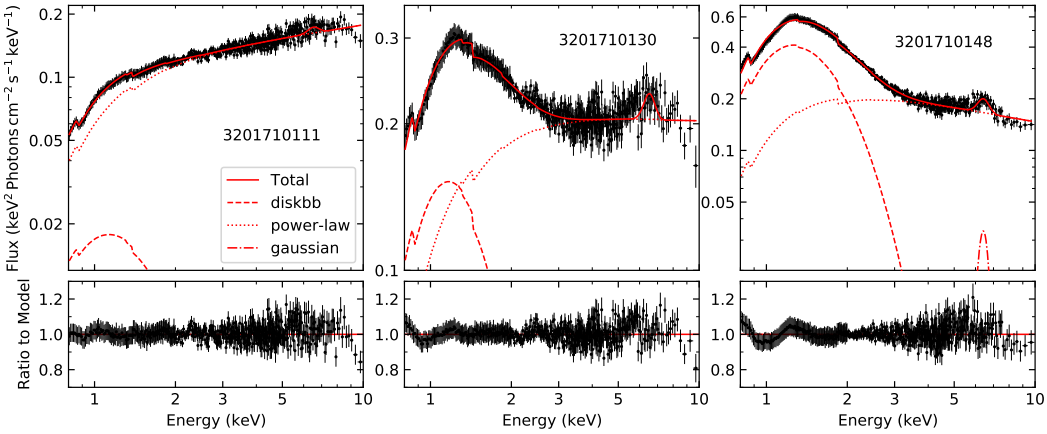

Figure 2.12: *NICER* spectra of AT2019wey at three representative epochs.

Figure 2.12 shows the *NICER* spectra at three representative epochs (59076, 59100, and 59113 MJD). The continuum can be described by a combination of a multi-color disk component, a power-law component, and a Gaussian line component at 6.3–6.5 keV. To investigate the evolution of spectral components, for each OBSID, we fitted a `tbfeo*(diskbb+pegpwrlw+gaussian)*edge` model to the 0.8–10 keV *NICER* spectrum. The `edge` feature at ≈1.4 keV was included, as found to be present in the *NICER* and *NuSTAR* joint spectral analysis (§2.4). In the `tbfeo` model, the O and Fe abundances were fixed at Solar values, and $N_{\rm H}$ was fixed at 5×10^{21} cm^{-2}. All data were fitted using χ^2-statistics. The best-fit models provided a reduced-χ^2 close to 1 in most of the cases.

The evolution of spectral parameters of the hydrogen column density $N_{\rm H}$, the power-law photon index Γ, the temperature at inner disk radius $T_{\rm disk}$, and the disk-blackbody normalization term $\mathrm{Norm_{disk}} = (R_{\rm in}/D_{10})^2 \cos i$ are shown in Figure 2.13. $\mathrm{Norm_{disk}}$ remained almost constant after 59082 MJD. This provides evidence that the inner disk radius ($R_{\rm in}$) remained at $\sim$ 100–1000 km assuming a range of distances from $D \sim 10$ kpc to 1 kpc.

In the bottom panel of Figure 2.13, we present the unabsorbed 0.4–10 keV fluxes in the disk-blackbody component, the power-law component, and the total (disk-blackbody + power-law + Gaussian). Note that the Fe line flux is significantly smaller than the other two components. The occasional enhancement observed in the source light curve matches to the brightening of the thermal component.

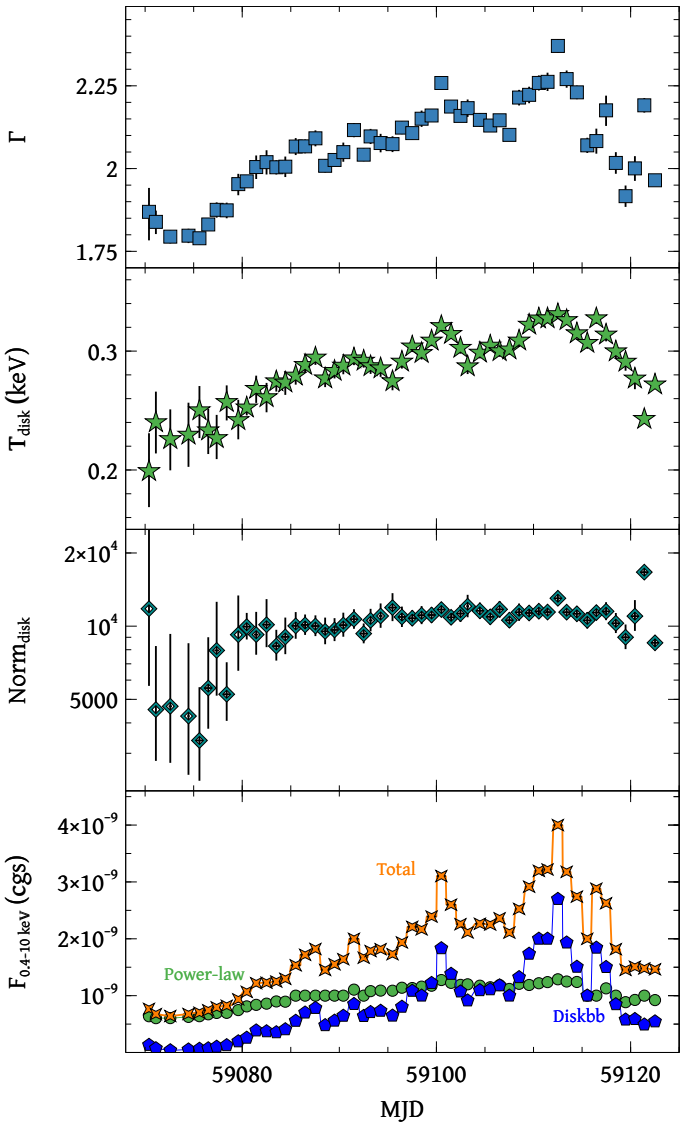

Figure 2.13: X-ray spectral parameters and flux from *NICER* observations of AT2019wey.

2.5 Discussion

X-ray States in AT2019wey

The X-ray spectral-timing properties of AT2019wey are in line with the typical properties of LMXBs in the LHS and HIMS.

From 2019 December to 59082 MJD (2020 August 21), AT2019wey stayed in the canonical LHS of LMXBs. In the first six months, the spectrum was dominated by a hard power-law component ($1.7 \lesssim \Gamma \lesssim 2.0$) with little contribution from the disk component (Figures 2.9 and 2.13). It moved along the HL on the RID (Figure 2.5), and the fractional rms stayed at ~30%. No QPO was observed (§2.3). The X-ray color softened as the source brightened (Figure 2.3). Toward the end of the brightening, spectral features of relativistic reflection were clearly seen (Figure 2.10). Modeling of the reflection spectrum suggests a small inclination ($i \lesssim 30^\circ$, see §2.7). The rms variability decreased with increasing photon energy (right panel of Figure 2.8), indicating that cooler regions of the source are more variable than hotter regions, perhaps due to inhomogeneities in an accretion disk.

Between 59082 MJD and 59122 MJD (2020 September 30), AT2019wey was in the canonical HIMS of LMXBs. The power-law component steepened ($2.0 \lesssim \Gamma \lesssim 2.3$), and the thermal disk emission became comparable to the power-law component in the 0.4–10 keV band (Figure 2.13). The excess in the very soft X-ray band (§2.4) might arise from reprocessing of X-rays in the outer accretion disk. Its soft X-ray light curve underwent a few episodes of mini-outbursts, which were correlated with the enhancement of a thermal component. At the same time, the source left the HL on the RID as the fractional rms decreased (Figure 2.5). A weak type-C LFQPO was observed, and its characteristic frequency increased from ~2 Hz to ~6.5 Hz as the disk flux increased. It did not reach the SIMS since the fractional rms was > 9% at the minimum (Figure 2.4).

AT2019wey likely stayed in the HIMS from 2020 October 1 to November 30, since the 2–10 keV and 15–50 keV light curves remained roughly constant (Figure 2.1). We note that after being active in X-ray for at least $\sim$ 12 months, AT2019wey had not transitioned to the SIMS or HSS. The lack of hysteresis in the HID (Figure 2.3) is similar to the BH candidate MAXI J1836−194 (Russell, Russell, et al., 2013).

Yao, Kulkarni, Burdge, et al. (2021) reported the radio brightening as AT2019wey transitioned from LHS to HIMS. Yadlapalli et al. (2021) reported the detection of a resolved radio source during the HIMS, which was interpreted as a steady compact jet. The evolution of the radio emission is consistent with LMXBs in the hard states

(Fender, Belloni, and Gallo, 2004; Migliari and Fender, 2006).

The X-ray properties observed in AT2019wey thus far make it a promising candidate for the population of "hard-only" outbursts (Tetarenko, Sivakoff, Heinke, et al., 2016). The distance of this system is poorly constrained to ∼1–10 kpc (Yao, Kulkarni, Burdge, et al., 2021). Given the brightness of AT2019wey in the optical ($r \approx 17.4$ mag), the *Gaia* mission will be able to determine the parallax to the source and thus settle the distance. Assuming a typical distance at 3–5 kpc, the 0.3–100 keV X-ray luminosity of AT2019wey remained at a few times 10^{35} erg s^{-1} for ∼ 6 months in the LHS, increased by a factor of ∼ 10 to a few times 10^{36} erg s^{-1} over ∼ 2 months, and stayed at this luminosity afterward in the HIMS. This range of X-ray luminosities is at the lower end of the whole population of BH transients, but is typical for "hard-only" outbursts (Tetarenko, Sivakoff, Heinke, et al., 2016).

Nature of the Compact Object

NS signatures of coherent pulsations and thermonuclear X-ray bursts were not detected in 394 ks of *NICER* and 80 ks of *NuSTAR* data (see §2.7). The X-ray spectral and timing properties shown in this paper are consistent with both NS and BH LMXB outbursts. However, a few properties of this source favor a BH accretor.

First of all, during the initial six months of the LHS, the power-law index was $\Gamma \approx 1.77$ and the 0.5–10 keV luminosity was 4.5×10^{33}–4.5×10^{35} erg s^{-1}. This makes AT2019wey closer to BH binaries on the Γ–$L_{\rm X}$ diagram (see Fig. 2 of Wijnands et al. 2015). Moreover, the positions of this source on the $L_{\rm radio}$–$L_{\rm X}$ and the $L_{\rm opt}$–$L_{\rm X}$ diagrams are also closer to BH binaries (Yao, Kulkarni, Burdge, et al., 2021).

Therefore, although we can not preclude the possibility of a NS at this time, it is highly suggestive that AT2019wey is a BH system.

The Slow Rise of the Outburst

LMXB outbursts (also termed as X-ray novae) span a wide range of morphological types (Chen, Shrader, and Livio, 1997). Theories for the canonical fast-rise exponential-decay (FRED) profile of X-ray novae have been developed based on the disk instability model (DIM), which was originally invoked to explain dwarf nova outbursts (Lasota, 2001). Disk truncation and irradiation are generally invoked to account for the longer evolution timescale and recurrence time of X-ray novae (van Paradijs, 1996; Dubus, Hameury, and Lasota, 2001). Recently, detailed

analysis of the decay profile of X-ray outbursts provides evidence for the existence of generic outflows and time-varying irradiation (Tetarenko, Lasota, et al., 2018; Tetarenko, Dubus, Lasota, et al., 2018; Shaw, Tetarenko, et al., 2019; Tetarenko, Dubus, Marcel, et al., 2020).

Table 2.6: Short-period ($P_{\rm orb} < 16$ hr) BH or BH candidate LMXB outbursts discovered from 2009 to 2020.

Name	$P_{\rm orb}$ (hr)	Discovery Instrument	Discovery Date	X-ray States	References
AT2019wey	< 16	ATLAS; *SRG*	2019 Dec 7	LHS, HIMS	1, 2, 23, 24
MAXI J1305−704	9.7	*MAXI*	2012 Apr 9	IMS	3, 4, 5, 25
Swift J1357.2−0933	2.8	*Swift*/BAT	2011 Jan 28	LHS	6, 7, 8
		CRTS	2017 Apr 20	LHS	9, 10
		ZTF	2019 Mar 31	–	11
MAXI 1659−152	2.4	*Swift*/BAT, *MAXI*	2010 Sep 25	LHS, IMS, HSS	5, 12, 13, 14
IGR J17451−3022	6.3	*INTEGRAL*	2014 Aug 22–24	HSS	20, 21, 22
XTE J1752−223	< 6.8	*RXTE*	2009 Oct 23	LHS, IMS, HSS	5, 15, 16
MAXI 1836−194	< 4.9	*MAXI*, *Swift*/BAT	2011 Aug 30	LHS, HIMS	17, 18, 19

Instruments: the International Gamma-Ray Astrophysics Laboratory (*INTEGRAL*; Winkler et al. 2003); the Rossi X-ray Timing Explorer (*RXTE*; Swank 1999); the Catalina Real-Time Transient Survey (CRTS; Drake, Djorgovski, Mahabal, Beshore, et al. 2009); the Zwicky Transient Facility (ZTF; Bellm, Kulkarni, Graham, et al. 2019; Graham et al. 2019).

References. (1) This work (2) Yao, Kulkarni, Burdge, et al. (2021) (3) Sato et al. (2012) (4) Shidatsu et al. (2013) (5) Tetarenko, Sivakoff, Heinke, et al. (2016) (6) Krimm, Barthelmy, et al. (2011) (7) Corral-Santana, Casares, Muñoz-Darias, Rodríguez-Gil, et al. (2013) (8) Armas Padilla et al. (2013) (9) Drake, Djorgovski, Mahabal, Graham, et al. (2017) (10) Beri, Tetarenko, et al. (2019) (11) van Velzen, Gezari, Cenko, et al. (2019) (12) Negoro, Yamaoka, et al. (2010) (13) Mangano, Hoversten, et al. (2010) (14) Kuulkers et al. (2013) (15) Markwardt et al. (2009) (16) Ratti et al. (2012) (17) Negoro, Nakajima, Nakahira, et al. (2011) (18) Ferrigno et al. (2012) (19) Russell, Soria, et al. (2014) (20) Chenevez et al. (2014) (21) Jaisawal et al. (2015) (22) Bozzo et al. (2016) (23) Tonry, Denneau, Heinze, Weiland, et al. (2019) (24) Mereminskiy et al. (2020) (25) Morihana et al. (2013)

Here we focus on the rise profile of AT2019wey. Yao, Kulkarni, Burdge, et al. (2021) shows that the orbital period of AT2019wey is likely less than 16 hours. To compare AT2019wey with other short-period LMXBs, we select outbursts discovered between 2009 and 2020 from the BlackCAT[5] catalog (Corral-Santana, Casares, Muñoz-Darias, Bauer, et al., 2016). Systems with $P_{\rm orb} \lesssim 16$ hours are summarized in Table 2.6. Figure 2.14 shows their *MAXI* 4-day binned 2–10 keV light curves. The dotted horizontal line marks *MAXI* 4 day 3σ detection limit of 7 mCrab. We excluded IGR J17451−3022 since its *MAXI* data was highly contaminated by the bright persistent source 1A 1742−294. We also excluded the 2017 and 2019 outbursts of Swift J1357.2−0933 since their X-ray fluxes were too faint to be seen by *MAXI*— they were only detected by follow-up observations conducted by *NuSTAR*, *Swift*/XRT, and *NICER* (Beri, Tetarenko, et al., 2019; Beri, Wijnands, et al., 2019; Gandhi et al., 2019; Rao et al., 2019).

[5] `https://www.astro.puc.cl/BlackCAT/transients.php`

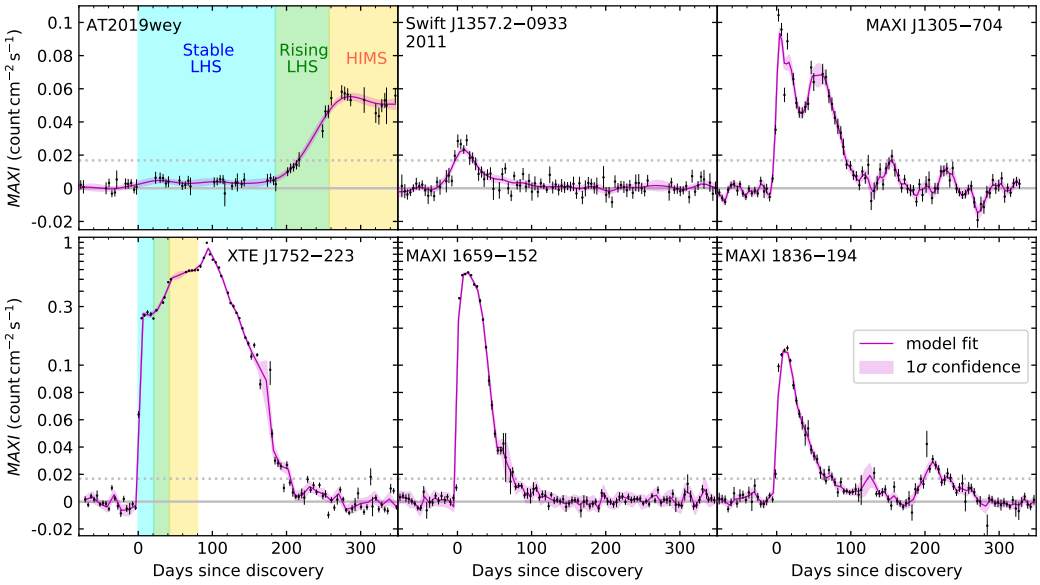

Figure 2.14: *MAXI* 2–10 keV light curves of outbursts from short-period LMXBs.

Figure 2.14 (middle and right panels) show that the 2–10 keV light curves of MAXI J1305−704, MAXI J1659−152, MAXI J1836−194, and the 2011 outburst of Swift J1357.2−0933 rose to maximum in 5–20 days. In comparison, the evolution of AT2019wey's light curve (upper left panel of Figure 2.14) is rather slow. Its 2–10 keV flux rose to $\sim$ 1 mCrab upon discovery, remained at this level for about 6 months, and brightened to a maximum of only $\sim$ 20 mCrab afterwards. This is similar to the initial evolution of XTE J1752−223 (lower left panel of Figure 2.14), where the source stayed in the hard state with two stable flux levels for about 3 months (Nakahira et al., 2010)[6]. In the left panels of Figure 2.14, we color-code the background of the two stable flux levels by blue and yellow, and the rising between the two stable levels by green. As mentioned by Nakahira et al. (2010), the long duration of the initial LHS and the two plateau phases are rather uncommon for recorded LMXB outbursts, and might be accounted for by a slow increase of $\dot{M}$. We note that XTE J1752−223 later transitioned to the HSS and completed the hysteresis pattern on the HID. It remains to be seen if AT2019wey will transition to the HSS.

2.6 Conclusion

In this paper, we present *NICER*, *NuSTAR*, *Chandra*, *Swift*, and *MAXI* observations of the X-ray transient AT2019wey. By analyzing its spectral-timing properties, we

[6]The exact time of the LHS → HIMS transition was not well determined for XTE J1752−223 (Brocksopp, Corbel, et al., 2013).

conclude that AT2019wey is a LMXB outburst with a BH or NS accretor. The source's evolution from 2019 December to 2020 November can be separated by three phases: the stable LHS from 2019 December to 2020 May ($\sim$ 1 mCrab), the rising LHS from 2020 June to August, and the stable HIMS from 2020 August to November ($\sim$ 20 mCrab).

The long duration of the initial LHS and the two plateau phases of AT2019wey (Figure 2.14) are not commonly seen. We searched the literature for analogs of AT2019wey. The closest analog we found is XTE J1752−223, a candidate BH LMXB with an orbital period of < 7 hr (Table 2.6).

If *SRG* had not discovered AT2019wey in 2020 March, the source would have probably been discovered by *MAXI* or BAT during the HIMS, and in a retrospective fashion, the initial $\sim$ 1 mCrab flux excess could have been revealed by *MAXI* long-term monitoring. However, the *SRG* discovery is important to trigger rapid X-ray follow-up observations, which classify the initial plateau phase as in the LHS.

The repeated *SRG* all-sky surveys that are being carried offer the opportunity to discover other events similar to AT2019wey at early epochs (and thus enable critical multi-wavelength follow-up). Furthermore, the eROSITA sensitivity is unprecedented: $< 5 \times 10^{-14}$ erg s^{-1} cm^{-2} (1.3 μCrab) in the 0.3–2.2 keV band, and $< 7 \times 10^{-13}$ erg s^{-1} cm^{-2} (36 μCrab) in the 2.3–8 keV band (Predehl, Andritschke, et al., 2021). This sensitivity should lead to the discovery of fainter versions of AT2019wey look-alikes.

2.7 Appendix

Observing Logs

Here we present observation logs of *NuSTAR* (Table 2.7) and *Swift*/XRT (Table 2.8).

Table 2.7: *NuSTAR* Observation Log

OBSID	Exp. (ks)	Start Time (UT)	Count Rate count s^{-1}
90601315002	38	2020-04-18 11:21	2.3 ± 0.7
90601315004	42	2020-08-16 12:16	30.8 ± 2.6
90601315006	37	2020-08-27 02:51	35.1 ± 2.7

Table 2.8: *Swift*/XRT Observation Log

OBSID	Exp. (s)	Start Time (UT)	Mode	Count Rate count s^{-1}
13313001	1523	2020-04-12 06:07	PC	0.645 ± 0.029
13313002	874	2020-04-17 19:55	PC	0.570 ± 0.035
13313003	1026	2020-04-24 14:28	PC	0.639 ± 0.036
13313004	1043	2020-04-28 13:56	PC	0.717 ± 0.051
13313010	434	2020-09-02 20:36	WT	$27.57^{+0.28}_{-0.31}$
13313011	1023	2020-09-09 16:40	WT	$42.50^{+1.58}_{-1.54}$
13313012	858	2020-09-16 16:01	WT	$43.32^{+0.26}_{-0.29}$
13313013	794	2020-09-23 20:03	WT	$40.53^{+2.35}_{-2.27}$

Count rate is given in the 0.3–10 keV band.

Details of Analysis

***NICER* Pulsation Search** — Pulsation searches were carried out for all *NICER* data up to 2020 September 28. The *NICER* data contains 2257 GTIs spread over 394 ks of observations. Upon cursory inspection of the data with `NICERsoft`[7], we found that detectors 34 and 43 suffered from high optical loading. Thus, the events in these detectors were excluded. The events were barycentered using `barycorr`. We employed acceleration search and stacked power spectral search schemes to search for pulsations.

To start with, we searched for pulsations using acceleration search. To account for possible frequency shifts due to binary Doppler motion, we employed an acceleration search algorithm over the f-$\dot{f}$ plane in the PulsaR Exploration and Search TOolkit (`PRESTO`[8]; Ransom 2011). The acceleration search is valid under the assumption that the pulsar has a constant acceleration throughout the observation, and is most effective for observation durations of $T \lesssim P_{\rm orb}/10$ (Ransom, Eikenberry, and Middleditch, 2002).

To determine the GTIs (and hence event files) used in the acceleration searches, we started from the 2257 GTIs in the original filtered event file. In order to prevent very short GTIs from being used, adjacent GTIs that were less than 11 s apart were combined. This resulted in a total of 445 GTIs, ranging in length from 1 s to 2648 s. We imposed a minimum GTI duration of 64 s to avoid spurious signals in short GTIs, leaving 378 GTIs with a median length of 883 s. For each of these GTIs

[7] `https://github.com/paulray/NICERsoft`

[8] `https://www.cv.nrao.edu/~sransom/presto/`

(considered independently), we further filtered events from three energy ranges: 0.5–2 keV, 2–12 keV, and 0.5–12 keV. The 1134 event files were then extracted with `niextract-events`. We then ran the search using the `accelsearch` task in `PRESTO` over the range 1–1000 Hz, positing that Doppler shifting would cause the possible signal to drift across a maximum of 100 Fourier frequency bins. For the median GTI length (883 s) and a fiducial fundamental pulsation frequency of 300 Hz, this corresponds to accelerations of up to $a = z_{\max} c/(fT^2) \approx 130\ \mathrm{m\,s^{-2}}$. The typical acceleration in a NS LXMB, say in a 12-hour orbit around a $0.2\,M_\odot$ companion, is approximately $5.7\,\mathrm{m\,s^{-2}}$. The acceleration searches yielded no candidate signals above the statistical significance threshold of 3-σ, after accounting for the total number of trials.

An alternative pulsation search algorithm involves stacking power spectra from M segments and calculating an averaged power spectrum. This is Bartlett's method (Bartlett, 1948), in which the original time series is broken up into M non-overlapping segments of equal length. The M segments were binned at $\Delta t = 0.5$ ms, such that we sampled at the Nyquist frequency of 1000 Hz. The Leahy-normalized power spectrum was then computed for each of the M segments, using the `realfft` task in `PRESTO` (Leahy et al., 1983). Finally, the M resulting spectra were averaged and the corresponding noise distributions were calculated. The detection level for any candidate signal was then determined by calculating the probability that the power in any frequency bin exceeded that of a detection threshold (say, 3-σ). This was calculated through the integrated probability of the χ^2 distribution with $2MW$ degrees of freedom, with W being the rebinning factor (van der Klis, 1988). The stacking procedure was done to enhance the signal of faint millisecond pulsars.

The stacked power spectra were calculated with segments of length 64, 128, 256, and 512 s, to account for possible orbital modulations in the pulsar frequency with yet unknown binary parameters. On top of stacking the power spectra from segments of the entire time series, the stacked power spectra were also calculated for various sub-time series, where the choices were informed by the overall light curve binned at 128 s and looking at the source brightness level. The number of segments admitted into the calculation for the stacked power spectrum also depends on a segment threshold (in %). That is, for each segment, a 1-s binned light curve was generated. If the fraction of bins with counts is less than the threshold, then that segment will not be used in the calculation. Segment thresholds used were 20%, 50%, 70%, and 100%. We also searched over energy ranges 0.5–2 keV, 2–12 keV, and 0.5–12 keV.

The averaged power spectrum was finally calculated by dividing the total power spectrum by the number of segments used.

From all of these stacked power spectra, there were no candidate signals that exceeded the 3-σ detection level, after accounting for the total number of trials.

***NuSTAR* Pulsation Search** — We used `HENDRICS` to perform the timing analysis. Initially developed as `MaLTPyNT` (Bachetti, 2015) for timing analysis of *NuSTAR* data, `HENDRICS` now comprises of tools such as acceleration searches, periodograms, Z_n^2 statistics to search for pulsations and extends to some other X-ray missions (e.g., *NICER*). We began this analysis by first calibrating the datafile by using the response file for each observation and constructing the light curve using `HENcalibrate`. The intent here was to check if AT2019wey exhibited rapid variability along with modality such that the light curve could be distributed into 'high,' 'low,' and 'flare' regions as seen in transitional millisecond pulsars. No modality was observed.

Similar to the techniques used in *NICER* pulsation search, we launched acceleration search using `PRESTO` to search for periodic pulsations. We split the observation into chunks of 720 s each and allowed for 5% overlap within these chunks. We then used `HENbinary` from `Hendrics` to render these time series in the format preferred by `accelsearch`. We binned the light curve to 1 ms bins. After that, we used the `accelsearch` routine in `PRESTO` and searched to a `zmax` depth of 10 and detection threshold of 2σ. No viable "candidates" were detected.

Modeling Relativistic Reflection — Here we present details of the spectral fitting in §2.4.

In the `relxillCp` model, the Γ parameter (power law index of the incident spectrum) was fixed at the same value as that in the `simpcutx` model. The outer disk radius ($R_{\rm out}$) was fixed at a fiducial value of $400\,r_{\rm g}$ (Choudhury et al., 2017), since it has little effect on the X-ray spectrum. Here $r_{\rm g} = GM/c^2$ is the gravitational radius. The electron temperature (kT_e) describes the observed high energy cutoff of the spectrum. Since no sign of a power-law cutoff was observed in the *NuSTAR* data, kT_e was fixed at the maximum value of 1 MeV. Redshift (z) was fixed at 0 since AT2019wey is a Galactic source. We included a cross-normalization term (`constant`) between FPMA, FPMB, and *NICER* data. To reduce the complexity of this model, we frozen the reflection fraction ($R_{\rm F} = 1$). The inner and outer emissivity index were set at the same value q throughout the accretion disk, making $R_{\rm break}$ obsolete.

If we fix the black hole spin parameter at $a = 0$ or $a = 0.998$, and let $R_{\rm in}$, q, and i be free, then the fitting will result in parameters loosely constrained, as most of these parameters are correlated (Dauser, Garcia, et al., 2013). Therefore, we experimented by fitting multiple models, and for each model we fixed two of the four parameters. First, we fixed $a = 0$, $q = 3$, and let $R_{\rm in}$ and i be free. The best-fit values are listed in Table 2.4.

Next, we fixed $a = 0.998$, the inclination to the value obtained in the previous fit ($i = 27.0^\circ$), and allowed $R_{\rm in}$ and q to be free. The best-fit model has similar statistics to that with $a = 0$ (Table 2.4). However, this model results in a flatter emissivity law ($q \sim 2.8$) with an inner radius still relatively close to ISCO ($R_{\rm in} \sim 4 \pm 3\, R_{\rm ISCO}$). This is contrary to the theoretical expectation of a steep emissivity profile for rapidly rotating black holes with compact coronae, unless the source of power-law photons is placed much farther along the rotational axis, which conversely will result in weaker reflection features (see Fig. 3 in Dauser, Garcia, et al. 2013).

Finally, we fixed $a = 0$ or $a = 0.998$, and i to higher values (45°, 60°). The fit quality decreases, with clear residuals around the Fe line. Therefore, from the point of view of reflection, the inclination (i) of the inner disk is well constrained to $i \lesssim 30^\circ$.

Chapter 3

MULTI-WAVELENGTH OBSERVATIONS OF AT2019WEY: A NEW CANDIDATE BLACK HOLE LOW-MASS X-RAY BINARY

Yao, Y. et al. (Oct. 2021). In: *ApJ* 920.2, 120, p. 120. DOI: 10.3847/1538-4357/ac15f9.

Yuhan Yao[1], S. R. Kulkarni[1], Kevin B. Burdge[1], Ilaria Caiazzo[1], Kishalay De[1], Dillon Dong[1], C. Fremling[1], Mansi M. Kasliwal[1], Thomas Kupfer[2], Jan van Roestel[1], Jesper Sollerman[3], Ashot Bagdasaryan[1], Eric C. Bellm[4], S. Bradley Cenko[5], Andrew J. Drake[1], Dmitry A. Duev[1], Matthew J. Graham[1], Stephen Kaye[6], Frank J. Masci[7], Nicolas Miranda[8], Thomas A. Prince[1], Reed Riddle[6], Ben Rusholme[7], and Maayane T. Soumagnac[9,10]

[1] Division of Physics, Mathematics and Astronomy, California Institute of Technology, Pasadena, CA 91125, USA
[2] Texas Tech University, Department of Physics & Astronomy, Box 41051, 79409, Lubbock, TX, USA
[3] The Oskar Klein Centre, Department of Astronomy, Stockholm University, AlbaNova, SE-10691 Stockholm, Sweden
[4] DIRAC Institute, Department of Astronomy, University of Washington, 3910 15th Avenue NE, Seattle, WA 98195, USA
[5] Astrophysics Science Division, NASA Goddard Space Flight Center, Greenbelt, MD 20771, USA
[6] Caltech Optical Observatories, California Institute of Technology, Pasadena, CA 91125, USA
[7] IPAC, California Institute of Technology, 1200 E. California Blvd, Pasadena, CA 91125, USA
[8] Institut für Informatik, Humboldt-Universität zu Berlin, Rudower Chaussee 25, 12489 Berlin, Germany
[9] Lawrence Berkeley National Laboratory, 1 Cyclotron Road, Berkeley, CA 94720, USA
[10] Department of Particle Physics and Astrophysics, Weizmann Institute of Science, Rehovot 76100, Israel

Abstract

AT2019wey (SRGA J043520.9+552226, SRGE J043523.3+552234) is a transient first reported by the ATLAS optical survey in 2019 December. It rose to prominence upon detection, three months later, by the *Spektrum-Roentgen-Gamma* (*SRG*) mission in its first all-sky survey. X-ray observations reported in Yao, De, et al. (2020) suggest that AT2019wey is a Galactic low-mass X-ray binary (LMXB) with a black hole (BH) or neutron star (NS) accretor. Here we present ultraviolet, optical, near-infrared, and radio observations of this object. We show that the companion is a short-period ($P \lesssim 16\,\mathrm{hr}$) low-mass ($< 1\,M_\odot$) star. We consider AT2019wey to be a candidate BH system since its locations on the L_{radio}–L_{X} and L_{opt}–L_{X} diagrams

are closer to BH binaries than NS binaries. We demonstrate that from 2020 June to August, despite the more than 10 times brightening at radio and X-ray wavelengths, the optical luminosity of AT2019wey only increased by 1.3–1.4 times. We interpret the UV/optical emission before the brightening as thermal emission from a truncated disk in a hot accretion flow and the UV/optical emission after the brightening as reprocessing of the X-ray emission in the outer accretion disk. AT2019wey demonstrates that combining current wide-field optical surveys and *SRG* provides a way to discover the emerging population of short-period BH LMXB systems with faint X-ray outbursts.

3.1 Introduction

Low-mass X-ray binaries (LMXBs) contain an accreting neutron star (NS) or black hole (BH) in orbit with a low-mass ($\lesssim 2\,M_\odot$) companion star. Most of the known BH LMXBs were discovered by X-ray all-sky monitors (ASMs) during X-ray outbursts induced by instabilities in the accretion processes. The most sensitive X-ray ASM to date, the Monitor of All-sky X-ray Image (*MAXI*; Matsuoka et al. 2009), has a transient triggering threshold of 8 mCrab (1 mCrab = 2.4×10^{-11} erg s^{-1} cm^{-2} over 2–10 keV) sustained for 4 days (Negoro, Kohama, et al., 2016). Due to the relatively shallow sensitivity of ASMs, the sample of LMXBs is biased toward nearby sources that exhibit bright X-ray outbursts.

Prior to 2020, the most sensitive all-sky X-ray imaging survey was carried out in 1990/1991 by *ROSAT* at 0.1–2.4 keV (Truemper, 1982; Voges et al., 1999). It cataloged X-ray sources brighter than $\sim 10\,\mu$Crab, providing the deepest X-ray all-sky reference at the time (Boller et al., 2016). Three decades after *ROSAT*, the dynamic X-ray sky is being surveyed by the eROSITA (0.2–10 keV; Predehl, Andritschke, et al. 2021) and the Mikhail Pavlinsky ART-XC (4–30 keV; Pavlinsky et al. 2021) telescopes on board the *Spektrum-Roentgen-Gamma* (*SRG*) mission (Sunyaev, Arefiev, et al., 2021). This planned four-year survey obtaining full-sky images created every six months is a powerful X-ray time domain facility. The first eROSITA All-Sky Survey (eRASS1; 2019 December–2020 June) was sensitive to point sources down to $\sim 0.8\,\mu$Crab (Predehl, Andritschke, et al., 2021).

On 2020 March 18, SRGA J043520.9+552226 (=SRGE J043523.3+552234) was discovered by *SRG* as a bright X-ray transient at ~ 1 mCrab (Mereminskiy et al., 2020). It coincided with an optical ($r \sim 17.5$) transient, AT2019wey, first reported by ATLAS (Tonry, Denneau, Heinze, Weiland, et al., 2019). This transient, bright at

both X-ray and optical wavelengths, and located at low Galactic latitude ($b = 5.3°$) was not present in the Palomar Observatory Sky Survey or the *ROSAT* catalog. We conducted an extensive follow-up campaign, revealing that AT2019wey is a Galactic LMXB with unique properties.

Yao, Kulkarni, Gendreau, et al. (2021) presented X-ray observations of AT2019wey from 2019 January to 2020 November, suggesting that AT2019wey is a LMXB with a BH or NS accretor. In this work, we present multi-wavelength observations of AT2019wey. We conclude that the compact object is probably a BH and the companion star must be of low mass ($< 1\,M_\odot$). We therefore call AT2019wey a candidate BH LMXB. This class of objects and the classification of their X-ray states is reviewed in McClintock and Remillard (2006), Remillard and McClintock (2006), Belloni, Motta, and Muñoz-Darias (2011), Zhang (2013), and Tetarenko, Sivakoff, Heinke, et al. (2016).

The paper is organized as follows. The association between the optical and X-ray transients is outlined in §3.2. We present optical and ultraviolet (UV) photometry in §3.3, optical and near-infrared (NIR) spectroscopy in §3.4, and radio observations in §3.5. We discuss the nature of the source in §3.6, and summarize out findings and conclusions in §3.7.

Throughout this paper, times are reported in UT. Optical magnitudes are reported in the AB system. We adopt the reddening law of Cardelli, Clayton, and Mathis (1989) with $R_V = 3.1$.

3.2 Association between the Optical and X-ray Transients

On 2019 December 2 05:18:40 (MJD 58819.2213), the Zwicky Transient Facility (ZTF; Bellm, Kulkarni, Graham, et al. 2019; Graham et al. 2019) detected AT2019wey at a g-band ($\lambda_{\rm eff} = 4810\,$Å) magnitude of $g_{\rm ZTF} = 19.30 \pm 0.05$. The last non-detection was obtained by ATLAS at an o-band ($\lambda_{\rm eff} = 6790\,$Å) magnitude of $o_{\rm ATLAS} > 18.3$, on 2019 December 1 12:18:30 (MJD 58818.5129).

In Figure 3.1, the eROSITA and ZTF (R.A=04h35m23.27s, Dec=+55d22m34.3s) positions are shown by "+" sign and "×", respectively. The circle indicates eROSITA's 68% error circle radius of 5″. The AT2019wey and SRGE J043523.3+552234 locations are separated by only 0.8″, well within the X-ray error circle radius, thereby confirming the association first suggested by Mereminskiy et al. (2020). The Galactic coordinates of AT2019wey, $l = 151.2°$ and $b = 5.3°$, *a priori* favors a Galactic source in the Galactic anti-center direction.

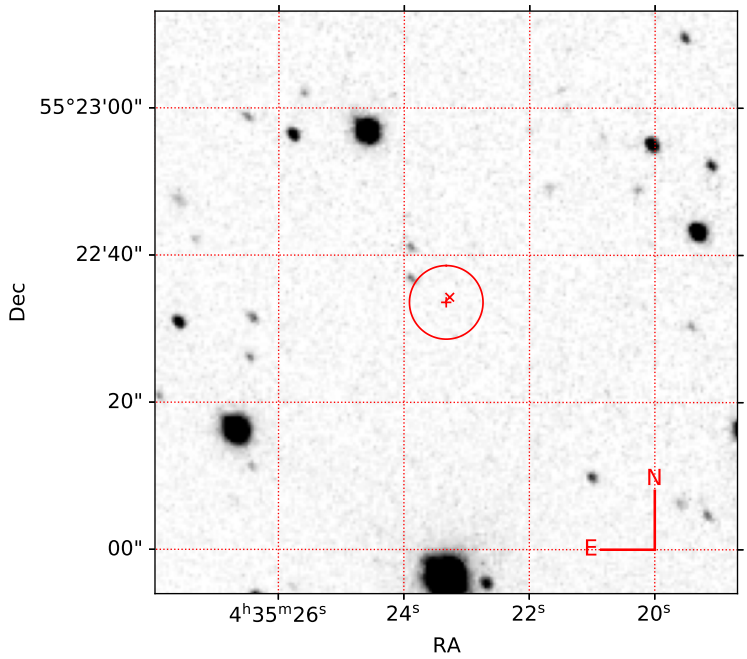

Figure 3.1: Localization of AT2019wey plotted on top of the SDSS z-band image.

3.3 Photometry

ZTF, ATLAS, and *Gaia* Photometry

We constructed the optical light curve using the forced-photometry services of ZTF (Masci et al., 2019) and ATLAS (Smith et al., 2020). We obtained *Gaia* photometry from the *Gaia* alerts page[1].

The upper panel of Figure 3.2 shows the ZTF, ATLAS, and *Gaia* light curves of AT2019wey. Over the first two weeks, the light curve rose to $r_{\rm ZTF} = 17.3$ mag. After that, the light curve displayed small amplitude ($\lesssim 0.3$ mag) variability for more than 300 days. The lack of photometry between MJD $\sim$ 58980 to MJD $\sim$ 59040 is due to the source being in the day sky. On September 9 and 13 we undertook continuous observations as part of the ZTF "deep drilling" program (Kupfer et al., 2021). On each day, ≈ 130 r-band exposure frames were obtained.

CHIMERA Photometry

On 2020 July 23 (MJD 59053), we obtained high-speed photometry in the SDSS g and i band using the Caltech HIgh-speed Multi-color camERA (CHIMERA; Harding et al. 2016) on the 200-inch Hale telescope of the Palomar Observatory. We operated the detectors using the 1 MHz conventional amplifier in frame-transfer

[1] `http://gsaweb.ast.cam.ac.uk/alerts/alert/Gaia20aua/`

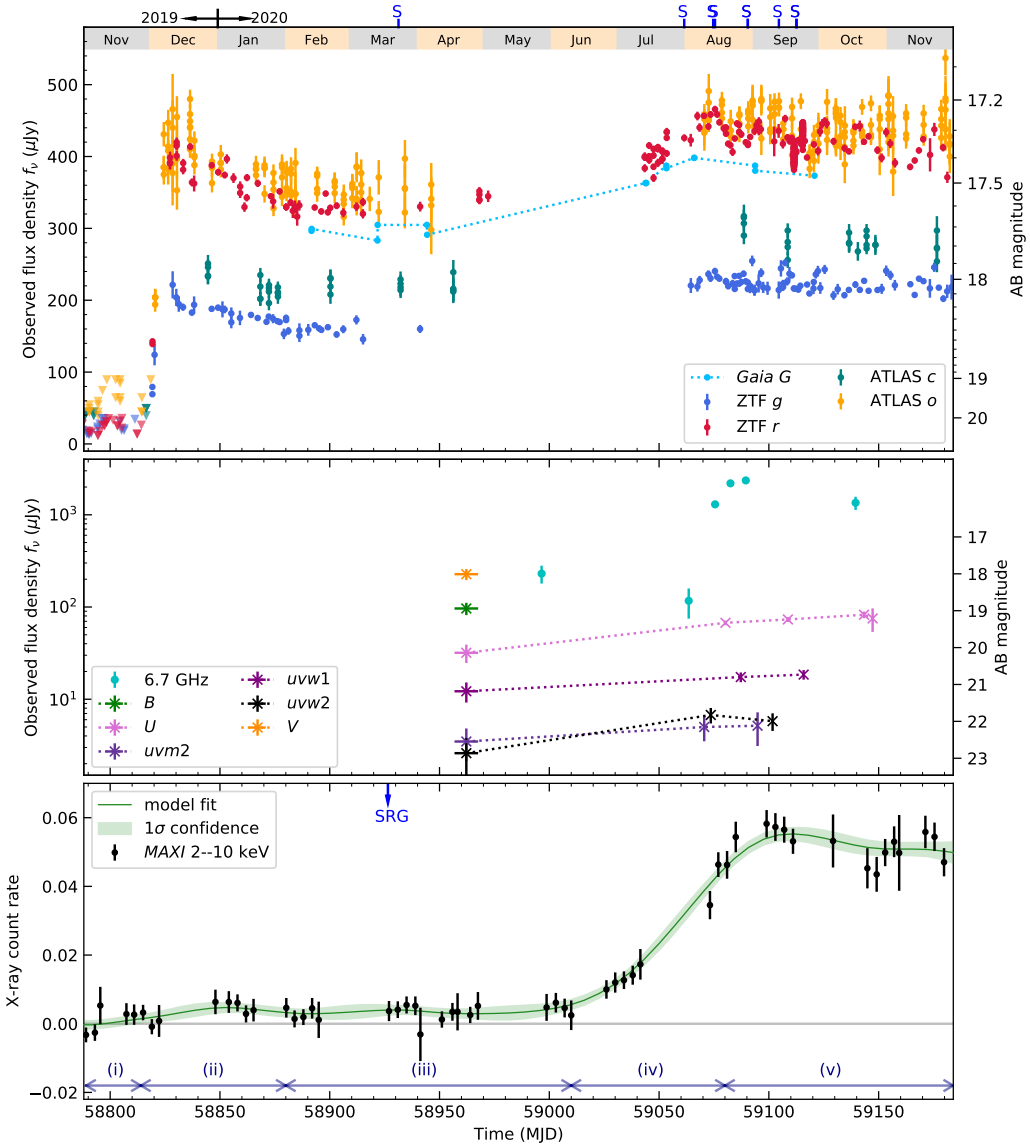

Figure 3.2: Multi-wavelength light curves of AT2019wey.

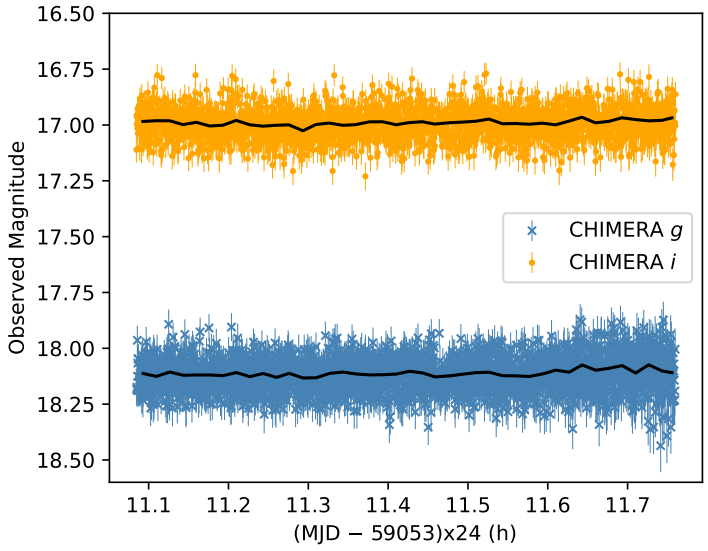

Figure 3.3: CHIMERA photometry of AT2019wey.

mode with a frame exposure time of 1 s, and obtained 3300 frames in each filter. We reduced the data with a custom pipeline[2]. Figure 3.3 shows the CHIMERA light curve. The black lines show light curves averaged to 1 min. AT2019wey appears to exhibit intra-night variability of ~ 0.1 mag. The median magnitudes are $i = 16.99 \pm 0.07$ and $g = 18.12 \pm 0.08$. The g-band rms increased toward the end of the observation due to the onset of twilight.

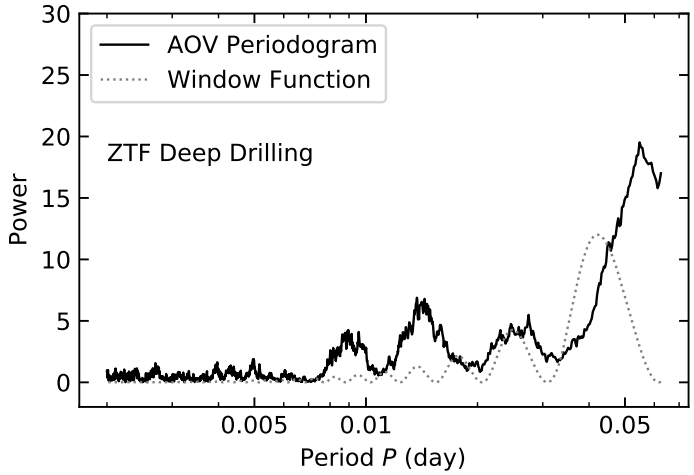

Figure 3.4: The periodogram and window function for the ZTF deep drilling dataset.

[2]https://github.com/mcoughlin/kp84

Period Search

We ran a periodicity search on the CHIMERA and the ZTF deep drilling datasets using the analysis of variance (AOV) method (Schwarzenberg-Czerny, 1998)[3]. We used a frequency grid from 16 d^{-1} to 500 d^{-1} for the ZTF data, and a frequency grid from 48 d^{-1} to 40,000 d^{-1} for the CHIMERA data. To see how the observational cadence affects the periodogram, we used the Lomb-Scargle algorithm (see a recent review by VanderPlas 2018) to compute the window function.

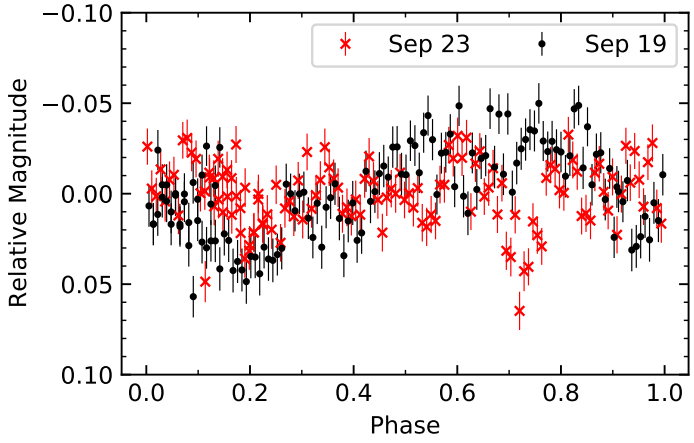

Figure 3.5: The ZTF deep-drilling light curve, relative to the median, folded on a period of 0.055 d.

We define "significance" of a period as the maximum value in the periodogram divided by the standard deviation of values across the full periodogram. A possible period at 0.055 d (1.3 hr) at a significance of 9.2 can be seen in the ZTF periodogram (see Figure 3.4). We note that the 1.3 hr peak is mainly caused by the sinusoidal-like structure observed on September 19, not the dip-like structure observed on September 23. Since the data on September 19 and 23 do not follow the same trend as a function of phase (see Figure 3.5), we consider the possible period at 1.3 hr to be spurious. No period above 8σ can be identified from the CHIMERA periodogram (see Figure 3.6).

UV Photometry

We obtained UV observations of AT2019wey with the Ultra-Violet/Optical Telescope (UVOT; Roming et al. 2005) on board the *Neil Gehrels Swift Observatory* (Gehrels et al., 2004) from 2020 April to September. The UVOT data were pro-

[3]We used the `python` script provided by `https://users.camk.edu.pl/alex/\#software`

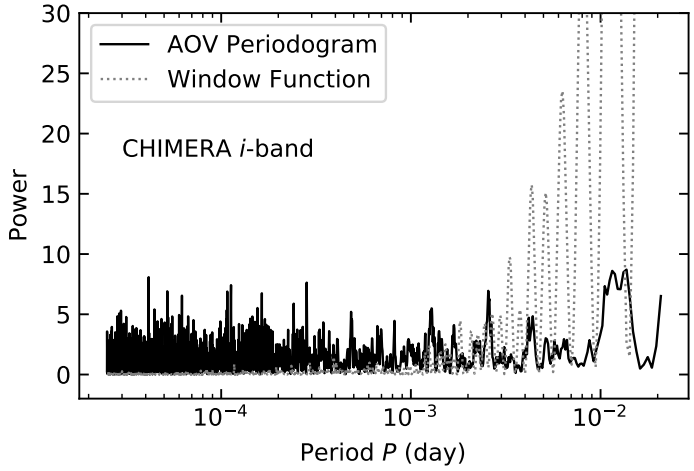

Figure 3.6: The periodogram and window function for CHIMERA *i* band.

cessed using `HEASoft`. We extracted the photometry with `uvotsource` using a 3″ circular aperture. Background counts were estimated in a 10″ source-free circular aperture. AT2019wey was only marginally detected in April. Therefore, for the April datasets, we undertook photometry on co-added images.

In October 2020, we obtained U-band photometry using the Spectral Energy Distribution Machine (SEDM, Blagorodnova, Neill, et al. 2018, Rigault et al. 2019) on the robotic Palomar 60-inch telescope (P60, Cenko, Fox, et al. 2006). Data reduction was performed using the `FPipe` pipeline (Fremling, Sollerman, et al., 2016). The UVOT and SEDM photometry are presented in Table 3.5 and is shown in the middle panel of Figure 3.2.

3.4 Optical and NIR Spectroscopy

A log of our spectroscopic observations is given in Table 3.1. The instrumental and observational details can be found in §3.8.

Optical Spectroscopy

We identify the following features at redshift $z = 0$ in all of our spectra: Balmer absorption lines, Ca II H and K lines, the Na I D doublet, diffuse interstellar band (DIB) λ5780, λ6283 absorption features, and the Balmer jump (Figure 3.7, 3.8). He II λ4686 emission seems to be detected in the spectra obtained on July 31, August 14, and September 20. We conclude that AT2019wey is a transient of Galactic stellar origin.

From March to September, the hydrogen profile clearly changed (Figure 3.8).

Table 3.1: Log of AT2019wey spectroscopy.

Date in 2020	Telescope/ Instrument	Range (Å)	Exp. (s)	Airmass
Mar 23	Keck-I/LRIS	3200–10250	300	2.22
Jul 31	P200/DBSP	3410–5550, 5750–9995	600	1.38
Aug 13	Keck-II/NIRES	9400–24650	360	1.38
Aug 14	P200/DBSP	3410–5550, 5750–9995	600	1.34
Aug 29	P200/DBSP	3410–5550, 5750–9995	600×2	1.40
Sep 12	Keck-II/ESI	3950–10200	1800	1.32
Sep 20	Keck-I/LRIS	3200–10250	300×2	1.28

All spectra have been uploaded to the TNS page of this source (`https://www.wis-tns.org/object/2019wey`). Multiple exposures were obtained on 2020 August 29 and September 20. Since no significant variability was observed on the timescale of 5–10 min, summed spectra were produced for the two dates.

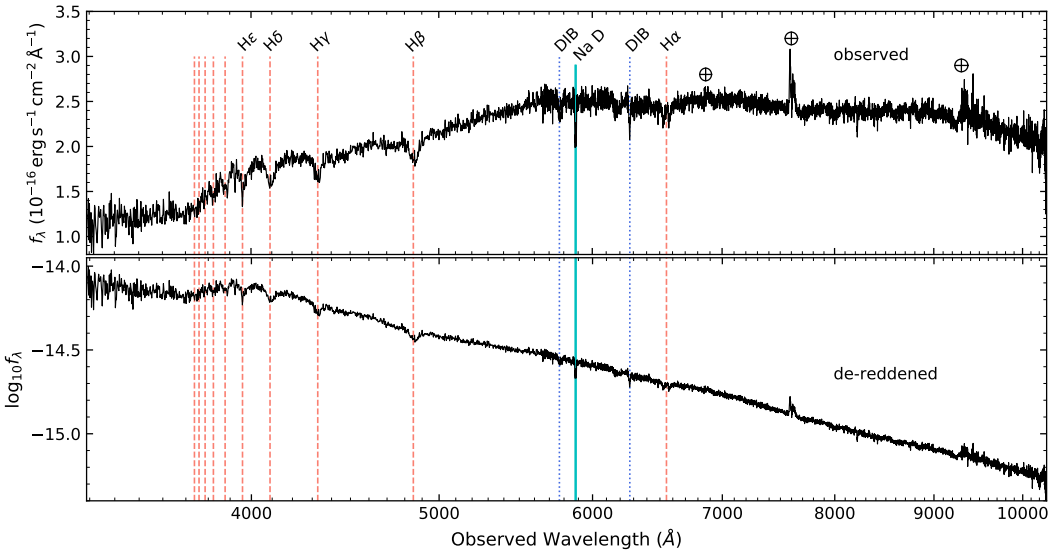

Figure 3.7: LRIS spectrum of AT2019wey obtained on 2020 March 18.

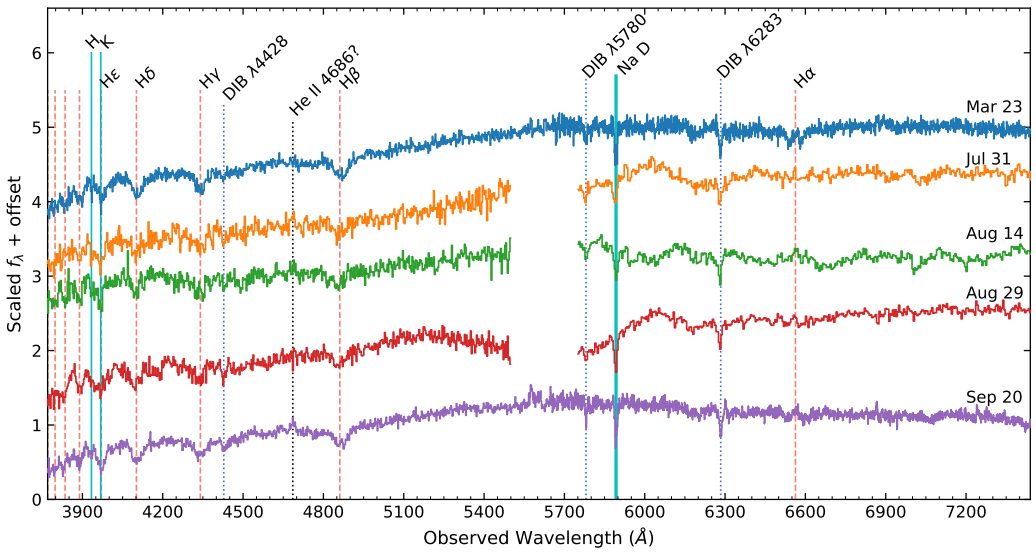

Figure 3.8: Low-resolution optical spectra of AT2019wey (Table 3.1).

Figure 3.9 presents the velocity profiles of Balmer lines in the March 23 and the September 12 spectra. On March 23, we observed a relatively narrower (FWHM$\sim$ 1200 km s^{-1}) emission component in the middle of a rotationally broadened (FWHM$\sim$ 2700 km s^{-1}) shallow absorption trough. At the same epoch, we also observed broad Hβ and Hγ absorption features with FWHM$\sim$ 2000–3000 km s^{-1}. There was a marginal detection of narrow emission cores redshifted by $\sim$ 300–400 km s^{-1} from the line center of the absorption troughs. On September 12, we observed flat-topped Hα in emission ($\sim$ 400 km s^{-1}), while the Hβ and Hγ profiles were similar to the Hα profile on March 23. The variable Balmer features are discussed further in §3.6.

The reddening of AT2019wey can be constrained to $0.8 < E(B-V) < 1.2$ (§3.8) using the equivalent width (EW) of the interstellar absorption lines. We find a lower limit to the distance of AT2019wey of $D > 1$ kpc using the velocities of the Na I doublet in the ESI spectrum (§3.8). In addition, since AT2019wey is in the Galactic anti-center direction, the distance to AT2019wey is likely less than $\sim$10 kpc. Taken together, we conclude that the distance of AT2019wey is between $\sim$1 kpc and $\sim$10 kpc.

NIR Spectroscopy

The NIR spectrum of AT2019wey is shown in Figure 3.10. Hydrogen emission lines of Paγ, Paβ, and Brγ are clearly distinguished. We tentatively attribute the emission

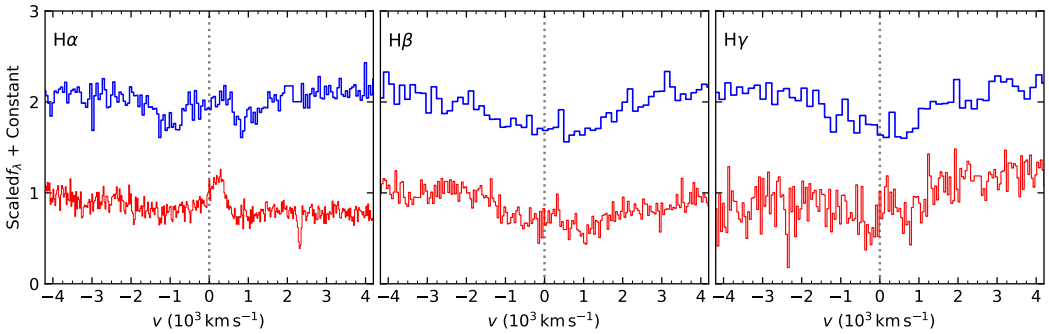

Figure 3.9: Velocity of the Balmer lines in AT2019wey. The 2020 March 23 LRIS spectrum is shown on the top (in blue) and the 2020 September 12 ESI spectrum is shown on the bottom (in red).

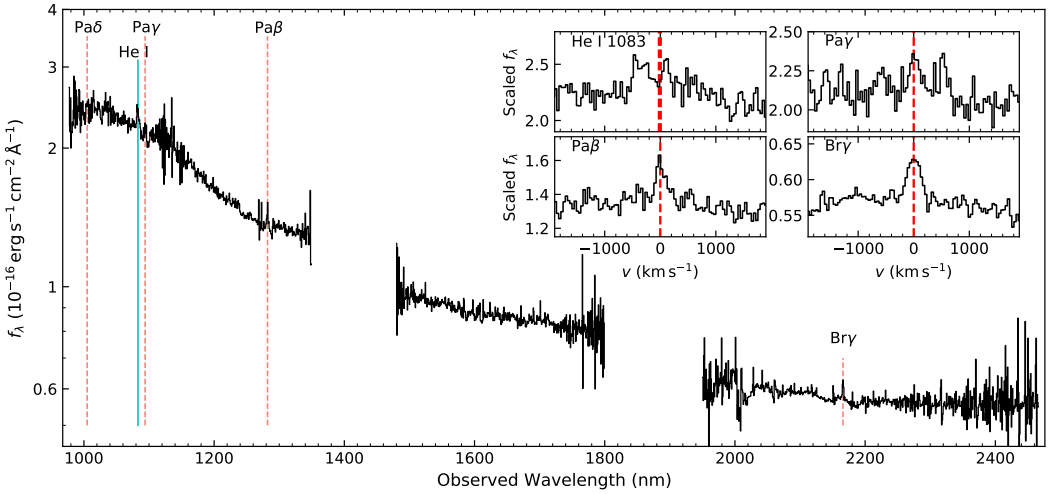

Figure 3.10: NIRES spectrum of AT2019wey. The insets show the zoom-in on emission lines in velocity space.

lines around 1083 nm to double-peaked He I. No absorption lines or molecular bands from the secondary star can be identified. With a FWHM of $\approx$ 200–300 km s^{-1}, the velocities of NIR emission features are much narrower than the Hα line, hinting at different formation locations in the accretion disk.

3.5 Radio Observations

We monitored AT2019wey with the VLA (Perley, Chandler, et al., 2011) under the Director's Discretionary Time programs 20A-591 and 20B-397 (PI: Y. Yao). The data were calibrated using the standard VLA Pipeline. We present the flux density of our VLA detections along with the radio detections reported by Cao, Frey, et al. (2020) and Cao, Giroletti, et al. (2020) in Table 3.2. We fit a power-law (PL)

Table 3.2: Radio observations of AT2019wey.

Date	ν_0 (GHz)	f_ν (μJy)	α
2020-05-27	5.0	197 ± 20	0.51 ± 0.69
	6.0	220 ± 22	
	7.0	234 ± 23	
2020-08-02	2.5	218 ± 49	−0.82 ± 0.23
	3.5	205 ± 16	
	10.0	82 ± 11	
2020-08-14	1.5	1023 ± 75	0.23 ± 0.02
	2.5	998 ± 59	
	3.5	1077 ± 18	
	8.5	1420 ± 12	
	9.5	1399 ± 11	
	10.5	1447 ± 13	
	11.5	1431 ± 13	
2020-08-21	1.5	1676 ± 102	0.19 ± 0.01
	2.5	1767 ± 51	
	3.5	1923 ± 18	
	8.5	2340 ± 18	
	9.5	2393 ± 18	
	10.5	2376 ± 18	
	11.5	2353 ± 19	
2020-08-28	1.5	1846 ± 128	0.20 ± 0.01
	2.5	1891 ± 34	
	3.5	2048 ± 15	
	8.5	2529 ± 11	
	9.5	2542 ± 16	
	10.5	2536 ± 18	
	11.5	2511 ± 20	
2020-10-17	6.7	1350 ± 220	—
2021-02-17	1.5	1565 ± 44	0.01 ± 0.01
	2.5	1394 ± 16	
	3.5	1435 ± 10	
	8.5	1658 ± 12	
	9.5	1553 ± 13	
	10.5	1407 ± 11	
	11.5	1295 ± 11	

ν_0 is central frequency. The spectral index α ($f_\nu \propto \nu^\alpha$) is fitted using the Markov chain Monte Carlo (MCMC) approach with `emcee` (Foreman-Mackey, Hogg, et al., 2013). The uncertainties are calculated using the 90% quantiles from the MCMC run.

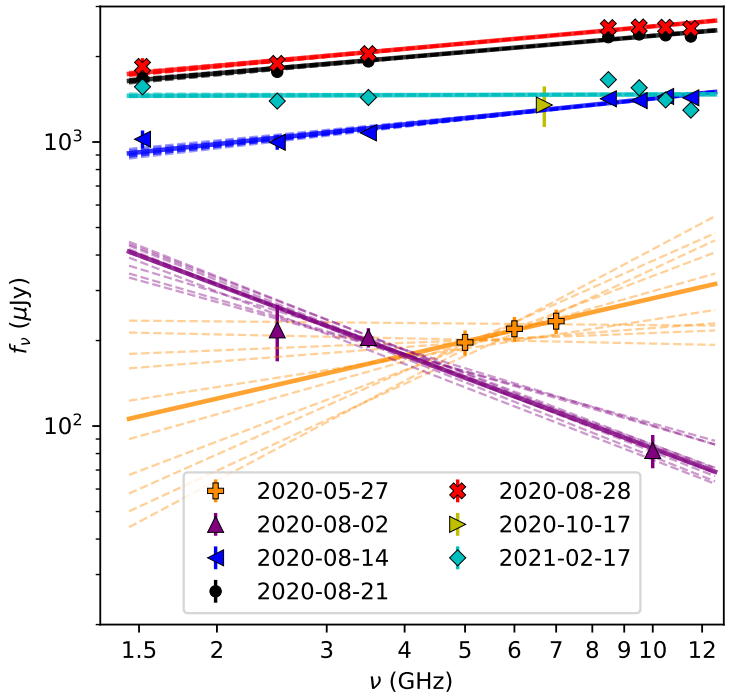

Figure 3.11: Radio SEDs of AT2019wey.

function ($f_\nu \propto \nu^\alpha$) to the data; see Figure 3.11 for model fits and Table 3.2 for the value of α.

Other than for August 2, the power law fit is flat or slightly inverted ($\alpha \approx 0$–0.5). Usually this is attributed to synchrotron self-absorption and is frequently seen in the low-hard-state (LHS) and hard-intermediate state (HIMS) of X-ray binaries (Fender, 2001; Fender, Belloni, and Gallo, 2004). On August 2, however, a "standard" spectral index of ~ -0.8 was observed. The change of spectral index may indicate the existence of a multi-zone jet. Yadlapalli et al. (2021) reported the detection of a resolved radio source by VLBA in 2020 September, which was interpreted as a steady compact jet.

3.6 Discussion

The archival (historical) optical data (see §3.8) establish a faint quiescent counterpart: $r_{\rm SDSS} > 22.6$. For $0.8 < E(B-V) < 1.2$, the corresponding extinction is $2.2 < A_{r_{\rm SDSS}} < 3.3$. Combined with our distance limit of $D < 10\,$kpc, this restricts the donor star to have an absolute magnitude of $M_R > 4.3$. For a main sequence star, this corresponds to a spectral type later than G2 and a stellar mass $< 1\,M_\odot$. For a subgiant star, the stellar mass is even smaller. Therefore, the companion is a

low mass ($< 1\,M_\odot$) late-type, likely evolved star. The optical outburst amplitude for AT2019wey is $\Delta r > (22.6 - 17.4) = 5.2$ mag. Using an empirical relation between Δr and $P_{\rm orb}$ for short-period LMXBs (Shahbaz and Kuulkers, 1998), we find the orbital period, $P_{\rm orb} \lesssim 16$ hr.

Radio–X-ray Correlation

Figure 3.12 shows AT2019wey on the $L_{\rm radio}$–$L_{\rm X}$ diagram, compared with quiescent/hard state BHs, NSs, accreting millisecond X-ray pulsars (AMXPs), transitional millisecond pulsars (tMSPs), and cataclysmic variables (CVs) (Bahramian, Miller-Jones, et al., 2018). We mark the positions of AT2019wey at four epochs for possible distances of 1–3–10 kpc. The position of AT2019wey is above the region occupied by the majority of NS binaries and is closer to BH binaries. Therefore, the bright radio luminosity favors a BH accretor.

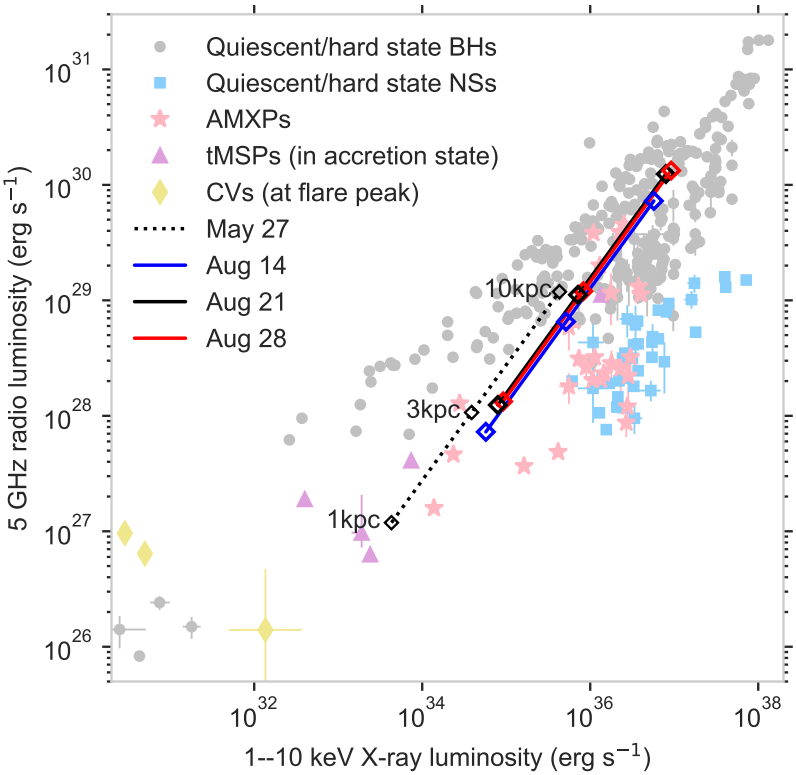

Figure 3.12: The $L_{\rm radio}$–$L_{\rm X}$ diagram of AT2019wey and various populations of X-ray sources.

Multi-wavelength Light Curve

We separate the multi-wavelength light curve of AT2019wey into five stages (see the bottom panel of Figure 3.2): (i) Before MJD~ 58814, the source was in quiescence; (ii) From MJD~ 58814 to MJD~ 58880, the optical light curve exhibited a fast-rise linear-decay outburst, after which it settled onto a r-band flux of $f_{\nu,r} \sim 315\,\mu$Jy. Around the same time, the X-ray flux rose to ~ 1 mCrab, and stayed in the LHS; (iii) From MJD~ 58880 to MJD~ 59010, the optical and X-ray light curves stayed almost flat; (iv) From MJD~ 59010 to MJD~ 59080, AT2019wey exhibited a multi-wavelength brightening, and the X-ray remained in the LHS (Yao, Kulkarni, Gendreau, et al., 2021); (v) From MJD~ 59081 to MJD~ 59180, the source entered into the HIMS (Yao, Kulkarni, Gendreau, et al., 2021). The optical stayed around $f_{\nu,r} \sim 400\,\mu$Jy, and X-ray stayed around ~ 20 mCrab (Yao, Kulkarni, Gendreau, et al., 2021).

Table 3.3: X-ray and optical luminosity of AT2019wey at different stages of the multi-wavelength evolution.

Stage	Band	Luminosity	Comments
(iii)	r & g	4.0×10^{34} & 6.1×10^{34}	Averaged between MJD~ 58880 and MJD~ 59010
(iii)	X-ray	1.0×10^{35}	Averaged between MJD~ 58951 and MJD~ 58967
(v)	r & g	4.9×10^{34} & 8.4×10^{34}	Averaged between MJD~ 59080 and MJD~ 59153
(v)	X-ray	$(1.3\text{–}1.7)\times10^{36}$	From minimum (MJD~ 59082) to maximum (MJD~ 59112)

Luminosity is given in units of $(D/5\,\mathrm{kpc})^2\,\mathrm{erg\,s^{-1}}$. X-ray column density corrected luminosity is given in 2–10 keV, assuming $N_\mathrm{H} = 5\times10^{21}\,\mathrm{cm^{-2}}$. Optical luminosity has been corrected for extinction, adopting $E(B-V) = 0.9$.

UV/optical–X-ray Correlation — During stage (iv), the X-ray and radio fluxes increased by a factor of $\gtrsim 10$ but in the optical/UV the increase was modest, between a factor of 1.3 and 2. During stages (iii) and (v), the source was stable and representative luminosities can be found in Table 3.3. For these two stages, following Russell, Fender, et al. (2006), we link the UV/optical and X-ray luminosities as

$$L_\mathrm{UV/opt} = A L_\mathrm{X}^\beta, \tag{3.1}$$

and find $\beta \sim 0.08$ in r band, $\beta \sim 0.12$ in g band, and $0.12 \lesssim \beta \lesssim 0.34$ in the UV bands. Russell, Fender, et al. (2006) derived $A = 10^{13.1\pm0.6}$, $\beta = 0.61 \pm 0.02$ for a sample of 15 BH LMXBs, and $A = 10^{10.8\pm1.4}$, $\beta = 0.63 \pm 0.04$ for a sample of 8 NS LMXBs. As can be seen from Figure 3.13, over the distance range of $1 \lesssim D \lesssim 10$ kpc, the inferred luminosities of AT2019wey are suggestive of an accreting BH system.

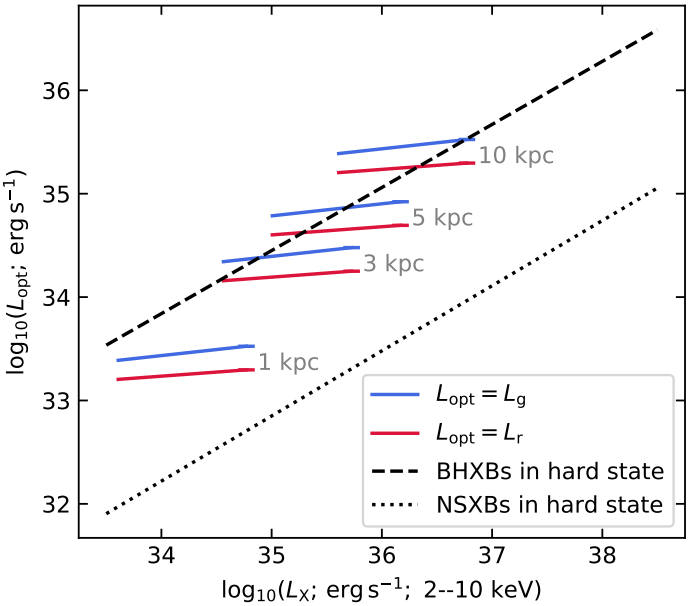

Figure 3.13: The correlation between optical and X-ray luminosities of AT2019wey from stage (iii) to stage (v).

Possible Mechanisms for the Optical Emission — In BH LMXBs in the hard state, the optical/UV emission can arise from (1) X-ray reprocessing in the outer accretion disk; (2) the optically thick jet spectrum extending from centimeter wavelengths; (3) intrinsic thermal emission from the viscously heated outer accretion disk. For processes (1) and (2), the expected slopes are $\beta \sim 0.5$ (van Paradijs and McClintock, 1994), and $\beta \sim 0.7$ (Corbel et al., 2003; Russell, Fender, et al., 2006), respectively. For process (3), β ranges from 0.13 (Rayleigh–Jeans or R–J tail) to 0.33 (between the R–J tail and the Wien cut-off) (Tetarenko, Dubus, Marcel, et al., 2020). Russell, Fender, et al. (2006) find $\beta \sim 0.6$ for BH LMXBs, which suggests that process (3) is not dominant. However, the observed $\beta \sim 0.1$ for AT2019wey favors process (3).

Curiously, we note that such small values of β have been observed in two BH LMXBs with short orbital periods: $\beta \sim 0.2$ (Armas Padilla et al., 2013) in Swift J1357.2−0933 ($P_{\rm orb} = 2.8$ h; Corral-Santana, Casares, Muñoz-Darias, Rodríguez-Gil, et al. 2013; Mata Sánchez et al. 2015) and $\beta \sim 0.2$ (Chiang et al., 2010) in Swift J1753.5−0127 ($P_{\rm orb} \lesssim 3.2$ h; Zurita, Durant, et al. 2008; Neustroev et al. 2014; Shaw, Charles, Casares, et al. 2016). Interestingly, the X-rays for these two systems are only observed in the LHS or HIMS, without successful transitions to the high/soft state (HSS) (Armas Padilla et al., 2013; Tetarenko, Sivakoff, Heinke, et al.,

2016). These similarities might be understood as characteristics of a sub-population of BH LMXBs (Shaw, Charles, Bird, et al. 2013, see §3.7).

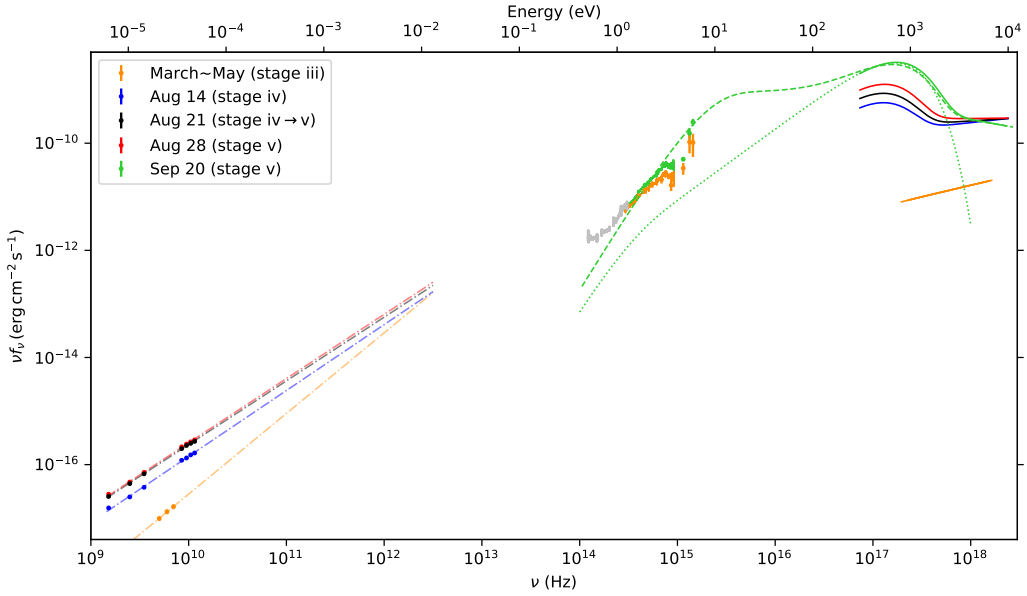

Figure 3.14: Multi-wavelength SED of AT2019wey.

Multi-wavelength SED

The spectral energy distribution (SED) of AT2019wey is shown in Figure 3.14. In the radio, we show the observed data and power-law fits (Table 3.2). In UV/optical/NIR, we show the dereddened photometry and spectra assuming $E(B-V) = 0.9$. Note that the silver NIR spectrum, the orange optical spectrum, and the green optical spectrum were obtained on August 13, March 20, and September 20, respectively (Table 3.1). In X-ray, we show the best fits to X-ray data corrected for a fixed column density of $N_{\rm H} = 5 \times 10^{21}$ cm^{-2}. The dashed and dotted green lines from optical to X-ray are illustrative models of irradiation and standard disk emission, respectively.

Below we first we briefly summarize the X-ray spectra. Next, based on radio data, we conclude that jet emission is unlikely to be the dominant mechanism in the optical. After that, we show that the UV/optical emission during stage (iii) originates from the intrinsic emission of a truncated accretion disk. Finally, we show that the UV/optical emission during stage (v) arises from X-ray reprocessing.

(1) The X-ray SED — Briefly speaking, the X-ray spectrum observed in stage (iii) can be described by an absorbed power-law with photon index $\Gamma = 1.8$. In stages (iv) and (v), the X-ray spectrum can be fitted with a combination of disk-

blackbody (`diskbb`, Shakura and Sunyaev 1973; Mitsuda et al. 1984) and power-law components (Yao, Kulkarni, Gendreau, et al., 2021). On August 14, 21, and 28, the fitted models have $\Gamma \sim 1.9$ and inner disk temperature $T_{\rm disk} \sim 0.21$ keV$\sim 2.4\times10^6$ K. The inner disk radius is

$$R_{\rm in} \sim (360\text{–}470) \left(\frac{\cos i}{1}\right)^{-1/2} \left(\frac{D}{5\,\rm kpc}\right) \rm km. \tag{3.2}$$

On September 20, the soft X-ray flux reached a local maximum in the HIMS, where the PL softened to $\Gamma = 2.3$ and the inner disk temperature increased to $T_{\rm disk} \sim 0.29$ keV$\sim 3.4 \times 10^6$ K, while the inner disk radius remains at ~ 400 km. The fitted $T_{\rm disk}$ and $R_{\rm in}$ are typical for thermal emission from a truncated accretion disk observed in the LHS and HIMS of BH LMXBs (Done, Gierliński, and Kubota, 2007). Denoting the innermost stable circular orbit radius as $R_{\rm ISCO} = 6GM/c^2$ and the Schwarzschild radius as $R_{\rm S} = 2GM/c^2$, then $R_{\rm in} \sim 15R_{\rm S} \sim 5R_{\rm ISCO}$ for a $10\,M_\odot$ non-spinning black hole.

(2) The Radio SED — The dashed-dotted lines shown in Figure 3.14 are best-fit power-laws for the radio data (Table 3.2) extrapolated to 3×10^{12} Hz. If the spectrum remains optically thick all the way to the optical and near-infrared (OIR) wavelengths, it will over-predict the observed OIR spectrum. Assuming a classical jet spectrum of a broken PL (Blandford and Königl, 1979), the break frequency must be $\ll 10^{14}$ Hz. The optically thin jet spectrum may contribute a fraction of NIR emission (grey data in Figure 3.14), but is unlikely to dominate in the optical.

(3) UV/Optical Emission in the Dim LHS — In Figure 3.15, we show the UV/optical data and the best-fit X-ray model in the dim LHS (stage iii) in orange. Single-temperature blackbody models are shown in the upper panel, while disk-blackbody models are shown in the lower panel. All models are normalized to match the flux in r band. $D = 5$ kpc and $\cos i = 1$ are assumed. The upper and lower bounds of the yellow region are obtained by dereddening the observed data using $E(B-V) = 1.2$ and 0.7, respectively. No detailed model fits are performed due to the uncertainty of $E(B-V)$. The low level of X-ray flux (compared to that in the UV/optical) suggests that there is not enough X-ray flux to illuminate the outer accretion disk. As a result, the UV/optical probably comes from the intrinsic thermal emission of an accretion disk.

To obtain a constraint on the outermost annulus of the accretion disk, we compute a set of simple blackbody models (upper panel of Figure 3.15). We adopt the 11,000 K blackbody as an approximation of the outer disk annulus, and compute a

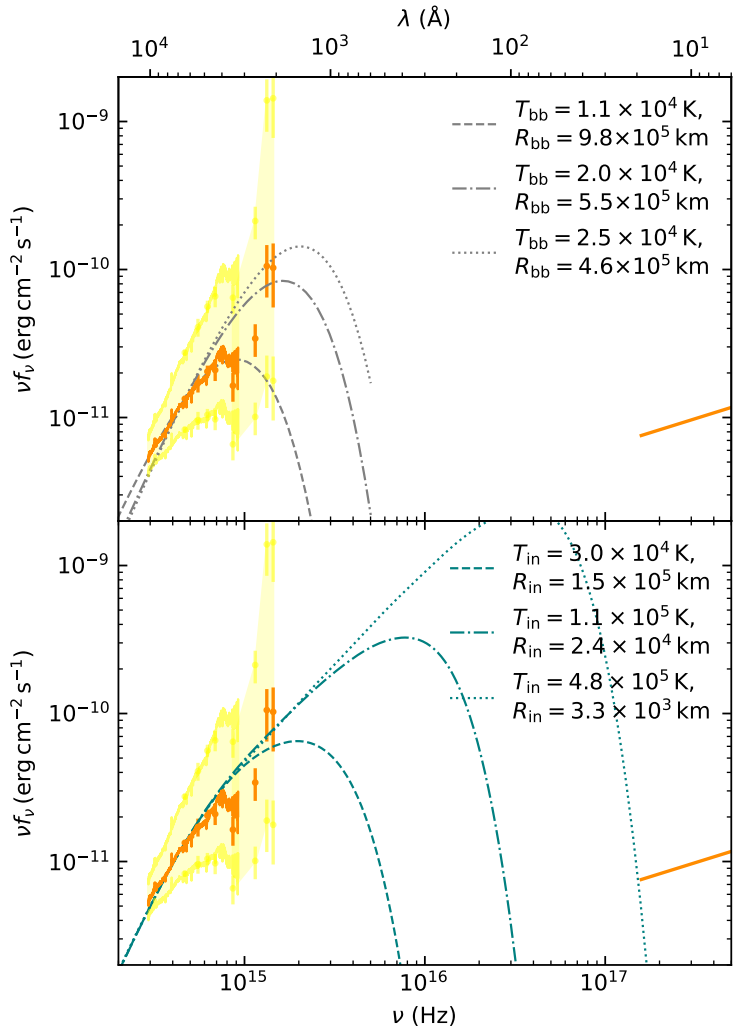

Figure 3.15: X-ray–UV–optical SED of AT2019wey in the dim LHS.

set of `diskbb` models to obtain a lower limit to the inner disk radius (and an upper limit to the inner disk temperature). The dotted line in the lower panel of Figure 3.15 suggests $T_{\rm in} < 4.8 \times 10^5$ K and $R_{\rm in} > 3.3 \times 10^3$ km$\sim 38 R_{\rm ISCO} \sim 114 R_{\rm S}$.

Similar SED shapes have been observed in the LHS of a few BH LMXBs, including XTE J1118+480 ($R_{\rm in} = 300 R_{\rm S}$; Yuan, Cui, and Narayan 2005) and Swift J1753.5−0127 ($R_{\rm in} > 100 R_{\rm S}$; Froning et al. 2014). The observed SED of AT2019wey in the dim LHS fits into the advection-dominated accretion flow (ADAF; Narayan and Yi 1994; Narayan and Yi 1995b) model of a hot accretion flow around a BH, which is predicted at low-accretion rates (see reviews by Done, Gierliński, and Kubota 2007; Yuan and Narayan 2014; Poutanen and Veledina 2014). If so, the X-ray PL comes from a high-temperature flow in the central regions close to the BH, while the UV/optical

thermal component comes from a geometrically thin, optically thick accretion disk truncated far from the ISCO (Yuan and Narayan, 2014).

(4) UV/Optical Emission in the HIMS — The dotted green line in Figure 3.14 shows an extrapolation of the `diskbb` fit on *NICER* data for September 20. It clearly under-predicts the observed UV/optical spectrum, making X-ray reprocessing the most likely origin of the UV/optical emission in the HIMS. We therefore attempt to fit the green data by the irradiation model `diskir` (Gierliński, Done, and Page, 2008; Gierliński, Done, and Page, 2009).

We set the inner disk temperature of the unilluminated disk and the asymptotic PL photon index to be the same as the best-fit September 20 model. The fraction of reprocessed luminosity in the Compton tail ($f_{\rm in}$) is fixed at 0.1. The electron temperature is fixed at 1000 keV as there is no sign of a high-energy PL cutoff (see Yao, Kulkarni, Gendreau, et al. 2021). The dashed green line in Figure 3.14 is a schematic fit with the following parameters: the ratio of luminosity in the Compton tail to that of the unilluminated disk $L_{\rm C}/L_{\rm d} = 0.22$, the radius of the Compton illuminated disk $R_{\rm irr} = 1.2R_{\rm in}$, the fraction of thermalized bolometric flux $f_{\rm out} = 0.08$, $R_{\rm out} = 10^{3.55}R_{\rm in}$, and the normalization parameter of the un-illuminated disk (Eq. 3.2) ≈ 370 km. We conclude that the UV/optical SED in the HIMS is due to reprocessing of the X-ray irradiation.

Optical Spectral Lines

The hydrogen lines in AT2019wey display both broad absorption and emission components (§3.4). This behavior is reminiscent of some LMXBs and CVs, where the hydrogen absorption and emission lines are thought to arise from different layers of the viscous accretion disk (Horne and Marsh, 1986; La Dous, 1989; Warner, 1995). In a few BH LMXBs, such as GRO J1655−40 (Soria, Wu, and Hunstead, 2000), GRO J0422+32 (Callanan et al., 1995), XTE J1118+480 (Dubus, Kim, et al., 2001; Torres, Callanan, et al., 2002), and Swift J1753.5−0127 (Rahoui et al., 2015), double-peaked Hα was observed. The single-peaked hydrogen line profile of AT2019wey is similar to that observed in MAXI J1836−194 (Russell, Soria, et al., 2014), suggesting a binary system viewed close to face-on. This is in agreement with the low inclination ($i \lesssim 30^\circ$) constraint from modeling the X-ray reflection spectrum (Yao, Kulkarni, Gendreau, et al., 2021).

We have shown that in the HIMS, the UV/optical emission comes from the reprocessing of inner disk and coronal emission. Irradiation of the outer disk may

form a thin temperature-inversion layer on the disk surface (Tuchman, Mineshige, and Wheeler, 1990). This naturally explains the enhanced Balmer emission lines observed during stage (iv) and stage (v).

Most BH LMXBs show strong He II emission during their outbursts (Zurita, Sánchez-Fernández, et al., 2002; Kaur et al., 2012; Jiménez-Ibarra et al., 2019; Russell, Soria, et al., 2014). A lack of significant He II was observed in the optical spectra of AT2019wey. This might also be present in the 2009 outburst of XTE J1752−223 (Torres, Steeghs, et al., 2009), and the 2021 outburst of XTE J1859+226 (Bellm 2021, Bellm et al. in prep). We note that the He II recombination line was also not significantly detected in the outburst spectra of a few CVs (Morales-Rueda and Marsh, 2002). A possible explanation for this is that the number of photons with energies between 54 eV (the ionization potential of He^+) and 280 eV (the ionization potential of the carbon K-edge) is not large enough (Patterson and Raymond, 1985).

3.7 Conclusion

We have undertaken a detailed multi-wavelength follow-up of the X-ray transient AT2019wey. This study builds upon X-ray observations reported in Paper I, which show that AT2019wey is a LMXB with a NS or BH accretor. In this paper, we present the high radio and optical (§3.6) luminosities of AT2019wey. These properties, combined with the hard X-ray spectrum reported in Yao, Kulkarni, Gendreau, et al. (2021), indicate that AT2019wey is likely a BH system.

Multi-wavelength evolution of AT2019wey can be separated into five distinct stages, as illustrated in Figure 3.2. In the dim LHS [i.e., stage (iii)], the UV/optical emission comes from intrinsic thermal emission of an accretion disk with $R_{\rm in} > 100R_{\rm S}$. In the HIMS [i.e., stage (v)], the UV/optical emission comes from reprocessing of X-rays, and the disk truncation radius has moved inward ($R_{\rm in} \sim 15R_{\rm S}$). The overall SED evolution fits into the picture of a hot accretion flow consisting of an inner ADAF and a truncated disk. This confirms the widely accepted model for short-period BH LMXBs in the hard state.

The optical light curve of AT2019wey is distinguished by its flatness during stages (iii) and (v). This is different from the majority of LMXBs and is similar to what was observed during the 12 yr outburst of Swift J1753.5−0127 (Shaw, Tetarenko, et al., 2019; Zhang, Bernardini, et al., 2019). The X-ray light curve is reminiscent of the 'flat top' profile in the 1996 outburst of GRO J1655−40 (Esin, Lasota, and Hynes, 2000). As noted before (Esin, Lasota, and Hynes, 2000; Shaw, Tetarenko,

et al., 2019), the 'standstill' outburst is analogous to the Z Cam class of dwarf novae (Osaki, 1996). In such systems, the mass transfer rate ($\dot{M}_2$) during quiescence is $\lesssim \dot{M}_{\rm crit}$. Here $\dot{M}_{\rm crit}$ is the critical mass-transfer rate, above which the disk remains stable (Dubus, Lasota, et al., 1999; Lasota, Dubus, and Kruk, 2008). During the outburst, $\dot{M}_2$ increased to $\gtrsim \dot{M}_{\rm crit}$, stabilizing the accretion. In AT2019wey, the second stable period in stage (v) indicates a further increase of $\dot{M}_2$, probably caused by irradiation on the accretion disk or the companion star.

We note that if AT2019wey continues to remain sufficiently bright in the optical for an extended period of time, the next data release of the *Gaia* mission may help further constrain the distance. Once the distance is settled, future studies can estimate $\dot{M}_2$ during the stable stages. Comparison between $\dot{M}_2$ and $\dot{M}_{\rm crit}$ can provide a key probe to the evolution of X-ray binaries.

As discussed in Yao, Kulkarni, Gendreau, et al. (2021), *SRG* is sensitive to the population of BH LMXBs with faint X-ray outbursts. These outbursts are generally associated with lower mass accretion rates and shorter orbital periods (Meyer-Hofmeister, 2004; Wu et al., 2010; Tetarenko, Sivakoff, Heinke, et al., 2016). The discovery of AT2019wey showcases the possibility of hunting for similar systems in wide-field optical surveys. This has also been demonstrated in the case of the BH LMXB ASASSN-18ey (MAXI J1820+070), which was first discovered in the optical (Tucker et al., 2018), and then in the X-ray (Kawamuro et al., 2018). Perhaps the easiest approach to identify similar LMXBs is to study optical light curves of *SRG* point sources in the Galactic plane.

3.8 Appendix

Archival Limits

Optical Limits — We conducted an archival search of optical photometry at the position of AT2019wey. The source was not detected by historical optical surveys, including the Palomar Observatory Sky Survey I (POSS-I, Minkowski and Abell 1963), the Second Palomar Observatory Sky Survey (POSS-II, Reid et al. 1991), SDSS, and the Panoramic Survey Telescope and Rapid Response System DR1 (Pan-STARRS, PS1) (Flewelling et al., 2020; Waters et al., 2020), the intermediate Palomar Transient Factory (iPTF; Law et al. 2009; Rau et al. 2009), and the ZTF. We list 5σ upper limits in Table 3.4.

Radio Limit — AT2019wey was not detected in any archival radio database. The NRAO VLA Sky Survey (NVSS, Condon, Cotton, et al. 1998) provides an upper

Table 3.4: Historical upper limits at the position of AT2019wey.

Survey	Time	Filter	$\lambda_{\rm eff}$ (Å)	Limit
POSS-I	1953-10-08	r	6500	19.5
POSS-II	1990-10-26	r	6500	20.8
SDSS	2004-10-15	u	3560	22.5
		g	4720	23.1
		r	6190	22.6
		i	7500	22.0
		z	8960	20.9
PS1	2010-02–2014-12	g	4870	22.7
		r	6210	22.3
		i	7540	22.1
		z	8680	21.8
		y	9630	20.8
iPTF	2014-01-24	R	6420	21.0
ZTF	2017-12–2019-11	g	4810	21.3
		r	6420	21.5

limit of 2 mJy at 1.4 GHz in 1993–1996. The Karl G. Jansky Very Large Array Sky Survey (VLASS, Lacy et al. 2020) provides a 3σ upper limit of 0.40 mJy at 2–4 GHz in March 2019.

Instrumental/Observational Information

UVOT and SEDM photometry is provided in Table 3.5.

We obtained optical spectroscopic follow-up observations of AT2019wey using the Low Resolution ($R \approx 1000$) Imaging Spectrograph (LRIS; Oke, Cohen, et al. 1995) on the Keck-I telescope, the Double Spectrograph (DBSP; $R \approx 1200$; Oke and Gunn 1982) on the 200-inch Hale telescope, and the medium-resolution ($R \approx 13000$) Echellette Spectrograph and Imager (ESI; Sheinis et al. 2002) on the Keck-II telescope. We obtained NIR spectroscopy using the Near infrared emission spectroscopy (NIRES; $R = 2700$) on the Keck-II telescope. Spectroscopic observations were coordinated with the GROWTH Marshal (Kasliwal et al., 2019).

The DBSP spectra were reduced using the `pyraf-dbsp` pipeline (Bellm and Sesar, 2016). The LRIS spectra were reduced and extracted using `Lpipe` (Perley, 2019). The flat-fielding, wavelength solution (using sky lines) and extraction for the NIRES spectrum was carried out using the `spextool` code (Cushing, Vacca, and Rayner, 2004). The extracted spectrum was flux calibrated using the telluric A0V standard

Table 3.5: UVOT and SEDM photometry of AT2019wey.

Date	Instrument	Filter	mag
2020-04 Coadd	*Swift*/UVOT	B	18.93 ± 0.17
2020-04 Coadd	*Swift*/UVOT	U	20.16 ± 0.24
2020-04 Coadd	*Swift*/UVOT	$uvm2$	22.55 ± 0.42
2020-04 Coadd	*Swift*/UVOT	$uvw1$	21.17 ± 0.27
2020-04 Coadd	*Swift*/UVOT	$uvw2$	22.86 ± 0.50
2020-04 Coadd	*Swift*/UVOT	V	18.00 ± 0.15
2020-08-05	*Swift*/UVOT	$uvm2$	> 21.16
2020-08-09	*Swift*/UVOT	$uvm2$	22.16 ± 0.33
2020-08-12	*Swift*/UVOT	$uvw2$	21.83 ± 0.21
2020-08-19	*Swift*/UVOT	U	19.35 ± 0.06
2020-08-26	*Swift*/UVOT	$uvw1$	20.78 ± 0.13
2020-09-02	*Swift*/UVOT	$uvm2$	22.12 ± 0.43
2020-09-09	*Swift*/UVOT	$uvw2$	22.00 ± 0.24
2020-09-16	*Swift*/UVOT	U	19.26 ± 0.07
2020-09-23	*Swift*/UVOT	$uvw1$	20.72 ± 0.13
2020-10-21	P60/SEDM	U	19.11 ± 0.09
2020-10-25	P60/SEDM	U	19.21 ± 0.31

magnitude is observed (without extinction correction).

star HIP 16652 with the `xtellcor` code (Vacca, Cushing, and Rayner, 2003). The ESI spectrum was reduced using the `MAKEE`[4] pipeline following the standard procedure. Flux calibration was not performed on the ESI spectrum.

Details of Analysis

Extinction Estimation — The EW of interstellar absorption lines has been observed to be correlated with the amount of reddening. To estimate the extinction of AT2019wey, we produced a summed spectrum from the LRIS and ESI spectra. We did not include DBSP spectra in this analysis since the CCD malfunction resulted in non-astrophysical structures between 5750 Å and 6200 Å in the continuum. This problem prevents EW of spectral lines from being accurately determined from DBSP spectra. The EW of DIB $\lambda\lambda$5780, λ6283 and Na I D lines were measured from the summed spectrum. As a result, we got $EW(\lambda 5780) = 0.56 \pm 0.02$ Å, and $EW(\lambda 6283) = 1.55 \pm 0.02$ Å. These can be converted to $E(B-V) = 0.92 \pm 0.02$ and 1.23 ± 0.02 using relations presented by Yuan and Liu (2012). We got EW(Na I D) $= 1.84 \pm 0.02$ Å, which can be converted to $E(B-V) = 2.01 \pm 0.38$ using the

[4] `http://www.astro.caltech.edu/~tb/ipac_staff/tab/makee/`

relation in Poznanski, Prochaska, and Bloom (2012).

The inferred $E(B-V)$ values are greater than the total Galactic extinction of $E(B-V) = 0.88$ (Schlafly and Finkbeiner, 2011). However, we note that at the measured EW, the calibration uncertainty is large. From Yuan and Liu (2012, upper panels of Fig. 4) and Poznanski, Prochaska, and Bloom (2012, bottom panel of Fig. 9), we infer that $E(B-V)$ towards AT2019wey should be $\gtrsim 0.8$.

We also attempt to infer the extinction by assuming that the 6000–10000 Å March 23 LRIS spectrum is in the Rayleigh–Jeans (R–J) tail of a blackbody ($f_\lambda \propto \lambda^{-4}$ when $h\nu \ll kT$), which yields $E(B-V) = 1.29$ and a blackbody radius ($R_{\rm bb}$) of

$$R_{\rm bb} = (4.5\times10^{10}\,{\rm cm})\left(\frac{D}{5\,{\rm kpc}}\right)\left(\frac{T_{\rm bb}}{5.0\times10^4\,{\rm K}}\right)^{-1/2} \tag{3.3}$$

Note that this is likely an overestimate of the true extinction (and a lower limit of the outer disk radius), since the optical is only in the R–J limit when $kT \gg 2\,{\rm eV}$ ($T \gg 2\times10^4\,{\rm K}$). For instance, for an extinction of $E(B-V) \sim 0.9$, we have

$$R_{\rm bb} = (1.0\times10^{11}\,{\rm cm})\left(\frac{D}{5\,{\rm kpc}}\right)\left(\frac{T_{\rm bb}}{1.1\times10^4\,{\rm K}}\right)^{-1/2} \tag{3.4}$$

Lower Limit of Distance — We have found that AT2019wey should have an extinction of $0.8 \lesssim E(B-V) \lesssim 1.2$. If this is from diffuse interstellar absorption, the distance of AT2019wey should be greater than 1 kpc using the map of STructuring by Inversion the Local Interstellar Medium (Stilism[5]; Capitanio, Lallement, et al. 2017).

We are able to put a lower limit to the distance using the velocity of the Na I D doublets in the ESI spectrum, given that the lines arise from interstellar absorption by a dust cloud along the line-of-sight to AT2019wey. The spectrum is heliocentric velocity corrected. The velocities of D1 and D2 lines were measured to be $-11.75\pm1.13\,{\rm km\,s^{-1}}$ and $-9.83\pm1.13\,{\rm km\,s^{-1}}$, respectively (see Figure 3.16). Assuming that the velocity of the dust cloud follows Galactic rotation, we have

$$V_{{\rm obs},r} = Ad\sin(2l) \tag{3.5}$$

where $A = 15.3\pm0.4\,{\rm km\,s^{-1}\,kpc^{-1}}$ is the Oort A constant (Bovy, 2017), $l = 151.2°$ is the Galactic longitude of AT2019wey, and d is distance to the dust cloud. Therefore, Eq. (3.5) gives $d = 0.83\,{\rm kpc}$.

[5] https://stilism.obspm.fr/

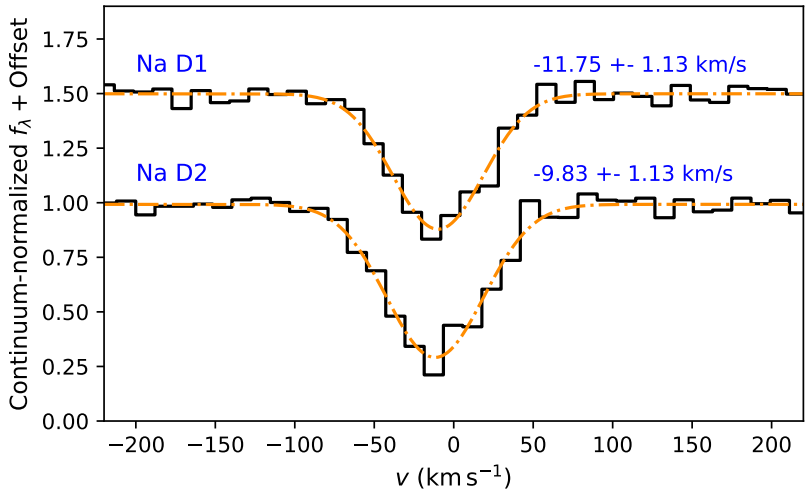

Figure 3.16: Na I D lines of AT2019wey.

Chapter 4

THE X-RAY AND RADIO LOUD FAST BLUE OPTICAL TRANSIENT AT2020MRF: IMPLICATIONS FOR AN EMERGING CLASS OF ENGINE-DRIVEN MASSIVE STAR EXPLOSIONS

Yao, Y. et al. (Aug. 2022). In: *ApJ* 934.2, 104, p. 104. DOI: 10.3847/1538-4357/ac7a41.

Yuhan Yao[1], Anna Y. Q. Ho[2,3], Pavel Medvedev[4], Nayana A. J.[5], Daniel A. Perley[6], S. R. Kulkarni[1], Poonam Chandra[7], Sergey Sazonov[4,8], Marat Gilfanov[4,9], Georgii Khorunzhev[4], David K. Khatami[2], and Rashid Sunyaev[4,9]

[1] Division of Physics, Mathematics and Astronomy, California Institute of Technology, Pasadena, CA 91125, USA
[2] Department of Astronomy, University of California, Berkeley, 501 Campbell Hall, Berkeley, CA, 94720, USA
[3] Miller Institute for Basic Research in Science, 468 Donner Lab, Berkeley, CA 94720, USA
[4] Space Research Institute, Russian Academy of Sciences, Profsoyuznaya ul. 84/32, Moscow, 117997, Russia
[5] Indian Institute of Astrophysics, II Block, Koramangala, Bangalore 560034, India
[6] Astrophysics Research Institute, Liverpool John Moores University, IC2, Liverpool Science Park, 146 Brownlow Hill, Liverpool L3 5RF, UK
[7] National Centre for Radio Astrophysics, Tata Institute of Fundamental Research, P.O. Box 3, Pune, 411007, India
[8] Moscow Institute of Physics and Technology, Institutsky per. 9, 141700 Dolgoprudny, Russia
[9] Max-Planck-Institut für Astrophysik, Karl-Schwarzschild-Str. 1, D-85741 Garching, Germany

Abstract

We present AT2020mrf (SRGe J154754.2+443907), an extra-galactic ($z = 0.1353$) fast blue optical transient (FBOT) with a rise time of $t_{g,\mathrm{rise}} = 3.7$ days and a peak luminosity of $M_{g,\mathrm{peak}} = -20.0$. Its optical spectrum around peak shows a broad ($v \sim 0.1c$) emission feature on a blue continuum ($T \sim 2 \times 10^4$ K), which bears a striking resemblance to AT2018cow. Its bright radio emission ($\nu L_\nu = 1.2 \times 10^{39}\,\mathrm{erg\,s^{-1}}$; $\nu_{\mathrm{rest}} = 7.4$ GHz; 261 days) is similar to four other AT2018cow-like events, and can be explained by synchrotron radiation from the interaction between a sub-relativistic ($\gtrsim 0.07$–$0.08c$) forward shock and a dense environment ($\dot{M} \lesssim 10^{-3}\,M_\odot\,\mathrm{yr^{-1}}$ for $v_{\mathrm{w}} = 10^3\,\mathrm{km\,s^{-1}}$). AT2020mrf occurs in a galaxy with $M_* \sim 10^8\,M_\odot$ and specific star formation rate $\sim 10^{-10}\,\mathrm{yr^{-1}}$, supporting the idea that AT2018cow-like events

are preferentially hosted by dwarf galaxies. The X-ray luminosity of AT2020mrf is the highest among FBOTs. At 35–37 days, *SRG*/eROSITA detected luminous ($L_X \sim 2 \times 10^{43}$ erg s^{-1}; 0.3–10 keV) X-ray emission. The X-ray spectral shape ($f_\nu \propto \nu^{-0.8}$) and erratic intraday variability are reminiscent of AT2018cow, but the luminosity is a factor of $\sim$ 20 greater than AT2018cow. At 328 days, *Chandra* detected it at $L_X \sim 10^{42}$ erg s^{-1}, which is $>$ 200 times more luminous than AT2018cow and CSS161010. At the same time, the X-ray emission remains variable on the timescale of $\sim$ 1 day. We show that a central engine, probably a millisecond magnetar or an accreting black hole, is required to power the explosion. We predict the rates at which events like AT2018cow and AT2020mrf will be detected by *SRG* and Einstein Probe.

4.1 Introduction

The past several years have shown that the landscape of massive-star death is unexpectedly rich and diverse. Of particular interest is the group of "fast blue optical transients" (FBOTs; Drout, Chornock, et al. 2014; Pursiainen et al. 2018). As implied by the name, these events exhibit blue colors of $(g - r) < -0.2$ mag at peak, and evolve faster than ordinary supernovae (SNe), with time above half-maximum $t_{1/2} \lesssim 12$ days.

The earliest studies were stymied by the identification of FBOTs after the transients had faded away. This situation has been rectified by cadenced wide-field optical sky surveys, such as the Zwicky Transient Facility (ZTF; Bellm, Kulkarni, Graham, et al. 2019; Graham et al. 2019) and the Asteroid Terrestrial-impact Last Alert System (ATLAS; Tonry, Denneau, Heinze, Stalder, et al. 2018), which enable real-time discovery and spectroscopic classification. Ho, Perley, Gal-Yam, et al. (2021) recently identified three distinct subtypes of FBOTs: (1) subluminous stripped-envelope SNe of type Ib/IIb, (2) luminous interaction-powered SNe of type IIn/Ibn/Icn, and (3) the most luminous ($-20 \lesssim M_{\rm peak} \lesssim -22$) and short-duration ($t_{1/2} \lesssim 5$ days) events with properties similar to AT2018cow.

The nature of AT2018cow-like events remains the most mysterious. Following the discovery of the prototype AT2018cow (z = 0.014, Prentice, Maguire, et al. 2018), only three analogs have been identified: AT2018lug (z = 0.271, Ho, Perley, Kulkarni, et al. 2020), CSS161010 (z = 0.034; Coppejans et al. 2020), and AT2020xnd (z = 0.243, Perley, Ho, et al. 2021). All of these events arose in low-mass star-forming galaxies, which suggests a massive star origin and disfavors

models invoking tidal disruption by an intermediate-mass black hole (Perley, Ho, et al., 2021). In the radio and millimeter band, their high luminosities imply the existence of dense circumstellar material (CSM), which points to significant mass-loss prior to the explosion (Ho, Goldstein, et al., 2019; Huang, Shimoda, et al., 2019; Margutti, Metzger, et al., 2019; Coppejans et al., 2020).

The X-ray luminosity of AT2018cow ($\sim 10^{43}\,\mathrm{erg\,s^{-1}}$) at early times ($\lesssim 20$ days) is similar to that of long-duration gamma-ray bursts (GRBs) (Rivera Sandoval et al., 2018). Its fast soft X-ray variability suggests the existence of a central energy source (also called central engine), and the relativistic reflection features seen in the hard X-ray spectrum point to equatorial materials (Margutti, Metzger, et al., 2019). The probable natures of the central engine include an accreting black hole, a rapidly spinning magnetar, and an embedded internal shock (Margutti, Metzger, et al., 2019; Pasham, Ho, et al., 2021). Meanwhile, AT2018cow's late-time ($\sim$ 20–45 days) optical spectra are dominated by hydrogen and helium (Perley, Mazzali, et al., 2019; Margutti, Metzger, et al., 2019; Xiang et al., 2021), which make it different from other engine-powered massive stellar transients such as long GRBs and hydrogen-poor super-luminous supernovae (i.e., SLSNe-I; see a recent review by Gal-Yam 2019) that are devoid of hydrogen and helium.

X-ray observations of AT2020xnd showed a luminosity consistent with that of AT2018cow at 20–40 days (Bright et al., 2022; Ho, Margalit, et al., 2022). Separately, late-time ($\gtrsim 100$ day) observations of AT2018cow and CSS161010 showed modest X-ray emission at $L_X \approx$ few $\times\, 10^{39}\,\mathrm{erg\,s^{-1}}$) (see §4.6 and Coppejans et al. 2020). AT2018cow-like events are thus promising X-ray transients to be discovered by the eROSITA (Predehl, Andritschke, et al., 2021) and the Mikhail Pavlinsky ART-XC (Pavlinsky et al., 2021) telescopes onboard the *Spektrum-Roentgen-Gamma* (*SRG*) satellite (Sunyaev, Arefiev, et al., 2021).

AT2020mrf is an FBOT that was first detected by ZTF on 2020 June 12. On June 14, it was also detected by ATLAS. On July 15, it was reported to the transient name server (TNS) by the ATLAS team. On June 17, an optical spectrum obtained by the "Global SN Project" displayed a featureless blue continuum. Burke, Howell, et al. (2020) assigned a spectral type of "SN II", and tentatively associated it with a $z = 0.059$ host galaxy ($109''$ offset). AT2020mrf was detected in the X-ray by *SRG* from 2020 July 21 to July 24 (§4.2), which made it a promising candidate AT2018cow analog and motivated our follow-up observations. Given that the *SRG* detection occurred $\sim$ 41 days after the first optical detection, and we became aware

of it even later, our follow-up started in April 2021.

This paper is organized as follows. We outline optical, X-ray, and radio observations, as well as analysis of AT2020mrf and its host galaxy ($z = 0.1353$) in §4.2. We provide the forward shock and CSM properties in §4.3, discuss possible power sources of the optical emission in §4.3, and present host galaxy properties in §4.3. We summarize AT2020mrf's key X-ray properties and discuss the implication in the context of engine driven explosions similar to AT2018cow in §4.3. We estimate the detection rates of events like AT2018cow and AT2020mrf in current and upcoming X-ray all-sky surveys in §4.4. We give a summary in §4.5.

UT time is used throughout the paper. We assume a cosmology of $\Omega_{\rm M} = 0.3$, $\Omega_\Lambda = 0.7$, and $h = 0.7$, implying a luminosity distance to AT2020mrf of $D_L = 637\,{\rm Mpc}$ and an angular-diameter distance of $D_\theta = 494\,{\rm Mpc}$. Optical magnitudes are reported in the AB system. We use the Galactic extinction from Schlafly and Finkbeiner (2011) and the extinction law from Cardelli, Clayton, and Mathis (1989). Coordinates are given in J2000.

4.2 Observations and Data Analysis

Optical Photometry

We obtained public ZTF[1] and ATLAS[2] forced photometry (Masci et al., 2019; Smith et al., 2020) using the median position of all ZTF alerts (R.A. = $15^{\rm h}47^{\rm m}54.17^{\rm s}$, decl. = $+44^\circ39'07.34''$). The 1-day binned optical light curve is shown in Figure 4.1, where data points are $> 2.5\sigma$ detections and semi-transparent downward triangles are 3σ upper limits. The rest-frame equivalent light curves of AT2018cow and AT2021csp are shown as dashed-dotted lines (based on blackbody parameters provided in Tab. 4 of Perley, Mazzali, et al. 2019) and dotted lines (based on Tab. 4 of Perley, Sollerman, et al. 2022), respectively. The solid and dashed black lines are observer-frame $r_{\rm ZTF}$-band light curves of AT2018lug ($\lambda_{\rm rest} = 5050\,$Å) and AT2020xnd ($\lambda_{\rm rest} = 5165\,$Å), respectively. Note that the apparent AB magnitude scale pertains to AT2020mrf only — the light curves of other objects are only shown in absolute magnitude.

Following Whitesides et al., 2017 and Ho, Perley, Kulkarni, et al. (2020), we compute absolute magnitude using

$$M = m_{\rm obs} - 5\log_{10}\left(\frac{D_L}{10\,{\rm pc}}\right) + 2.5\log_{10}(1+z). \tag{4.1}$$

[1] `https://ztfweb.ipac.caltech.edu/cgi-bin/requestForcedPhotometry.cgi`
[2] `https://fallingstar-data.com/forcedphot/`

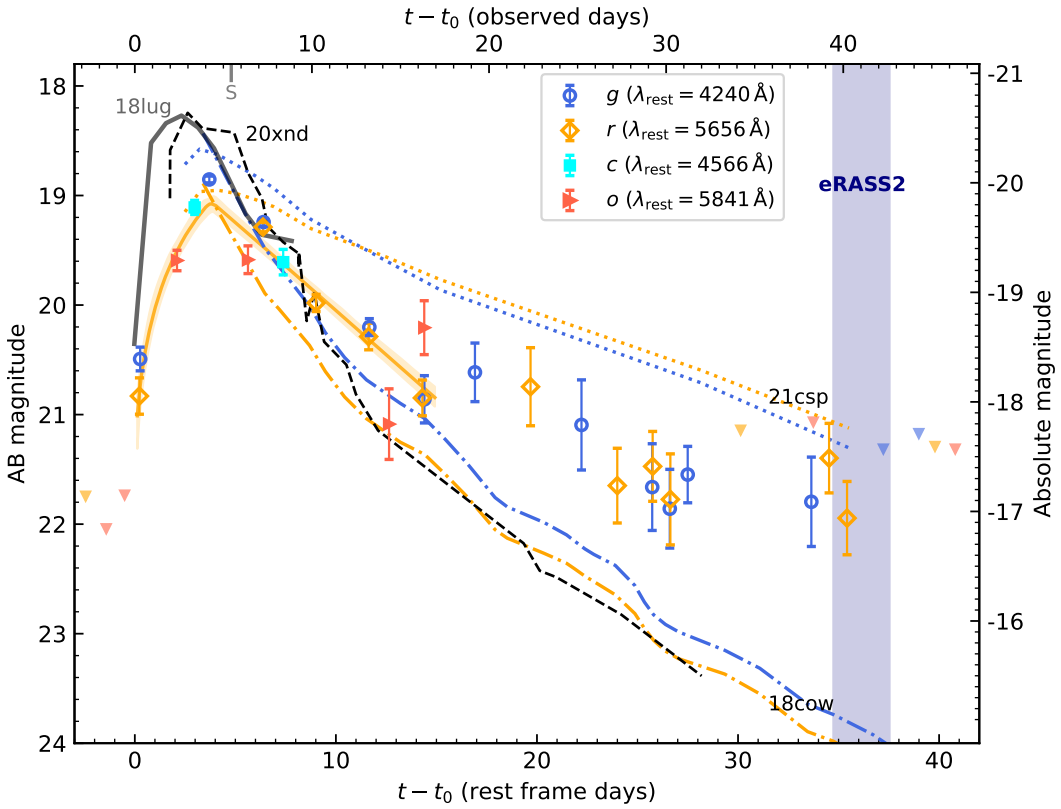

Figure 4.1: Optical light curve of AT2020mrf.

The last term in Equation (4.1) is a rough estimation of the K-correction, and introduces an error of 0.1 mag.

The first detection is $r = 20.88 \pm 0.17$, on 2020-06-12T06:14:12 (59012.2599 MJD) and the last non-detection is $o > 21.73$, on 2020-06-11T10:12:13 (59011.4252 MJD). Therefore, we assume an explosion epoch of $t_0 = 59012.0$ MJD. Hereafter, we use Δt to denote rest-frame time with respect to t_0. At $\Delta t = 3.7$ days, AT2020mrf peaked at $M_g = -20.0$ mag.

Optical Spectroscopy

The transient spectrum[3] was obtained on 2020 June 17 ($\Delta t = 4.8$ days) with the FLOYDS-N spectrograph on the 2 m Faulkes Telescope North (Burke, Howell, et al., 2020). In Figure 4.2, the dashed line is a blackbody with $T = 2 \times 10^4$ K and $R = 7.9 \times 10^{14}$ cm. The spectrum of AT2020mrf is similar to that of AT2018cow at similar phases — a single broad feature at $\sim$ 5600 Å was observed to span ±600 Å, indicating a velocity of $0.1c$. The origin of this broad line in AT2018cow

[3] Available at `https://www.wis-tns.org/object/2020mrf`

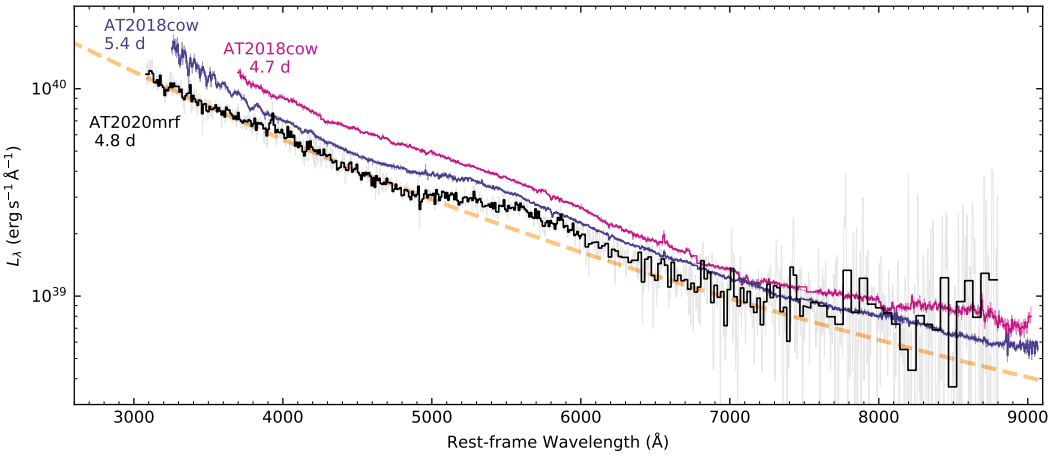

Figure 4.2: Optical spectrum of AT2020mrf, compared with AT2018cow at similar phases (Perley, Mazzali, et al., 2019).

remains an open question. Perley, Mazzali, et al. (2019) note that although it is vaguely reminiscent of the Fe II feature in Ic broad-line (Ic-BL) SNe around peak (Galama et al., 1998), in SNe Ic-BL the blueshifted absorption trough strengthens at later times, while in AT2018cow this line vanished at $\Delta t \sim 8$ days. In terms of other AT2018cow-like objects, the peak-light optical spectra of AT2018lug and AT2020xnd are consistent with being blue and featureless (Ho, Perley, Kulkarni, et al., 2020; Perley, Ho, et al., 2021), and there exists no published optical spectra of CSS161010.

A blackbody fit to AT2020mrf's optical spectrum suggests a temperature of $T \approx 2 \times 10^4$ K and a radius of $R = 7.9 \times 10^{14}$ cm. This temperature is typical of AT2018cow-like events.

Early-time X-rays: *SRG*

SRG is a space satellite at the L2 Lagrange point with a drafting rate of $\approx 1^\circ$ day^{-1}. It is conducting eight all-sky surveys from the beginning of 2020 to the end of 2023, with a cadence of 6 months. Hereafter, eRASS*n* refers to the *n*'th eROSITA all-sky survey. *SRG*'s rotational axis points toward the Sun, and the rotational period is 4 hr. The eROSITA field-of-view (FoV) is 1 deg^2. Therefore, during a single sky survey, a particular region of the sky will be scanned by eROSITA at least ~ 6 times (~ 1 day), where each scan lasts for ≈ 40 s (see details in Sunyaev, Arefiev, et al. 2021). AT2020mrf, at a relatively high ecliptic latitude of $b_{\rm ecl} = 61.9^\circ$, was scanned for ≈ 3 days in each all-sky survey.

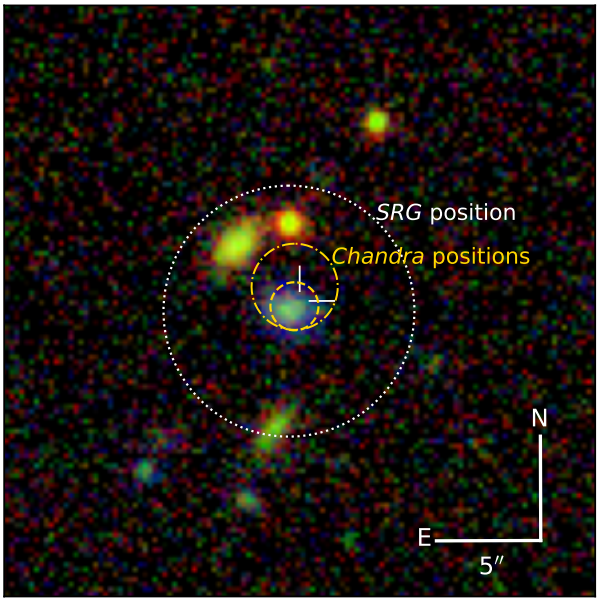

Figure 4.3: HSC-SSP RGB false-color *g*/*i*/*z* image centered at the ZTF position of AT2020mrf (marked by the white crosshairs).

During eRASS2 ($\Delta t \sim 36$ days), *SRG*/eROSITA discovered an X-ray transient SRGe J154754.2+443907, with a 98% localization radius of 4.28″. This X-ray transient is only 0.56″ from AT2020mrf (see Figure 4.3), suggesting an association between the X-ray and the optical transients. Figure 4.4 shows that the source exhibits significant variability — the 0.2–2.2 keV count rate increased from ≈ 0.053 count s^{-1} ($\Delta t \sim 35$ days) to ≈ 0.32 count s^{-1} ($\Delta t \sim 36$ days), and then decreased to ≈ 0.051 count s^{-1} ($\Delta t \sim 37$ days).

Table 4.1: Modeling of the eRASS2 spectrum of AT2020mrf.

Component	Parameter	Power-law Model		Thermal Plasma Model	
		(a) Fixed $N_{\rm H}$	(b) Free $N_{\rm H}$	(a) Fixed $N_{\rm H}$	(b) Free $N_{\rm H}$
`tbabs`	$N_{\rm H}$ (10^{20} cm^{-2})	1.38	$15.32^{+14.06}_{-10.70}$	1.38	$9.04^{+7.10}_{-6.99}$
`zpowerlw`	Γ	1.81 ± 0.26	$2.79^{+1.00}_{-0.80}$	...	...
	$\mathrm{norm_{pl}}$ (10^{-5})	$8.0^{+1.1}_{-1.0}$	$14.8^{+11.8}_{-5.7}$	...	...
`apec`	$k_{\rm B}T$	...	...	$2.0^{+1.9}_{-0.7}$	$1.0^{+1.1}_{-0.3}$
	$\mathrm{norm_{apec}}$ (10^{-4})	...	...	$3.8^{+0.9}_{-0.7}$	$7.2^{+5.2}_{-3.3}$
cstat/*dof*		25.94/35	24.09/34	24.80/35	23.60/34
$f_{\rm X}$ (10^{-13} erg s^{-1} cm^{-2})		$3.90^{+1.32}_{-1.00}$	$2.48^{+0.51}_{-0.83}$	$2.40^{+0.54}_{-0.75}$	$1.92^{+0.15}_{-1.37}$

$\mathrm{norm_{pl}}$ and $\mathrm{norm_{apec}}$ are the normalization parameters in the model components (see the `xspec` documentation for units). Uncertainties are represented by the 68% confidence intervals.
$f_{\rm X}$ is the observed 0.3–10 keV flux.

Figure 4.5 shows the average eRASS2 spectrum of AT2020mrf, which has been

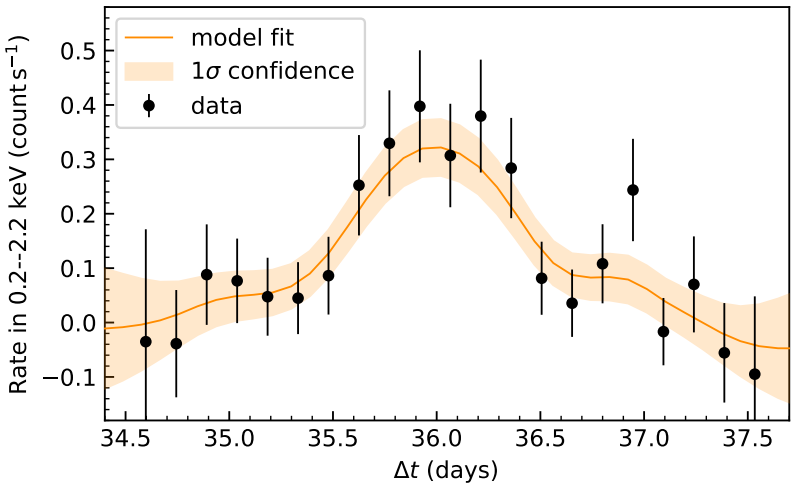

Figure 4.4: eRASS2 light curve of AT2020mrf.

grouped via `ftgrouppha` to have at least five counts per bin in the background spectrum. We fit the 0.3–10 keV spectrum using `xspec` (12.11, Arnaud 1996) and C-statistics. The data are modeled first with an absorbed power-law (`zpowerlw`) and then with an absorbed thermal plasma (`apec`). For each model, we first fix the column density at the Galactic value of $N_{\rm H} = 1.38 \times 10^{20}\,{\rm cm}^{-2}$ (Willingale et al., 2013), and then free this parameter. The models with fixed $N_{\rm H}$ are shown in Table 4.1. The data do not favor any particular model because the *cstat/dof* (C-statistics divided by degrees of freedom) values have small differences between the four fits.

Although we are unable to distinguish between the power-law and thermal models using the eROSITA data, the optical/radio similarities between AT2020mrf and AT2018cow (§4.2, §4.2, §4.3), and the non-thermal nature of AT2018cow's X-rays ($f_\nu \propto \nu^{-0.7}$, 36.5 days, 0.3–30 keV, see Fig. 6 of Margutti, Metzger, et al. 2019) motivate us to adopt the power-law model in the following discussion.

AT2020mrf was not detected in eRASS1, eRASS3 and eRASS4. Using the eROSITA sensitivity maps, we calculate the 0.3–2.2 keV flux upper limits to be $(1.12, 1.35, 1.54) \times 10^{-14}\,{\rm erg\,s^{-1}\,cm^{-2}}$ at the confidence level likelihood of 6 ($\approx 2.8\sigma$).

Late-time X-rays: *Chandra*

We conducted deep X-ray observations of AT2020mrf with the *Chandra* X-ray Observatory (Wilkes and Tucker, 2019) under a DDT program (PI Yao) on 2021

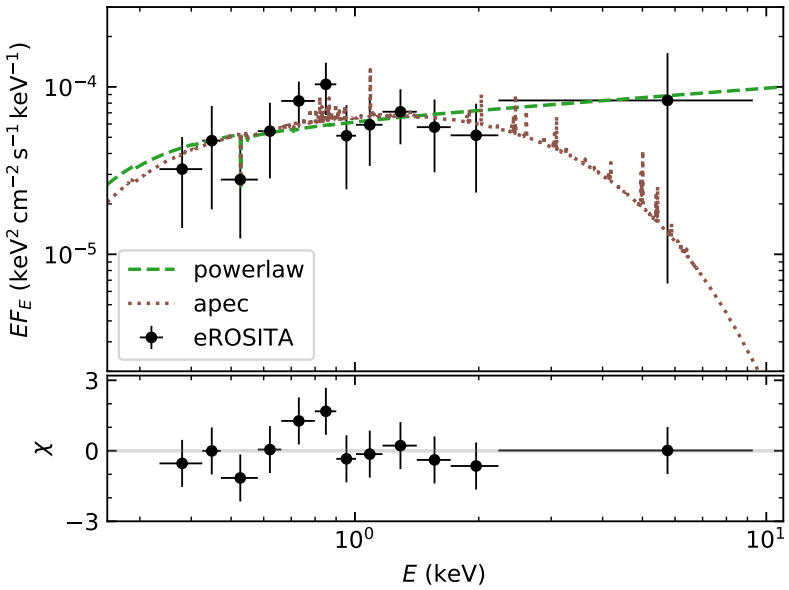

Figure 4.5: eRASS2 spectrum of AT2020mrf.

June 18 (22.0 ks, obsID 25050) and June 19 (19.8 ks, obsID 25064). We used the Advanced CCD Imaging Spectrometer (ACIS; Garmire et al. 2003), with the aim point on the back illuminated CCD S3. The data were reduced with the `CIAO` package (v4.14).

To determine the astrometric shifts of *Chandra* images, we first ran the `CIAO` tool `wavdetect` to obtain lists of positions for all sources in the *Chandra* FoV. Wavelet scales of 1, 2, 4, and 8 pixels and a significance threshold of 10^{-6} were used. A total of 8 and 12 X-ray sources were detected in obsID 25050 and obsID 25064, respectively. We cross matched the X-ray source lists with the *Gaia* EDR3 catalog (Gaia Collaboration et al., 2021), using a radius of 2″. This left two *Chandra*/*Gaia* sources from both obsIDs. We define the astrometric shifts as the mean difference in R.A. and decl. between the two matched sources. For obsID 25050, δR.A. = $-1.88 \pm 0.42''$ and δdecl. = $-0.58 \pm 0.75''$; For obsID 25064, δR.A. = $-0.62 \pm 0.27''$ and δdecl = $+0.61 \pm 0.29''$.

Having applied the astrometric shifts, we found that an X-ray source at the location of AT2020mrf was detected in both obsIDs. The position of the X-ray source from obsID 25050 is R.A. = $15^{\rm h}47^{\rm m}54.18^{\rm s}$, decl. = $+44°39'07.83''$, with an astrometric uncertainty of 1.47″ from the residual offsets with the *Gaia* catalog; The position of the X-ray source from obsID 25064 is R.A. = $15^{\rm h}47^{\rm m}54.18^{\rm s}$, decl. = $+44°39'07.16''$, with an astrometric uncertainty of 0.82″ from the residual offsets with the *Gaia*

catalog. The *Chandra* positions are shown in Figure 4.3, which are more accurate than the eROSITA position, and clearly associate the X-ray emission with the ZTF position of AT2020mrf.

For each obsID, we extracted the source spectrum using a source region of $r_{\rm src} = 1.5''$ centered on the X-ray position determined by `wavdetect`. A total of 30 and 10 counts (0.5–10 keV) were detected within the source regions of obsID 25050 and obsID 25064, respectively. The background spectrum was extracted using nearby source-free regions. The 0.5–10 keV net count rate at 90% credible interval is $1.61^{+0.32}_{-0.28} \times 10^{-3}$ count s^{-1} for obsID 25050, and $0.56^{+0.21}_{-0.17} \times 10^{-3}$ count s^{-1} for obsID 25064, indicating that X-ray net count rate has dropped by a factor of 2.9 ± 1.1. Such a large flux decrease reflects intrinsic X-ray variability.

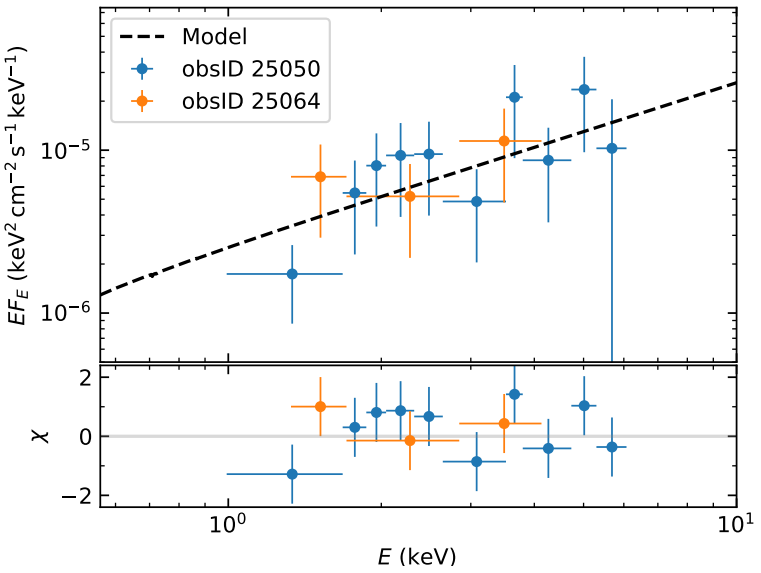

Figure 4.6: *Chandra* spectrum of AT2020mrf at $\Delta t \approx 328$ days.

We groupped the *Chandra* spectrum to at least one count per bin, and modeled the data using C-statistics. We used a model of `tbabs*zpowerlw`, with $N_{\rm H}$ fixed at the Galactic value. Since the count rate has significantly decreased between the two obsIDs, we include a constant scaling factor C between the two *Chandra* observations (Madsen et al., 2017), with the constant for obsID 25050 (C_1) fixed at 1. The result, with $cstat/dof = 32.25/34$, gives $\Gamma = 1.00 \pm 0.35$ and $C_2 = 0.39^{+0.17}_{-0.13}$, where uncertainties are represented by the 68% confidence intervals. The best-fit model is shown in Figure 4.6. To account for the flux variation (see text), the obsID 25064 data has been divided by 0.39.

Table 4.2: X-ray flux measurements of AT2020mrf.

Δt (days)	Telescope	Observed 0.3–10 keV flux (10^{-14} erg s^{-1} cm^{-2})
−127	*SRG*/eRASS1	< 2.93
34.5–37.6	*SRG*/eRASS2	$39.0^{+13.2}_{-10.0}$
192	*SRG*/eRASS3	< 7.24
327.4	*Chandra*	$4.00^{+0.68}_{-1.24}$
328.2		$1.57^{+0.27}_{-0.49}$
355	*SRG*/eRASS4	< 8.26

To convert the 0.3–2.2 keV eROSITA upper limits to 0.3–10 keV, we assume the eRASS2 best-fit spectral model for the eRASS1 epoch, and the *Chandra* spectral model for the eRASS3 and eRASS4 epochs.

The difference between the *SRG* and *Chandra* power-law indices is $\Gamma_{36\,\mathrm{d}} - \Gamma_{328\,\mathrm{d}} = 0.81 \pm 0.44$. Therefore, we conclude that a change of Γ is marginally detected at 1.9σ. Table 4.2 summarizes the 0.3–10 keV fluxes.

Figure 4.7 compares the X-ray luminosity evolution of AT2020mrf with AT2018cow (Rivera Sandoval et al. 2018; Margutti, Metzger, et al. 2019, §4.6), CSS161010 (Coppejans et al., 2020), AT2020xnd (Bright et al., 2022; Ho, Margalit, et al., 2022), cosmological long GRBs (light blue solid lines; §4.6), GRBs associated with SNe (dashed grey lines; Kouveliotou et al. 2004; Tiengo et al. 2004; Campana et al. 2006; Soderberg et al. 2006; Margutti, Soderberg, et al. 2013), SLSNe-I (Levan, Read, et al. 2013; Margutti, Chornock, et al. 2018), the jetted TDE SwiftJ1644 (Mangano, Burrows, et al., 2016), interacting SNe of type IIn (dashed-dotted green lines; Chandra, Chevalier, Chugai, Fransson, Irwin, et al. 2012; Chandra, Chevalier, Chugai, Fransson, and Soderberg 2015; Dwarkadas, Romero-Cañizales, et al. 2016; Katsuda et al. 2016) and type Ibn (dotted cyan lines; Immler et al. 2008; Ofek et al. 2013), as well as normal CCSNe (Dwarkadas and Gruszko, 2012). AT2020mrf is as luminous as cosmological GRBs. We further discuss this figure in §4.3.

Search for Prompt γ-rays

Given that cosmological long GRBs are the only type of massive-star explosion with X-ray luminosities known to be comparable to AT2020mrf (see Figure 4.7), we are motivated to search for bursts of prompt γ-rays between the last ZTF non-detection and the first ZTF detection (§4.2).

During this time interval, only one burst was detected by the interplanetary network

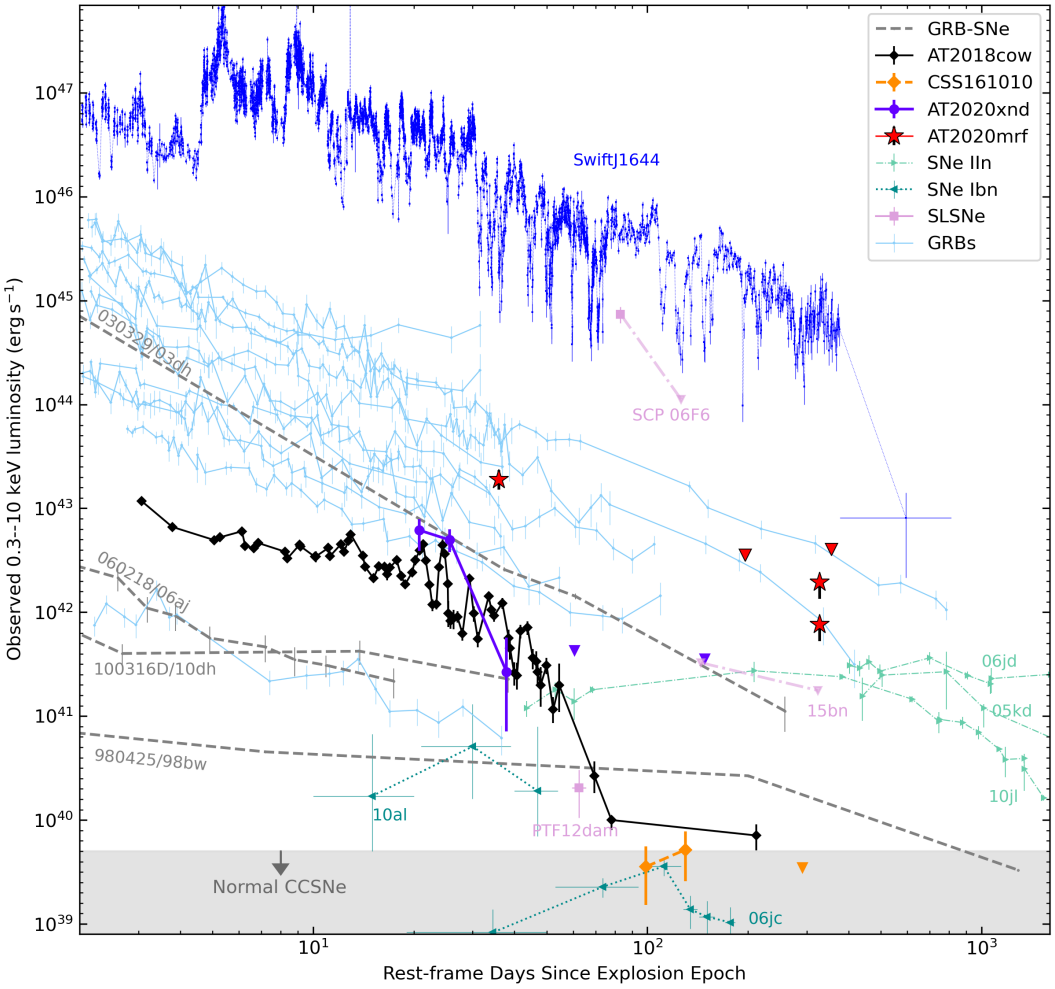

Figure 4.7: X-ray luminosities of AT2020mrf, compared with other types of explosions.

(IPN; Hurley et al. 2010). The position of this burst (Sonbas et al., 2020) is inconsistent with that of AT2020mrf. To obtain a constraint on the γ-ray flux of AT2020mrf, we use the Konus instrument (Aptekar et al., 1995) on the *Wind* spacecraft. Unlike other high energy telescopes on low Earth orbit (LEO) spacecrafts (such as *Swift*/BAT and *Fermi*/GBM), Konus-*Wind* (KW) continuously observe the whole sky without Earth blocking and with a very stable background, thanks to its orbit around the L1 Lagrange point (see, e.g., Tsvetkova et al. 2021). During the interval of interest, KW was taking data (total duration of data gaps was $< 1\%$ of the total time). Assuming a typical long GRB spectrum[4] and a timescale of 2.944 s, KW gives a 20–1000 keV upper limit of $< 2 \times 10^{-7}$ erg s^{-1} cm^{-2}. This corresponds

[4]The Band function with peak energy $E_{\rm peak} = 300$ keV, low-energy photon index $\alpha = -1$, and high energy photon index $\beta = -2$ (Band et al., 1993).

to an isotropic luminosity of $L_{\rm iso} < 1.0 \times 10^{49}\,{\rm erg\,s^{-1}}$, which strongly disfavors an on-axis classical GRB (Frail et al., 2001).

Radio: VLA and uGMRT

Table 4.3: Radio observations of AT2020mrf.

Date in 2021	Δt (days)	Telescope/ Receiver	ν_0 (GHz)	f_ν (μJy)
Apr 2	259.5	VLA/C	4.30	254 ± 25
			4.94	234 ± 22
			5.51	330 ± 18
			6.49	327 ± 20
			7.06	336 ± 17
			7.70	349 ± 18
Apr 6	262.9	VLA/S	3.00	165 ± 26
		VLA/X	8.49	277 ± 23
			9.64	271 ± 20
			11.13	223 ± 17
		VLA/Ku	12.78	213 ± 19
			14.32	189 ± 16
			16.62	153 ± 15
		VLA/K	20.00	149 ± 8
			24.00	103 ± 8
May 19	300.9	uGMRT/B5	1.25	< 45
May 29	309.5	VLA/S	3.00	206 ± 48
Aug 13	376.6	uGMRT/B5	1.25	< 105
Sep 28	416.8	uGRMT/B5	1.36	68 ± 15
Sep 28–29	417.5	VLA/S	3.00	81 ± 10
		VLA/C	6.00	87 ± 7
		VLA/X	10.00	49 ± 8
		VLA/Ku	13.55	65 ± 6
			16.62	51 ± 7

ν_0 is observed central frequency. f_ν is the observed flux density values. Upper limits are 3σ.

We began a monitoring program of AT2020mrf using the VLA (Perley, Chandler, et al., 2011) under Program 21A-308 (PI Ho), and the upgraded Giant Metrewave Radio Telescope (uGMRT; Swarup 1991; Gupta et al. 2017) under Program 40_077 (PI Nayana). The data were analyzed following the standard radio continuum image analysis procedures in the Common Astronomy Software Applications (`CASA`; McMullin et al. 2007). The results are presented in Table 4.3. Incidentally, AT2020mrf

was not detected in the Karl G. Jansky Very Large Array Sky Survey (VLASS, Lacy et al. 2020), which provides a 3-σ upper limit of 0.42 mJy at 2–4 GHz in March 2019. Hereafter radio flux density values have been K-corrected and frequency values are reported in the rest-frame. K-correction was performed following Condon and Matthews (2018), assuming a steep synchrotron spectrum with a spectral index of $\beta = -1$ ($f_\nu \propto \nu^\beta$).

Regarding data obtained within $(\Delta t/10)$ days as coeval, we model the radio spectral energy distribution (SED) at $\Delta t \approx 261$ days and $\Delta t \approx 417$ days with a broken power-law (Granot and Sari, 2002):

$$L_\nu = L_{\nu\,\mathrm{peak}} \left[\left(\frac{\nu}{\nu_\mathrm{peak}} \right)^{-s\beta_1} + \left(\frac{\nu}{\nu_\mathrm{peak}} \right)^{-s\beta_2} \right]^{-1/s} \tag{4.2}$$

where ν and L_ν are quantities in the object's rest-frame, $L_{\nu\,\mathrm{peak}}$ is the peak specific luminosity, ν_peak is the peak frequency, β_1 and β_2 are the asymptotic spectral indices below and above the break, and s is a smoothing parameter. We perform the fit using the Markov chain Monte Carlo (MCMC) approach with `emcee` (Foreman-Mackey, Hogg, et al., 2013). The reported uncertainties follow the 68% credible region.

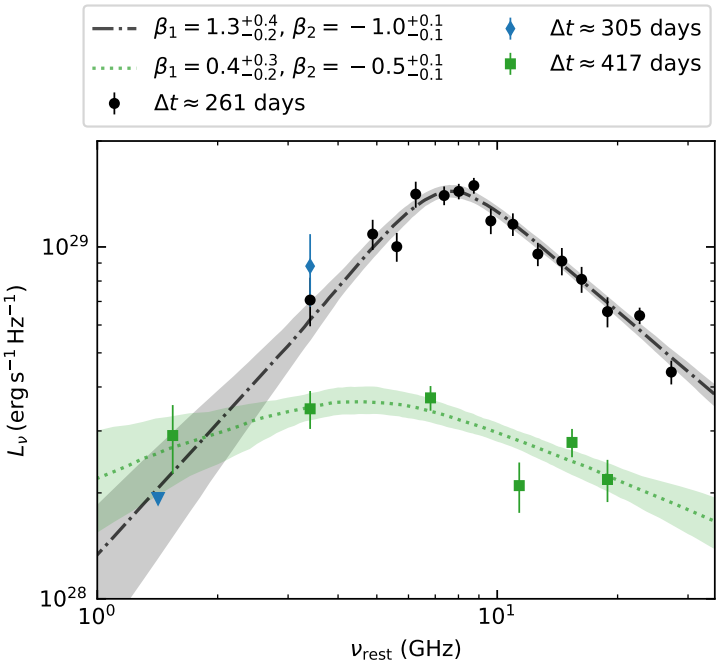

Figure 4.8: Radio observations of AT2020mrf, overplotted with the best-fit broken power-law models.

The best-fit models are shown in Figure 4.8. At $\Delta t \approx 261$ days, $\nu_\mathrm{peak} = 7.44^{+0.44}_{-0.52}$ GHz, $L_{\nu\,\mathrm{peak}} = 1.70^{+0.23}_{-0.09} \times 10^{29}$ erg s^{-1} Hz^{-1}, $\beta_1 = 1.3^{+0.4}_{-0.2}$, and $\beta_2 = -1.0 \pm 0.1$. At $\Delta t \approx$

305 days, the 1–4 GHz band probably remains below the broken frequency, and the blue data in Figure 4.8 suggests $\beta_1 > 1.7$. At $\Delta t \approx 417$ days, $\nu_{\rm peak} = 4.82^{+1.36}_{-1.18}$ GHz, $L_{\nu\,\rm peak} = 4.33^{+0.36}_{-0.34} \times 10^{28}$ erg s^{-1} Hz^{-1}, $\beta_1 = 0.4^{+0.3}_{-0.2}$, and $\beta_2 = -0.5 \pm 0.1$. Equation (4.2) does not provide a decent description for the data.

The radio observations will further be discussed in §4.3.

The Host Galaxy

Table 4.4: Observed photometry of AT2020mrf's host galaxy.

Instrument	Band	$\lambda_{\rm eff}$ (Å)	Magnitude
GALEX	FUV	1528	> 23.276
GALEX	NUV	2271	> 23.579
HSC	g	4755	23.282 ± 0.029
HSC	r	6184	23.152 ± 0.046
HSC	i	7661	22.635 ± 0.040
HSC	z	8897	22.721 ± 0.079
HSC	y	9762	22.359 ± 0.133

The HSC Kron radius is 0.705″. *GALEX* upper limits are given in 3σ.

Deep pre-explosion images of the target field are available in the Hyper Suprime-Cam Subaru Strategic Program (HSC-SSP; Aihara, Arimoto, et al. 2018) second Public Data Release (PDR2; Aihara, AlSayyad, et al. 2019) and the *Galaxy Evolution Explorer* (*GALEX*; Martin et al. 2005) UV imaging survey. As is shown in Figure 4.3, AT2020mrf is 0.50″ offset from an extended blue source (R.A. = $15^{\rm h}47^{\rm m}54.20^{\rm s}$, decl. = +44°39′07.01″), which is considered to be the host galaxy. At the host redshift, the spatial offset corresponds to a physical distance of 1.19 kpc. The photometry of the host is shown in Table 4.4.

On 2021 April 14 ($\Delta t = 267.0$ days), we obtained a spectrum of the host galaxy using the Low Resolution Imaging Spectrometer (LRIS; Oke, Cohen, et al. 1995) on the Keck I 10 m telescope. We used the 560 dichroic, the 400/3400 grism on the blue side, the 400/8500 grating on the red side, and the 1″ slit width. This setup gives a full-width half maximum (FWHM) of ≈ 6.8 Å. Exposure times were 3650 and 3400 s for the blue and red cameras, respectively. The spectrum was reduced and extracted using `LPipe` (Perley, 2019). The upper panel of Figure 4.9 shows the Galactic extinction corrected host spectrum, overplotted with HSC $griz$ photometry.

To determine the redshift and emission line fluxes of the host, we fit the Galactic

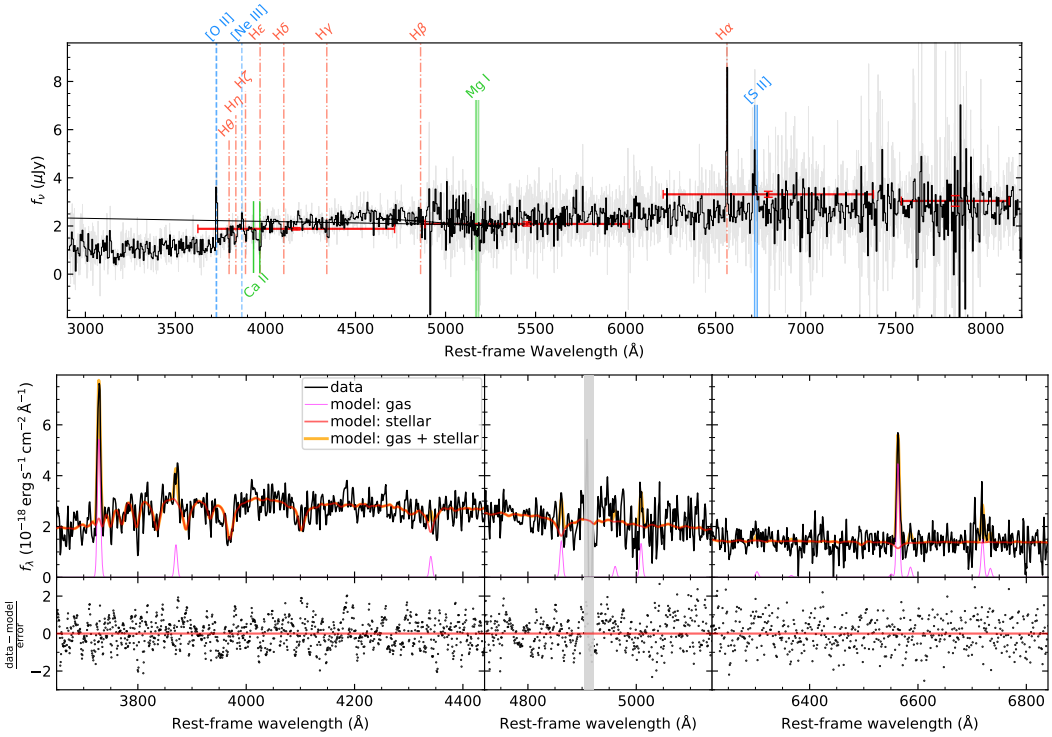

Figure 4.9: Spectrum of AT2020mrf's the host galaxy.

extinction corrected LRIS spectrum with stellar population models using the penalized pixel-fitting (`ppxf`) software (Cappellari and Emsellem, 2004; Cappellari, 2017). We use the MILES library (FWHM=2.5 Å; Falcón-Barroso et al. 2011) and commonly observed galaxy emission lines, including Hα, Hβ, Hγ, [O II], [S II], [O III], [O I], and [N II]. The [O I] $\lambda\lambda$6300, 6364, [O III] $\lambda\lambda$4959, 5007 and [N II] $\lambda\lambda$6548, 6583 doublets are fixed at the theoretical flux ratio of 3.

The best-fit model suggests a redshift of $z = 0.1353 \pm 0.0002$. Zoom-in portions of the spectrum around regions of emission lines are shown in the bottom panel of Figure 4.9. The line fluxes are presented in Table 4.5. Note that because the [O II] doublets are not resolved, the derived individual line fluxes are not reliable and we only report the total flux of the doublets.

The calculated line ratios are given in Table 4.6. Uncertainties in line ratios are calculated by performing 10^4 Monte Carlo (MC) trials using the measured flux uncertainties. Figure 4.10 shows the location of the host galaxy on the Baldwin, Phillips, & Terlevich (BPT) diagrams (Baldwin, Phillips, and Terlevich, 1981). Under the diagnostic definitions of Kewley et al. (2006), the host falls in the region of star-forming galaxies.

Table 4.5: Emission line fluxes of AT2020mrf's host galaxy.

Line	Flux (10^{-18} erg s^{-1} cm^{-2} Å^{-1})
[O II] $\lambda\lambda$3726, 3729	53.00 ± 6.09
[Ne III] λ3869	10.96 ± 1.97
Hγ λ4340	6.31 ± 1.55
Hβ λ4861	9.81 ± 1.87
[O III] $\lambda\lambda$4959, 5007	11.67 ± 4.57 (2.6σ)
[O I] $\lambda\lambda$6300, 6364	1.59 ± 1.17 (1.4σ)
Hα λ6563	22.82 ± 0.89
[N II] $\lambda\lambda$6548, 6583	2.72 ± 1.71 (1.6σ)
[S II] λ6716	7.32 ± 2.01
[S II] λ6731	1.77 ± 1.26 (1.4σ)

Marginally detected emission lines are indicated with the detection significance shown in the parenthesis.

Table 4.6: Emission line ratios of AT2020mrf's host galaxy.

Definition	Value
[O III]λ5007/Hβ	$0.90^{+0.78}_{-0.58}$
log{[O III]λ5007/Hβ}	$-0.05^{+0.27}_{-0.45}$
[N II]λ6583/Hα	< 0.18
N2 $\equiv$ log{[N II]λ6583/Hα}	< -0.73
O3N2 $\equiv$ log{[O III]λ5007/Hβ}$-$N2	< -1.71
[S II]$\lambda\lambda$6716,31/Hα	0.40 ± 0.17
log{[S II]$\lambda\lambda$6716,31/Hα}	$-0.40^{+0.16}_{-0.24}$
[O I]λ6300/Hα	< 0.12
log{[O I]λ6300/Hα}	< -0.94

Line ratios and their uncertainties are estimated using the 5$^{\text{th}}$, 50$^{\text{th}}$ and 95$^{\text{th}}$ percentiles of the MC simulations. When the 5$^{\text{th}}$ percentile value is negative, we present the 95$^{\text{th}}$ percentile as an upper limit.

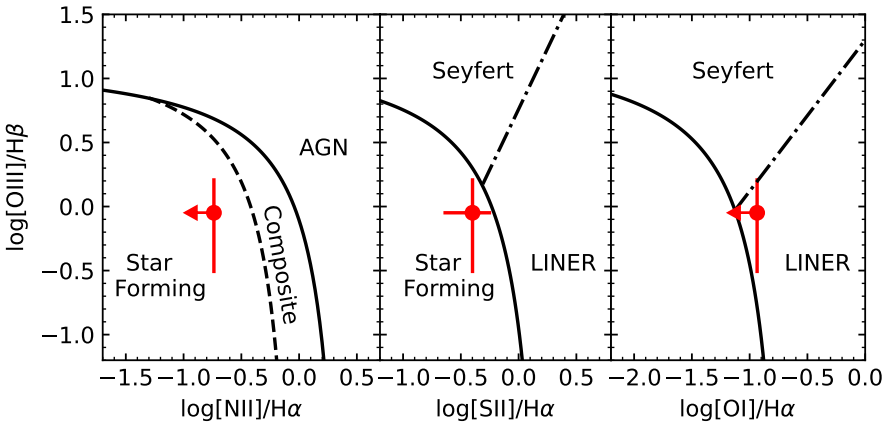

Figure 4.10: The host galaxy of AT2020mrf on the BPT diagrams.

We measure the oxygen abundance using two metallicity indicators N2 and O3N2 (Pettini and Pagel, 2004), defined in Table 4.6. Using the calibration reported by Marino et al. (2013), the gas-phase oxygen abundance is $< 8.40 \pm 0.16$(sys) in the N2 scale, and $> 8.17 \pm 0.18$(sys) in the O3N2 scale. Compared with the solar metallicity ($Z_\odot$) of $12 + \log(\mathrm{O/H}) = 8.69$ (Asplund et al., 2009), our constraints suggest a metallicity of $10^{-0.70}$–$10^{-0.13} Z_\odot$.

To obtain an estimate of the host galaxy total stellar mass (M_*), we fit the host SED with flexible stellar population synthesis (FSPS; Conroy, Gunn, and White 2009) models (Foreman-Mackey, Sick, and Johnson, 2014). We adopt a delayed exponentially declining star-formation history (SFH) characterized by the e-folding timescale τ_{SFH}, such that the time-dependent star-formation rate $\psi_*(t) \propto te^{-(t/\tau_{\mathrm{SFH}})}$. The `Prospector` package (Johnson et al., 2021) was used to run a Markov Chain Monte Carlo (MCMC) sampler (Foreman-Mackey, Hogg, et al., 2013). We use log-uniform priors for the following three parameters: M_* in the range $[10^7\ M_\odot, 10^9\ M_\odot]$, τ_{SFH} in the range [0.1 Gyr, 100 Gyr], the metallicity $\log(Z/Z_\odot)$ in the range -0.70 and -0.13, and the population age t_{age} in the range [0.1 Gyr, 12.5 Gyr]. Host galaxy extinction was included, with $E(B-V)_{\mathrm{host}}$ uniformly sampled between 0 and 1. From the marginalized posterior probability functions we obtain $\log(M_*/M_\odot) = 7.94^{+0.22}_{-0.39}$, $\log(Z/Z_\odot) = -0.46^{+0.20}_{-0.17}$, $\tau_{\mathrm{SFH}} = 11.6^{+45.6}_{-10.0}$ Gyr, $t_{\mathrm{age}} = 1.82^{+4.07}_{-1.50}$ Gyr, and $E(B-V)_{\mathrm{host}} = 0.21^{+0.10}_{-0.12}$, where uncertainties are represented by the 68% confidence intervals.

Using the 90% confidence interval of the M_* posterior probability function and the mass–metallicity relation (MZR) of low-mass galaxies (Berg et al., 2012), we infer

that the typical $\log(Z/Z_\odot)$ at the host mass should be $-0.78^{+0.10}_{-0.16} \pm 0.15$(sys). The measured metallicity is therefore on the high end of the distribution.

We convolve the observed LRIS spectrum with the HSC i-band filter and compare the flux with the host photometry (Table 4.4), which suggests that 80.6% of the total host flux is captured by the LRIS slit. Subsequently, we assume the same fraction of total Hα flux is captured by the slit and no host extinction, and calculate the Hα luminosity to be $L_{\mathrm{H}\alpha} = (1.39 \pm 0.05) \times 10^{39}\,\mathrm{erg\,s^{-1}}$. Using the Kennicutt (1998) relation converted to a Chabrier initial mass function (Chabrier, 2003; Madau and Dickinson, 2014), we infer a star formation rate (SFR) of $(6.93 \pm 0.27) \times 10^{-3}\,M_\odot\ \mathrm{yr^{-1}}$. An extinction of $E(B-V)_{\mathrm{host}} \sim 0.21$ will render the SFR higher by a factor of ~ 1.5. Therefore, hereafter we adopt SFR $= 6.93^{+3.90}_{-0.27} \times 10^{-3}\,M_\odot\ \mathrm{yr^{-1}}$. The specific star formation rate is sSFR $\equiv$ SFR$/M_* = 0.80^{+0.45}_{-0.03} \times 10^{-10}\ \mathrm{yr^{-1}}$, where we only consider the uncertainty of SFR but exclude the uncertainty of M_*.

4.3 Inferences and Discussion

A Mildly Relativistic Shock in a Dense Environment

Standard SSA Modeling — At $\Delta t \approx 261$ days, the observed spectral index of $\beta_2 \approx -1$ (§4.2) in the optically thin regime of the radio SED motivates us to adopt the standard model given by Chevalier (1998), where the electrons in the CSM are accelerated by the forward shock into a power-law distribution of energy $N(E) = N_0 E^{-p}$. We do not consider the alternative of a relativistic Maxwellian electron-energy distribution, in which case we expect a much steeper β_2 (see, e.g., Fig. 11 of Ho, Margalit, et al. 2022) and a shock speed of $v_{\mathrm{sh}} \gtrsim 0.2c$ (Margalit and Quataert, 2021). The v_{sh} inferred from our observations is much slower (see below). We note that the standard model might not be fully appropriate since the observed spectral index of β_1 in the optically thick regime is much shallower than the $\beta_1 = 2.5$ expected from SSA. We investigate the effects of CSM inhomogeneity and scintillation in later in this section.

In the standard model of Chevalier (1998), the minimum electron energy is $E_{\mathrm{min}} = 511\,\mathrm{keV}$; the peak of the SED is governed by synchrotron self-absorption (SSA) such that $\tau(\nu_{\mathrm{peak}}) = 1$; the radio emitting region is approximated by a sphere with radius R and volume filling factor f (hereafter assumed to be 0.5); the magnetic energy density ($U_B \propto B^2$) and the relativistic electron energy density ($U_e \propto N_0$) are assumed to scale as the total (thermalized) post-shock energy density U, such that $U_B = \epsilon_B U$ and $U_e = \epsilon_e U$.

We define $L_{\theta\nu} \equiv 4\pi D_\theta^2 f_\nu = L_\nu/(1+z)^4$, $L_{\theta\nu,29} \equiv L_{\theta\nu,\rm peak}/(10^{29}\,{\rm erg\,s^{-1}\,Hz^{-1}})$ and $\nu_5 \equiv \nu_{\rm peak}/(5\,{\rm GHz})$, such that

$$R = 7.1\times10^{16}\left(\frac{\epsilon_e}{\epsilon_B}\right)^{-1/19} L_{\theta\nu,29}^{9/19}\nu_5^{-1}\,{\rm cm} \tag{4.3a}$$

$$B = 0.36\left(\frac{\epsilon_e}{\epsilon_B}\right)^{-4/19} L_{\theta\nu,29}^{-2/19}\nu_5\,{\rm G} \tag{4.3b}$$

$$U = 4.0\times10^{48}\frac{1}{\epsilon_B}\left(\frac{\epsilon_e}{\epsilon_B}\right)^{-11/19} L_{\theta\nu,29}^{23/19}\nu_5^{-1}\,{\rm erg}. \tag{4.3c}$$

The upstream CSM density can be estimated under the conditions of strong shocks and fully ionized hydrogen (see Eq. 16 of Ho, Goldstein, et al. 2019):

$$n_e = 61\frac{1}{\epsilon_B}\left(\frac{\epsilon_e}{\epsilon_B}\right)^{-6/19} L_{\theta\nu,29}^{-22/19}\nu_5^4\left(\frac{\Delta t}{100\,{\rm days}}\right)^2\,{\rm cm^{-3}}. \tag{4.4}$$

Assuming that the CSM density profile is determined by a pre-explosion steady wind with mass-loss rate $\dot{M}$ and velocity $v_{\rm w}$, we have (see Eq. 23[5] of Ho, Goldstein, et al. 2019):

$$\frac{\dot{M}}{v_{\rm w}}\left(\frac{1000\,{\rm km\,s^{-1}}}{10^{-4}\,M_\odot\,{\rm yr^{-1}}}\right) = 0.10\left(\frac{1}{\epsilon_B}\right)\left(\frac{\epsilon_e}{\epsilon_B}\right)^{-8/19}\times L_{\theta\nu,29}^{-4/19}\nu_5^2\left(\frac{\Delta t}{100\,{\rm days}}\right)^2. \tag{4.5}$$

We adopt $L_{\theta\nu\,\rm peak} = L_{\nu\,\rm peak}/(1+z)^4 \approx 1.0\times10^{29}\,{\rm erg\,s^{-1}\,Hz^{-1}}$ and $\nu_{\rm peak}\approx 7\,{\rm GHz}$ at $\Delta t = 261$ days. Assuming $\epsilon_e = \epsilon_B = 1/3$, we have $R\approx 5.1\times10^{16}\,{\rm cm}$, $B\approx 0.50\,{\rm G}$, $U\approx 1.7\times10^{49}\,{\rm erg}$, and $n_e\approx 3.5\times10^3\,{\rm cm^{-3}}$. Assuming $\epsilon_e = 0.1$, $\epsilon_B = 0.01$, we have $R\approx 4.6\times10^{16}\,{\rm cm}$, $B\approx 0.31\,{\rm G}$, $U\approx 1.5\times10^{50}\,{\rm erg}$, and $n_e\approx 5.6\times10^4\,{\rm cm^{-3}}$. The average shock velocity ($v_{\rm sh} = R/\Delta t$) is 0.07–0.08c, suggesting a mildly relativistic shock. The derived R, U, $v_{\rm sh}$ should be taken as upper limits, B, n_e, $\dot{M}/v_{\rm w}$ should be taken as upper limits.

Figure 4.11 compares AT2020mrf with normal SNe (Bietenholz et al., 2021), SNe associated with long GRBs, and four AT2018cow-like objects in the literature. Note that all GRB-SNe are of type Ic-BL. Under the assumptions of the standard SSA model, dotted lines mark constant time-averaged velocity; Dashed lines mark constant mass-loss rate ($\dot{M}_{-4}\equiv\dot{M}/(10^{-4}\,M_\odot\,{\rm yr^{-1}})$) scaled to wind velocity ($v_{\rm w,\,3}\equiv v_{\rm w}/(10^3\,{\rm km\,s^{-1}})$). The two panels show the results with different assumptions of ϵ_e and ϵ_B. The data of AT2018cow-like objects and GRB-SNe are based on Fig. 9 of Ho, Margalit, et al. 2022 and Fig. 3 of Nayana and Chandra (2021).

[5]The normalization constant in Eq. 23 of Ho, Goldstein, et al. 2019 is off by a factor of ~ 10. Here we update the equation with the correct constant.

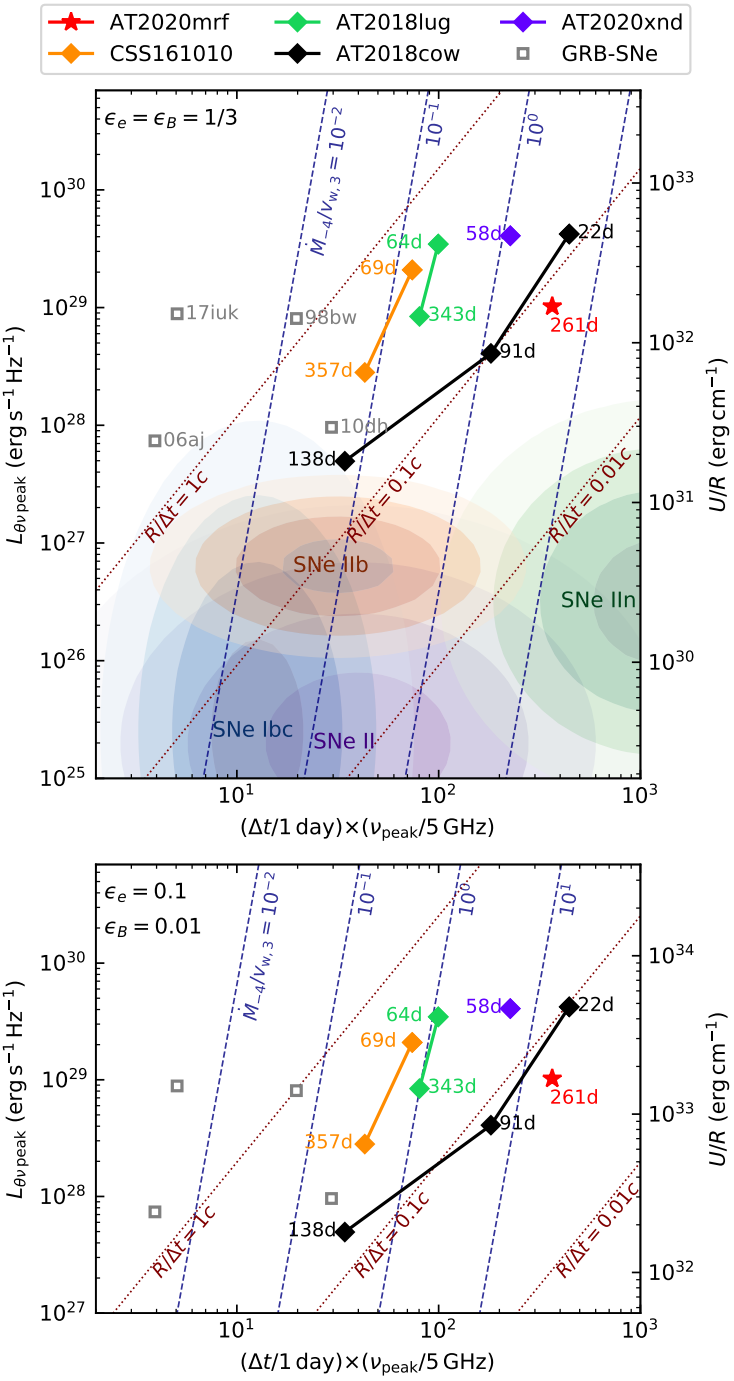

Figure 4.11: AT2020mrf and other transients on the diagram of peak radio luminosity ($L_{\nu\,\mathrm{peak}}$) versus the product of peak time and ν_{peak}.

The peak radio luminosity of AT2020mrf is much greater than normal SNe and is in the same regime as other AT2018cow-like objects. A physical interpretation is that the energy divided by the shock radius ($U/R \propto L_{\theta\nu\,\mathrm{peak}}^{14/19}$) is greater. This indicates a more efficient conversion/thermalization of energy, which can come from a higher explosion energy or a higher ambient density (Ho, Goldstein, et al., 2019).

Moreover, we see that the CSM "surface density" ($n_e R^2 \propto \dot{M}/v_\mathrm{w}$) of AT2020mrf at 261 days is similar to AT2018cow at 22 days. At a similar shock radius of $R \sim 6 \times 10^{16}$ cm, the CSM number density of AT2018cow is $n_e < 33\,\mathrm{cm}^{-3}$ (Nayana and Chandra, 2021) — more than 100 times smaller than that in AT2020mrf. Since $\dot{M}/v_\mathrm{w}$ generally decreases at later times (i.e., the density profile is steeper than $n_e \propto r^{-2}$), the immediate environment of AT2020mrf is probably denser than all other AT2018cow-like events.

CSM Inhomogeneity and Scintillation — The small values of β_1 and the flat-topped radio SEDs (Figure 4.8) motivate us to assume an inhomogeneous CSM, which means that the distribution of electrons or magnetic field strength varies within the synchrotron source (Björnsson and Keshavarzi, 2017). In this model, between the standard SSA optically thick $F_\nu \propto \nu^{5/2}$ regime and the optically thin $F_\nu \propto \nu^{-(p+1)/2}$ regimes, there is a transition regime with a spectral index of $0 < \beta < 2.5$. Since the measured β_1 remains below 2.5, we assume that the standard SSA optically thick regime is at frequencies lower than our observations.

Following Chandra, Nayana, et al. (2019), we fit the full set of radio data with the function

$$L(\nu, t) = K_1 \nu_5^\beta \left(\frac{\Delta t}{100\,\mathrm{days}}\right)^a \left[1 - \exp\left(-\tau_\mathrm{ssa}(\nu, t)\right)\right], \tag{4.6}$$

where τ_ssa is the SSA optical depth

$$\tau_\mathrm{ssa}(\nu, t) = K_2 \nu_5^{-(\beta + \frac{p-1}{2})} \left(\frac{\Delta t}{100\,\mathrm{days}}\right)^{-(a+b)}. \tag{4.7}$$

The best-fit model is shown in Figure 4.12, with $K_1 = 5.4^{+14.6}_{-4.4} \times 10^{29}\,\mathrm{erg\,s^{-1}\,Hz^{-1}}$, $K_2 = 13^{+53}_{-10}$, $\beta = 1.6^{+0.8}_{-0.6}$, $p = 3.3^{+0.4}_{-0.3}$, $a = -1.6^{+1.8}_{-1.4}$, and $b = 3.0^{+0.3}_{-0.4}$. Evidence of source inhomogeneities has also been found in AT2018cow (Nayana and Chandra, 2021). With an inhomogeneous CSM, the R, U, v_sh values derived in the standard SSA modeling should be taken as lower limits, and B, n_e, $\dot{M}/v_\mathrm{w}$ should be taken as upper limits.

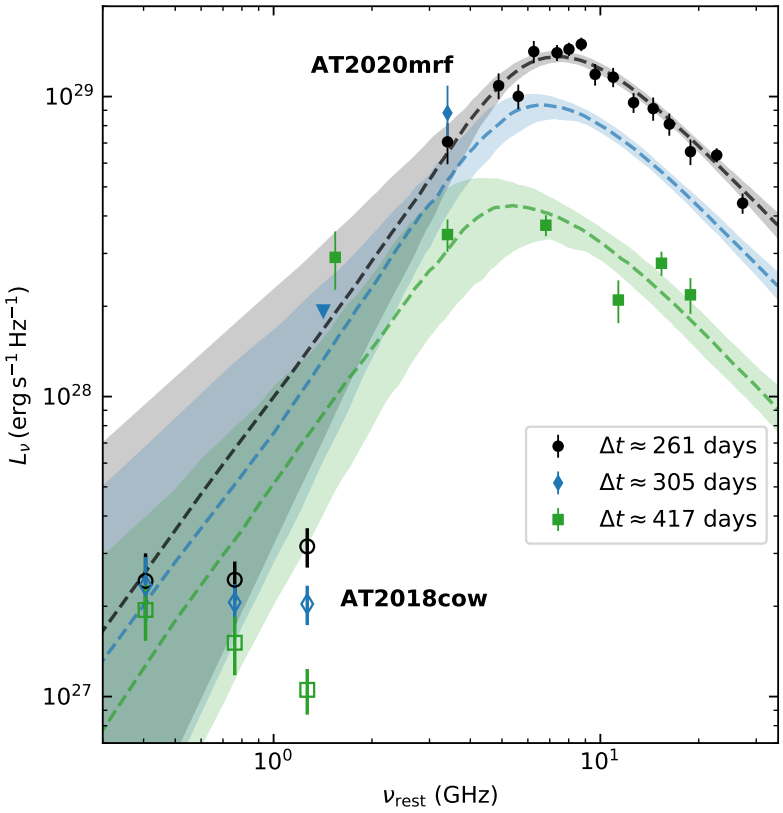

Figure 4.12: Radio SEDs of AT2020mrf, compared with the that of AT2018cow at similar phases.

A few datapoints at $\Delta t > 300$ days are not well fitted by the inhomogeneous SSA model. We estimate the effects of interstellar scintillation (ISS) to our radio observations using the `NE2001` model (Cordes and Lazio, 2002) of the Galactic distribution of free electrons. The transition frequency below which strong scattering occurs is (Goodman, 1997):

$$\nu_{\rm ss} = 10.4 ({\rm SM}_{-3.5})^{6/17} d_{\rm scr,\,kpc}^{5/17}\ {\rm GHz}, \tag{4.8}$$

where ${\rm SM}_{-3.5} \equiv {\rm SM}/(10^{-3.5}\ {\rm m}^{-20/3}\ {\rm kpc})$ is the scintillation measure, and $d_{\rm scr,\,kpc}$ is the distance to the electron scattering screen in kpc. For the line of sight to AT2020mrf (Galactic coordinates $l = 71.339°$, $b = 50.806°$), `NE2001` predicts $\nu_{\rm ss} = 8.3$ GHz and ${\rm SM}_{-3.5} = 0.53$, implying $d_{\rm scr,\,kpc} = 1.0$. This suggests that the 11.35 GHz "dip" (or 15–19 GHz "excess") cannot be explained by ISS.

AT2020mrf is subject to diffractive or refractive ISS if the source angular size satisfies $\theta_{\rm s} < 3.3 \nu_{10}^{6/5}\ \mu$as or $\theta_{\rm s} < 2.0 \nu_{10}^{-11/5}\ \mu$as (Goodman, 1997). We have shown that the shock radius at times of our radio observations is $R \gtrsim 5{\times}10^{16}$ cm, corresponding

to $\theta_s \gtrsim 6.8\,\mu$as. Therefore, the 3.4 GHz "excess" at $\Delta t \approx 305$ days and the 1.5 GHz "excess" at $\Delta t \approx 417$ days are likely caused by refractive ISS.

Properties of the Optical Emission

Rise and Decline Timescales — To constrain the optical evolution of AT2020mrf around maximum, we model the multi-band photometry using a power-law rise and an exponential decay. For simplicity we assume a blackbody SED and a single temperature for data at $\Delta t < 15$ days. The best-fit model in the $r_{\rm ZTF}$ band is shown as the solid orange line in Figure 4.1.

To compare AT2020mrf with the sample of spectroscopically classified FBOTs presented by Ho, Perley, Gal-Yam, et al. (2021), we calculate the time it takes for AT2020mrf to rise from half-max to max ($t_{1/2,\rm rise} = 2.4 \pm 0.2$ days), and to decline from max to half-max ($t_{1/2,\rm fade} = 4.8 \pm 0.2$ days). Its total duration above half-max is $t_{1/2} = 7.1^{+0.3}_{-0.2}$ days. On the $M_{\rm peak}$ versus $t_{1/2}$ diagram (see, e.g., Fig. 1 of Ho, Perley, Gal-Yam, et al. 2021 and Fig. 7 of Perley, Sollerman, et al. 2022), AT2020mrf lies between previously studied AT2018cow-like events ($t_{1/2} \lesssim 5$ days, $M_{\rm peak} \lesssim -20.5$) and interacting SNe of type IIn/Ibn/Icn ($t_{1/2} \gtrsim 7$ days, $M_{\rm peak} \gtrsim -20.0$).

Color Evolution — The $g - r$ color of AT2020mrf is -0.34 ± 0.20 mag at the day of discovery ($\Delta t \approx 0.25$ day), and reddens at later times. At $\Delta t \approx 6.4$, 11.7, and 23–28 days, the $g - r$ values are -0.05 ± 0.06 mag, -0.09 ± 0.14 mag, and 0.05 ± 0.27 mag, respectively. Assuming that the optical SED can be modeled by a blackbody, the blackbody temperature ($T_{\rm bb}$) decreases from $\sim 2 \times 10^4$ K to $\sim 10^4$ K. Similar cooling signatures have also been observed in AT2018lug, while both AT2018cow and AT2020xnd remain blue post-peak.

Figure 4.13 compares the color evolution of AT2020mrf with other FBOTs. We have included AT2018cow (Perley, Mazzali, et al., 2019), AT2018lug (Ho, Perley, Kulkarni, et al., 2020), AT2020xnd (Perley, Ho, et al., 2021), the type Icn SNe 2019hgp (Gal-Yam et al., 2022) and 2021csp (Perley, Sollerman, et al., 2022), as well as the gold sample of 22 spectroscopically classified FBOTs presented by Ho, Perley, Gal-Yam, et al. (2021). The calculated $g - r$ color has been corrected for Galactic extinction but assumes no host reddening. As can be seen, the amount of $g - r$ increase observed in AT2020mrf is closer to other multi-wavelength FBOTs and interacting SNe, but smaller than events shown in the lower panels.

Possible Power Sources — Like many other FBOTs, the fast rise and luminous optical peak of AT2020mrf is unlikely to be powered by radioactive ^{56}Ni decay,

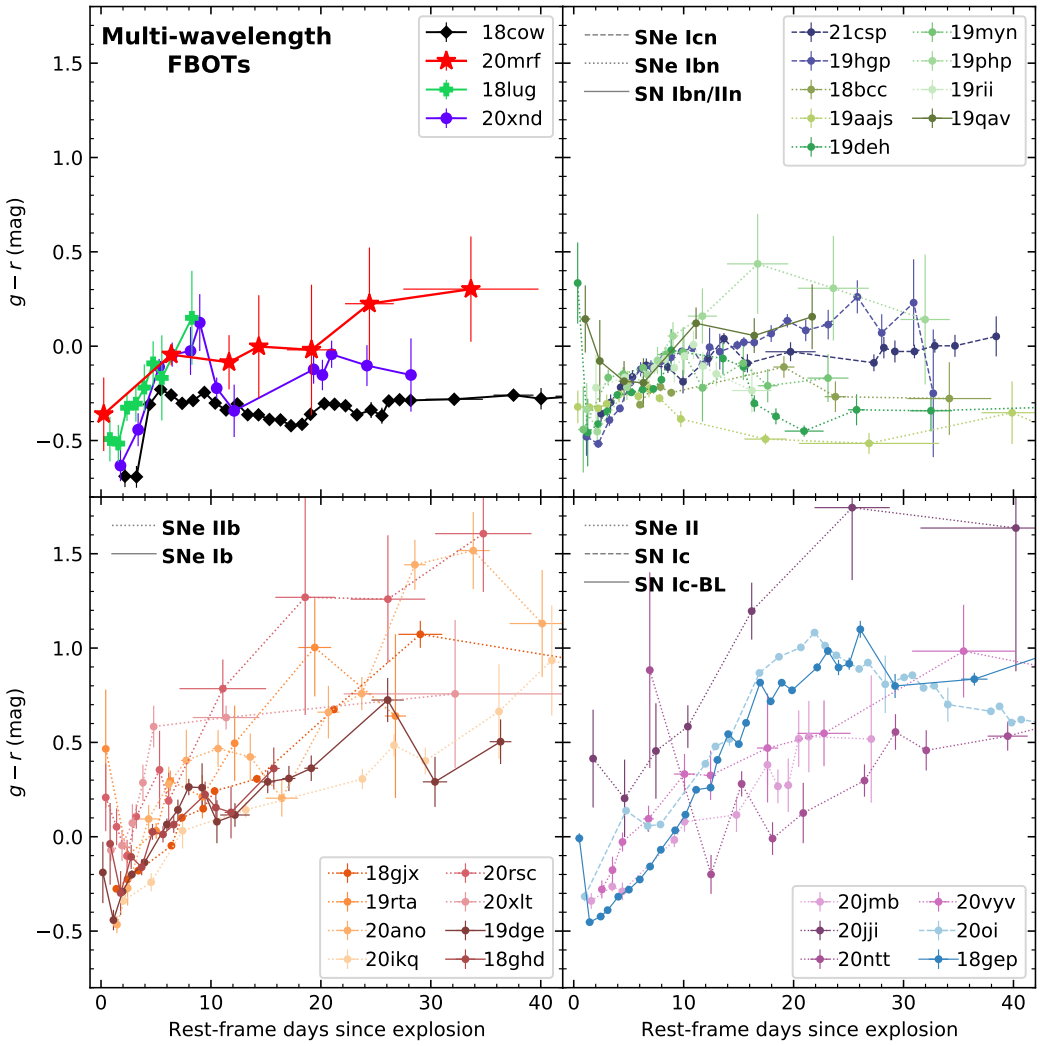

Figure 4.13: Color evolution of FBOTs.

which would require the nickel mass $M_{\rm Ni}$ to be greater than the ejecta mass $M_{\rm ej}$ (see, e.g., Fig. 1 of Kasen 2017). Possible emission mechanisms include shock breakout (SBO) from extended CSM (Waxman and Katz, 2017), shock cooling emission (SCE) from an extended envelope (Piro, Haynie, and Yao, 2021), continued interaction between the SN ejecta and the CSM (Smith, 2017; Fox and Smith, 2019), and reprocessing of X-ray/UV photons (potentially deposited by a central engine) by dense outer ejecta (Margutti, Metzger, et al., 2019) or an optically think wind (Piro and Lu, 2020). We do not attempt to distinguish between these scenarios due to a lack of multi-wavelength observations at early times.

The decay rate of AT2020mrf is significantly slower than that of AT2018cow and AT2020xnd (Figure 4.1). This is similar to the post-peak decay of AT2018lug,

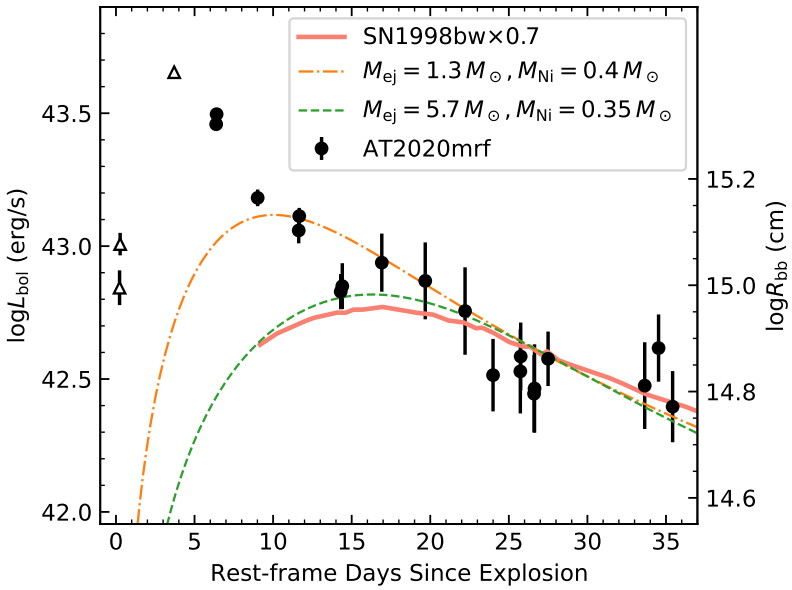

Figure 4.14: Bolometric light curve of AT2020mrf converted from ZTF photometry, assuming $T_{bb} = 10^4$ K.

which also slows down at $\Delta t \approx 6$–8 days (see Figure 4.1). The slower decay can be caused either by the emergence of a radioactivity powered SN or continued CSM interaction. Since the color evolution of AT2020mrf is most similar to interacting SNe shown in the upper right panel of Figure 4.13, we slightly favor the CSM interaction scenario. In §4.6, we attempt to fit the multi-band light curve using the one-zone SBO+SCE model presented by Margalit (2021), but no satisfactory fit is obtained. However, given that the CSM interaction model has many free parameters (e.g., anisotropy, radial density structure), more detailed modeling would be required to determine whether it is a viable emission mechanism.

Assuming $T_{bb} = 10^4$ K, the bolometric luminosity and blackbody radius of AT2020mrf are shown in Figure 4.14. The L_{bol} of SN1998bw (Galama et al., 1998) is shown for comparison. We show two models of radioactivity powered SN in the photospheric phase (Valenti et al., 2008; Lyman, Bersier, et al., 2016), adopting an opacity of $\kappa = 0.07\,\mathrm{cm^2\,g^{-1}}$ (typical for stripped envelope SNe; Taddia et al. 2018), and a photospheric velocity of $v_{phot} = 2 \times 10^4\,\mathrm{km\,s^{-1}}$ (typical for GRB-SNe; Modjaz et al. 2016).

Although radioactivity is not required to explain the optical emission, the light curve at $\Delta t \gtrsim 10$ days is consistent with being dominated by nickel decay with $M_{ej} \sim 1$–$6\,M_\odot$ and $M_{Ni} \sim 0.3$–$0.4\,M_\odot$. Improved analytic relations (compared to

the "Arnett model" shown in Figure 4.14) have been presented by Khatami and Kasen (2019). Adopting $L_{\rm peak} \approx 10^{42.8}$, $t_{\rm peak} \approx 17$ days, and the dimensionless parameter $\beta \approx 1$, we use Eq. 21 of Khatami and Kasen (2019) to estimate $M_{\rm Ni}$, which gives $M_{\rm Ni} \approx 0.26\,M_{\odot}$. In summary, the inferred $M_{\rm ej}$ and $M_{\rm Ni}$ are broadly consistent with stripped envelope SNe of all types (IIb, Ib, Ic, and Ic-BL; Drout, Soderberg, et al. 2011; Taddia et al. 2018; Prentice, Ashall, et al. 2019), but can not accommodate normal hydrogen-rich type II SNe (Meza and Anderson, 2020; Afsariardchi et al., 2021).

A Dwarf Host Galaxy

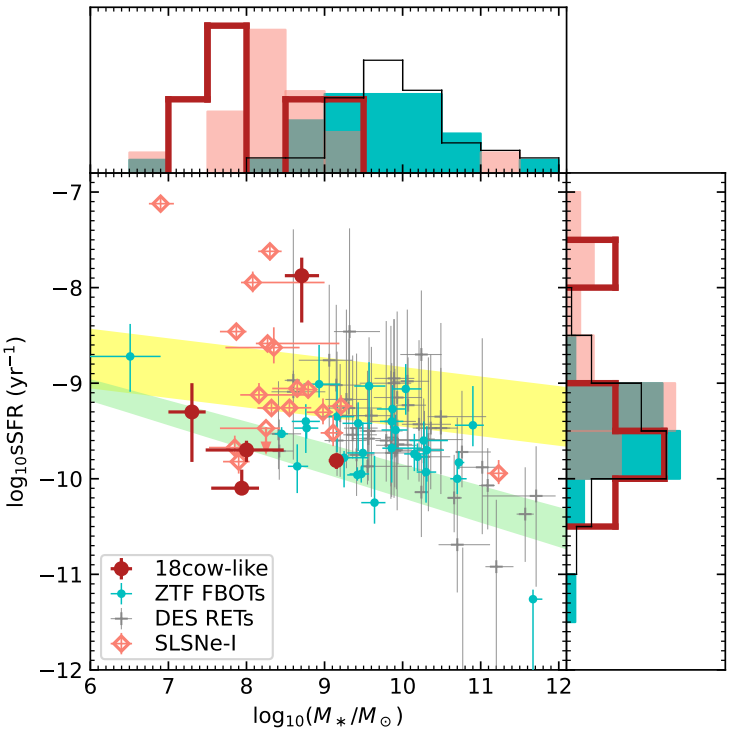

Figure 4.15: The host galaxy of AT2020mrf on the SFR–M_* diagram.

Figure 4.15 and Figure 4.16 show the position of AT2020mrf on the SFR–M_* and the sSFR–M_* diagrams. For comparison, hosts of other AT2018cow-like events: AT2018cow itself (Perley, Mazzali, et al., 2019), AT2018lug (Ho, Perley, Kulkarni, et al., 2020), CSS161010 (Coppejans et al., 2020), and AT2020xnd (Perley, Ho, et al., 2021). We also show the 28 FBOTs selected from ZTF (note that we excluded the three 18cow-like events from the 31 objects in Tab. 17 of Ho, Perley, Gal-Yam, et al. 2021), the 49 rapidly evolving transients (RETs) from the dark energy survey (DES) (Wiseman et al., 2020), 18 PTF SLSNe-I from Perley, Quimby, et al. (2016).

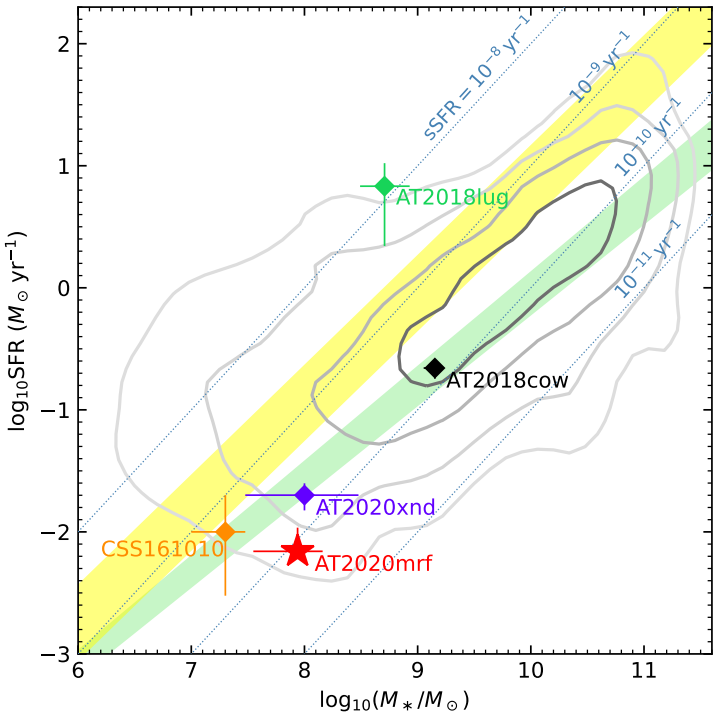

Figure 4.16: The host galaxies of AT2018cow-like events and other massive star explosions on the sSFR–M_* diagram.

The grey contours show the PTF/iPTF CCSNe host galaxy sample (Schulze et al., 2021), from 0.5σ to 2σ in steps of 0.5σ. The light green and yellow bands show the main sequence of star-forming galaxies at $0.02 < z < 0.085$ (Renzini and Peng, 2015) and $z \sim 1$ (Eq. 4 of Elbaz et al. 2007), respectively.

Compared with normal CCSNe (Schulze et al., 2021) and X-ray/radio-faint FBOTs, the M_* of AT2018cow-like events (a sample of five) is much smaller. Indeed, all AT2018cow-like events are hosted by dwarf galaxies with $M_* < 2 \times 10^9\ M_\odot$. This trend has been previously reported by Perley, Ho, et al. (2021), and argues for a massive star origin. Several types of the most powerful explosions from massive stars are also preferentially hosted by dwarf galaxies, including long GRBs (Vergani et al., 2015; Perley, Tanvir, et al., 2016), hydrogen-poor SLSNe (Leloudas, Schulze, et al., 2015; Perley, Quimby, et al., 2016; Taggart and Perley, 2021), and SNe Ic-BL (Schulze et al., 2021).

Perley, Ho, et al. (2021) have suggested that an elevated level of SFR or sSFR is not a requirement for producing AT2018cow and similar explosions. The properties of AT2020mrf's host further support this suggestion. At $M_* \sim 10^8\ M_\odot$, the SFR

of AT2020mrf lies below the main-sequence (MS) of local star-forming galaxies. Moreover, among the 369 PTF/iPTF normal CCSNe hosted by galaxies with $M_* < 2 \times 10^9\,M_\odot$ (Schulze et al., 2021), the host galaxies of only 30 objects (8%) have sSFR $< 8 \times 10^{-11}$ yr^{-1}. This indicates that AT2020mrf does not occur during a vigorous starburst, and that progenitor scenarios with a slightly longer delay time than that of a typical CCSN are favored. Zapartas et al. (2017) performed a population synthesis study of CCSNe, finding that a prolonged delay time can be achieved by binary interactions, through common envelope evolution, mass transfer episodes, and/or merging. Explosions driven by the merging of a compact object with a massive star inside a common envelope have indeed been proposed as promising channels for producing AT2018cow-like events (Soker, Grichener, and Gilkis, 2019; Schrøder et al., 2020; Soker, 2022; Metzger, 2022b).

Among the five AT2018cow-like events, only AT2018lug lies above the local MS of star-forming galaxies. For comparison, the majority (15/18) of SLSNe-I presented by Perley, Quimby, et al. (2016) lie above the local MS[6]. We perform a two-sided Kolmogorov-Smirnov (K-S) test for the null hypothesis that the host galaxy sSFR of SLSNe-I and AT2018cow-like events are drawn from the same distribution. The returned p-value of 0.23 is too high to reject the null hypothesis. A larger sample size is clearly needed to test if the host sSFR between AT2018cow-like events and other powerful massive star explosions are statistically different.

An Engine Driven Explosion

X-ray Properties — We have shown that the radio (§4.3) and early-time optical (§4.2, §4.3) properties of AT2020mrf are similar to other AT2018cow-like events. Here we summarize the key X-ray observables of AT2020mrf, and compare them with other AT2018cow-like events.

At $\sim$ 36 days, the mean 0.3–10 keV luminosity of AT2020mrf is $(1.9 \pm 0.4) \times 10^{43}$ erg s^{-1}, a factor of $\sim$ 20 brighter than AT2018cow and AT2020xnd at similar phases (Figure 4.7). The best-fit powerlaw of $f_\nu \propto \nu^{-0.8}$ (Figure 4.5) is similar to the 0.3–10 keV spectral shape of AT2018cow and AT2020xnd (Margutti, Metzger, et al., 2019; Bright et al., 2022; Ho, Margalit, et al., 2022). From 34.5 to 37.6 days, the 0.2–2.2 keV flux varies by a factor of ≈ 6 on the timescale of ≈ 1 day (Figure 4.4), similar to the fast soft X-ray variability observed in AT2018cow at similar phases

[6]Compared with AT2018cow-like events, the sample of SLSNe-I is at slightly higher redshifts (the median is $z \sim 0.2$). We note that for $M_* \approx 10^8\,M_\odot$, the sSFR at $z \approx 0.2$ is only slightly (≈ 0.2 dex) higher than that at $z \approx 0$ (Speagle et al., 2014).

(Figure 4.7).

At 328 days, the mean 0.3–10 keV luminosity of AT2020mrf is $\sim 1.4 \times 10^{42}$ erg s^{-1}, which is $\sim$ 300 times brighter than the upper limit of CSS161010 at 291 days, and $\sim$ 200 times brighter than AT2018cow itself at 212 days. The spectrum of AT2020mrf has probably hardened to $f_\nu \propto \nu^0$. From 327.4 to 328.2 days, the X-ray flux decreases by a factor of ~ 2.6.

Among AT2018cow-like events, intraday X-ray variability has only been detected in AT2018cow and AT20202mrf. This is probably because CSS161010, AT2018lug, and AT2020xnd were not observed often enough to detect it. The isotropic equivalent observed X-ray luminosity of AT2020mrf is as luminous as long GRBs. The X-ray emission of long GRBs are produced by the afterglow synchrotron radiation of electrons accelerated by a ultra-relativistic shock (Sari, Piran, and Narayan, 1998). However, given the lack of a prompt γ-ray emission (§4.2) and the sub-relativistic shock velocity (§4.3) observed in AT2020mrf, the nature of its X-rays should be different from that of long GRBs.

As shown in Figure 4.7, in AT2018cow (and perhaps AT2020xnd), the 0.3–10 keV light curve decay steepens from $L \propto t^{-1}$ ($t \lesssim 25$ days) to $L \propto t^{-4}$ ($25 \lesssim t \lesssim 100$ days). The overall decay shape of AT2020mrf is consistent with a $L \propto t^{-1.3}$ power-law. However, we can not rule out the existence of a steeper decay. Below we discuss the physical origin of the X-ray emission associated with AT2020mrf.

General Considerations — First, the dashed blue line in Figure 4.17 shows an example synchrotron spectrum one would expect at the epoch of the *Chandra* observation ($\Delta t \approx 328$ days). Here we have assumed $B \sim 0.2$ G, and a cooling frequency of $\nu_c = \gamma_c^2 \nu_g \sim 3 \times 10^{11}$ Hz, where $\gamma_c = 6\pi m_e c/(\sigma_{\rm T} B^2 t)$ and $\nu_g = eB/(2\pi m_e c)$ (Sari, Piran, and Narayan, 1998; Granot and Sari, 2002). Therefore, the late-time X-ray luminosity of AT2020mrf is too bright to be an extension of the radio synchrotron spectrum.

Second, inverse-Compton (IC) scattering of the radiation field (i.e., UV/optical photons) by electrons accelerated in the forward shock is found to be the main early-time ($t \lesssim 40$ days) X-ray emission mechanism for SNe Ib/c exploding in low-density environments (Fransson, Lundqvist, and Chevalier, 1996; Kamble et al., 2016). The ratio of IC to synchrotron radiation losses is $P_{\rm IC}/P_{\rm syn} = u_{\rm rad}/u_B$, where $u_{\rm rad}$ is the energy density in seed photons, and $u_B = U_B/(4\pi R_{\rm sh}^3/3)$. To first order, $P_{\rm IC}/P_{\rm syn} \sim L_{\rm X}/L_{\rm radio}$. At $\Delta t \approx 36$ days, the bolometric luminosity of the optical

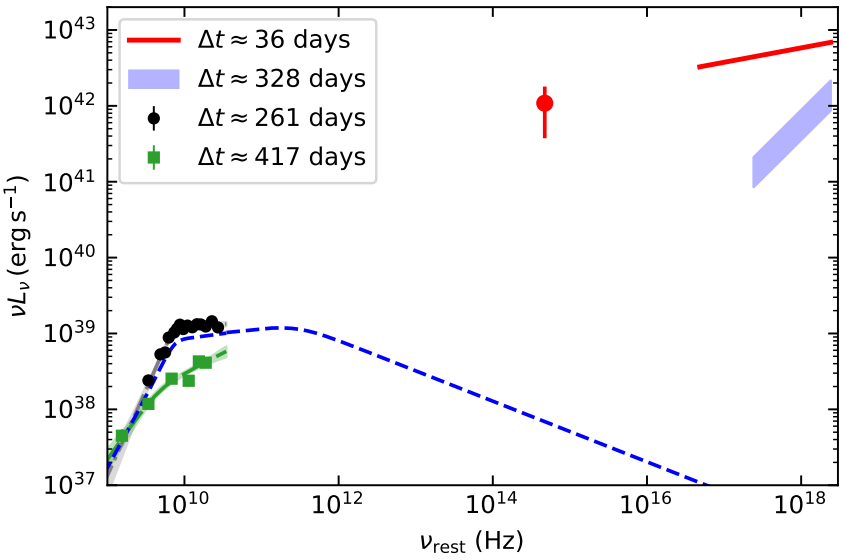

Figure 4.17: Broadband SED of AT2020mrf.

transient is $L_{\rm bol} \sim 10^{42.3}\,{\rm erg\,s^{-1}}$ (see Figure 4.14). Assuming $v_{\rm sh} \sim 0.07$–$0.08c$, the shock radius is $R_{\rm sh} \sim 7 \times 10^{15}\,{\rm cm}$. Therefore $u_{\rm rad}/L_{\rm X} = L_{\rm bol}/(4\pi c R_{\rm sh}^2)/L_{\rm X} \sim (0.1\,{\rm erg\,cm^{-3}})/(2\times10^{43}\,{\rm erg\,s^{-1}}) \sim 5.4\times10^{-45}\,{\rm s\,cm^{-3}}$. Assuming that the standard SSA model applies at $\Delta t \approx 36\,{\rm days}$[7], from Equation (4.3c) we have $u_B/L_{\rm radio} \sim 8\times10^{-31} L_{\theta\nu,29}^{4/19}(\epsilon_e/\epsilon_B)^{-11/19}\nu_{100}^{-1} > 2\times10^{-31}\,{\rm s\,cm^{-3}}$, where we have assumed that the early-time synchrotron emission peaks at $\sim 100\,{\rm GHz}$ and $L_{\theta\nu} > 10^{29}\,{\rm erg\,s^{-1}\,Hz^{-1}}$. Therefore, $u_{\rm rad}/L_{\rm X} \ll u_B/L_{\rm radio}$, and IC is not likely to be the dominant mechanism for the X-ray emission. At $\Delta t \approx 328\,{\rm days}$, the observed X-ray spectral shape of $f_\nu \propto \nu^0$ is too hard to be consistent with IC.

Finally, X-rays from most normal CCSNe and interacting SNe have been successfully modeled by thermal bremsstrahlung from supernova reverse-shock-heated ejecta or the forward-shock-heated CSM (Chevalier and Fransson, 1994; Dwarkadas and Gruszko, 2012). The shortest variability timescale expected from clumpy CSM encountered by a forward shock is much slower — $\Delta t/t = v_{\rm sh}/c \sim 0.1$ (see Section 3.3.1 of Margutti, Metzger, et al. 2019). In contrast, the X-ray relative variability and flux contrast are $\Delta t/t \approx 0.03$, $\Delta F/F \approx 2.5$ at $t \approx 36\,{\rm days}$ and $\Delta t/t \lesssim 0.003$, $\Delta F/F \approx 1$ at $t \approx 328\,{\rm days}$.

Some previous studies have interpreted AT2018cow as the tidal disruption of a

[7]This assumption will not be accurate if $v_{\rm sh} \gtrsim 0.2c$, at which condition we expect thermal electrons to contribute significantly to the synchrotron spectrum (Ho, Margalit, et al., 2022; Margalit and Quataert, 2021).

white dwarf or star by an IMBH (Kuin et al., 2019; Perley, Mazzali, et al., 2019). Since the observed early-time non-thermal X-ray spectrum and fast variability are not consistent with observations of thermal X-ray loud TDEs (Sazonov et al., 2021), the X-rays are thought to be powered by a jet similar to that observed in the jetted TDE SwiftJ1644 (Burrows, Kennea, et al., 2011; Bloom et al., 2011). However, for AT2020mrf and AT2018cow-like events in general, the TDE scenario is disfavored by the dense environment (§4.3) and the host properties (§4.3).

Therefore, the most natural origin of the X-rays in AT2020mrf is a central compact object — either a neutron star or a black hole — formed in a massive star explosion. Since the UV/optical luminosity of AT2020mrf remains much lower than $L_{\rm X}$ throughout the evolution, we can assume that the central engine luminosity $L_{\rm e}$ is mostly tracked by $L_{\rm X}$. The engine timescale is set by the duration of the X-ray emission $t_{\rm e} > 328\,{\rm days}$. The total energy release in the X-ray is $E_{\rm e} > (2\times10^{43}\,{\rm erg\,s^{-1}})\times(36\,{\rm days})+(10^{42}\,{\rm erg\,s^{-1}})\times[(328-36)\,{\rm days}] = 9\times10^{49}\,{\rm erg}$.

Stellar Mass Black Hole Engine — The engine of AT2020mrf can be a stellar mass BH, where X-rays are powered by accretion. The isotropic equivalent luminosity of 10^{42}–$10^{43}\,{\rm erg\,s^{-1}}$ corresponds to an Eddington ratio of $L_{\rm engine}/L_{\rm Edd} > 10^{4}$–$10^{3}$ for a $10\,M_\odot$ BH, suggesting that the emission is likely beamed.

In the case of a failed explosion, $t_{\rm e}$ is determined by the free-fall of the stellar envelope (Quataert and Kasen, 2012; Fernández et al., 2018):

$$t_{\rm ff} = \frac{\pi r^{3/2}}{(2GM_\star)^{1/2}} = 706\left(\frac{r}{10^{14}\,{\rm cm}}\right)^{3/2}\left(\frac{M_\star}{10\,M_\odot}\right)^{-1/2}\,{\rm day}. \tag{4.9}$$

In order to power AT2020mrf's X-ray emission out to 328 days, a weakly bound red supergiant (RSG) progenitor with $r > 6\times10^{13}\,{\rm cm}$ is required. The amount of mass around the disk circularization radius is much smaller than that in the stellar envelope, and the fast X-ray variability is related to the change of angular momentum in the accreting material (Quataert, Lecoanet, and Coughlin, 2019).

In the case of a successful explosion, the accretion is supplied by fallback of bound material (Dexter and Kasen, 2013). In compact progenitors such as blue supergiants (BSGs), a reverse shock decelerates the inner layers of the ejecta, resulting in enhanced fallback mass (Zhang, Woosley, and Heger, 2008). The fast X-ray variability might be caused by disk instability since the viscous time is much shorter than the fallback time. The temporal coverage of our X-ray data is poor. It is possible that $L_{\rm e}$ decays shallower than $t^{-1.3}$ initially, followed by a steeper decay (e.g. $L_{\rm e} \propto t^{-5/3}$)

due to fallback. This might be consistent with a range of SN energies, with lower energies corresponding to later transition times between an early less steep light curve to a later steeper fallback light curve (Quataert and Kasen, 2012).

Millisecond Magnetar Engine — Another speculation is that the engine of AT2020mrf is a young magnetar (i.e., an extremely magnetized neutron star), where $L_{\rm e}$ is primarily provided by rotational energy loss due to spindown. For a neutron star with a spin period of $P_{\rm ms} \equiv P/(1\,{\rm ms})$ and a mass of $1.4\,M_\odot$, the rotational energy is $E_{\rm rot} \approx 2.5\times10^{52}P_{\rm ms}^{-2}$ erg (Kasen and Bildsten, 2010; Kasen, 2017). The spin period required to power $E_{\rm e}$ is thus $P \lesssim 17$ ms. If the NS has a radius of 10 km and a magnetic field of $B_{14} \equiv B/(10^{14}\,{\rm G})$, the characteristic spindown timescale is $t_{\rm spindown} \approx 0.5 B_{14}^{-2}P_{\rm ms}^{2}$ day. The luminosity extracted from spindown is roughly constant when $t \lesssim t_{\rm spindown}$, and decays as $L_{\rm e} \propto t^{-2}$ afterwards. Extrapolating the *Chandra* detection back to the *SRG* luminosity suggests that the transition occurs at ~ 73 days, which implies $B \lesssim 1.4\times10^{14}$ G. This is similar to the B field required to power AT2018cow inferred by Margutti, Metzger, et al. (2019).

In this scenario, X-rays are generated in a "nebula" region of electron/positron pairs and radiation inflated by a relativistic wind behind the SN ejecta (Vurm and Metzger, 2021). Additional energy injection by fallback accretion widens the parameter space of magnetar birth properties, and predicts a late-time light curve decay shallower or steeper than $L_{\rm e} \propto t^{-2}$ (Metzger, Beniamini, and Giannios, 2018). The day-timescale X-ray variability can be accounted for by magnetically driven mini-outbursts.

4.4 The Detection Rate in X-ray Surveys

Table 4.7: The detection rates ($\dot{N}_{\rm det}$ in yr^{-1}) of events similar to AT2018cow and AT2020mrf in X-ray surveys, under three different assumptions of the event volumetric rates ($\mathcal{R}$ in Gpc^{-3} yr^{-1}).

Survey	f_{-13}	$D_{\rm max}$	$\dot{N}_{\rm det}$ if $\mathcal{R}=2.1$	$\dot{N}_{\rm det}$ if $\mathcal{R}=70$	$\dot{N}_{\rm det}$ if $\mathcal{R}=420$
SRG/eROSITA	1.8	373	0.080	2.7	16
		964	1.7	57	340
Einstein Probe	20	112	0.012	0.41	2.5
		289	0.21	7.1	43

$D_{\rm max}$ is given in Mpc. The values in the first and third rows assume an X-ray light-curve shape similar to AT2018cow. The values in the second and fourth rows assume a conservative light-curve shape similar to AT2020mrf, and therefore the derived $\dot{N}_{\rm det}$ should be taken as lower limits.

AT2020mrf is the first multi-wavelength FBOT identified from X-ray surveys. This

motivates us to estimate the rate of such events in present and future X-ray surveys. The core collapse SN rate is $R = 7 \times 10^4\,\mathrm{Gpc^{-3}\,yr^{-1}}$ (Li et al., 2011). The birthrate of 18cow-like events estimated by ZTF is $\mathcal{R} = 3 \times 10^{-5}$–$6 \times 10^{-3} R$ (Ho, Perley, Gal-Yam, et al., 2021), or 2.1–420 $\mathrm{Gpc^{-3}\,yr^{-1}}$.

Here we assume that a multi-wavelength FBOT has an X-ray light curve either similar to AT2018cow itself or similar to AT2020mrf. We approximate the 0.3–10 keV X-ray luminosity of AT2018cow as a plateau with a luminosity of $L_{\mathrm{X,\,p0}} = 3 \times 10^{42}$ erg $\mathrm{s^{-1}}$ and a duration of $t_{\mathrm{X,\,p0}} = 30$ days (Figure 4.7). The light curve shape of AT2020mrf is less well constrained. For simplicity, we assume a conservative shape consisting of two plateaus, with $L_{\mathrm{X,\,p1}} = 2 \times 10^{43}\,\mathrm{erg\,s^{-1}}$, $t_{\mathrm{X,\,p1}} = 36$ days, $L_{\mathrm{X,\,p2}} = 1 \times 10^{42}\,\mathrm{erg\,s^{-1}}$, and $t_{\mathrm{X,\,p2}} = 350$ days.

The transient detection rate is

$$\dot{N}_{\mathrm{det}} = \frac{\Omega}{3} D_{\mathrm{max}}^3 \mathcal{R} \cdot p_{\mathrm{s}} \tag{4.10}$$

where Ω is the solid angle of the surveyed area ($\Omega = 4\pi$ for an all-sky survey), D_{max} is the maximum distance out to which the source can be detected, and p_{s} is the probability that the transient is "on" when being scanned by the X-ray survey. If the survey cadence is shorter than the transient duration, $p_{\mathrm{s}} = 1$. Setting a survey flux threshold of $f_{\mathrm{thre}} = 10^{-13} f_{-13}\,\mathrm{erg\,cm^{-2}\,s^{-1}}$, we have $4\pi D_{\mathrm{max}}^2 f_{\mathrm{thre}} = L_{\mathrm{X,\,p}}$.

On average, every 0.5 yr, *SRG*/eROSITA samples the same region of the sky over $\sim$ 12 passes within $\sim$ 2 days. For a single event, somewhere on the sky, with an X-ray light curve shape similar to AT2018cow, the probability of being imaged by *SRG* during its X-ray active phase is $p_{\mathrm{s0}} = 2 \times (t_{\mathrm{X,\,p0}} + 2)/365 = 0.175$. For a light curve shape similar to AT2020mrf, $p_{\mathrm{s1}} = 2 \times (t_{\mathrm{X,\,p1}} + 2)/365 = 0.208$, and $p_{\mathrm{s2}} \sim 1$. The sensitivity of an eROSITA single sky survey is $\approx 2.5 \times 10^{-14}\,\mathrm{erg\,s^{-1}\,cm^{-2}}$ (see Fig. 17 of Sunyaev, Arefiev, et al. 2021). In reality, to be selected as a transient by eRASSn ($n > 1$), the source needs to exceed the eRASS1 sensitivity limit by a factor of ≈ 7. Therefore, the flux threshold is $f_{-13} \approx 1.8$.

Einstein Probe (EP) is a lobster-eye telescope for monitoring the X-ray sky (Yuan, Zhang, et al., 2018) to be launched in 2023. With an orbital period of 97 min, the entire sky can be covered over three successive orbits. Here we assume that its Wide-field X-ray telescope (WXT) is 2 orders of magnitude more sensitive than the Monitor of All-sky X-ray Image (*MAXI*) mission[8]. *MAXI* has a transient triggering

[8]From slide #32 of `https://sites.astro.caltech.edu/~srk/XC/Notes/EP_20200923.pdf`.

threshold of 8 mCrab for 4 days (Negoro, Kohama, et al., 2016), leading us to assume $f_{-13} \approx 20$ for EP.

The calculated detection rates in eROSITA and EP are summarized in Table 4.7. The rate of similar events in present and future millimeter transient surveys is given by Ho, Margalit, et al. (2022) and Eftekhari, Berger, Metzger, et al., 2022.

4.5 Summary

We report multi-wavelength observations of AT2020mrf, the fifth member of the class of AT2018cow-like events (i.e., FBOTs with luminous multi-wavelength counterparts). Among the four 18cow-like events ever detected in the X-ray (i.e., AT2018cow, CSS161010, AT2020xnd, AT2020mrf), AT2020mrf is the most luminous object, exhibiting day-timescale X-ray variability both at early (≈ 36 days) and late times (≈ 328 days), with a luminosity between 10^{42} and few$\times 10^{43}$ erg s^{-1}. Previously, the only object showing evidence of a NS/BH central engine was AT2018cow (Margutti, Metzger, et al., 2019; Pasham, Ho, et al., 2021). Here we show that a compact object — a young millisecond magnetar or an accreting black hole — is required to be the central energy source of AT2020mrf (see §4.3).

AT2020mrf also provides accumulating evidence to show that AT2018cow-like events form another class of engine-driven massive star explosions, after long GRBs and SLSNe-I. Intriguingly, all three classes of events are preferentially hosted by dwarf galaxies. Given the MZR (Gallazzi et al., 2005; Berg et al., 2012; Kirby et al., 2013), low metallicity probably plays an important role in the formation of such exotic explosions by reducing angular momentum loss of their progenitors (Kudritzki and Puls, 2000). Local environment studies with integral-field unit (IFU) observations (e.g., Lyman, Galbany, et al. 2020) and high spatial resolution images (e.g., with the Hubble Space Telescope) can further illuminate the nature of their progenitors.

Although AT2018cow, AT2018lug, and AT2020xnd are FBOTs with $-20.5 < M_{g,\mathrm{peak}} < -21.5$ and $t_{1/2} < 5$ day, the optical light curve of AT2020mrf is of lower peak luminosity ($M_{g,\mathrm{peak}} = -20$) and slower evolution timescale ($t_{1/2} = 7$ days). This should guide searches of such events in optical wide field surveys to be more agnostic of the light curve decay rate. Real-time identification of FBOTs and comprehensive spectroscopic follow up observations are necessary to distinguish between different emission mechanisms: shock interaction with extended CSM, radioactivity, or wind reprocessing. The discovery of X-ray emission in AT2020mrf

also showcases how X-ray surveys such as *SRG* can be essential in the identification of multi-wavelength FBOTs.

Once identified, millimeter and radio follow-up observations are needed to reveal the CSM density as a function of distance to the progenitor, which contains information about the mass-loss history (§4.3). X-ray light curves provide diagnostics for the nature of the power source (§4.3), while broad-band X-ray spectroscopy can constrain the evolution of the geometry of the material closest to the central engine (Margutti, Metzger, et al., 2019). Given the late-time X-ray detections of AT2018cow at $\Delta t \approx 212$ days (§4.6) and of AT2020mrf at $\Delta t \approx 328$ days (§4.2), future *Chandra* observations of these two objects may further constrain the timescales of their central engines.

4.6 Appendix

XMM-Newton Late-time Detection of AT2018cow

AT2018cow was observed by *XMM-Newton*/EPIC on three epochs (PI Margutti) at rest-frame 29.6, 78.1, and 211.8 days since explosion. The first two epochs yielded clear X-ray detections, which have been reported by Margutti, Metzger, et al. (2019). Pasham, Ho, et al. (2021) analyzed the 0.25–2.5 keV EPIC/MOS1 data of the third epoch, and reported a non detection. Here we analyze the third epoch EPIC/pn data to derive the flux (or upper limit) in 0.3–10 keV, which is important to be compared with the late-time X-ray detection of AT2020mrf. The pn instrument generally has better sensitivity than MOS1 and MOS2.

We reduced the pn data using the *XMM-Newton* Science Analysis System (SAS) and relevant calibration files. Events were filtered with the conditions `PATTERN<=4` and `(FLAG&0xfb0825)==0`. We removed high background time windows and retained 43178 s good times among the total exposure time of of 53163 s. Following Margutti, Metzger, et al. (2019), we extracted the source using a circular region with a radius of $r_{\rm src} = 20''$ to avoid contamination from a nearby source located 36.8″ southwest form AT2018cow. The background is extracted from a source-free circular region with a radius of $r_{\rm bkg} = 30''$ on the same CCD (see Figure 4.18).

The average count rate of the source is $0.00486\,{\rm count\,s^{-1}}$. The average count rate of the background (multiplied by $r_{\rm src}^2/r_{\rm bkg}^2$ to match the area of the source region) is $0.00360\,{\rm count\,s^{-1}}$. Therefore, AT2018cow is detected at a (Gaussian equivalent) confidence limit of 4.2σ. Assuming an absorbed power-law model with $\Gamma \approx 2$ and $N_{\rm H} \approx 7{\times}10^{20}\,{\rm cm^{-2}}$, the 0.3–10 keV flux is $\sim 1.6{\times}10^{-14}\,{\rm erg\,s^{-1}\,cm^{-2}}$, corresponding

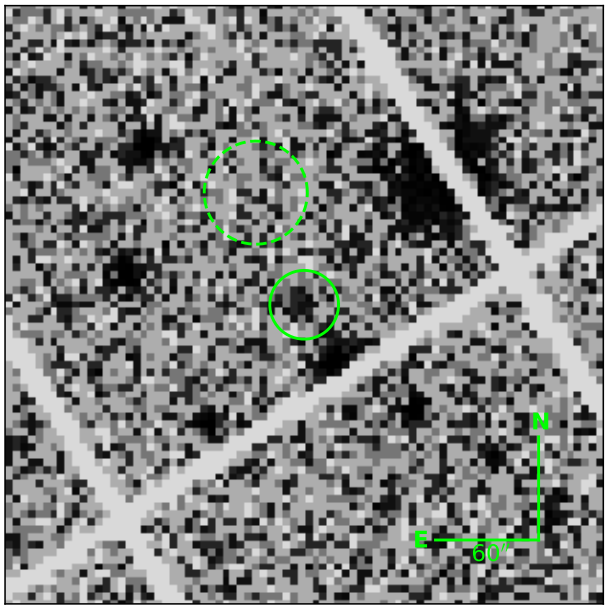

Figure 4.18: *XMM-Newton*/pn 0.3–10 keV image centered on AT2018cow, obtained at $\Delta t = 212$ days.

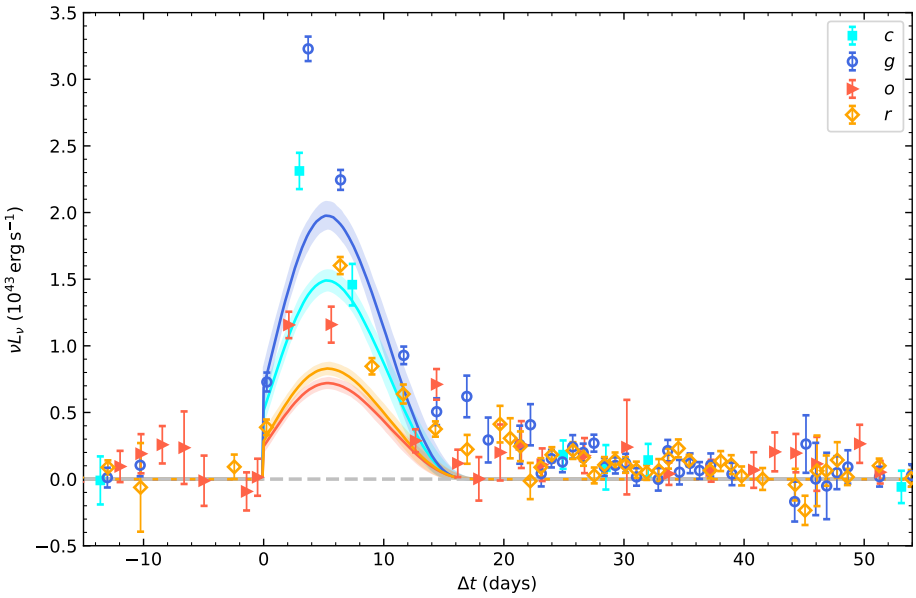

Figure 4.19: Dense CSM shock breakout and cooling model fit to the multi-band light curve of AT2020mrf. The maximum a posteriori model is shown via solid lines.

to a luminosity of $\sim 7 \times 10^{39}\,\mathrm{erg\,s^{-1}}$.

A Sample of GRB X-ray Light Curves

The sample of GRB light curves shown in Figure 4.7 is collected as follows. We start with the list of GRBs given by the *Swift* GRB Table[9]. Next, we retain the 339 long GRBs ($T_{90} > 2$ s) with reported redshifts. After that, we require the last *Swift*/XRT detection to be at $[(t - T_0)/(1 + z)] > 20$ days, where T_0 is the GRB trigger time. This step selects 12 events, including GRB171205A ($z = 0.0368$), GRB190829A ($z = 0.078$), GRB180728A ($z = 0.12$), GRB161219B ($z = 0.15$), GRB130427A ($z = 0.34$), GRB061021 ($z = 0.35$), GRB091127 ($z = 0.49$), GRB060729 ($z = 0.54$), GRB090618 ($z = 0.54$), GRB090424 ($z = 0.54$), GRB080411 ($z = 1.0$), and GRB100814A ($z = 1.4$). We supplement the XRT light curves with deep late-time X-ray observations reported in the literature (Grupe, Burrows, et al., 2010; De Pasquale et al., 2016).

Modeling the Optical Light Curve with CSM SBO+SCE

For simplicity, we adopt the one-zone model presented in Margalit (2021) to fit the optical light curve of AT2020mrf. Following Yao, Miller, et al. (2019), we add a constant additional variance σ_0^2 to each of the measurement variance σ_i^2 to account for systematic uncertainties. The multi-band light curves are parameterized using five free parameters: t_0, $t_{\rm dyn}$, $t_{\rm a}$, β, and E_0 (see Table 1 of Margalit 2021 for the definitions of these variables). The best-fit model is shown in Figure 4.19, and the posterior distribution is shown in Figure 4.20.

We are not able to obtain a decent fit to the observed light curves. This is due to the fact that in the CSM shock breakout and cooling model, the light curve decay can not be significantly slower than the rise, making it difficulty to reproduce the "flux excess" observed at $\Delta t \sim$15–35 days.

[9] `https://swift.gsfc.nasa.gov/archive/grb_table/fullview/`.

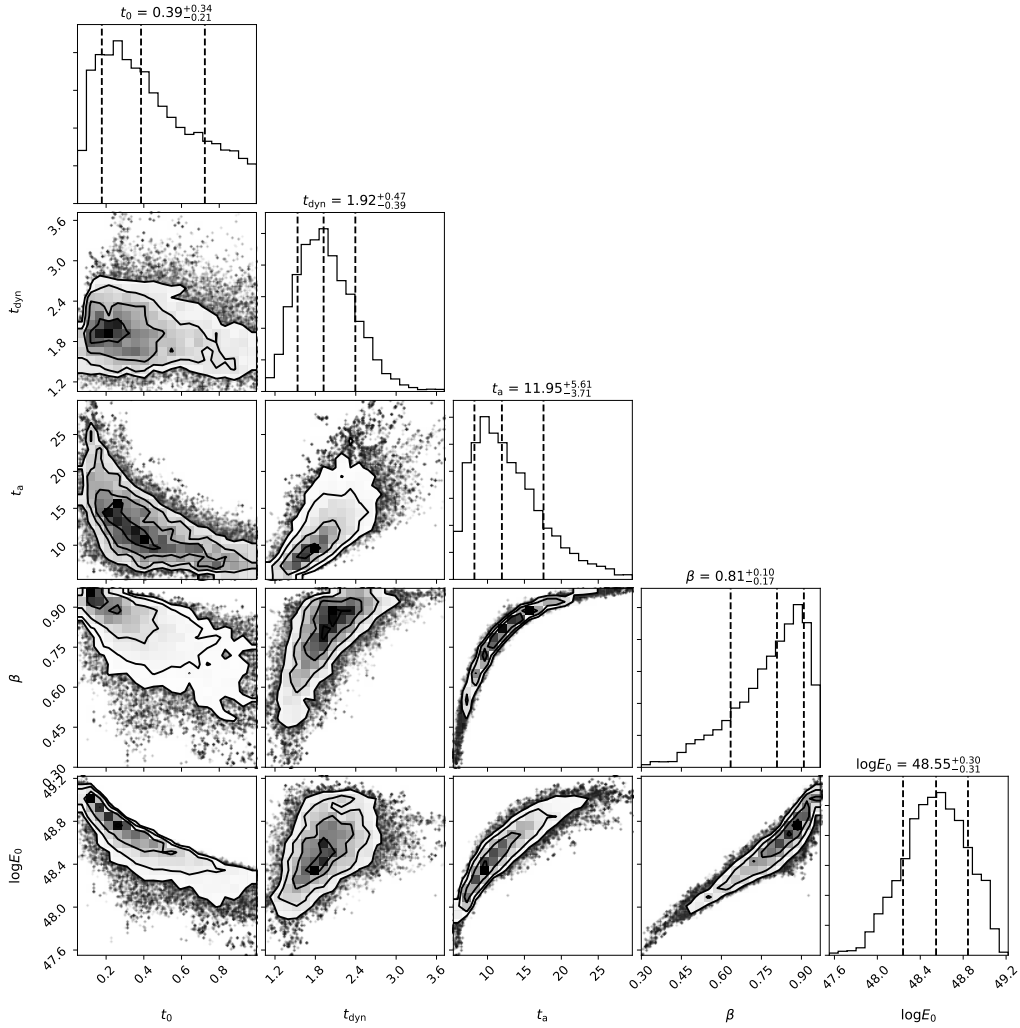

Figure 4.20: Corner plot showing the posterior constraints on the model parameters. Each parameter is marginalized over σ_0.

Chapter 5

THE TIDAL DISRUPTION EVENT AT2021EHB: EVIDENCE OF RELATIVISTIC DISK REFLECTION, AND RAPID EVOLUTION OF THE DISK–CORONA SYSTEM

Yao, Y. et al. (Sept. 2022). In: *ApJ* 937.1, 8, p. 8. DOI: 10.3847/1538-4357/ac898a.

Yuhan Yao[1], Wenbin Lu[2,3], Muryel Guolo[4], Dheeraj R. Pasham[5], Suvi Gezari[6], Marat Gilfanov[7,8], Keith C. Gendreau[9], Fiona Harrison[1], S. Bradley Cenko[9], S. R. Kulkarni[1], Jon M. Miller[10], Dominic J. Walton[11,12], Javier A. García[1,13], Sjoert van Velzen[14], Kate D. Alexander[15], James C. A. Miller-Jones[16], Matt Nicholl[17], Erica Hammerstein[18], Pavel Medvedev[7], Daniel Stern[19], Vikram Ravi[1], R. Sunyaev[7,8], Joshua S. Bloom[3,20], Matthew J. Graham[1], Erik C. Kool[21], Ashish A. Mahabal[1,22], Frank J. Masci[23], Josiah Purdum[24], Ben Rusholme[23], Yashvi Sharma[1], Roger Smith[24], and Jesper Sollerman[21]

[1] Division of Physics, Mathematics and Astronomy, California Institute of Technology, Pasadena, CA 91125, USA

[2] Department of Astrophysical Sciences, 4 Ivy Lane, Princeton University, Princeton, NJ 08544, USA

[3] Department of Astronomy, University of California, Berkeley, CA 94720-3411, USA

[4] Department of Physics and Astronomy, Johns Hopkins University, 3400 N. Charles Street, Baltimore, MD 21218, USA

[5] Kavli Institute for Astrophysics and Space Research, Massachusetts Institute of Technology, Cambridge, MA 02139, USA

[6] Space Telescope Science Institute, 3700 San Martin Drive, Baltimore, MD 21218, USA

[7] Space Research Institute, Russian Academy of Sciences, Profsoyuznaya ul. 84/32, Moscow, 117997, Russia

[8] Max-Planck-Institut für Astrophysik, Karl-Schwarzschild-Str. 1, D-85741 Garching, Germany

[9] Astrophysics Science Division, NASA Goddard Space Flight Center, Greenbelt, MD 20771, USA

[10] Department of Astronomy, The University of Michigan, 1085 South University Avenue, Ann Arbor, MI 48103, USA

[11] Centre for Astrophysics Research, University of Hertfordshire, College Lane, Hatfield AL10 9AB, UK

[12] Institute of Astronomy, University of Cambridge, Madingley Road, Cambridge CB3 0HA, UK

[13] Dr. Karl Remeis-Observatory and Erlangen Centre for Astroparticle Physics, Sternwartstr. 7, D-96049 Bamberg, Germany

[14] Leiden Observatory, Leiden University, Postbus 9513, 2300 RA, Leiden, The Netherlands

[15] Center for Interdisciplinary Exploration and Research in Astrophysics (CIERA) and Department of Physics and Astronomy, Northwestern University, Evanston, IL 60208, USA

[16] International Centre for Radio Astronomy Research, Curtin University, GPO Box U1987, Perth, WA 6845, Australia

[17] Birmingham Institute for Gravitational Wave Astronomy and School of Physics and Astronomy, University of Birmingham, Birmingham B15 2TT, UK

[18] Department of Astronomy, University of Maryland, College Park, MD 20742, USA
[19] Jet Propulsion Laboratory, California Institute of Technology, 4800 Oak Grove Drive, Pasadena, CA 91109, USA
[20] Lawrence Berkeley National Laboratory, 1 Cyclotron Road, MS 50B-4206, Berkeley, CA 94720, USA
[21] The Oskar Klein Centre, Department of Astronomy, Stockholm University, AlbaNova, SE-10691, Stockholm, Sweden
[22] Center for Data Driven Discovery, California Institute of Technology, Pasadena, CA 91125, USA
[23] IPAC, California Institute of Technology, 1200 E. California Boulevard, Pasadena, CA 91125, USA
[24] Caltech Optical Observatories, California Institute of Technology, Pasadena, CA 91125, USA

Abstract

We present X-ray, UV, optical, and radio observations of the nearby (≈78 Mpc) tidal disruption event (TDE) AT2021ehb/ZTF21aanxhjv during its first 430 days of evolution. AT2021ehb occurs in the nucleus of a galaxy hosting a $\approx 10^7\,M_\odot$ black hole ($M_{\rm BH}$ inferred from host galaxy scaling relations). High-cadence *Swift* and *NICER* monitoring reveals a delayed X-ray brightening. The spectrum first undergoes a gradual soft → hard transition and then suddenly turns soft again within 3 days at $\delta t \approx 272$ days during which the X-ray flux drops by a factor of ten. In the joint *NICER*+*NuSTAR* observation ($\delta t = 264$ days, harder state), we observe a prominent non-thermal component up to 30 keV and an extremely broad emission line in the iron K band. The bolometric luminosity of AT2021ehb reaches a maximum of $6.0^{+10.4}_{-3.8}\%L_{\rm Edd}$ when the X-ray spectrum is the hardest. During the dramatic X-ray evolution, no radio emission is detected, the UV/optical luminosity stays relatively constant, and the optical spectra are featureless. We propose the following interpretations: (i) the soft → hard transition may be caused by the gradual formation of a magnetically dominated corona; (ii) hard X-ray photons escape from the system along solid angles with low scattering optical depth (∼ a few) whereas the UV/optical emission is likely generated by reprocessing materials with much larger column density — the system is highly aspherical; (iii) the abrupt X-ray flux drop may be triggered by the thermal-viscous instability in the inner accretion flow, leading to a much thinner disk.

5.1 Introduction

A star getting too close to a massive black hole (MBH) can get disrupted by the tidal forces in a Tidal Disruption Event (TDE; see recent review by Gezari 2021). The first observational evidence for TDEs came from the detection of X-ray flares from the centers of quiescent galaxies during the *ROSAT* (0.1–2.4 keV) all-sky survey (RASS) in 1990–1991 (Donley et al., 2002). The flares exhibit soft spectra that are consistent with blackbody radiation with temperatures $T_{\rm bb} \sim 10^6$ K and radii

$R_{\rm bb} \sim$ few $\times 10^{11}$ cm (Saxton et al., 2020). Since 2020, the *Spektrum-Roentgen-Gamma* (*SRG*) mission (Sunyaev, Arefiev, et al., 2021), with its sensitive eROSITA telescope (0.2–8 keV; Predehl, Andritschke, et al. 2021) and six month cadenced all-sky surveys, has become the most prolific discoverer of TDEs in X-rays. The majority of X-ray selected TDEs are faint in the optical (Sazonov et al., 2021).

In the UV and optical sky, TDEs have been identified as blue nuclear transients in surveys such as the *Galaxy Evolution Explorer* (Martin et al., 2005), the Panoramic Survey Telescope and Rapid Response System DR1 (Pan-STARRS, PS1; Flewelling et al. 2020; Waters et al. 2020), the Sloan Digital Sky Survey (SDSS, Alam et al. 2015), the All-Sky Automated Survey for SuperNovae (ASAS-SN; Shappee et al. 2014), the Palomar Transient Factory (PTF; Law et al. 2009; Rau et al. 2009), the intermediate PTF (iPTF), the Asteroid Terrestrial-impact Last Alert System (ATLAS; Tonry, Denneau, Heinze, Stalder, et al. 2018), and the Zwicky Transient Facility (ZTF; Bellm, Kulkarni, Graham, et al. 2019; Graham et al. 2019). In most cases, the UV/optical spectral energy distribution (SED) can be described by blackbody radiation with larger radii ($R_{\rm bb} \sim$ few $\times 10^{14}$ cm) and lower temperatures ($T_{\rm bb} \sim$ few $\times 10^4$ K) than those of the X-ray discovered events. The origin of this blackbody component has been attributed to reprocessing of disk emission by an optically thick gas layer (Metzger and Stone, 2016; Roth, Kasen, et al., 2016; Lu and Bonnerot, 2020), stream self-intersecting shocks formed as a result of general relativistic apsidal precession (Piran et al., 2015; Jiang, Guillochon, and Loeb, 2016), or intrinsic thermal emission from the viscously heated accretion disk (Wevers, Pasham, van Velzen, Miller-Jones, et al., 2021).

Among the UV/optically selected TDEs with simultaneous X-ray observations, about two dozen events have been detected in the X-rays (e.g., Auchettl, Guillochon, and Ramirez-Ruiz 2017; Wevers 2020). Their X-ray light curves show a wide range of properties. For example, the X-ray emission of ASASSN-14li lags behind its UV/optical emission by one month (Pasham, Cenko, Sadowski, et al., 2017); ASASSN-15oi, AT2018fyk, and AT2019azh exhibit a gradual X-ray brightening long after the UV/optical peak (Gezari, Cenko, and Arcavi, 2017; Wevers, Pasham, van Velzen, Miller-Jones, et al., 2021; Hinkle et al., 2021); AT2019ehz and OGLE16aaa show extreme X-ray flares on a timescale of a few days (van Velzen, Gezari, Hammerstein, et al., 2021; Kajava et al., 2020; Shu et al., 2020); and the probable neutrino emitter AT2019dsg has a rapid X-ray decline (Stein et al., 2021). Understanding the co-evolution between the X-ray and UV/optical emission may

hold the key in deciphering the origin of these two components.

The majority of TDEs are not associated with on-axis relativistic jets (Alexander, van Velzen, et al., 2020) (hereafter non-jetted TDEs). The sample of jetted TDEs includes four objects: Sw J1644+57 (Bloom et al., 2011; Burrows, Kennea, et al., 2011; Zauderer, Berger, Soderberg, et al., 2011), Sw J2058+05 (Cenko, Krimm, et al., 2012; Pasham, Cenko, Levan, et al., 2015), and Sw J1112−82 (Brown, Levan, Stanway, Tanvir, et al., 2015) were discovered by the hard X-ray Burst Alert Telescope (BAT) on board *Swift*, whereas AT2022cmc was discovered by ZTF in the optical (Andreoni, Coughlin, Ahumada, et al., 2022; Yao, Pasham, Gendreau, et al., 2022; Pasham, Yao, et al., 2022). Among them, Sw J1644+57 is the most well studied. Its fast X-ray variability and extremely high isotropic equivalent X-ray luminosity ($\sim 10^{47}$ erg s^{-1}) suggest that the early-time X-rays are powered by internal dissipation within a jet. A sudden X-ray flux drop by a factor of $\sim 10^2$ indicates a jet shut off at rest-frame 370 days after discovery (Zauderer, Berger, Margutti, et al., 2013), after which the X-ray emission is consistent with being powered by a forward shock (Eftekhari, Berger, Zauderer, et al., 2018; Cendes, Eftekhari, et al., 2021).

During the outburst of a stellar-mass black hole X-ray binary (XRB), as the mass accretion rate ($\dot{M}_{\rm acc}$) varies, the X-ray source transitions between distinct spectral states governed by the global evolution of the disk–corona system (Remillard and McClintock, 2006). A major question in accretion physics is whether a similar geometry operates in the environment around MBHs. Recent studies of a sample of Changing-Look Active Galactic Nuclei (CLAGNs) support a scale-invariant nature of black hole accretion flows (McHardy et al., 2006; Walton, Reis, et al., 2012; Ruan et al., 2019). However, the preexisting gas and dusty torus sometimes complicate interpretation of the observables in CLAGNs (Guolo et al., 2021). On the other hand, the majority of TDEs are hosted by otherwise quiescent galaxies (French, Wevers, et al., 2020). Therefore, TDEs provide ideal laboratories for studying MBH accretion in different regimes (Ulmer, 1999; Strubbe and Quataert, 2009).

ZTF conducts multiple time-domain surveys using the ZTF mosaic camera (Dekany et al., 2020) on the Palomar Oschin Schmidt 48-inch (P48) telescope. The ZTF team selects TDE candidates by imposing a set of criteria, such as proximity to a galaxy nucleus, a lack of pre-flare nuclear activity, a lack of $g - r$ color change, etc (see detailed descriptions in van Velzen, Gezari, Cenko, et al. 2019; van Velzen, Gezari, Hammerstein, et al. 2021). The filter is executed by AMPEL (Nordin et al., 2019).

We use the Fritz marshal[1] to coordinate our follow-up classifications. Thanks to its fast survey speed, ZTF is now reporting $\sim$ 15 TDEs per year (van Velzen, Gezari, Hammerstein, et al., 2021; Hammerstein, van Velzen, et al., 2023).

AT2021ehb/ZTF21aanxhjv was first detected by the ZTF public 2-day cadence all-sky survey at a brightness of $g_{\rm ZTF} = 19.10 \pm 0.22$ on 2021 March 1. On 2021 March 3, it was reported to the Transient Name Server (TNS) by the ALeRCE broker (Munoz-Arancibia et al., 2021). On 2021 March 25, AT2021ehb passed our TDE selection filter. *Swift* observations were triggered while the TDE was still on the rise to peak. On 2021 March 26, we classified AT2021ehb as a TDE based on its nuclear location, persistent blue color, and bright UV emission (Gezari, Hammerstein, et al., 2021; Yao, 2021a). Four *Swift* snapshots from 2021 March 26 to April 2 yielded no X-ray detections. From 2021 April 12 to June 16, AT2021ehb was not observed due to occultation by the Sun. On 2021 June 17, ZTF observations resumed. On 2021 July 1, X-rays were detected with *Swift* (Yao, Brightman, et al., 2021). Its bright X-ray emission ($\sim 10^{42}\,{\rm erg\,s^{-1}}$) and the subsequent X-ray brightening motivated us to conduct a comprehensive monitoring campaign.

At a spectroscopic redshift of $z = 0.0180$ (see §5.3), AT2021ehb is the third closest TDE discovered by optical sky surveys. The previously known lower-redshift events, AT2019qiz (Nicholl, Wevers, et al., 2020) and iPTF16fnl (Blagorodnova, Gezari, et al., 2017), were too faint in the X-ray to be carefully characterized. AT2021ehb, with a peak 0.3–10 keV X-ray flux of 1 mCrab, is the brightest non-jetted TDE in the X-ray sky. We are therefore able to conduct high-cadence monitoring (with *Swift* and *NICER*) and obtain high signal-to-noise ratio (SNR) X-ray spectra (with *NuSTAR*, *NICER*, *XMM-Newton*, and *SRG*/eROSITA), which allows for the search of spectral line features in the X-ray continuum.

Unlike the X-ray spectra of most other non-jetted TDEs (Saxton et al., 2020; Sazonov et al., 2021), the X-ray spectrum of AT2021ehb drastically evolves over the X-ray observing campaign of $\sim$ 370 days, and at a certain stage exhibits prominent non-thermal hard emission. Therefore, AT2021ehb is only the second non-jetted TDE, after AT2018fyk (Wevers, Pasham, van Velzen, Miller-Jones, et al., 2021), which allows us to investigate the rapid evolution between the UV/optical, soft X-ray, and hard X-ray components. Different from the result presented by Wevers, Pasham, van Velzen, Miller-Jones, et al. (2021), we find that the disk–corona system of AT2021ehb is dissimilar to XRBs.

[1] `https://github.com/fritz-marshal/fritz`

In this paper, we present an in-depth study of the X-ray, UV, optical, and radio emission of AT2021ehb, using observations obtained from 2021 March 1 to 2022 May 31. We outline the observations in §5.2. We analyze the host galaxy in §5.3, including measurements of the central black hole mass ($M_{\rm BH}$) and the SED. We study the light curve and spectral evolution of the TDE emission in §5.4. We provide a discussion in §5.5, and conclude in §5.6.

UT time is used throughout the paper. We adopt a standard ΛCDM cosmology with matter density $\Omega_{\rm M} = 0.3$, dark energy density $\Omega_\Lambda = 0.7$, and the Hubble constant $H_0 = 70\,{\rm km\,s^{-1}\,Mpc^{-1}}$, implying a luminosity distance to AT2021ehb of $D_L = 78.2\,{\rm Mpc}$. UV and optical magnitudes are reported in the AB system. We use the extinction law from Cardelli, Clayton, and Mathis (1989), and adopt a Galactic extinction of $E_{B-V,{\rm MW}} = 0.123\,{\rm mag}$ (Schlafly and Finkbeiner, 2011). Uncertainties of X-ray model parameters are reported at the 90% confidence level. Other uncertainties are 68% confidence intervals, and upper limits are reported at 3σ. Coordinates are given in J2000.

5.2 Observations and Data Reduction

ZTF Optical Photometry

We obtained ZTF forced photometry (Masci et al., 2019) in the g and the r bands using the median position of all ZTF alerts up to MJD 59550 (α = 03h07m47.82s, $\delta = +40^\circ18'40.85''$). We performed baseline correction following the procedures outlined in Yao, Miller, et al. (2019).

The peak of the optical light curve probably occurred during Sun occultation and cannot be robustly determined. Therefore, we fitted a five-order polynomial function to the $r_{\rm ZTF}$-band observations, which suggested that the optical maximum light was around MJD $\approx$ 59321. Hereafter we use δt to denote rest-frame days relative to MJD 59321. The Galactic extinction-corrected ZTF difference photometry are shown in Figure 5.1. The lack of data at $0 \lesssim \delta t \lesssim 50$ days is due to Sun occultation. The lack of data at $220 \lesssim \delta t \lesssim 290$ days and $310 \lesssim \delta t \lesssim 340$ days is due to performance issues with the cooling system for the ZTF Camera (Fremling, Graham, et al., 2021).

Optical Spectroscopy

We obtained low-resolution optical spectroscopic observations using the Low Resolution Imaging Spectrograph (LRIS; Oke, Cohen, et al. 1995) on the Keck-I telescope, the Double Spectrograph (DBSP; Oke and Gunn 1982) on the 200-inch Hale telescope, the integral field unit (IFU; $R \approx 100$) spectrograph of SEDM, and the De

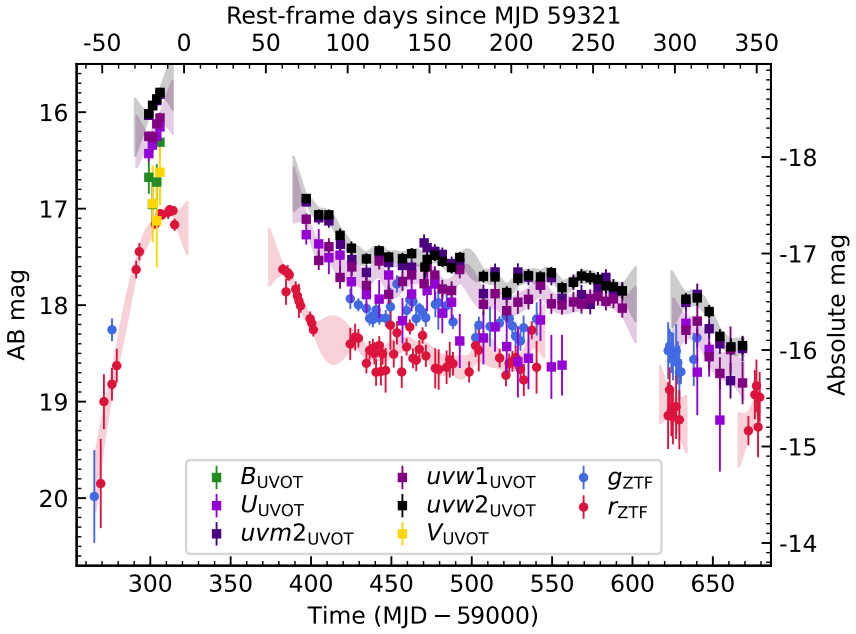

Figure 5.1: Optical and UV light curves of AT2021ehb.

Veny Spectrograph on the Lowell Discovery Telescope (LDT). We also obtained a medium-resolution spectrum using the Echellette Spectrograph and Imager (ESI; Sheinis et al. 2002) on the Keck-II telescope.

Figure 5.2 shows the low-resolution spectra. The observed spectra have been corrected for Galactic extinction. The vertical lines mark observed strong host absorption lines and spectral features common in TDEs. The vertical grey bands mark atmospheric telluric features and strong telluric features have been masked. The best-fit galaxy model is shown at the bottom (see §5.3). A log of optical spectroscopic observation is given in Table 5.1.

For LRIS observations, we used the 560 dichroic, the 400/3400 grism on the blue side, the 400/8500 grating on the red side, and the 1″ slit width, which gives $\sigma_{\rm inst} \approx 173\,{\rm km\,s^{-1}}$ on the blue side and $\sigma_{\rm inst} \approx 126\,{\rm km\,s^{-1}}$ on the red side. The LRIS spectra were reduced and extracted using `Lpipe` (Perley, 2019).

For DBSP observations, we used the D-55 dichroic filter, the 600/4000 grating on the blue side, the 316/7500 grating on the red side. With a slit width of 1.5″ (2.0″), this gives $\sigma_{\rm inst} \approx 106\,{\rm km\,s^{-1}}$ ($\sigma_{\rm inst} \approx 141\,{\rm km\,s^{-1}}$) on the blue side and $\sigma_{\rm inst} \approx 143\,{\rm km\,s^{-1}}$ ($\sigma_{\rm inst} \approx 190\,{\rm km\,s^{-1}}$) on the red side.

The DBSP spectra were reduced using the `dbsp_drp` pipeline (Roberson, Fremling,

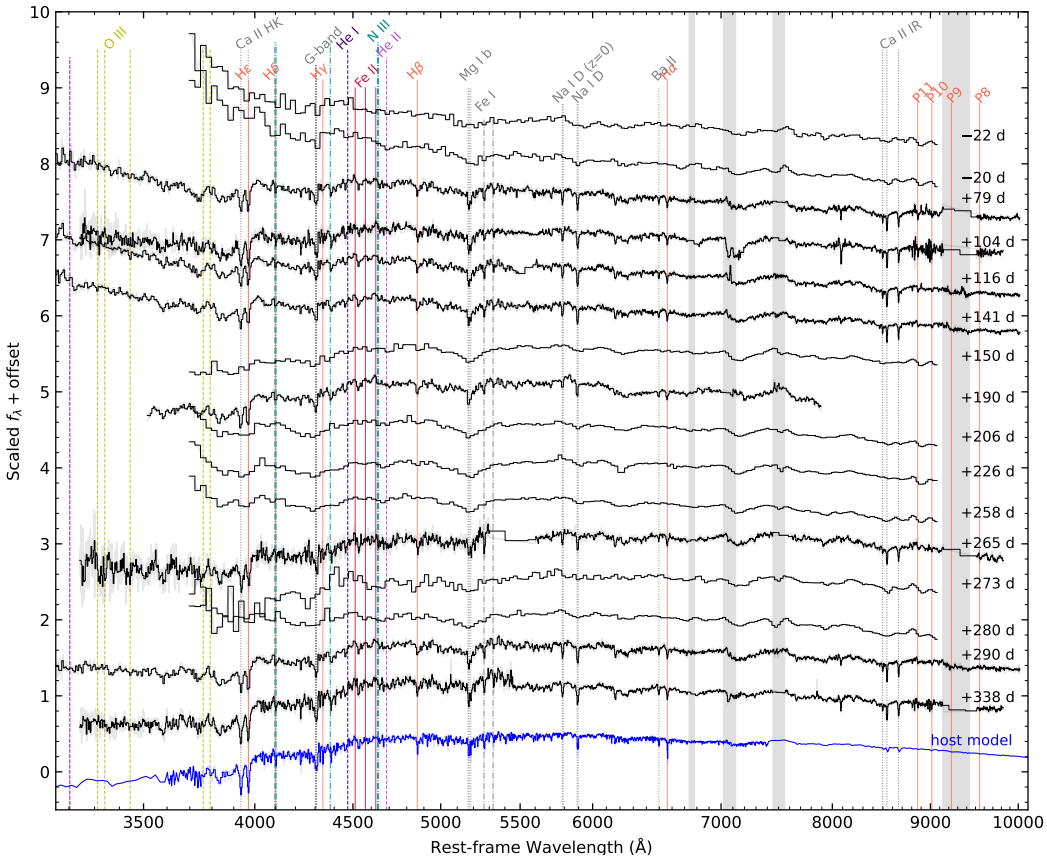

Figure 5.2: Optical spectroscopic evolution of AT2021ehb.

Table 5.1: Log of AT2021ehb optical spectroscopy.

Start Date	δt (days)	Telescope	Instrument	Wavelength range (Å)	Slit width (″)	Exp. (s)
2021-03-25.1	−22	P60	SEDM	3770–9223	—	2160
2021-03-27.1	−20	P60	SEDM	3770–9223	—	2160
2021-07-06.6	+79	Keck-I	LRIS	3200–10250	1.0	300
2021-08-01.4	+104	P200	DBSP	3410–5550, 5750–9995	1.5	900
2021-08-13.6	+116	Keck-I	LRIS	3200–10250	1.0	300
2021-09-07.6	+141	Keck-I	LRIS	3200–10250	1.0	300
2021-09-17.4	+150	P60	SEDM	3770–9223	—	2700
2021-10-27.5	+190	LDT	DeVeny	3586–8034	1.5	2400
2021-11-13.3	+206	P60	SEDM	3770–9223	—	2700
2021-12-03.3	+226	P60	SEDM	3770–9223	—	2700
2021-12-28.4	+250	Keck-II	ESI	4000–10250	0.75	300
2022-01-05.2	+258	P60	SEDM	3770–9223	—	2700
2022-01-12.2	+265	P200	DBSP	3410–5550, 5750–9995	2.0	600
2022-01-20.3	+273	P60	SEDM	3770–9223	—	2700
2022-01-27.3	+280	P60	SEDM	3770–9223	—	2700
2022-02-06.3	+290	Keck-I	LRIS	3200–10250	1.0	300
2022-03-27.1	+338	P200	DBSP	3410–5550, 5750–9995	1.5	1200

and Kasliwal, 2022), which is based on `PypeIt` (Prochaska et al., 2020).

The ESI observation was performed in the Echellette mode with a 0.75″ wide slit, which gives a resolving power of $R = 5350$ (i.e., $\sigma_{\rm inst} = 24\,{\rm km\,s^{-1}}$). The ESI spectrum was reduced using the `MAKEE` pipeline following standard procedures. Flux calibration was not performed. We normalized the spectra by fitting third-order cubic splines to the continuum, with prominent emission and absorption lines masked.

Observations with DeVeny were performed with the 300/4000 grating, with a grating tilt angle of 23.13° to yield a central wavelength of 5800 Å, the clear rear filter, and a slit width of 1.5″. This gives $\sigma_{\rm inst} \approx 169\,{\rm km\,s^{-1}}$. DeVeny spectra were reduced with `PyRAF`, including bias correction and flat-fielding.

Swift

AT2021ehb was observed by the X-Ray Telescope (XRT; Burrows, Hill, et al. 2005) and the Ultra-Violet/Optical Telescope (UVOT; Roming et al. 2005) on board *Swift* under our GO program 1619088 (as ZTF21aanxhjv; target ID 14217; PI: Gezari) and a series of time-of-opportunity (ToO) requests (PI: Yao). The lack of data at $270 \lesssim \delta t \lesssim 300$ days is due to an issue with one of the *Swift* reaction wheels (Cenko, 2022). All *Swift* data were processed with `heasoft` v6.29c.

All XRT observations were obtained in the photon-counting mode. First, we ran `ximage` to select snapshots where AT2021ehb was detected above 3σ. For X-ray non-detections, we computed upper limits within a circular region with a radius of 30″, assuming Poisson statistics. For X-ray detections, to calculate the background-subtracted count rates, we filtered the cleaned event files using a source region with $r_{\rm src} = 30''$, and eight background regions with $r_{\rm bkg} = 25''$ evenly spaced at 80″ from AT2021ehb. A log of XRT observations is given in Table 5.2.

We generated XRT spectra using an automated online tool[2] (Evans, Beardmore, Page, Osborne, et al., 2009). To improve the SNR of each spectrum, we stacked consecutive observations with a similar hardness ratio (HR; see details in §5.4).

The first four UVOT epochs (obsID 14217001–14217005) were conducted with *UBV*+All UV filters. Subsequent observations were conducted with *U*+All UV filters.

[2] `https://www.swift.ac.uk/user_objects`

Table 5.2: Log of *Swift*/XRT observations of AT2021ehb.

obsID	Start Date	δt (days)	Exp. (s)	Net Count Rate (count s^{-1})	f_X (10^{-13} erg s^{-1} cm^{-2})	$f_{X,0}$ (10^{-13} erg s^{-1} cm^{-2})
14217001	2021-03-26.0	−21.6	2669	< 0.0019	< 0.66	< 1.25
14217003	2021-03-28.2	−19.4	1475	< 0.0027	< 0.96	< 1.82
14217004	2021-03-31.0	−16.7	1683	< 0.0024	< 0.84	< 1.59
14217005	2021-04-02.0	−14.7	1336	< 0.0030	< 1.06	< 2.01
14217006	2021-07-01.2	+73.9	4078	0.0339 ± 0.0029	12.01 ± 3.21	22.73 ± 6.08
14217007	2021-07-09.8	+82.3	1366	0.0120 ± 0.0030	4.27 ± 1.52	8.08 ± 2.88
14217008	2021-07-16.1	+88.5	1348	0.0184 ± 0.0037	6.52 ± 2.11	12.34 ± 4.00
14217009	2021-07-23.1	+95.4	1141	0.0343 ± 0.0056	12.13 ± 3.65	22.96 ± 6.90
14217010	2021-07-30.1	+102.3	1366	0.0502 ± 0.0061	16.57 ± 2.23	44.04 ± 5.92
14217011	2021-08-08.1	+111.1	1925	0.0863 ± 0.0067	28.44 ± 2.76	75.62 ± 7.34
14217012	2021-08-15.9	+118.8	1653	0.1635 ± 0.0100	53.90 ± 4.54	143.32 ± 12.08
14217013	2021-08-22.1	+124.8	2065	0.1958 ± 0.0098	64.56 ± 4.94	171.64 ± 13.13
14217014	2021-08-30.9	+133.5	1583	0.2268 ± 0.0120	74.78 ± 5.87	198.82 ± 15.61
14217015	2021-09-05.5	+139.0	1830	0.2548 ± 0.0119	94.07 ± 7.27	200.69 ± 15.51
14217016	2021-09-12.8	+146.2	641	0.2061 ± 0.0180	76.09 ± 8.13	162.34 ± 17.35
14217017	2021-09-15.0	+148.4	1503	0.1281 ± 0.0093	47.29 ± 4.51	100.90 ± 9.63
14217018	2021-09-19.7	+153.0	1580	0.1974 ± 0.0112	72.90 ± 6.12	155.52 ± 13.05
14217019	2021-09-24.2	+157.4	2045	0.1959 ± 0.0098	72.33 ± 5.76	154.31 ± 12.28
14217020	2021-09-30.4	+163.5	1867	0.2675 ± 0.0120	98.74 ± 7.54	210.67 ± 16.09
14217021	2021-10-05.5	+168.5	1595	0.2775 ± 0.0132	104.81 ± 9.01	170.40 ± 14.65
14217022	2021-10-20.2	+182.9	1618	0.2865 ± 0.0134	108.22 ± 9.24	175.94 ± 15.02
14217023	2021-10-27.4	+190.0	1480	0.2698 ± 0.0136	101.93 ± 8.91	165.71 ± 14.48
14217024	2021-11-03.5	+197.0	2010	0.2124 ± 0.0103	80.23 ± 6.94	130.44 ± 11.29
14217025	2021-11-10.7	+204.0	1286	0.3132 ± 0.0157	149.64 ± 15.02	210.15 ± 21.10
14217026	2021-11-17.2	+210.4	1813	0.1251 ± 0.0084	59.75 ± 6.57	83.92 ± 9.23
14217027	2021-11-24.7	+217.7	1957	0.2718 ± 0.0119	129.86 ± 12.64	182.38 ± 17.75
14217028	2021-12-01.5	+224.4	1967	0.2600 ± 0.0116	124.20 ± 12.14	174.42 ± 17.05
14217029	2021-12-08.1	+230.9	2317	0.2596 ± 0.0107	126.84 ± 9.59	168.93 ± 12.77
14217030	2021-12-15.2	+237.9	2010	0.5234 ± 0.0162	255.79 ± 18.06	340.66 ± 24.05
14217031	2021-12-20.3	+242.9	1293	0.5445 ± 0.0206	266.11 ± 19.65	354.40 ± 26.17
14217032	2021-12-25.6	+248.2	1395	0.7108 ± 0.0227	347.35 ± 24.66	462.59 ± 32.84
14217033	2021-12-30.5	+253.0	1371	0.9721 ± 0.0268	551.93 ± 41.79	691.67 ± 52.37
14217034	2022-01-04.5	+257.8	1410	0.9675 ± 0.0263	549.33 ± 41.53	688.41 ± 52.05
14217035	2022-01-09.2	+262.4	1361	0.8629 ± 0.0253	489.92 ± 37.43	613.96 ± 46.91
14217036	2022-01-14.7	+267.9	1423	0.9218 ± 0.0256	523.38 ± 39.68	655.88 ± 49.72
14217041	2022-02-23.1	+306.6	2594	0.0745 ± 0.0054	26.05 ± 3.06	47.73 ± 5.60
14217042	2022-03-02.2	+313.5	3888	0.0706 ± 0.0043	24.72 ± 2.73	45.29 ± 5.01
14217043	2022-03-09.7	+320.9	2766	0.0918 ± 0.0058	32.11 ± 3.59	58.83 ± 6.58
14217044	2022-03-16.1	+327.2	2956	0.0122 ± 0.0022	5.03 ± 1.40	14.35 ± 3.98
14217045	2022-03-23.0	+334.0	3263	0.0197 ± 0.0025	8.08 ± 2.01	23.04 ± 5.73
14217046	2022-03-30.5	+341.3	2354	0.0246 ± 0.0033	10.11 ± 2.55	28.81 ± 7.26

All measurements are given in 0.3–10 keV. f_X and $f_{X,0}$ are converted using the scaling factors derived in Table 5.11.

We measured the UVOT photometry using the `uvotsource` tool. We used a circular source region with $r_{\rm src} = 12''$, and corrected for the enclosed energy within the aperture[3]. We measured the background using two nearby circular source-free regions with $r_{\rm bkg} = 15''$. Following the procedures outlined in van Velzen, Gezari, Hammerstein, et al. (2021), we estimated the host-galaxy flux in the UVOT bandpass from the population synthesis models (see §5.3). The host-subtracted UVOT light curves are presented in Figure 5.1.

NICER

AT2021ehb was observed by the Neutron Star Interior Composition Explorer (*NICER*; Gendreau et al. 2016) under Director's Discretionary Time (DDT) programs on 2021 March 26, 2021 July 2–7, and from 2021 November 13 to 2022 March 29 (PIs: Yao, Gendreau, Pasham). The *NICER* data were processed using `nicerdas` v9 (`2021-08-31_V008c`). We ran `nicerl2` to obtain the cleaned and screened event files. Background was computed using the `nibackgen3C50` tool (Remillard, Loewenstein, et al., 2022). Following the screening criteria suggested by Remillard, Loewenstein, et al. (2022), we removed GTIs with `hbgcut=0.05` and `s0cut=2.0`.

We extracted one spectrum for each obsID, excluding obsIDs with 0.3–1 keV background rate $> 0.2\,{\rm count\,s^{-1}}$ or 4–12 keV background rate $> 0.1\,{\rm count\,s^{-1}}$. Using observations bracketed by the two *NuSTAR* observations, we also produced two *NICER* spectra with exposure times of 8.2 ks and 36.6 ks, which we jointly analyzed with the *NuSTAR* spectra (see §5.4).

All *NICER* spectra were binned using the optimal binning scheme (Kaastra and Bleeker, 2016), requiring at least 20 counts per bin. Following the *NICER* calibration memo[4], we added systematic errors of 1.5% with `grppha`.

XMM-Newton

We obtained two epochs of follow-up observations with *XMM-Newton* under our Announcement of Opportunity (AO) program (PI: Gezari), on 2021 August 4 (obsID 0882590101) and 2022 January 25 (obsID 0882590901). The observations were taken in Full Frame mode with the thin filter using the European Photon Imaging Camera (EPIC; Strüder et al. 2001).

The observation data files (ODFs) were reduced using the *XMM-Newton* Standard

[3] A large aperture is chosen to make sure that all of the flux of the host galaxy is captured.

[4] See `https://heasarc.gsfc.nasa.gov/docs/nicer/data_analysis/nicer_analysis_tips.html`.

Analysis Software (Gabriel et al., 2004). The raw data files were then processed using the `epproc` task. Since the pn instrument generally has better sensitivity than MOS1 and MOS2, we only analyze the pn data. Following the *XMM-Newton* data analysis guide, to check for background activity and generate "good time intervals" (GTIs), we manually inspected the background light curves in the 10–12 keV band. Using the `evselect` task, we only retained patterns that correspond to single and double events (`PATTERN<=4`).

The source spectra were extracted using a source region of $r_{\rm src} = 35''$ around the peak of the emission. The background spectra were extracted from a $r_{\rm bkg} = 108''$ region located in the same CCD. The ARFs and RMF files were created using the `arfgen` and `rmfgen` tasks, respectively. We grouped the spectra to have at least 25 counts per bin, and limited the over-sampling of the instrumental resolution to a factor of 5.

NuSTAR

We obtained Nuclear Spectroscopic Telescope ARray (*NuSTAR*; Harrison et al. 2013) observations under a pre-approved ToO program (PI: Yao; obsID 80701509002) and a DDT program (PI: Yao; obsID 90801501002). The first epoch was conducted from 2021 November 18.8 to 19.9 with an exposure time of 43.2 ks. The second epoch was conducted from 2022 January 10.4 to 12.1 with an exposure time of 77.5 ks.

To generate the first epoch's spectra for the two photon-counting detector modules (FPMA and FPMB), source photons were extracted from a circular region with a radius of $r_{\rm src} = 40''$ centered on the apparent position of the source in both FPMA and FPMB. The background was extracted from a $r_{\rm bkg} = 80''$ region located on the same detector. For the second epoch, since the source was brighter, we used a larger source radius of $r_{\rm src} = 70''$, and a smaller background radius of $r_{\rm bkg} = 65''$.

All spectra were binned first with `ftgrouppha` using the optimal binning scheme developed by Kaastra and Bleeker (2016), and then further binned to have at least 20 counts per bin.

***SRG*/eROSITA**

The location of AT2021ehb was scanned by eROSITA as part of the planned eight all-sky surveys. Hereafter eRASS*n* refers to the *n*'th eROSITA all-sky survey[5]. During

[5]Here *n* runs from 1 to 8. As of April 2022, eRASS1–eRASS4 have been completed, and 38% (sky area) of eRASS5 has been completed.

Table 5.3: Log of *SRG* observations of AT2021ehb.

eRASS	MJD	δt (days)	0.3–10 keV flux (10^{-13} erg s^{-1} cm^{-2})
1	58903.59–58904.59	−409.5	< 0.25
2	59083.36–59084.70	−232.8	< 0.23
3	59253.16–59254.16	−66.1	< 0.23
4	59442.45–59443.62	+119.9	$76.8^{+2.5}_{-2.4}$
5	59624.53–59625.70	+298.7	$30.7^{+2.4}_{-2.3}$

Upper limits are computed assuming an absorbed PL spectrum with $\Gamma = 2.5$ and $N_{\rm H} = 9.97 \times 10^{20}$ cm^{-2}, and presented at 90% confidence.

eRASS4, AT2021ehb was independently identified by *SRG* as a TDE candidate. A log of *SRG* observations is given in Table 5.3. We grouped the eRASS4 and eRASS5 spectra to have at least 3 counts per bin.

VLA

Table 5.4: Radio observations of AT2021ehb.

Date	Δt (days)	ν (GHz)	f_ν (μJy)	νL_ν (10^{36} erg s^{-1})
2021 Mar 28.85	−18.8	15.0	< 16	< 1.8
2021 Jul 10.53	83.0	10.0	< 16	< 1.1
2021 Dec 5.09	228.0	10.0	< 16	< 1.1
2022 May 6.96	378.1	10.0	< 14	< 1.1

We began a monitoring program of AT2021ehb using the Very Large Array (VLA; Perley, Chandler, et al. 2011) under Program 20B-377 (PI Alexander). All of the data were analyzed following standard radio continuum image analysis procedures in the Common Astronomy Software Applications (`CASA`; McMullin et al. 2007). The first three observations used a custom data reduction pipeline (`pwkit`; Williams et al. 2017), while the final observation used the standard NRAO pipeline. AT2021ehb was not detected in any of our observations. All data were imaged using the CASA task `clean`. We computed 3σ upper limits using the `stats` command within the `imtool` package of `pwkit`. The results are presented in Table 5.4.

In Figure 5.3, we compare the radio luminosity of AT2021ehb with other UV- and optically-selected TDEs, including ASASSN-14li (Alexander, Berger, et al., 2016), ASASSN-15oi (Horesh, Cenko, and Arcavi, 2021), iPTF16fnl (Horesh, Sfaradi, et al., 2021), AT2018fyk (Wevers, Pasham, van Velzen, Leloudas, et al., 2019; Wevers,

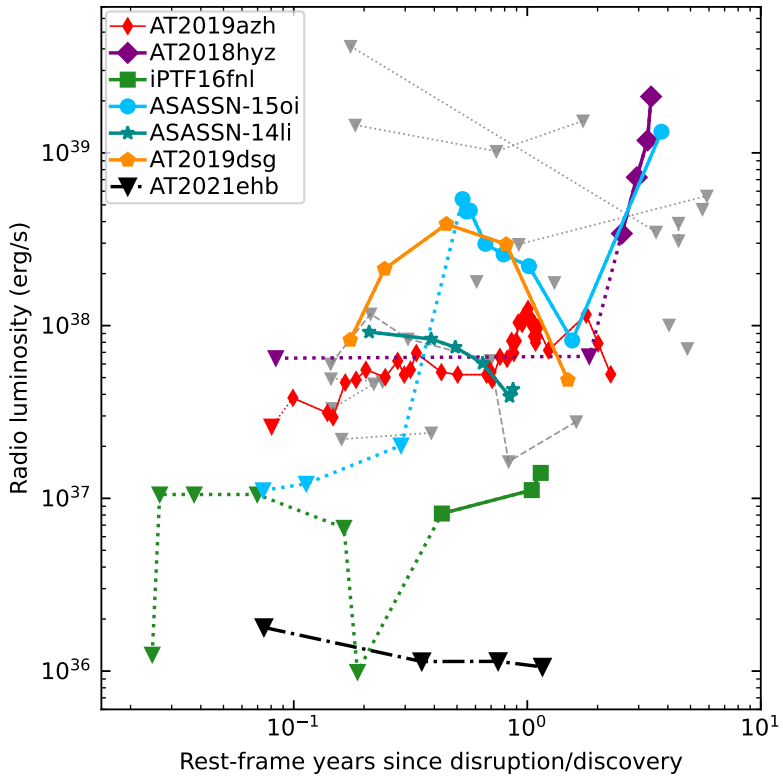

Figure 5.3: Radio upper limits for AT2021ehb in the context of other UV- and optically-discovered TDEs with radio data.

Pasham, van Velzen, Miller-Jones, et al., 2021), AT2018hyz (Cendes, Berger, et al., 2022), AT2019azh (Goodwin et al., 2022; Sfaradi et al., 2022), AT2019dsg (Cendes, Alexander, et al., 2021), and upper limits listed in Tab. 2 of Alexander, van Velzen, et al. (2020). We note that AT2021ehb looks to be significantly (by more than an order of magnitude) radio-underluminous compared to previously observed non-jetted TDEs at similar times post-peak. It has the deepest limits on any TDE radio emission at > 150 days post-discovery.

5.3 Host Galaxy Analysis

Figure 5.4 shows the pre-TDE optical image centered on AT2021ehb, using data from PS1. The host galaxy appears to be close to edge-on.

Velocity Dispersion and Black Hole Mass

The host galaxy absorption lines are prominent in the optical spectra (see Figure 5.2). Using our medium-resolution ($R = 5350$) spectrum taken with Keck-II/ESI, we measured the line centers of strong absorption lines, and determined the redshift to

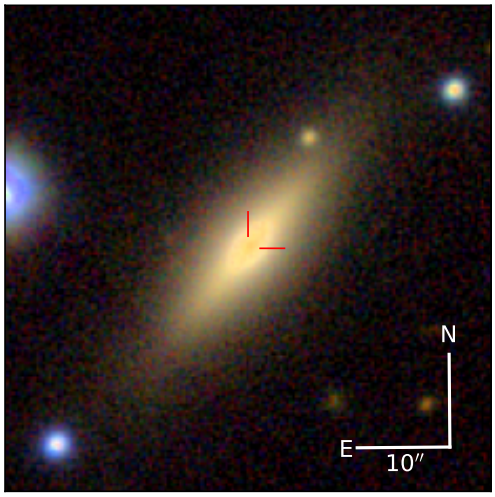

Figure 5.4: PS1 RGB false-color *g*/*i*/*z* image centered on AT2021ehb.

be $z = 0.0180$.

Following previous TDE work (Wevers, van Velzen, et al., 2017; Wevers, Stone, et al., 2019; French, Wevers, et al., 2020), we measured the stellar velocity dispersion by fitting the normalized ESI spectrum with the penalized pixel-fitting (`pPXF`) software (Cappellari and Emsellem, 2004; Cappellari, 2017). `pPXF` fits the absorption line spectrum by convolving a library of stellar spectra with Gauss-Hermite functions. We adopted the ELODIE v3.1 high resolution ($R = 42000$) template library (Prugniel and Soubiran, 2001; Prugniel, Soubiran, et al., 2007).

To robustly measure the velocity dispersion and the associated uncertainties, we performed 1000 Monte Carlo (MC) simulations, following the approach adopted by Wevers, van Velzen, et al. (2017). In each fitting routine, we masked wavelength ranges of common galaxy emission lines and hydrogen Balmer lines. The derived velocity dispersion is $\sigma = 92.9^{+5.3}_{-5.2}$ km s^{-1} at 95% confidence interval.

According to the $M_{\rm BH}$–σ relation (Kormendy and Ho, 2013), the measured σ corresponds to a black hole mass of $\log(M_{\rm BH}/M_\odot) = 7.03 \pm 0.15\,({\rm stat}) \pm 0.29\,({\rm sys})$, where 0.29 is the intrinsic scatter of the $M_{\rm BH}$–σ relation. If adopting the Ferrarese and Ford, 2005 $M_{\rm BH}$–σ relation, then $\log(M_{\rm BH}/M_\odot) = 6.60 \pm 0.20\,({\rm stat}) \pm 0.34\,({\rm sys})$. Hereafter we adopt the result from the Kormendy and Ho (2013) relation because it includes more low-mass galaxies.

We note that although the Kormendy and Ho (2013) relation was originally calibrated mainly at a $M_{\rm BH}$ regime that is too massive to produce a TDE, recent studies show

that the same relation holds in the dwarf galaxy regime (Baldassare et al., 2020).

Host SED Model

We constructed the pre-TDE host galaxy SED using photometry from SDSS, the Two Micron All-Sky Survey (2MASS; Skrutskie et al. 2006), and the AllWISE catalog (Cutri et al., 2021). The photometry of the host is shown in Table 5.5 and as open squares in Figure 5.5.

Table 5.5: Observed photometry of the host galaxy.

Catalog	Band	$\lambda_{\rm eff}$ (nm)	Magnitude
SDSS	u	355	17.748 ± 0.019
SDSS	g	467	15.814 ± 0.003
SDSS	r	616	14.901 ± 0.002
SDSS	i	747	14.443 ± 0.003
SDSS	z	892	14.094 ± 0.004
2MASS	J	1232	13.951 ± 0.025
2MASS	H	1642	13.676 ± 0.034
2MASS	$K_{\rm s}$	2157	13.893 ± 0.043
AllWISE	$W1$	3346	14.816 ± 0.024
AllWISE	$W2$	4595	15.535 ± 0.022
AllWISE	$W3$	11553	16.756 ± 0.229

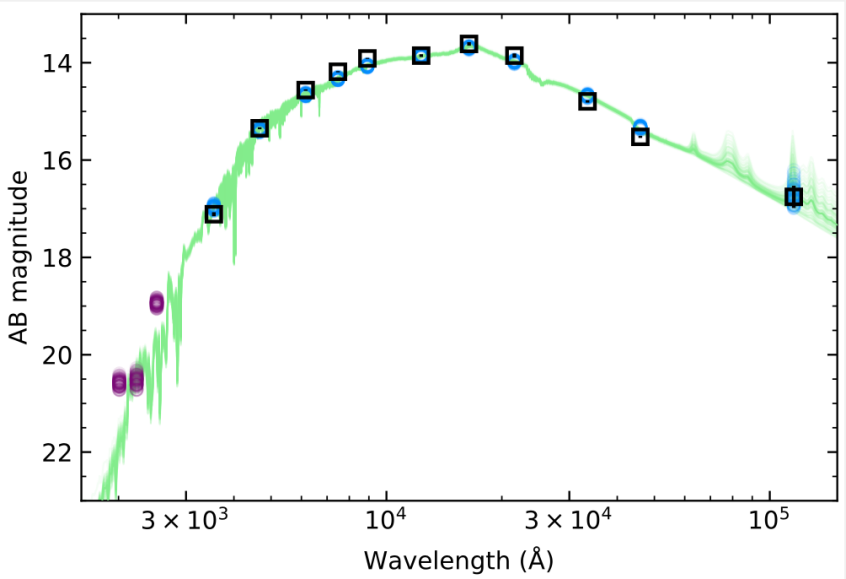

Figure 5.5: Host galaxy SED of AT2021ehb.

Our SED fitting approach is similar to that described in van Velzen, Gezari, Hammerstein, et al. (2021). We used the flexible stellar population synthesis (FSPS) code

(Conroy, Gunn, and White, 2009), and adopted a delayed exponentially declining star-formation history (SFH) characterized by the e-folding timescale $\tau_{\rm SFH}$. The `Prospector` package (Johnson et al., 2021) was utilized to run a Markov Chain Monte Carlo sampler (Foreman-Mackey, Hogg, et al., 2013). We show the best-fit model prediction of the host galaxy optical spectrum at the bottom of Figure 5.2.

From the marginalized posterior probability functions we obtain the total galaxy stellar mass $\log(M_*/M_\odot) = 10.18^{+0.01}_{-0.02}$, the metallicity, $\log Z = -0.57 \pm 0.04$, $\tau_{\rm SFH} = 0.19^{+0.18}_{-0.07}$ Gyr, the population age, $t_{\rm age} = 12.1^{+0.3}_{-0.6}$ Gyr, and negligible host reddening ($E_{B-V,\rm host} = 0.01 \pm 0.01$ mag). The best-fit SED model is shown in Figure 5.5. The green lines are samples from the posterior distribution of host galaxy SED models. The open circles are the synthetic host galaxy magnitudes in the observed bands (shown in blue) and in the UV filters of *Swift*/UVOT (shown in purple).

Following Gezari (2021), we use the $M_{\rm BH}$–M_* relation from Greene, Strader, and Ho (2020) to obtain a black hole mass of $\log(M_{\rm BH}/M_\odot) = 7.14 \pm (0.10 + 0.79)$, where 0.79 is the intrinsic scatter of the scaling relation. This is consistent with the $M_{\rm BH}$ inferred from the $M_{\rm BH}$–σ relation (§5.3).

To summarize, the host galaxy of AT2021ehb has a total stellar mass of $M_* \approx 10^{10.18}\,M_\odot$ and a BH mass of $M_{\rm BH} \approx 10^{7.03}\,M_\odot$. The measured black hole mass is on the high end of the population of optically selected TDEs (French, Wevers, et al., 2020; Nicholl, Lanning, et al., 2022), and is too massive to disrupt a white dwarf (Rosswog, Ramirez-Ruiz, and Hix, 2009).

5.4 Analysis of the TDE Emission

UV/optical Photometric Analysis

To capture the general trend of AT2021ehb's UV/optical photometric evolution, we fit the data in each filter using a combination of five-order polynomial functions and Gaussian process smoothing, following procedures described in Appendix B.4 of Yao, De, et al. (2020). The model fits in $r_{\rm ZTF}$, $uvw1$, and $uvw2$ are shown as semi-transparent lines in Figure 5.1.

We then define a set of "good epochs" close in time to actual multiband measurements, and fit a Planck function to each set of fluxes to determine the effective temperature $T_{\rm bb}$, photospheric radius $R_{\rm bb}$, and blackbody luminosity of the UV/optical emitting component $L_{\rm bb}$. We initially assume $E_{B-V,\rm host} = 0$ mag, and then repeat the procedure under different assumptions about the host reddening. We find that

the fitting residual monotonically increases as $E_{B-V,\mathrm{host}}$ increases from 0 mag to 0.2 mag, suggesting negligible host reddening. Therefore, for the reminder of the discussion we assume $E_{B-V,\mathrm{host}} = 0$ mag.

We also define a set of "ok epochs" where we only have photometric observations in the optical (or only in the UV). Due to a lack of wavelength coverage, T_{bb} and R_{bb} can not be simultaneously constrained. As such we fix the T_{bb} values by interpolating the T_{bb} evolution of "good epochs," and fit for R_{bb} values of "ok epochs."

The physical parameters derived from the blackbody fits are presented in Table 5.6 and shown in Figure 5.6, where they are compared with a sample of recent TDEs with multiple X-ray detections, including AT2018fyk (Wevers, Pasham, van Velzen, Leloudas, et al., 2019; Wevers, Pasham, van Velzen, Miller-Jones, et al., 2021), AT2019dsg (Stein et al., 2021), AT2019azh (Hinkle et al., 2021), AT2020ocn, and AT2019ehz (van Velzen, Gezari, Hammerstein, et al., 2021). The results of "good epochs" are shown in high-opacity colors, whereas results of "ok epochs" are shown in semi-transparent. We have measured the blackbody parameters of other TDEs using the same procedures described above.

While the temperature of AT2021ehb ($T_{\mathrm{bb}} \sim 2.5 \times 10^4$ K) is typical among optical and X-ray bright TDEs, its peak radius ($R_{\mathrm{bb}} \sim 3 \times 10^{14}$ cm) and luminosity ($L_{\mathrm{bb}} \sim 3 \times 10^{43}$ erg s^{-1}) are at the low end of the distributions. We note that in the ZTF-I sample of 30 TDEs (Hammerstein, van Velzen, et al., 2023), only two objects (AT2020ocn and AT2020wey) have peak radii smaller than that of AT2021ehb.

Optical Spectral Analysis

Figure 5.2 shows that no broad line is evident in the optical spectra of AT2021ehb. To search for weak spectral features from the TDE, we fit the Galactic extinction-corrected long-slit spectra in rest-frame 3600–5400 Å using a combination of blackbody emission and host galaxy contribution: $f_{\lambda,\mathrm{obs}} = A_1 f_{\lambda,\mathrm{BB}} + A_2 f_{\lambda,\mathrm{host}}$. Here $f_{\lambda,\mathrm{BB}} = \pi B_\lambda(T_{\mathrm{bb}})(R_{\mathrm{bb}}^2/D_L^2)$, where T_{bb} and R_{bb} are obtained by linearly interpolating the blackbody parameters derived in §5.4 at the relevant δt. $f_{\lambda,\mathrm{host}}$ is the predicted host galaxy spectrum obtained in §5.3 convolved with the instrumental broadening σ_{inst}. A_1 and A_2 are constants added to account for unknown factors, including the varying amount of host galaxy flux falling within the slit (which depends on the slit width, slit orientation, seeing conditions and target acquisition), uncertainties in the absolute flux calibration and the adopted blackbody parameters. We note that $f_{\lambda,\mathrm{host}}$ is the predicted spectrum for the whole galaxy, and therefore

Table 5.6: UV/optical blackbody parameters of AT2021ehb.

δt (days)	$L_{\rm bb}$ (10^{43} erg s^{-1})	$R_{\rm bb}$ (10^{14} cm)	$T_{\rm bb}$ (10^3 K)
−50.0	0.39 ± 0.15	0.91 ± 0.03	2.85
−45.0	0.67 ± 0.25	1.19 ± 0.01	2.85
−40.0	1.01 ± 0.38	1.46 ± 0.05	2.85
−30.0	2.10 ± 0.78	2.11 ± 0.04	2.85
−25.0	2.62 ± 0.96	2.36 ± 0.03	2.85
−21.5	2.77 ± 1.19	2.42 ± 0.27	2.85 ± 0.26
−19.2	2.92 ± 1.30	2.51 ± 0.29	2.84 ± 0.27
−16.7	3.00 ± 0.89	2.70 ± 0.20	2.75 ± 0.18
−14.7	3.13 ± 0.65	2.80 ± 0.14	2.73 ± 0.13
−10.0	3.31 ± 0.62	2.89 ± 0.02	2.73
70.0	1.33 ± 0.29	1.91 ± 0.02	2.67
74.7	1.12 ± 0.29	1.75 ± 0.12	2.67 ± 0.15
82.4	1.06 ± 0.86	1.45 ± 0.31	2.90 ± 0.50
88.6	1.27 ± 1.46	1.18 ± 0.34	3.36 ± 0.84
95.4	0.79 ± 0.67	1.42 ± 0.33	2.72 ± 0.48
102.3	0.55 ± 0.18	1.79 ± 0.17	2.22 ± 0.15
111.5	0.52 ± 0.12	1.70 ± 0.10	2.24 ± 0.11
119.3	0.60 ± 0.10	1.56 ± 0.07	2.43 ± 0.09
125.1	0.54 ± 0.20	1.67 ± 0.18	2.28 ± 0.18
133.6	0.50 ± 0.18	1.82 ± 0.19	2.14 ± 0.16
139.2	0.52 ± 0.13	1.80 ± 0.12	2.18 ± 0.11
147.0	0.57 ± 0.15	1.65 ± 0.11	2.32 ± 0.13
153.3	0.60 ± 0.25	1.51 ± 0.18	2.47 ± 0.22
157.9	0.57 ± 0.30	1.47 ± 0.21	2.47 ± 0.27
163.6	0.54 ± 0.19	1.50 ± 0.15	2.41 ± 0.18
168.6	0.63 ± 0.25	1.31 ± 0.14	2.68 ± 0.23
178.0	0.42 ± 0.18	1.65 ± 0.18	2.16 ± 0.20
183.1	0.44 ± 0.25	1.51 ± 0.25	2.28 ± 0.26
190.2	0.43 ± 0.22	1.55 ± 0.23	2.24 ± 0.23
197.3	0.37 ± 0.13	1.76 ± 0.17	2.02 ± 0.14
204.1	0.43 ± 0.19	1.53 ± 0.18	2.25 ± 0.20
210.5	0.44 ± 0.25	1.59 ± 0.26	2.22 ± 0.26
217.8	0.44 ± 0.20	1.56 ± 0.05	2.24
224.5	0.42 ± 0.18	1.51 ± 0.07	2.26
231.0	0.40 ± 0.17	1.44 ± 0.05	2.27
238.0	0.42 ± 0.17	1.47 ± 0.04	2.29
242.9	0.42 ± 0.16	1.45 ± 0.05	2.30
248.2	0.42 ± 0.16	1.43 ± 0.05	2.32
253.0	0.43 ± 0.16	1.43 ± 0.04	2.33
257.8	0.43 ± 0.15	1.42 ± 0.03	2.34
262.4	0.42 ± 0.14	1.39 ± 0.03	2.35
267.9	0.41 ± 0.13	1.35 ± 0.03	2.37
276.0	0.39 ± 0.12	1.29 ± 0.04	2.39
296.0	0.42 ± 0.11	1.29 ± 0.03	2.44
302.0	0.38 ± 0.11	1.22 ± 0.08	2.45 ± 0.15
306.7	0.39 ± 0.10	1.22 ± 0.02	2.45
313.7	0.39 ± 0.10	1.23 ± 0.04	2.45
320.9	0.32 ± 0.08	1.11 ± 0.04	2.45
327.5	0.26 ± 0.07	1.01 ± 0.03	2.45
334.3	0.24 ± 0.06	0.97 ± 0.03	2.45
341.4	0.25 ± 0.06	0.98 ± 0.03	2.45

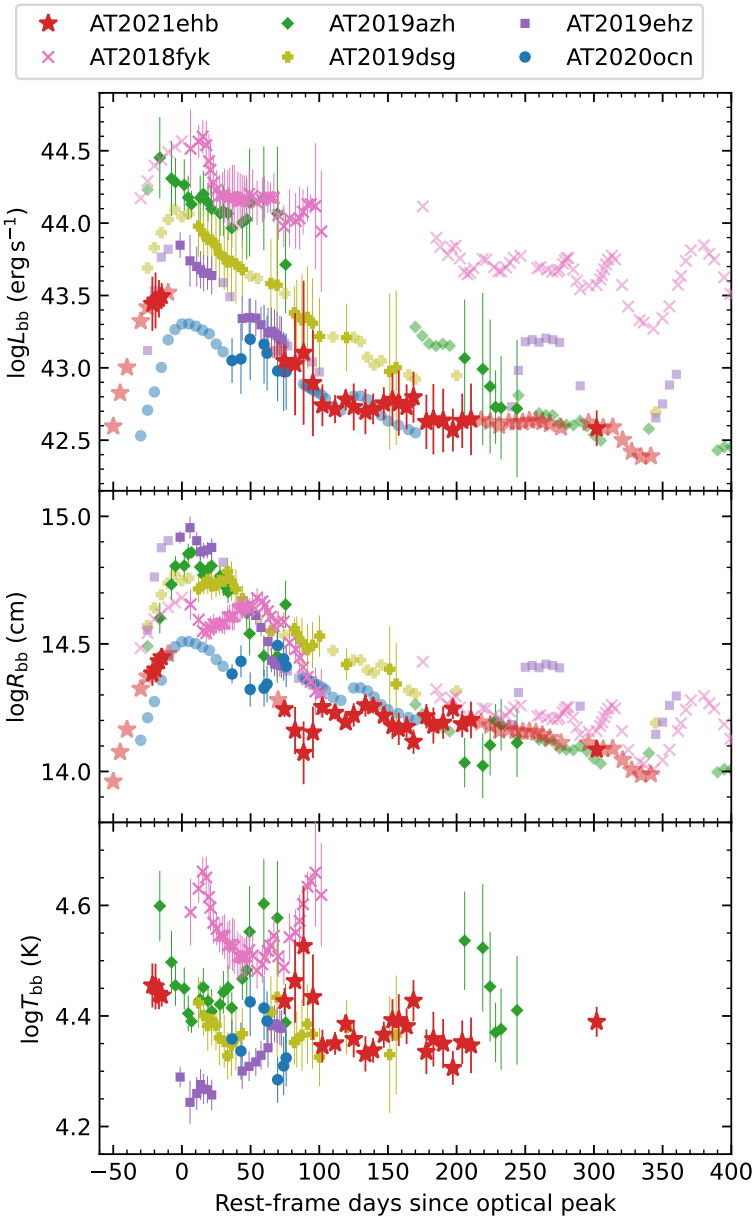

Figure 5.6: Evolution of the UV/optical blackbody properties of AT2021ehb compared with a sample of X-ray bright TDEs in the literature.

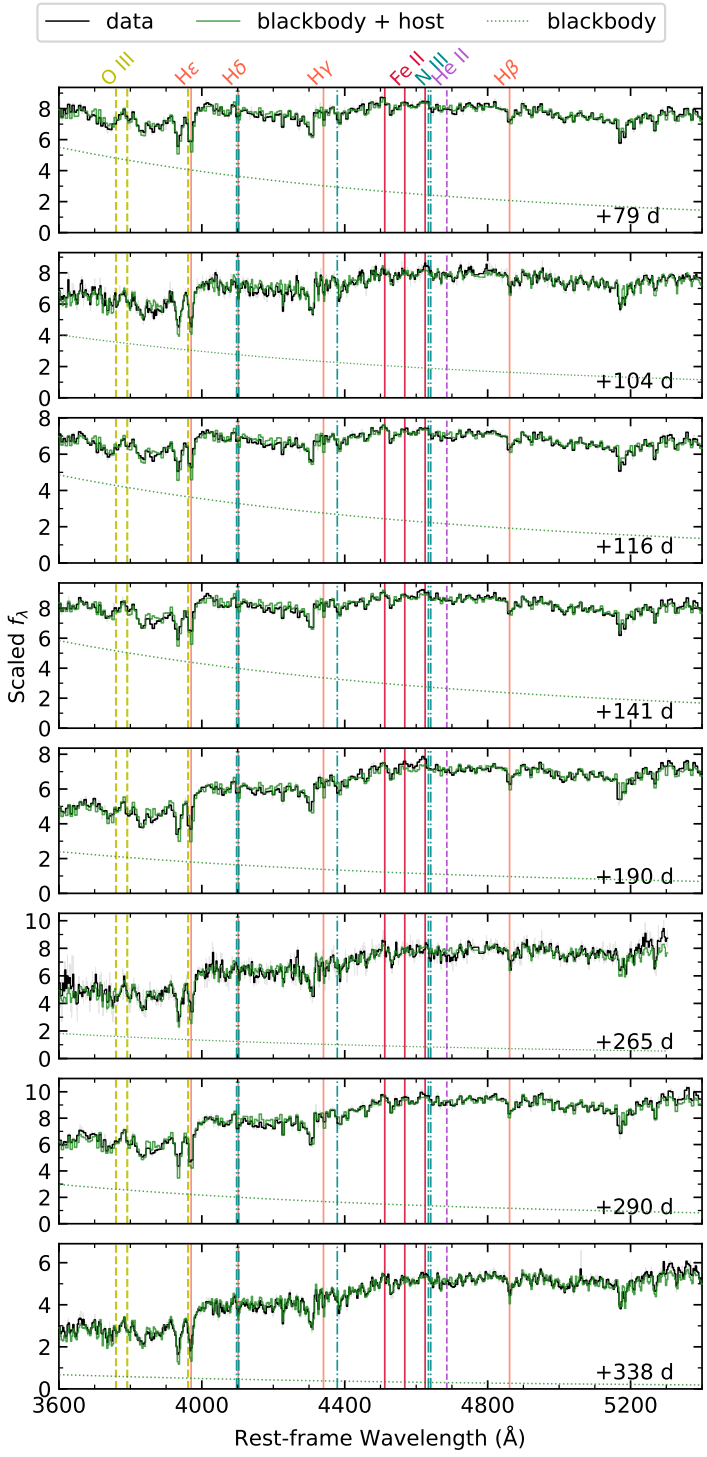

Figure 5.7: Long-slit optical spectra of AT2021ehb, overplotted with the blackbody continuum ($A_1 f_{\lambda,\mathrm{BB}}$; dotted lines) plus host galaxy spectrum ($A_2 f_{\lambda,\mathrm{host}}$).

might not be a perfect description of the bulge spectrum.

The fitting results are shown in Figure 5.7. We mark locations of emission lines commonly seen in TDEs, including Balmer lines, He II, the Bowen fluorescence lines of N III and O III, as well as low-ionization Fe II lines (Blanchard et al., 2017; Wevers, Pasham, van Velzen, Leloudas, et al., 2019; van Velzen, Gezari, Hammerstein, et al., 2021). The observed spectra of AT2021ehb can be well described by a blackbody continuum (dotted lines) plus host galaxy contribution. The spectra at $\delta t > 170$ days are mostly from the host, and therefore it is not very surprising that no discernible TDE lines were detected. However, at $\delta t < 170$ days, the blackbody component contributes 25%–80% of the total flux. As such, it is surprising that no prominent lines from the TDE itself can be identified.

X-ray Light Curve Analysis

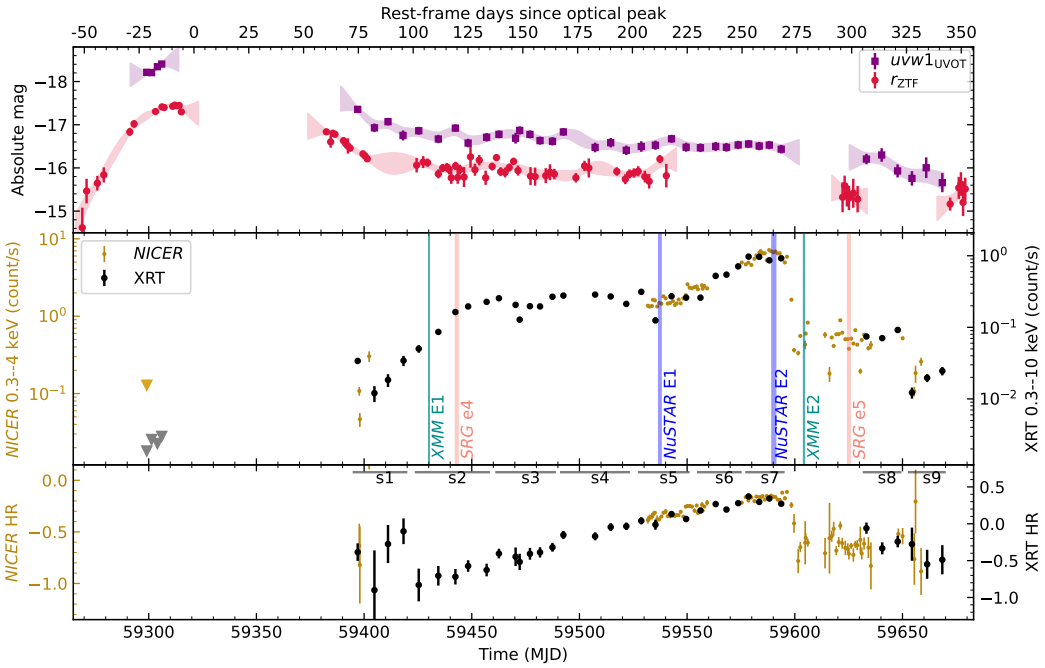

Figure 5.8: *Upper & Middle*: UV, optical, and X-ray light curves of AT2021ehb. *Bottom*: X-ray HR evolution of AT2021ehb.

The middle panel of Figure 5.8 shows the XRT and *NICER* (all binned by obsID) light curves. The lower panel of Figure 5.8 shows the evolution of the hardness ratio, defined as HR $\equiv (H - S)/(H + S)$, where H is the number of net counts in the hard band, and S is the number of net counts in 0.3–1 keV. For XRT we take 1–10 keV as the hard band, while for *NICER* we take 1–4 keV.

X-rays were not detected at $\delta t < 0$. Pre-peak X-ray upper limits are provided by *Swift*/XRT ($< 10^{40.9}$ erg s^{-1}, Table 5.2) and *SRG*/eROSITA ($< 10^{40.2}$ erg s^{-1}, Table 5.3).

X-rays were first detected by XRT at $\delta t = 73.9$ days. The exact time of the X-ray onset cannot be accurately constrained. The count rate initially exhibited strong variability from $\delta t = 73.9$ days to $\delta t = 82.3$ days, and then gradually increased out to $\delta t = 250$ days. At the same time, the HR gradually increased. From $\delta t = 250$ days to $\delta t = 271$ days, both the X-ray flux and the hardness stayed at the maximum values.

From $\delta t = 271.0$ days to $\delta t = 273.7$ days, the *NICER* net count rate suddenly decreased by a factor of 10 (Yao, Pasham, Gendreau, et al., 2022). At the same time, the HR significantly decreased. After an X-ray plateau of ≈ 50 days, the XRT net count rate further decreased drastically by a factor of 6 (from $\delta t = 320.9$ days to $\delta t = 327.2$ days).

X-ray Spectral Analysis

In this subsection, we first present a joint spectral analysis of contemporaneous data sets obtained from *NICER* and *NuSTAR*, including the first epoch in 2021 November 18–19 and the second epoch in 2022 January 10–12. These observations are of high SNR and cover a wide energy range. As such, the fitting results can guide us to choose appropriate spectral models to fit spectra with lower SNR. We adopt the `wilm` abundances (Wilms, Allen, and McCray, 2000).

We then perform analysis on data sets obtained by single telescopes, including *XMM-Newton*, *SRG*, *Swift*/XRT, and *NICER*, where the Anders and Grevesse (1989) abundances were adopted.

All spectral fitting was performed with `xspec` (v12.12, Arnaud 1996). We used the `vern` cross sections (Verner et al., 1996).

(I) *NICER*+*NuSTAR* First Epoch, 2021 November

We chose energy ranges where the source spectrum dominates over the background. For *NICER* we used 0.3–4 keV. For *NuSTAR*/FPMA we used 3–23 keV, and for FPMB we used 3–20 keV[6]. All data were fitted using χ^2-statistics.

For all spectral models described below, we included the Galactic absorption using the `tbabs` model (Wilms, Allen, and McCray, 2000), with the hydrogen-equivalent

[6]In this *NuSTAR* observation, FPMB is more affected by a nearby bright source.

Table 5.7: Modeling of the first joint *NICER* and *NuSTAR* observations of AT2021ehb.

Component	Parameter	(1a)
`constant`	$C_{\rm FPMB}$	$1.03^{+0.06}_{-0.05}$
	$C_{\rm NICER}$	$0.85^{+0.06}_{-0.05}$
`ztbabs`	$N_{\rm H}$ (10^{20} cm^{-2})	< 0.75
`simpl`	Γ	2.29 ± 0.05
	$f_{\rm sc}$	$0.35^{+0.02}_{-0.03}$
`diskbb`	$T_{\rm in}$ (eV)	164^{+6}_{-9}
	$R^{*}_{\rm in}$ (10^4 km)	$25.5^{+4.4}_{-2.0}$
—	χ^2/dof	$163.17/142 = 1.15$

column density $N_{\rm H}$ fixed at 9.97×10^{20} cm^{-2} (HI4PI Collaboration et al., 2016). We shifted the TDE emission using the convolution model `zashift`, with the redshift z fixed at 0.018. We included possible absorption intrinsic to the source using the `ztbabs` model. We also included a calibration coefficient (`constant`; Madsen et al. 2017) between FPMA, FPMB, and *NICER*, with $C_{\rm FPMA} \equiv 1$. This term also accounts for the differences in the mean flux between *NuSTAR* and *NICER* that results from intrinsic source variability.

First, we fitted the spectrum with a power-law (PL), and obtained a photon index of $\Gamma \approx 2.7$. The fit is unacceptable, with the reduced χ^2 being $\chi^2_{\rm r} = 3.44$ for 144 degrees of freedom (*dof*). The residuals are most significant between 0.3 and 2 keV, suggesting the existence of a (thermal) soft component. Therefore, we changed the PL to `simpl*thermal_model`. Here `simpl` is a Comptonization model that generates the PL component via Compton scattering of a fraction ($f_{\rm sc}$) of input seed photons (Steiner, Narayan, et al., 2009). The flag $R_{\rm up}$ was set to 1 to only include upscattering. We experimented with three different thermal models: a blackbody (`bbody`), a multicolor disk (MCD; `diskbb`; Mitsuda et al. 1984), and a single-temperature thermal plasma (`bremss`; Kellogg, Baldwin, and Koch 1975), resulting in $\chi^2_{\rm r} = 1.33$, 1.15, and 1.35 (for $dof = 142$), respectively. The fit statistics favors a MCD.

The best-fit result with a MCD, defined as model (1a), is shown in Figure 5.9. We present the best-fit parameters in Table 5.7. Here $T_{\rm in}$ is the inner disk temperature, and $R^{*}_{\rm in} \equiv R_{\rm in}\sqrt{\cos i}$ is the apparent inner disk radius times square root of $\cos i$, where i is the system inclination. $R^{*}_{\rm in}$ is inferred from the normalization parameter of `diskbb`. Model (1a) gives a good fit with $\chi^2_{\rm r} = 163/142 = 1.15$.

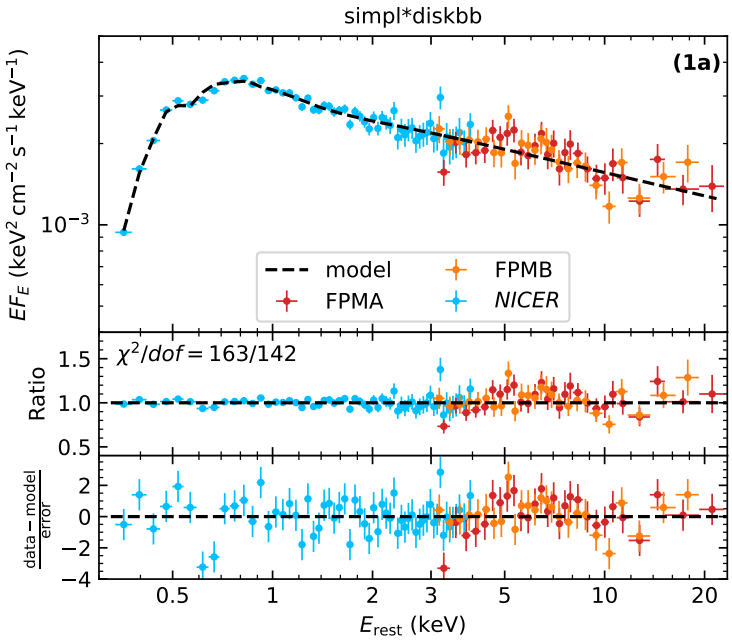

Figure 5.9: The spectrum of the first joint *NICER* and *NuSTAR* observations of AT2021ehb (2021 November).

(II) *NICER*+*NuSTAR* Second Epoch, 2022 January

We chose energy ranges where the source spectrum dominates over the background. For *NICER* we used 0.3–7.0 keV; For *NuSTAR* FPMA and FPMB we used 3–30 keV. All data were fitted using χ^2-statistics. Here we use `tbfeo` to model the Galactic absorption. Compared with `tbabs`, `tbfeo` allows the O and Fe abundances ($A_{\rm O}$, $A_{\rm Fe}$) to be free.

We adopted a continuum model of `simpl*diskbb`, defined as (2a). The result, with $\chi^2_{\rm r} = 2.04$, is shown in Figure 5.10 and the upper left panel of Figure 5.11. The residual plot clearly indicates the existence of unmodeled spectral features and a significant offset between *NuSTAR* and *NICER* at 6–7 keV.

First, we study whether this offset is brought about by a cross-calibration difference between *NICER* and *NuSTAR*. To this end, we replaced `constant` with `crabcorr` (Ludlam, Cackett, García, Miller, Stevens, et al., 2022), which multiplies the spectrum by a power-law of $C \cdot E^{-\Delta\Gamma}$. When $\Delta\Gamma = 0$, `crabcorr` is equivalent to `constant`. We fixed $\Delta\Gamma_{\rm FPMA} = \Delta\Gamma_{\rm FPMB} = 0$, and allow $\Delta\Gamma_{NICER}$ to be free. The best-fit model gives $\Delta\Gamma_{NICER} = -0.128^{+0.014}_{-0.023}$, which is too large compared with the value of $\Delta\Gamma_{NICER} \approx -0.06$ found by Ludlam, Cackett, García, Miller, Stevens, et al. (2022). Therefore, we conclude that a difference in the cross-calibration slope is

Table 5.8: Modeling of the second joint *NICER* and *NuSTAR* observations of AT2021ehb.

Component	Parameter	(2b)	(2c)	(2d)
`constant`	$C_{\rm FPMB}$	1.03 ± 0.01	1.03 ± 0.01	1.03 ± 0.01
	$C_{\rm NICER}$	1.02 ± 0.01	1.02 ± 0.01	1.03 ± 0.01
`tbfeo`	$A_{\rm O}$	$1.48^{+0.11}_{-0.08}$	1.26 ± 0.13	$1.45^{+0.10}_{-0.07}$
	$A_{\rm Fe}$	$2.07^{+0.63}_{-0.64}$	$1.99^{+0.61}_{-0.62}$	$2.37^{+0.50}_{-0.39}$
`ztbabs`	$N_{\rm H}$ (10^{20} cm^{-2})	< 0.12	0.70 ± 0.28	< 0.01
`diskbb`	$T_{\rm in}$ (eV)	198^{+8}_{-6}	257 ± 8	180^{+7}_{-2}
	$R^{*}_{\rm in}$ (10^{4} km)	$28.4^{+1.2}_{-1.7}$	$10.5^{+1.0}_{-0.9}$	47.3 ± 2.8
`simpl`	Γ	2.11 ± 0.01	...	2.26 ± 0.01
	$f_{\rm sc}$	$0.49^{+0.02}_{-0.03}$	...	0.61 ± 0.01
`gaussian`	$E_{\rm line}$ (keV)	$4.92^{+0.36}_{-0.71}$	...	...
	$\sigma_{\rm line}$ (keV)	$2.18^{+0.50}_{-0.32}$	...	...
	Norm (10^{-4} ph cm^{-2} s^{-1})	$2.52^{+1.01}_{-0.51}$	...	...
`relxill`	$q_1 = q_2$	...	3 (frozen)	...
	a	...	0 (frozen)	...
	i (°)	...	$43.4^{+8.5}_{-9.6}$	...
	$R_{\rm in}$ ($R_{\rm ISCO}$)	...	1 (frozen)	...
	$R_{\rm out}$ ($R_{\rm g}$)	...	400 (frozen)	...
	Γ	...	1.86 ± 0.02	...
	logξ (erg cm s^{-1})	...	$4.09^{+0.20}_{-0.12}$	...
	$A_{\rm Fe}$	...	$1.86^{+1.46}_{-0.63}$	...
	$E_{\rm cut}$ (keV)	...	$54.0^{+13.4}_{-9.5}$	...
	$R_{\rm F}$	...	1 (frozen)	...
	Norm (10^{-5})	...	$6.1^{+0.40}_{-0.40}$	...
`xstar`	$N_{\rm H}$ (10^{23} cm^{-2})	...	...	$2.22^{+0.49}_{-0.86}$
	logξ (erg cm s^{-1})	...	...	$1.51^{+0.34}_{-0.32}$
	$f_{\rm cover}$	...	...	0.31 ± 0.02
	Redshift	...	...	0 (frozen)
—	χ^2/dof	330.72/296 = 1.12	306.64/295 = 1.04	318.23/296 = 1.08

likely not the primary reason for the 6–7 keV offset.

Next, we investigate whether this offset is caused by imperfect *NICER* calibration at 2–3 keV. *NICER* effective area changes rapidly in the 2–3 keV band. Calibration issues in that range may cause the model to over-estimate the data at 2–3 keV, and to badly under-estimate it above 3 keV. As a test, we performed the fit omitting the 2–3 keV region in the *NICER* data. However, the best-fit result still leaves a significant offset between *NICER* and *NuSTAR* at 6–7 keV, similar to that shown in Figure 5.10.

We are left to conclude that the offset is likely caused by either an underestimate of *NICER* background at the high energy end or systematic uncertainties in *NICER* calibration that is not well characterized. This conjecture is based on the fact that *NICER* uses X-ray concentrators optics and its 3–7 keV background is > 10 times brighter than that of *NuSTAR* (Figure 5.10). On the other hand, *NuSTAR* adopts X-

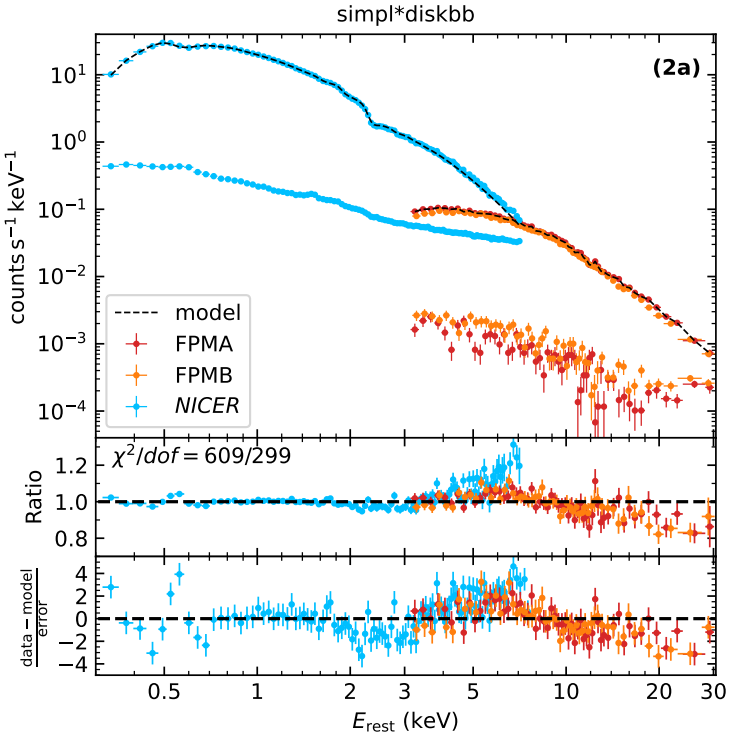

Figure 5.10: The spectrum of the second joint *NICER* and *NuSTAR* observations (2022 January), overplotted with the simple model (2a).

ray focusing optics, which enables more robust background estimation using regions close to the object of interest.

In the following, we attempted to improve the fit by three approaches: adding a Gaussian line, adding reflection emission features, and adding absorption features.

(i) Modeling with a Gaussian Line Profile

The result with adding a `gaussian` line component is shown in the upper-right panel of Figure 5.11. This model, defined as (2b), provides a much better fit compared with (2a). The best-fit parameters (Table 5.8) give a very broad emission profile with a central energy at $E_{\rm line} \sim 5\,{\rm keV}$ and a line width of $\sigma_{\rm line} \sim 2\,{\rm keV}$. If the 3–7 keV spectral feature indeed comes from an emission line, its central energy is different from the emission line at $E_{\rm line} \sim 8\,{\rm keV}$ that has been found in the jetted TDE Sw J1644+57, which has been interpreted as highly ionized iron Kα emission blueshifted by $\sim 0.15c$ (Kara, Miller, et al., 2016; Thomsen, Lixin Dai, et al., 2019). Instead, what is shown here indicate the possible existence of a relativistically broadened iron line (either redshifted or with a more distorted red wing).

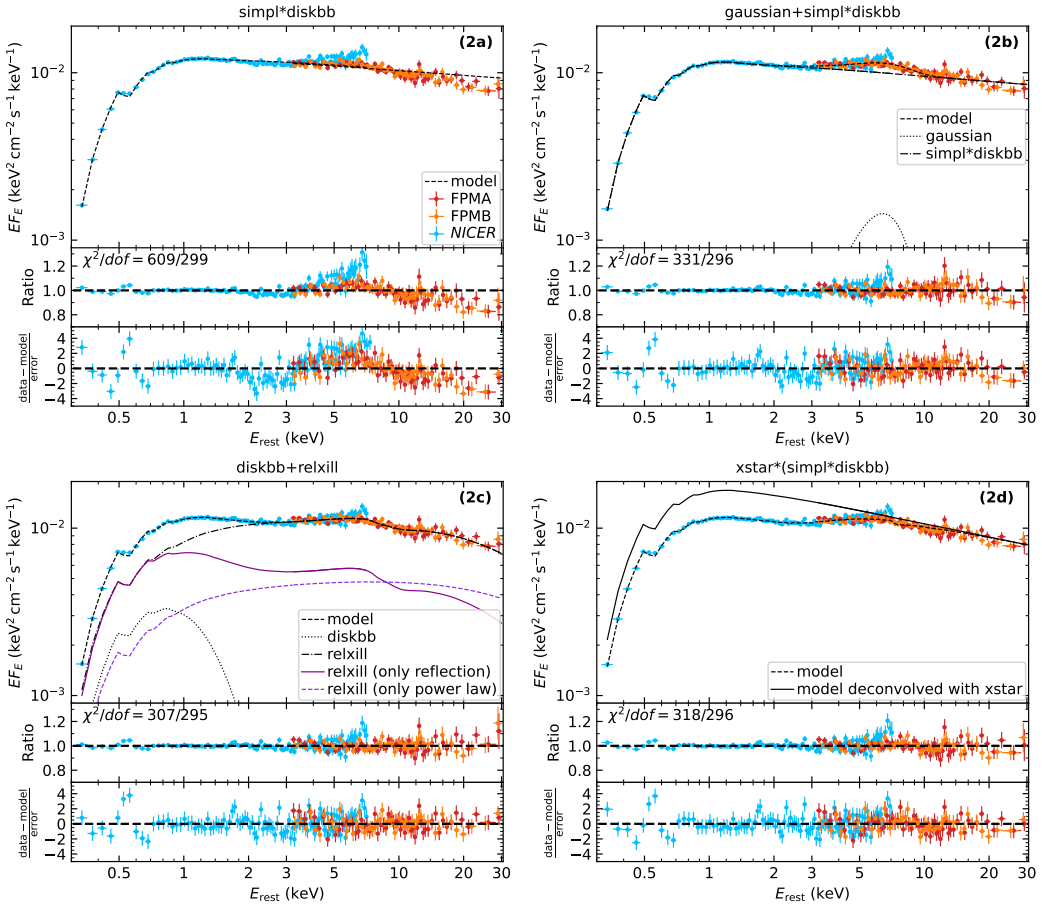

Figure 5.11: The spectrum of the second joint *NICER* and *NuSTAR* observations (2022 January). The four panels show four different model fitting results.

(ii) Modeling with Disk Reflection

In this method, we fit the data using a combination of MCD and relativistic reflection from an accretion disk.

We utilize the self-consistent `relxill` model to describe the direct power-law component and the reflection part (García, Dauser, et al., 2014; Dauser, García, Parker, et al., 2014). In `relxill`, we fixed the outer disk radius ($R_{\rm out}$) at a fiducial value of 400 $R_{\rm g}$, since it has little effect on the X-ray spectrum. The redshift parameter in `relxill` was fixed at 0 since the host redshift was already included by the `zashift` model. To reduce the complexity of this model, we froze the reflection fraction $R_{\rm F}$ (ratio of the reflected to primary emission; Dauser, García, Walton, et al. 2016) at 1. The inner and outer emissivity index q were fixed at 3 throughout the accretion disk, making $R_{\rm break}$ obsolete. We assume the inner disk radius is at the innermost stable circular orbit (ISCO), i.e., $R_{\rm in} = R_{\rm ISCO}$. Other parameters in

`relxill` include the power-law index of the incident spectrum Γ, the cutoff energy of the power-law $E_{\rm cut}$, the black hole spin a, the inclination i, the ionization of the accretion disk ξ, the iron abundance of the accretion disk $A_{\rm Fe}$, and the normalization parameter $\rm Norm_{rel}$. We first fit the data allowing a to be free, finding that the fit is not sensitive to a. Therefore, we performed the fit with a fixed at zero.

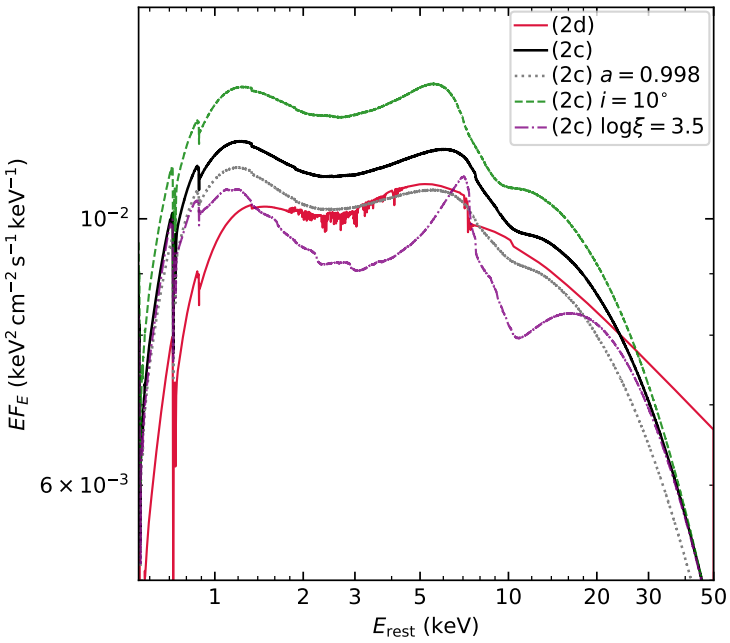

Figure 5.12: Best-fit incident model spectra of (2c) and (2d), as well as modifications of (2c) if one parameter is changed.

The best-fit model, hereafter (2c), gives $\chi^2/dof = 306.65/296 = 1.04$ and is shown in the lower-left panel of Figure 5.11. The best-fit model parameters are given in Table 5.8. In Figure 5.12, the solid black line shows the best-fit model; Modifications of the best-fit model are shown as dotted (if a is changed from 0 to 0.998), dashed (if i is changed from 43.4° to 70°), and dash-dotted (if $\log\xi$ is changed from 4.09 to 3.50) lines. The shape and width of the extremely broad iron emission are mainly determined by the high disk ionization state and the moderate inclination. We note that the best-fit ionization of $\xi \sim 10^4\,\rm erg\,cm\,s^{-1}$ is greater than the typical values observed in Seyfert 1 AGN (Walton, Nardini, et al., 2013; Ezhikode et al., 2020).

(iii) Modeling with Absorbers

In this method, we attempt to improve the fit by adding absorption features. First, we added partial covering of a neutral absorber using the `pcfabs` model. In `pcfabs`, a fraction $f_{\rm cover}$ of the X-ray source is seen through a neutral absorber with hydrogen-

equivalent column density $N_{\rm H}$, while the rest is assumed to be observed directly. The best-fit model gives $\chi^2/dof = 386/297 = 1.30$. If we add a new free parameter (redshift of the neutral absorber) by replacing `pcfabs` with `zpcfabs`, χ^2/dof becomes $370/296 = 1.25$. However, both models leave 5–8 keV flux excess in the residual.

Therefore, we next allow the absorber to be partially ionized by replacing `zpcfabs` with a photoionized absorber. This is also motivated by the fact that a good fit to the *Chandra* LETG observation conducted on 2021 November 29 was found with such a model by Miller, Reynolds, Yun, et al. (2022). This fit utilized the `zxipcf` model (Reeves et al., 2008), which is a grid of photoionization models computed by the `XSTAR` code (Kallman and Bautista, 2001). However, Reynolds et al. (2012) noted that `zxipcf` only has a very coarse sampling in ionization space, and so in this work, we use an updated `XSTAR` grid that is suitable for use with AGNs (computed in Walton, Alston, et al. 2020). This grid assumes an ionizing continuum of $\Gamma = 2$ and a velocity broadening of $100\,{\rm km\,s^{-1}}$, and allows the ionization parameter, column density, absorber redshift, and both the oxygen and iron abundances to be varied as free parameters (although for simplicity we assume these abundances are solar). Fitting the data with the redshift of the absorber fixed at zero yields $\chi^2/dof = 318.2/296 = 1.08$. If the redshift is allowed to be free, we have $\chi^2/dof = 317.7/295 = 1.08$. Since χ^2 only reduces by 0.5 for 1 *dof*, the redshift parameter cannot be well constrained by our data. Therefore, we name the model with the absorber redshift fixed at zero as (2d), and show it in the lower-right panel of Figure 5.11. The model parameters are given in Table 5.8. In Figure 5.12, the solid crimson line shows a high-resolution version of model (2d).

Model Comparison and Comments — Between (2b) and (2c), we consider (2c) to be superior since (*i*) its χ^2 is smaller by 24 for only 1 *dof* and (*ii*) it adopts a physically motivated model instead of a mathematical function.

To compare (2c) and (2d), we use the Bayesian information criterion (BIC) to assess the goodness of fit. Here

$$\begin{aligned} {\rm BIC} &= k \cdot \ln(N) - 2\ln\mathcal{L} && (5.1)\\ &= k \cdot \ln(N) + \chi^2 + {\rm constant} && (5.2) \end{aligned}$$

where k is the number of free parameters, N is the number of spectral bins, and $\mathcal{L}$ is the maximum of the likelihood function. Models with lower BIC values are favored. According to Raftery (1995), a BIC difference between 2 and 6 is positive,

a difference between 6 and 10 is strong, and a difference greater than 10 is very strong. Since BIC(2c) − BIC(2d) = −5.9, model (2c) is slightly favored over (2d). The energy range over which model (2c) performs better than (2d) is ∼ 8–12 keV. This is because absorption by ionized iron adds a relatively sharp flux decrease at ∼ 7 keV, while the blue wing of the iron emission in `relxill` is smoother (see the lower-right panel of Figure 5.11).

We note that the residual below 0.7 keV is strong in all model fits, and is likely caused by underestimated *NICER* calibration uncertainties at the lowest energies.

(III) *XMM-Newton* Analysis

Table 5.9: Modeling of two *XMM-Newton* observations of AT2021ehb.

Component	Parameter	XMM E1	XMM E2
`ztbabs`	$N_{\rm H}$ (10^{20} cm^{-2})	$1.09^{+0.99}_{-0.45}$	< 1.22
`diskbb`	$T_{\rm in}$ (eV)	68^{+1}_{-4}	125 ± 8
	$R^{*}_{\rm in}$ (10^4 km)	511^{+144}_{-75}	39^{+10}_{-6}
`simpl`	Γ	> 4.57 †	2.92 ± 0.15
	$f_{\rm sc}$	$0.13^{+0.03}_{-0.01}$	0.16 ± 0.03
—	χ^2/dof	$70.26/52 = 1.35$	$97.49/82 = 1.19$

† Upper limit of Γ is at 5.

We chose energy ranges where the source spectrum dominates over the background. For XMM E1 this is 0.2–2.6 keV, while for XMM E2 this is 0.2–7.0 keV. All data were fitted using χ^2-statistics. Following §5.4 and §5.4, all models described below have been multiplied by `tbabs*ztbabs*zashift` to include Galactic absorption, host absorption, and host redshift.

Although the XMM E1 spectrum is very soft, a single MCD results in a poor fit and leaves a large residual above 1 keV, suggesting the existence of a non-thermal component. A continuum model of `simpl*diskbb` gives a much better fit with $\chi^2_{\rm r} = 1.35$. The best-fit model is shown in the upper panel of Figure 5.13. The XMM E2 spectrum is much harder than that from XMM E1. Fitting with `simpl*diskbb` gives a good fit with $\chi^2_{\rm r} = 1.19$ (see Figure 5.13, lower panel).

We note that although the $\chi^2_{\rm r}$ of our best-fit *XMM-Newton* models are acceptable, there seems to be some systematic residuals. For example, eight consecutive bins of positive residuals are seen in the 1.7–2.6 keV XMM E1 data. A possible explanation is that there exist spectral features created by absorbing materials in the TDE system,

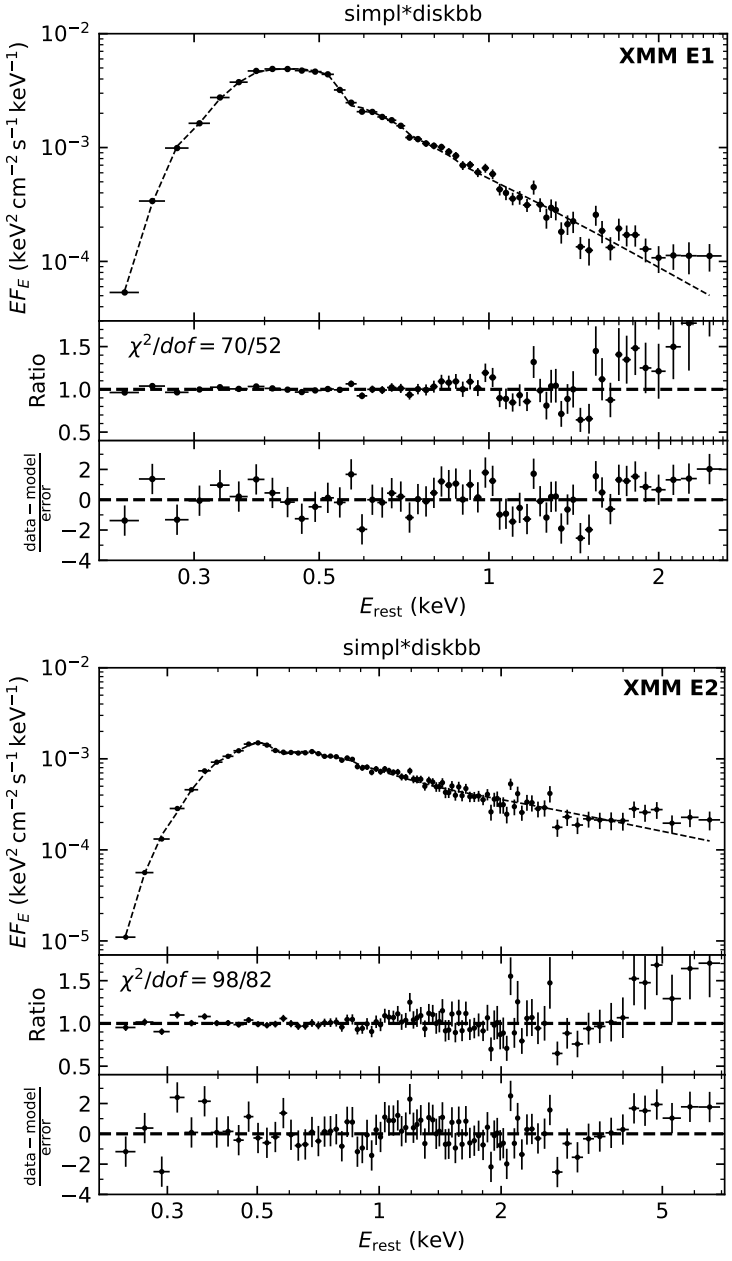

Figure 5.13: The *XMM-Newton* spectra of AT2021ehb.

such as the blueshifted absorption lines reported in the TDE ASASSN-14li (Miller, 2015; Kara, Dai, et al., 2018). Seven consecutive bins of positive residuals are seen in the 4.0–7.0 keV XMM E2 data. This might indicate the existence of disk reflection features, such as an iron emission line. We note that 2–4 days after our second *XMM-Newton* epoch, *XMM-Newton*/EPIC observations obtained under another program also reveals the existence of interesting features in the iron K band (Miller, Reynolds, Zoghbi, et al., 2022). More detailed modeling of the *XMM-Newton* spectra is beyond the scope of this paper, and is encouraged in future work.

(IV) *SRG*/eROSITA Analysis

We chose energy ranges where the source spectrum dominates over the background. For eRASS4 this range is 0.2–3 keV, while for eRASS5 this range is 0.2–2 keV. All data were fitted with the C-statistic (Cash, 1979).

Table 5.10: Modeling of two *SRG*/eROSITA observations of AT2021ehb.

Component	Parameter	eRASS4	eRASS5
`ztbabs`	$N_{\rm H}$ (10^{20} cm^{-2})	$0.21^{+2.19}_{-0.20}$	< 3.41
`diskbb`	$T_{\rm in}$ (eV)	89^{+7}_{-13}	96^{+32}_{-22}
	$R^{*}_{\rm in}$ (10^{4} km)	210^{+179}_{-38}	73^{+243}_{-21}
`simpl`	Γ	$4.15^{+0.82}_{-0.73}$	2.92 (frozen)
	$f_{\rm sc}$	$0.14^{+0.12}_{-0.08}$	$0.21^{+0.06}_{-0.09}$
—	$cstat/dof$	126.43/140	76.45/85

Following the *NICER*+*NuSTAR* and *XMM-Newton* spectral analysis, we fitted the *SRG*/eROSITA spectra with `tbabs*ztbabs*zashift*simpl*diskbb`. For the eRASS5 spectrum, since the source is only above background at 0.2–2 keV, the powerlaw index cannot be constrained from the *SRG*/eROSITA spectrum alone. Therefore, we fixed Γ at the best-fit value of the XMM E2 spectrum (Table 5.9, $\Gamma = 2.92$), and allowed other parameters to be free. This choice is based on the fact that the XMM E2 and eRASS5 observations appear to show the same properties on the light curve and hardness evolution diagrams (Figure 5.8).

The fitting results are shown in Figure 5.14. The best-fit parameters are shown in Table 5.10.

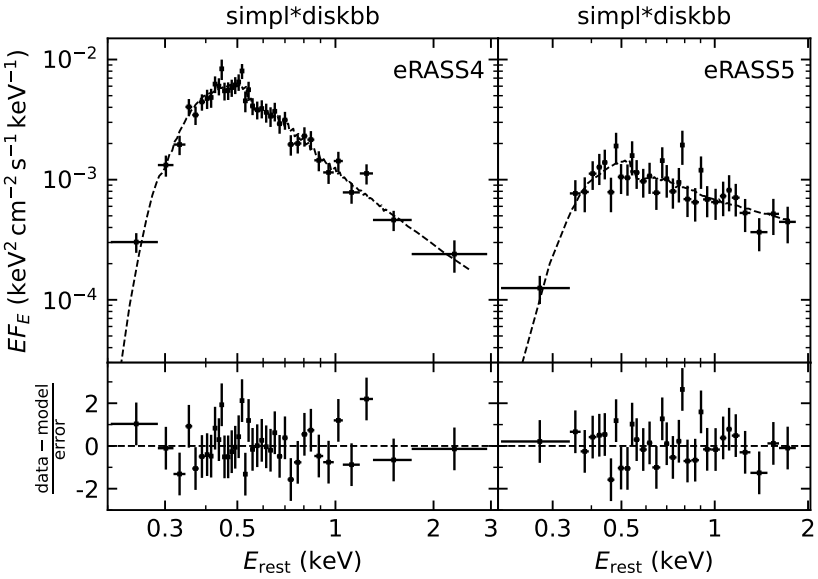

Figure 5.14: *SRG*/eROSITA spectra of AT2021ehb.

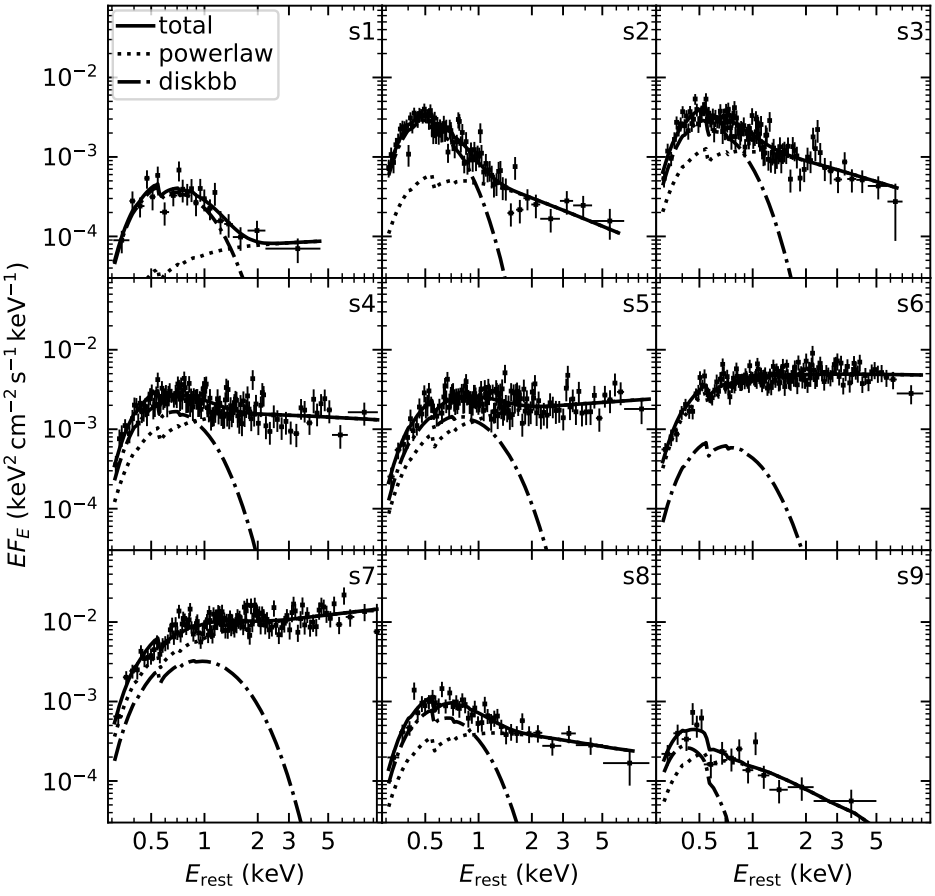

Figure 5.15: XRT time-averaged spectra of AT2021ehb.

(V) XRT Analysis

The temporal coverage of each time-averaged XRT spectrum is shown as 's1', 's2', ..., 's9' in the lower panel of Figure 5.8. We fitted the 0.3–10 keV spectra using a simple model of `tbabs*zashift*(diskbb+powerlaw)`. We did not include the `ztbabs` component, as host galaxy absorption was found to be negligible or much smaller than the Galactic absorption in all previous spectral analyses (see Tables 5.7, 5.8, 5.9, and 5.3). The adopted continuum model does not give realistic model parameters. For example, the disk radii will be underestimated when the source spectrum is hard (see a detailed discussion in Steiner, Narayan, et al. 2009). The main goal of this fitting is to compute the multiplicative factor to convert the 0.3–10 keV XRT net count rate to X-ray fluxes, including (i) the observed 0.3–10 keV flux $f_{\rm X}$ (0.3–10 keV), (ii) the Galactic absorption corrected 0.3–10 keV flux $f_{\rm X,\,0}$ (0.3–10 keV), (iii) the Galactic absorption corrected 0.5–10 keV flux $f_{\rm X,\,0}$ (0.5–10 keV), (iv) the Galactic absorption corrected flux density at the rest-frame energies of 0.5 keV and 2 keV (i.e., f_ν(0.5 keV) and f_ν(2 keV)). All data were fitted using C-statistics.

Table 5.11: X-ray Fluxes of AT2021ehb from Modeling of XRT spectra.

Obs	Net 0.3–10 keV Rate (count s^{-1})	f_ν(0.5 keV) (μJy)	f_ν(2 keV) (μJy)	$f_{\rm X}$ (0.3–10 keV)	$f_{\rm X,\,0}$ (0.3–10 keV) (10^{-13} erg s^{-1} cm^{-2})	$f_{\rm X,\,0}$ (0.5–10 keV)
s1	0.0276 ± 0.0019	$1.133^{+0.103}_{-0.185}$	$0.030^{+0.002}_{-0.023}$	$9.76^{+1.39}_{-1.08}$	$18.47^{+2.63}_{-2.05}$	$11.34^{+0.37}_{-2.72}$
s2	0.1476 ± 0.0041	$9.639^{+0.178}_{-0.595}$	$0.106^{+0.008}_{-0.012}$	$48.67^{+1.79}_{-1.03}$	$129.40^{+4.76}_{-2.74}$	$48.96^{+1.34}_{-2.53}$
s3	0.2116 ± 0.0047	$10.930^{+0.287}_{-0.694}$	$0.312^{+0.017}_{-0.018}$	$78.12^{+2.87}_{-1.95}$	$166.66^{+6.13}_{-4.15}$	$86.04^{+1.75}_{-3.95}$
s4	0.2584 ± 0.0062	$7.565^{+0.224}_{-0.683}$	$0.544^{+0.026}_{-0.035}$	$97.63^{+3.67}_{-3.31}$	$158.72^{+5.97}_{-5.37}$	$109.87^{+2.56}_{-5.73}$
s5	0.2382 ± 0.0058	$5.485^{+0.211}_{-0.583}$	$0.678^{+0.029}_{-0.054}$	$113.80^{+5.90}_{-4.00}$	$159.82^{+8.29}_{-5.62}$	$127.47^{+3.50}_{-7.81}$
s6	0.4776 ± 0.0083	$8.675^{+0.247}_{-1.257}$	$1.702^{+0.057}_{-0.063}$	$233.38^{+8.72}_{-4.48}$	$310.81^{+11.61}_{-5.97}$	$256.24^{+7.73}_{-11.39}$
s7	0.9314 ± 0.0129	$14.647^{+0.724}_{-1.061}$	$3.575^{+0.082}_{-0.164}$	$528.81^{+20.29}_{-13.21}$	$662.69^{+25.43}_{-16.55}$	$579.24^{+11.66}_{-27.10}$
s8	0.0780 ± 0.0029	$2.843^{+0.121}_{-0.351}$	$0.132^{+0.010}_{-0.014}$	$27.30^{+1.56}_{-0.96}$	$50.03^{+2.85}_{-1.77}$	$30.99^{+1.06}_{-2.74}$
s9	0.0185 ± 0.0015	$1.218^{+0.006}_{-0.741}$	$0.027^{+0.006}_{-0.005}$	$7.59^{+1.11}_{-0.52}$	$21.62^{+3.15}_{-1.48}$	$6.78^{+0.48}_{-1.38}$

The best-fit models are shown in Figure 5.15. Scaling factors to convert 0.3–10 keV net count rate to X-ray fluxes can be computed using values provided in Table 5.11. The observed isotropic equivalent 0.3–10 keV X-ray luminosity, $L_{\rm X}$, is shown in the upper panel of Figure 5.16. Note that for the initial four XRT non-detections, we assume a spectral shape similar to 's1'.

(VI) *NICER* Analysis

We started with the obsID-binned *NICER* spectra generated in §5.2. We only performed spectral fitting on obsIDs with more than 500 total net counts in 0.3–4 keV. Following §5.4, we fitted a `tbabs*zashift*(diskbb+powerlaw)` model to the 0.3–4 keV spectra and inferred $f_{\rm X}$ from the best-fit models. All data were

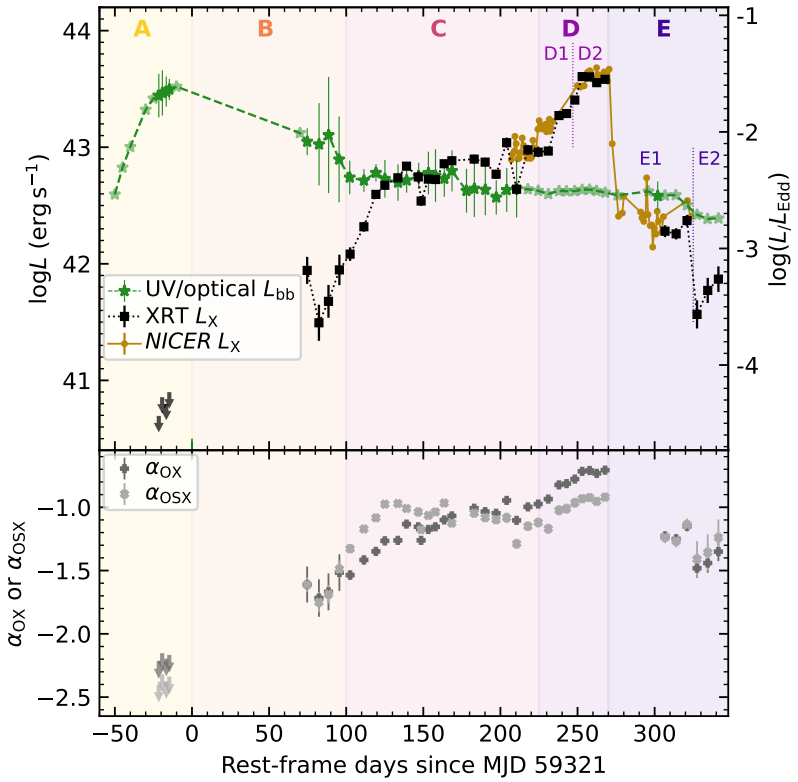

Figure 5.16: Multi-wavelength evolution of AT2021ehb. *Upper*: UV/optical L_{bb} compared with the observed isotropic equivalent 0.3–10 keV X-ray luminosity of AT2021ehb. *Lower*: UV to X-ray spectral slope of AT2021ehb measured by *Swift* observations.

fitted using χ^2-statistics. The best-fit models provided a χ^2_r close to 1 in most cases. The L_X evolution inferred from *NICER* spectral fitting is also shown in the upper panel of Figure 5.16.

Spectral Indices α_{OX} and α_{OSX}

To assist comparison with TDEs from the literature, we computed the UV to X-ray spectral index α_{OX} (Tananbaum et al., 1979; Ruan et al., 2019; Wevers, Pasham, van Velzen, Miller-Jones, et al., 2021) and α_{OSX} (Gezari, 2021), which are commonly used in AGN and TDE literature to characterize the ratio of UV to X-ray fluxes[7].

[7]Note that some papers use these indices with a minus sign in front of our definitions.

Here

$$\alpha_{\rm OX} \equiv \frac{\log[L_\nu(2500\,\text{Å})/L_\nu(2\,\text{keV})]}{\log[\nu(2500\,\text{Å})/\nu(2\,\text{keV})]}, \tag{5.3}$$

$$\alpha_{\rm OSX} \equiv \frac{\log[L_\nu(2500\,\text{Å})/L_\nu(0.5\,\text{keV})]}{\log[\nu(2500\,\text{Å})/\nu(0.5\,\text{keV})]}, \tag{5.4}$$

where L_ν is the luminosity at a certain frequency (corrected for $N_{\rm H}$ and $E_{B-V,{\rm MW}}$). We use the *Swift uvw1* host-subtracted luminosities (rest-frame effective wavelength at 2459 Å for $T_{\rm eff} = 3 \times 10^4$ K) as a proxy for $L_\nu(2500\,\text{Å})$. We measure $f_\nu(0.5\,\text{keV})$ and $f_\nu(2\,\text{keV})$ by converting the XRT net count rates to flux densities using the scaling factors derived in §5.4. We note that $f_\nu(2\,\text{keV})$ mainly traces the evolution of the non-thermal X-ray component, while $f_\nu(0.5\,\text{keV})$ traces both the thermal and non-thermal components. The results are shown in the lower panel of Figure 5.16.

Based on Figure 5.16, we divide the evolution of AT2021ehb into five phases. In phase A ($\delta t \lesssim 0$ days), the UV/optical luminosity brightens, while X-rays are not detected ($< 10^{40.9}\,\text{erg}\,\text{s}^{-1}$). In phase B ($0 \lesssim \delta t \lesssim 100$ days), the UV/optical luminosity declines, and X-rays emerge. Entering into phase C ($100 \lesssim \delta t \lesssim 225$ days), the X-ray spectrum gradually hardens, while the UV/optical luminosity stays relatively flat. In phase D ($225 \lesssim \delta t \lesssim 270$ days), the X-ray further brightens two times (indicated by D1 and D2), and the UV/optical plateau persists. In phase E, the X-ray luminosity drops two times (indicated by E1 and E2), while the UV/optical luminosity only slightly declines. Interestingly, the dramatic X-ray evolution in phase D+E does not have much effect on the UV/optical luminosity. Typical SEDs in each phase are shown in Figure 5.17. The data has been corrected for extinction (in UV/optical) and column density absorption (in the X-ray). The solid lines are the blackbody fits to UV/optical data.

Bolometric Luminosity $L_{\rm bol}$

To calculate the bolometric luminosity $L_{\rm bol}$ at the epochs of the *Swift* observations, we assume that the bulk of the radiation is between 10000 Å and 10 keV. We estimate that when the X-ray spectrum is the hardest (i.e., model 2c), the 0.3–10 keV flux still constitutes 72% of the 0.3–100 keV flux. Therefore, this assumption at most underestimates $\log L_{\rm bol}$ by 0.14 dex.

We compute the 10000 Å to 10 keV luminosity by adding the luminosities in three energy ranges (see a demonstration in Figure 5.18). The data has been corrected for extinction (in UV/optical) and Galactic absorption (in the X-ray). The solid lines

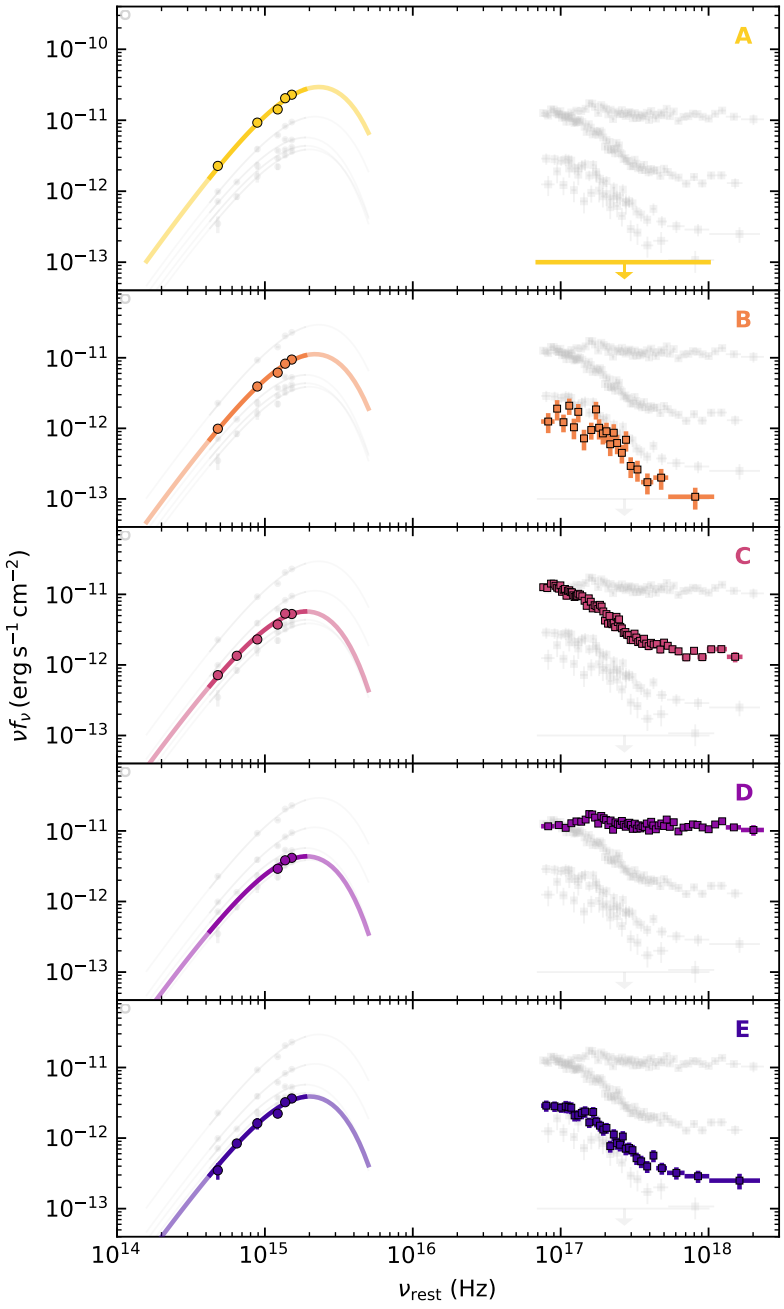

Figure 5.17: Typical SEDs of AT2021ehb in five phases.

are the blackbody fits to UV/optical data (§5.4) and the XRT 's3' spectrum best-fit model (§5.4).

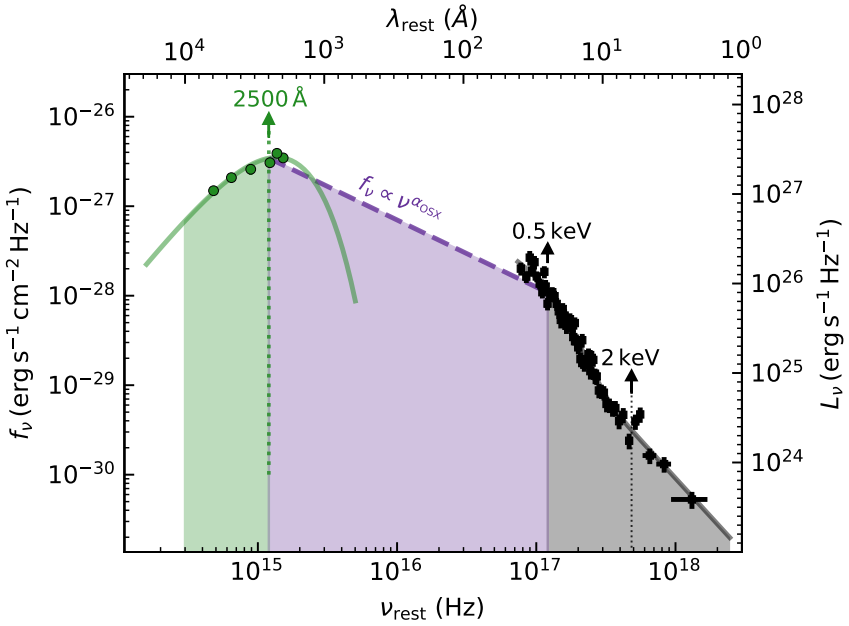

Figure 5.18: A snapshot SED of AT2021ehb at $\delta t \approx 147$ days.

From 10000 Å to 2500 Å, we integrate below the blackbody model fitted to the UV/optical photometry (§5.4).

From 2500 Å to 0.5 keV, we assume that the TDE spectrum is continuous and can be approximated by a power-law of $f_\nu \propto \nu^{\alpha_{\rm OSX}}$. Hence, the luminosity is

$$L = \int_{\nu_1}^{\nu_2} L_\nu d\nu \approx \int_{\nu_1}^{\nu_2} \frac{L_\nu(\nu_1)}{\nu_1^{\alpha_{\rm OSX}}} \nu^{\alpha_{\rm OSX}} d\nu \tag{5.5}$$

$$= \frac{L_\nu(\nu_1)}{\nu_1^{\alpha_{\rm OSX}}} \times \begin{cases} \dfrac{\nu_2^{\alpha_{\rm OSX}+1} - \nu_1^{\alpha_{\rm OSX}+1}}{\alpha_{\rm OSX}+1} & \text{if } \alpha_{\rm OSX} \neq -1 \\ \ln(\nu_2/\nu_1) & \text{if } \alpha_{\rm OSX} = -1 \end{cases} \tag{5.6}$$

where $\nu_1 = 10^{15.08}$ Hz, $\nu_2 = 10^{17.08}$ Hz. In this range, we assume that the uncertainty of L is $0.3L$.

From 0.5 keV to 10 keV, we calculate the luminosity by converting the 0.3–10 keV XRT net count rate to Galactic absorption corrected 0.5–10 keV luminosity using the scaling factors derived in §5.4.

Note that for the first four *Swift* epochs, since X-rays were not detected, we use the UV/optical blackbody luminosity $L_{\rm bb}$ as an approximation of $L_{\rm bol}$.

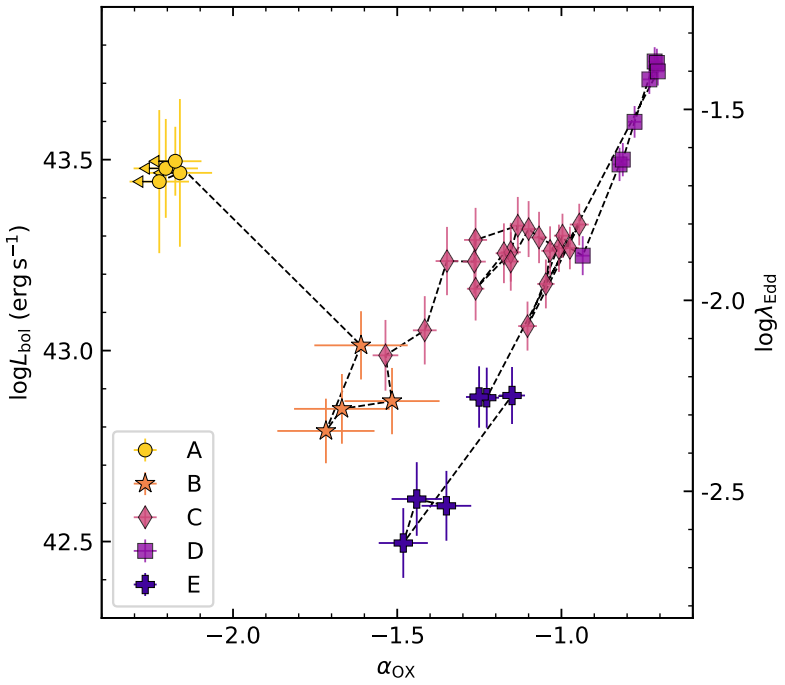

Figure 5.19: The bolometric luminosity $L_{\rm bol}$ and the corresponding $\lambda_{\rm Edd}$ as a function of $\alpha_{\rm OX}$ in AT2021ehb.

The evolution of $\log L_{\rm bol}$ as a function of $\alpha_{\rm OX}$ is shown in Figure 5.19. The data points are color coded by their phases (from A to E, see Figure 5.16). The right y-axis converts $L_{\rm bol}$ to the Eddington ratio $\lambda_{\rm Edd} \equiv L_{\rm bol}/L_{\rm Edd}$. For pure hydrogen, a $M_{\rm BH}$ of $10^{7.03}\,M_\odot$ (§5.3) implies an Eddington luminosity of $L_{\rm Edd} \approx 10^{45.13}\,{\rm erg\,s^{-1}}$. We further discuss this figure in §5.5. The maximum luminosity was reached at $\delta t = 253$ days, with $L_{\rm bol} = (7.94 \pm 0.66) \times 10^{43}\,{\rm erg\,s^{-1}}$ and $\lambda_{\rm Edd} = 6.0^{+10.4}_{-3.8}\%$. As a cautionary note, the relatively low value of $\lambda_{\rm Edd}$ ($< 16\%$) does not necessarily imply that the accretion is in the sub-Eddington regime, as the TDE broadband SED may peak in the extreme-UV (EUV) band (Dai, McKinney, Roth, et al., 2018; Mummery and Balbus, 2020).

5.5 Discussion

Hereafter we define $M_7 \equiv M_{\rm BH}/(10^7\,M_\odot)$, $\dot{m} \equiv \dot{M}_{\rm acc}/\dot{M}_{\rm Edd}$, $\dot{M}_{\rm Edd} \equiv L_{\rm Edd}/(\eta c^2)$, $\eta_{-1} \equiv \eta/10^{-1}$, where $\dot{M}_{\rm acc}$ is the mass accretion rate and η is the accretion radiative efficiency. With $M_7 \approx 1$, the gravitational radius is $R_{\rm g} = GM_{\rm BH}/c^2 \approx 10^{12.20}\,{\rm cm}$. For a solar type star, the tidal radius is $R_{\rm T} = 10^{13.19}\,{\rm cm} \approx 10R_{\rm g}$, within which the tidal force exceeds the star's self-gravity (Rees, 1988).

Origin of the Soft X-ray Emission

The soft X-ray emission of many TDEs has been attributed to the inner regions of an accretion disk (Saxton et al., 2020). Assuming $R_{\rm in} \approx 6R_{\rm g} \approx 10^{13}$ cm, the maximum effective temperature of an optically thick, geometrically thin accretion disk is $T_{\rm eff} \approx 20(\frac{\dot{m}}{M_7\eta_{-1}})^{1/4}$ eV (Shakura and Sunyaev, 1973). With a maximum black hole spin of $a \to 1$, $R_{\rm in} \to R_{\rm g}$, and $T_{\rm eff} \approx 78(\frac{\dot{m}}{M_7\eta_{-1}})^{1/4}$ eV.

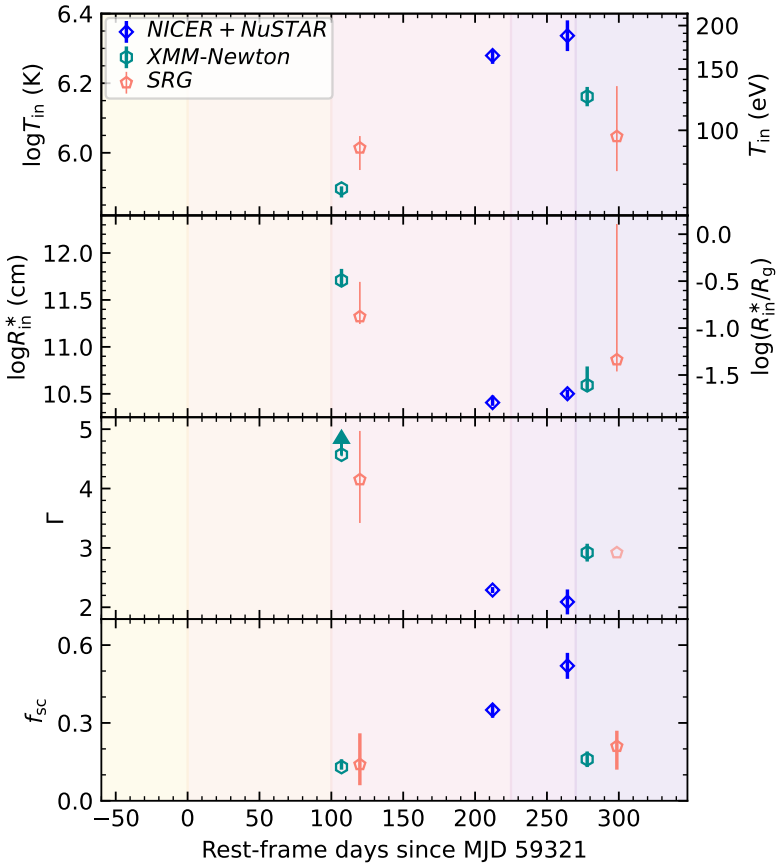

Figure 5.20: Evolution of best-fit X-ray spectral parameters of AT2021ehb.

Figure 5.20 shows the evolution of the best-fit X-ray parameters, including log$T_{\rm in}$ and log$R^*_{\rm in}$ in the `diskbb` component (top two panels), Γ and $f_{\rm sc}$ in the `simpl` component (third and fourth panels). Note that the uncertainty of log($R^*_{\rm in}/R_{\rm g}$) is greater than the uncertainty of $R^*_{\rm in}$ by 0.44 dex (i.e., the uncertainty of $M_{\rm BH}$; §5.3), which is not included in the figure. Data are from model (1a) in Table 5.7, model (2a) in Table 5.8, Table 5.9, and Table 5.10. For parameters in model (2a), we assume an uncertainty of 10%. Fixed values are shown as semi-transparent symbols. Background colors follow the scheme shown in Figure 5.16.

In phase D, when the X-ray spectrum is the hardest, the measured $T_{\rm in}$ is ~ 2.5 times greater than the maximum allowed $T_{\rm eff}$. This high color temperature causes the inferred disk radius $R_{\rm d,in} = R^*_{\rm in}/\sqrt{\cos i}$ to be much less than $R_{\rm g}$ throughout the evolution. The projection factor $\sqrt{\cos i}$ should not be much less than unity, since for a nearly edge-on viewing angle, the X-rays from the inner disk will be obscured by the gas at larger radii. The relativistic disk reflection model (2c) also suggests $\sqrt{\cos i} = 0.85^{+0.06}_{-0.07}$. We note that disk radii much less than $R_{\rm g}$ have also been inferred in a few other X-ray bright TDEs (see, e.g., Fig. 8 of Gezari 2021).

This discrepancy may be due to Compton scattering (Shimura and Takahara, 1995), which makes the measured temperature greater than the effective inner disk temperature by a factor of f_c (Davis and El-Abd, 2019), i.e., $T_{\rm in} = f_c T_{\rm eff}$. The physical reason is that, as the X-ray photons propagate in the vertical direction away from the disk mid-plane, the color temperature is determined by the thermalization depth (corresponding to the last absorption), which could be located at a high scattering optical depth $\tau \gg 1$ — this causes $T_{\rm in}$ to be higher than $T_{\rm eff}$ by a factor of $\sim \tau^{1/4}$. As a result of ongoing fallback, the vertical structure of the TDE disk (see Bonnerot, Lu, and Hopkins, 2021) is likely substantially different from the standard thin disk as studied by Davis and El-Abd (2019, who concluded $f_{\rm c} \lesssim 2$), so the color correction factor may be different. More detailed radiative transport calculations in the TDE context are needed to provide a reliable $f_{\rm c}$ based on first principles.

Another possible reason for the seemingly small disk radii is that a scattering dominated, Compton-thick gas layer can suppress the X-ray flux without causing any significant change to the spectral shape. For a spatially uniform layer, the transmitted flux is exponentially suppressed for a large scattering optical depth $\gg 1$. A more likely configuration is that the layer is like an obscuring wall with small holes where a fraction of the source X-rays can get through, and the rest of the area contributes negligibly to the observed flux. In this scenario, the inferred disk radius is reduced by a factor of the square root of the transmitted over emitted fluxes.

Implications of the Hard X-ray Emission

Hard X-rays can be generated by Compton up-scattering of soft X-rays from the accretion disk by the hot electrons in the (magnetically dominated) coronal regions above the disk, as is the case in AGNs and XRBs. The physical situation in TDEs is more complicated than in AGNs in that the hard X-rays must make their way out of the complex hydrodynamic structures. An X-ray photon undergoes $\sim \tau^2$ electron

scatterings as it propagates through a gas slab of Thomson optical depth τ. In each scattering, the photon loses a fraction $E_\gamma/m_e c^2$ of its energy (where E_γ is the photon energy) as a result of Compton recoil, and hence the cumulative fractional energy loss is $\sim \tau^2 E_\gamma/m_e c^2$. This means that photons above an energy threshold of $\sim 1\,\mathrm{keV}(\tau/20)^{-2}$ will be Compton down-scattered by the gas.

Our *NuSTAR* observations clearly detected hard X-ray photons up to 30 keV, which requires that the optical depth along the pathways of these photons from the inner disk ($\gtrsim R_\mathrm{g} \sim 10^{12.2}$ cm) to the observer is less than about 4. On the other hand, the UV/optical emission indicates that the reprocessing layer is optically thick up to a radius of the order of $R_\mathrm{bb} \sim 10^{14}$ cm. Therefore, our observations favor a highly non-spherical system — there are viewing angles that have very large optical depths such that most X-ray photons are absorbed (and reprocessed into the UV/optical bands), and there are other viewing angles with scattering optical depth $\tau \lesssim 4$ so that hard X-ray photons can escape.

X-ray Spectral Evolution

Soft to Hard Transition: Corona Formation — The top two panels of Figure 5.20 show that, during the soft → hard transition, AT2021ehb's inferred inner disk radius "moves" inward. We find that the main cause of this behavior is that the inner disk temperature increases with time as the spectrum hardens. The gradual hardening is consistent with a picture where it takes $\sim 10^2$ days to build up the magnetically dominated hot corona region. It is possible that the initially weak magnetic fields in the bound debris are amplified by differential rotation of the disk and the magnetorotational instability (Balbus and Hawley, 1991; Miller and Stone, 2000).

Hard to Soft Transition: Thermal-viscous Instability? — The rapid X-ray flux drop (D→E) is likely due to a state transition in the innermost regions of the accretion disk. Under the standard α-viscosity prescription where the viscous stress is proportional to the total (radiation + gas) pressure (Shakura and Sunyaev, 1973), the disk undergoes a thermal-viscous instability as the accretion rate drops from super- to sub-Eddington regimes (Lightman and Eardley, 1974; Shakura and Sunyaev, 1976). This instability causes the disk material to suddenly transition from radiation pressure-dominated to gas pressure-dominated state on a sound-crossing timescale, and the consequence is that the disk becomes much thinner and hence the accretion rate drops. Shen and Matzner, 2014 considered the thermal-viscous

instability in the TDE context but concluded that the instability should occur within a few months since the disruption and the accretion rate drops by several orders of magnitude — these, taken at face value, are inconsistent with our observations. More detailed work on the disk evolution is needed to draw a firm conclusion. Here, we provide two arguments for the disk state transition explanation.

First, TDEs with relativistic jets (e.g., Bloom et al., 2011; Burrows, Kennea, et al., 2011; Cenko, Krimm, et al., 2012; Pasham, Cenko, Levan, et al., 2015) also show a sharp drop in X-ray luminosity 200 to 300 days (in the rest frame) after the discovery and that has been interpreted as the thick-to-thin transition of the inner disk (Tchekhovskoy, Metzger, et al., 2014). Second, from the mass fallback rate $\dot{M}_{\rm fb} \simeq M_*/3P_{\rm min}(t/P_{\rm min})^{-5/3}$ (M_* being the stellar mass and $P_{\rm min}$ being the minimum period of the fallback material), one can estimate the time $t_{\rm Edd}$ at which the fallback rate drops below the Eddington accretion rate of $\sim 10L_{\rm Edd}/c^2$, and the result is (Lu and Kumar, 2018)

$$t_{\rm Edd} \simeq 309\,{\rm d}\,M_{\rm h,7}^{-2/5}\left(\frac{M_*}{M_\odot}\right)^{(1+3q)/5}, \tag{5.7}$$

where we have taken the normal mass-radius relation of main sequence stars $R_* \simeq R_\odot(M_*/M_\odot)^q$ ($q = 0.8$ below one solar mass stars and $q = 0.57$ above one solar mass stars). We expect the inner disk to collapse into a thin state on the timescale of $t_{\rm Edd}$, under the condition that an order-unity fraction of the fallback rate directly reaches near the innermost regions of the disk. We note that the condition is satisfied for a $\approx 10^7 M_\odot$ MBH since the tidal radius is only $\approx 10R_{\rm g}$ for a solar-type star.

If the rapid X-ray flux drop (D→E) is indeed caused by a disk state transition, then after the transition, the disk mass will accumulate over time due to ongoing fallback. This causes the accretion rate to increase, and eventually the disk briefly goes back to a thick state (with a very short viscous time) followed by another transition to the thin state. This is qualitatively consistent with the second rapid X-ray flux decline at $\delta t \approx 325$ days (E1→E2 in Figure 5.16).

Unusual UV/optical Behavior

Featureless Optical Spectrum — As shown in §5.4, AT2021ehb's optical spectroscopic properties are dissimilar to the majority of previously known TDEs (i.e., H-rich, He-rich, N-rich, Fe-rich; Leloudas, Dai, et al. 2019; van Velzen, Gezari, Hammerstein, et al. 2021; Wevers, Pasham, van Velzen, Leloudas, et al. 2019). It is most similar to a few recently reported TDEs with blue and featureless spectra

(Brightman, Ward, et al., 2021; Hammerstein, van Velzen, et al., 2023). Hammerstein, van Velzen, et al. (2023) found that compared with TDEs that develop broad emission lines, the UV/optical emission of four featureless events have larger peak $L_{\rm bb}$, peak $T_{\rm bb}$, and peak $R_{\rm bb}$.

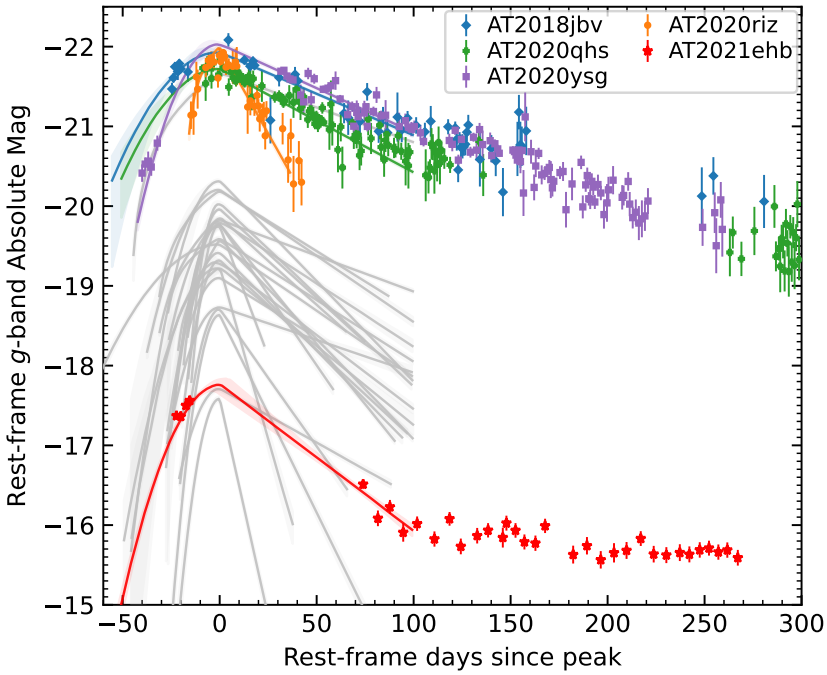

Figure 5.21: Rest-frame g-band light curve of AT2021ehb compared with that of the 30 TDEs presented by Hammerstein, van Velzen, et al. (2023).

Figure 5.21 compares the rest-frame g-band light curve of AT2021ehb with 30 TDEs from phase-I of ZTF (Hammerstein, van Velzen, et al., 2023). Solid lines are the results of fitting the multi-band light curves ($\delta t < 100$ days) with a Gaussian rise + exponential decay model (see Section 5.1 of van Velzen, Gezari, Hammerstein, et al. 2021). We highlight the TDEs lacking line features by plotting the data as colored symbols. Here we have chosen an observing band with good temporal sampling, and converted the observations in this band into $\nu_0 = 6.3 \times 10^{14}$ Hz by performing a color correction.

Our study suggests that not all featureless TDEs are overluminous. In fact, the peak g-band magnitude ($M_{g,\rm peak}$) and peak $L_{\rm bb}$ of AT2021ehb are faint compared with other optically selected TDEs (Figure 5.6, Figure 5.21). It is unclear whether $M_{g,\rm peak}$ of the TDE-featureless class forms a continuous or bimodal distribution between -17 and -22. This question will be addressed in a forthcoming publication (Yao et

al. in preparation). A detailed analysis of Hubble Space Telescope UV spectroscopy (Hammerstein et al. in preparation) will be essential to reveal if AT2021ehb exhibits any spectral lines in the UV.

Origin of the NUV/optical Emission — Here we discuss possible origins of AT2021ehb's NUV/optical emission: stream self-crossing shock, reprocessing, and thermal emission from disk accretion.

In the self-crossing shock model, since the radius of the self-crossing shock is determined by the amount of general relativistic apsidal precession as given by the pericenter of the initial stellar orbit (Dai, McKinney, and Miller, 2015), we expect the power of the self-crossing shock to track the fallback rate and decay with time as $\sim t^{-5/3}$. This is inconsistent with the flat light curve observed in AT2021ehb in the UV/optical bands (phase C–E), unless there is an additional mechanism that modulates the radiative efficiency of the self-crossing shock such that it roughly cancels the effects of the dropping shock dissipation power. Therefore, the energy dissipated by the stream-stream collision cannot be the primary source of emission during the plateau phase, although it may contribute to the early-time UV/optical emission.

In the reprocessing model, the nature of the reprocessing layer could originate from either a disk wind (Strubbe and Quataert, 2009; Miller, 2015; Dai, McKinney, Roth, et al., 2018; Parkinson et al., 2022; Thomsen, Kwan, et al., 2022) or an outflow from the self-crossing shock (Jiang, Guillochon, and Loeb, 2016; Lu and Bonnerot, 2020). The outflow scenario is favored with two reasons. First, a radiation pressure-driven disk wind originates from the innermost regions of the disk and the wind density is geometrically diluted as it propagates to a distance of the order $R_{\rm bb} \sim 10^{14}$ cm, whereas the outflow from the self-crossing shock is expected to be much denser near the self-crossing point and is hence more capable of reprocessing the hard emission from the disk (Bonnerot, Lu, and Hopkins, 2021). Second, as the accretion flow goes from super-Eddington to sub-Eddington, one may expect the reduction in radiation pressure to reduce the strength of the wind outflows. The fact that the UV/optical luminosity only slightly decreases from phase D to phase E suggests that the reprocessing layer is not sensitive to the innermost accretion flow.

Finally, if the UV/optical emission is powered by disk accretion, then the outer disk radius must be located at $\gtrsim 10R_{\rm T} \approx 100R_{\rm g}$. Recent simulations show that it is possible that a small fraction of the bound debris circularizes at $\sim 10R_{\rm T}$ (Bonnerot, Lu, and Hopkins, 2021), but the accretion power at such large radii may be too low

to produce the observed UV/optical emission, since the outermost regions of the disk is expected to be geometrically thin (due to efficient radiative cooling) with a very long viscous time. More detailed disk evolution modeling is needed to evaluate this possibility.

To summarize, we infer that the early-time UV/optical light may be thermal radiation emitted at the photosphere of a stream-stream collision shock. The late-time UV/optical emission likely comes from reprocessing by the outflow launched from the self-crossing shock, although thermal emission from the outer regions of an accretion flow is not ruled out.

Comparison to Other Accreting Black Holes

In stellar-mass black hole XRB outbursts, some objects are observed to transition between a soft disk-dominated state (SDS) and a hard Comptonized state (HCS). In the SDS of XRBs, the inner radius ($R_{\rm in,\,d}$) of an optically thick, geometrically thin disk stays around the ISCO of $R_{\rm ISCO} \sim$ a few $\times R_{\rm g}$. When the outbursts transition to the HCS, $\dot{M}_{\rm acc}$ decreases, $R_{\rm in,\,d}$ progressively moves outwards to $\sim$ few $\times 100 R_{\rm g}$, leaving a radiatively inefficient, advection-dominated accretion flow (Yuan, Cui, and Narayan, 2005; Yuan and Narayan, 2014). At the same time, a region of hot corona is formed close to the BH (Done, Gierliński, and Kubota, 2007). For MBH accretors, Seyferts have been proposed as the high-$M_{\rm BH}$ analogs of XRBs in the SDS, whereas low-luminosity AGNs and low-ionization nuclear emission-line regions are considered similar to XRBs in the HCS (Falcke, Körding, and Markoff, 2004).

We have proposed that in phases B–D, the accretion flow of AT2021ehb is in a radiation-trapped, super-Eddington regime (see, e.g., Fig. 2 of Narayan and Quataert 2005), which is different from the typical sub-Eddington X-ray states observed in AGNs and XRBs. Such a difference is further corroborated by two properties. First, on the hardness–intensity diagram (HID; see Figure 5.22), the evolution of AT2021ehb is neither similar to the "turtlehead" pattern observed in XRBs (Fender, Belloni, and Gallo, 2004; Muñoz-Darias, Coriat, et al., 2013; Tetarenko, Sivakoff, Heinke, et al., 2016), nor similar to the "brighter when softer" trend observed in X-ray bright AGNs (Auchettl, Ramirez-Ruiz, and Guillochon, 2018). On the $L_{\rm bol}$–$\alpha_{\rm OX}$ diagram (Figure 5.19), its evolution is also different from that observed in CLAGNs (Ruan et al., 2019). Second, in the canonical hard state (i.e. sub-Eddington accretion rates), there is a correlation among radio luminosity, X-ray luminosity, and $M_{\rm BH}$,

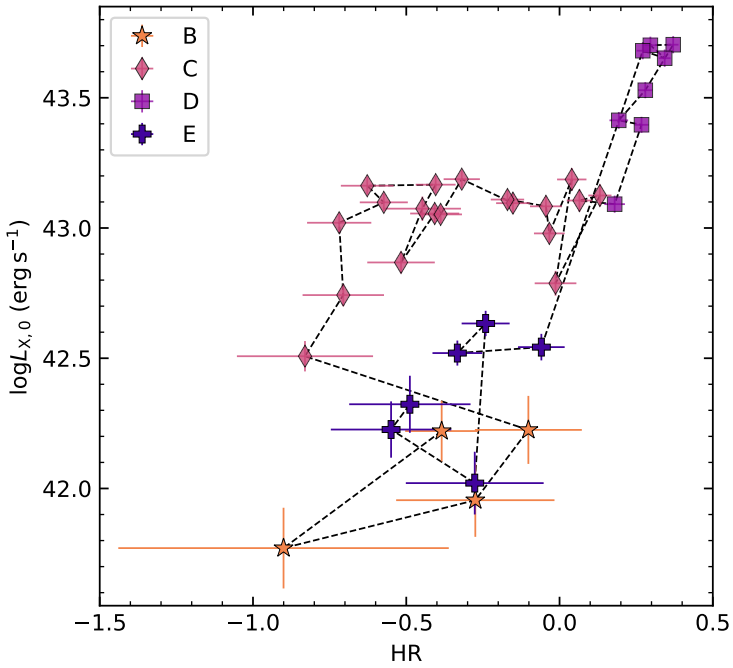

Figure 5.22: AT2021ehb's Galactic extinction-corrected 0.3–10 keV X-ray luminosity ($L_{X,0}$) as a function of hardness ratio for *Swift*/XRT detections only.

which applies to both XRBs and hard-state AGN (Merloni, Heinz, and di Matteo, 2003; Falcke, Körding, and Markoff, 2004). A recent fit to this "fundamental plane of black hole activity" was provided by Gültekin, King, et al. (2019):

$$(1.09 \pm 0.10)R = (\log M_7 - 1) - (0.55 \pm 0.22) - (-0.59^{+0.16}_{-0.15})X, \tag{5.8}$$

where $R \equiv \log[L_{5\,\mathrm{GHz}}/(10^{38}\,\mathrm{erg\,s^{-1}})]$ and $X \equiv \log[L_{2\text{-}10\,\mathrm{keV}}/(10^{40}\,\mathrm{erg\,s^{-1}})]$. In the hard state of AT2021ehb, the 2–10 keV luminosity in the *Swift*/XRT 's6' spectrum gives $X = 2.96 \pm 0.02$. Using Eq. (5.8), the expected 5 GHz radio luminosity on the fundamental plane is $\log[L_{5\,\mathrm{GHz}}/(\mathrm{erg\,s^{-1}})] = R + 38 = 38.21 \pm 0.59$. The uncertainty of R is calculated from the distribution of 10^5 MC trials. Using our radio limit at $\delta t = 228$ days (Table 5.4) and assuming a flat radio spectrum of $f_\nu \propto \nu^0$, we find a 5 GHz equivalent radio upper limit of $\log[L_{5\,\mathrm{GHz}}/(\mathrm{erg\,s^{-1}})] < 35.76$. According to Gültekin, King, et al. (2019), the scatter on the fundamental plane correlation is a factor of ~ 7.6 in the $L_{5\,\mathrm{GHz}}$ direction (or ~ 10 in the M_{BH} direction), which is not enough to solve the discrepancy. This again argues that AT2021ehb is not in a canonical hard state where we would expect a radio jet to be launched.

The radio behavior of BH binaries at the Eddington accretion rates might be more relevant to AT2021ehb (at least in phases B–D). A few XRBs get above the Eddington

limit for brief periods, when they are seen to undergo a sequence of bright radio flares for a short period of time. Examples include the 2015 outburst of V404 Cygni (Tetarenko, Sivakoff, Miller-Jones, Rosolowsky, et al., 2017; Tetarenko, Sivakoff, Miller-Jones, Bremer, et al., 2019) and the ultraluminous X-ray source in M31 (Middleton et al., 2013). In AT2021ehb, the slow cadence of our radio follow-up observations does not allow us to rule out the existence of such radio flares, which last for hours to weeks, not months.

Finally, we note that the evolution of the X-ray properties of AT2021ehb are different from a few other TDEs. For example, Wevers, Pasham, van Velzen, Miller-Jones, et al. (2021) constructed the $\log\lambda_{\rm Edd}$–$\alpha_{\rm OX}$ diagram for AT2018fyk, finding that the 2 keV (corona) emission is stronger when $\lambda_{\rm Edd}$ is lower. Figure 5.19 shows that this is clearly not the case for AT2021ehb. Separately, Hinkle et al. (2021) studied the evolution of AT2019azh on the canonical HID, showing that when the X-ray luminosity is higher, the X-ray spectrum is softer. Figure 5.22 shows that AT2021ehb does not follow this trend either. It remains to be seen whether AT2021ehb is peculiar among the sample of optically selected TDEs with significant X-ray spectral evolution. To this end, constructing a systematically selected sample and analyzing the multi-wavelength data in a homogeneous fashion is the key.

5.6 Conclusion

We have presented an extensive multi-wavelength study of the TDE AT2021ehb. Its peak 0.3–10 keV flux of $\sim$ 1 mCrab is brighter than any other non-jetted TDE in the literature, allowing us to obtain a series of high-quality X-ray spectra, including the first hard X-ray spectrum of a non-jetted TDE up to 30 keV. The detection of hard X-ray photons favors a highly aspherical geometry (§5.5), and detailed modeling of the *NICER* +*NuSTAR* spectrum shows evidence of relativistic disk reflection (§5.4).

The emission from the self-crossing shock itself might contribute to the early-time UV/optical emission, while the post-peak (phase C–E) emission is either dominated by reprocessing of X-ray photons by the outflow launched from the shock, or by thermal emission in the outer regions of an accretion flow. More detailed hydrodynamic and radiative transfer calculations (e.g., Roth, Kasen, et al., 2016) are needed to test if such scenarios can reproduce the observed UV/optical plateau and the featureless optical spectra.

We observed a soft $\rightarrow$ hard $\rightarrow$ soft spectral transition in the X-ray. The initial soft-to-hard transition happened gradually over $\sim$ 170 days. A possible explanation

is that magnetic fields grow with time due to differential rotation, resulting in the formation of a magnetically dominated hot corona. The bolometric luminosity of AT2021ehb is the highest when the X-ray spectrum is the hardest — a property that is different from XRBs, X-ray bright AGNs, and many other TDEs (§5.5). The latter hard-to-soft transition happened drastically within 3 days at $\delta t \approx 272$ days, and might be due to thermal–viscous instability in the inner disk. Such an instability typically occurs when $L_{\rm bol} \sim 0.3 L_{\rm Edd}$ (Tchekhovskoy, Metzger, et al., 2014). This requires that most of the luminosity of AT2021ehb is emitted in the EUV band that is not observed.

Systems similar to AT2021ehb are excellent targets for X-ray telescopes to study the real-time formation of the accretion disk and corona around MBHs. The detection of relativistic disk reflection features demonstrates the possibility of constraining the spin of normally quiescent MBHs via reflection spectroscopy — an opportunity enabled by combining modern time-domain surveys with systematic multi-wavelength follow-up observations.

Chapter 6

THE ON-AXIS RELATIVISTIC TIDAL DISRUPTION EVENT AT2022CMC: X-RAY OBSERVATIONS AND BROADBAND SPECTRAL MODELING

Yuhan Yao[1], Wenbin Lu[2], Fiona Harrison[1], S. R. Kulkarni[1], Suvi Gezari[3,4], Muryel Guolo[4], S. Bradley Cenko[5,6], Anna Y. Q. Ho[7]

[1] Cahill Center for Astrophysics, California Institute of Technology, MC 249-17, 1200 E California Boulevard, Pasadena, CA 91125, USA
[2] Department of Astronomy, University of California, Berkeley, CA 94720-3411, USA
[3] Space Telescope Science Institute, 3700 San Martin Drive, Baltimore, MD 21218, USA
[4] Department of Physics and Astronomy, Johns Hopkins University, Baltimore, MD 21218
[5] Astrophysics Science Division, NASA Goddard Space Flight Center, Greenbelt, MD 20771, USA
[6] Joint Space-Science Institute, University of Maryland, College Park, MD 20742, USA
[7] Department of Astronomy, Cornell University, Ithaca, NY 14853, USA

Abstract

AT2022cmc was recently reported as the first on-axis relativistic tidal disruption event (RTDE) discovered in the last decade, and the fourth on-axis RTDE known so far. In this work, we present *NuSTAR* high-energy X-ray (3–30 keV) observations of AT2022cmc, as well as lower energy X-ray (0.3–6 keV) observations obtained by *NICER*, *Swift*, and *XMM-Newton*. Our analysis reveals that the broadband X-ray spectra can be well described by a broken power-law with $f_\nu \propto \nu^{-0.5}$ ($f_\nu \propto \nu^{-1}$) below (above) the rest-frame break energy of $E_{\rm bk} \sim 10$ keV at observer-frame $t_{\rm obs} = 7.8$ and 17.6 days since discovery. At $t_{\rm obs} = 36.2$ days, the X-ray spectrum is consistent with either a single power-law of $f_\nu \propto \nu^{-0.8}$ or a broken power-law with spectral slopes similar to the first two epochs. By modeling the spectral energy distribution evolution from radio to hard X-ray across the three *NuSTAR* observing epochs, we inferred that the sub-millimeter/radio synchrotron emission originates from a forward shock, the UV/optical light comes from a thermal envelope, and the X-ray emission can be modeled with synchrotron radiation powered by internal energy dissipation within a Poynting flux dominated jet. Our interpretation differs from the matter dominated jet model proposed by Pasham, Lucchini, et al. (2023) for this source, highlighting the similarities between the jets observed in gamma-ray bursts and on-axis RTDEs.

6.1 Introduction

An unlucky star coming too close to a massive black hole gets disrupted by the tidal forces and the subsequent accretion gives rise to a luminous transient. A fraction of such tidal disruption events (TDEs) launch collimated relativistic jets (hereafter relativistic TDEs, or RTDEs; see De Colle and Lu 2020 for a review). So far, only four RTDEs with on-axis jets have been found, including three objects discovered by the hard X-ray burst alert telescope (BAT) on board *Swift* more than a decade ago, Sw J1644+57 (Bloom et al., 2011; Burrows, Kennea, et al., 2011; Levan, Tanvir, et al., 2011; Zauderer, Berger, Soderberg, et al., 2011), Sw J2058+05 (Cenko, Krimm, et al., 2012; Pasham, Cenko, Levan, et al., 2015), Sw J1112-82 (Brown, Levan, Stanway, Tanvir, et al., 2015; Brown, Levan, Stanway, Krühler, et al., 2017), and AT2022cmc discovered by the Zwicky Transient Facility (ZTF) in 2022 (Andreoni, Coughlin, Perley, et al., 2022; Pasham, Lucchini, et al., 2023). These objects exhibit rapidly variable, super-Eddington early-time X-ray emission ($> 10^{47}\,\mathrm{erg\,s^{-1}}$) with a power-law secular decline, as well as extremely bright and long-lived radio afterglow emission ($> 10^{40}\,\mathrm{erg\,s^{-1}}$).

RTDEs form a rare class of transients with limited observational data. They are similar to blazars — active galactic nuclei with powerful jets beamed towards the observer. However, the broadband spectral energy distribution (SED) of RTDEs do not follow the ensemble properties of blazars in the sense that the ratio of X-ray to radio luminosity is extremely high (Cenko, Krimm, et al., 2012). In addition, RTDEs might be similar to gamma-ray busts (GRBs, see Piran 2004 for a review), as both are triggered by super/hyper-Eddington accretion onto black holes (BHs) that produce jets. In the standard GRB fireball model, the long-lasting afterglow emission comes from external shocks propagating into the ambient medium, whereas the seconds-long prompt γ-ray emission comes from energy dissipation (by internal shocks or magnetic reconnection) in a region closer to the BH (Zhang, 2018).

Among the *Swift* RTDEs, Sw J1644+57 is the most well observed event. Evolution of its millimeter (mm) and radio SED over a decade can be well described by synchrotron emission from an outgoing forward shock (Zauderer, Berger, Soderberg, et al., 2011; Berger et al., 2012; Zauderer, Berger, Margutti, et al., 2013; Mimica et al., 2015; Eftekhari, Berger, Zauderer, et al., 2018; Cendes, Eftekhari, et al., 2021), indeed similar to GRB afterglows. As the blast wave travels through the the circumnuclear medium (CNM), the shock is decelerated and the CNM density decreases, resulting in the radio SED moving to lower frequencies over time.

Unlike the better-understood radio SED, the site and radiation mechanism(s) of the early-time ($\lesssim 1$ yr) bright X-ray emission in RTDEs remains actively debated. Burrows, Kennea, et al. (2011) showed that the X-ray spectrum of Sw J1644+57 is consistent with synchrotron emission of a particle-starved magnetically-dominated jet, whereas Bloom et al. (2011) found acceptable fits with synchrotron self-Compton (SSC) and external inverse Compton (EIC) models. Reis et al. (2012) detected a 5 mHz quasi-periodic oscillation in X-ray observations of Sw J1644+57, suggesting that the jet production is modulated by accretion variability near the event horizon. Crumley et al. (2016) studied a wide range of emission mechanisms and concluded that the X-ray emission can be produced by either synchrotron emission or EIC scattering off optical photons from the thermal envelope. Kara, Miller, et al. (2016) found a blueshifted ($\sim$0.1–0.2c) Fe Kα line and the associated reverberation lags in the *XMM-Newton* data. Different interpretations for the reflector have been proposed, including a radiation pressure driven sub-relativistic outflow close to the black hole ($\sim 30R_{\rm g}$ where $R_{\rm g}$ is the gravitational radius; Kara, Miller, et al. 2016; Thomsen, Dai, et al. 2022), and a gas layer accelerated by the interaction between the jet X-rays and a thermal envelope ($\sim 300R_{\rm g}$; Lu, Krolik, et al. 2017).

AT2022cmc was a fast optical transient discovered by the ZTF on 2022 February 11 10:42:40 (Andreoni, 2022). Shortly afterwards, it was detected by follow up observations in the radio (Perley, 2022) and X-ray (Pasham, Gendreau, et al., 2022) bands. An optical spectrum obtained by ESO's Very Large Telescope reveals host galaxy lines at the redshift of $z = 1.193$ (Tanvir et al., 2022). At the cosmological distance, its X-ray and radio luminosities are comparable to Sw J1644+47 at similar phases (Yao, Pasham, and Gendreau, 2022). Further multi-wavelength follow-up observations reveal the remarkable similarities between AT2022cmc and Sw J1644+57, suggesting that AT2022cmc is indeed a RTDE (Andreoni, Coughlin, Perley, et al., 2022; Pasham, Lucchini, et al., 2023; Rhodes et al., 2023).

As the only RTDE discovered in the last decade, AT2022cmc offers a great opportunity to address several key questions related to RTDEs' X-ray emission, such as the jet composition, the particle acceleration and energy dissipation processes, and the emission mechanisms. By computing the X-ray power density spectrum, Pasham, Lucchini, et al. (2023) demonstrated that the rest-frame systematic X-ray variability timescale is $t_{\rm var,min} \lesssim 10^3/(1+1.193)$ s. By requiring that $t_{\rm var,min}$ exceed the light-crossing time of the Schwarzschild radius of the BH, an upper limit of the BH mass can be derived as $M_{\rm BH} \lesssim 5 \times 10^7\, M_\odot$.

Pasham, Lucchini, et al. (2023) fitted the radio and soft X-ray SEDs of AT2022cmc with SSC/EIC models, concluding that the relativistic jet exhibits a high ratio of electron-to-magnetic-field energy densities. In this work, we present *NuSTAR* hard X-ray observations, independently analyze the soft X-ray and UV data, and reexamine the broadband SED evolution across nine orders of magnitude in frequency. We follow the physical picture outlined in Andreoni, Coughlin, Perley, et al. (2022) and propose that the observed broken power-law X-ray spectrum can be explained with a synchrotron origin.

The paper is organized as follows. We describe the observations and data reduction in §6.2. In §6.3, we first outline the rationales of treating the broadband radiation with three separate emission components, and then perform model fitting on the sub-mm/radio, UV/optical, and X-ray SEDs. A discussion is given in §6.4.

Hereafter we use $t_{\rm obs}$ ($t_{\rm rest}$) to denote observer-frame (rest-frame) time relative to the first ZTF detection. We adopt a redshift of $z = 1.1933$ (Andreoni, Coughlin, Perley, et al., 2022), a standard ΛCDM cosmology with $\Omega_{\rm M} = 0.3$, $\Omega_\Lambda = 0.7$, and $H_0 = 70\,{\rm km\,s^{-1}\,Mpc^{-1}}$. Throughout the paper, we use UT time and the usual notation $Q_n = Q/10^n$. Uncertainties are reported at the 68% confidence intervals, and upper limits are reported at 3σ.

6.2 Observation and Data Analysis

All X-ray observations were processed using `HEASoft` version 6.31.1. X-ray spectral fitting was performed with `xspec` (v12.13, Arnaud 1996). We used the `vern` cross sections (Verner et al., 1996) and the Anders and Grevesse (1989) abundances.

NuSTAR

We obtained Nuclear Spectroscopic Telescope ARray (*NuSTAR*; Harrison et al. 2013) observations under a pre-approved Target of Opportunity (ToO) program (PI: Y. Yao; obsID 80701510002) and Director's Discretionary Time (DDT) programs (PI: Y. Yao; obsIDs 90801501002, 90802306004). The three epochs of observations are summarized in Table 6.1 and marked as the vertical orange bands in Figure 6.1. The first two *NuSTAR* observations were conducted jointly with *NICER*, and the last *NuSTAR* observation was conducted jointly with *Swift*/XRT.

To generate the first epoch's spectra for the two photon counting detector modules (FPMA and FPMB), source photons were extracted from a circular region with a radius of $r_{\rm src} = 45''$ centered on the apparent position of the source in both FPMA

Table 6.1: Log of X-ray Observations Used in Joint Spectral Analysis.

Epoch	$t_{\rm obs}$ (d)	$t_{\rm rest}$ (d)	Mission	OBSID	Exp. (ks)	Count Rate [Energy Range] (count s^{-1} [keV])
1	7.8	3.6	*NuSTAR*	80701510002	47.9	0.2167 ± 0.0022 [3–27]
			NICER	4656010102	13.5	1.216 ± 0.010 [0.3–5]
				4656010103	9.6	
2	17.6	8.0	*NuSTAR*	90801501002	44.5	0.0899 ± 0.0015 [3–24]
			NICER	4202560109	5.9	0.287 ± 0.009 [0.3–4]
				5202560101	9.2	
3	36.2	16.5	*NuSTAR*	90802306004	44.6	0.0063 ± 0.0003 [3–17]
			Swift	15023014	12.5	0.0111 ± 0.0010 [0.3–10]

The last column is the mean net count rate within the energy range where the source is above background. For *NuSTAR* observations we show the total count rate in the two optical modules (FPMA and FPMB).

and FPMB. The background was extracted from a $r_{\rm bkg} = 80''$ region located on the same detector. For the second and third epochs, since the source became fainter, we used $r_{\rm src} = 40''$ and $r_{\rm src} = 35''$, respectively.

All spectra were binned with `ftgrouppha` using the optimal binning scheme developed by Kaastra and Bleeker (2016). For the first two *NuSTAR* epochs, we further binned the spectra to have at least 20 counts per bin.

NICER

AT2022cmc was observed by the Neutron Star Interior Composition Explorer (*NICER*; Gendreau et al. 2016) under ToO (PI: D. R. Pasham) and DDT (PI: Y. Yao) programs from 2022 February 16 to 2022 June 11.

First, we ran `nicerl2` to obtain the cleaned and screened event files, and ran `nicerl3-lc` to obtain light curves in the 0.3–1 keV, 1–5 keV, 0.3–5 keV and 13–15 keV bands with a time bin of 30 s. `nicerl3-lc` estimates the background using a space weather model. For good time intervals (GTIs) where more than four focal plane modules (FPMs) were turned off, we scaled the count rate up to an effective area with 52 FPMs. We removed four obsIDs where the background count rate is NaN, and removed time bins where the 13–15 keV count rate is above 0.1 count s^{-1}. AT2022cmc was detected above 3-σ in both 0.3–1 keV and 1–5 keV in 39 obsIDs. For the remaining 30 obsIDs, we computed the 3-σ upper limits.

For each of the 39 obsIDs with significant detections, we ran `nicerl3-spec` to extract one spectrum using the default parameters. Using C-statistics (Cash, 1979),

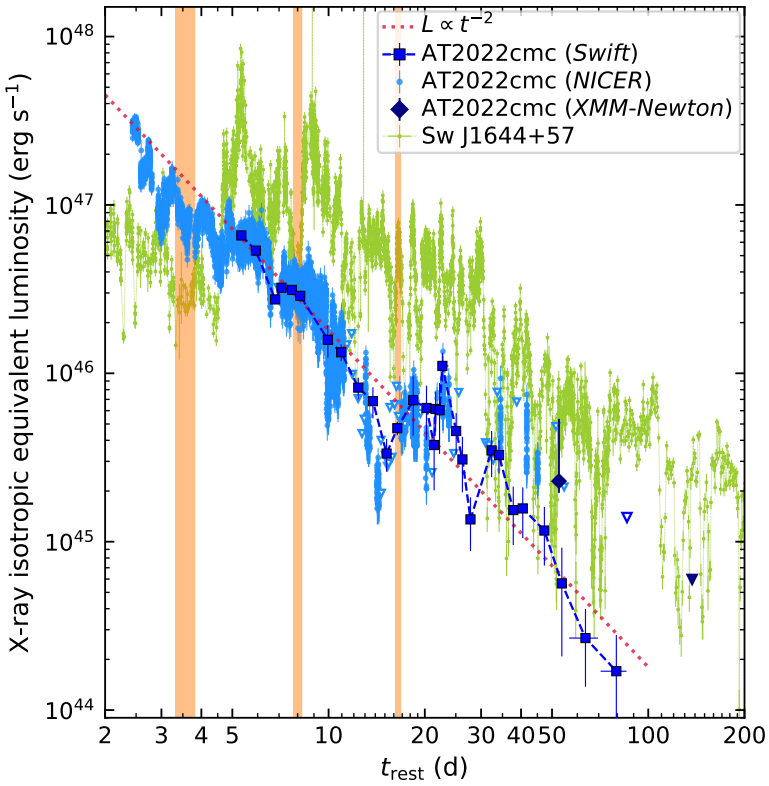

Figure 6.1: X-ray light curve of AT2022cmc and Sw J1644+57 in the observer-frame 0.3–10 keV.

we fitted each spectrum in the 0.22–15 keV energy range with a combination of source and background models. The source model is an absorbed power-law (i.e., `tbabs*ztbabs*zashift*(cglumin*powerlaw)` in `xspec`). The background model includes both X-ray and non-X-ray components[1]. We fixed the Galactic hydrogen-equivalent column density to be $N_{\rm H} = 8.88 \times 10^{19}$ cm^{-2} (HI4PI Collaboration et al., 2016), and the host absorption to be $N_{\rm H,\,host} = 10^{21}$ cm^{-2}, which is the best-fit value found in the joint spectral analysis (see below). When $t_{\rm rest} > 10$ d, the source flux was too faint to provide stringent constraints on both the power-law index and the normalization. Therefore, we further fixed the power-law index $\Gamma = 1.6$. Using the best-fit spectral models, we obtained the conversion factors to convert 0.3–5 keV count rate to 0.3–10 keV flux (in both observer frame and the rest frame). Figure 6.1 shows the resulting *NICER* light curve.

Using observations contemporaneously obtained with the first two *NuSTAR* observations, we also produced two *NICER* spectra to be jointly analyzed with the *NuSTAR*

[1]See `https://heasarc.gsfc.nasa.gov/docs/nicer/analysis_threads/scorpeon-xspec/` for details.

spectra (see below). The obsIDs of the *NICER* data used in this step is shown in Table 6.1. The source and background spectra were created with `nibackgen3C50`. Following the screening criteria suggested by Remillard, Loewenstein, et al. (2022), we removed GTIs with `hbgcut=0.05` and `s0cut=2.0`, and added systematic errors of 1.5% with `grppha`.

***Swift*/XRT**

AT2022cmc was observed by the X-Ray Telescope (XRT; Burrows, Hill, et al. 2005) on board *Swift* following a series of ToO requests (submitted by Y. Yao and D. R. Pasham). All XRT observations were obtained under the photon counting (PC) mode.

We generated the XRT light curve using an automated online tool[2] (Evans, Beardmore, Page, Tyler, et al., 2007; Evans, Beardmore, Page, Osborne, et al., 2009). For data at $t_{\rm rest} < 19$ d, we binned the light curve by obsID. For data at $t_{\rm rest} > 19$ d, we used dynamic binning to ensure a minimum of five counts per bin. Using the same tool, we also created three stacked XRT spectra for data at $t_{\rm rest} < 9$ d, $9 < t_{\rm rest} < 19$ d, and $t_{\rm rest} > 19$ d. We then fitted the three spectra using the same absorbed power-law model as described above in the *NICER* spectral analysis. From the best-fit models, we obtained conversion factors to convert 0.3–10 keV net count rate to 0.3–10 keV flux (in both observer frame and the rest frame). The XRT light curve is shown in Figure 6.1.

To generate an XRT spectrum for obsID 15023014 (to be jointly analyzed with the third *NuSTAR* epoch), we processed the data using `xrtproducts`. We extracted source photons from a circular region with a radius of $r_{\rm src} = 30''$, and background photons from eight background regions with $r_{\rm bkg} = 25''$ evenly spaced at $80''$ from AT2022cmc. The spectrum was first binned with `ftgrouppha` using the optimal binning scheme (Kaastra and Bleeker, 2016), and then further binned to have at least one count per bin.

XMM-Newton

AT2022cmc was observed two times by *XMM-Newton* as part of our GO program (PI: S. Gezari, ObsIDs 0882591301, 0882592101), the first on 2022 June 6 (MJD 59736) for $\sim$ 18 ks, and a second time on 2022 December 9 (MJD 59922) for $\sim$ 21 ks. For the EPIC camera, since the pn instrument has larger effective area than MOS1

[2] `https://www.swift.ac.uk/user_objects`

and MOS2, we only analyze the pn data. The raw data files were then processed using the `epproc` task. Following the *XMM-Newton* data analysis guide, to check for background activity and generate GTIs, we manually inspected the background light curves in the 10–12 keV band. The source was detected in the first epoch, but not in the second one.

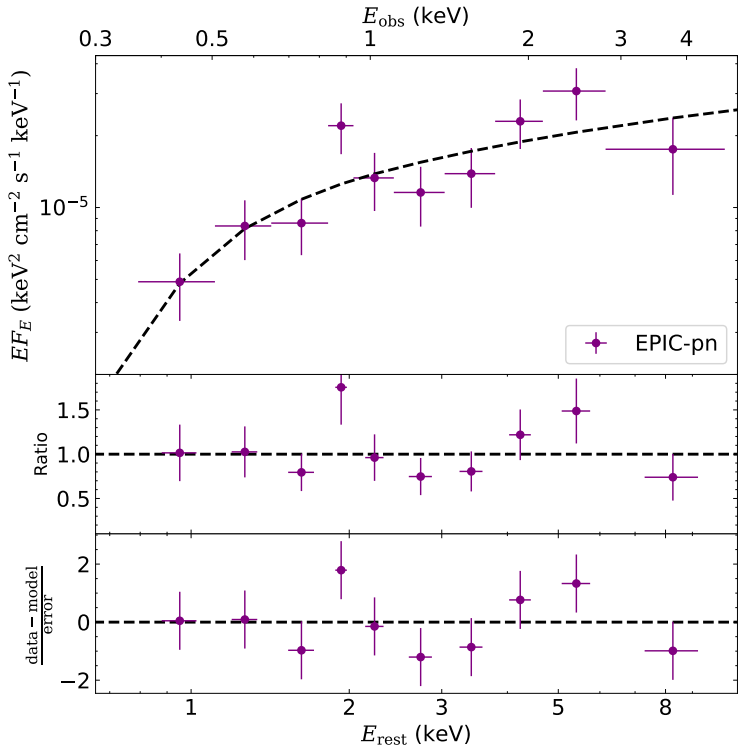

Figure 6.2: The *XMM-Newton* EPIC-pn X-ray spectrum at $t_{\rm rest} \approx 52.6$ d.

For the first epoch, source photons were extracted from a circular region with a radius of 33″ centered on the position of the source. The background was extracted from a 45″ region located on the same detector. The observation data files (ODFs) were reduced using the *XMM-Newton* Standard Analysis Software (SAS; Gabriel et al., 2004). The ARFs and RMF files were created using the `arfgen` and `rmfgen` tasks, respectively. The resulting EPIC-pn spectrum from the first visit has ~ 200 background subtracted counts, at a rate of ~ 0.023 counts s^{-1}, and was binned using the optimal binning criteria (Kaastra and Bleeker, 2016) also ensuring that each bin had at least 1 count.

For the second epoch, we ran `eregionanalyse` task using the same apertures as in the first epoch, and obtained a background-subtracted 3σ upper limit of of ~ 0.006 count s^{-1}.

XMM-Newton EPIC-pn data from the first were fitted with C-statistics, we chose energy ranges where the source spectrum dominates over the background, i.e. 0.35–4.5 keV (observed frame). The data was modeled with an absorbed power-law. The best-fit model parameters are $N_{\rm H,\,host} = 0.26^{+0.27}_{-0.23} \times 10^{22}\,{\rm cm}^{-2}$, $\Gamma = 1.65^{+0.25}_{-0.23}$, and $cstat/dof = 11/8$. In Figure 6.2 we show our *XMM-Newton* EPIC-pn spectrum and best-fitting model. The X-ray luminosity at this first epoch is $L_{\rm X} = 2.29^{+3.07}_{0.34} \times 10^{45}\,{\rm erg\,s}^{-1}$. Assuming the same spectrum we estimate the 3σ upper-limit luminosity of the second epoch to be $L_{\rm X} \leq 5.97 \times 10^{44}\,{\rm erg\,s}^{-1}$.

Joint X-ray Spectral Analysis

Here performed joint spectral analysis between *NuSTAR* and soft X-ray observations (*NICER* or XRT). Data were fitted with χ^2-statistics for the first two epochs, and with C-statistics for the third epoch. Uncertainties of X-ray model parameters are reported at the 90% confidence level. For all models described below, we included a calibration coefficient (`constant`; Madsen et al. 2017) between FPMA, FPMB, and *NICER* (or XRT), with $C_{\rm FPMA}$ fixed at one.

Epoch 1 — We chose energy ranges where the source spectrum dominates over the background. For *NICER* we used 0.3–5.0 keV; For *NuSTAR* FPMA and FPMB we used 3–27 keV. Fitting the data with a single power-law results in a poor fit with a χ^2 over degrees of freedom (*dof*) of $302/206 = 1.47$. Replacing the single power-law with a broken power-law (`bknpower`) gives a good fit. This model assumes that the photon energy distribution takes the form $n(E)dE \propto E^{-\Gamma_1}$ below a break energy $E_{\rm bk}$, and that $n(E)dE \propto E^{-\Gamma_2}$ where $E > E_{\rm bk}$

The best-fit model is presented in the top panel of Figure 6.3. The best-fit parameters are: $C_{\rm FPMB} = 0.99 \pm 0.03$, $C_{NICER} = 1.11 \pm 0.05$, $N_{\rm H,\,host} = 1.03^{+0.11}_{-0.10} \times 10^{21}\,{\rm cm}^{-2}$, $\Gamma_1 = 1.66 \pm 0.02$, $\Gamma_2 = 1.96^{+0.08}_{-0.05}$, $E_{\rm bk} = 11.1^{+2.7}_{-2.3}\,{\rm keV}$, and $\chi^2/dof = 174/204$. The isotropic-equivalent 0.5–50 keV X-ray luminosity is $L_{\rm X} = (1.30 \pm 0.03) \times 10^{47}\,{\rm erg\,s}^{-1}$.

Epoch 2 — We chose energy ranges where the source spectrum dominates over the background. For *NICER* we used 0.3–4.0 keV; For *NuSTAR* FPMA and FPMB we used 3–24 keV. Similar to what was found in the first epoch, a single power-law leaves an unacceptable χ^2/dof of $204/150 = 1.36$, whereas a broken power-law describes the data much better.

The best-fit model is presented in the bottom panel of Figure 6.3. The best-fit model parameters are: $C_{\rm FPMB} = 1.00^{+0.06}_{-0.05}$, $C_{NICER} = 0.86 \pm 0.06$, $N_{\rm H,\,host} = 0.55^{+0.23}_{-0.22} \times$

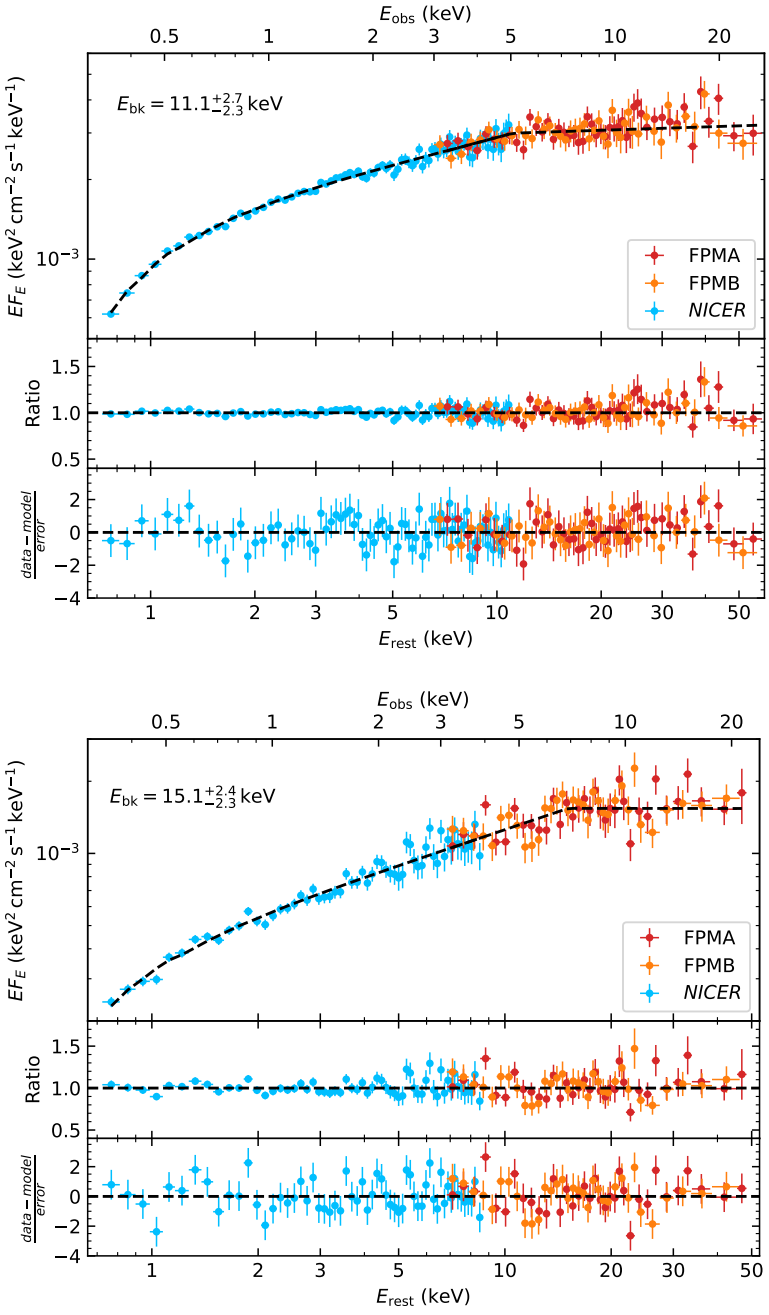

Figure 6.3: The X-ray spectrum of AT2022cmc at $t_{\rm rest} \approx 3.6$ d (top) and 8.0 d (bottom).

$10^{21}\,\mathrm{cm}^{-2}$, $\Gamma_1 = 1.51 \pm 0.04$, $\Gamma_2 = 2.00^{+0.15}_{-0.12}$, $E_{\rm bk} = 15.1^{+2.4}_{-2.3}\,\mathrm{keV}$, and $\chi^2/dof = 146/148$. The isotropic-equivalent 0.5–50 keV X-ray luminosity is $L_{\rm X} = (0.60 \pm 0.02) \times 10^{47}\,\mathrm{erg\,s^{-1}}$.

Epoch 3 — We chose energy ranges where the source spectrum dominates over the background. For XRT we used 0.3–10.0 keV; For *NuSTAR* FPMA and FPMB we used 3–15 keV. Compared with the previous two *NuSTAR* epochs, AT2022cmc has become much fainter at this observing epoch. Both a single power-law and a double power-law give acceptable fits.

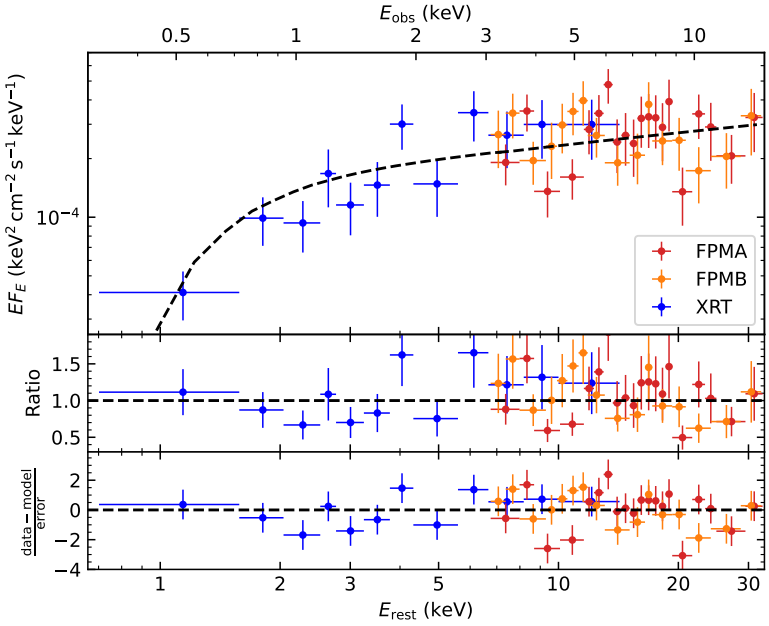

Figure 6.4: The X-ray spectrum of AT2022cmc at $t_{\rm rest} \approx 16.5$ d.

First, we model the X-ray spectrum with a double power-law with $\Gamma_1 = 1.5$ and $\Gamma_2 = 2.0$ (similar to the previous two epochs). The best-fit model parameters are: $C_{\rm FPMB} = 0.92^{+0.15}_{-0.13}$, $C_{\rm XRT} = 0.81^{+0.19}_{-0.25}$, $N_{\rm H,\,host} = 0.26^{+0.37}_{-0.25} \times 10^{21}\,\mathrm{cm}^{-2}$, $E_{\rm bk} = 11.7^{+3.6}_{-6.5}\,\mathrm{keV}$, and $cstat/dof = 140/98$. Next, we model the X-ray spectrum with a single power-law. The best-fit model parameters are: $C_{\rm FPMB} = 0.92^{+0.15}_{-0.13}$, $C_{\rm XRT} = 0.68^{+0.22}_{-0.17}$, $N_{\rm H,\,host} = 0.56^{+0.54}_{-0.36} \times 10^{21}\,\mathrm{cm}^{-2}$, $\Gamma = 1.79^{+0.18}_{-0.17}\,\mathrm{keV}$, and $cstat/dof = 129/98$. Figure 6.4 shows the single power-law fit, which is favored by the fit statistics. The X-ray luminosity at this epoch is $L_{\rm X} = (0.12 \pm 0.01) \times 10^{47}\,\mathrm{erg\,s^{-1}}$.

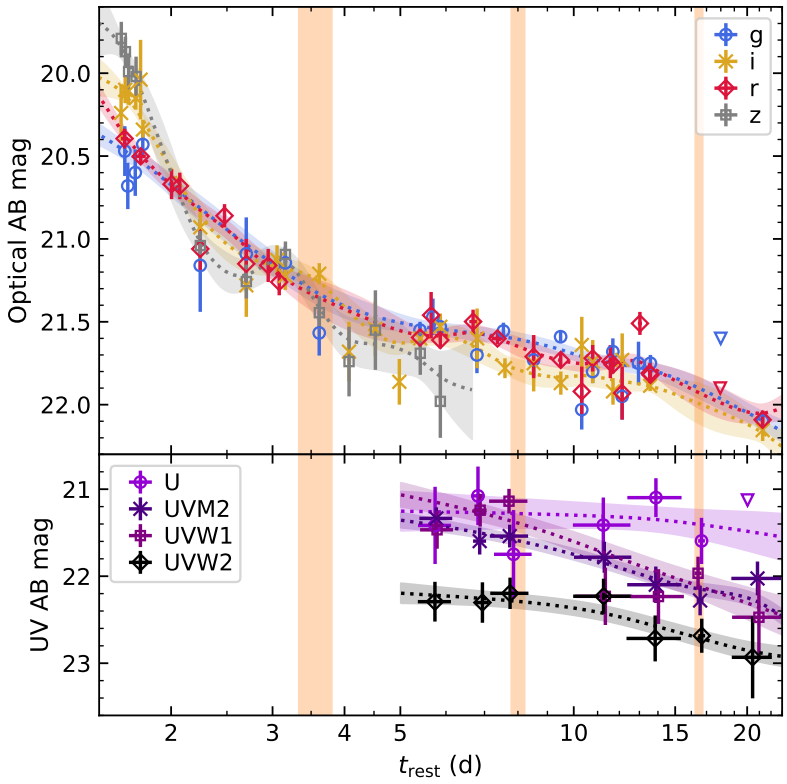

Figure 6.5: Optical and UV photometry of AT2022cmc.

UV and optical

The top panel of Figure 6.5 shows the optical data reported in Andreoni, Coughlin, Perley, et al. (2022, Supplementary table 1). For UV data taken by the Ultra-Violet/Optical Telescope (UVOT; Roming et al. 2005) on board *Swift*, we stacked a few adjacent obsIDs with `uvotimsum` to improve the sensitivity, and performed photometry on the stacked images with `uvotsource`. The bottom panel of Figure 6.5 shows the results.

We note that the UV and optical photometry exhibits short-timescale (~hr–day) wiggles (either due to intrinsic stochastic variability or underestimated systematic uncertainties across multiple instruments). Therefore, to capture the general trend of the photometric evolution, we fit the UV and optical data in each filter with Gaussian process models, following the same procedures described in Yao, Lu, et al. (2022). We then infer the photometry at the *NuSTAR* observing epochs using the best-fit models (shown as the transparent lines in Figure 6.5).

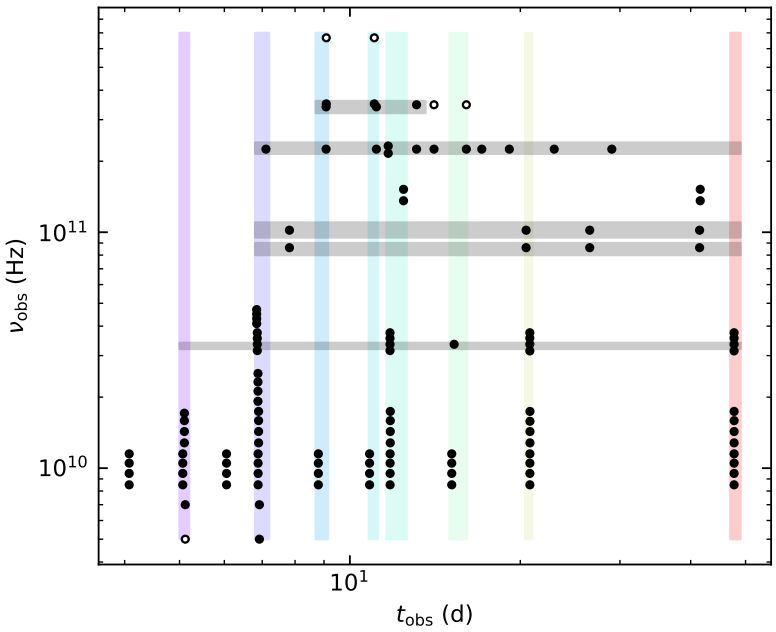

Figure 6.6: Radio/mm observing time and frequency of AT2022cmc.

Radio/sub-mm

In this work, we analyze radio and sub-mm observations of AT2022cmc reported in Andreoni, Coughlin, Perley, et al. (2022). Figure 6.6 shows the time and frequency of the observations. Detections are shown in solid circles and upper limits are shown as hollow circles.

We prepare eight epochs (indicated by the vertical colored bands) of SEDs with good frequency sampling to be analyzed in §6.3. Since the sub-mm observations were much sparser, we fitted the light curves at five frequencies (indicated by the horizontal grey bands) with Gaussian process models to infer the high-frequency flux densities. The resulting SED at the eight epochs are shown in Figure 6.7.

6.3 Broadband SED Modeling

Preliminary Considerations

The broadband SED of AT2022cmc is shown in Figure 6.8. Since Pasham, Lucchini, et al. (2023) is the only previous work that have modeled the radio-to-X-ray SED of AT2022cmc, we briefly summarize their results here.

Pasham, Lucchini, et al. (2023) consider the scenario where the X-ray and radio photons are emitted from the same region at the jet front, whereas the UV/optical emission originates from a quasi-isotropic thermal envelope (modeled with a black-

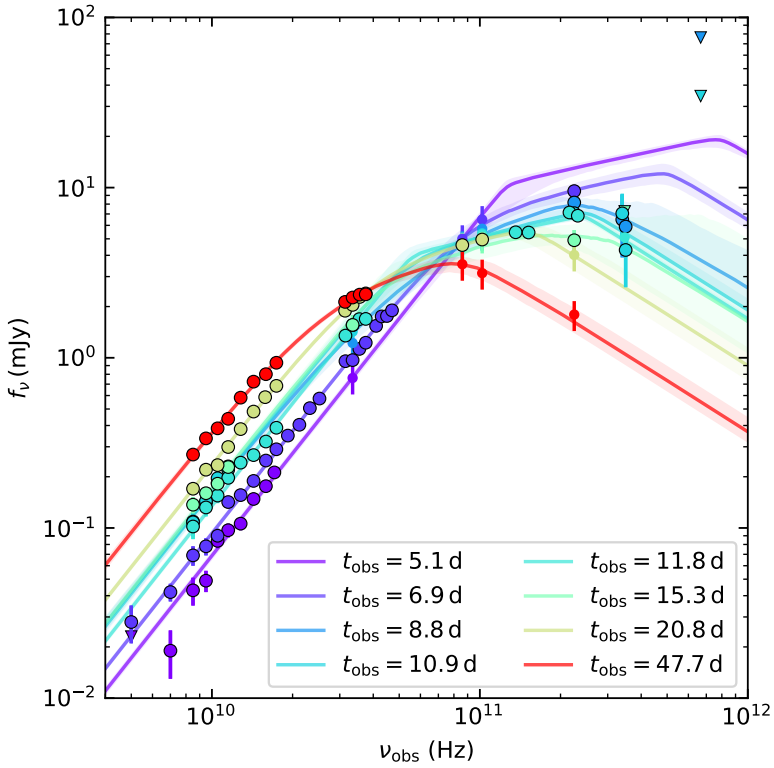

Figure 6.7: Radio SED of AT2022cmc.

body). In their model 1 (synchrotron+SSC), the jet synchrotron photons are inverse Compton scattered by relativistic electrons to produce the X-ray emission; in their model 2 (synchrotron+EIC), seed photons from a thermal envelope outside the jet are inverse Compton scattered to produce the X-ray light. SED fitting was performed at three epochs with good multi-wavelength coverage (t_{obs} = 15–16 d, 25–27 d, and 41–46 d) using the `BHjet` code developed by Lucchini et al. (2022). Pasham, Lucchini, et al. (2023) find that model 1 was favored over model 2.

The upper panel of Figure 6.8 displays the best-fit synchrotron+blackbody+SSC models from Pasham, Lucchini, et al. (2023). Although the 15–16 d model is fitted to data obtained close in time to the second *NuSTAR* epoch (t_{obs} = 17.6 d), it fails to match the observed optical spectral slope or produce the broken power-law shape in the X-ray band. Moreover, both the 25–27 d model and the 41–46 d model significantly under-predict the 30–300 GHz flux, which likely results from the fact that sub-mm data was not included in the SED fitting. Notably, the models are in conflict with the observed 100 GHz light curve of AT2022cmc, which exhibits a slight monotonic decline from t_{obs} = 16 d to 60 d (see Andreoni, Coughlin, Perley,

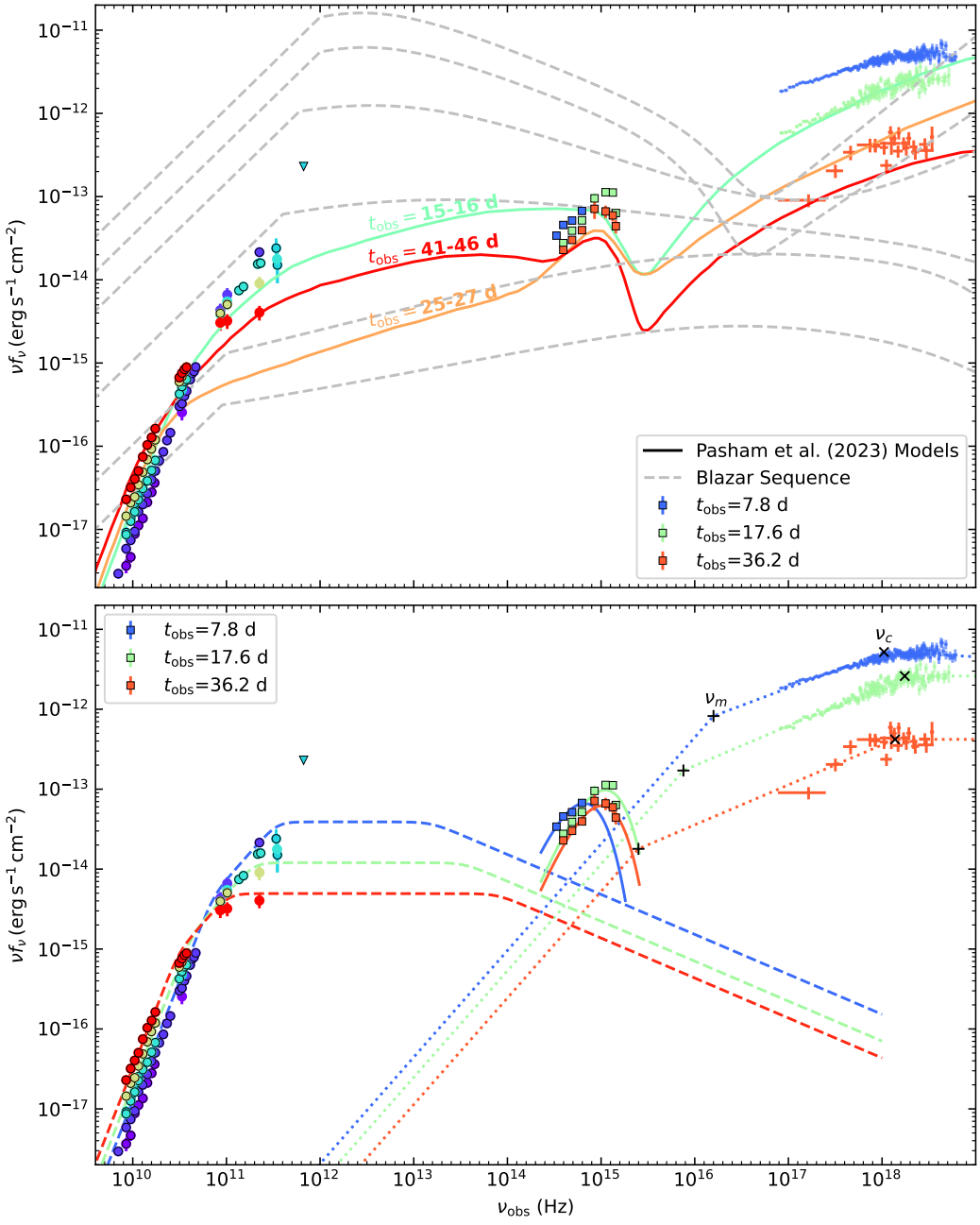

Figure 6.8: Broadband SED of AT2022cmc.

et al. 2022, Fig. 1).

A novel result from our joint *NICER* and *NuSTAR* observations is that the X-ray spectrum exhibits a relatively sharp break (at least in the first two epochs, see Figure 6.3), whereas the spectra produced by the SSC process are quite smooth (Ghisellini, 2013).

Given the aforementioned issues of the synchrotron+SSC models, hereafter we consider an alternative scenario where the X-ray and radio photons arise from two separate regions, akin to the prompt and afterglow emitting sites observed in GRBs. This physical picture is motivated by the success of applying the forward shock model developed for GRB afterglows in the radio/mm observations of Sw J1644+57 (Zauderer, Berger, Soderberg, et al., 2011; Berger et al., 2012; Zauderer, Berger, Margutti, et al., 2013; Mimica et al., 2015; Eftekhari, Berger, Zauderer, et al., 2018; Cendes, Eftekhari, et al., 2021). When modeled as a forward shock, the radio SED of AT2022cmc places a lower limit on the size of the radio emitting region $R > 10^{17}$ cm (see §6.3), whereas the X-ray variability timescale of $t_{\rm var,\,min} = 10^3$ s places an upper limit on the size of the X-ray emitting region $R_{\rm X} \sim 2\Gamma_{\rm j}^2 c t_{\rm var,\,min} = 6 \times 10^{15} (\Gamma_{\rm j}/10)^2$ cm. This further argues that as long as $\Gamma_{\rm j} < 40$, we can robustly infer that the X-ray and radio emission come from different regions.

A similar interpretation has also been adopted by several previous works to explain Sw J1644+57 (Crumley et al., 2016; Lu, Krolik, et al., 2017) and AT2022cmc (Andreoni, Coughlin, Perley, et al., 2022; Matsumoto and Metzger, 2023). For the X-ray emission of AT2022cmc, we explore the possibility of a pure synchrotron origin, which is the leading emission mechanism for the GRB prompt emission (Oganesyan et al., 2019; Zhang, Altamirano, et al., 2020).

Sub-mm/Radio: Forward Shock

Here we provide a brief description of the afterglow model (Sari, Piran, and Narayan, 1998; Granot and Sari, 2002). Let $n_{\rm ext}$ be the upstream unshocked particle density, $\Gamma = 1/\sqrt{1-\beta^2}$ be the bulk Lorentz factor of the shock front, and γ be the Lorentz factor of the shocked fluid. Under the Hygoniot shock jump conditions (Blandford and McKee, 1976), $\Gamma^2 = 2\gamma^2$, the downstream shock energy is $e = 4\gamma^2 n_{\rm ext} m_p c^2$, and the particle density is $n = 4\gamma n_{\rm ext}$.

Here the electrons in the shock are accelerated into a power-law distribution, $N(\gamma_e) \propto \gamma_e^{-p}$ for $\gamma_e > \gamma_m$, where γ_m is the minimum Lorentz factor of the relativistic electrons.

At each γ_e, the characteristic synchrotron frequency is

$$\nu(\gamma_e) = \gamma\gamma_e^2 \frac{eB}{2\pi m_e c} \tag{6.1}$$

The injection frequency is $\nu_m \equiv \nu(\gamma_m)$. Assuming a fraction ϵ_e of the shock energy goes into electrons and a fraction ϵ_B of shock energy goes into magnetic energy density, we have $B = (32\pi m_p \epsilon_B n_{\rm ext})^{1/2}\gamma c$ and

$$\gamma_m = \epsilon_e \left(\frac{p-2}{p-1}\right)\frac{m_p}{m_e}\gamma. \tag{6.2}$$

The critical electron Lorentz factor is

$$\gamma_c = \frac{6\pi m_e c}{\sigma_{\rm T}\gamma B^2 t} = \frac{3m_e}{16\epsilon_B\sigma_{\rm T} m_p c}\frac{1}{t\gamma^3 n_{\rm ext}} \tag{6.3}$$

$$= 5.1\times 10^9 \frac{1}{\epsilon_B t n_{\rm ext}\gamma^3} \tag{6.4}$$

where t is the time in the observer frame. The cooling frequency

$$\nu_c \equiv \nu(\gamma_c) = 2.8\times 10^6 \gamma\gamma_c^2 B \tag{6.5}$$

From the observed radio spectra, we infer that the system is in the the slow cooling regime, i.e., $\nu_m < \nu_c$. In this regime, one can use spectrum 1 and spectrum 2 of Granot and Sari (2002). The self-absorption frequency is ν_a, below which the synchrotron spectrum is optically thick.

For the standard Blandford and McKee (1976) evolution, at sufficiently early times, $\nu_a \ll \nu_m$, the synchrotron spectrum is given by

$$\begin{aligned} F_{\nu,1}(\nu) =& F_\nu(\nu_a)\left[\left(\frac{\nu}{\nu_a}\right)^{-s_1\beta_1} + \left(\frac{\nu}{\nu_a}\right)^{-s_1\beta_2}\right]^{-1/s_1} \\ &\times\left[1+\left(\frac{\nu}{\nu_m}\right)^{s_2(\beta_2-\beta_3)}\right]^{-1/s_2} \end{aligned} \tag{6.6}$$

where s_1 and s_2 are smoothing parameters, $\beta_1 = 2$, $\beta_2 = 1/3$, $\beta_3 = (1-p)/2$ are the power-law indices of each segment.

At late times, $\nu_m \ll \nu_a$,

$$\begin{aligned} F_{\nu,2}(\nu) =& F_\nu(\nu_m)\left[\left(\frac{\nu}{\nu_m}\right)^2 e^{-s_4\left(\frac{\nu}{\nu_m}\right)^{2/3}} + \left(\frac{\nu}{\nu_m}\right)^{5/2}\right] \\ &\times\left[1+\left(\frac{\nu}{\nu_a}\right)^{s_5(\beta_2-\beta_3)}\right]^{-1/s_5} \end{aligned} \tag{6.7}$$

where s_4 and s_5 are smoothing parameters, $\beta_2 = 5/2$, and $\beta_3 = (1-p)/2$.

To smoothly connect the evolution in the two phases, one uses a weighted average

$$F_\nu(\nu) = \frac{w_1 F_{\nu,1} + w_2 F_{\nu,2}}{w_1 + w_2} \tag{6.8}$$

where $w_1 = (\nu_m/\nu_a)^2$ and $w_2 = (\nu_a/\nu_m)^2$.

As the optically thin radio spectrum is not well sampled at early times, hereafter we assume $p = 3$. We perform the fit using the Markov chain Monte Carlo (MCMC) approach with `emcee` (Foreman-Mackey, Hogg, et al., 2013). The best-fit models are shown in Figure 6.7. For all radio epochs analyzed in this paper, $w_1 \gg 1$, $F_\nu(\nu) \approx F_{\nu,1}$, the observed peak frequency $\nu_p = \nu_m$, and the observed peak specific flux $F_p = F_\nu(\nu_p)$.

Using equipartition analysis in the relativistic regime (Barniol Duran, Nakar, and Piran, 2013), we computed the equipartition radius

$$R_{\rm eq} \approx (1.7 \times 10^{17}\,{\rm cm}) \left[\frac{F_{p,\,{\rm mJy}}^{8/17} d_{L,28}^{16/17} \eta^{35/51}}{\nu_{p,10}(1+z)^{25/17}}\right] \frac{\Gamma^{10/17}}{f_A^{7/17} f_V^{1/17}}, \tag{6.9}$$

and the minimal total energy

$$E_{\rm eq} \approx (2.5 \times 10^{49}\,{\rm erg}) \left[\frac{F_{p,{\rm mJy}}^{20/17} d_{L,28}^{40/17} \eta^{15/17}}{\nu_{p,10}(1+z)^{37/17}}\right] \frac{f_V^{6/17}}{f_A^{9/17}\Gamma^{26/17}}. \tag{6.10}$$

Here f_V and f_A are geometry factors, and $\eta = \nu_m/\nu_a$. We consider a narrow jet with a half-opening angle of $\theta_j = 0.1 < 1/\Gamma$, such that $f_A = f_V = (\theta_j\Gamma)^2$.

Following Barniol Duran and Piran (2013) and Barniol Duran, Nakar, and Piran (2013) and Eftekhari, Berger, Zauderer, et al. (2018), we assume $\epsilon_e = 0.1$, $\epsilon_B = 10^{-3}$, and that the kinetic energy of hot protons is 10 times more than the electrons. Defining $\xi \equiv 1 + \epsilon_e = 11$, the equipartition radius will be increased by a factor of $\xi^{1/17} = 1.15$ and the total minimal energy will be increased by a factor of $\xi^{11/17} = 4.72$. Defining $\epsilon \equiv (\epsilon_B/\epsilon_e)/(6/11)$, the actual radius R is different from $R_{\rm eq}$ by a multiplicative factor of $\epsilon^{1/17} = 0.79$ and the total energy $E_{\rm T}$ is greater than $E_{\rm eq}$ by a multiplicative factor of $(11/17)\epsilon^{-6/17} + (6/17)\epsilon^{11/17} = 2.68$.

The magnetic field in the source frame is

$$B = (1.3 \times 10^{-2}\,{\rm G}) \left[\frac{\nu_{p,10}^5 (1+z)^7}{F_{p,{\rm mJy}}^2 d_{L,28}^4 \eta^{10/3}}\right] \frac{f_A^2 R_{17}^4}{\Gamma^3}. \tag{6.11}$$

Γ is related to the shock radius R by

$$t \approx \frac{R(1-\beta)(1+z)}{\beta c}. \tag{6.12}$$

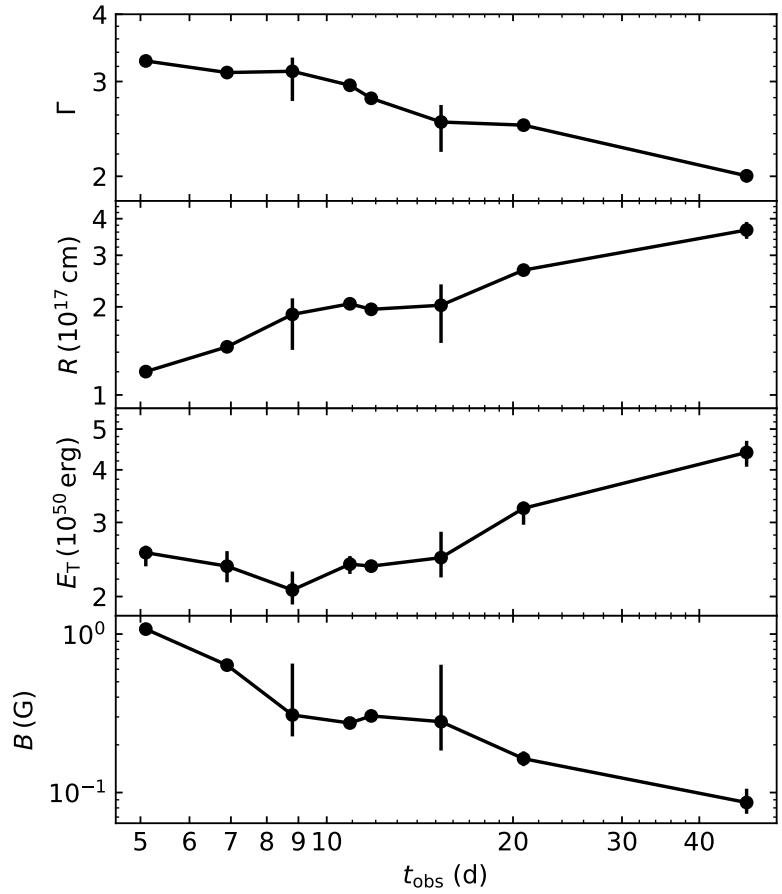

Figure 6.9: Evolution of physical properties inferred by fitting the sub-mm/radio SEDs of AT2022cmc.

Figure 6.9 shows the evolution of Γ, R, $E_{\rm T}$, and B. Similar parameters of Γ and R have also been obtained with afterglow model fitting performed by Matsumoto and Metzger (2023). The cooling frequency ν_c, computed with Eq. (6.5), lie in the infrared band. The best-fit afterglow models at the three *NuSTAR* observing epochs are shown as the dashed lines in the lower panel of Figure 6.8.

UV/optical: Thermal Envelope

The optical (*griz*) spectral slopes α (for $f_\nu \propto \nu^\alpha$) at $t_{\rm obs}$ = 7.8, 17.6, and 36.2 d are 0.03 ± 0.15, 0.36 ± 0.14, and 0.18 ± 0.26, respectively. The optical emission is therefore not an extension of the radio/mm synchrotron SED, consistent with the

analysis in §6.3. In the UV bands, the spectral slope at the second and third *NuSTAR* epochs are -1.43 ± 0.31 and -1.76 ± 0.54. Following Andreoni, Coughlin, Perley, et al. (2022) and Pasham, Lucchini, et al. (2023), we fit the UV/optical SED of AT2022cmc with a blackbody function. The best-fit blackbody radius, temperature, and luminosity are presented in Table 6.2.

Table 6.2: Best-fit Parameters of the Thermal Envelope.

$t_{\rm obs}$ (d)	$\log T_{\rm bb}$ (K)	$\log R_{\rm bb}$ (cm)	$\log L_{\rm bb}$ (erg s^{-1})
7.8	4.25 ± 0.03	15.51 ± 0.04	44.87 ± 0.03
17.6	4.47 ± 0.03	15.14 ± 0.05	45.03 ± 0.04
36.2	4.44 ± 0.02	15.12 ± 0.03	44.84 ± 0.03

By fitting the UV/optical SED as a blackbody, we are agnostic of the nature of this thermal component, which might be generated either by energy dissipation in stellar debris self-collision shocks (Piran et al., 2015; Jiang, Guillochon, and Loeb, 2016) or by reprocessing in an optically thick wind (Miller, 2015; Dai, McKinney, Roth, et al., 2018; Thomsen, Kwan, et al., 2022). A peak blackbody luminosity of $L_{\rm bb} \approx 10^{45}\,{\rm erg\,s^{-1}}$ is on the high end of the bolometric luminosity function of ZTF-selected non-relativistic TDEs (see Fig. 14 of Yao, Ravi, et al. 2023).

X-ray: Internal Energy Dissipation in the Jet

In the first two *NuSTAR* observing epochs, the X-ray spectral shape steepens from $f_\nu \propto \nu^{-0.5}$ to $f_\nu \propto \nu^{-1}$ at $\nu_{\rm bk} \approx 3 \times 10^{18}\,{\rm Hz}$ — the spectral slope difference of ≈ 0.5 can be naturally explained with a synchrotron spectrum if $\nu_{\rm bk}$ is consistent with either ν_c in the slow cooling regime or ν_m in the fast cooling regime.

We assume the electrons have a power-law energy distribution with a power-law index p and minimum Lorentz factor γ_{em}. If the electrons are accelerated by internal shocks, $\gamma_{em} \approx m_p/m_e = 1836$ provides a rough estimate. If the electrons are accelerated by magnetic reconnection (Kumar and Crumley, 2015), higher values of γ_{em} might also be achieved.

The X-ray is variable on $t_{\rm var} \approx 1\,{\rm hr}$, which is the timescale over which we expect the plasma (that emits X-rays) to undergo significant expansion. Internal dissipation occurs at a distance of $R = 2\Gamma^2 c t_{\rm var} = 2 \times 10^{16} (\Gamma/10)^2 (t_{\rm var}/{\rm h})\,{\rm cm}$. The isotropic equivalent luminosity $L_{\rm X} = 4\pi R^2 \Gamma^2 u c$, where u is the energy density in the jet rest

frame. Since the magnetic field energy density $B^2/(8\pi) = \epsilon_B u$, we have

$$B = 12 L_{47}^{1/2} \epsilon_B^{1/2} (\Gamma/10)^{-3} (t_{\rm var}/{\rm h})^{-1}\,{\rm G} \tag{6.13}$$

The injection frequency $\nu_m = \Gamma \gamma_{em}^2 eB/(2\pi m_e c)$. The Lorentz factor of electrons that correspond to the cooling frequency can be computed with $\Gamma \gamma_{ec} m_e c^2 = P(\gamma_{ec}) t_{\rm var}$, which gives

$$\gamma_{ec} = \frac{3 m_e c}{4 \sigma_{\rm T} \Gamma t_{\rm var} \epsilon_B u} \tag{6.14}$$

and $\nu_c = \Gamma \gamma_{ec}^2 eB/(2\pi m_e c)$.

For the first *NuSTAR* epoch, $L_{47} = 1.3$ and $\nu_{\rm bk} = 10^{18.4}$ Hz. We assume $t_{\rm var} = 500$ s and $\epsilon_B = 0.3$. In order to make sure that the model does not overpredict the observed optical flux, both ν_m and ν_c needs to be above $\approx 10^{16.5}$ Hz, and one of the frequencies should correspond to the break frequency $\nu_{\rm bk}$. The top panel of Figure 6.10 shows the expected ν_m and ν_c as a function of γ_{em} and Γ. The observed data can be explained by the synchrotron model if $\Gamma \approx 52$, $\gamma_{em} \approx 2.5 \times 10^4$, and $p \approx 2.12$, which is shown as the dotted blue line in the bottom panel of Figure 6.8.

For the second *NuSTAR* epoch, $L_{47} = 0.6$ and $\nu_{\rm bk} = 10^{18.6}$ Hz. We assume $t_{\rm var} = 10^3$ s and $\epsilon_B = 0.3$. The break frequency can be reconciled with ν_c. To ensure that the synchrotron flux in the UV/optical band is below the observed value, we rule out parameter space where $\nu_m < 10^{16}$ Hz. The observed data can be explained by the synchrotron model if $\Gamma \approx 44$, $\gamma_{em} \approx 2.5 \times 10^4$, and $p \approx 2$, which is shown as the dotted green line in the bottom panel of Figure 6.8.

For the third *NuSTAR* epoch, we assume that ν_c still lies in the X-ray band and adopt the broken power-law fit, which gives $L_{47} = 0.12$ and $\nu_{\rm bk} = 10^{18.5}$ Hz. Assuming $t_{\rm var} = 1$ hr and $\epsilon_B = 0.3$. The observed data can be explained by the synchrotron model if $\Gamma \approx 27$, $\gamma_{em} \approx 2.5 \times 10^4$, and $p \approx 2$, which is shown as the dotted orange line in the bottom panel of Figure 6.8.

The self-absorption frequency can be derived as the intersection between the Rayleigh-Jeans part of a blackbody spectrum and the synchortron spectrum. We consider that in the electron's rest frame

$$I'_\nu = \frac{2\nu_a'^2 k_B T_e}{c^2} = j'_\nu \left(\frac{R}{\Gamma^2} \Gamma \right) \tag{6.15}$$

The temperature of the blackbody is taken as $k_B T_e \approx \gamma_m m_e c^2$.

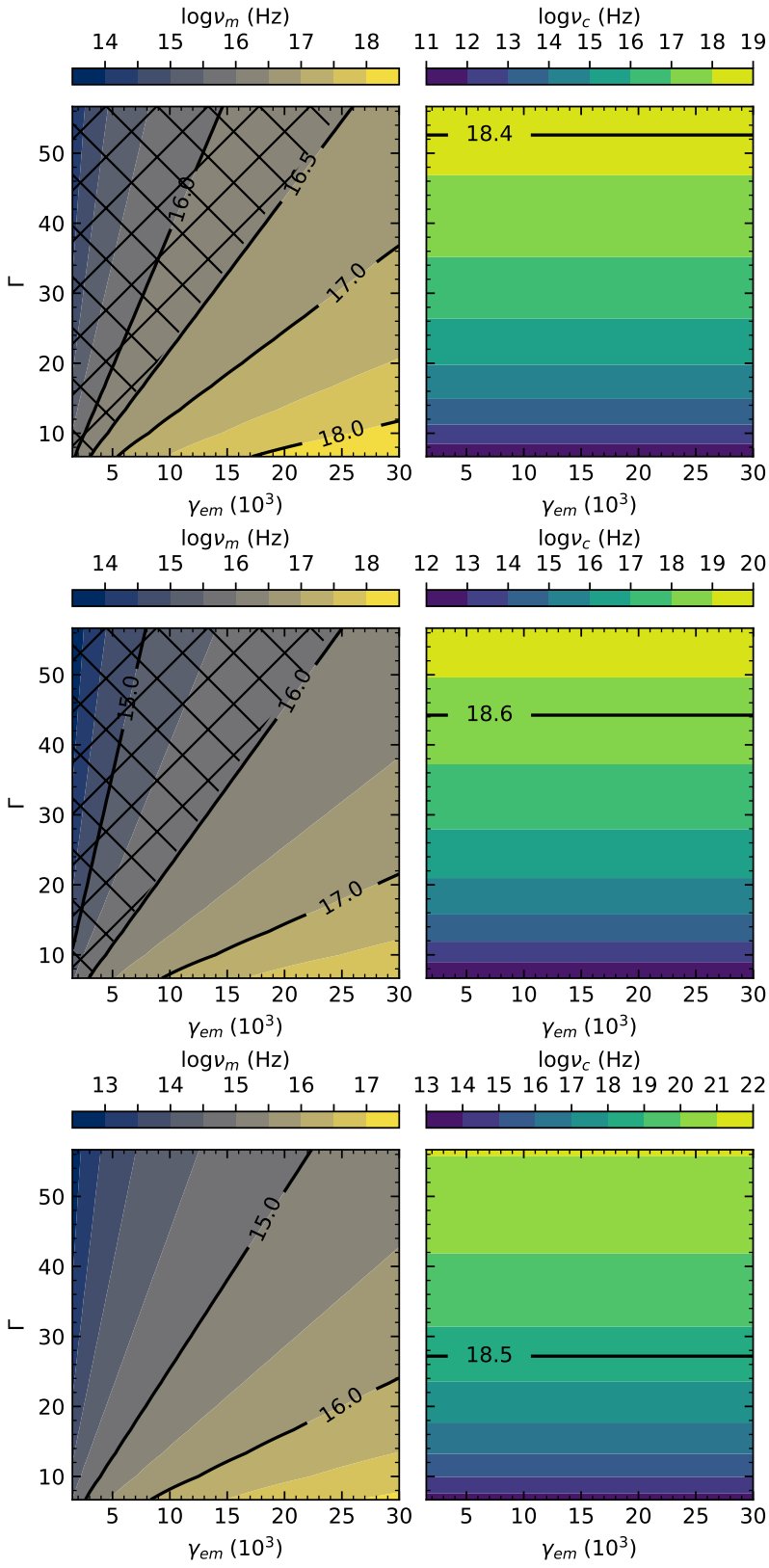

Figure 6.10: ν_m and ν_c as a function of γ_{em} and Γ.

In the slow cooling regime ($\nu_m < \nu_c$), we have

$$j'_\nu \approx \left(\frac{\nu'_a}{\nu'_m}\right)^{1/3} \frac{P(\nu'_m)}{\nu'_m} n_e \tag{6.16a}$$

$$= \left(\frac{\nu'_a}{\nu'_m}\right)^{1/3} \frac{\gamma_{em}^2 \frac{4}{3}\sigma_{\rm T} c \frac{B^2}{8\pi}}{\gamma_{em}^2 \frac{eB}{2\pi m_e c}} n_e \tag{6.16b}$$

$$= \left(\frac{\nu'_a}{\nu'_m}\right)^{1/3} n_e \frac{\sigma_{\rm T} m_e c^2}{3e} B. \tag{6.16c}$$

The self-absorption frequency in all three epochs are in the GHz band.

6.4 Discussion

AT2022cmc is the first on-axis RTDE ever observed with *NICER* and *NuSTAR*. Joint X-ray analysis reveals a broken powerlaw spectral shape. We interpret the rest-frame break energy of few $\times 10^{18}$ Hz as the cooling frequency in a synchrotron spectrum, which is generated by internal dissipation within the jet. The inferred jet Lorentz factor Γ decreases from ~ 52 to ~ 27 from $t_{\rm rest} \approx 3.6$ to 36.2 d, implying that the radiation is beamed into a cone with an opening angle of $\approx 1/\Gamma$ that increases from 1° to 2° thorough this time period.

Using a simple electron-synchrotron model, we infer that the particle distribution has a low-energy cut-off at the minimum Lorentz factor of $\gamma_{em} \sim 10^4$, otherwise the UV flux will be over-predicted. The high value of γ_{em} indicates that the particle is probably accelerated by magnetic reconnection instead of internal shocks. However, detailed theoretical calculations and simulations are needed to address the nature of the dissipative mechanism.

At late time during the X-ray evolution of on-axis RTDEs, a sudden flux drop has been observed in both Sw J1644+57 (at rest-frame days since discovery $t_{\rm rest} \approx$ 370 days; Zauderer, Berger, Margutti, et al. 2013) and Sw J2058+05 ($t_{\rm rest} \approx 200$ days; Pasham, Cenko, Levan, et al. 2015), which has been explained by a jet shut-off as the accretion flow transitions from a supercritical "slim" disk to a geometrically thin disk state (Tchekhovskoy, Metzger, et al., 2014). Such a disk instability triggered state transition is naturally predicted as a result of the decreasing mass accretion rate (Shen and Matzner, 2014; Lu, 2022), and has recently also been observed in the non-jetted TDE AT2021ehb (Yao, Lu, et al., 2022). Future *Chandra* X-ray monitoring observations of AT2022cmc will reveal if the luminosity continues to follow the $L \propto t^{-2}$ decay (Figure 6.1) and verify the existence of such a disk state transition.

The rate of on-axis RTDEs with prompt X-ray luminosity above $10^{48}\,\mathrm{erg\,s^{-1}}$ has been estimated to be $0.03^{+0.04}_{-0.02}\,\mathrm{Gpc^{-3}\,yr^{-1}}$ from *Swift*/BAT (Sun, Zhang, and Li, 2015). The inferred Γ of the relativistic jet of AT2022cmc is greater than the $\Gamma \approx 10$ estimate in Sw J1644+57 (Bloom et al., 2011). Taking a median value of $\Gamma \approx 30$ indicates that the volumetric rate of RTDEs is $\sim 100\,\mathrm{Gpc^{-3}\,yr^{-1}}$. The volumetric rates of TDEs with soft X-ray and UV/optical thermal emission above $10^{43}\,\mathrm{erg\,s^{-1}}$ is $\sim$230 $\mathrm{Gpc^{-3}\,yr^{-1}}$ and $\sim 310\,\mathrm{Gpc^{-3}\,yr^{-1}}$, respectively (Sazonov et al., 2021; Yao, Ravi, et al., 2023). Given the recent infrared discovery of a nearby heavily extincted TDE (Panagiotou et al., 2023), we assume a comparable fraction of TDEs are missed by soft X-ray/optical time domain surveys, implying a total TDE rate of $\sim 10^3\,\mathrm{Gpc^{-3}\,yr^{-1}}$. This implies that the fraction of TDEs that launch relativistic jets is $\sim 10\%$, similar to the fraction of AGN with radio-loud jets.

Chapter 7

TIDAL DISRUPTION EVENT DEMOGRAPHICS WITH THE ZWICKY TRANSIENT FACILITY: VOLUMETRIC RATES, LUMINOSITY FUNCTION, AND IMPLICATIONS FOR THE LOCAL BLACK HOLE MASS FUNCTION

Yao, Y. et al. (Mar. 2023). In: *arXiv e-prints*, arXiv:2303.06523, arXiv:2303.06523. DOI: 10.48550/arXiv.2303.06523.

Yuhan Yao[1], Vikram Ravi[1], Suvi Gezari[2,3], Sjoert van Velzen[4], Wenbin Lu[5], Steve Schulze[6], Jean J. Somalwar[1], S. R. Kulkarni[1], Erica Hammerstein[7], Matt Nicholl[8,9], Matthew J. Graham[1], Daniel A. Perley[10], S. Bradley Cenko[11,12], Robert Stein[1], Angelo Ricarte[13,14], Urmila Chadayammuri[13], Eliot Quataert[15], Eric C. Bellm[16], Joshua S. Bloom[5], Richard Dekany[17], Andrew J. Drake[1], Steven L. Groom[18], Ashish A. Mahabal[19,20], Thomas A. Prince[1], Reed Riddle[17], Ben Rusholme[18], Yashvi Sharma[1], Jesper Sollerman[21], and Lin Yan[1]

[1] Cahill Center for Astrophysics, California Institute of Technology, MC 249-17, 1200 E California Boulevard, Pasadena, CA 91125, USA
[2] Space Telescope Science Institute, 3700 San Martin Drive, Baltimore, MD 21218, USA
[3] Department of Physics and Astronomy, Johns Hopkins University, Baltimore, MD 21218
[4] Leiden Observatory, Leiden University, Postbus 9513, 2300 RA, Leiden, The Netherlands
[5] Department of Astronomy, University of California, Berkeley, CA 94720-3411, USA
[6] Department of Physics, The Oskar Klein Centre, Stockholm University, AlbaNova, SE-10691 Stockholm, Sweden
[7] Department of Astronomy, University of Maryland, College Park, MD 20742, USA
[8] Birmingham Institute for Gravitational Wave Astronomy and School of Physics and Astronomy, University of Birmingham, Birmingham B15 2TT, UK
[9] Astrophysics Research Centre, School of Mathematics and Physics, Queens University Belfast, Belfast BT7 1NN, UK
[10] Astrophysics Research Institute, Liverpool John Moores University, IC2, Liverpool Science Park, 146 Brownlow Hill, Liverpool L3 5RF, UK
[11] Astrophysics Science Division, NASA Goddard Space Flight Center, Greenbelt, MD 20771, USA
[12] Joint Space-Science Institute, University of Maryland, College Park, MD 20742, USA
[13] Center for Astrophysics | Harvard & Smithsonian, 60 Garden Street, Cambridge, MA 02138, USA
[14] Black Hole Initiative at Harvard University, 20 Garden Street, Cambridge, MA 02138, USA
[15] Department of Astrophysical Sciences, Princeton University, Princeton, NJ 08544, USA
[16] DIRAC Institute, Department of Astronomy, University of Washington, 3910 15th Avenue NE, Seattle, WA 98195, USA
[17] Caltech Optical Observatories, California Institute of Technology, Pasadena, CA 91125, USA
[18] IPAC, California Institute of Technology, 1200 E. California Blvd, Pasadena, CA 91125, USA

[19] Division of Physics, Mathematics and Astronomy, California Institute of Technology, Pasadena, CA 91125, USA
[20] Center for Data Driven Discovery, California Institute of Technology, Pasadena, CA 91125, USA
[21] Department of Astronomy, The Oskar Klein Centre, Stockholm University, AlbaNova, SE-10691 Stockholm, Sweden

Abstract

We conduct a systematic tidal disruption event (TDE) demographics analysis using the largest sample of optically selected TDEs. A flux-limited, spectroscopically complete sample of 33 TDEs is constructed using the Zwicky Transient Facility (ZTF) over three years (from October 2018 to September 2021). We infer the black hole (BH) mass ($M_{\rm BH}$) with host galaxy scaling relations, showing that the sample $M_{\rm BH}$ ranges from $10^{5.1}\,M_\odot$ to $10^{8.2}\,M_\odot$. We developed a survey efficiency corrected maximum volume method to infer the rates. The rest-frame g-band luminosity function (LF) can be well described by a broken power-law of $\phi(L_g) \propto [(L_g/L_{\rm bk})^{0.3} + (L_g/L_{\rm bk})^{2.6}]^{-1}$, with $L_{\rm bk} = 10^{43.1}\,{\rm erg\,s^{-1}}$. In the BH mass regime of $10^{5.2} \lesssim (M_{\rm BH}/M_\odot) \lesssim 10^{7.2}$, the TDE mass function follows $\phi(M_{\rm BH}) \propto M_{\rm BH}^{-0.25}$, which favors a flat local BH mass function ($dn_{\rm BH}/d\log M_{\rm BH} \approx$ constant). We confirm the significant rate suppression at the high-mass end ($M_{\rm BH} \gtrsim 10^{7.5}\,M_\odot$), which is consistent with theoretical predictions considering direct capture of hydrogen-burning stars by the event horizon. At a host galaxy mass of $M_{\rm gal} \sim 10^{10}\,M_\odot$, the average optical TDE rate is $\approx 3.2 \times 10^{-5}\,{\rm galaxy^{-1}\,yr^{-1}}$. We constrain the optical TDE rate to be [3.7, 7.4, and 1.6] $\times 10^{-5}\,{\rm galaxy^{-1}\,yr^{-1}}$ in galaxies with red, green, and blue colors.

7.1 Introduction

In the local universe, a small fraction ($\sim 10\%$) of galaxies host active massive black holes (BHs) in their nuclei (Kewley et al., 2006; Aird et al., 2012). The remaining massive BHs are quiescent, but can be temporarily "awakened" when a star comes too close to it and becomes disrupted by tidal forces. The stellar debris evolves into an elongated stream, approximately half of which comes back to get accreted (Rees, 1988). This produces an electromagnetic flare if the tidal radius $R_{\rm T}$ (where the self gravity of the star balances the tidal forces) is greater than the size of the BH event horizon. Since $R_{\rm T} \propto M_{\rm BH}^{1/3}$ and the event horizon size $\propto M_{\rm BH}$, there exists a maximum BH mass for an observable TDE — the so-called Hills mass. For Sun-like stars, $M_{\rm Hills} \sim 10^8\,M_\odot$ (Hills 1975).

The first tidal disruption event (TDE) was identified with the *ROSAT* all-sky X-ray

survey, where the soft X-rays are thought to come from a newly-formed accretion disk (Bade, Komossa, and Dahlem, 1996; Grupe, Thomas, and Leighly, 1999; Saxton et al., 2020). Recently, the eROSITA telescope (Predehl, Andritschke, et al., 2021) on-board the *SRG* X-ray mission (Sunyaev, Arefiev, et al., 2021) reported 13 TDEs selected from the second eROSITA all-sky survey (Sazonov et al., 2021). Low-temperature (few $\times 10^4$ K) thermal emission from TDEs has been discovered with UV/optical sky surveys (Gezari, Martin, et al., 2006; van Velzen, Farrar, et al., 2011; Gezari, Chornock, et al., 2012; Arcavi, Gal-Yam, et al., 2014; Holoien et al., 2014; Hung et al., 2017), which has been postulated to arise from either energy dissipation within a stream-stream collision shock (Piran et al., 2015; Jiang, Guillochon, and Loeb, 2016) or reprocessing of high-energy photons (Metzger and Stone, 2016; Roth, Kasen, et al., 2016). In the latter scenario, the physical origin of the "reprocessing layer" may be the optically thick gas from the self-collision shock (Lu and Bonnerot, 2020), a radiation-driven outflow formed under super-Eddington accretion (Miller, 2015; Dai, McKinney, Roth, et al., 2018; Thomsen, Kwan, et al., 2022), or a quasi-static weakly bound envelope (Loeb and Ulmer, 1997; Coughlin and Begelman, 2014; Metzger, 2022a).

Theoretically, the TDE rate is determined by processes that govern stellar diffusion into the "loss cone," which defines a phase-space volume of orbits with angular momentum $J \leq J_{\rm lc} \equiv \sqrt{2GM_{\rm BH}R_{\rm T}}$ (Alexander, 2017; Stone, Vasiliev, et al., 2020). Observational constraints on TDE demography can help address various open questions in astrophysics. First, the TDE luminosity function (LF) provides clues to how the emission mechanism is tied to the loss cone filling (Kochanek, 2016; Stone and Metzger, 2016; Stone, Vasiliev, et al., 2020) and provides an essential input to predict TDE rates in future sky surveys.

Moreover, measuring the volumetric rate of TDEs as a function of $M_{\rm BH}$ offers a unique approach to trace the local BH population. At the low-mass end ($M_{\rm BH} \lesssim 10^6\,M_\odot$), the TDE mass function depends on the unknown bottom end of the massive black hole mass function (BHMF). The space density of such intermediate-mass black holes (IMBHs) encodes formation mechanisms of primordial BHs in the early Universe at redshifts of $z > 10$ (Ricarte and Natarajan, 2018b; Woods et al., 2019; Greene, Strader, and Ho, 2020; Chadayammuri et al., 2023). Mergers of IMBHs and extreme mass-ratio inspirals (EMRIs) are prime targets for the upcoming space-based gravitational-wave detector Laser Interferometer Space Antenna (*LISA*; Amaro-Seoane et al. 2017; Jani, Shoemaker, and Cutler 2020; Amaro Seoane 2022).

At the high-mass end, the location of the TDE mass function's cut-off is set by the size of the event horizon, which probes the spin distribution of BHs in the mass range of $10^{7.5}\,M_\odot \lesssim M_{\rm BH} \lesssim 10^{8.5}\,M_\odot$ (Kesden, 2012; Stone, Kesden, et al., 2019; Du et al., 2022; Huang and Lu, 2022). The spin of such quiescent BHs can not be measured via the traditional method of X-ray reflection spectroscopy (Reynolds, 2021) developed for X-ray binaries and active galactic nulei (AGN).

van Velzen, 2018 made the first attempt to construct the TDE LF and mass function. Using a sample of 13 objects selected from five different UV/optical sky surveys, the authors inferred a rest-frame g-band LF of $dN/dL_g \propto L_g^{-3/2}$ for $L_g \in (10^{42.3}, 10^{44.8})\,{\rm erg\,s^{-1}}$ and a nearly constant TDE mass function for $M_{\rm BH} \in (10^{5.8}, 10^{7.3})\,M_\odot$. While these early results have demonstrated the important role that TDEs play in understanding BH demographics, they are susceptible to small number statistics and the heterogeneous nature of the sample.

Over the past few years, time domain sky surveys have led to a surge of TDE discoveries. The Zwicky Transient Facility (ZTF; Bellm, Kulkarni, Graham, et al. 2019; Graham et al. 2019) is one of the most prolific optical discovery engines. Previous ZTF TDE sample studies have made significant progress on characterizing the photometric and spectroscopic properties of TDEs (van Velzen, Gezari, Hammerstein, et al., 2021; Hammerstein, van Velzen, et al., 2023). However, little has been done regarding TDE rates. This is mainly because the spectroscopic classification completeness of photometric candidates in previous TDE samples was not assessed. In this work, we aim to put new observational constraints on TDE demography. To this end, we constructed a flux-limited, spectroscopically complete sample of 33 TDEs selected from three years of the ZTF operation.

This paper is organized as follows. Procedures of the TDE sample selection, observation, and classification are outlined in §7.2. UV/optical light curve fitting is described in §7.3. Host galaxy observation and analysis (including measurements of the $M_{\rm BH}$) are presented in §7.4. The survey efficiency is assessed in §7.5. We compute and discuss the volumetric rate of optical TDEs as a function of $M_{\rm BH}$, L_g, as well as other host galaxy and transient properties in §7.6. We summarize our conclusions in §7.7.

UT time is used throughout the paper. We assume a basic cosmology of $\Omega_{\rm M} = 0.3$, $\Omega_\Lambda = 0.7$, and $h = 0.7$. Optical magnitudes are reported in the AB system. Assuming $R_V = 3.1$,we correct the observed photometry for Galactic extinction using the Cardelli, Clayton, and Mathis (1989) extinction law and the Schlafly and

Finkbeiner (2011) extinction map. Coordinates are given in J2000. We use t to denote rest-frame time relative to the maximum-light epoch.

7.2 Sample Construction

The ZTF TDE Experiment

ZTF is an optical time domain sky survey operated by the Palomar Observatory. It uses the Palomar Oschin Schmidt 48-inch telescope (P48) equipped with a 47 $\deg^2$ camera (Dekany et al., 2020) to scan the entire northern visible sky at declination $> -35.2°$. The three ZTF filters (g, r, and i) were designed to maximize throughput by avoiding major Palomar sky lines. The typical survey depth is ~ 20.5 mag (Graham et al., 2019).

Image processing and reference subtraction are performed by the ZTF Science Data System (ZSDS, Masci et al. 2019). Five-σ point-source detections are saved as "alerts" in the Avro format and distributed to community brokers via the ZTF Alert Distribution System (ZADS, Patterson, Bellm, et al. 2019). Alerts are enhanced with additional contextual information such as the machine learning real-bogus score (Mahabal et al., 2019; Duev et al., 2019), the proximity to the nearest object in archival catalogs (Soumagnac and Ofek, 2018), and the star-galaxy classifier (Tachibana and Miller, 2018).

ZTF phase I (hereafter ZTF-I) ran from March 2018 to September 2020, during which 40% of the time was dedicated to two public sky surveys, including a Northern sky survey (one g + one r every three days) and a Galactic Plane survey (Bellm, Kulkarni, Barlow, et al., 2019). On 2020 October 1, ZTF increased the MSIP/NSF-funded public program to 50% of the total time, and the Northern sky survey cadence was shortened from 3 days to 2 days. Therefore, in this paper, we use 2020 October 1 as the start of ZTF phase II (hereafter ZTF-II) [1].

The ZTF team selects nuclear transients in real-time by filtering public alerts with the `AMPEL` broker (Nordin et al., 2019). Details of our filtering techniques are described in van Velzen, Gezari, Cenko, et al. (2019) and van Velzen, Gezari, Hammerstein, et al. (2021). AT2018zr is the first TDE selected by the ZTF nuclear transient filter (van Velzen, Gezari, Cenko, et al., 2019). Afterwards, van Velzen, Gezari, Hammerstein, et al. (2021) presented 17 TDEs selected within the first 1.5 yr of ZTF-I operation, and introduced three distinct spectroscopic sub-classes of optically selected TDEs

[1] Note that some other publications from the ZTF collaboration (such as Hammerstein, van Velzen, et al. 2023) consider December 2020 as the start of ZTF-II, as the Phase II Partnership surveys did not begin until that time.

(TDE-H, TDE-H+He, and TDE-He) based on the existence of a combination of broad emission lines around Hα, Hβ, and He II λ4686. Recently, Hammerstein, van Velzen, et al. (2023) presented a sample of 30 spectroscopically classified TDEs from the entirety of ZTF-I, and reported a new spectroscopic subclass called "TDE-featureless," which is characterized by a lack of broad emission lines in optical spectra.

Entering into ZTF-II, the TDE experiment was carried out with more spectroscopic follow-up resources allocated from the Keck and Palomar Observatories, which allowed us to classify a larger number of fainter TDE candidates.

The follow-up campaign in ZTF was conducted on a best effort basis. We tried to classify as many TDE candidates as possible, with higher priorities of spectroscopic observations given to objects with brighter peak magnitudes. Unlike previous ZTF work, we here seek to construct a flux-limited sample of TDEs, enabling a systematic study of optical TDE demographics. Therefore, we performed a retrospective search of nuclear transients using historical ZTF alerts, and applied a set of well-defined criteria to select TDE candidates (see §7.2). We then find the peak magnitude limits (in ZTF-I and ZTF-II separately) below which our spectroscopic classification is almost ($\gtrsim$ 90%) complete (see step 7 below). And for the few candidates with no (or ambiguous) spectroscopic classification, we determine the transient type using the photometric properties and other information (see details below).

Retrospective Candidate Filtering

Table 7.1: Steps for selecting TDE candidates.

Step	Criteria	# TDE candidates
1	Initial cuts to select nuclear transients	890,266
2	More detailed cuts to select nuclear transients	143,731
3	Cuts on peak magnitude, transient duration, and number of detections	9,426
4	Cuts on the peak color, ML classification, IR variability; remove quasars	1,390
5	Alert photometry: cuts on color, cooling rate, and rise/decline timescales	174
6	Forced photometry: cuts on color, cooling rate, and rise/decline timescales	90
7	Cuts on peak magnitude (of forced photometry)	55
8	Spectroscopic classification & photometric/contextual classification	33

Table 7.1 presents a summary of the candidate filtering steps.

1. We applied basic cuts to select nuclear transients. We kept alerts with a real-bogus score `rb>0.5` (Mahabal et al., 2019) or a deep learning score

drb>0.65 (Duev et al., 2019)[2], a position within 0.6″ to the location of the nearest object in the Panoramic Survey Telescope and Rapid Response System Data Release 1 (PS1; Chambers et al. 2016) catalog (distpsnr1<0.6) or hostless (distpsnr1==-999). We removed alerts in negative subtractions. We kept alerts in coincidence with objects with galaxy-like morphologies, selected using a cut on the star-galaxy score (Tachibana and Miller, 2018) of sgscore1<0.8. This step left 890,266 unique sources.

2. We kept objects first detected between 2018 October 1 and 2021 September 30, i.e., the last two years of ZTF-I[3] and the first year of ZTF-II. We require that in either g or r band, the transient is within 0.6″ to the location of the nearest object in the ZTF reference image (distnr<0.6). If the nearest reference object is brighter than 15 mag (magnr<=15), we require sgscore1<0.2; Similarly, we require sgscore1<=0.5 for 15<magnr<=18 and sgscore1<0.8 for magnr>18. This left 143,731 sources.

3. We define n_g (n_r) as the number of detections in g band (r band), and $t_{\rm dur}$ as the duration of all detections. The peak magnitudes in the g and r bands are $m_{g,\rm peak}$ and $m_{r,\rm peak}$, respectively. We required $m_{g,\rm peak} < 19.5$ mag, $m_{r,\rm peak} < 19.5$ mag, $t_{\rm dur} > 30$ d, $n_g > 10$ and $n_r > 10$. This left 9,426 sources.

4. We applied a few cuts to remove stellar and AGN variability. We required $m_{g,\rm peak} - m_{r,\rm peak} < 1$, and that the closest object in the "Pan-STARRS1 Source Types and Redshifts with Machine learning" (PS1-STRM) catalog (Beck et al., 2021) is not classified as "QSO" or "STAR." We removed objects with a counterpart in the Million Quasars catalogue (Milliquas v6.3, Flesch 2019). We constructed a $W1$-band light curve from the NeoWISE (Mainzer et al., 2011) photometry prior to the first ZTF detection, and rejected any galaxies with significant variability in the $W1$ band ($\chi^2/dof > 10$). This left 1,390 sources.

5. We selected candidates based on the alert photometry. We kept objects with at least 5 nights of post-peak multi-band photometry. We required the rate of post-peak $g-r$ color change to be < 0.02 mag day^{-1}, and the mean $g-r$ color

[2]The deep learning score was not included in the alert packets until June 19 2019. Therefore, we used rb and drb for alerts released before and after that date, respectively.

[3]Due to a likely low recovery efficiency for TDEs detected in the reference images, we do not consider events first detected before October 1 2018, when ZTF reference images for most fields were still being constructed.

to be < 0.2 mag. We calculated the rise and decay e-folding times in the alert photometry light curve (smoothed with a Gaussian process). We required the rise e-folding time to be $2 < t_{e,\mathrm{rise}} < 300$ d, and the decline e-folding time to be $2 < t_{e,\mathrm{decline}} < 300$ d. This step left 174 sources, including 104 sources first detected during ZTF-I, and 70 sources first detected during the first year of ZTF-II.

6. We ran forced point spread function (PSF) photometry which provide more accurate light curves. We also visually examined the light curves and excluded 8 objects[4] that are reminiscent of AGN and one object[5] with a typical dwarf nova light curve. We applied the criteria outlined in step 4 to the ZTF forced photometry. This left 90 sources, including 54 in ZTF-I and 36 in ZTF-II.

7. We found that for candidates in ZTF-I, our spectroscopic classification completeness was $\sim 93\%$ at $m_{\mathrm{peak}} < 18.75$; for candidates in ZTF-II, our spectroscopic classification completeness was $\sim 89\%$ complete at $m_{g,\mathrm{peak}} < 19.1$ (see Figure 7.1). Therefore, we kept ZTF-I sources with $m_{\mathrm{peak}} < 18.75$, and ZTF-II sources with $m_{g,\mathrm{peak}} < 19.1$. This left 55 sources, including 27 in ZTF-I and 28 in ZTF-II.

A few notes are worth mentioning. First, as pointed out in van Velzen, Gezari, Hammerstein, et al. (2021), by applying step 4, our search is biased against TDEs hosted by AGN, such as PS1-16dtm (Blanchard et al., 2017) and ZTF20abisysx/AT2020nov (Dahiwale and Fremling, 2020e). The local AGN fraction for galaxies throughout the stellar mass range of $9.5 < \log(M_{\mathrm{gal}}/M_{\odot}) < 12$ is $\lesssim 10\%$ (Kewley et al., 2006; Aird et al., 2012), and the fraction is even lower in dwarf galaxies (Latimer, Reines, Bogdan, et al., 2021). Therefore, the majority of TDEs should be hosted by quiescent galaxies without strong AGN activity, unless the rate is enhanced by a factor ~ 10 in AGN. Second, unlike previous ZTF TDE sample studies, we do not reject candidates based on the mean $W1 - W2$ color of their host galaxies, since recent studies have found that some star-forming dwarf galaxies also exhibit red neoWISE colors (Latimer, Reines, Hainline, et al., 2021). Third, in steps 5 and 6, the cuts on color and cooling rate are defined such that all TDEs presented in van Velzen, Gezari, Hammerstein, et al. (2021), Angus et al. (2022), and Hammerstein, van

[4]ZTF18accdkxa, ZTF18acenyfr, ZTF18acpjddi, ZTF19acblzqb, ZTF19abkftuu, ZTF19abukbuc, ZTF20absxaaj, and ZTF20abzpysa show stochastic variability.

[5]ZTF21abiplqz has a fast rise, a rapid decline followed by a sudden flux frop, and a blue optical conterpart.

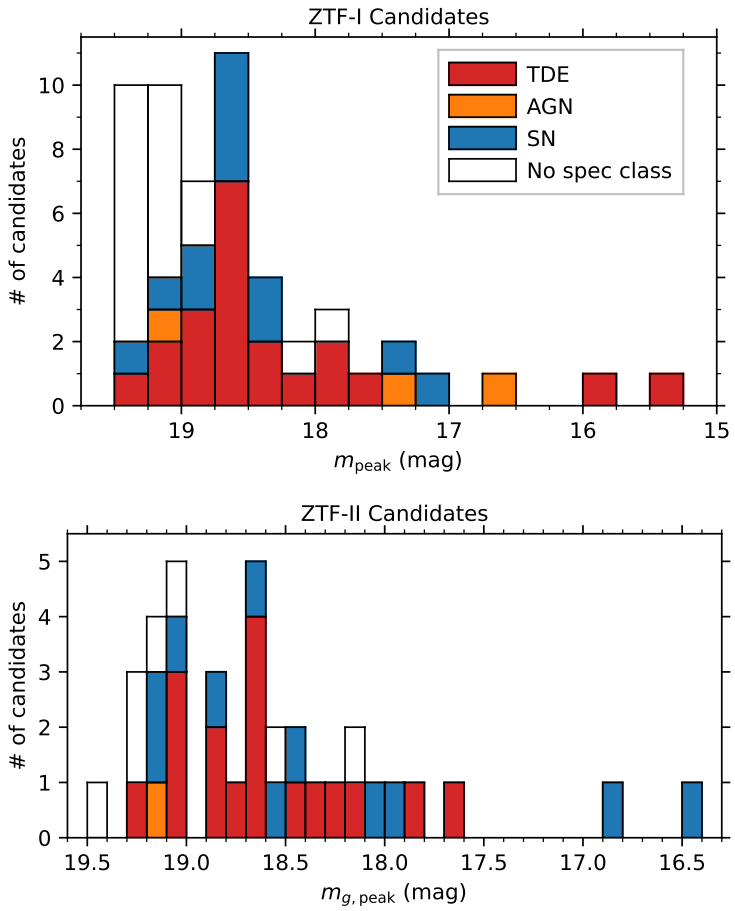

Figure 7.1: Histograms of the photometric TDE candidates that passed the filtering step 6, color-coded by their spectroscopic classifications.

Velzen, et al. (2023) satisfy the selection criteria. Finally, we show in §7.8 that our cuts on `sgscore1`, $t_{e,\mathrm{rise}}$ and $t_{e,\mathrm{decline}}$ do not hit the boundary of the selection.

Observations

UV/Optical Photometry — For all TDE candidates, we constructed the optical and UV light curves using data from ZTF, the Asteroid Terrestrial-impact Last Alert System (ATLAS; Tonry, Denneau, Heinze, Stalder, et al. 2018; Smith et al. 2020; Shingles et al. 2021), and the Ultra-Violet/Optical Telescope (UVOT; Roming et al. 2005) onboard the *Neil Gehrels Swift Observatory* (Gehrels et al., 2004). Data reduction procedures follow those outlined in van Velzen, Gezari, Hammerstein, et al. (2021) and Hammerstein, van Velzen, et al. (2023). We show the Galactic extinction corrected $g - r$ evolution in ZTF forced photometry in Figure 7.2.

Optical Spectroscopy — To spectroscopically classify the TDE candidates, we ob-

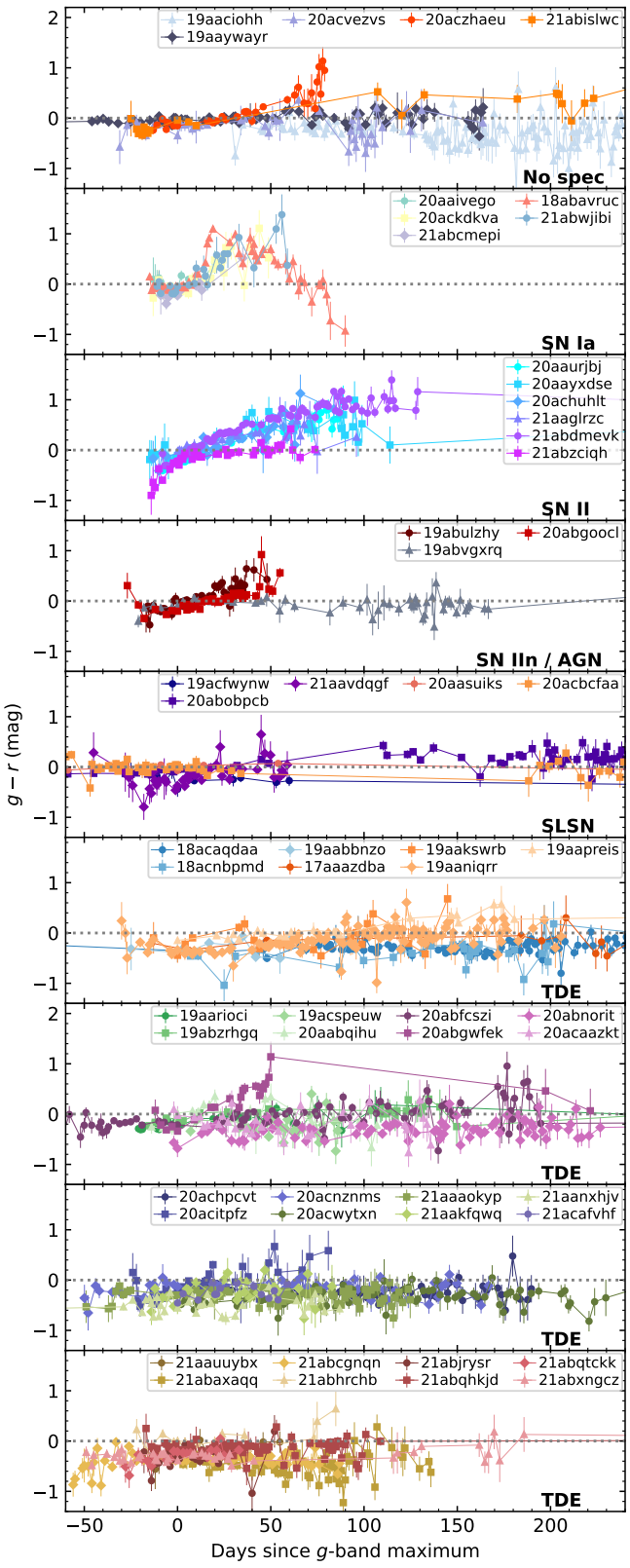

Figure 7.2: $g - r$ evolution of the 55 ZTF phtometric TDE candidates.

tained low-resolution optical spectra with the Spectral Energy Distribution Machine (SEDM, Blagorodnova, Neill, et al. 2018, Rigault et al. 2019, Kim et al. 2022) on the robotic Palomar 60 inch telescope (P60, Cenko, Fox, et al. 2006), the Low Resolution Imaging Spectrograph (LRIS; Oke, Cohen, et al. 1995) on the Keck-I telescope, the Double Spectrograph (DBSP; Oke and Gunn 1982) on the 200-inch Hale telescope, and the De Veny Spectrograph on the Lowell Discovery Telescope (LDT). Note that all DBSP observations are affected by a CCD malfunction, which results in a wavelength gap between 5750 Å and 6200 Å. The instrument configurations and data reduction procedures follow that described in Appendix B of Yao, Lu, et al. (2022).

We also made use of spectra uploaded to the transient name server (TNS) by other groups. For each TDE that was not previously reported in the literature, we release at least one optical spectrum in this paper. An observing log of the released data is provided in §7.8 (Table 7.7).[6]

Classification

As mentioned in §7.2, five of the 55 photometrically selected TDE candidates do not have spectroscopic classifications. Using light curves, host galaxy spectroscopy, and multi-wavelength information (see details below), we classify ZTF19aaciohh and ZTF20acvezvs as 'TDE?', ZTF19aaywayr as 'AGN?', and ZTF20aczhaeu and ZTF21abislwc as 'SN?'. Table 7.2 and Table 7.3 summarize 22 false positives and 33 TDEs. Below we comment on the individual events.

(I) False Positives — Among the list of 22 false positives, spectroscopic classifications are available for 19 objects: five were classified as Type Ia supernovae (SNe Ia); six were classified as Type II SNe (SNe II); two were classified as Type IIn SNe (SNe IIn); three were classified as hydrogen-poor superluminous SNe (SLSNe-I); two were classified as hydrogen-rich SLSNe (SLSNe-II); one was classified as AGN.

ZTF20aczhaeu and ZTF21abislwc are probably SNe since their post-peak color reddened significantly, which is different from known TDEs (see Figure 7.2).

ZTF19aaywayr is probably a slow AGN flare. In the forced photometry light curve, it has two peaks: the first at $m_r = 19.9$ mag in 2019 June, and the second at $m_r = 18.1$ mag in 2020 September. The rise time of the second peak is ≈ 400 d,

[6]Upon publication, all spectra in Table 7.7 will be available in electronic format on the Weizmann Interactive Supernova Data Repository (WISEReP, Yaron and Gal-Yam 2012).

Table 7.2: Spectroscopic classifications of 22 false positives.

ZTF name	Class	Reference
ZTF18abavruc	SN Ia	Angus (2021)
ZTF20aaivego	SN Ia	Dahiwale and Fremling (2020a)
ZTF20ackdkva	SN Ia	Dahiwale and Fremling (2020d)
ZTF21abcmepi	SN Ia	SNIascore (2021)
ZTF21abwjibi	SN Ia	Yao (2022)
ZTF20aaurjbj	SN II	Siebert (2020)
ZTF20aayxdse	SN II	Dahiwale and Fremling (2020c)
ZTF20achuhlt	SN II	Yan et al. (2020)
ZTF21aaglrzc	SN II	Dahiwale and Fremling (2021)
ZTF21abdmevk	SN II	Bruch et al. (2021)
ZTF21abzciqh	SN II	Chu, Dahiwale, and Fremling (2021c)
ZTF19abulzhy	SN IIn	Dahiwale and Fremling (2020b)
ZTF20abgoocl	SN IIn	Perley, Taggart, et al. (2020)
ZTF19acfwynw	SLSN-I	Nicholl, Short, et al., 2019
ZTF20abobpcb	SLSN-I	Perez-Fournon et al. (2020)
ZTF21aavdqgf	SLSN-I	Yao, Hammerstein, et al. (2021)
ZTF20aasuiks	SLSN-II	Tucker (2021)
ZTF20acbcfaa	SLSN-II	Pessi et al. (2020)
ZTF19abvgxrq	AGN	Frederick et al. (2021) and Yu, Kochanek, et al. (2022)
ZTF21abislwc	SN?	This work
ZTF20aczhaeu	SN?	This work
ZTF19aaywayr	AGN?	This work

which is a factor of ~ 10 longer than the typical rise time of the spectroscopically classified TDE sample. Therefore, we think it is more likley to be an AGN.

True Positives — The TDE classifications of 15 objects (ID 1–3, 5–6, 8–15, 18, 24) have been previously reported in refereed papers (Arcavi, Burke, et al., 2020; Nicholl, Wevers, et al., 2020; Hinkle et al., 2021; Stein et al., 2021; van Velzen, Gezari, Hammerstein, et al., 2021; Angus et al., 2022; Yao, Lu, et al., 2022; Hammerstein, van Velzen, et al., 2023).

Two objects were detected in the radio band with the VLA Sky Survey (VLASS; Lacy et al. 2020). In short, **ZTF19aaciohh/AT2019baf (ID 4)** is hosted by a galaxy with Seyfert-like emission line ratios. Multi-wavelength properties suggest that it is likely a TDE associated with a jet. **ZTF20acaazkt/AT2020vdq (ID 16)** can be spectroscopically classified as a TDE based on the existence of intermediate-width ($\sim 700\,\mathrm{km\,s^{-1}}$) transient Balmer lines, He II, and Fe X emission lines. Detailed properties of these two events will be presented as part of a sample of VLASS-selected TDE (candidates) with optical flares (see J. Somalwar et al. in prep).

ZTF19aaniqrr/AT2019cmw (ID 7) was first reported by Perley, Fremling, et al. (2020) as a peculiar transient discovered in the ZTF Bright Transient Survey (BTS;

Table 7.3: Basic information of 33 TDEs in our sample.

ID	ZTF Name	IAU Name	Redshift	TDE Report	Spectral Subtype
1	ZTF18acaqdaa	AT2018iih	0.212	1	TDE-He
2	ZTF18acnbpmd	AT2018jbv	0.340	2	TDE-featureless
3	ZTF19aabbnzo	AT2018lna	0.0914	1	TDE-H+He
4	ZTF19aaciohh	AT2019baf	0.0890	3; 4	Unknown
5	ZTF17aaazdba	AT2019azh	0.0222	5	TDE-H+He
6	ZTF19aakswrb	AT2019bhf	0.121	1	TDE-H
7	ZTF19aaniqrr	AT2019cmw	0.519	3; 6	TDE-featureless
8	ZTF19aapreis	AT2019dsg	0.0512	7	TDE-H+He
9	ZTF19aarioci	AT2019ehz	0.0740	1	TDE-H
10	ZTF19abzrhgq	AT2019qiz	0.0151	8	TDE-H+He
11	ZTF19acspeuw	AT2019vcb	0.0890	2	TDE-H+He
12	ZTF20aabqihu	AT2020pj	0.0680	2	TDE-H+He
13	ZTF20abfcszi	AT2020mot	0.0690	2	TDE-H+He
14	ZTF20abgwfek	AT2020neh	0.0620	9	TDE-H+He
15	ZTF20abnorit	AT2020ysg	0.277	2	TDE-featureless
16	ZTF20acaazkt	AT2020vdq	0.0450	3; 4	Unknown
17	ZTF20achpcvt	AT2020vwl	0.0325	10	TDE-H+He
18	ZTF20acitpfz	AT2020wey	0.0274	11	TDE-H+He
19	ZTF20acnznms	AT2020yue	0.204	3	TDE-H?
20	ZTF20acvezvs	AT2020abri	0.178	3	Unknown
21	ZTF20acwytxn	AT2020acka	0.338	12	TDE-featureless
22	ZTF21aaaokyp	AT2021axu	0.192	13	TDE-H+He
23	ZTF21aakfqwq	AT2021crk	0.155	3	TDE-H+He?
24	ZTF21aanxhjv	AT2021ehb	0.0180	14	TDE-featureless
25	ZTF21aauuybx	AT2021jjm	0.153	15	TDE-H
26	ZTF21abaxaqq	AT2021mhg	0.0730	16	TDE-H+He
27	ZTF21abcgnqn	AT2021nwa	0.0470	17	TDE-H+He
28	ZTF21abhrchb	AT2021qth	0.0805	3	TDE-coronal
29	ZTF21abjrysr	AT2021sdu	0.0590	18	TDE-H+He
30	ZTF21abqhkjd	AT2021uqv	0.106	19	TDE-H+He
31	ZTF21abqtckk	AT2021utq	0.127	3	TDE-H
32	ZTF21abxngcz	AT2021yzv	0.286	20	TDE-featureless
33	ZTF21acafvhf	AT2021yte	0.0530	21	TDE-H+He

The first 16 objects were selected from ZTF-I (from 2018 October 1 to 2020 September 30) with $m_{\rm peak} < 18.75$. The last 17 objects were selected from the first year of ZTF-II (from 2020 October 1 to 2021 September 30) with $m_{g,\rm peak} < 19.1$.

In the "TDE report" column, we include a refereed paper if existent. (1) van Velzen, Gezari, Hammerstein, et al. (2021) (2) Hammerstein, van Velzen, et al. (2023) (3) This paper (4) J. Somalwar et al. (in prep) (5) Hinkle et al. (2021) (6) J. Wise et al. (in prep) (7) Stein et al. (2021) (8) Nicholl, Wevers, et al. (2020) (9) Angus et al. (2022) (10) Hammerstein, Gezari, van Velzen, Kulkarni, et al. (2021a) (11) Arcavi, Burke, et al. (2020) (12) Hammerstein, Gezari, van Velzen, Kulkarni, et al. (2021b) (13) Hammerstein, Gezari, van Velzen, Yao, et al. (2021) (14) Yao, Lu, et al. (2022) (15) Yao, van Velzen, et al. (2021) (16) Chu, Dahiwale, and Fremling (2021a) (17) Yao, Gezari, et al. (2021) (18) Chu, Dahiwale, and Fremling (2021b) (19) Yao (2021b) (20) Chu, Dahiwale, and Fremling (2022) (21) Yao, Chu, et al. (2021)

Fremling, Miller, et al. 2020; Perley, Fremling, et al. 2020). With an absolute magnitude of $M < -23$ mag, it was the most luminous event in the BTS sample. Its high luminosity and featureless optical spectra make it similar to events previously classified as TDE-featureless by Hammerstein, van Velzen, et al. (2023). Detailed analysis and modeling of this object will be presented by J. Wise et al. (in preparation).

ZTF20acnznms/AT2020yue (ID 19) was previously classified as a SLSN-II by Kangas et al. (2022). However, some observed properties of this object favor a TDE interpretation. The upper panel of Figure 7.3 shows the UV and optical light curves. The color $uvm2 - r$ is 1.56 ± 0.19, 1.47 ± 0.22, and 0.37 ± 0.19 mag at $t \approx 14$ d, 37 d, and 278 d, respectively. This indicates a significant increase of temperature from 37 d to 278 d post peak, which is not uncommon in TDEs (Hammerstein, van Velzen, et al., 2023), but not observed in SLSNe.

The middle panel of Figure 7.3 shows the three optical spectra published in Kangas et al. (2022), as well as a deep late-time optical spectrum obtained by us in November 2022 using 85 min of LRIS on-source time (see details in Table 7.7). Broad Hα emission is seen in the −13 d, +6 d, and +39 d spectra. In the +6 d LRIS spectrum, we clearly identified narrow absorption lines of the Mg II λ2800 doublet as well as a broad absorption trough around rest-frame 2660 Å, which can be attributed to blueshifted Mg II absorption. Such NUV features have been observed in both SLSNe (Quimby et al., 2011; Chomiuk et al., 2011) and the TDE PS1-11af (Chornock et al., 2014).

At $\approx$ 595 d, the transient flux is still detected at $r = 22.3 \pm 0.3$ in the ZTF forced photometry. No broad lines characteristic of SLSN nebular emission (such as [O I] λ6300 and [Ca II] λ7300; Nicholl, Berger, et al. 2019) are observed. The 6500–6640 Å spectrum can be decomposed into three narrow components (from the host galaxy) and a broader component that originates from the transient (see the bottom panel of Figure 7.3). The late-time luminosity of the broad Hα component is 1.8×10^{40} erg s^{-1}, which is a factor of 5–10 times brighter than that observed in the optically selected TDEs ASASSN-14li and ASASSN-14ae (Brown, Holoien, et al., 2017) but similar to the radio-selected TDE VLASS J1008 (Somalwar et al. in prep). The full-width half-maximum (FWHM) of the transient Hα line decreased from $\approx$ 14000 km s^{-1} at early time to $\approx$ 2250 km s^{-1} at $\approx$ 595 d. Such a narrowing phenomenon has been observed in a few known TDEs (Brown, Holoien, et al., 2017; Onori et al., 2019; Nicholl, Wevers, et al., 2020) and can be explained by a decrease

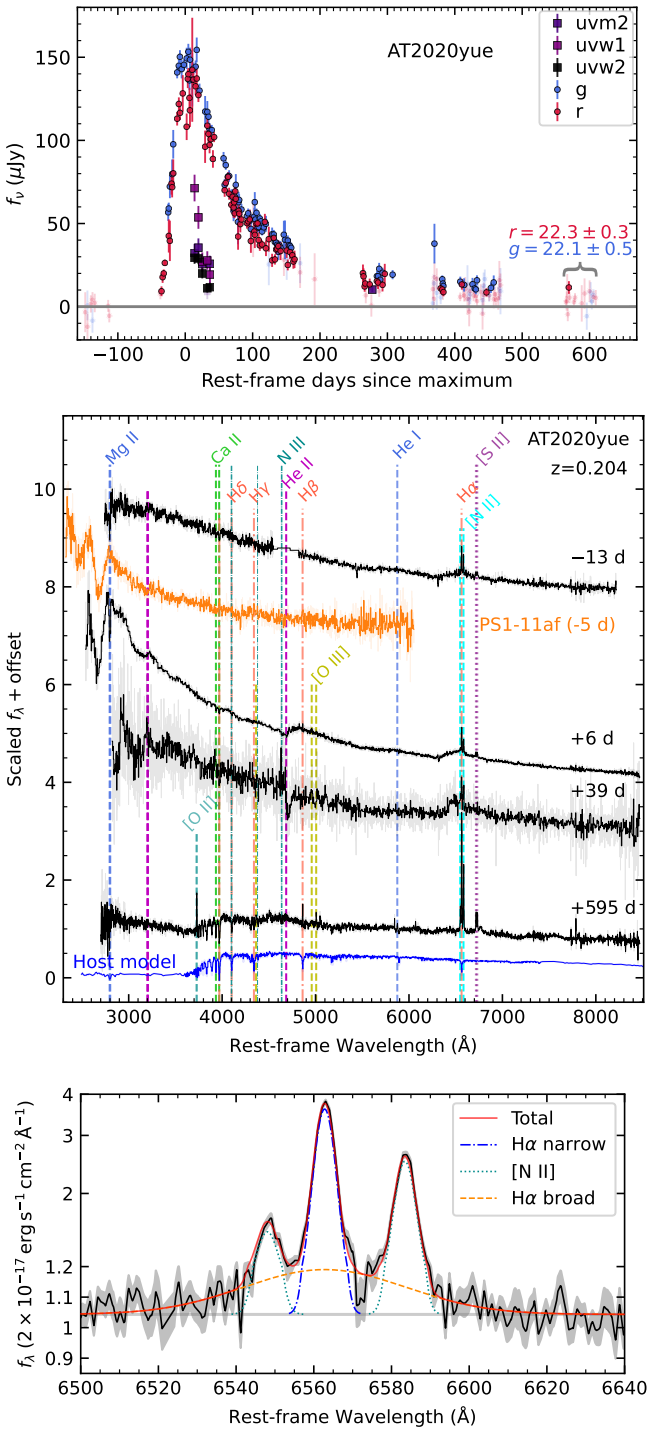

Figure 7.3: UV/optical properties of AT2020yue. *Upper*: ZTF and UV light curves. *Middle*: Optical spectra. *Bottom*: The +595 d spectrum zoomed around Hα.

in the optical depth of the line-emitting region (Roth and Kasen, 2018).

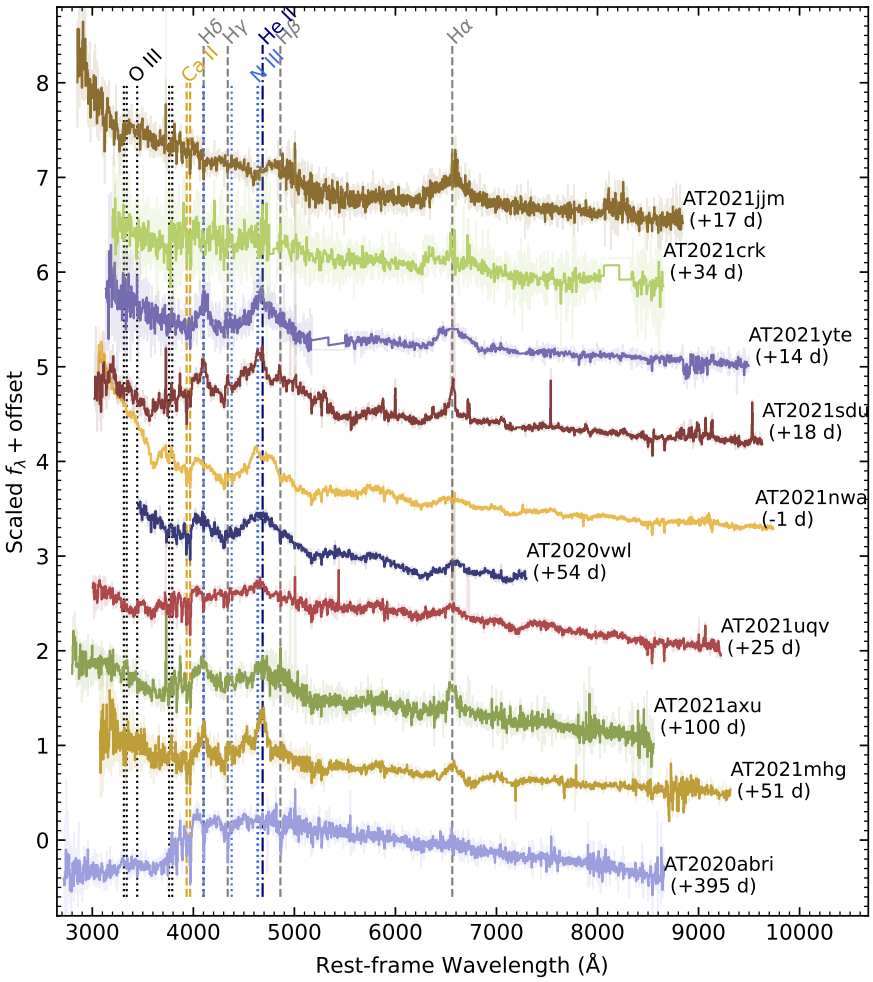

Figure 7.4: Optical spectra of 10 objects. The top 9 objects show broad emission lines characteristic of spectral classes of TDE-H, TDE-H+He, and TDE-He. The bottom spectrum was obtained for the host galaxy of AT2020abri.

ZTF20acvezvs/AT2020abri (ID 20) has no optical spectrum obtained during the optical flare. A post-flare spectrum clearly shows host galaxy absorption lines at $z = 0.178$ (see Figure 7.4). Following the procedures adopted by Sazonov et al. (2021), we measure the equivalent width (EW) of the Hα emission line and the Lick H$\delta_{\rm A}$ index, resulting in EW(H$\alpha_{\rm em}$) = 3.22 Å and Lick H$\delta_{\rm A,\,abs}$ = 5.52 Å. We consider this object to be a probable TDE since (*i*) its color remains blue ($g - r \approx -0.2$ mag) for ∼200 days (see Figure 7.2) and the lack of cooling makes it different from most SNe, (*ii*) the relatively strong Hδ absorption and weak Hα emission suggest that the host is a post-starburst galaxy, which is over-represented

in previous samples of TDE host galaxies (French, Arcavi, and Zabludoff, 2016; Law-Smith et al., 2017; French, Wevers, et al., 2020; Hammerstein, Gezari, van Velzen, Cenko, et al., 2021).

ZTF21aakfqwq/AT2021crk (ID 23) has a DBSP spectrum obtained during the optical flare, which is not of high signal-to-noise ratio (SNR) (see Figure 7.4). A broad emission line at Hα is clearly present (with the red wing slightly affected by telluric absorptions), while the He II wavelength region is affected by the DBSP CCD malfunction. Therefore, we tentatively assign a spectral subtype of TDE-H+He? for this object.

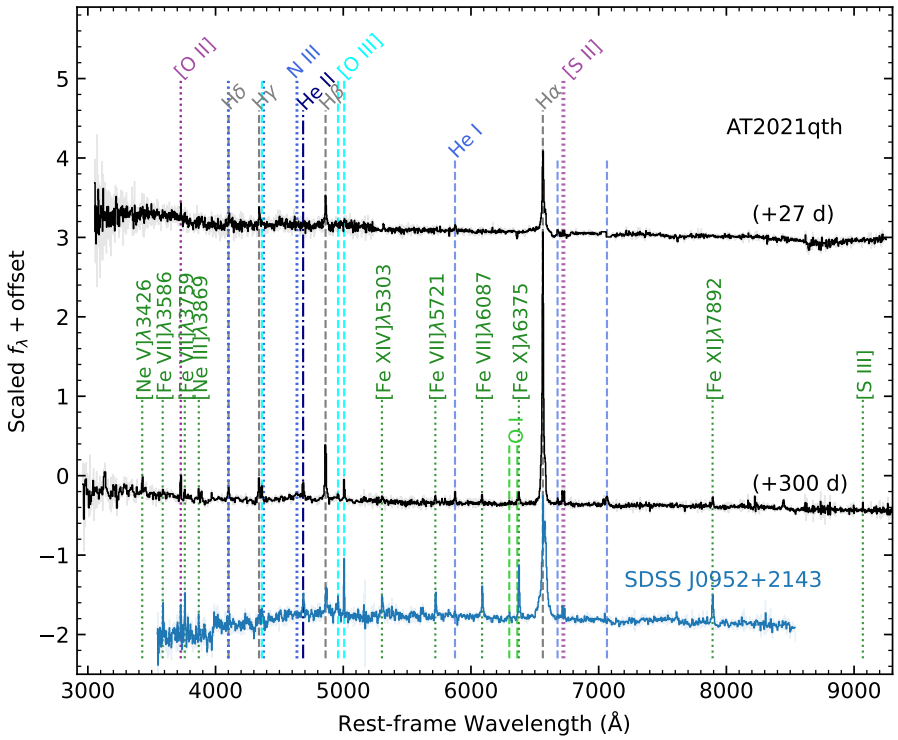

Figure 7.5: Optical spectra of AT2021qth, compared with the SDSS spectrum of the prototype extreme coronal line emitter SDSS J0952+2143 (Komossa et al., 2008; Palaversa et al., 2016).

ZTF21abhrchb/AT2021qth (ID 28) was missed by real-time selection with optical surveys, but was later revealed to be a TDE based on an X-ray detection at $L_{\rm X} \sim 6 \times 10^{42}\,{\rm erg\,s^{-1}}$ from eROSITA/*SRG* (private communication). X-ray data of this object will be presented as part of a sample of *SRG*-selected TDEs with strong optical flares by M. Gilfanov et al. (in prep). Such a high X-ray luminosity is not theoretically expected in interaction-powered SNe (see Fig. 3 of Margalit, Quataert, and Ho 2022), and $> \times 10$ brighter than the peak of the most X-ray luminous known

SN IIn (see, e.g., Fig. 7 of Yao, Ho, et al. 2022). Figure 7.5 shows that its late-time optical spectrum exhibits highly ionized narrow emission lines of [Ne III], [Ne V], [Fe VII], [Fe X], [Fe XI], and [Fe XIV] — reminiscent of the known class of extreme coronal line emitters (ECLEs; Komossa et al. 2008; Somalwar et al. 2022).

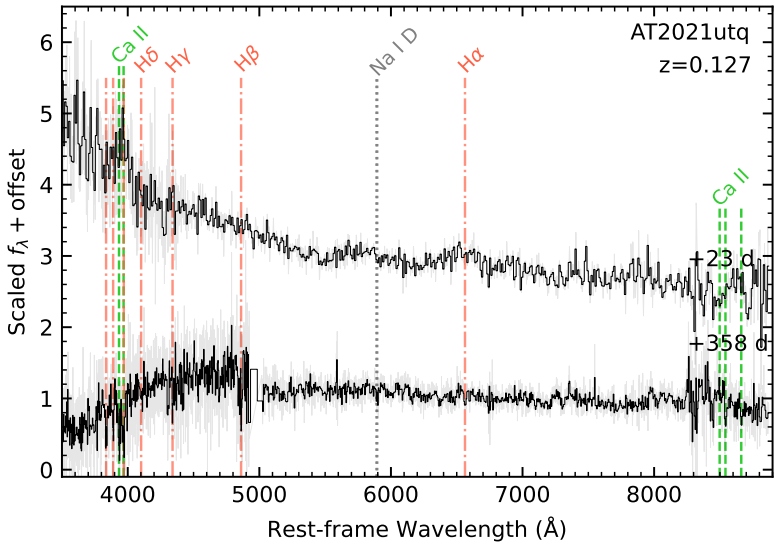

Figure 7.6: Optical spectra of AT2021utq.

ZTF21abqtckk/AT2021utq (ID 31) was previously classified as a variable star on TNS based on the fact that its parallax was reported by *Gaia* DR2 and that the distance was estimated by Bailer-Jones et al. (2018) to be ~ 1 kpc (Burke, Arcavi, et al., 2021). However, both the *Gaia* parallax ($\varpi = -0.91 \pm 1.51$ mas) and the distance estimate ($1.16^{+0.81}_{-0.50}$ kpc) have large uncertainties. Moreover, a post-flare optical spectrum reveals host galaxy absorption lines at $z = 0.127$ (see Figure 7.6). At this redshift, the early-time spectrum reported by Burke, Arcavi, et al. (2021) exhibits a board emission line at Hα, suggesting a spectral class of TDE-H.

The TDE classifications of the remaining 10 objects have been previously reported to TNS by the ZTF group. Their optical spectra are shown in Figure 7.4 for objects with broad emission lines, and in Figure 7.7 for two objects in the TDE-featureless spectral class.

We note that although TDEs can evolve and change spectroscopic subtypes (Nicholl, Blanchard, et al., 2019; van Velzen, Holoien, et al., 2020), a precise labeling of the subtype is not important for this work.

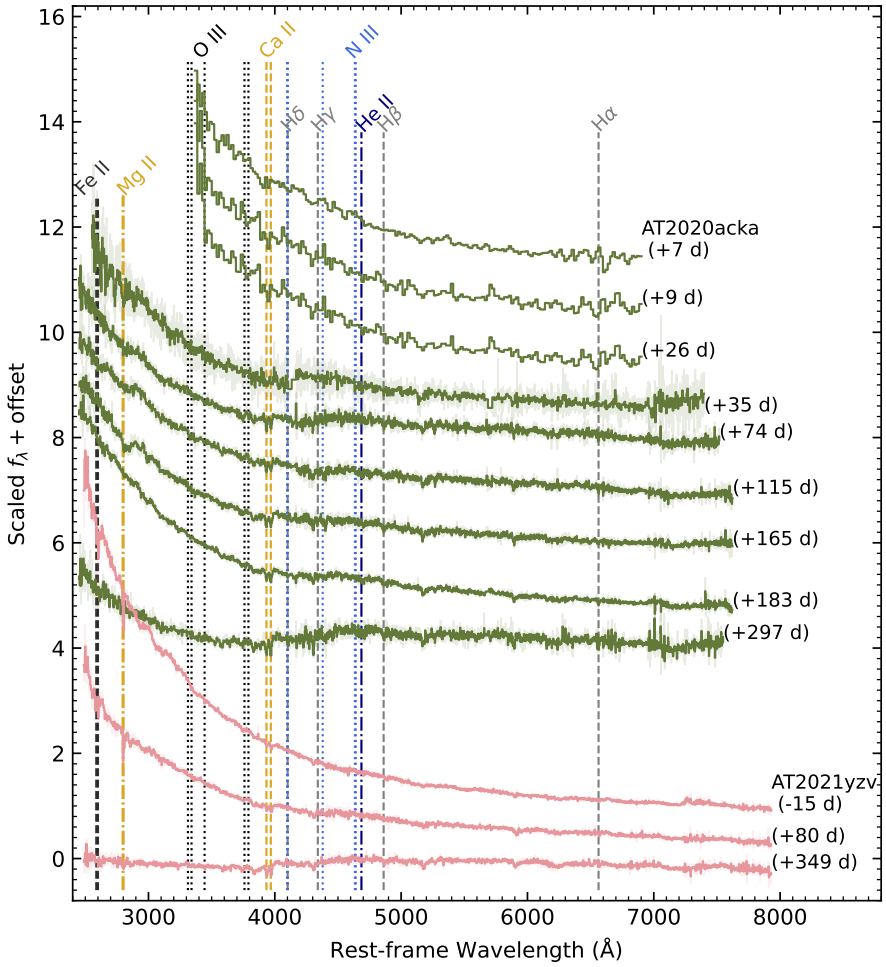

Figure 7.7: Optical spectra of two TDEs that belong to the TDE-featureless subclass.

7.3 Light Curve Characterization

In this section, we aim to systematically estimate the peak-light properties and light curve evolution timescales of the 33 TDEs. Below we outline the procedures of the fitting routine, describe the choice of the light curve model, and summarize the results.

The Fitting Routine

Model fitting was performed using the Markov chain Monte Carlo (MCMC) approach with the `emcee` sampler (Foreman-Mackey, Hogg, et al., 2013). For each TDE (at redshift z) and each observation i, the input data are t_i (rest-frame days relative to the visually-determined light curve maximum), L_i, σ_i (Galactic extinction corrected luminosity and its uncertainty in the observed band), and ν_i (rest-frame

effective frequency of the observed band). We assume negligible host galaxy extinction.

Following Yao, Miller, et al. (2019), we add a constant additional variance σ_0^2 to each of the measurement variance σ_i^2 to account for systematic uncertainties. We use 100 walkers and N steps, where N is typically 1000–3000. We visually inspect the walker values as a function of step to ensure convergence. The posterior distribution is obtained after discarding the first $N - 500$ steps.

The Light Curve Model

The SED Shape — It has been shown that the UV/optical emission of TDEs can be described with a thermal blackbody (Gezari, 2021). Therefore, we assume that the UV/optical spectrum follows a blackbody $B_\nu(T_{\rm bb})$. Our goal is to determine the blackbody parameters (temperature $T_{\rm bb}$, radius $R_{\rm bb}$, and luminosity $L_{\rm bb}$) at maximum light.

Since the majority of known TDEs show little temperature evolution (van Velzen, Holoien, et al., 2020), we assume the temperature is fixed to that near peak. However, this assumption is not appropriate for a few TDEs in our sample (ID 2, 5, 7, 8, 10, 13, 14, 18, 21, 24, 27) with significant post-peak $uvw2 - r$ color change. Since our goal is to constrain the peak-light blackbody parameters, we excluded late-time UVOT data for these objects.[7]

The Rise Function — Following van Velzen, Gezari, Hammerstein, et al. (2021), we first model the light curve at $t < 100\,{\rm d}$ with a Gaussian rise and an exponential decay:

$$L_\nu(t) = A_\nu \times \begin{cases} e^{(t-t_{\rm peak})^2/(2\sigma^2_{\rm rise})} & t \le t_{\rm peak} \\ e^{-(t-t_{\rm peak})/\tau_{\rm decay}} & t > t_{\rm peak} \end{cases} \tag{7.1}$$

where $A_\nu = L_{\nu_0\,{\rm peak}} \frac{B_\nu(T_0)}{B_{\nu_0}(T_0)}$. Here $L_{\nu_0\,{\rm peak}}$ is the rest-frame g-band ($\nu_0 = 6.3 \times 10^{14}$ Hz) peak luminosity, and $t_{\rm peak}$ is the epoch of rest-frame g-band maximum.

A Gaussian function is generally a good model when the data sampling is sparse on the rise, since it reduces the model complexity by imposing strong assumptions on the shape of the light curve profile. However, it can not describe a rise where the flux increase rate decreases as a function of time (e.g., see Figure 7.8). Therefore,

[7] We removed UVOT data at $t \gtrsim t_{\rm c/h}$, where $t_{\rm c/h}$ is the time when clear evidence of post-peak cooling/heating is observed. We chose $t_{\rm c/h} \in (5, 100)\,{\rm d}$ for each of the 10 objects by visually inspecting their multi-band light curves.

Table 7.4: Light curve properties of 33 ZTF TDEs.

ID	Model	$t_{\rm peak}$ (MJD)	$\log T_{\rm bb}$ (K)	$\log L_g$ (erg s^{-1})	$\log L_{\rm bb}$ (erg s^{-1})	$\log R_{\rm bb}$ (cm)	$t_{1/2,\rm rise}$ (days)	$t_{1/2,\rm decline}$ (days)
1	r2+d2	$58451.13^{+2.78}_{-2.20}$	4.22	44.11	44.59	15.43	$31.0^{+2.5}_{-1.5}$	$86.5^{+3.3}_{-5.0}$
2	r1+d2	$58470.36^{+0.00}_{-0.00}$	4.50	44.23	45.33	15.24	$34.4^{+2.1}_{-1.4}$	$65.9^{+2.3}_{-1.7}$
3	r1+d1	$58507.31^{+1.20}_{-0.95}$	4.49	43.21	44.27	14.73	$15.5^{+1.3}_{-1.0}$	$30.2^{+1.3}_{-1.1}$
4	r2+d6	$58514.16^{+0.82}_{-0.78}$	4.10	43.52	43.81	15.28	$23.2^{+0.9}_{-1.0}$	$27.6^{+0.6}_{-0.9}$
5	r2+d2	$58561.39^{+1.05}_{-0.77}$	4.46	43.30	44.31	14.80	$24.7^{+1.3}_{-1.0}$	$44.1^{+1.1}_{-0.9}$
6	r1+d2	$58544.78^{+1.10}_{-1.34}$	4.14	43.46	43.81	15.20	$9.9^{+0.7}_{-0.9}$	$29.1^{+1.9}_{-1.4}$
7	r2+d2	$58588.82^{+0.00}_{-0.00}$	4.34	44.68	45.41	15.60	$14.0^{+0.3}_{-0.3}$	$28.9^{+0.7}_{-0.5}$
8	r1+d1	$58606.97^{+3.51}_{-3.22}$	4.41	43.18	44.05	14.79	$19.7^{+2.3}_{-2.0}$	$43.1^{+1.0}_{-1.1}$
9	r2+d6	$58618.69^{+0.70}_{-0.51}$	4.29	43.28	43.90	14.94	$15.7^{+0.7}_{-0.8}$	$28.0^{+0.0}_{-1.0}$
10	r1+d4	$58766.50^{+0.25}_{-0.26}$	4.23	42.90	43.40	14.81	$11.6^{+0.3}_{-0.3}$	$17.9^{+0.7}_{-0.8}$
11	r1+d1	$58819.83^{+1.08}_{-0.89}$	4.11	43.35	43.65	15.19	$13.6^{+1.1}_{-0.8}$	$24.6^{+0.4}_{-0.4}$
12	r1+d2	$58866.42^{+0.58}_{-0.55}$	4.10	42.95	43.24	14.99	$12.4^{+0.7}_{-0.5}$	$17.2^{+1.3}_{-1.1}$
13	r1+d4	$59082.04^{+1.24}_{-1.30}$	4.29	43.22	43.84	14.92	$42.6^{+1.3}_{-1.6}$	$46.1^{+1.9}_{-2.1}$
14	r1+d1	$59030.93^{+0.53}_{-0.39}$	4.19	43.26	43.70	15.04	$6.4^{+0.4}_{-0.4}$	$16.4^{+0.6}_{-0.6}$
15	r1+d2	$59094.32^{+3.30}_{-3.03}$	4.37	44.24	45.04	15.35	$24.0^{+2.1}_{-1.5}$	$72.5^{+2.1}_{-3.3}$
16	r1+d2	$59113.09^{+1.00}_{-0.93}$	4.16	42.62	42.99	14.76	$11.9^{+1.7}_{-1.3}$	$23.3^{+1.5}_{-1.7}$
17	r1+d4	$59166.88^{+1.17}_{-1.14}$	4.30	43.13	43.77	14.86	$22.2^{+0.8}_{-0.7}$	$27.4^{+1.9}_{-1.7}$
18	r1+d5	$59155.84^{+0.19}_{-0.20}$	4.32	42.47	43.15	14.51	$13.9^{+0.4}_{-0.4}$	$5.2^{+0.2}_{-0.2}$
19	r1+d4	$59179.44^{+1.25}_{-1.12}$	4.06	44.00	44.24	15.57	$19.5^{+1.0}_{-0.9}$	$62.8^{+2.0}_{-1.9}$
20	r2+d3	$59208.56^{+0.83}_{-0.80}$	4.10	43.66	43.95	15.35	$16.7^{+1.2}_{-0.9}$	$31.7^{+0.7}_{-0.8}$
21	r1+d5	$59217.15^{+1.38}_{-1.14}$	4.45	44.47	45.44	15.39	$26.9^{+1.6}_{-1.8}$	$28.8^{+0.7}_{-0.5}$
22	r1+d2	$59252.50^{+0.55}_{-0.50}$	4.58	43.75	45.05	14.93	$23.9^{+0.5}_{-0.6}$	$33.4^{+0.9}_{-1.0}$
23	r1+d2	$59273.90^{+0.53}_{-0.52}$	4.30	43.50	44.14	15.05	$10.2^{+0.7}_{-0.4}$	$20.9^{+1.1}_{-1.1}$
24	r1+d3	$59314.51^{+2.78}_{-1.90}$	4.44	42.58	43.54	14.46	$23.7^{+1.9}_{-1.4}$	$50.5^{+3.6}_{-3.8}$
25	r1+d1	$59327.68^{+0.99}_{-0.93}$	4.17	43.59	43.99	15.23	$9.1^{+0.7}_{-0.7}$	$29.1^{+2.6}_{-1.7}$
26	r1+d4	$59370.28^{+0.89}_{-0.85}$	4.49	43.22	44.28	14.74	$17.2^{+0.7}_{-0.7}$	$14.7^{+1.1}_{-1.0}$
27	r1+d3	$59402.51^{+0.64}_{-0.68}$	4.51	42.68	43.81	14.45	$27.1^{+0.6}_{-0.8}$	$76.2^{+1.9}_{-1.6}$
28	r2+d4	$59401.88^{+1.26}_{-1.26}$	3.96	43.14	43.30	15.30	$15.8^{+1.2}_{-1.3}$	$39.1^{+1.3}_{-2.0}$
29	r1+d3	$59419.36^{+0.33}_{-0.36}$	4.30	43.09	43.73	14.84	$12.2^{+0.4}_{-0.4}$	$11.0^{+0.3}_{-0.4}$
30	r1+d5	$59446.39^{+0.66}_{-0.63}$	4.29	43.15	43.77	14.87	$14.9^{+0.7}_{-0.7}$	$36.0^{+2.2}_{-2.0}$
31	r1+d6	$59457.51^{+0.83}_{-0.85}$	4.39	43.39	44.22	14.91	$14.6^{+0.6}_{-0.6}$	$43.4^{+5.8}_{-4.3}$
32	r2+d2	$59511.50^{+1.35}_{-1.38}$	4.43	44.07	45.01	15.21	$51.8^{+1.4}_{-1.2}$	$69.9^{+2.6}_{-2.6}$
33	r1+d3	$59484.99^{+0.59}_{-0.60}$	4.29	42.90	43.52	14.75	$18.4^{+0.5}_{-0.6}$	$23.7^{+0.7}_{-0.7}$

Column 2 indicates the light curve rise and decline functional forms of the adopted model. `r1`: Gaussian rise, `r2`: power-law rise. See text for the meaning of the six decline models.
Columns 3–9 are light curve properties (see text for definitions).

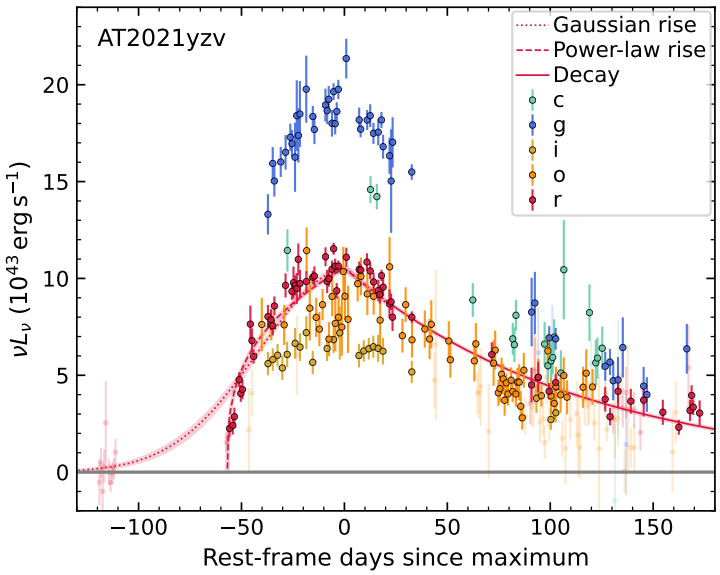

Figure 7.8: ZTF and ATLAS light curves of AT2021yzv, overplotted with the best-fit models in the ZTF r band.

for objects with good sampling on the rise[8], we also fit the rise with a power-law function:

$$L_\nu(t) = A_\nu \times \begin{cases} 0 & t \leq t_{\rm fl} \\ \frac{(t-t_{\rm fl})^n}{(t_{\rm peak}-t_{\rm fl})^n} & t_{\rm fl} < t \leq t_{\rm peak} \end{cases} \tag{7.2}$$

where $t_{\rm fl}$ is the first-light epoch and n is the rise power-law index. We consider the power-law rise model to be superior to the Gaussian rise model if the best-fit σ_0 is smaller *and* the 68% confidence region of n is < 0.5. The adopted rise function for each TDE is given in the 'Model' column of Table 7.4.

The Decline Function — Having decided on the rise function, we fit the light curve within $t < 365$ d with six types of decline functions:

1. An exponential decline (model `d1`; Eq. 7.1)

2. A power-law decline (model `d2`):

$$L_\nu(t) = A_\nu \left(\frac{t - t_{\rm peak} + t_0}{t_0} \right)^p \quad t > t_{\rm peak} \tag{7.3}$$

[8]Here "good sampling" is defined as follows. For each object, we select data within $[t_{\rm peak} - 2\sigma_{\rm rise}, t_{\rm peak} + \sigma_{\rm rise}]$, where $t_{\rm peak}$ and $\sigma_{\rm rise}$ are best-fit model parameters from Eq. 7.1. We require that the maximum time separation in consecutive pairs of observations is less than $\sigma_{\rm rise}$.

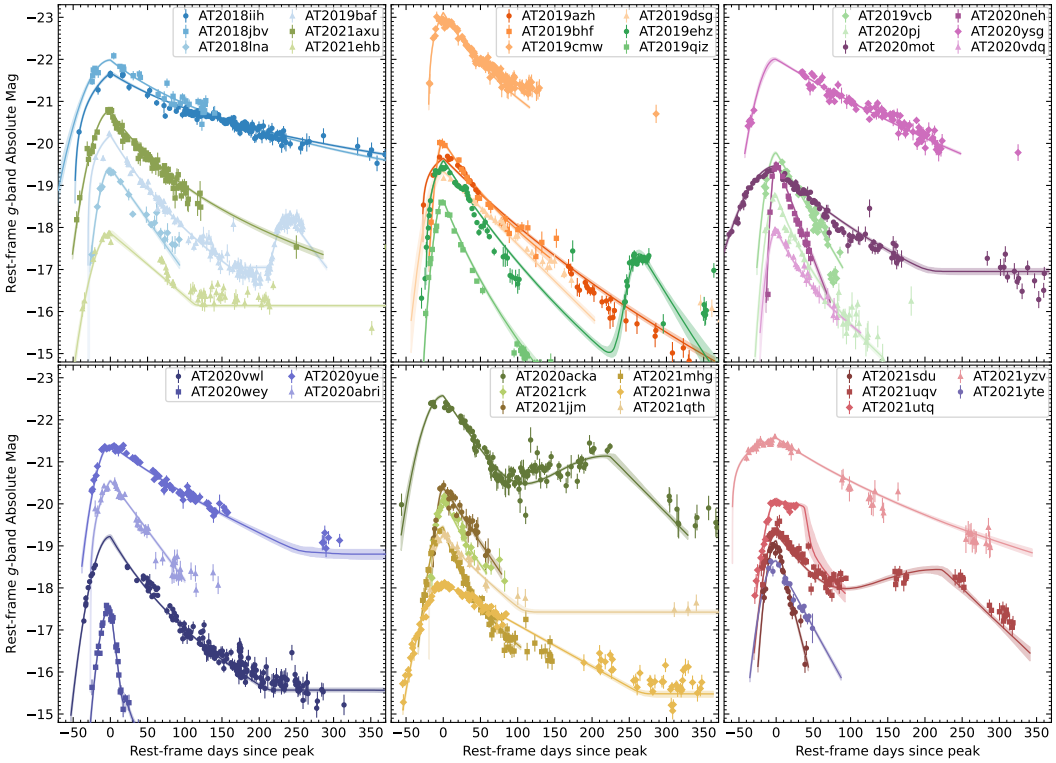

Figure 7.9: Rest-frame g-band light curves of the 33 TDEs in our sample. The solid lines show the best-fit models.

3. An exponential decline followed by a late-time plateau (model `d3`),
4. A power-law decline followed by a late-time plateau (model `d4`).
5. An exponential decline with a secondary peak on top of that (model `d5`),
6. A power-law decline with a secondary peak on top of that (model `d6`).

In functions `d5` and `d6`, we assume that the secondary peak has a Gaussian rise and an exponential decline. We compare the Bayesian information criterion (BIC) of the six model fits and choose the one with the smallest value of BIC. The adopted decline function for each TDE is given in the 'Model' column of Table 7.4.

The Fitting Results

Figure 7.9 shows the fitting results. The light curve properties obtained with the best-fit models are provided in Table 7.4, where $t_{\rm peak}$ is the peak light epoch, $T_{\rm bb}$, $L_{\rm bb}$, and $R_{\rm bb}$ are the blackbody parameters at peak, L_g is the rest-frame g-band luminosity at peak (corrected for Galactic extinction). Following conventions of transient studies

(Ho, Perley, Gal-Yam, et al., 2021; Yao, Ho, et al., 2022), we characterize the light curve evolution speed by calculating the rest-frame duration it takes for a TDE to rise from half-max to max ($t_{1/2,\mathrm{rise}}$) and to decline from max to half-max ($t_{1/2,\mathrm{decline}}$). The rest-frame duration above half-max light is $t_{1/2} \equiv t_{1/2,\mathrm{rise}} + t_{1/2,\mathrm{decline}}$.

7.4 Host Galaxies

Observation

For the TDE host galaxies, we retrieved science-ready coadded images from the *Galaxy Evolution Explorer* (*GALEX*) general release 6/7 (Martin et al., 2005), the Sloan Digital Sky Survey data release 9 (SDSS DR9; Ahn et al. 2012), the PS1, the Two Micron All Sky Survey (2MASS; Skrutskie et al. 2006), and the unWISE archive (Lang, 2014). We measured the brightness of the host galaxies using the `Lambda Adaptive Multi-Band Deblending Algorithm in R` (`LAMBDAR`; Wright, Robotham, Bourne, et al. 2016) and the methods described in Schulze et al. (2021).

We note that some fields were observed more than once with *GALEX*, while the Schulze et al. (2021) pipeline only utilizes the deepest *GALEX* exposure. Therefore, in two objects (ID 8, 28), to make the most of *GALEX* observations, we supplemented the `LAMBDAR` measurements with *GALEX* photometry extracted by `gPhoton` (Million et al., 2016). We adopted an aperture of 10″ and 5″ for the host galaxies of AT2019dsg and AT2021qth, respectively. §7.8 presents the photometry in different bands.

To measure the velocity dispersion of TDE host galaxies, we obtained medium-resolution spectra using the Echellette Spectrograph and Imager (ESI; Sheinis et al. 2002) on the Keck-II telescope. In all observations, we used the Echelle mode. Spectra were obtained for the host galaxies of 15 TDEs (see Table 7.8 in §7.8 for details). A slit width of 0.3″, 0.5″, and 0.75″ gives an instrumental broadening of σ_{inst} = 9.5, 15.8, and 23.7 km s^{-1}. We reduced the ESI spectra with the `makee` pipeline. We extracted the spectrum using a radius of r_{extract}, which was implemented by specifying the `hw` and `uop` parameters in `makee`. For most objects, r_{extract} was chosen to match the half-light radius (see $r_{1/2}$ in Table 7.5). For a few faint host galaxies, r_{extract} was chosen to enclose a larger aperture to maximize the SNR.

Analysis

ESI Spectral Fitting — The galaxy central velocity dispersion σ_* (i.e., the intensity weighted mean of the root-mean-square of the line-of-sight stellar velocity) is known

Table 7.5: Parameters Related to Survey Efficiency and $M_{\rm BH}$.

ID	$D_{\rm max,\,t}$ (Mpc)	$z_{\rm max,\,t}$	$f_{\rm loss}$	$\log M_{\rm BH}$ ($M_\odot$)	σ_* (km s^{-1})	$r_{1/2}$ ($''$)	$z_{\rm max,\,h}$
1	1501	0.291	0.525	7.93 ± 0.35	148.64 ± 14.42	1.5	0.60
2	2052	0.381	0.328	6.72 ± 0.40	—	1.0	0.52
3	488	0.106	0.241	5.59 ± 0.53	—	1.4	0.26
4	668	0.141	0.475	6.83 ± 0.27	—	1.8	0.43
5	547	0.118	0.652	6.44 ± 0.33	67.99 ± 2.03	4.0	0.41
6	630	0.134	0.207	7.03 ± 0.26	—	1.7	0.45
7	3714	0.626	0.288	7.82 ± 0.42	—	1.0	0.63
8	465	0.101	0.526	6.90 ± 0.32	86.89 ± 3.92	2.5	0.42
9	521	0.112	0.380	5.82 ± 0.48	—	1.7	0.32
10	322	0.0714	0.545	6.48 ± 0.33	69.70 ± 2.30	9.9	0.27
11	546	0.117	0.309	6.03 ± 0.39	—	1.2	0.44
12	335	0.0742	0.158	6.41 ± 0.33	—	1.7	0.35
13	485	0.105	0.515	6.66 ± 0.34	76.61 ± 5.33	1.4	0.49
14	501	0.108	0.269	5.43 ± 0.46	40.00 ± 6.00	1.7	0.38
15	1963	0.367	0.463	7.52 ± 0.28	—	1.2	0.56
16	227	0.0511	0.210	5.59 ± 0.37	43.56 ± 3.07	1.3	0.27
17	515	0.111	0.623	5.79 ± 0.35	48.49 ± 2.00	2.4	0.27
18	228	0.0514	0.302	5.40 ± 0.38	39.36 ± 2.79	2.1	0.24
19	1399	0.274	0.465	6.71 ± 0.33	—	1.5	0.59
20	948	0.194	0.261	5.65 ± 0.53	—	0.9	0.36
21	3629	0.614	0.514	8.23 ± 0.40	174.47 ± 25.30	1.1	0.70
22	1253	0.249	0.368	6.59 ± 0.55	73.50 ± 17.26	1.2	0.51
23	831	0.173	0.216	6.12 ± 0.39	57.62 ± 6.29	1.6	0.48
24	265	0.0593	0.661	7.16 ± 0.32	99.58 ± 3.83	3.3	0.27
25	893	0.184	0.304	5.54 ± 0.54	—	0.7	0.52
26	595	0.127	0.399	6.13 ± 0.37	57.78 ± 5.25	1.0	0.31
27	301	0.0669	0.483	7.22 ± 0.32	102.44 ± 5.37	1.7	0.36
28	481	0.104	0.374	5.95 ± 0.49	—	1.2	0.31
29	488	0.106	0.340	6.64 ± 0.31	—	2.6	0.42
30	525	0.113	0.251	6.27 ± 0.39	62.30 ± 7.08	1.4	0.49
31	736	0.155	0.390	5.85 ± 0.45	—	1.1	0.45
32	1920	0.360	0.456	7.74 ± 0.36	—	1.5	0.61
33	385	0.0847	0.413	5.13 ± 0.45	34.22 ± 4.81	1.6	0.29

Columns 2–4, and 8 are parameters relevant to the survey efficiencies (see §7.5 for definitions).

The black hole mass $M_{\rm BH}$ is inferred using the $M_{\rm BH}$–σ_* scaling relation for the 17 objects with available σ_* measurements, and using the $M_{\rm BH}$–$M_{\rm gal}$ scaling relation for the remaining 16 objects.

$r_{1/2}$ is the mean of (seeing-corrected) half-light radii in the g-, r-, and i-band images as measured by `LAMBDAR`.

to be correlated with the central massive black hole mass (Merritt and Ferrarese, 2001; Pinkney et al., 2003; Gültekin, Richstone, et al., 2009; Kormendy and Ho, 2013). Following previous works (Wevers, van Velzen, et al., 2017; Somalwar et al., 2022), we measured σ_* with the penalized pixel-fitting (`pPXF`) software (Cappellari and Emsellem, 2004; Cappellari, 2017), which fits the ESI absorption line spectrum by convolving a template stellar spectral library with Gauss-Hermite functions.

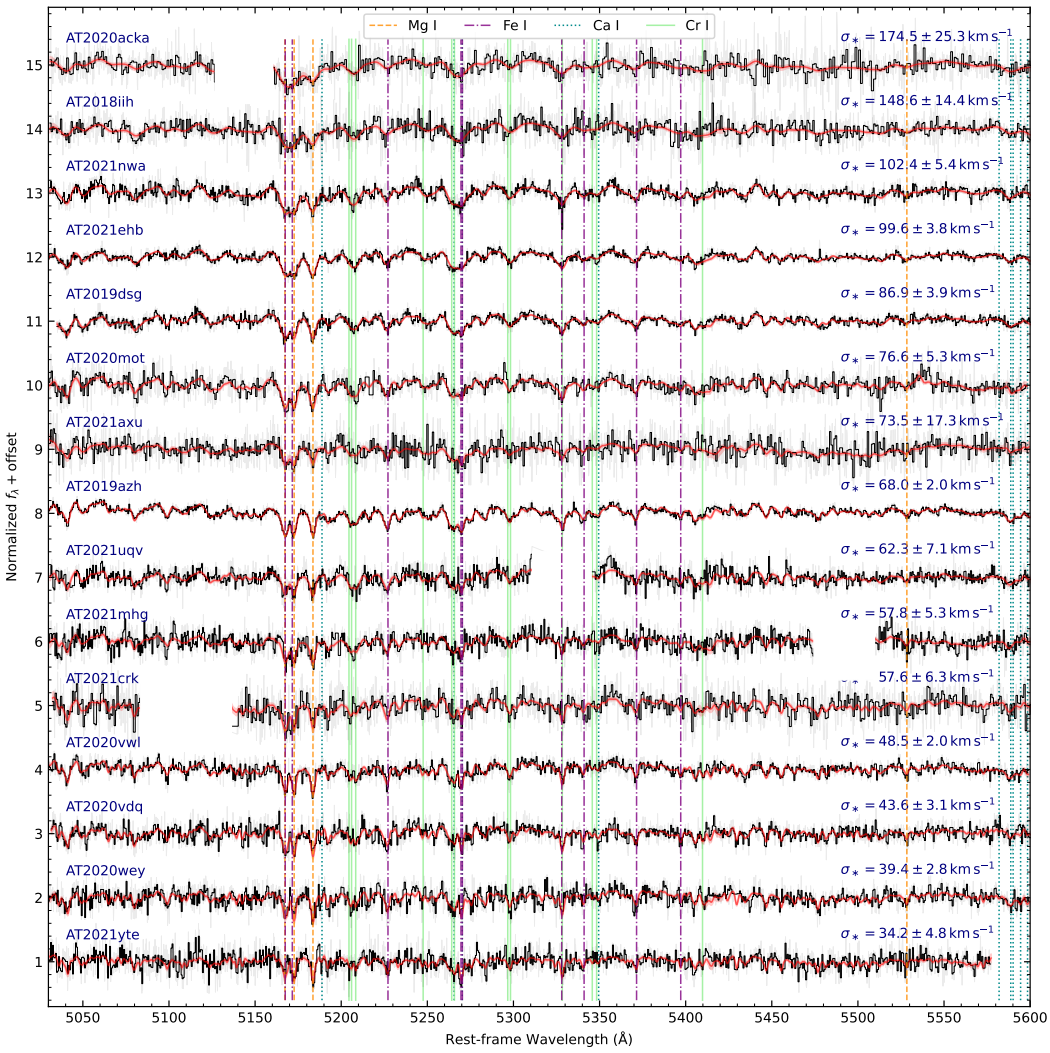

Figure 7.10: ESI spectra of 15 TDE host galaxies arranged in order of decreasing σ_*.

We used the ELODIE v3.1 high resolution ($R = 42000$) library (Prugniel and Soubiran, 2001; Prugniel, Soubiran, et al., 2007). For all ESI spectra, we fit the rest-frame wavelength range from 5030 Å to 5600 Å. Prominent galaxy absorption

lines[9] of Mg I, Fe I, Ca I, and Cr I in this wavelength range are shown in Figure 7.10. We masked wavelength ranges of common galaxy emission lines, hydrogen Balmer lines, telluric regions, an instrument artifact feature at observer-frame ~ 4510 Å, and the Na I D doublet at $z = 0$ if Galactic absorption is strong.

Following previous works (Wevers, van Velzen, et al., 2017; Wevers, Stone, et al., 2019; French, Wevers, et al., 2020), we performed 1000 Monte Carlo (MC) simulations to robustly determine σ_*. In each MC simulation, the observed spectrum was re-sampled within its error spectrum and re-fitted with `pPXF`. By visually examining results of the simulations, we confirmed that the distributions of the velocity dispersion are well-behaved (i.e., not double-peaked or skewed). We took the median of the distribution as the velocity dispersion, and the difference between the $84^{\rm th}/16^{\rm th}$ percentiles as the uncertainty. The best-fit spectra and the measured σ_* are shown in Figure 7.10.

SED Fitting — We modelled the photometric spectral energy distribution of host galaxies with the software package `prospector` version 1.1 (Johnson et al., 2021). `prospector` uses the `Flexible Stellar Population Synthesis` (`FSPS`) code (Conroy, Gunn, and White, 2009) to generate the underlying physical model and `python-fsps` (Foreman-Mackey, Sick, and Johnson, 2014) to interface with `FSPS` in python. We assumed a Chabrier initial mass function (Chabrier, 2003) and approximated the star formation history (SFH) by a delayed exponentially declining function. The model was attenuated with the Calzetti et al. (2000) model. The fitted parameters are presented in Table 7.6, where $M_{\rm gal}$ is the host galaxy total stellar mass, ${}^{0,0}u - r$ is the Galactic extinction-corrected, synthetic rest-frame $u - r$ color, $\tau_{\rm SFH}$ is the characteristic e-folding timescale of the SFH, $t_{\rm age}$ is the stellar age, Z is the metallicity, and $E(B-V)_{\rm h}$ is the host galaxy extinction. The best-fit galaxy SEDs are shown in §7.8.

A fraction of our TDE host galaxies have been analyzed with similar approaches in the literature (Ramsden et al., 2022; Hammerstein, van Velzen, et al., 2023). In §7.8, we show that our estimates of $M_{\rm gal}$ and ${}^{0,0}u - r$ are mostly consistent with previous results, and point out possible reasons for the differences.

Black Hole Mass Estimates — Here we estimate the BH mass $M_{\rm BH}$ of our TDE sample using host galaxy scaling relations.

[9] We take the strong lines table in the National Institute of Standards and Technoloty (NIST) atomic database.

Table 7.6: Host galaxy properties.

ID	$\log M_{\rm gal}$ ($M_\odot$)	${}^{0,0}u-r$ (mag)	$\tau_{\rm SFR}$ (Gyr)	$t_{\rm age}$ (Gyr)	$\log Z$ ($Z_\odot$)	$E(B-V)_{\rm h}$ (mag)
1	$10.69^{+0.12}_{-0.16}$	$2.17^{+0.09}_{-0.13}$	$0.33^{+0.54}_{-0.19}$	$8.59^{+2.81}_{-3.63}$	$-1.02^{+0.43}_{-0.65}$	$0.13^{+0.10}_{-0.09}$
2	$10.20^{+0.17}_{-0.19}$	$1.98^{+0.18}_{-0.19}$	$0.71^{+1.29}_{-0.50}$	$7.87^{+3.38}_{-3.73}$	$-1.27^{+0.61}_{-0.51}$	$0.15^{+0.08}_{-0.09}$
3	$9.50^{+0.12}_{-0.17}$	$1.84^{+0.11}_{-0.19}$	$0.37^{+0.60}_{-0.22}$	$8.33^{+2.66}_{-3.29}$	$-1.43^{+0.43}_{-0.39}$	$0.06^{+0.04}_{-0.04}$
4	$10.27^{+0.04}_{-0.05}$	$1.75^{+0.05}_{-0.04}$	$3.23^{+0.76}_{-0.95}$	$10.57^{+1.35}_{-2.40}$	$-0.54^{+0.27}_{-0.39}$	$0.17^{+0.04}_{-0.04}$
5	$9.88^{+0.03}_{-0.03}$	$1.76^{+0.01}_{-0.01}$	$0.29^{+0.05}_{-0.04}$	$2.26^{+0.28}_{-0.24}$	$-0.63^{+0.10}_{-0.10}$	$0.06^{+0.01}_{-0.01}$
6	$10.39^{+0.05}_{-0.06}$	$1.96^{+0.04}_{-0.04}$	$1.74^{+0.35}_{-0.47}$	$10.45^{+1.49}_{-2.29}$	$-0.95^{+0.42}_{-0.44}$	$0.12^{+0.05}_{-0.05}$
7	$10.88^{+0.17}_{-0.20}$	$2.22^{+0.12}_{-0.24}$	$0.40^{+1.00}_{-0.23}$	$7.40^{+3.39}_{-3.61}$	$-0.74^{+0.60}_{-0.85}$	$0.16^{+0.09}_{-0.10}$
8	$10.34^{+0.06}_{-0.05}$	$2.12^{+0.04}_{-0.04}$	$0.49^{+0.13}_{-0.09}$	$4.30^{+0.96}_{-0.69}$	$0.11^{+0.05}_{-0.07}$	$0.01^{+0.02}_{-0.01}$
9	$9.65^{+0.13}_{-0.16}$	$1.93^{+0.05}_{-0.04}$	$0.76^{+0.67}_{-0.58}$	$6.08^{+4.18}_{-3.05}$	$-1.36^{+0.53}_{-0.46}$	$0.13^{+0.04}_{-0.06}$
10	$10.28^{+0.04}_{-0.06}$	$2.36^{+0.04}_{-0.06}$	$0.26^{+0.34}_{-0.13}$	$10.95^{+1.16}_{-1.88}$	$-0.41^{+0.14}_{-0.18}$	$0.03^{+0.03}_{-0.02}$
11	$9.77^{+0.03}_{-0.07}$	$1.54^{+0.02}_{-0.03}$	$3.00^{+0.57}_{-0.84}$	$10.46^{+1.50}_{-2.48}$	$-0.95^{+0.23}_{-0.22}$	$0.10^{+0.02}_{-0.02}$
12	$10.01^{+0.07}_{-0.08}$	$2.01^{+0.07}_{-0.05}$	$1.43^{+0.47}_{-0.88}$	$9.28^{+2.32}_{-3.84}$	$-1.35^{+0.53}_{-0.34}$	$0.17^{+0.03}_{-0.05}$
13	$10.40^{+0.06}_{-0.08}$	$2.20^{+0.05}_{-0.05}$	$1.18^{+0.35}_{-0.50}$	$9.52^{+2.09}_{-2.65}$	$-0.73^{+0.32}_{-0.38}$	$0.12^{+0.05}_{-0.05}$
14	$9.80^{+0.05}_{-0.06}$	$1.49^{+0.03}_{-0.03}$	$3.25^{+0.71}_{-0.94}$	$10.41^{+1.46}_{-2.36}$	$-1.19^{+0.26}_{-0.24}$	$0.12^{+0.02}_{-0.02}$
15	$10.70^{+0.06}_{-0.07}$	$2.09^{+0.17}_{-0.12}$	$1.63^{+0.43}_{-0.71}$	$10.24^{+1.65}_{-2.79}$	$-0.12^{+0.20}_{-0.37}$	$0.07^{+0.06}_{-0.05}$
16	$9.25^{+0.07}_{-0.11}$	$1.69^{+0.09}_{-0.07}$	$1.34^{+0.81}_{-1.08}$	$8.18^{+2.95}_{-3.71}$	$-1.10^{+0.30}_{-0.53}$	$0.06^{+0.04}_{-0.04}$
17	$9.89^{+0.08}_{-0.08}$	$2.08^{+0.03}_{-0.04}$	$0.36^{+0.42}_{-0.21}$	$8.81^{+2.18}_{-2.16}$	$-0.84^{+0.17}_{-0.28}$	$0.05^{+0.04}_{-0.03}$
18	$9.67^{+0.09}_{-0.12}$	$2.05^{+0.04}_{-0.03}$	$0.61^{+0.40}_{-0.39}$	$7.92^{+2.39}_{-1.85}$	$-1.18^{+0.59}_{-0.56}$	$0.11^{+0.04}_{-0.08}$
19	$10.19^{+0.10}_{-0.14}$	$1.48^{+0.10}_{-0.07}$	$4.18^{+2.94}_{-2.02}$	$7.68^{+3.07}_{-2.93}$	$-0.51^{+0.25}_{-0.34}$	$0.16^{+0.04}_{-0.04}$
20	$9.54^{+0.14}_{-0.17}$	$1.85^{+0.07}_{-0.08}$	$0.29^{+0.46}_{-0.15}$	$6.74^{+3.73}_{-3.04}$	$-1.29^{+0.49}_{-0.48}$	$0.05^{+0.05}_{-0.04}$
21	$11.03^{+0.15}_{-0.19}$	$2.21^{+0.08}_{-0.09}$	$0.56^{+0.98}_{-0.40}$	$7.21^{+3.58}_{-3.71}$	$-1.20^{+0.83}_{-0.50}$	$0.21^{+0.07}_{-0.09}$
22	$10.20^{+0.11}_{-0.13}$	$1.78^{+0.05}_{-0.05}$	$0.42^{+0.74}_{-0.26}$	$7.82^{+3.16}_{-3.24}$	$-1.57^{+0.33}_{-0.29}$	$0.06^{+0.04}_{-0.03}$
23	$9.89^{+0.11}_{-0.10}$	$1.28^{+0.11}_{-0.06}$	$2.90^{+2.62}_{-1.57}$	$8.59^{+2.90}_{-3.79}$	$-1.09^{+0.40}_{-0.53}$	$0.06^{+0.04}_{-0.04}$
24	$10.23^{+0.01}_{-0.02}$	$2.34^{+0.01}_{-0.02}$	$0.20^{+0.21}_{-0.08}$	$11.96^{+0.41}_{-0.72}$	$-0.43^{+0.04}_{-0.04}$	$0.01^{+0.01}_{-0.00}$
25	$9.47^{+0.13}_{-0.14}$	$1.13^{+0.08}_{-0.08}$	$4.53^{+3.34}_{-2.85}$	$6.38^{+3.41}_{-2.76}$	$-1.23^{+0.54}_{-0.52}$	$0.11^{+0.03}_{-0.05}$
26	$9.65^{+0.12}_{-0.14}$	$2.05^{+0.07}_{-0.07}$	$0.26^{+0.45}_{-0.12}$	$7.71^{+3.14}_{-2.99}$	$-1.27^{+0.57}_{-0.55}$	$0.12^{+0.05}_{-0.07}$
27	$10.13^{+0.03}_{-0.05}$	$2.24^{+0.02}_{-0.02}$	$1.09^{+0.12}_{-0.16}$	$10.94^{+1.06}_{-1.55}$	$-0.58^{+0.12}_{-0.12}$	$0.06^{+0.02}_{-0.02}$
28	$9.73^{+0.14}_{-0.21}$	$1.91^{+0.24}_{-0.17}$	$2.65^{+3.63}_{-1.82}$	$5.17^{+4.93}_{-3.60}$	$-0.94^{+0.67}_{-0.70}$	$0.40^{+0.15}_{-0.17}$
29	$10.15^{+0.07}_{-0.09}$	$1.45^{+0.07}_{-0.06}$	$2.22^{+2.47}_{-1.28}$	$6.63^{+3.86}_{-2.88}$	$-0.01^{+0.09}_{-0.11}$	$0.07^{+0.02}_{-0.02}$
30	$10.14^{+0.08}_{-0.11}$	$1.65^{+0.04}_{-0.03}$	$2.18^{+1.16}_{-1.03}$	$7.70^{+3.07}_{-2.87}$	$-1.54^{+0.42}_{-0.33}$	$0.21^{+0.02}_{-0.03}$
31	$9.66^{+0.09}_{-0.12}$	$1.49^{+0.11}_{-0.08}$	$2.44^{+1.32}_{-1.15}$	$8.81^{+2.64}_{-3.79}$	$-0.94^{+0.48}_{-0.55}$	$0.09^{+0.06}_{-0.06}$
32	$10.83^{+0.12}_{-0.15}$	$2.15^{+0.08}_{-0.08}$	$0.29^{+0.38}_{-0.15}$	$8.35^{+2.87}_{-3.23}$	$-1.13^{+0.61}_{-0.55}$	$0.13^{+0.07}_{-0.08}$
33	$9.17^{+0.17}_{-0.21}$	$1.38^{+0.24}_{-0.17}$	$3.40^{+3.48}_{-2.60}$	$6.38^{+3.82}_{-3.57}$	$-1.24^{+0.77}_{-0.58}$	$0.15^{+0.06}_{-0.06}$

For objects with σ_* measurements, we use the Kormendy and Ho (2013, Eq. 3) $M_{\rm BH}$–σ_* relation:

$$\log M_{\rm BH,9} = -(0.509 \pm 0.049) + (4.384 \pm 0.287) \times \log\left(\frac{\sigma_*}{200\,{\rm km/s}}\right) \qquad (7.4)$$

with an intrinsic scatter of 0.29 dex, where $M_{\rm BH,9} \equiv M_{\rm BH}/10^9\,M_\odot$. In addition to the 15 objects with ESI spectra (Table 7.8), we adopt $\sigma_* = 69 \pm 2\,{\rm km\,s^{-1}}$ for AT2019qiz (Nicholl, Wevers, et al., 2020) and $\sigma_* = 40 \pm 6\,{\rm km\,s^{-1}}$ for AT2020neh (Angus et al., 2022).

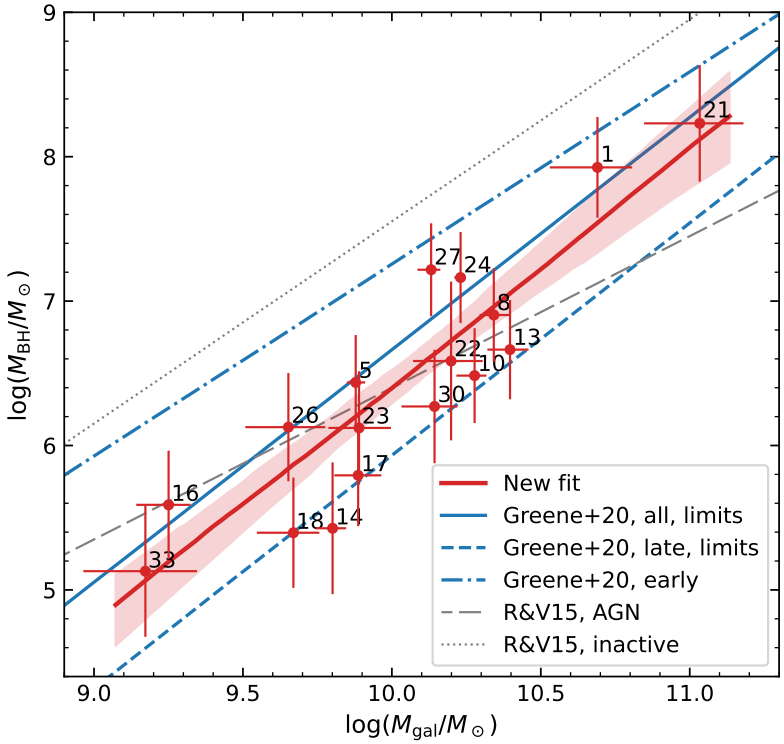

Figure 7.11: $M_{\rm BH}$ versus $M_{\rm gal}$ for 17 TDEs with $M_{\rm BH}$ measurements inferred from σ_*, labelled by the IDs in Table 7.3.

Figure 7.11 shows the inferred $M_{\rm BH}$ versus $M_{\rm gal}$ (derived from galaxy SED fitting) of these 17 objects. We fit a linear relation to these objects:

$$\log M_{\rm BH,9} = -(1.83 \pm 0.16) + (1.62 \pm 0.26) \times \log\left(\frac{M_{\rm gal}}{3 \times 10^{10}\,M_\odot}\right), \qquad (7.5)$$

which has an intrinsic scatter of 0.18 dex and is shown as the solid red line. For reference, we also show empirical relations from the literature. Reines and Volonteri (2015) adopt dynamical BH masses for inactive galaxies (Kormendy and Ho, 2013), and use $M_{\rm BH}$ derived from the width and luminosity of the Hα broad line for AGN.

Greene, Strader, and Ho (2020) adopt dynamical BH masses provided by Kormendy and Ho (2013) and recent literatures (see details in §8.2 of Greene, Strader, and Ho 2020). We use Eq. (7.5) to infer the $M_{\rm BH}$ for the remaining 16 objects without σ_* measurements.

The inferred values of $M_{\rm BH}$ and the used equation numbers are shown in the last two columns of Table 7.5. The majority of events (25/33) in our sample are hosted by BHs with $M_{\rm BH} \in (10^5, 10^7)\,M_\odot$. We computed the Eddington ratio of the UV/optical emitting component $\lambda_{\rm Edd} \equiv L_{\rm bb}/L_{\rm Edd}$, where $L_{\rm Edd} \equiv (M_{\rm BH}/M_\odot) \times 1.25 \times 10^{38}\,{\rm erg\,s^{-1}}$.

Among our sample, the $M_{\rm BH}$ of AT2020acka (ID 21) is above $10^8\,M_\odot$. For a Schwarzschild BH, the maximum mass at which a star of mass m_* (in $M_\odot$) and radius r_* (in $R_\odot$) can be tidally disrupted outside the horizon is given by

$$M_{\rm Hills}(m_*) = 1.1 \times 10^8\,M_\odot m_*^{-1/2} r_*^{3/2}. \tag{7.6}$$

Assuming $r_* \sim m_*^{0.6}$ for $m_* > 1$ (Demircan and Kahraman, 1991), $M_{\rm Hills} = 10^{8.4}\,M_\odot (m_*/10)^{0.4}$. Therefore, the $M_{\rm BH}$ of AT2020acka is still below $M_{\rm Hills}$ of a massive star ($m_* \gtrsim 4$). The disruption of a low-mass main-sequence star requires a rapid BH spin (Kesden, 2012). Given that the $t_{\rm age}$ of its host galaxy is not young, the relatively large $M_{\rm BH}$ can also be explained by the disruption of evolved stars (MacLeod, Guillochon, and Ramirez-Ruiz, 2012; MacLeod, Ramirez-Ruiz, et al., 2013).

7.5 Survey Efficiency

For an ideal survey that scans the entire sky to a given flux limit, the volumetric rate of a given type of transient can be estimated using (Schmidt, 1968):

$$\mathcal{R} = \sum_{i=1}^{N} \mathcal{R}_i = \sum_{i=1}^{N} \frac{1}{T_{{\rm span},i}/(1+z_i)} \frac{1}{V_{{\rm max},i}}, \tag{7.7}$$

where $T_{{\rm span},i}/(1+z_i)$ is the rest-frame duration of the experiment within which the $i^{\rm th}$ transient is selected, N is the number of transients that have passed the flux limit, the maximum volume $V_{{\rm max},i} \equiv \frac{4\pi}{3} D^3_{{\rm max},i}$ and $D_{\rm max}$ is the maximum luminosity distance (see §7.5). In this work, $N = 33$. For the 16 ZTF-I TDEs, $T_{{\rm span},i} = 2$ yr (from 2018 October 1 to 2020 September 30); while for the 17 ZTF-II TDEs, $T_{{\rm span},i} = 1$ yr (from 2020 October 1 to 2021 September 30).

Loss Function

For a realistic sky survey, $V_{\rm max}$ in Eq. (7.7) needs to be replaced by the effective volume $\mathcal{V}_{\rm max} = V_{\rm max} f_{\rm loss}$ (Perley, Fremling, et al., 2020). Here the loss factor $f_{\rm loss}$ takes into account the facts that the survey coverage is not all-sky, that the Galactic extinction reduces the survey volume, that the limiting magnitude of observations is not constant (it depends strongly on the moon phase, weather, and airmass), and that fast-evolving TDEs with fainter peak magnitudes are easier to be missed.

To estimate $f_{\rm loss}$, we took the observation history of ZTF. We obtained the limiting magnitude for each observation (with a certain field ID and MJD) from the exposure table of ZTF DR14[10]. For each TDE, using the light curve model obtained in §7.3, we simulated fake ZTF observations by inserting 10^5 light curves uniformly across all sky and $T_{{\rm span},i}$. We then applied the cuts outlined in §7.2 to compute the fraction of observations that would have passed our selection criteria. The values of $f_{\rm loss}$ are given in Table 7.5.

Maximum Volume

If the TDE candidate selection only depends on transient photometric properties, then $D_{\rm max} = D_{\rm max,\,t}$, where $D_{\rm max,\,t}$ is the distance out to which a transient can be detected above the flux limit of our experiments (i.e., $m_{\rm peak} < 18.75$ for ZTF-I TDEs, and $m_{g,{\rm peak}} < 19.1$ for ZTF-II TDEs). $D_{\rm max,\,t}$ can be computed using the redshifts and the best-fit values of $T_{\rm bb}$, $L_{\rm bb}$ (§7.3). The results of $D_{\rm max,\,t}$ and the corresponding maximum redshift $z_{\rm max,\,t}$ are shown in Table 7.5.

However, in Steps 1 and 2 of our TDE selection criteria (§7.2), we required the detection of each host galaxy in the ZTF reference image, the depth of which (for point sources) is $m \lesssim 23$ (Masci et al., 2019). It is easy to imagine that TDEs hosted by lower mass galaxies and galaxies with redder colors can only be selected out to a smaller volume (because at higher redshifts, these galaxies will not be cataloged in the ZTF reference and the transient will appear as "hostless").

Therefore, for each of the TDE host galaxies, we estimated $z_{\rm max,\,h}$, which is the maximum redshift out to which the observer-frame PSF AB magnitude (in either g or r band) will be < 23. We computed $z_{\rm max,\,h}$ using the best-fit `prospector` models derived in §7.4. To include the effects of PSF photometry on extended sources, we multiplied the model SED fluxes by a factor of $10^{-0.4(m_{\rm PSF} - m_{\rm LAMBDAR})}$, where $m_{\rm PSF}$

[10] Accessible at `https://irsa.ipac.caltech.edu/data/ZTF/docs/ztf_metadata_latest.db`

is the `rPSFMag` column in the PS1 `StackObjectView` catalog (Flewelling et al., 2020), and $m_{\texttt{LAMBDAR}}$ is the PS1 r-band magnitude in the `LAMBDAR` photometry (see Table 7.10 in §7.8). The derived values of $z_{\mathrm{max,\,h}}$ are given in Table 7.5.

Taken together,

$$z_{\mathrm{max},i} = \min(z_{\mathrm{max,\,t},i}, z_{\mathrm{max,\,h},i}). \tag{7.8}$$

We find that all 33 TDEs in our sample satisfy $z_i < z_{\mathrm{max,\,t},i} < z_{\mathrm{max,\,h},i}$. Therefore, for this TDE sample, $z_{\mathrm{max}} = z_{\mathrm{max,\,t}}$.

7.6 Results and Discussion

Correlations Between TDE Photometric and Galaxy Properties

Here we investigate the correlations between the TDE photometric and host galaxy properties. We focus on the three blackbody parameters, $t_{1/2}$ (defined in §7.3), λ_{Edd}, and M_{BH}. We did not include M_{gal} since it is strongly correlated with M_{BH} (Figure 7.11). We also dis not include $t_{1/2,\mathrm{rise}}$ and $t_{1/2,\mathrm{decline}}$, because both parameters are strongly correlated with $t_{1/2}$ (this can be seen in Figure 7.9, where TDEs that rise fast generally also decline fast). The p-value of a Kendall's tau test between $t_{1/2,\mathrm{rise}}$ and $t_{1/2,\mathrm{decline}}$ is 1.29×10^{-5}. This result is in agreement with Hammerstein, van Velzen, et al. (2023). We note that the first ZTF TDE sample study found no correlation between the TDE rise and decline rates (van Velzen, Gezari, Hammerstein, et al., 2021), which possibly results from the smaller sample size.

Figure 7.12 shows the distribution of our sample on various diagrams. Symbol colors follow the same convention as in Figure 7.2 and Figure 7.9. Hollow markers show objects at $z > 0.24$, where there is an observational bias towards selecting TDEs in higher-mass galaxies. Panel (p) shows the p-values of a Kendall's tau test between any two of the six quantities of interest, using the total sample of 33 TDEs and the subset of 28 TDEs at $z < 0.24$ (see reasons for this cut below). Significant correlations with $p < 0.05$ are highlighted in red colors.

The Selection Effects — Considering the whole sample of 33 TDEs, the correlations between eight pairs of parameters appear to be significant. While a few similar correlations have also been reported by Hammerstein, van Velzen, et al. (2023), we note that such correlations might be promoted by selection effects. To be in our sample, the host galaxies needs to be bright enough to be detected in the ZTF reference catalog (§7.2). Since $M_{\mathrm{BH}} \propto M_{\mathrm{gal}}^{1.6}$ (see Eq. 7.5) and $M_{\mathrm{gal}} \propto L_{\mathrm{gal}}$, we can find luminous TDEs hosted by higher-mass black holes even at high redshifts.

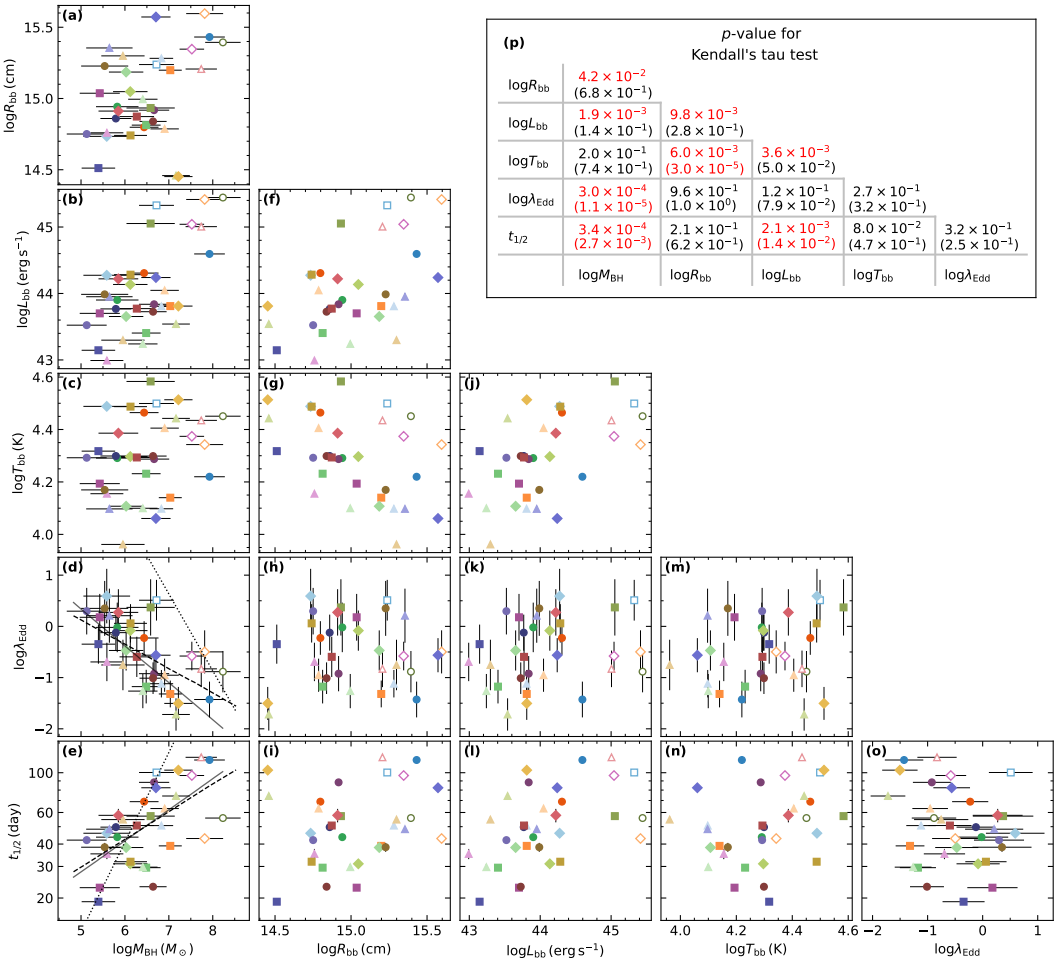

Figure 7.12: Correlations between TDE photometric properties, $\lambda_{\rm Edd}$, and $M_{\rm BH}$.

Based on the the values of $z_{\rm max,\,h}$ computed in §7.5 (see Table 7.6), within $z < 0.24$, even the faintest host galaxy of our sample (i.e., the host of AT2020wey) can be detected in the ZTF reference catalog. Therefore, within this volume, there should be no observational bias towards bright galaxies[11].

Restricting ourselves to the 28 TDEs at $z < 0.24$, the correlation between a few pairs of parameters become statistically less insignificant. The correlation between $R_{\rm bb}$ and $T_{\rm bb}$ become even more significant, as expected in a flux-limited sample if many TDEs have a similar peak blackbody luminosity. Below we discuss the other two strong correlations.

Duration above half-max vs. Black Hole Mass — The correlation between the light curve evolutionary speed and black hole mass has been reported in the literature

[11]Note that here we do not consider galaxies with an absolute r-band PSF magnitude fainter than that of AT2020wey.

(van Velzen, Holoien, et al., 2020; Gezari, 2021; Hammerstein, van Velzen, et al., 2023), which we confirm in panel (e) of Figure 7.12. We note that the p-values between $t_{1/2,\rm rise}$ and $\log M_{\rm BH}$ (1.7×10^{-3}) and between $\log M_{\rm BH}$ and $t_{1/2,\rm decline}$ (9.3×10^{-4}) are comparable to (but slightly greater than) the p-value between $t_{1/2}$ and $\log M_{\rm BH}$ (3.4×10^{-4}).

We define $M_6 \equiv M_{\rm BH}/(10^6\,M_\odot)$. A log-linear fit between $t_{1/2}$ and $M_{\rm BH}$ for 33 TDEs yields (see the dashed line):

$$\frac{t_{1/2}}{42.7^{+3.9}_{-3.5}\,\rm d} = M_6^{0.15\pm0.04}, \tag{7.9}$$

which has an intrinsic scatter of 0.17 dex. Restricting to the 28 TDEs at $z < 0.24$, we obtain a similar power-law relation of (see the solid line):

$$\frac{t_{1/2}}{41.6^{+3.7}_{-3.4}\,\rm d} = M_6^{0.17\pm0.05}, \tag{7.10}$$

which has an intrinsic scatter of 0.15 dex.

Equations (7.9, 7.10) can be compared with the fall-back timescale of the most bound debris (see the dotted line):

$$\frac{t_{\rm fb}}{41\,\rm d} = M_6^{1/2} m_*^{-1} r_*^{3/2}. \tag{7.11}$$

The observed shallow power-law index may be caused by other processes. For example, the circularization of the stellar debris has been shown to be more rapid around higher-mass black holes (Bonnerot, Rossi, et al., 2016; Bonnerot and Lu, 2020).

Eddington Ratio vs. Black Hole Mass — The distribution of our sample on the Eddington ratio and black hole mass diagram is shown in panel (d) of Figure 7.12. A log-linear fit between $\lambda_{\rm Edd}$ and $M_{\rm BH}$ for 33 TDEs yields (see the dashed line):

$$\frac{\lambda_{\rm Edd}}{0.46^{+0.13}_{-0.10}} = M_6^{-0.49\pm0.12}, \tag{7.12}$$

which has an intrinsic scatter of 0.31 dex. To correct for the selection bias, we also fit for the 28 TDEs at $z < 0.24$, obtaining a steeper power-law of (see the solid line):

$$\frac{\lambda_{\rm Edd}}{0.42^{+0.11}_{-0.09}} = M_6^{-0.72\pm0.13}, \tag{7.13}$$

which has an intrinsic scatter of 0.10 dex. This relatively tight correlation is not surprising since by definition $\log\lambda_{\rm Edd} \equiv \log L_{\rm bb} - \log M_{\rm BH} - 38.10$. And Eq. (7.13)

comes from the fact that $L_{\rm bb}$ is only weakly positively correlated with $M_{\rm BH}$ (see the filled markers in panel b).

Eq. (7.13) can also be compared with the expected peak fall-back rate of $\dot{M}_{\rm fb} \approx M_*/(3t_{\rm fb})$ relative to the Eddington accretion rate (see the dotted line):

$$\frac{\dot{M}_{\rm fb}}{\dot{M}_{\rm Edd}} = 136\,\eta_{-1} m_*^2 r_*^{-3/2} M_6^{-3/2} \tag{7.14}$$

where η is the accretion radiative efficiency and $\eta_{-1} \equiv \eta/0.1$. The observed power-law is much shallower than Eq. (7.14). In fact, the majority of TDEs in panel (d) lie well below the dotted line. One likely reason might be Eddington-limited accretion. Indeed, none of the TDEs in our sample appear to have a peak blackbody luminosity that is significantly super-Eddington. Another natural explanation is that the UV/optical peak blackbody luminosity only captures a fraction of the total bolometric luminosity, with the EUV and X-ray luminosity unaccounted for.

Luminosity Functions

While theoretical calculations show that the TDE rate may decline by a factor of 5 from $z = 0$ to $z = 1$ (Kochanek, 2016), a detailed discussion of the redshift evolution of TDE rates is beyond the scope of this work. Hereafter we assume that the TDE rate remains the same out to the highest redshift object in our sample (i.e., $z < 0.519$).

(I) Rest-frame g-band LF — In the upper panel of Figure 7.13, we show the distribution of the 33 TDEs in the observed redshift vs. peak rest-frame g-band luminosity diagram, where boundaries of the nine $\log L_g$ bins are indicated with vertical lines. For a certain bin j with n_j TDEs and width $\Delta_j \log L_g$, the rate $\phi_j = \left[\sum_{i=1}^{n_j} 1/(T_{{\rm span},i}\mathcal{V}_{{\rm max},i})\right]/\Delta_j \log L_g$, and we compute the corresponding uncertainty of ϕ_j based on the Poisson error (Gehrels, 1986). For example, when $n_j = 4$, the upper and lower limits of ϕ_j are $\phi_j^u = \phi_j \times 7.163/4$ and $\phi_j^l = \phi_j \times 2.086/4$.

First, we fit the seven solid data points in the lower panel of Figure 7.13 with a single power-law of

$$\phi(L_g) = \frac{d\mathcal{R}(L_g)}{d\log L_g} = \dot{N}_0 \left(\frac{L_g}{L_0}\right)^{-\gamma}. \tag{7.15}$$

For $L_0 = 10^{43}\,{\rm erg\,s^{-1}}$, we have $\dot{N}_0 = 1.82^{+0.48}_{-0.39} \times 10^{-7}\,{\rm Mpc^{-3}\,yr^{-1}}$, and $\gamma = 2.00^{+0.15}_{-0.14}$. The best-fit model, shown as the dotted gray line in Figure 7.13, is steeper than the power-law model with $\gamma = 1.6 \pm 0.2$ presented by van Velzen (2018).

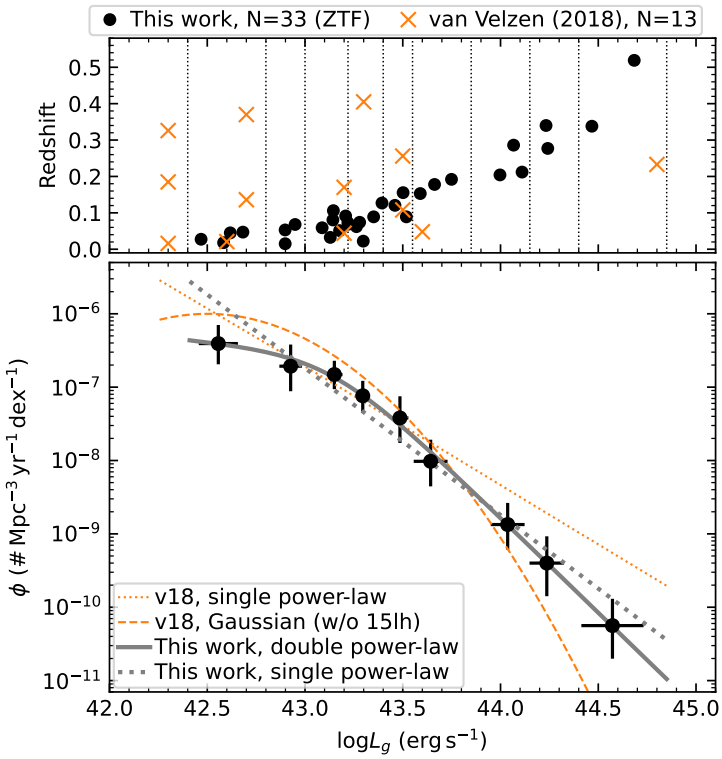

Figure 7.13: *Upper*: Redshift versus log$L_{\rm g}$ for 33 TDEs in this work (circles) and 13 TDEs used by van Velzen (2018) (crosses). *Lower*: ZTF TDE LF in rest-frame g band.

Next, we describe the LF with a double power-law of:

$$\phi(L_g) = \dot{N}_0 \left[\left(\frac{L_g}{L_{\rm bk}} \right)^{\gamma_1} + \left(\frac{L_g}{L_{\rm bk}} \right)^{\gamma_2} \right]^{-1} \tag{7.16}$$

where $-\gamma_1$ is the faint-end slope, $-\gamma_2$ is the bright-end slope, and $L_{\rm bk}$ is the characteristic break luminosity. We perform the fit with MCMC, obtaining $L_{\rm bk} = 1.36^{+0.89}_{-0.48} \times 10^{43}\,{\rm erg\,s^{-1}}$, $\dot{N}_0 = 2.87^{+2.98}_{-1.68} \times 10^{-7}\,{\rm Mpc^{-3}\,yr^{-1}}$, $\gamma_1 = 0.26^{+0.61}_{-0.80}$, and $\gamma_2 = 2.58^{+0.27}_{-0.25}$. This model is shown as the solid gray line in Figure 7.13.

The BIC value of the double power-law fit is smaller than the single power-law fit by 6.07. According to Raftery (1995), a BIC difference of 0–2 is weak, and a of 2–6 is positive, and a difference of 6–10 is strong. Therefore, we conclude that a double power-law LF provides a better description of the data.

Our result of $\phi(L_g)$ is consistent with that provided by van Velzen (2018) at $L_g \sim 10^{43.5}\,{\rm erg\,s^{-1}}$. For over-luminous events, ASASSN-15lh is the only object with $L_g > 10^{43.6}\,{\rm erg\,s^{-1}}$ in the van Velzen (2018) sample. The fact that nine objects in

our sample have $L_g > 10^{43.6}\,\mathrm{erg\,s^{-1}}$ allow us to constrain the upper end of the LF more precisely.

For sub-luminous events, the LF measured with the ZTF sample is shallower and the rate is about a factor of two smaller than that measured by van Velzen (2018). No objects in our sample have $L_g < 10^{42.4}\,\mathrm{erg\,s^{-1}}$, while three objects in the van Velzen (2018) sample (*GALEX*-D1-9, *GALEX*-D23H-1, and iPTF16fnl) have $L_g \approx 10^{42.3}\,\mathrm{erg\,s^{-1}}$. However, the two *GALEX* events have relatively sparse light curves (note the lack of data points on the rise in Fig. 15 of Gezari, Basa, et al. 2008 and Fig. 2 of Gezari, Heckman, et al. 2009), which can possibly lead to an underestimation of their peak g-band luminosity.

(II) UV/Optical Blackbody LF — Following the procedures outlined above, we compute the TDE rate as a function of the peak UV/optical blackbody luminosity (see Figure 7.14).

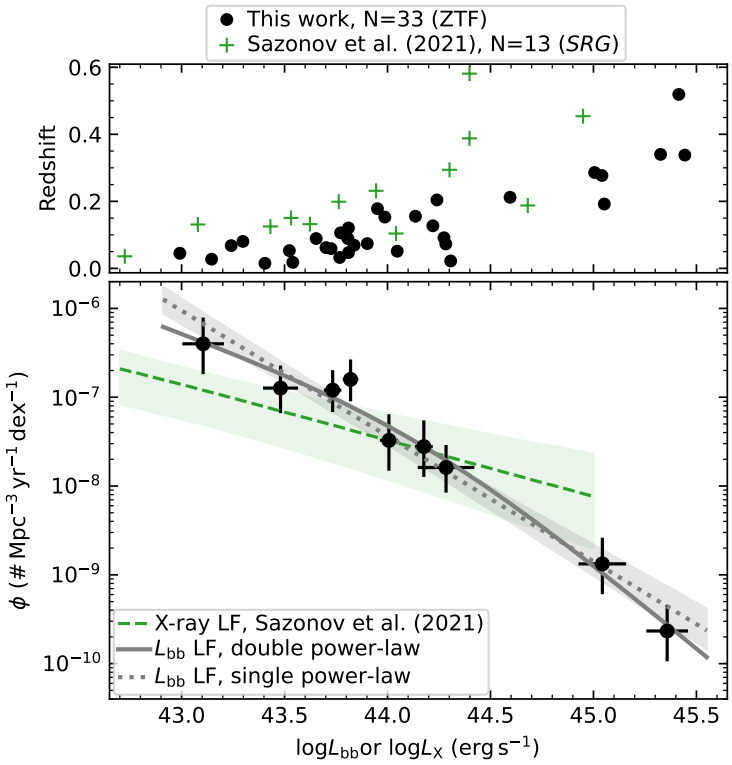

Figure 7.14: *Upper*: Redshift versus $\log L_{\rm bb}$ for 33 TDEs in this work (circles), and versus the peak X-ray luminosity for 13 *SRG*-selected TDEs presented by Sazonov et al. (2021). *Lower*: X-ray and UV/optical bolometric TDE LFs.

With $L_0 = 10^{43}\,\mathrm{erg\,s^{-1}}$, a single power-law fit yields

$$\phi(L_{\rm bb}) = (9.43^{+4.53}_{-3.04} \times 10^{-7}\,\mathrm{Mpc^{-3}\,yr^{-1}}) \left(\frac{L_{\rm bb}}{L_0}\right)^{-1.41\pm0.14}. \tag{7.17}$$

A double power-law fit yields

$$\phi(L_{\rm bb}) = (5.72^{+7.08}_{-3.29} \times 10^{-8}\,\mathrm{Mpc^{-3}\,yr^{-1}}) \times \left[\left(\frac{L_{\rm bb}}{L_{\rm bk}}\right)^{0.84^{+0.30}_{-0.36}} + \left(\frac{L_{\rm bb}}{L_{\rm bk}}\right)^{1.93^{+0.32}_{-0.27}}\right]^{-1}, \tag{7.18}$$

where $L_{\rm bk} = 1.46^{+1.20}_{-0.64} \times 10^{44}\,\mathrm{erg\,s^{-1}}$. The BIC value of the double power-law fit is greater than the single power-law fit by 2.2. Therefore, the single power-law fit is slightly favored.

With Eq. (7.17), the integrated volumetric rate of optical TDEs with $L_{\rm bb} > 10^{43}\,\mathrm{erg\,s^{-1}}$ is $3.1^{+0.6}_{-1.0} \times 10^{-7}\,\mathrm{Mpc^{-3}\,yr^{-1}}$. This can be compared with the volumetric rate of X-ray selected TDEs. Using a sample of 13 TDEs selected from *SRG*/eROSITA, Sazonov et al. (2021) found that the majority of X-ray selected events are intrinsically faint in the optical. Previous studies also implied that the majority of ZTF-selected TDEs are intrinsically faint in the X-ray band (see Fig. 8 of Hammerstein, van Velzen, et al. 2023). Using the LF provided by Sazonov et al. (2021), the rate of X-ray TDEs with $L_{\rm X} > 10^{43}\,\mathrm{erg\,s^{-1}}$ is $\sim 2.3 \times 10^{-7}\,\mathrm{Mpc^{-3}\,yr^{-1}}$. Therefore, we conclude that the rates of optically loud and X-ray loud TDEs are comparable to each other.

Rate Dependence on $R_{\rm bb}$

Following the procedures outlined above, we compute the TDE rate as a function of the peak blackbody radius $R_{\rm bb}$ (see Figure 7.15). A double power-law fit gives

$$\phi(R_{\rm bb}) = (1.00^{+1.33}_{-0.62} \times 10^{-7}\,\mathrm{Mpc^{-3}\,yr^{-1}}) \times \left[\left(\frac{R_{\rm bb}}{R_{\rm bk}}\right)^{0.97^{+0.59}_{-0.67}} + \left(\frac{R_{\rm bb}}{R_{\rm bk}}\right)^{5.81^{+2.16}_{-1.57}}\right]^{-1}, \tag{7.19}$$

where $R_{\rm bk} = 1.46^{+1.20}_{-0.64} \times 10^{44}\,\mathrm{cm}$. Compared with the $\phi(R_{\rm bb}) \propto R_{\rm bb}^{-2}$ relation found by van Velzen, Gezari, Hammerstein, et al. (2021), our results indicate a slope that is much shallower/deeper at small/large radii.

van Velzen, Gezari, Hammerstein, et al. (2021) suggested that the observed $R_{\rm bb}$ in the majority of TDEs can be explained by the self-intersection radius ($R_{\rm I}$) of the debris stream for disruptions of stars with $0.2 \lesssim m_* \lesssim 3$ and impact parameter $R_{\rm p}/R_{\rm T} \approx 1$ (Dai, McKinney, and Miller, 2015). For TDEs hosted by the most

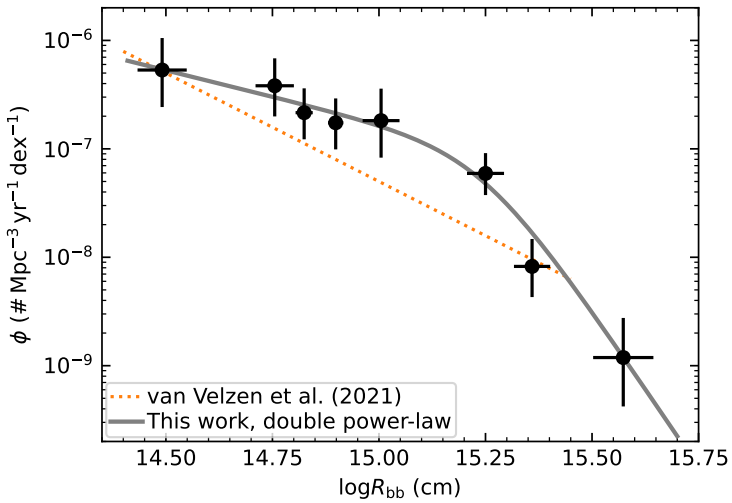

Figure 7.15: TDE rate as a function of $R_{\rm bb}$.

massive BHs, we find $R_{\rm bb} \gg R_{\rm I}$ because the self-intersection radius decreases with $M_{\rm BH}$ for $M_{\rm BH} \gtrsim 10^{6.5}\,M_\odot$ (see Fig. 8 of Gezari 2021). In fact, we find that TDEs at a given $M_{\rm BH}$ show a broad range of $R_{\rm bb}$ [see panel (a) of Figure 7.12]. As suggested by Nicholl, Lanning, et al. (2022), $R_{\rm bb}$ can vary a lot even for the same $M_{\rm BH}$ depending on the impact parameter — it could be set by the collision-induced outflow in shallow encounters, but by the disk wind in deep encounters.

The steep upper power-law index ($\gamma_2 \sim 5.8$ in Eq. 7.19) suggests that there is a physical maximum blackbody radius for TDEs: $R_{\rm bb,max} \sim$ few $\times\, 10^{15}$ cm. One possibility is that this maximum radius corresponds to the semimajor axis of the most bound tidal debris $a \simeq 0.5 R_* (M_{\rm BH}/M_*)^{2/3} \simeq 3\times10^{15}\,{\rm cm}\,(M_{\rm BH}/10^{7.5}M_\odot)^{2/3}$, where we have taken the mass–radius relation $R_* \propto M_*^{\approx 2/3}$ for main-sequence stars. Under this hypothesis, the fact that the TDE rate is strongly suppressed at $M_{\rm BH} \gtrsim 10^{7.5} M_\odot$ (see §7.6) would lead to a maximum blackbody radius that is in reasonable agreement with observations. However, we leave detailed theoretical considerations to future works.

Optical TDE Black Hole Mass Function

Since the uncertainty of log$M_{\rm BH}$ is relatively large (0.1–0.4 dex), instead of the binning method utilized in §7.6 and §7.6, we compute the optical TDE black hole mass function using KDEs. We adopt a Gaussian kernel with the same variance as the uncertainties of the log$M_{\rm BH}$ measurements.

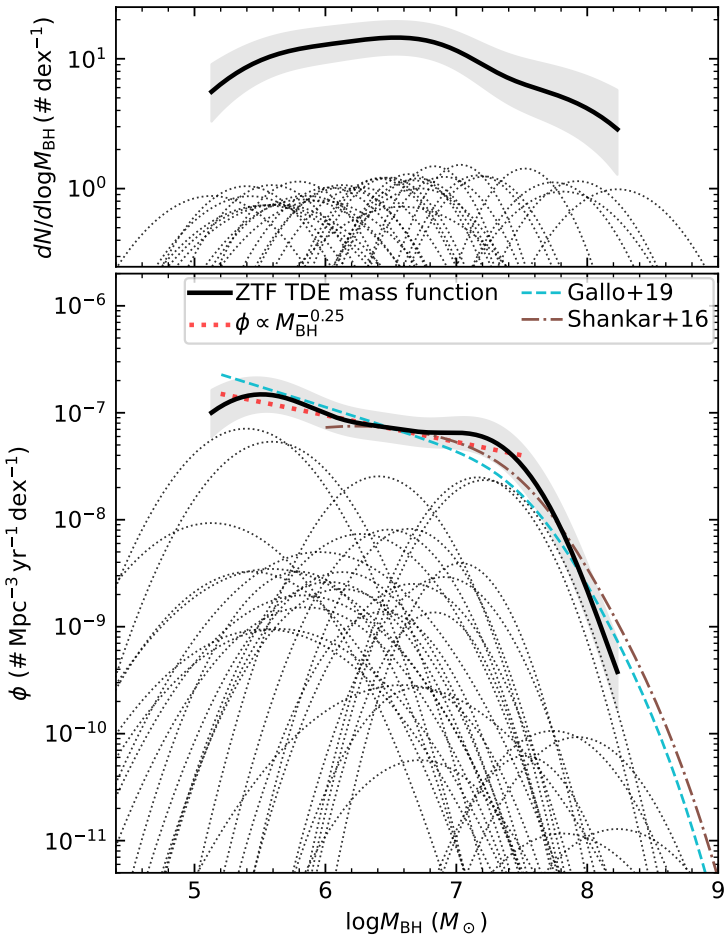

Figure 7.16: *Upper*: The raw observed number of TDEs per BH mass dex. *Lower*: The optical TDE rate with respect to $M_{\rm BH}$.

In the upper panel of Figure 7.16, the thin lines are the $\log M_{\rm BH}$ PDFs of the 33 TDE host galaxies. The think black line shows the total number of detected TDEs per dex, computed by summing over the individual Gaussians and plotted between the peak of the PDF of the lowest BH mass ($10^{5.13}\,M_\odot$) and highest BH mass ($10^{8.23}\,M_\odot$). We estimated the 1-σ Poisson single-sided upper and lower limits (the semitransparent region) by interpolating Tab. 1 and Tab. 2 of Gehrels (1986). The curve of $dN/d\log M_{\rm BH}$ peaks at $M_{\rm BH} \approx 10^{6.5}\,M_\odot$.

In the lower panel of Figure 7.16, the thin dotted lines are the PDFs (in the upper panel) multiplied by $\mathcal{R}_i$. The solid black curve shows the total optical TDE rate as a function of $M_{\rm BH}$. From $10^{5.2}\,M_\odot$ to $10^{7.4}\,M_\odot$, the slope follows a power-law of $\phi \propto \log M_{\rm BH}^{-0.25}$ (red dotted line). Predictions of two BHMFs (Shankar, Bernardi, et al., 2016; Gallo and Sesana, 2019) are normalized to match the black curve at

$M_{\rm BH} = 10^{6.5}\,M_\odot$. We observed a significant drop of $\phi(M_{\rm BH})$ from $10^{7.4}\,M_\odot$ to $10^{8.2}\,M_\odot$. This roughly corresponds to $M_{\rm Hills}$ for main-sequence stars. A similar result was first reported by van Velzen (2018, Fig. 3) and later updated by van Velzen, Holoien, et al. (2020, Fig. 13). While more massive galaxies exhibit shallower ("cored") stellar density profiles that can also lead to a suppression of TDE rates by a factor of $\lesssim 10$ (see Fig. 5 of Magorrian and Tremaine 1999 and Fig. 4 of Stone and Metzger 2016), this effect alone does not account for the observed (much steeper) rate suppression.

To compare our observations to theoretical predictions, we write the mass function for the BHs that are causing TDEs as

$$\phi(M_{\rm BH}) = \dot{N}_0 \times M_6^{\beta} \times \frac{dn_{\rm BH}}{d\log M_{\rm BH}} g(M_{\rm BH}), \tag{7.20}$$

where $\dot{N}_0 \times M_6^{\beta}$ is the rate at which stars are scattered into the loss cone ($\dot{N}_0$ being a normalization constant and β will be explained shortly), $dn_{\rm BH}/d\log M_{\rm BH}$ is the local BHMF, and $g(M_{\rm BH})$ is the event-horizon suppression factor that describes the fraction of stars that produce observable optical flares.

Most TDEs originate from the BH's sphere of influence $R_{\rm infl}$ (Wang and Merritt, 2004), where the number of stars within $R_{\rm infl}$ is $N \sim M_{\rm BH}/M_*$. Since $R_{\rm infl} \approx GM_{\rm BH}/\sigma_*^2 \propto \sigma_*^2 \sim M_{\rm BH}^{1/2}$, the orbital period at $R_{\rm infl}$ is $P_{\rm orb} \propto R_{\rm infl}^{3/2}/M_{\rm BH}^{1/2} \propto M_{\rm BH}^{1/4}$. The two-body relaxation timescale at $R_{\rm infl}$ is $t_{\rm rel} \propto (P_{\rm orb}/N)(\frac{M_{\rm BH}}{M_*})^2 \propto M_{\rm BH}^{5/4}$ (Alexander, 2017). The TDE rate is expected to be the total number of stars within the sphere of influence divided by $t_{\rm rel}$, which is $\sim N/t_{\rm rel} \propto M_{\rm BH}/t_{\rm rel} \propto M_{\rm BH}^{-1/4}$. Therefore, in Eq. (7.20), we adopt $\beta = -0.25$. For reference, Stone and Metzger (2016) performed the most recent detailed theoretical calculations by applying loss cone dynamics to observations of nearby galactic nuclei, finding $\beta = -0.247$ for core nuclei and $\beta = -0.223$ for cusp nuclei.

The rate suppression factor $g(M_{\rm BH}) \sim 1$ at $M_{\rm BH} \lesssim 10^7\,M_\odot$, and drops at higher BH masses because stars are swallowed by the event horizon. The shape of $g(M_{\rm BH})$ depends on the stellar age, the stellar metallicity, the BH spin distribution, the stellar density structure (how centrally concentrated the star is), the exact boundary between full and partial TDEs, and the rate at which stars of different masses are scattered into the loss cone (see more detailed theoretical calculations in Huang and Lu 2022). We compute $g(M_{\rm BH})$ as the fraction of stars in a given stellar population that satisfies $M_{\rm Hills}(m_*, M_{\rm BH}) < M_{\rm BH}$. The stellar population we consider has metallicity [Fe/H] = 0.3 (twice solar, appropriate for stars near galactic centers) and

a single age of 100 Myr. Our small sample is insufficient to differentiate models of different stellar ages, BH spins, and loss-cone filling mechanisms.

We computed $\phi(M_{\rm BH})$ using Eq. (7.20), and convolved it with a Gaussian kernel of the typical $\log M_{\rm BH}$ measurement uncertainty of 0.3 dex. The convolution is needed since the measurement error blurs and broadens the distribution of quantities (Kelly and Merloni, 2012). The dashed cyan and dash-dotted brown lines in the lower panel of Figure 7.16 show the predictions with two BHMFs (Shankar, Bernardi, et al., 2016; Gallo and Sesana, 2019), scaled at $M_{\rm BH} = 10^{6.5}\,M_\odot$ to match the observation (the thick black line). We confirm that the observed high-mass rate drop is consistent with theoretical expectation of the event horizon effect.

A novel result in Figure 7.16 is that the optical TDE mass function roughly follows a power-law of $\phi \propto M_{\rm BH}^{-0.25}$ for $10^{5.2}\,M_\odot \lesssim M_{\rm BH} \lesssim 10^{7.4}\,M_\odot$. We discuss the implications of this result for the local BHMF later in this section.

Rate Enhancement/Suppression in Green/Blue Galaxies

Following the procedures outlined above, we compute the TDE rate as a function of $M_{\rm gal}$. We limit the minimum kernel bandwidth to be 0.15. In panel (a) of Figure 7.17, the thin lines show the probability density function of each host's $\log M_{\rm gal}$ multiplied by $\mathcal{R}_i$. The thick line shows the observed optical TDE galaxy mass function $\phi(M_{\rm gal})$, plotted between the peak of the PDF of the lowest galaxy mass ($10^{9.17}\,M_\odot$) and highest galaxy mass ($10^{11.03}\,M_\odot$). The semitransparent region represents the 1-σ uncertainties.

Using Eq. (7.5) and Eq. (7.20) and assuming that the occupation fraction of black holes is close to unity, the observed TDE galaxy mass function should follow

$$\phi(M_{\rm gal}) \approx \dot{N}_0' M_{\rm gal}^{-0.41} \frac{dn_{\rm gal}}{d\log M_{\rm gal}} g(M_{\rm gal}), \tag{7.21}$$

where $dn_{\rm gal}/d\log M_{\rm gal}$ is the local galaxy mass function (GMF). We took the GMF given by Baldry et al. (2012), which is similar to the most recent GMF (Wright, Robotham, Driver, et al., 2017) at $M_{\rm gal} \gtrsim 10^9\,M_\odot$. At a typical galaxy mass of $M_{\rm gal} = 10^{10}\,M_\odot$, the optical TDE rate is $3.2^{+0.8}_{-0.6}\times10^{-5}$ galaxy^{-1} yr^{-1}, as shown by the dashed purple line in panel (a) of Figure 7.17. This generally agrees with theoretical calculations, which predict a per-galaxy TDE rate between 10^{-5} galaxy^{-1} yr^{-1} and 10^{-4} galaxy^{-1} yr^{-1} (Wang and Merritt, 2004; Stone and Metzger, 2016; Teboul, Stone, and Ostriker, 2022).

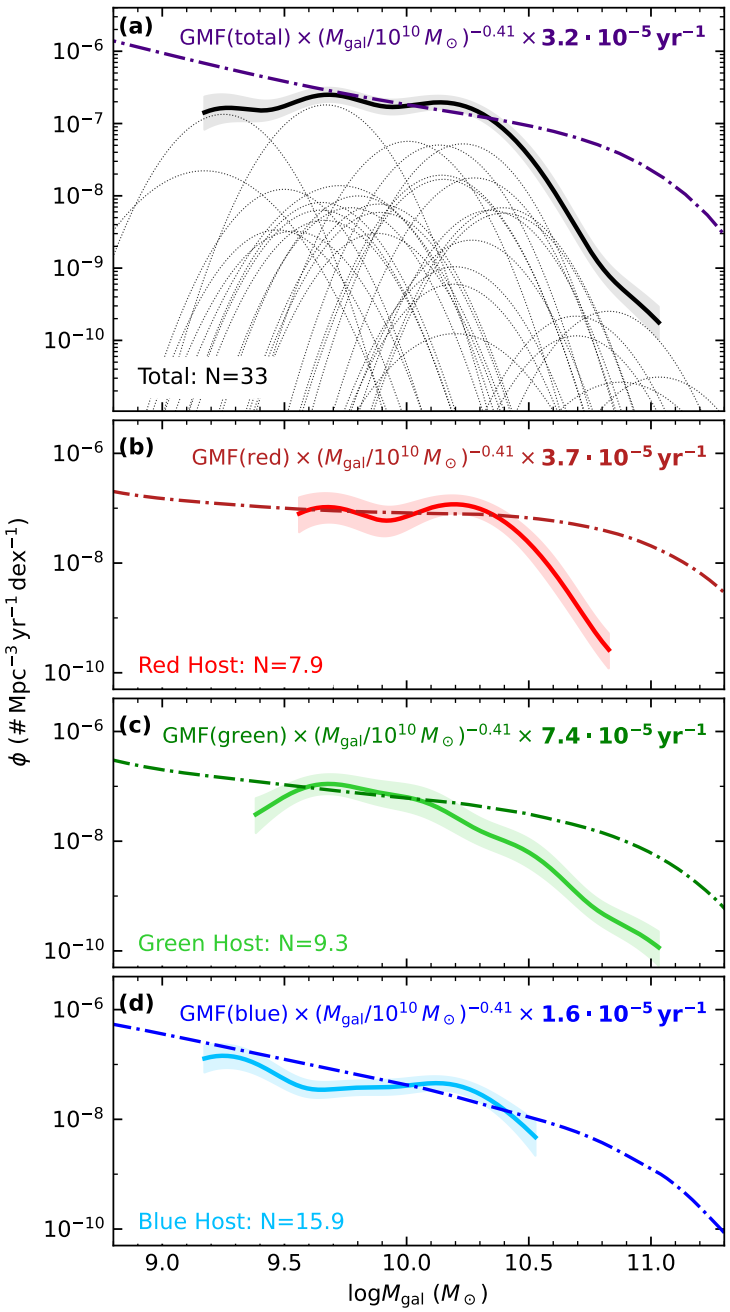

Figure 7.17: Panel (a): The total optical TDE rate as a function of $M_{\rm gal}$. Panels (b)–(d): The observed optical TDE galaxy mass functions in three bins of C (Eq. 7.23). The dash-dotted lines show the local GMFs multiplied by $M_{\rm gal}^{-0.41}$ and scaled to match the observation at $M_{\rm gal} = 10^{10}\,M_\odot$.

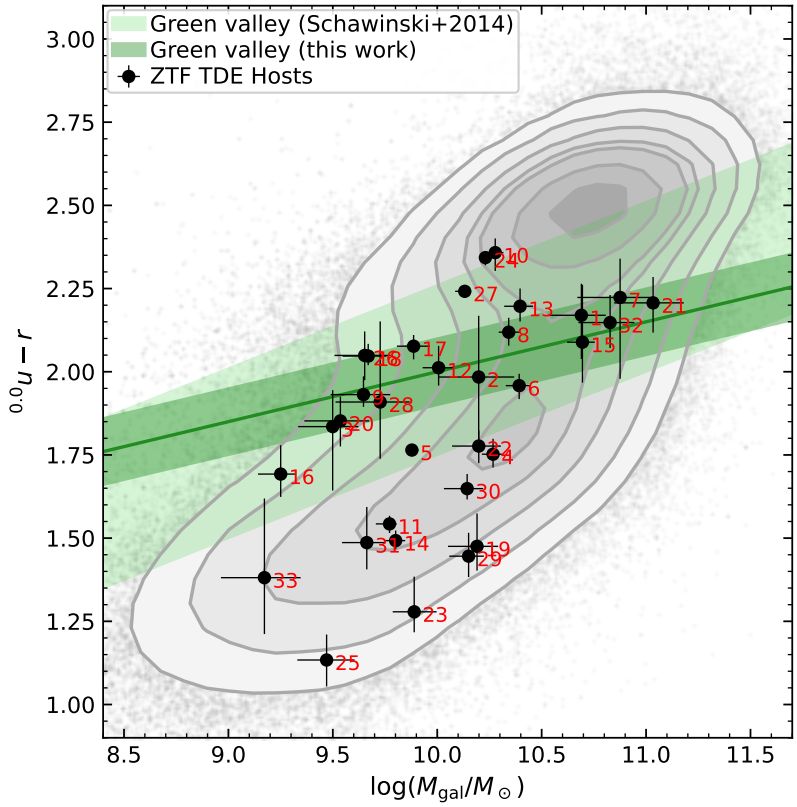

Figure 7.18: Host galaxies of the ZTF TDE sample on the $^{0,0}u - r$ versus $M_{\rm gal}$ diagram. The background contours represent a comparison sample of galaxies from SDSS.

Next, we aim to quantify the relative optical TDE rate in galaxies with different colors. In Figure 7.18, we show the host galaxy distribution on the $^{0,0}u - r$ versus $M_{\rm gal}$ diagram. To compare the properties of TDE hosts to the population of local galaxies, we started with the flux-limited ($14 \leq m_r \leq 17.77$) sample of $\sim 6.6 \times 10^5$ spectroscopically classified SDSS galaxies (Strauss et al., 2002) with $M_{\rm gal}$ estimated by Mendel et al. (2014, Tab. 4). We computed $^{0,0}u - r$ using the rest-frame absolute magnitude in u and r bands provided by the `Photoz` table in SDSS DR7 (Abazajian et al., 2009). To build a comparison sample representative of galaxies that our ZTF TDE selection is sensitive to, for each TDE in our sample, we randomly select 10^3 galaxies with $z < z_{\rm max}$, where z is the redshift of the SDSS galaxy, and $z_{\rm max}$ is computed in §7.5. The grey contours in Figure 7.18 are regions encircling 6.7, 16, 31, 50, 69, 84, and 93.3% (i.e., in steps of 0.5σ) of the final sample of 3.3×10^4 galaxies.

The region of green valley galaxies defined by Schawinski et al. (2014) is marked

by the light green band in Figure 7.18, which already enclosed galaxies in the "red sequence" and "blue cloud" loci of the SDSS comparison sample. Therefore, we define a new green valley locus (shown as the solid green line):

$$^{0,0}u - r = 0.5 + 0.15 \times \log(M_{\rm gal}/M_\odot). \tag{7.22}$$

Based on Eq. (7.22), we define a new quantity of $M_{\rm gal}$-corrected color:

$$C \equiv {}^{0,0}u - r - 0.5 - 0.15 \times \log(M_{\rm gal}/M_\odot), \tag{7.23}$$

which represents the vertical distance to the green valley loci on the color–mass diagram. We define red, green, and blue galaxies to be those with $C > 0.1$, $|C| \leq 0.1$, and $C < -0.1$, respectively.

We compute $\phi(M_{\rm gal})$ for red, green, and blue galaxies. Note that the uncertainty of C is not negligible and is dominated by the uncertainty of $^{0,0}u - r$. Therefore, for each TDE host, we compute the PDF of its C (assuming Gaussian distributions), and computed the probabilities of it being a red/green/blue galaxy. For example, the host position of AT2018iih/ZTF18acaqdaa (ID 1) is in the green valley, but the probability of it being a red/green/blue galaxy is 0.40/0.52/0.08. The resulting $\phi(M_{\rm gal})$ for three C bins are shown as the solid thick curves in panels (b)–(d) of Figure 7.17.

The GMFs for the three C bins are computed using the Mendel et al. (2014) sample. By definition, GMF(red) + GMF(green) + GMF(blue) = GMF(total). We compute $M_{\rm gal}^{-0.41} \times$GMF, and scale it to match the observed optical TDE galaxy mass function at the typical galaxy mass of $10^{10}\,M_\odot$. Considering red, green, and blue galaxies, the per-galaxy TDE rate is $3.7^{+2.3}_{-1.5} \times 10^{-5}$ galaxy^{-1} yr^{-1}, $7.4^{+5.0}_{-3.2} \times 10^{-5}$ galaxy^{-1} yr^{-1}, and $1.6^{+0.6}_{-0.4} \times 10^{-5}$ galaxy^{-1} yr^{-1}, respectively. At a typical galaxy mass of $M_{\rm gal} = 10^{10}\,M_\odot$, the relative ratio of optical TDE rate in red, green, and blue galaxies is $1 : \frac{7.4^{+5.0}_{-3.2}}{3.7^{+2.3}_{-1.5}} : \frac{1.6^{+0.6}_{-0.4}}{3.7^{+2.3}_{-1.5}} = 1 : 2.0^{+1.1}_{-0.7} : 0.4^{+0.2}_{-0.1}$.

The rate suppression in blue galaxies may come from the fact that star-forming galaxies exhibit larger amounts of dust in the galaxy nuclei. It is expected that optical searches, which generally select blue transients, will be biased against TDEs which are intrinsically redder due to dust extinction (Roth, van Velzen, et al., 2021). The rate enhancement in green-valley galaxies can be attributed to the higher number density of stars scattered into the loss cone following recent star formation or galaxy mergers (e.g., French, Wevers, et al. 2020; Hammerstein, Gezari, van Velzen, Cenko, et al. 2021). We note that the rate enhancement we found appears to be smaller

than previous observational constrains (Law-Smith et al., 2017; French, Wevers, et al., 2020; Hammerstein, Gezari, van Velzen, Cenko, et al., 2021), although instead of using the "green-valley" definition, some other studies focus on the over-representation factor in E+A galaxies.

Implications of the Local BHMF

Here, we aim to independently measure the shape of the local BHMF in the mass range of $10^{5.2}\,M_\odot \lesssim M_{\rm BH} \lesssim 10^{7.2}\,M_\odot$. Below we briefly review literature estimates of the local BHMFs, present the results, and comment on some caveats in our assessment.

Literature BHMFs — The traditional approach to calculate the local BHMF is to convert the observed galaxy distribution $\Phi(y)$ into the BHMF using a $M_{\rm BH}$–y scaling relation with a certain slope a, intercept b, and intrinsic scatter η (see reviews by Kelly and Merloni 2012; Shankar 2013):

$$\Phi(M_{\rm BH}) = \int \Phi(y) \frac{1}{\sqrt{2\pi\eta^2}} \exp\left[-\frac{(M_{\rm BH} - [a + by])^2}{2\eta^2}\right] dy. \tag{7.24}$$

A key assumption here is that BHs exist ubiquitously in galaxy nuclei, which has been justified in high-mass galaxies ($M_{\rm gal} \gtrsim 10^{10}\,M_\odot$; Miller, Gallo, Greene, et al. 2015). This approach has been widely applied (Marconi et al., 2004; Merloni and Heinz, 2008; Yu and Lu, 2008; Shankar, Weinberg, and Miralda-Escudé, 2009; Vika et al., 2009) to compute the BHMF at $M_{\rm BH} \gtrsim 10^6\,M_\odot$. Shankar, Weinberg, and Miralda-Escudé (2009) showed the range of BHMFs derived with different scaling relations. This has been updated using newly calibrated scaling relations (Shankar, Bernardi, et al., 2016). See the hatched regions in the lower panel of Figure 7.19.

In a few nearby dwarf galaxies, however, stellar dynamical measurements have placed stringent upper limits on $M_{\rm BH}$ (e.g., Gebhardt et al. 2001; Valluri et al. 2005), suggesting that the occupation fraction in low-mass galaxies is <100%. An empirical method to constrain the occupation fraction is to use high spatial resolution *Chandra* X-ray observations (Gallo, Treu, Jacob, et al., 2008; Gallo, Treu, Marshall, et al., 2010; Miller, Gallo, Treu, et al., 2012). Assume that the nuclear X-ray luminosity $L_{\rm X}$ is a power-law function of $M_{\rm gal}$ with Gaussian scatter (Gallo, Hodges-Kluck, et al., 2019), and that the occupation fraction $f_{\rm occ}(M_{\rm gal})$ follows

$$0.5 + 0.5 \times \tanh\left[2.5^{|8.9 - \log M_{\rm gal,\,0}|} \log(M_{\rm gal}/M_{\rm gal,\,0})\right], \tag{7.25}$$

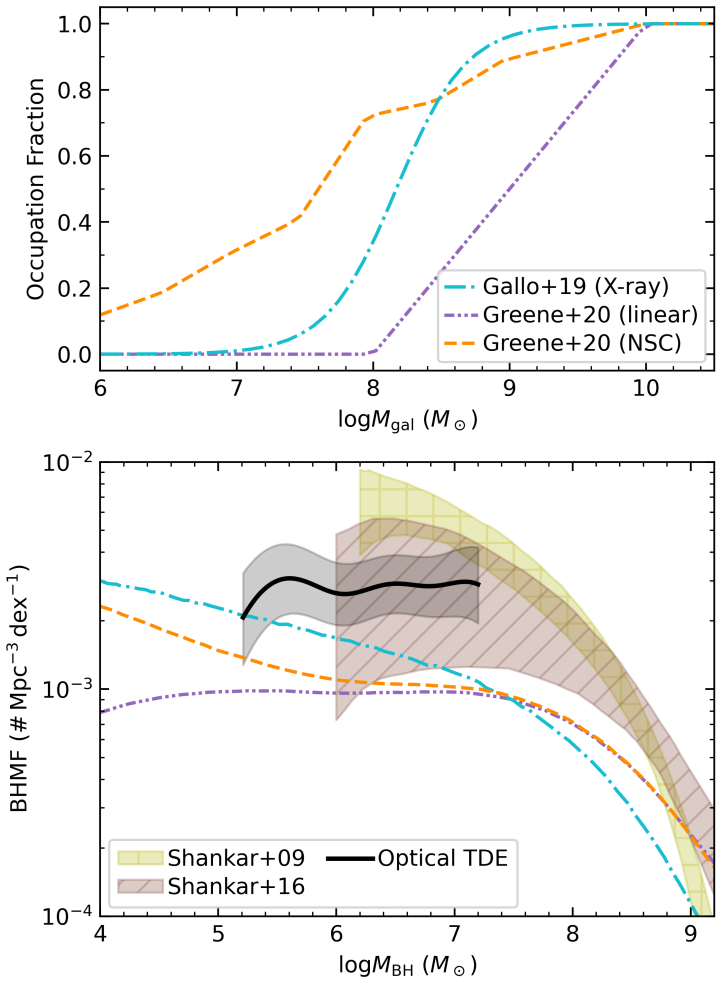

Figure 7.19: *Upper*: Black hole occupation fraction from the literature. *Lower*: The local BHMF inferred with the optical TDE mass function, compared with those inferred using other methods and scaling relations (see text).

by measuring $L_{\rm X}$ of a large sample of nearby galaxies across a wide range of $M_{\rm gal}$, one can simultaneously constrain the slope, intercept, and scatter of the $L_{\rm X}$–$M_{\rm gal}$ relation, as well as the critical galaxy mass $M_{\rm gal,\,0}$ at which $f_{\rm occ} = 0.5$. This approach is first adopted by Miller, Gallo, Greene, et al. (2015) using 194 early-type galaxies, and later updated by Gallo and Sesana (2019) using 326 early-type galaxies. The best-fit curves of Gallo and Sesana (2019) are shown as the dash-dotted cyan lines in Figure 7.19. Using *Chandra* archive, She, Ho, and Feng (2017) found a similar occupation fraction in late-type spirals.

The actual $f_{\rm occ}(M_{\rm gal})$ does not necessarily follow the functional form of Eq. (7.25). Greene, Strader, and Ho (2020) assumed two different shapes of $f_{\rm occ}$ (see Fig-

ure 7.19), with the pessimistic case drawn as a linear curve and the optimistic case provided by the fraction of nuclear star cluster (NSC) from Sánchez-Janssen et al. (2019). The authors then converted the GMF of Wright, Robotham, Driver, et al. (2017) into the local BHMF using the $M_{\rm BH}$–$M_{\rm gal}$ relation (gray lines in Figure 7.11).

Optical TDE Black Hole Mass Function Favors a Flat BHMF — Assuming $g(M_{\rm BH}) = 1$ for $M_{\rm BH} < 10^{7.2}\,M_\odot$ and using Eq. (7.20), we determined the shape of the local BHMF (at $M_{\rm BH} > 10^{5.2}\,M_\odot$) using the observed optical TDE black hole mass function (lower panel of Figure 7.16). To correct for the relative rate differences in red/green/blue galaxies (§7.6), we compute the corrected $\phi_{\rm corr}(M_{\rm BH}) = \phi_{\rm red}(M_{\rm BH}) \times \frac{3.2}{3.7} + \phi_{\rm green}(M_{\rm BH}) \times \frac{3.2}{7.4} + \phi_{\rm blue}(M_{\rm BH}) \times \frac{3.2}{1.6}$. Given the theoretical uncertainties of $\dot{N}_0$, we determine the normalization by matching the Shankar, Bernardi, et al. (2016) curve at $M_{\rm BH} = 10^{6.5}\,M_\odot$.

The result is shown as the solid black line in the lower panel of Figure 7.19. Generally speaking, our result favors a flat BHMF (i.e., $dn_{\rm BH}/d\log M_{\rm BH} \approx$ constant) in the mass range of $10^{5.2}\,M_\odot \lesssim M_{\rm BH} \lesssim 10^{7.2}\,M_\odot$. The derived shape of the BHMF is consistent with observational constraints using other method (Gallo and Sesana, 2019; Greene, Strader, and Ho, 2020). However, with the current sample size, we are not able to differentiate the nuances under various $f_{\rm occ}$ assumptions.

Comparison with Semi-Analytical Models — Here, we also explore physically motivated BHMFs from the semi-analytic models presented in Ricarte and Natarajan (2018a), Ricarte and Natarajan (2018b), Ricarte, Pacucci, et al. (2019), and Chadayammuri et al. (2023). These semi-analytic models include halo masses down to $10^7\,M_\odot$ from redshifts $20 > z > 0$, with the aim of comparing BH seeding prescriptions via electromagnetic and gravitational wave signatures (Ricarte and Natarajan, 2018b).

The semi-analytic models considered here explore two different BH seeding models, and three different BH growth prescriptions. Population III (Pop III) models place a "light" seed initialized at approximately $10^2\,M_\odot$ in almost all dwarf galaxies by $z = 0$. Meanwhile, the direct collapse black hole (DCBH) models place a "heavy" seed of approximately $10^5\,M_\odot$ in a subset of these halos. Fundamentally, DCBHs start off more massive than Pop IIIs, but occupy fewer halos.

These semi-analytic models do not model the astrophysics of galaxy formation, and instead use empirical relations and simple prescriptions to determine the BH growth rate across cosmic time. Each of them includes a "burst" mode triggered during a

major merger until the BH reaches the $M_{\rm BH}$–σ_* relation, and a "steady" mode that operates otherwise.

- PL: BHs grow at the Eddington rate during the burst mode, and otherwise draw from a universal power law Eddington ratio distribution. The power law does not substantially affect BH growth, but it helps reproduce the AGN luminosity function.
- AGN-MS: BHs grow at the Eddington rate during the burst mode, and otherwise accrete at a fixed fraction of the star formation rate, motivated by observations. This mode helps grow BHs in low-mass halos, but fails to produce high-luminosity AGN at low-redshift without additional variability.
- BLQ: During the burst mode, BHs grow at an Eddington ratio drawn from a log-normal distribution that was fit to broad-line quasars (Kelly and Shen, 2013; Tucci and Volonteri, 2017). This model does the best of the three at reproducing the quasar luminosity function, but does not produce enough accretion in dwarf galaxies due to the lack of a steady mode.

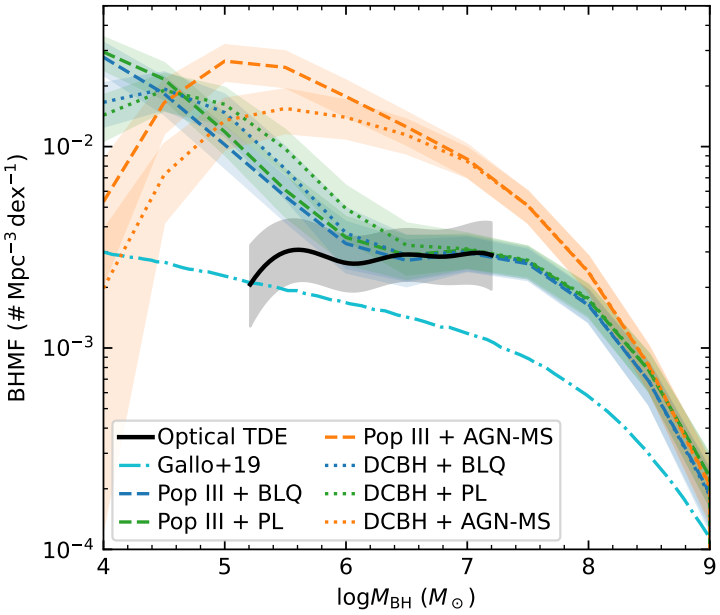

Figure 7.20: BHMF obtained by Gallo and Sesana (2019) and optical TDEs, compared with theoretical predictions from semi-analytical models.

These models all match the $M_{\rm BH}$–σ_* relation at high masses but deviate at lower masses depending on the seeding and accretion prescriptions. The resulting BHMFs

are shown in Figure 7.20. Interestingly, all models except the AGN-MS models produce a somewhat flat feature in the BHMF between 10^6–$10^7\,M_\odot$. However, the steep rise towards lower masses shown in the models are not seen in the BHMF shape determined by optical TDEs.

Caveats — The above analysis only includes the optical TDE sample. Therefore, the implications for the local BHMF is only robust if the $M_{\rm BH}$ distribution of optical TDEs is representative of the underlying $M_{\rm BH}$ distribution of all TDEs. While previous studies do not find a significant difference in the $M_{\rm BH}$ distributions between optically and X-ray selected TDE samples (Wevers, Stone, et al., 2019; French, Wevers, et al., 2020), we note that the literature samples consist of events from various surveys with different sensitivity and selection criteria. A robust assessment requires detailed understanding of how TDE emission properties (across the electromagnetic spectrum from X-ray to radio) depend on $M_{\rm BH}$ in a way that biases the sample $M_{\rm BH}$ distributions under different selection criteria.

We also note that in order to obtain the BHMF, we assumed that the $M_{\rm BH}$–σ_* relation remains valid down to $M_{\rm BH} \sim 10^5\,M_\odot$. There are two caveats associated with this assumption: (i) the number of dynamical $M_{\rm BH}$ measurements at $M_{\rm BH} \lesssim 10^6\,M_\odot$ is still insufficient to robustly test the $M_{\rm BH}$–σ_* relation in the IMBH regime (Greene, Strader, and Ho, 2020), (ii) the Kormendy and Ho (2013, Eq. 3) relation is mainly based on massive elliptical galaxies. If using the $M_{\rm BH}$–σ_* relations derived by Gültekin, Richstone, et al. (2009) and Greene, Strader, and Ho (2020), the inferred $M_{\rm BH}$ will be lower by by 0.2–0.4 dex across the range of σ_* measurements, whereas the shape of the inferred black hole mass function remains the same.

7.7 Summary

We present a complete flux-limited sample of 55 blue nuclear transients systematically selected with ZTF. Among the 55 objects, 33 are classified as TDEs. Their black hole masses are inferred with host galaxy scaling relations (using central velocity dispersion σ_* for 17 objects, and using galaxy total stellar mass $M_{\rm gal}$ in for the other 16 objects). We recovered a number of correlations between $M_{\rm BH}$ and photometric properties (§7.6).

For rate inferences, we develop a survey efficiency corrected maximum volume method. We present the rest-frame g-band luminosity function, precisely constrain the upper end ($10^{43.5} \lesssim L_g \lesssim 10^{44.7}\,{\rm erg\,s^{-1}}$) for the first time, and observe a shallower slope (compared to van Velzen 2018) at the low end ($10^{42.5} \lesssim L_g \lesssim$

$10^{43.1}$ erg s^{-1}) that drives a $\approx 2\times$ reduction in the inferred volumetric rate. Using a newly determined LF in terms of the peak UV/optical blackbody luminosity, we find the rates of optically loud and X-ray loud TDEs are comparable.

We construct the optical TDE mass function, confirming the previous result of rate suppression due to event horizon, and revealing a $\phi(M_{\rm BH}) \propto M_{\rm BH}^{-0.25}$ dependence at $10^{5.2}\,M_\odot \lesssim M_{\rm BH} \lesssim 10^{7.4}\,M_\odot$. This indicates that the local BHMF is relatively flat. At a typical galaxy mass of $10^{10}\,M_\odot$, we constrain the per-galaxy TDE rate to be [3.7, 7.4, and 1.6] $\times\,10^{-5}$ galaxy^{-1} yr^{-1} in galaxies with red, green, and blue colors, respectively.

While we have mainly focused on TDE demographics in this paper, the TDE sample presented here can also be used to address the origin of TDE's UV/optical emission, and to train machine learning algorithms (e.g., Gomez et al. 2022) for real-time photometric selection of TDE candidates. The luminosity and mass functions of optical TDEs should ultimately be compared to that of X-ray-, infrared- and radio-selected TDEs.

Over the next few years, we expect substantial progresses to be made in studies of TDE demographics. The excellent angular resolution and depth of the Vera Rubin Observatory Legacy Survey of Space and Time (LSST; Ivezić et al. 2019) will enable the creation of a reference galaxy catalog that is complete to low-mass galaxies out to higher redshifts. Since TDE black hole mass scales positively with transient duration [see Eq. (7.10) and panel (e) of Figure 7.12], the selection of fast-evolving TDEs will rely on high-cadence wide-field experiments such as those conducted by ZTF, the La Silla Schmidt Southern Survey (LS4), and the wide-field (200 deg^2) *Ultraviolet Transient Astronomy Satellite* (*ULTRASAT*; Ben-Ami et al. 2022).

7.8 Appendix

Supplementary Tables

The observing logs of low-resolution spectroscopy and ESI spectroscopy are provided in Table 7.7 and Table 7.8, respectively. The pre-flare host galaxy photometry is provided in Table 7.9, Table 7.10, Table 7.11.

Details of Sample Selection

Here we justify a few selection cuts adopted in §7.2.

The `sgscore1` (star-galaxy classification score) parameter is close to one (zero) for a star-like (galaxy-like) morphology. Its value is set to 0.5 if the PS1 counterpart is

Table 7.7: Log of low-resolution optical spectroscopy of the ZTF TDE Sample.

ID	Start Date	t (days)	Telescope	Instrument	Wavelength range (Å)	Exp. (s)
17	2021-01-11.5	+54	LDT	DeVeny	3586–8034	2700
19	2022-11-17.6†	+599	Keck-I	LRIS	3200–10250	2700
	2022-11-25.6†	+605	Keck-I	LRIS	3200–10250	2400
20	2022-04-07.5	+395	Keck-I	LRIS	3200–10250	1500
21	2021-01-14.5	+7	P60	SEDM	3770–9223	2700
	2021-01-16.5	+9	P60	SEDM	3770–9223	2700
	2021-02-08.5	+26	P60	SEDM	3770–9223	2700
	2021-02-20.5	+31	P200	DBSP	3410–5550, 5750–9995	1200
	2021-04-14.5	+70	Keck-I	LRIS	3200–10250	400
	2021-06-07.5	+111	Keck-I	LRIS	3200–10250	430
	2021-08-13.3	+161	Keck-I	LRIS	3200–10250	430
	2021-09-07.3	+179	Keck-I	LRIS	3200–10250	900
	2022-02-06.6	+293	Keck-I	LRIS	3200–10250	900
22	2021-06-07.3	+100	Keck-I	LRIS	3200–10250	485
23	2021-04-09.4	+34	P200	DBSP	3410–5550, 5750–9995	1200
25	2021-05-13.5	+17	Keck-I	LRIS	3200–10250	300
26	2021-08-01.4	+51	P200	DBSP	3410–5550, 5750–9995	1800
27	2021-07-06.3	−1	Keck-I	LRIS	3200–10250	300
28	2021-08-04.2	+27	P200	DBSP	3410–5550, 5750–9995	900
	2022-05-26.3	+300	Keck-I	LRIS	3200–10250	900
29	2021-08-13.4	+18	Keck-I	LRIS	3200–10250	750
30	2021-09-17.5	+25	Keck-I	LRIS	3200–10250	600
31	2022-10-03.2	+353	P200	DBSP	3410–5550, 5750–9995	1500
32	2021-10-04.6	−15	Keck-I	LRIS	3200–10250	600
	2022-02-05.3	+80	Keck-I	LRIS	3200–10250	900
	2023-01-16.4	+349	Keck-I	LRIS	3200–10250	1200
33	2021-10-14.5	+14	P200	DBSP	3410–5550, 5750–9995	900

†: On 2022-11-17, one exposure (900 s) on the red CCD is badly affected by cosmic rays and is therefore not included in spectral extraction. We stack the observations on 2022-11-17 and 2022-11-25 together to create a deep spectrum for analysis.
LRIS data are taken with the 1.0″ slit; DBSP and DeVeny data are taken with the 1.5″ slit.

Table 7.8: Details of ESI spectroscopy of the ZTF TDE Sample.

ID	Start Date	Slit width (″)	Exp. (s)	$r_{\rm extract}$ (pixel)	Fitted $\lambda_{\rm rest}$ (Å)	σ_* (km s^{-1})	SNR
1	2022-07-04.5	0.5	1200	4.2	5030–5600	148.6 ± 14.4	6.9
5	2022-10-21.6	0.5	1200	5.7	5030–5600	68.0 ± 2.0	33.3
8	2022-08-24.4	0.5	900	4.3	5030–5600	86.9 ± 3.9	16.9
13	2022-10-21.4	0.5	1200	9.3	5030–5600	76.6 ± 5.3	8.8
16	2022-11-25.5	0.3	2700	5.8	5030–5600	43.6 ± 3.1	12.0
17	2022-03-07.6	0.5	600	4.2	5030–5600	48.5 ± 2.0	11.6
18	2022-10-22.6	0.5	600	8.2	5030–5600	40.1 ± 3.1	7.4
21	2022-03-07.6	0.5	2400	6.0	5030–5127,5159–5600	174.5 ± 25.3	9.1
22	2022-03-07.3	0.5	1500	4.3	5030–5600	73.5 ± 17.3	7.2
	2022-11-25.6	0.5	2400				
23	2022-03-07.3	0.5	1600	5.6	5030–5083, 5137–5600	57.6 ± 6.3	6.8
	2022-11-25.6	0.5	2400				
24	2021-12-28.4	0.75	300	5.0	5030–5600	99.6 ± 3.8	18.4
26	2022-10-22.3	0.5	1800	4.2	5030–5196, 5200–5600	57.8 ± 5.3	8.1
27	2022-03-07.7	0.5	600	4.6	5030–5600	102.4 ± 5.4	11.3
30	2022-08-24.5	0.5	1200	5.0	5030–5310, 5346–5600	62.3 ± 7.1	10.6
33	2022-03-07.2	0.5	1120	3.8	5030–5578	34.2 ± 4.8	7.3

All ESI spectra were obtained after the optical TDE flux has faded to $< 10\%$ of the host galaxy flux. $r_{\rm extract}$ can be converted to angular scale using a conversion factor of 0.154″ per pixel.

Table 7.9: *GALEX* and SDSS Photometry of ZTF TDE Host Galaxies.

ID	FUV	NUV	SDSS/*u*	SDSS/*g*	SDSS/*r*	SDSS/*i*	SDSS/*z*
1				20.55 ± 0.19	19.24 ± 0.16	18.80 ± 0.17	18.28 ± 0.17
2		23.73 ± 0.89		22.73 ± 0.28	21.32 ± 0.13	20.95 ± 0.14	20.23 ± 0.17
3							
4	20.91 ± 0.27	20.19 ± 0.12	19.63 ± 0.13	18.37 ± 0.03	17.69 ± 0.01	17.28 ± 0.02	17.11 ± 0.19
5	19.24 ± 0.18	17.83 ± 0.03	16.51 ± 0.08	15.01 ± 0.02	14.49 ± 0.01	14.20 ± 0.01	14.04 ± 0.04
6	22.51 ± 1.04	21.12 ± 0.23	20.13 ± 0.28	19.00 ± 0.04	18.24 ± 0.02	17.81 ± 0.03	17.71 ± 0.10
7							
8	21.19 ± 0.32	21.22 ± 0.26					
9		22.54 ± 0.19	20.29 ± 0.30	19.28 ± 0.06	18.52 ± 0.07	18.24 ± 0.07	17.96 ± 0.18
10							
11	21.12 ± 0.09	20.87 ± 0.04	20.04 ± 0.10	19.07 ± 0.02	18.55 ± 0.01	18.23 ± 0.02	17.97 ± 0.06
12			20.05 ± 0.09	18.63 ± 0.02	17.90 ± 0.01	17.50 ± 0.02	17.33 ± 0.04
13	22.65 ± 0.64	21.56 ± 0.25					
14	20.91 ± 0.34	19.61 ± 0.11	19.18 ± 0.09	18.20 ± 0.01	17.68 ± 0.02	17.35 ± 0.02	17.23 ± 0.05
15		21.97 ± 0.25	21.79 ± 0.70	21.14 ± 0.26	19.81 ± 0.07	19.22 ± 0.07	19.46 ± 0.35
16			19.80 ± 0.14	18.87 ± 0.02	18.26 ± 0.02	18.05 ± 0.02	17.94 ± 0.12
17			18.81 ± 0.12	17.24 ± 0.02	16.53 ± 0.02	16.18 ± 0.01	15.90 ± 0.05
18	21.82 ± 0.34	21.61 ± 0.09	18.88 ± 0.09	17.40 ± 0.01	16.70 ± 0.01	16.34 ± 0.01	16.11 ± 0.02
19	21.98 ± 0.34	21.09 ± 0.15					
20			23.14 ± 0.64	21.83 ± 0.14	21.00 ± 0.07	20.63 ± 0.07	20.83 ± 0.35
21			22.84 ± 0.89	21.07 ± 0.11	19.71 ± 0.07	19.09 ± 0.08	18.66 ± 0.17
22				20.34 ± 0.04	19.57 ± 0.03	19.29 ± 0.06	18.77 ± 0.15
23			20.52 ± 0.21	19.51 ± 0.04	19.04 ± 0.05	18.68 ± 0.07	18.50 ± 0.28
24			17.66 ± 0.06	15.86 ± 0.01	14.98 ± 0.01	14.50 ± 0.01	14.18 ± 0.02
25							
26							
27	23.29 ± 0.17	22.05 ± 0.09	19.22 ± 0.10	17.67 ± 0.01	16.90 ± 0.01	16.51 ± 0.01	16.24 ± 0.03
28		22.51 ± 0.38					
29		20.01 ± 0.14					
30	21.76 ± 0.39	20.76 ± 0.13	20.33 ± 0.39	18.79 ± 0.05	18.14 ± 0.05	17.78 ± 0.04	17.62 ± 0.07
31	21.88 ± 0.51	21.61 ± 0.31					
32							
33			20.62 ± 0.36				

not "detected" in the PS1 `StackObjectAttributes` table (see details in Tachibana and Miller 2018; Miller and Hall 2021). In Figure 7.21, we show the distribution of the 55 photometric TDE candidates (after step 7 in §7.2) on the `magnr` (magnitude of the nearest object in the ZTF reference image) versus `sgscore1` diagram. Symbol colors follow the same convention as in Figure 7.2. The 33 TDEs are shown in solid markers and the 22 false positives are shown in hollow markers. We show the ZTF names for objects with `sgscore1>0.2`. The highest value of `sgscore` is 0.5, implying that our selection cut of `sgscore1` is sufficiently liberal.

In Figure 7.22, the observer-frame e-folding rise and decline timescales (computed using the best-fit models derived in §7.3) are shown versus $M_{\rm BH}$. The values are well within the boundaries of 2 and 300 days, implying that our criteria adopted in steps 5 and 6 of §7.2 are not at the boundaries.

Table 7.10: PS1 Photometry of ZTF TDE Host Galaxies.

ID	PS1/g	PS1/r	PS1/i	PS1/z	PS1/y
1	20.42 ± 0.22	19.18 ± 0.15	18.74 ± 0.15	18.54 ± 0.16	18.55 ± 0.27
2	23.02 ± 0.67	21.55 ± 0.17	20.96 ± 0.15	20.72 ± 0.18	20.78 ± 0.34
3	20.41 ± 0.26	19.57 ± 0.14	19.20 ± 0.13	19.16 ± 0.22	18.93 ± 0.15
4	18.34 ± 0.05	17.70 ± 0.03	17.29 ± 0.01	17.10 ± 0.03	16.82 ± 0.06
5	14.99 ± 0.03	14.48 ± 0.01	14.26 ± 0.01	14.09 ± 0.02	13.88 ± 0.03
6	18.94 ± 0.03	18.24 ± 0.02	17.85 ± 0.03	17.57 ± 0.05	17.34 ± 0.05
7		21.53 ± 0.15	20.63 ± 0.10	20.63 ± 0.14	20.11 ± 0.22
8	17.03 ± 0.04	16.20 ± 0.02	15.83 ± 0.02	15.57 ± 0.03	15.39 ± 0.06
9	19.30 ± 0.07	18.65 ± 0.10	18.28 ± 0.06	18.21 ± 0.08	18.03 ± 0.11
10	15.01 ± 0.05	14.33 ± 0.03	13.91 ± 0.06	13.69 ± 0.04	13.44 ± 0.05
11	19.03 ± 0.02	18.52 ± 0.01	18.27 ± 0.02	18.05 ± 0.03	17.97 ± 0.06
12	18.54 ± 0.03	17.92 ± 0.02	17.51 ± 0.02	17.34 ± 0.03	17.06 ± 0.05
13	17.99 ± 0.03	17.20 ± 0.01	16.76 ± 0.01	16.53 ± 0.02	16.39 ± 0.05
14	18.10 ± 0.04	17.68 ± 0.04	17.33 ± 0.02	17.20 ± 0.02	17.07 ± 0.06
15	21.44 ± 0.26	19.88 ± 0.09	19.37 ± 0.04	19.10 ± 0.08	19.26 ± 0.28
16	18.79 ± 0.06	18.30 ± 0.03	18.03 ± 0.02	17.88 ± 0.03	17.82 ± 0.09
17	17.17 ± 0.05	16.51 ± 0.03	16.16 ± 0.03	16.03 ± 0.03	15.87 ± 0.06
18	17.32 ± 0.01	16.69 ± 0.01	16.36 ± 0.01	16.15 ± 0.01	16.00 ± 0.03
19	19.74 ± 0.11	19.33 ± 0.05	18.89 ± 0.09	18.71 ± 0.21	18.40 ± 0.16
20	22.00 ± 0.15	20.87 ± 0.05	20.64 ± 0.06	20.63 ± 0.09	20.26 ± 0.19
21		19.84 ± 0.13	19.17 ± 0.07	18.89 ± 0.07	18.69 ± 0.24
22	20.32 ± 0.05	19.53 ± 0.05	19.17 ± 0.04	19.01 ± 0.07	
23	19.66 ± 0.07	19.09 ± 0.06	18.86 ± 0.05	18.63 ± 0.07	18.62 ± 0.15
24	15.73 ± 0.02	14.93 ± 0.01	14.49 ± 0.01	14.21 ± 0.01	13.98 ± 0.02
25	20.44 ± 0.06	20.08 ± 0.04	19.82 ± 0.05	19.58 ± 0.04	19.67 ± 0.12
26	19.63 ± 0.07	18.93 ± 0.03	18.55 ± 0.08	18.33 ± 0.07	18.25 ± 0.09
27	17.56 ± 0.02	16.88 ± 0.02	16.52 ± 0.01	16.27 ± 0.02	16.17 ± 0.04
28	19.84 ± 0.09	19.01 ± 0.09	18.58 ± 0.13	18.33 ± 0.09	18.09 ± 0.12
29	17.49 ± 0.02	16.84 ± 0.02	16.39 ± 0.05	16.18 ± 0.05	15.93 ± 0.06
30	18.79 ± 0.03	18.19 ± 0.03	17.88 ± 0.01	17.78 ± 0.04	17.53 ± 0.11
31	20.03 ± 0.06	19.53 ± 0.08	19.19 ± 0.07	18.98 ± 0.11	18.91 ± 0.11
32	20.96 ± 0.15	19.90 ± 0.14	19.25 ± 0.06	19.04 ± 0.12	18.80 ± 0.13
33	19.34 ± 0.22	18.65 ± 0.26	18.18 ± 0.25	18.09 ± 0.33	17.77 ± 0.24

Table 7.11: 2MASS and WISE Photometry of ZTF TDE Host Galaxies.

ID	2MASS/J	2MASS/H	2MASS/K_s	WISE/$W1$	WISE/$W2$
1	18.66 ± 0.41	17.99 ± 0.32	17.66 ± 0.28		
2				20.59 ± 0.57	20.66 ± 0.45
3				19.57 ± 0.19	20.91 ± 0.62
4				17.02 ± 0.04	17.47 ± 0.04
5	13.71 ± 0.01	13.61 ± 0.02	13.77 ± 0.03	14.60 ± 0.01	15.23 ± 0.02
6		17.17 ± 0.12		17.78 ± 0.04	18.36 ± 0.05
7				19.22 ± 0.13	19.89 ± 0.17
8	15.02 ± 0.02	15.02 ± 0.03	15.13 ± 0.04	15.65 ± 0.02	16.16 ± 0.02
9				18.50 ± 0.07	19.08 ± 0.09
10	13.26 ± 0.02	12.95 ± 0.02	13.26 ± 0.03	13.95 ± 0.02	14.60 ± 0.04
11	17.62 ± 0.12	17.69 ± 0.16		18.40 ± 0.05	18.90 ± 0.07
12	16.72 ± 0.05	16.83 ± 0.10	17.04 ± 0.12	17.56 ± 0.04	18.13 ± 0.04
13	16.05 ± 0.04		15.98 ± 0.06	16.66 ± 0.03	17.21 ± 0.03
14				17.53 ± 0.05	18.01 ± 0.05
15				18.59 ± 0.07	19.10 ± 0.08
16				18.48 ± 0.11	18.98 ± 0.12
17	15.77 ± 0.05	15.38 ± 0.05	15.67 ± 0.08	16.48 ± 0.03	17.16 ± 0.04
18				16.63 ± 0.03	17.22 ± 0.03
19				18.49 ± 0.07	19.10 ± 0.09
20				20.75 ± 0.20	
21	18.32 ± 0.17	18.01 ± 0.21	17.67 ± 0.15	18.18 ± 0.14	18.65 ± 0.16
22				19.33 ± 0.10	20.15 ± 0.20
23				18.98 ± 0.10	19.80 ± 0.18
24	13.83 ± 0.01	13.62 ± 0.01	13.80 ± 0.01	14.57 ± 0.02	15.25 ± 0.02
25				19.98 ± 0.19	20.11 ± 0.17
26	18.26 ± 0.18	18.30 ± 0.26	18.07 ± 0.22	18.70 ± 0.10	19.30 ± 0.10
27	15.87 ± 0.04	15.59 ± 0.04	15.91 ± 0.07	16.69 ± 0.03	17.29 ± 0.03
28					
29	15.73 ± 0.03	15.79 ± 0.05	15.46 ± 0.04	16.11 ± 0.04	16.62 ± 0.03
30	17.35 ± 0.13	17.29 ± 0.17		17.72 ± 0.06	18.16 ± 0.07
31	19.08 ± 0.52			19.55 ± 0.44	20.49 ± 1.05
32		18.09 ± 0.29		18.68 ± 0.11	19.19 ± 0.16
33	17.90 ± 0.14	17.92 ± 0.23		18.03 ± 0.25	18.73 ± 0.30

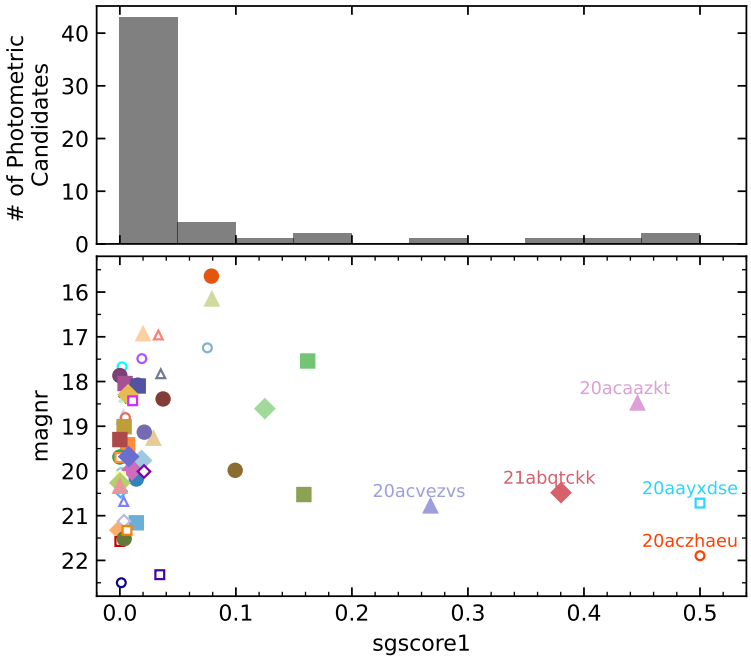

Figure 7.21: The `sgscore1` and `magnr` parameters of 55 photometric ZTF TDE candidates.

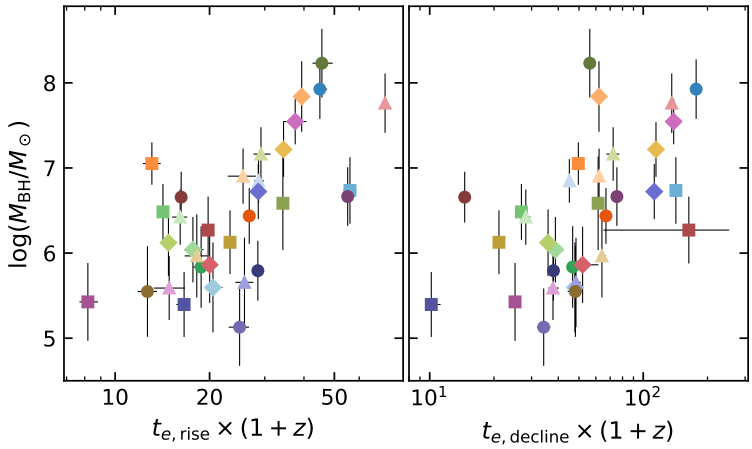

Figure 7.22: The black hole mass and observer-frame e-folding rise/decline timescales of 33 TDEs.

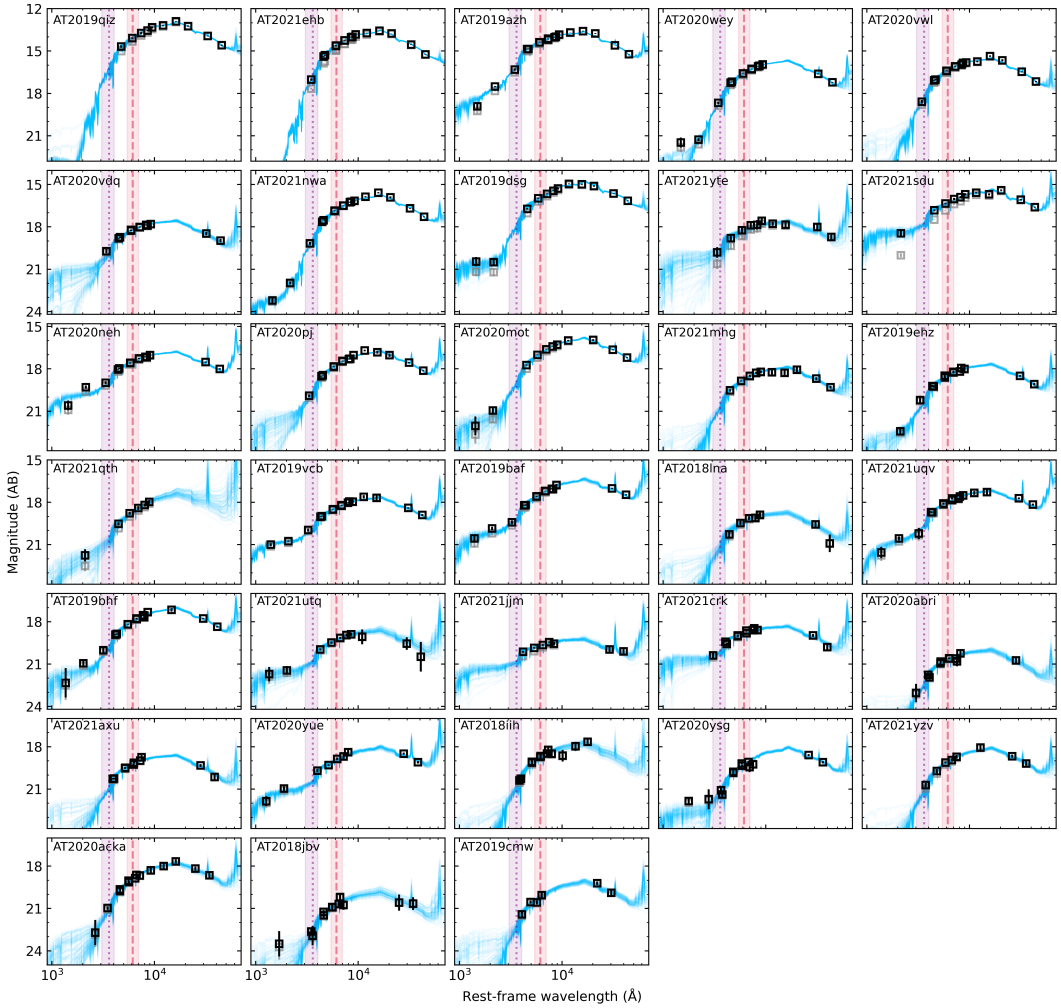

Figure 7.23: ZTF TDE host galaxy SEDs (sorted by redshift).

Host Galaxy SEDs and Comparison with Previous Studies

Figure 7.23 shows the SEDs of 33 TDE host galaxies. The grey and black squares show the observed and Galactic extinction corrected photometry, respectively. The blue lines show models of the 100 walkers in the MCMC sampler. The dotted and dashed vertical lines mark rest-frame wavelength of the SDSS u and r filters.

There are 13 galaxies in common between our sample and Hammerstein, van Velzen, et al. (2023). The left panel of Figure 7.24 shows the distributions of these objects on the galaxy color–mass diagram, using values derived in this work and Hammerstein, van Velzen, et al. (2023). Data points for the same object are connected with the solid black lines. The dahsed green line show the green valley defined by Eq. (7.22). For nine of the 13 objects, the $\log(M_{\rm gal}/M_\odot)$ and ${}^{0,0}u-r$ parameters are consistent with each other (to within 2-σ). For the other four objects (AT2019qiz, AT2019vcb,

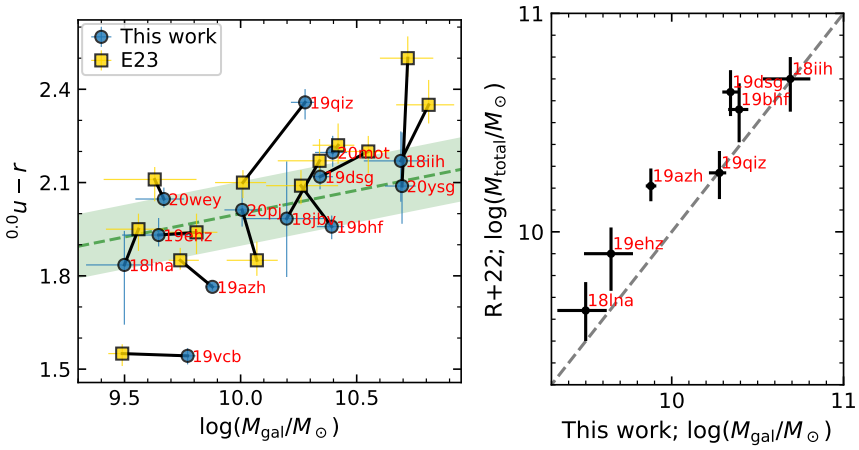

Figure 7.24: Comparison between host galaxy properties derived in this work, Hammerstein, van Velzen, et al. (2023), and Ramsden et al. (2022).

AT2019azh, and AT2020ysg), the difference probably comes from the different source of photometry: Hammerstein, van Velzen, et al. (2023) obtained photometry from various catalogs whereas we measured the host brightness using `LAMBDAR` (see §7.4).

There are 7 galaxies in common between our sample and Ramsden et al. (2022). The mean offset in $\log(M_{\rm gal}/M_\odot)$ between this work and Ramsden et al. (2022) is -0.17 dex (see the right panel of Figure 7.24). The difference could be because Ramsden et al. (2022) used a non-parametric SFH, whereas we assumed a delayed exponentially declining function.

Chapter 8

SUMMARY AND FUTURE DIRECTIONS

8.1 Thesis Summary

In this thesis, I have conducted a series of observational studies on high-energy transients powered by black holes, utilizing a plethora of multi-wavelength facilities from the γ-ray to the radio bands. The central engines vary from stellar-mass black holes at birth (Chapter 4) or during binary stellar evolution (Chapters 2–3), to massive black holes at the bottom end of the known supermassive black hole population (Chapters 5–7). These transients illuminates the dynamic Universe, probe black holes in a diverse range of environments, and help us understand the fundamental physics of black hole accretion. Below I summarize the main results of my thesis:

1. AT2019wey is an X-ray transient discovered by *SRG* during the first all-sky survey. Based on the X-ray spectral and timing characteristics, I classify it as a LMXB with long durations in the hard states. Unlike other transient BHBs with progressive state transitions, the X-ray evolution of AT2019wey follows an oscillatory track (e.g., on the HID, HRD, and RID).

2. Combining the X-ray results with UV, optical, and radio properties, I show that the central engine of AT2019wey is probably a BH. The accretion flow in the LHS and HIMS is consistent with ADAF and standard accretion, respectively. The unique light curve plateaus resemble those seen in the Z Cam type of dwarf novae, indicating that the mass transfer rate from the secondary star is probably very close to the critical mass accretion rate $\dot{M}^{+}_{\rm crit}$.

3. AT2020mrf is an X-ray transient discovered by *SRG* during the second all-sky survey. I associate with a fast blue optical transient (FBOT) in ZTF, and establish it as the 5$^{\rm th}$ member of the the emerging population of radio and X-ray loud FBOTs. My *Chandra* observation reveals late-time X-ray emission as luminous as lGRBs (10^{42} erg s^{-1}) with day-timescale variability, supporting a central BH or magnetar as the power source. The host galaxy properties of known LFBOTs point to progenitor systems that involve massive stars.

4. I have played a leading role in the discovery of the nearby TDE AT2021ehb, and designed a massive X-ray follow-up campaign, which led to the identification of a soft → hard → soft X-ray spectral evolution. I attribute the former transition to the gradual magnetic field amplification in a newly formed corona, and interpret the latter as a disk instability triggered state transition. With *NICER* and *NuSTAR*, I have identified evidence of relativistic disk reflection, which suggests that the disk surface material is highly ionized in the super-Eddington phase.

5. Using *NuSTAR*, *NICER* and *Swift*/XRT, I demonstrate that the early-time X-ray spectrum of the jetted TDE AT2022cmc remains a broken power-law. By modeling the broadband SED, I propose that the X-ray prompt emission has a synchrotron origin.

6. I develop a set of clearly defined selection criteria to select TDE candidates from ZTF, and undertake spectroscopic observations of all candidates to obtain a complete flux-limited TDE sample. I derive robust optical TDE rate and find that the luminosity function can be best described with a broken power-law, which removes a major uncertainty towards predicting TDE detection rates in future UV/optical sky surveys. By computing TDE rate as a function of black hole mass, I infer that the shape of the local BHMF from $2 \times 10^5\ M_\odot$ to $2 \times 10^7\ M_\odot$ is consistent with being flat. My work on TDE demographics lays a clear foundation for both future survey work and theoretical inquiry.

8.2 Upcoming Prospects for Using Transients as a Black Hole Census

High energy transients powered by black holes are fascinating objects because they offer excellent laboratories to study not only accretion and jet physics, but also other fundamental open questions in astrophysics, including SN mechanisms, binary evolution, as well as black hole formation in the early universe and the processes that govern their growth. Building upon my thesis work, I list below several promising directions for future research in this field.

Uncover the Sub-luminous Population of BHB Transients

The X-ray luminoisty funciton of LMXBs is a borken power-law flattening below $\sim 10^{36}$–$10^{37}\,\mathrm{erg\,s^{-1}}$. While more than two dozen low-luminosity LMXBs are expected to be found by *SRG* (Doroshenko et al., 2014), AT2019wey remains the only known *SRG*-discovered LMXB thus far. Given the cadence and the localization un-

certainty of eROSITA and ART-XC, identifying the nature of these X-ray transients requires extensive follow-up observations. One ideal starting point is to leverage legacy all-sky archives (*GALEX*, SDSS, PS1, *Gaia*, etc), time-domain datasets, and multiplexed optical spectroscopic instruments (e.g., with SDSS-V, LAMOST, and DESI) to efficiently obtain basic classifications for *SRG* objects (Galactic or extra-galactic, accretion powered or stellar dominated, etc).

Once the subluminous population of LMXBs are recovered, detailed observations are needed to decipher the nature of the accretors. The spacial distribution of BH LMXBs at high Galactic scale heights encodes the magnitude of natal kick the BH receives at birth (Repetto and Nelemans, 2015). The kinematics of the binary systems provide important constrains for population synthesis, binary evolution, and disk instability behaviors (Siegel et al., 2022). The mass and spin distributions of a greater sample of BHBs can be directly compared with GW-detected BH mergers and inform theoretical calculations of various black hole formation channels.

Map the Media Surrounding Massive Star Explosions

The formation of stellar-mass black holes is uniquely probed by the final gravitational collapse of massive stars that manifest themselves as spectacular explosions. A major recent development is the realization that a large fraction of massive stars undergo significant episodic mass losses, and in some cases these losses serve as omens of their deaths. A celebrated example is the LFBOT phenomena. In the prototype LFBOT AT2018cow, early-time X-ray observations reveal prominent spectral features reminiscent of relativistic disk reflection, which fades away over $\approx$ 1 month (Margutti, Metzger, et al., 2019). This gives direct evidence of the existence of dense equatorial material prior to the explosion. Continued monitoring observations in the millimeter and radio bands track the CSM density profile, which traces back the mass loss history of the progenitor star.

This frontier of massive star deaths will continue to be vigorous with ongoing and upcoming time domain surveys. The Vera Rubin Observatory Legacy Survey of Space and Time (LSST) will come online in 2025. With an unprecedented survey sensitivity of ≈ 24 mag, LSST will routinely detect pre-SN outbursts at $M_V < -14$. *SRG* and X-ray monitoring observations on nearby events will uniquely probe the inverse Compton and thermal bremsstrahlung emission from SN shocks interacting with the CSM. Upcoming sensitive surveys in the radio (DSA-2000) and millimeter (CMB-S4, CMB-HD) bands will map out the SN environments on timescales from

days to centuries prior to their explosion. Such mass loss tracers will constrain the final evolution of massive stars, allowing comprehensive investigation of the explosion energies and mass ranges of stars that give birth to NSs and BHs.

Reveal the Long-term Evolution of TDEs

Moving from stellar-mass black holes to more massive black holes, we are in a golden era of TDE studies. Recent monitoring observation of individual TDEs have revealed that delayed brightening in the X-ray (Chapter 5), optical (Chapter 7), infrared (Jiang, Wang, et al., 2021), and radio bands (Horesh, Cenko, and Arcavi, 2021; Cendes, Berger, et al., 2022) are not uncommon. Moving forward, systematic long-term multi-wavelength follow-up programs are required to reveal the frequency, timescale, and accretion regime of corona formation, disk state transition, and wind/jet launching.

High-resolution spectroscopy with *XMM-Newton*, *Chandra*, and the upcoming *XRISM* mission are particularly exciting to study the energetics and structure of the accretion flow closest to the black hole. The UV/optical emission is likely produced by multiple emission mechanisms. Early-time UV observations with *HST* and the upcoming UV satellite (*UVEX* or STAR-X) will provide a key diagnostic for differentiating between various power sources. Realistic simulations spanning a range of physical parameters are on the horizon of determining the origin and internal energy source of the UV/optical emitting layer.

By modeling the TDE radio synchrotron emission, one can map out the circum-nuclear density profile across various types of galaxies. With recent (modest) associations between a few PeV-scale IceCube neutrinos and TDE candidates, the multi-messenger front is also advancing rapidly (Stein et al., 2021; Reusch et al., 2022; van Velzen, Stein, et al., 2021).

Explore New TDE Types & New BH Environments

Most of current TDE searches are restricted to slow-evolving transients in galaxy centers, which select against certain TDE types and BH environments. For example, partially disrupted events might exhibit multiple peaks or short-duration periodic flares. Such a transient can be produced when a binary is destroyed by the tides of the BH via the Hills mechanism, leading to an ejected hypervelocity star and a star in tightly bound orbit around the massive BH (Lu and Quataert, 2022; Linial and Metzger, 2023). Recently, partial TDEs have gained significant interest, as they are closely related to quasi-periodic eruptions (QPEs) and extreme mass-ratio inspirals

(EMRIs). The former are rare enigmatic transients in galactic nuclei characterized by short duty cycle large amplitude increases in X-ray luminosity with periods of $\sim$ 10 hr (Miniutti et al., 2019; Giustini, Miniutti, and Saxton, 2020; Arcodia et al., 2021); the latter are inspirals of stellar-mass compact objects captured by massive BHs, which are especially interesting GW sources for the planned Laser Interferometer Space Antenna (*LISA*). Therefore, exploring the phenomenology of partial TDEs and their connection to other stellar dynamical processes in galactic nuclei is a timely research topic.

Another under-explored front is TDEs in wandering BHs or stripped galaxy nuclei. Recent cosmological simulations suggest that in the local universe, a significant fraction of BHs are offset from the center of the host halo via disruption of satellite galaxies or ejections due to gravitational recoils (Izquierdo-Villalba et al., 2020; Ricarte, Tremmel, et al., 2021). Using an indirect indicator of high mass fraction BHs, Voggel et al. (2019) estimates that 8–32% of the local BH number density are in nuclear star clusters of stripped galaxies. So far, only one promising off-nuclear TDE has been found (archival searches with *XMM-Newton*), which was associated with a compact star cluster with a mass of $\sim 10^7\ M_\odot$ (Lin et al., 2018). Looking forward, the excellent angular resolution of LSST opens up the discovery space of similar transients. If a large sample of off-nuclear TDEs can be found, they can be used to constrain the fraction of wandering BHs as a function of $M_{\rm BH}$, which is a sensitive diagnostic for distinguishing between different scenarios of BH formation in the early Universe (Greene, Strader, and Ho, 2020).

BIBLIOGRAPHY

Abazajian, K. N. et al. (June 2009). In: *ApJS* 182.2, pp. 543–558. DOI: 10.1088/0067-0049/182/2/543.

Abbott, R. et al. (Jan. 2023). In: *Physical Review X* 13.1, 011048, p. 011048. DOI: 10.1103/PhysRevX.13.011048.

Abramowicz, M. A., B. Czerny, et al. (Sept. 1988). In: *ApJ* 332, p. 646. DOI: 10.1086/166683.

Abramowicz, M. A., X. Chen, et al. (Jan. 1995). In: *ApJL* 438, p. L37. DOI: 10.1086/187709.

Abramowicz, M. A. and P. C. Fragile (Jan. 2013). In: *Living Reviews in Relativity* 16.1, 1, p. 1. DOI: 10.12942/lrr-2013-1.

Afsariardchi, N. et al. (Sept. 2021). In: *ApJ* 918.2, 89, p. 89. DOI: 10.3847/1538-4357/ac0aeb.

Ahn, C. P. et al. (Dec. 2012). In: *ApJS* 203, 21, p. 21. DOI: 10.1088/0067-0049/203/2/21.

Aihara, H., Y. AlSayyad, et al. (Dec. 2019). In: *PASJ* 71.6, 114, p. 114. DOI: 10.1093/pasj/psz103.

Aihara, H., N. Arimoto, et al. (Jan. 2018). In: *PASJ* 70, S4, S4. DOI: 10.1093/pasj/psx066.

Aird, J. et al. (Feb. 2012). In: *ApJ* 746.1, 90, p. 90. DOI: 10.1088/0004-637X/746/1/90.

Alam, S. et al. (July 2015). In: *ApJS* 219.1, 12, p. 12. DOI: 10.1088/0067-0049/219/1/12.

Alexander, K. D., E. Berger, et al. (Mar. 2016). In: *ApJL* 819.2, L25, p. L25. DOI: 10.3847/2041-8205/819/2/L25.

Alexander, K. D., S. van Velzen, et al. (June 2020). In: *SSRv* 216.5, 81, p. 81. DOI: 10.1007/s11214-020-00702-w.

Alexander, T. (Aug. 2017). In: *ARA&A* 55.1, pp. 17–57. DOI: 10.1146/annurev-astro-091916-055306.

Amaro Seoane, P. (2022). In: *Handbook of Gravitational Wave Astronomy. Edited by C. Bambi*, 17, p. 17. DOI: 10.1007/978-981-15-4702-7_17-1.

Amaro-Seoane, P. et al. (Feb. 2017). In: *arXiv e-prints*, arXiv:1702.00786, arXiv:1702.00786.

Andalman, Z. L. et al. (Feb. 2022). In: *MNRAS* 510.2, pp. 1627–1648. DOI: 10.1093/mnras/stab3444.

Anders, E. and N. Grevesse (Jan. 1989). In: *GeCoA* 53.1, pp. 197–214. DOI: 10.1016/0016-7037(89)90286-X.

Andreoni, I. (Feb. 2022). In: *Transient Name Server Discovery Report* 2022-397, p. 1.

Andreoni, I., M. Coughlin, T. Ahumada, et al. (Feb. 2022). In: *GRB Coordinates Network* 31590, p. 1.

Andreoni, I., M. W. Coughlin, D. A. Perley, et al. (Dec. 2022). In: *Nature* 612.7940, pp. 430–434. DOI: 10.1038/s41586-022-05465-8.

Angus, C. R. (July 2021). In: *Transient Name Server Classification Report* 2021-2291, pp. 1–2291.

Angus, C. R. et al. (Dec. 2022). In: *Nature Astronomy* 6, pp. 1452–1463. DOI: 10.1038/s41550-022-01811-y.

Aptekar, R. L. et al. (Feb. 1995). In: *SSRv* 71.1-4, pp. 265–272. DOI: 10.1007/BF00751332.

Arcavi, I., J. Burke, et al. (Oct. 2020). In: *Transient Name Server Classification Report* 2020-3228, p. 1.

Arcavi, I., A. Gal-Yam, et al. (Sept. 2014). In: *ApJ* 793.1, 38, p. 38. DOI: 10.1088/0004-637X/793/1/38.

Arcodia, R. et al. (Apr. 2021). In: *Nature* 592.7856, pp. 704–707. DOI: 10.1038/s41586-021-03394-6.

Armas Padilla, M. et al. (Feb. 2013). In: *MNRAS* 428.4, pp. 3083–3088. DOI: 10.1093/mnras/sts255.

Arnaud, K. A. (1996). In: *Astronomical Data Analysis Software and Systems V*. Ed. by G. H. Jacoby and J. Barnes. Vol. 101. Astronomical Society of the Pacific Conference Series, p. 17.

Asplund, M. et al. (Sept. 2009). In: *ARA&A* 47.1, pp. 481–522. DOI: 10.1146/annurev.astro.46.060407.145222.

Auchettl, K., J. Guillochon, and E. Ramirez-Ruiz (Apr. 2017). In: *ApJ* 838.2, 149, p. 149. DOI: 10.3847/1538-4357/aa633b.

Auchettl, K., E. Ramirez-Ruiz, and J. Guillochon (Jan. 2018). In: *ApJ* 852.1, 37, p. 37. DOI: 10.3847/1538-4357/aa9b7c.

Bachetti, M. (Feb. 2015). ascl: 1502.021.

Bachetti, M., F. A. Harrison, et al. (Feb. 2015). In: *ApJ* 800.2, 109, p. 109. DOI: 10.1088/0004-637X/800/2/109.

Bachetti, M., C. B. Markwardt, et al. (Feb. 2021). In: *ApJ* 908.2, 184, p. 184. DOI: 10.3847/1538-4357/abd1d6.

Bade, N., S. Komossa, and M. Dahlem (May 1996). In: *A&A* 309, pp. L35–L38.

El-Badry, K. et al. (May 2023). In: *MNRAS* 521.3, pp. 4323–4348. DOI: 10.1093/mnras/stad799.

Bahramian, A. and N. Degenaar (June 2022). In: *arXiv e-prints*, arXiv:2206.10053, arXiv:2206.10053. DOI: 10.48550/arXiv.2206.10053.

Bahramian, A., J. Miller-Jones, et al. (May 2018). DOI: 10.5281/zenodo.1252036. URL: https://doi.org/10.5281/zenodo.1252036.

Bailer-Jones, C. A. L. et al. (Aug. 2018). In: *AJ* 156.2, 58, p. 58. DOI: 10.3847/1538-3881/aacb21.

Balbus, S. A. and J. F. Hawley (July 1991). In: *ApJ* 376, p. 214. DOI: 10.1086/170270.

Baldassare, V. F. et al. (July 2020). In: *ApJL* 898.1, L3, p. L3. DOI: 10.3847/2041-8213/aba0c1.

Baldry, I. K. et al. (Mar. 2012). In: *MNRAS* 421.1, pp. 621–634. DOI: 10.1111/j.1365-2966.2012.20340.x.

Baldwin, J. A., M. M. Phillips, and R. Terlevich (Feb. 1981). In: *PASP* 93, pp. 5–19. DOI: 10.1086/130766.

Band, D. et al. (Aug. 1993). In: *ApJ* 413, p. 281. DOI: 10.1086/172995.

Banerjee, S. et al. (Nov. 2020). In: *MNRAS* 498.4, pp. 5353–5360. DOI: 10.1093/mnras/staa2788.

Barniol Duran, R., E. Nakar, and T. Piran (July 2013). In: *ApJ* 772.1, 78, p. 78. DOI: 10.1088/0004-637X/772/1/78.

Barniol Duran, R. and T. Piran (June 2013). In: *ApJ* 770.2, 146, p. 146. DOI: 10.1088/0004-637X/770/2/146.

Bartlett, M. S. (May 1948). In: *Nature* 161.4096, pp. 686–687. DOI: 10.1038/161686a0.

Beck, R. et al. (Jan. 2021). In: *MNRAS* 500.2, pp. 1633–1644. DOI: 10.1093/mnras/staa2587.

Begelman, M. C. and D. L. Meier (Feb. 1982). In: *ApJ* 253, pp. 873–896. DOI: 10.1086/159688.

Bellm, E. C. (Feb. 2021). In: *The Astronomer's Telegram* 14372, p. 1.

Bellm, E. C., S. R. Kulkarni, T. Barlow, et al. (June 2019). In: *PASP* 131.1000, p. 068003. DOI: 10.1088/1538-3873/ab0c2a.

Bellm, E. C., S. R. Kulkarni, M. J. Graham, et al. (Jan. 2019). In: *PASP* 131.995, p. 018002. DOI: 10.1088/1538-3873/aaecbe.

Bellm, E. C. and B. Sesar (Feb. 2016). ascl: 1602.002.

Belloni, T., A. P. Colombo, et al. (July 2002). In: *A&A* 390, pp. 199–204. DOI: 10.1051/0004-6361:20020703.

Belloni, T. and G. Hasinger (Jan. 1990). In: *A&A* 227, pp. L33–L36.

Belloni, T., J. Homan, et al. (Sept. 2005). In: *A&A* 440.1, pp. 207–222. DOI: 10.1051/0004-6361:20042457.

Belloni, T. M., S. E. Motta, and T. Muñoz-Darias (Sept. 2011). In: *Bulletin of the Astronomical Society of India* 39.3, pp. 409–428.

Belloni, T. (2010). Vol. 794. DOI: 10.1007/978-3-540-76937-8.

Belloni, T., D. Psaltis, and M. van der Klis (June 2002). In: *ApJ* 572.1, pp. 392–406. DOI: 10.1086/340290.

Ben-Ami, S. et al. (Aug. 2022). In: *Society of Photo-Optical Instrumentation Engineers (SPIE) Conference Series*. Ed. by J.-W. A. den Herder, S. Nikzad, and K. Nakazawa. Vol. 12181. Society of Photo-Optical Instrumentation Engineers (SPIE) Conference Series, 1218105, p. 1218105. DOI: 10.1117/12.2629850.

Berg, D. A. et al. (Aug. 2012). In: *ApJ* 754.2, 98, p. 98. DOI: 10.1088/0004-637X/754/2/98.

Berger, E. et al. (Mar. 2012). In: *ApJ* 748.1, 36, p. 36. DOI: 10.1088/0004-637X/748/1/36.

Beri, A., B. E. Tetarenko, et al. (May 2019). In: *MNRAS* 485.3, pp. 3064–3075. DOI: 10.1093/mnras/stz616.

Beri, A., R. Wijnands, et al. (May 2019). In: *The Astronomer's Telegram* 12816, p. 1.

Bhattacharyya, S. (2009). In: *Current Science* 97.6, pp. 804–820. ISSN: 00113891. URL: http://www.jstor.org/stable/24112117.

Bietenholz, M. F. et al. (Feb. 2021). In: *ApJ* 908.1, 75, p. 75. DOI: 10.3847/1538-4357/abccd9.

Björnsson, C. I. and S. T. Keshavarzi (May 2017). In: *ApJ* 841.1, 12, p. 12. DOI: 10.3847/1538-4357/aa6cad.

Blagorodnova, N., S. Gezari, et al. (July 2017). In: *ApJ* 844.1, 46, p. 46. DOI: 10.3847/1538-4357/aa7579.

Blagorodnova, N., J. D. Neill, et al. (Mar. 2018). In: *PASP* 130.985, p. 035003. DOI: 10.1088/1538-3873/aaa53f.

Blanchard, P. K. et al. (July 2017). In: *ApJ* 843.2, 106, p. 106. DOI: 10.3847/1538-4357/aa77f7.

Blandford, R. D. and A. Königl (Aug. 1979). In: *ApJ* 232, pp. 34–48. DOI: 10.1086/157262.

Blandford, R. D. and C. F. McKee (Aug. 1976). In: *Physics of Fluids* 19, pp. 1130–1138. DOI: 10.1063/1.861619.

Blandford, R. D. and R. L. Znajek (May 1977). In: *MNRAS* 179, pp. 433–456. DOI: 10.1093/mnras/179.3.433.

Bloom, J. S. et al. (July 2011). In: *Science* 333.6039, p. 203. DOI: 10.1126/science.1207150.

Bogdanov, S. et al. (Dec. 2019). In: *ApJL* 887.1, L25, p. L25. DOI: 10.3847/2041-8213/ab53eb.

Boller, T. et al. (Apr. 2016). In: *A&A* 588, A103, A103. DOI: 10.1051/0004-6361/201525648.

Bonnerot, C. and N. C. Stone (Feb. 2021). In: *SSRv* 217.1, 16, p. 16. DOI: 10.1007/s11214-020-00789-1.

Bonnerot, C. and W. Lu (June 2020). In: *MNRAS* 495.1, pp. 1374–1391. DOI: 10.1093/mnras/staa1246.

Bonnerot, C., W. Lu, and P. F. Hopkins (July 2021). In: *MNRAS* 504.4, pp. 4885–4905. DOI: 10.1093/mnras/stab398.

Bonnerot, C., E. M. Rossi, et al. (Jan. 2016). In: *MNRAS* 455.2, pp. 2253–2266. DOI: 10.1093/mnras/stv2411.

Bovy, J. (June 2017). In: *MNRAS* 468.1, pp. L63–L67. DOI: 10.1093/mnrasl/slx027.

Bozzo, E. et al. (May 2016). In: *A&A* 589, A42, A42. DOI: 10.1051/0004-6361/201527501.

Bright, J. S. et al. (Feb. 2022). In: *ApJ* 926.2, 112, p. 112. DOI: 10.3847/1538-4357/ac4506.

Brightman, M., H. Earnshaw, et al. (June 2020). In: *ApJ* 895.2, 127, p. 127. DOI: 10.3847/1538-4357/ab7e2a.

Brightman, M., C. Ward, et al. (Mar. 2021). In: *ApJ* 909.2, 102, p. 102. DOI: 10.3847/1538-4357/abde34.

Brocksopp, C., R. M. Bandyopadhyay, and R. P. Fender (May 2004). In: *NatAs* 9.4, pp. 249–264. DOI: 10.1016/j.newast.2003.11.002.

Brocksopp, C., S. Corbel, et al. (June 2013). In: *MNRAS* 432.2, pp. 931–943. DOI: 10.1093/mnras/stt493.

Brown, G. C., A. J. Levan, E. R. Stanway, T. Krühler, et al. (Dec. 2017). In: *MNRAS* 472.4, pp. 4469–4479. DOI: 10.1093/mnras/stx2193.

Brown, G. C., A. J. Levan, E. R. Stanway, N. R. Tanvir, et al. (Oct. 2015). In: *MNRAS* 452.4, pp. 4297–4306. DOI: 10.1093/mnras/stv1520.

Brown, J. S., T. W. S. Holoien, et al. (Apr. 2017). In: *MNRAS* 466.4, pp. 4904–4916. DOI: 10.1093/mnras/stx033.

Bruch, R. et al. (July 2021). In: *Transient Name Server AstroNote* 200, pp. 1–200.

Burke, J., I. Arcavi, et al. (Sept. 2021). In: *Transient Name Server Classification Report* 2021-3259, pp. 1–3259.

Burke, J., D. A. Howell, et al. (June 2020). In: *Transient Name Server Classification Report* 2020-1846, p. 1.

Burrows, D. N., J. A. Kennea, et al. (Aug. 2011). In: *Nature* 476.7361, pp. 421–424. DOI: 10.1038/nature10374.

Burrows, D. N., J. E. Hill, et al. (Oct. 2005). In: *SSRv* 120.3-4, pp. 165–195. DOI: 10.1007/s11214-005-5097-2.

Callanan, P. J. et al. (Mar. 1995). In: *ApJ* 441, p. 786. DOI: 10.1086/175402.

Calzetti, D. et al. (Apr. 2000). In: *ApJ* 533.2, pp. 682–695. DOI: 10.1086/308692.

Campana, S. et al. (Aug. 2006). In: *Nature* 442.7106, pp. 1008–1010. DOI: 10.1038/nature04892.

Canizares, C. R. et al. (Oct. 2005). In: *PASP* 117.836, pp. 1144–1171. DOI: 10.1086/432898.

Cao, H., S. Frey, et al. (Aug. 2020). In: *The Astronomer's Telegram* 13984, p. 1.

Cao, H., M. Giroletti, et al. (Nov. 2020). In: *The Astronomer's Telegram* 14168, p. 1.

Capitanio, F., T. Belloni, et al. (Sept. 2009). In: *MNRAS* 398.3, pp. 1194–1200. DOI: 10.1111/j.1365-2966.2009.15196.x.

Capitanio, L., R. Lallement, et al. (Oct. 2017). In: *A&A* 606, A65, A65. DOI: 10.1051/0004-6361/201730831.

Cappellari, M. (Apr. 2017). In: *MNRAS* 466.1, pp. 798–811. DOI: 10.1093/mnras/stw3020.

Cappellari, M. and E. Emsellem (Feb. 2004). In: *PASP* 116.816, pp. 138–147. DOI: 10.1086/381875.

Cardelli, J. A., G. C. Clayton, and J. S. Mathis (Oct. 1989). In: *ApJ* 345, p. 245. DOI: 10.1086/167900.

Casella, P., T. Belloni, and L. Stella (Aug. 2005). In: *ApJ* 629.1, pp. 403–407. DOI: 10.1086/431174.

Cash, W. (Mar. 1979). In: *ApJ* 228, pp. 939–947. DOI: 10.1086/156922.

Cendes, Y., K. D. Alexander, et al. (Oct. 2021). In: *ApJ* 919.2, 127, p. 127. DOI: 10.3847/1538-4357/ac110a.

Cendes, Y., E. Berger, et al. (Oct. 2022). In: *ApJ* 938.1, 28, p. 28. DOI: 10.3847/1538-4357/ac88d0.

Cendes, Y., T. Eftekhari, et al. (Feb. 2021). In: *ApJ* 908.2, 125, p. 125. DOI: 10.3847/1538-4357/abd323.

Cenko, B. (Jan. 2022). In: *GRB Coordinates Network* 31500, p. 1.

Cenko, S. B., D. B. Fox, et al. (Oct. 2006). In: *PASP* 118.848, pp. 1396–1406. DOI: 10.1086/508366.

Cenko, S. B., H. A. Krimm, et al. (July 2012). In: *ApJ* 753.1, 77, p. 77. DOI: 10.1088/0004-637X/753/1/77.

Chabrier, G. (July 2003). In: *PASP* 115.809, pp. 763–795. DOI: 10.1086/376392.

Chadayammuri, U. et al. (Mar. 2023). In: *ApJ* 946.1, 51, p. 51. DOI: 10.3847/1538-4357/acbea6.

Chambers, K. C. et al. (Dec. 2016). In: *arXiv e-prints*, arXiv:1612.05560, arXiv:1612.05560.

Chandra, P., R. A. Chevalier, N. Chugai, C. Fransson, C. M. Irwin, et al. (Aug. 2012). In: *ApJ* 755.2, 110, p. 110. DOI: 10.1088/0004-637X/755/2/110.

Chandra, P., R. A. Chevalier, N. Chugai, C. Fransson, and A. M. Soderberg (Sept. 2015). In: *ApJ* 810.1, 32, p. 32. DOI: 10.1088/0004-637X/810/1/32.

Chandra, P., A. J. Nayana, et al. (June 2019). In: *ApJ* 877.2, 79, p. 79. DOI: 10.3847/1538-4357/ab1900.

Chen, W., C. R. Shrader, and M. Livio (Dec. 1997). In: *ApJ* 491.1, pp. 312–338. DOI: 10.1086/304921.

Chenevez, J. et al. (Sept. 2014). In: *The Astronomer's Telegram* 6451, p. 1.

Chevalier, R. A. (May 1998). In: *ApJ* 499.2, pp. 810–819. DOI: 10.1086/305676.

Chevalier, R. A. and C. Fransson (Jan. 1994). In: *ApJ* 420, p. 268. DOI: 10.1086/173557.

Chiang, C. Y. et al. (Apr. 2010). In: *MNRAS* 403.3, pp. 1102–1112. DOI: 10.1111/j.1365-2966.2009.16129.x.

Cho, H. and R. Narayan (June 2022). In: *ApJ* 932.2, 97, p. 97. DOI: 10.3847/1538-4357/ac6d5c.

Chomiuk, L. et al. (Dec. 2011). In: *ApJ* 743.2, 114, p. 114. DOI: 10.1088/0004-637X/743/2/114.

Chornock, R. et al. (Jan. 2014). In: *ApJ* 780.1, 44, p. 44. DOI: 10.1088/0004-637X/780/1/44.

Choudhury, K. et al. (Dec. 2017). In: *ApJ* 851.1, 57, p. 57. DOI: 10.3847/1538-4357/aa9925.

Christie, I. M. et al. (Dec. 2019). In: *MNRAS* 490.4, pp. 4811–4825. DOI: 10.1093/mnras/stz2552.

Chu, M., A. Dahiwale, and C. Fremling (Aug. 2021a). In: *Transient Name Server Classification Report* 2021-2672, pp. 1–2672.

Chu, M., A. Dahiwale, and C. Fremling (Aug. 2021b). In: *Transient Name Server Classification Report* 2021-2712, pp. 1–2712.

Chu, M., A. Dahiwale, and C. Fremling (Oct. 2021c). In: *Transient Name Server Classification Report* 2021-3438, pp. 1–3438.

Chu, M., A. Dahiwale, and C. Fremling (Feb. 2022). In: *Transient Name Server Classification Report* 2022-363, p. 1.

Collin, S. and T. Kawaguchi (Nov. 2004). In: *A&A* 426, pp. 797–808. DOI: 10.1051/0004-6361:20040528.

Condon, J. J., W. D. Cotton, et al. (May 1998). In: *AJ* 115.5, pp. 1693–1716. DOI: 10.1086/300337.

Condon, J. J. and A. M. Matthews (July 2018). In: *PASP* 130.989, p. 073001. DOI: 10.1088/1538-3873/aac1b2.

Connors, R. M. T. et al. (Mar. 2020). In: *ApJ* 892.1, 47, p. 47. DOI: 10.3847/1538-4357/ab7afc.

Conroy, C., J. E. Gunn, and M. White (July 2009). In: *ApJ* 699.1, pp. 486–506. DOI: 10.1088/0004-637X/699/1/486.

Coppejans, D. L. et al. (May 2020). In: *ApJL* 895.1, L23, p. L23. DOI: 10.3847/2041-8213/ab8cc7.

Corbel, S. et al. (Mar. 2003). In: *A&A* 400, pp. 1007–1012. DOI: 10.1051/0004-6361:20030090.

Cordes, J. M. and T. J. W. Lazio (July 2002). In: *arXiv e-prints*, astro-ph/0207156, astro–ph/0207156.

Coriat, M., R. P. Fender, and G. Dubus (Aug. 2012). In: *MNRAS* 424.3, pp. 1991–2001. DOI: 10.1111/j.1365-2966.2012.21339.x.

Corral-Santana, J. M., J. Casares, T. Muñoz-Darias, F. E. Bauer, et al. (Mar. 2016). In: *A&A* 587, A61, A61. DOI: 10.1051/0004-6361/201527130.

Corral-Santana, J. M., J. Casares, T. Muñoz-Darias, P. Rodríguez-Gil, et al. (Mar. 2013). In: *Science* 339.6123, pp. 1048–1051. DOI: 10.1126/science.1228222.

Coughlin, E. R. and M. C. Begelman (Feb. 2014). In: *ApJ* 781.2, 82, p. 82. DOI: 10.1088/0004-637X/781/2/82.

Crumley, P. et al. (July 2016). In: *MNRAS* 460.1, pp. 396–416. DOI: 10.1093/mnras/stw967.

Curd, B. and R. Narayan (Feb. 2019). In: *MNRAS* 483.1, pp. 565–592. DOI: 10.1093/mnras/sty3134.

Cushing, M. C., W. D. Vacca, and J. T. Rayner (Apr. 2004). In: *PASP* 116, pp. 362–376. DOI: 10.1086/382907.

Cutri, R. M. et al. (Feb. 2021). In: *VizieR Online Data Catalog*, II/328, pp. II/328.

Dahiwale, A. and C. Fremling (Feb. 2020a). In: *Transient Name Server Classification Report* 2020-534, p. 1.

Dahiwale, A. and C. Fremling (Feb. 2020b). In: *Transient Name Server Classification Report* 2020-601, p. 1.

Dahiwale, A. and C. Fremling (June 2020c). In: *Transient Name Server Classification Report* 2020-1756, p. 1.

Dahiwale, A. and C. Fremling (Oct. 2020d). In: *Transient Name Server Classification Report* 2020-3308, p. 1.

Dahiwale, A. and C. Fremling (Dec. 2020e). In: *Transient Name Server Classification Report* 2020-3800, p. 1.

Dahiwale, A. and C. Fremling (Apr. 2021). In: *Transient Name Server Classification Report* 2021-1378, pp. 1–1378.

Dai, J. L., G. Lodato, and R. Cheng (Feb. 2021). In: *SSRv* 217.1, 12, p. 12. DOI: 10.1007/s11214-020-00747-x.

Dai, L., J. C. McKinney, and M. C. Miller (Oct. 2015). In: *ApJL* 812.2, L39, p. L39. DOI: 10.1088/2041-8205/812/2/L39.

Dai, L., J. C. McKinney, N. Roth, et al. (June 2018). In: *ApJL* 859.2, L20, p. L20. DOI: 10.3847/2041-8213/aab429.

Dauser, T., J. Garcia, et al. (Apr. 2013). In: *MNRAS* 430.3, pp. 1694–1708. DOI: 10.1093/mnras/sts710.

Dauser, T., J. García, M. L. Parker, et al. (Oct. 2014). In: *MNRAS* 444, pp. L100–L104. DOI: 10.1093/mnrasl/slu125.

Dauser, T., J. García, D. J. Walton, et al. (May 2016). In: *A&A* 590, A76, A76. DOI: 10.1051/0004-6361/201628135.

Davis, S. W. and S. El-Abd (Mar. 2019). In: *ApJ* 874.1, 23, p. 23. DOI: 10.3847/1538-4357/ab05c5.

De Colle, F. and W. Lu (Sept. 2020). In: *NewAR* 89, 101538, p. 101538. DOI: 10.1016/j.newar.2020.101538.

De Pasquale, M. et al. (Oct. 2016). In: *MNRAS* 462.1, pp. 1111–1122. DOI: 10.1093/mnras/stw1704.

Dekany, R. et al. (Mar. 2020). In: *PASP* 132.1009, 038001, p. 038001. DOI: 10.1088/1538-3873/ab4ca2.

Demircan, O. and G. Kahraman (July 1991). In: *Ap&SS* 181.2, pp. 313–322. DOI: 10.1007/BF00639097.

Dexter, J. and D. Kasen (July 2013). In: *ApJ* 772.1, 30, p. 30. DOI: 10.1088/0004-637X/772/1/30.

Done, C. and M. Gierliński (July 2003). In: *MNRAS* 342.4, pp. 1041–1055. DOI: 10.1046/j.1365-8711.2003.06614.x.

Done, C., M. Gierliński, and A. Kubota (Dec. 2007). In: *A&ARv* 15.1, pp. 1–66. DOI: 10.1007/s00159-007-0006-1.

Donley, J. L. et al. (Sept. 2002). In: *AJ* 124.3, pp. 1308–1321. DOI: 10.1086/342280.

Doroshenko, V. et al. (July 2014). In: *A&A* 567, A7, A7. DOI: 10.1051/0004-6361/201423766.

Drake, A. J., S. G. Djorgovski, A. Mahabal, E. Beshore, et al. (May 2009). In: *ApJ* 696.1, pp. 870–884. DOI: 10.1088/0004-637X/696/1/870.

Drake, A. J., S. G. Djorgovski, A. A. Mahabal, M. J. Graham, et al. (Apr. 2017). In: *The Astronomer's Telegram* 10297, p. 1.

Drout, M. R., R. Chornock, et al. (Oct. 2014). In: *ApJ* 794.1, 23, p. 23. DOI: 10.1088/0004-637X/794/1/23.

Drout, M. R., A. M. Soderberg, et al. (Nov. 2011). In: *ApJ* 741.2, 97, p. 97. DOI: 10.1088/0004-637X/741/2/97.

Du, P. et al. (Aug. 2022). In: *Nature Communications* 13, 4626, p. 4626. DOI: 10.1038/s41467-022-32301-4.

Dubus, G., J. M. Hameury, and J. P. Lasota (July 2001). In: *A&A* 373, pp. 251–271. DOI: 10.1051/0004-6361:20010632.

Dubus, G., R. S. J. Kim, et al. (May 2001). In: *ApJ* 553.1, pp. 307–320. DOI: 10.1086/320648.

Dubus, G., J.-P. Lasota, et al. (Feb. 1999). In: *MNRAS* 303.1, pp. 139–147. DOI: 10.1046/j.1365-8711.1999.02212.x.

Duev, D. A. et al. (Nov. 2019). In: *MNRAS* 489.3, pp. 3582–3590. DOI: 10.1093/mnras/stz2357.

Dwarkadas, V. V. and J. Gruszko (Jan. 2012). In: *MNRAS* 419.2, pp. 1515–1524. DOI: 10.1111/j.1365-2966.2011.19808.x.

Dwarkadas, V. V., C. Romero-Cañizales, et al. (Oct. 2016). In: *MNRAS* 462.1, pp. 1101–1110. DOI: 10.1093/mnras/stw1717.

Eftekhari, T., E. Berger, B. D. Metzger, et al. (Aug. 2022). In: *ApJ* 935.1, 16, p. 16. DOI: 10.3847/1538-4357/ac7ce8.

Eftekhari, T., E. Berger, B. A. Zauderer, et al. (Feb. 2018). In: *ApJ* 854.2, 86, p. 86. DOI: 10.3847/1538-4357/aaa8e0.

Elbaz, D. et al. (June 2007). In: *A&A* 468.1, pp. 33–48. DOI: 10.1051/0004-6361:20077525.

Esin, A. A., J. P. Lasota, and R. I. Hynes (Feb. 2000). In: *A&A* 354, pp. 987–994.

Evans, C. R. and C. S. Kochanek (Nov. 1989). In: *ApJL* 346, p. L13. DOI: 10.1086/185567.

Evans, P. A., A. P. Beardmore, K. L. Page, J. P. Osborne, et al. (Aug. 2009). In: *MNRAS* 397, pp. 1177–1201. DOI: 10.1111/j.1365-2966.2009.14913.x.

Evans, P. A., A. P. Beardmore, K. L. Page, L. G. Tyler, et al. (July 2007). In: *A&A* 469, pp. 379–385. DOI: 10.1051/0004-6361:20077530.

Event Horizon Telescope Collaboration, K. Akiyama, A. Alberdi, W. Alef, J. C. Algaba, et al. (May 2022). In: *ApJL* 930.2, L12, p. L12. DOI: 10.3847/2041-8213/ac6674.

Event Horizon Telescope Collaboration, K. Akiyama, A. Alberdi, W. Alef, K. Asada, et al. (Apr. 2019). In: *ApJL* 875.1, L6, p. L6. DOI: 10.3847/2041-8213/ab1141.

Ezhikode, S. H. et al. (Jan. 2020). In: *MNRAS* 495.3, pp. 3373–3386. DOI: 10.1093/mnras/staa1288.

Fabian, A. C. (Sept. 2012). In: *ARA&A* 50, pp. 455–489. DOI: 10.1146/annurev-astro-081811-125521.

Falcke, H., E. Körding, and S. Markoff (Feb. 2004). In: *A&A* 414, pp. 895–903. DOI: 10.1051/0004-6361:20031683.

Falcke, H., F. Melia, and E. Agol (Jan. 2000). In: *ApJL* 528.1, pp. L13–L16. DOI: 10.1086/312423.

Falcón-Barroso, J. et al. (Aug. 2011). In: *A&A* 532, A95, A95. DOI: 10.1051/0004-6361/201116842.

Fender, R. P. (Mar. 2001). In: *MNRAS* 322.1, pp. 31–42. DOI: 10.1046/j.1365-8711.2001.04080.x.

Fender, R. P., T. M. Belloni, and E. Gallo (Dec. 2004). In: *MNRAS* 355.4, pp. 1105–1118. DOI: 10.1111/j.1365-2966.2004.08384.x.

Feng, H. and R. Soria (Nov. 2011). In: *NewAR* 55.5, pp. 166–183. DOI: 10.1016/j.newar.2011.08.002.

Fernández, R. et al. (May 2018). In: *MNRAS* 476.2, pp. 2366–2383. DOI: 10.1093/mnras/sty306.

Ferrarese, L. and H. Ford (Feb. 2005). In: *SSRv* 116.3-4, pp. 523–624. DOI: 10.1007/s11214-005-3947-6.

Ferrigno, C. et al. (Jan. 2012). In: *A&A* 537, L7, p. L7. DOI: 10.1051/0004-6361/201118474.

Flesch, E. W. (July 2019). In: *VizieR Online Data Catalog*, VII/283, pp. VII/283.

Flewelling, H. A. et al. (Nov. 2020). In: *ApJS* 251.1, 7, p. 7. DOI: 10.3847/1538-4365/abb82d.

Foreman-Mackey, D., J. Sick, and B. Johnson (Oct. 2014). Version v0.1.1. DOI: 10.5281/zenodo.12157. URL: https://doi.org/10.5281/zenodo.12157.

Foreman-Mackey, D., D. W. Hogg, et al. (Mar. 2013). In: *Publications of the Astronomical Society of the Pacific* 125.925, p. 306. DOI: 10.1086/670067.

Fox, O. D. and N. Smith (Sept. 2019). In: *MNRAS* 488.3, pp. 3772–3782. DOI: 10.1093/mnras/stz1925.

Frail, D. A. et al. (Nov. 2001). In: *ApJL* 562.1, pp. L55–L58. DOI: 10.1086/338119.

Frank, J. and M. J. Rees (Sept. 1976). In: *MNRAS* 176, pp. 633–647. DOI: 10.1093/mnras/176.3.633.

Frank, J., A. King, and D. J. Raine (2002).

Fransson, C., P. Lundqvist, and R. A. Chevalier (Apr. 1996). In: *ApJ* 461, p. 993. DOI: 10.1086/177119.

Frederick, S. et al. (Oct. 2021). In: *ApJ* 920.1, 56, p. 56. DOI: 10.3847/1538-4357/ac110f.

Fremling, C., M. Graham, et al. (Dec. 2021). In: *Transient Name Server AstroNote* 318, pp. 1–318.

Fremling, C., A. A. Miller, et al. (May 2020). In: *ApJ* 895.1, 32, p. 32. DOI: 10.3847/1538-4357/ab8943.

Fremling, C., J. Sollerman, et al. (Sept. 2016). In: *A&A* 593, A68, A68. DOI: 10.1051/0004-6361/201628275.

French, K. D., I. Arcavi, and A. Zabludoff (Feb. 2016). In: *ApJL* 818.1, L21, p. L21. DOI: 10.3847/2041-8205/818/1/L21.

French, K. D., T. Wevers, et al. (Mar. 2020). In: *SSRv* 216.3, 32, p. 32. DOI: 10.1007/s11214-020-00657-y.

Froning, C. S. et al. (Jan. 2014). In: *ApJ* 780.1, 48, p. 48. DOI: 10.1088/0004-637X/780/1/48.

Gabriel, C. et al. (July 2004). In: *Astronomical Data Analysis Software and Systems (ADASS) XIII*. Ed. by F. Ochsenbein, M. G. Allen, and D. Egret. Vol. 314. Astronomical Society of the Pacific Conference Series, p. 759.

Gaia Collaboration et al. (May 2021). In: *A&A* 649, A1, A1. DOI: 10.1051/0004-6361/202039657.

Gal-Yam, A. et al. (Jan. 2022). In: *Nature* 601.7892, pp. 201–204. DOI: 10.1038/s41586-021-04155-1.

Gal-Yam, A. (Aug. 2019). In: *ARA&A* 57, pp. 305–333. DOI: 10.1146/annurev-astro-081817-051819.

Galama, T. J. et al. (Oct. 1998). In: *Nature* 395.6703, pp. 670–672. DOI: 10.1038/27150.

Galeev, A. A., R. Rosner, and G. S. Vaiana (Apr. 1979). In: *ApJ* 229, pp. 318–326. DOI: 10.1086/156957.

Gallazzi, A. et al. (Sept. 2005). In: *MNRAS* 362.1, pp. 41–58. DOI: 10.1111/j.1365-2966.2005.09321.x.

Gallo, E., E. Hodges-Kluck, et al. (May 2019). In: *BAAS* 51.3, 35, p. 35. DOI: 10.48550/arXiv.1903.06629.

Gallo, E. and A. Sesana (Sept. 2019). In: *ApJL* 883.1, L18, p. L18. DOI: 10.3847/2041-8213/ab40c6.

Gallo, E., T. Treu, J. Jacob, et al. (June 2008). In: *ApJ* 680.1, pp. 154–168. DOI: 10.1086/58801210.48550/arXiv.0711.2073.

Gallo, E., T. Treu, P. J. Marshall, et al. (May 2010). In: *ApJ* 714.1, pp. 25–36. DOI: 10.1088/0004-637X/714/1/2510.48550/arXiv.1002.3619.

Gandhi, P. et al. (May 2019). In: *The Astronomer's Telegram* 12801, p. 1.

García, J., T. Dauser, et al. (Feb. 2014). In: *ApJ* 782.2, 76, p. 76. DOI: 10.1088/0004-637X/782/2/76.

García, J., T. R. Kallman, and R. F. Mushotzky (Apr. 2011). In: *ApJ* 731.2, 131, p. 131. DOI: 10.1088/0004-637X/731/2/131.

Garmire, G. P. et al. (Mar. 2003). In: *X-Ray and Gamma-Ray Telescopes and Instruments for Astronomy*. Ed. by J. E. Truemper and H. D. Tananbaum. Vol. 4851. Society of Photo-Optical Instrumentation Engineers (SPIE) Conference Series, pp. 28–44. DOI: 10.1117/12.461599.

Gebhardt, K. et al. (Nov. 2001). In: *AJ* 122.5, pp. 2469–2476. DOI: 10.1086/323481.

Gehrels, N. (Apr. 1986). In: *ApJ* 303, p. 336. DOI: 10.1086/164079.

Gehrels, N. et al. (Aug. 2004). In: *ApJ* 611.2, pp. 1005–1020. DOI: 10.1086/422091.

Gendreau, K. C. et al. (July 2016). In: *Space Telescopes and Instrumentation 2016: Ultraviolet to Gamma Ray*. Vol. 9905. Society of Photo-Optical Instrumentation Engineers (SPIE) Conference Series, 99051H, 99051H. DOI: 10.1117/12.2231304.

Gezari, S. (Sept. 2021). In: *ARA&A* 59, pp. 21–58. DOI: 10.1146/annurev-astro-111720-030029.

Gezari, S., S. Basa, et al. (Apr. 2008). In: *ApJ* 676.2, pp. 944–969. DOI: 10.1086/529008.

Gezari, S., S. B. Cenko, and I. Arcavi (Dec. 2017). In: *ApJL* 851.2, L47, p. L47. DOI: 10.3847/2041-8213/aaa0c2.

Gezari, S., R. Chornock, et al. (May 2012). In: *Nature* 485.7397, pp. 217–220. DOI: 10.1038/nature10990.

Gezari, S., E. Hammerstein, et al. (Mar. 2021). In: *Transient Name Server AstroNote* 103, pp. 1–103.

Gezari, S., T. Heckman, et al. (June 2009). In: *ApJ* 698.2, pp. 1367–1379. DOI: 10.1088/0004-637X/698/2/1367.

Gezari, S., D. C. Martin, et al. (Dec. 2006). In: *ApJL* 653.1, pp. L25–L28. DOI: 10.1086/509918.

Ghisellini, G. (2013). Vol. 873. DOI: 10.1007/978-3-319-00612-3.

Gierliński, M., C. Done, and K. Page (Aug. 2008). In: *MNRAS* 388.2, pp. 753–760. DOI: 10.1111/j.1365-2966.2008.13431.x.

Gierliński, M., C. Done, and K. Page (Jan. 2009). In: *MNRAS* 392.3, pp. 1106–1114. DOI: 10.1111/j.1365-2966.2008.14166.x.

Gilfanov, M. (2010). In: *Lecture Notes in Physics, Berlin Springer Verlag*. Ed. by T. Belloni. Vol. 794, p. 17. DOI: 10.1007/978-3-540-76937-8_2.

Gilfanov, M., M. Revnivtsev, and S. Molkov (Oct. 2003). In: *A&A* 410, pp. 217–230. DOI: 10.1051/0004-6361:20031141.

Giustini, M., G. Miniutti, and R. D. Saxton (Apr. 2020). In: *A&A* 636, L2, p. L2. DOI: 10.1051/0004-6361/202037610.

Gomez, S. et al. (Oct. 2022). In: *arXiv e-prints*, arXiv:2210.10810, arXiv:2210.10810.

Goodman, J. (Nov. 1997). In: *NatAs* 2.5, pp. 449–460. DOI: 10.1016/S1384-1076(97)00031-6.

Goodwin, A. J. et al. (Apr. 2022). In: *MNRAS* 511.4, pp. 5328–5345. DOI: 10.1093/mnras/stac333.

Graham, M. J. et al. (July 2019). In: *PASP* 131.1001, p. 078001. DOI: 10.1088/1538-3873/ab006c.

Granot, J. and R. Sari (Apr. 2002). In: *ApJ* 568.2, pp. 820–829. DOI: 10.1086/338966.

Greene, J. E., J. Strader, and L. C. Ho (Aug. 2020). In: *ARA&A* 58, pp. 257–312. DOI: 10.1146/annurev-astro-032620-021835.

Grupe, D., H. C. Thomas, and K. M. Leighly (Oct. 1999). In: *A&A* 350, pp. L31–L34. DOI: 10.48550/arXiv.astro-ph/9909101.

Grupe, D., D. N. Burrows, et al. (Mar. 2010). In: *ApJ* 711.2, pp. 1008–1016. DOI: 10.1088/0004-637X/711/2/1008.

Gültekin, K., A. L. King, et al. (Jan. 2019). In: *ApJ* 871.1, 80, p. 80. DOI: 10.3847/1538-4357/aaf6b9.

Gültekin, K., D. O. Richstone, et al. (June 2009). In: *ApJ* 698.1, pp. 198–221. DOI: 10.1088/0004-637X/698/1/198.

Guolo, M. et al. (Nov. 2021). In: *MNRAS* 508.1, pp. 144–156. DOI: 10.1093/mnras/stab2550.

Gupta, Y. et al. (Aug. 2017). In: *Current Science* 113.4, pp. 707–714.

Hameury, J. M. (Sept. 2020). In: *Advances in Space Research* 66.5, pp. 1004–1024. DOI: 10.1016/j.asr.2019.10.022.

Hameury, J. M. and J. P. Lasota (Nov. 2020). In: *A&A* 643, A171, A171. DOI: 10.1051/0004-6361/202038857.

Hammerstein, E., S. Gezari, S. van Velzen, S. B. Cenko, et al. (Feb. 2021). In: *ApJL* 908.1, L20, p. L20. DOI: 10.3847/2041-8213/abdcb4.

Hammerstein, E., S. Gezari, S. van Velzen, S. Kulkarni, et al. (Jan. 2021a). In: *Transient Name Server Classification Report* 2021-159, pp. 1–159.

Hammerstein, E., S. Gezari, S. van Velzen, S. Kulkarni, et al. (Jan. 2021b). In: *Transient Name Server Classification Report* 2021-262, pp. 1–262.

Hammerstein, E., S. Gezari, S. van Velzen, Y. Yao, et al. (Mar. 2021). In: *Transient Name Server Classification Report* 2021-955, pp. 1–955.

Hammerstein, E., S. van Velzen, et al. (Jan. 2023). In: *ApJ* 942.1, 9, p. 9. DOI: 10.3847/1538-4357/aca283.

Harding, L. K. et al. (Apr. 2016). In: *MNRAS* 457.3, pp. 3036–3049. DOI: 10.1093/mnras/stw094.

Harrison, F. A. et al. (June 2013). In: *ApJ* 770.2, 103, p. 103. DOI: 10.1088/0004-637X/770/2/103.

Hasinger, G. and M. van der Klis (Nov. 1989). In: *A&A* 225, pp. 79–96.

Heckman, T. M. and P. N. Best (Aug. 2014). In: *ARA&A* 52, pp. 589–660. DOI: 10.1146/annurev-astro-081913-035722.

Heger, A. et al. (July 2003). In: *ApJ* 591.1, pp. 288–300. DOI: 10.1086/375341.

HI4PI Collaboration et al. (Oct. 2016). In: *A&A* 594, A116, A116. DOI: 10.1051/0004-6361/201629178.

Hills, J. G. (Mar. 1975). In: *Nature* 254.5498, pp. 295–298. DOI: 10.1038/254295a0.

Hinkle, J. T. et al. (Jan. 2021). In: *MNRAS* 500.2, pp. 1673–1696. DOI: 10.1093/mnras/staa3170.

Ho, A. Y. Q. (July 2020). PhD thesis. California Institute of Technology.

Ho, A. Y. Q., D. A. Goldstein, et al. (Dec. 2019). In: *ApJ* 887.2, 169, p. 169. DOI: 10.3847/1538-4357/ab55ec.

Ho, A. Y. Q., B. Margalit, et al. (June 2022). In: *ApJ* 932.2, 116, p. 116. DOI: 10.3847/1538-4357/ac4e97.

Ho, A. Y. Q., D. A. Perley, A. Gal-Yam, et al. (May 2021). In: *arXiv e-prints*, arXiv:2105.08811, arXiv:2105.08811.

Ho, A. Y. Q., D. A. Perley, S. R. Kulkarni, et al. (May 2020). In: *ApJ* 895.1, 49, p. 49. DOI: 10.3847/1538-4357/ab8bcf.

Ho, L. C. (Sept. 2008). In: *ARA&A* 46, pp. 475–539. DOI: 10.1146/annurev.astro.45.051806.110546.

Holoien, T. W. S. et al. (Dec. 2014). In: *MNRAS* 445.3, pp. 3263–3277. DOI: 10.1093/mnras/stu1922.

Homan, J. and T. Belloni (Nov. 2005). In: *Ap&SS* 300.1-3, pp. 107–117. DOI: 10.1007/s10509-005-1197-4.

Horesh, A., S. B. Cenko, and I. Arcavi (Jan. 2021). In: *Nature Astronomy* 5, pp. 491–497. DOI: 10.1038/s41550-021-01300-8.

Horesh, A., I. Sfaradi, et al. (Oct. 2021). In: *ApJL* 920.1, L5, p. L5. DOI: 10.3847/2041-8213/ac25fe.

Hori, T. et al. (Mar. 2018). In: *ApJS* 235.1, 7, p. 7. DOI: 10.3847/1538-4365/aaa89c.

Horne, K. and T. R. Marsh (Feb. 1986). In: *MNRAS* 218, pp. 761–773. DOI: 10.1093/mnras/218.4.761.

Houck, J. C. and L. A. Denicola (Jan. 2000). In: *Astronomical Data Analysis Software and Systems IX*. Ed. by N. Manset, C. Veillet, and D. Crabtree. Vol. 216. Astronomical Society of the Pacific Conference Series, p. 591.

Huang, H.-T. and W. Lu (Dec. 2022). In: *arXiv e-prints*, arXiv:2301.00259, arXiv:2301.00259.

Huang, K., J. Shimoda, et al. (June 2019). In: *ApJL* 878.1, L25, p. L25. DOI: 10.3847/2041-8213/ab23fd.

Hung, T. et al. (June 2017). In: *ApJ* 842.1, 29, p. 29. DOI: 10.3847/1538-4357/aa7337.

Huppenkothen, D. et al. (Aug. 2019). In: *ApJ* 881.1, 39, p. 39. DOI: 10.3847/1538-4357/ab258d.

Hurley, K. et al. (Oct. 2010). In: *Deciphering the Ancient Universe with Gamma-ray Bursts*. Ed. by N. Kawai and S. Nagataki. Vol. 1279. American Institute of Physics Conference Series, pp. 330–333. DOI: 10.1063/1.3509301.

Immler, S. et al. (Feb. 2008). In: *ApJL* 674.2, p. L85. DOI: 10.1086/529373.

Inayoshi, K., E. Visbal, and Z. Haiman (Aug. 2020). In: *ARA&A* 58, pp. 27–97. DOI: 10.1146/annurev-astro-120419-014455.

Ingram, A. R. and S. E. Motta (Sept. 2019). In: *NewAR* 85, 101524, p. 101524. DOI: 10.1016/j.newar.2020.101524.

Ivezić, Ž. et al. (Mar. 2019). In: *ApJ* 873.2, 111, p. 111. DOI: 10.3847/1538-4357/ab042c.

Izquierdo-Villalba, D. et al. (July 2020). In: *MNRAS* 495.4, pp. 4681–4706. DOI: 10.1093/mnras/staa1399.

Jaisawal, G. K. et al. (Apr. 2015). In: *The Astronomer's Telegram* 7361, p. 1.

Jani, K., D. Shoemaker, and C. Cutler (Jan. 2020). In: *Nature Astronomy* 4, pp. 260–265. DOI: 10.1038/s41550-019-0932-7.

Jiang, N., T. Wang, et al. (Apr. 2021). In: *ApJ* 911.1, 31, p. 31. DOI: 10.3847/1538-4357/abe772.

Jiang, Y.-F., J. Guillochon, and A. Loeb (Oct. 2016). In: *ApJ* 830.2, 125, p. 125. DOI: 10.3847/0004-637X/830/2/125.

Jiang, Y.-F., J. M. Stone, and S. W. Davis (Aug. 2019). In: *ApJ* 880.2, 67, p. 67. DOI: 10.3847/1538-4357/ab29ff.

Jiménez-Ibarra, F. et al. (Nov. 2019). In: *MNRAS* 489.3, pp. 3420–3426. DOI: 10.1093/mnras/stz2393.

Johnson, B. D. et al. (June 2021). In: *ApJS* 254.2, 22, p. 22. DOI: 10.3847/1538-4365/abef67.

Kaaret, P., H. Feng, and T. P. Roberts (Aug. 2017). In: *ARA&A* 55.1, pp. 303–341. DOI: 10.1146/annurev-astro-091916-055259.

Kaastra, J. S. and J. A. M. Bleeker (Mar. 2016). In: *A&A* 587, A151, A151. DOI: 10.1051/0004-6361/201527395.

Kajava, J. J. E. et al. (July 2020). In: *A&A* 639, A100, A100. DOI: 10.1051/0004-6361/202038165.

Kallman, T. and M. Bautista (Mar. 2001). In: *ApJS* 133.1, pp. 221–253. DOI: 10.1086/319184.

Kamble, A. et al. (Feb. 2016). In: *ApJ* 818.2, 111, p. 111. DOI: 10.3847/0004-637X/818/2/111.

Kangas, T. et al. (Oct. 2022). In: *MNRAS* 516.1, pp. 1193–1218. DOI: 10.1093/mnras/stac2218.

Kara, E., L. Dai, et al. (Mar. 2018). In: *MNRAS* 474.3, pp. 3593–3598. DOI: 10.1093/mnras/stx3004.

Kara, E., J. M. Miller, et al. (July 2016). In: *Nature* 535.7612, pp. 388–390. DOI: 10.1038/nature18007.

Kasen, D. (2017). In: *Handbook of Supernovae*. Ed. by A. W. Alsabti and P. Murdin, p. 939. DOI: 10.1007/978-3-319-21846-5_32.

Kasen, D. and L. Bildsten (July 2010). In: *ApJ* 717.1, pp. 245–249. DOI: 10.1088/0004-637X/717/1/245.

Kasliwal, M. M. et al. (Mar. 2019). In: *PASP* 131.3, p. 038003. DOI: 10.1088/1538-3873/aafbc2.

Kato, S., J. Fukue, and S. Mineshige (2008). Kyoto University Press.

Katsuda, S. et al. (Dec. 2016). In: *ApJ* 832.2, 194, p. 194. DOI: 10.3847/0004-637X/832/2/194.

Kaur, R. et al. (Feb. 2012). In: *ApJL* 746.2, L23, p. L23. DOI: 10.1088/2041-8205/746/2/L23.

Kawamuro, T. et al. (Mar. 2018). In: *The Astronomer's Telegram* 11399, p. 1.

Kellogg, E., J. R. Baldwin, and D. Koch (July 1975). In: *ApJ* 199, pp. 299–306. DOI: 10.1086/153692.

Kelly, B. C. and A. Merloni (Jan. 2012). In: *Advances in Astronomy* 2012, 970858, p. 970858. DOI: 10.1155/2012/970858.

Kelly, B. C. and Y. Shen (Feb. 2013). In: *ApJ* 764.1, 45, p. 45. DOI: 10.1088/0004-637X/764/1/45.

Kennicutt Robert C., J. (May 1998). In: *ApJ* 498.2, pp. 541–552. DOI: 10.1086/305588.

Kesden, M. (Jan. 2012). In: *Physical Review D* 85.2, 024037, p. 024037. DOI: 10.1103/PhysRevD.85.024037.

Kewley, L. J. et al. (Nov. 2006). In: *MNRAS* 372.3, pp. 961–976. DOI: 10.1111/j.1365-2966.2006.10859.x.

Khatami, D. K. and D. N. Kasen (June 2019). In: *ApJ* 878.1, 56, p. 56. DOI: 10.3847/1538-4357/ab1f09.

Kim, Y. L. et al. (Feb. 2022). In: *PASP* 134.1032, 024505, p. 024505. DOI: 10.1088/1538-3873/ac50a0.

King, A. R. (Mar. 2008). In: *MNRAS* 385.1, pp. L113–L115. DOI: 10.1111/j.1745-3933.2008.00444.x.

King, A. R. et al. (May 2001). In: *ApJL* 552.2, pp. L109–L112. DOI: 10.1086/320343.

Kirby, E. N. et al. (Dec. 2013). In: *ApJ* 779.2, 102, p. 102. DOI: 10.1088/0004-637X/779/2/102.

Klein-Wolt, M. and M. van der Klis (Mar. 2008). In: *ApJ* 675.2, pp. 1407–1423. DOI: 10.1086/525843.

Kochanek, C. S. (Sept. 2016). In: *MNRAS* 461.1, pp. 371–384. DOI: 10.1093/mnras/stw1290.

Komossa, S. et al. (May 2008). In: *ApJL* 678.1, p. L13. DOI: 10.1086/588281.

Kormendy, J. and L. C. Ho (Aug. 2013). In: *ARA&A* 51.1, pp. 511–653. DOI: 10.1146/annurev-astro-082708-101811.

Kouveliotou, C. et al. (June 2004). In: *ApJ* 608.2, pp. 872–882. DOI: 10.1086/420878.

Kremer, K. et al. (Apr. 2021). In: *ApJ* 911.2, 104, p. 104. DOI: 10.3847/1538-4357/abeb14.

Krimm, H. A., S. D. Barthelmy, et al. (Jan. 2011). In: *The Astronomer's Telegram* 3138, p. 1.

Krimm, H. A., S. T. Holland, et al. (Nov. 2013). In: *ApJS* 209.1, 14, p. 14. DOI: 10.1088/0067-0049/209/1/14.

Kudritzki, R.-P. and J. Puls (Jan. 2000). In: *ARA&A* 38, pp. 613–666. DOI: 10.1146/annurev.astro.38.1.613.

Kuin, N. P. M. et al. (Aug. 2019). In: *MNRAS* 487.2, pp. 2505–2521. DOI: 10.1093/mnras/stz053.

Kumar, P. and P. Crumley (Oct. 2015). In: *MNRAS* 453.2, pp. 1820–1828. DOI: 10.1093/mnras/stv1696.

Kupfer, T. et al. (May 2021). In: *MNRAS*. DOI: 10.1093/mnras/stab1344.

Kuulkers, E. et al. (Apr. 2013). In: *A&A* 552, A32, A32. DOI: 10.1051/0004-6361/201219447.

La Dous, C. (Feb. 1989). In: *A&A* 211.1, pp. 131–155.

Lacy, M. et al. (Mar. 2020). In: *PASP* 132.1009, p. 035001. DOI: 10.1088/1538-3873/ab63eb.

Lang, D. (May 2014). In: *AJ* 147.5, 108, p. 108. DOI: 10.1088/0004-6256/147/5/108.

Lasota, J. P., G. Dubus, and K. Kruk (Aug. 2008). In: *A&A* 486.2, pp. 523–528. DOI: 10.1051/0004-6361:200809658.

Lasota, J.-P. (June 2001). In: *NewAR* 45.7, pp. 449–508. DOI: 10.1016/S1387-6473(01)00112-9.

Lasota, J.-P. (Jan. 2016). In: *Astrophysics of Black Holes: From Fundamental Aspects to Latest Developments*. Ed. by C. Bambi. Vol. 440. Astrophysics and Space Science Library, p. 1. DOI: 10.1007/978-3-662-52859-4_1.

Latimer, L. J., A. E. Reines, A. Bogdan, et al. (Dec. 2021). In: *ApJL* 922.2, L40, p. L40. DOI: 10.3847/2041-8213/ac3af6.

Latimer, L. J., A. E. Reines, K. N. Hainline, et al. (June 2021). In: *ApJ* 914.2, 133, p. 133. DOI: 10.3847/1538-4357/abfe0c.

Law, N. M. et al. (Dec. 2009). In: *PASP* 121.886, p. 1395. DOI: 10.1086/648598.

Law-Smith, J. et al. (Nov. 2017). In: *ApJ* 850.1, 22, p. 22. DOI: 10.3847/1538-4357/aa94c7.

Leahy, D. A. et al. (Mar. 1983). In: *ApJ* 266, pp. 160–170. DOI: 10.1086/160766.

Leloudas, G., S. Schulze, et al. (May 2015). In: *MNRAS* 449.1, pp. 917–932. DOI: 10.1093/mnras/stv320.

Leloudas, G., L. Dai, et al. (Dec. 2019). In: *ApJ* 887.2, 218, p. 218. DOI: 10.3847/1538-4357/ab5792.

Levan, A. J., A. M. Read, et al. (July 2013). In: *ApJ* 771.2, 136, p. 136. DOI: 10.1088/0004-637X/771/2/136.

Levan, A. J., N. R. Tanvir, et al. (July 2011). In: *Science* 333.6039, p. 199. DOI: 10.1126/science.1207143.

Lewin, W. H. G., J. van Paradijs, and R. E. Taam (Sept. 1993). In: *SSRv* 62.3-4, pp. 223–389. DOI: 10.1007/BF00196124.

Li, W. et al. (Apr. 2011). In: *MNRAS* 412.3, pp. 1473–1507. DOI: 10.1111/j.1365-2966.2011.18162.x.

Lightman, A. P. and D. M. Eardley (Jan. 1974). In: *ApJL* 187, p. L1. DOI: 10.1086/181377.

Lin, D. et al. (June 2018). In: *Nature Astronomy* 2, pp. 656–661. DOI: 10.1038/s41550-018-0493-1.

Linial, I. and B. D. Metzger (Mar. 2023). In: *arXiv e-prints*, arXiv:2303.16231, arXiv:2303.16231. DOI: 10.48550/arXiv.2303.16231.

Liska, M. et al. (July 2019). In: *MNRAS* 487.1, pp. 550–561. DOI: 10.1093/mnras/stz834.

Liu, B. F. and E. Qiao (Jan. 2022). In: *iScience* 25.1, p. 103544. DOI: 10.1016/j.isci.2021.103544.

Liu, T., W.-M. Gu, and B. Zhang (Nov. 2017). In: *NewAR* 79, pp. 1–25. DOI: 10.1016/j.newar.2017.07.001.

Loeb, A. and A. Ulmer (Nov. 1997). In: *ApJ* 489.2, pp. 573–578. DOI: 10.1086/304814.

Lu, W. (2022). In: *Handbook of X-ray and Gamma-ray Astrophysics. Edited by Cosimo Bambi and Andrea Santangelo*, 3, p. 3. DOI: 10.1007/978-981-16-4544-0_127-1.

Lu, W. and C. Bonnerot (Feb. 2020). In: *MNRAS* 492.1, pp. 686–707. DOI: 10.1093/mnras/stz3405.

Lu, W., J. Krolik, et al. (Oct. 2017). In: *MNRAS* 471.1, pp. 1141–1152. DOI: 10.1093/mnras/stx1668.

Lu, W. and P. Kumar (Oct. 2018). In: *ApJ* 865.2, 128, p. 128. DOI: 10.3847/1538-4357/aad54a.

Lu, W. and E. Quataert (Oct. 2022). In: *arXiv e-prints*, arXiv:2210.08023, arXiv:2210.08023. DOI: 10.48550/arXiv.2210.08023.

Lucchini, M. et al. (Dec. 2022). In: *MNRAS* 517.4, pp. 5853–5881. DOI: 10.1093/mnras/stac2904.

Ludlam, R. M., E. M. Cackett, J. A. García, J. M. Miller, P. M. Bult, et al. (May 2020). In: *ApJ* 895.1, 45, p. 45. DOI: 10.3847/1538-4357/ab89a6.

Ludlam, R. M., E. M. Cackett, J. A. García, J. M. Miller, A. L. Stevens, et al. (Mar. 2022). In: *ApJ* 927.1, 112, p. 112. DOI: 10.3847/1538-4357/ac5028.

Lyapin, A. et al. (Mar. 2020). In: *The Astronomer's Telegram* 13576, p. 1.

Lyman, J. D., D. Bersier, et al. (Mar. 2016). In: *MNRAS* 457.1, pp. 328–350. DOI: 10.1093/mnras/stv2983.

Lyman, J. D., L. Galbany, et al. (June 2020). In: *MNRAS* 495.1, pp. 992–999. DOI: 10.1093/mnras/staa1243.

MacLeod, M., J. Guillochon, and E. Ramirez-Ruiz (Oct. 2012). In: *ApJ* 757.2, 134, p. 134. DOI: 10.1088/0004-637X/757/2/134.

MacLeod, M., E. Ramirez-Ruiz, et al. (Nov. 2013). In: *ApJ* 777.2, 133, p. 133. DOI: 10.1088/0004-637X/777/2/133.

Madau, P. and M. Dickinson (Aug. 2014). In: *ARA&A* 52, pp. 415–486. DOI: 10.1146/annurev-astro-081811-125615.

Madsen, K. K. et al. (Jan. 2017). In: *AJ* 153.1, 2, p. 2. DOI: 10.3847/1538-3881/153/1/2.

Magorrian, J. and S. Tremaine (Oct. 1999). In: *MNRAS* 309.2, pp. 447–460. DOI: 10.1046/j.1365-8711.1999.02853.x.

Mahabal, A. et al. (Mar. 2019). In: *PASP* 131.997, p. 038002. DOI: 10.1088/1538-3873/aaf3fa.

Mainzer, A. et al. (Apr. 2011). In: *ApJ* 731.1, 53, p. 53. DOI: 10.1088/0004-637X/731/1/53.

Mangano, V., D. N. Burrows, et al. (Feb. 2016). In: *ApJ* 817.2, 103, p. 103. DOI: 10.3847/0004-637X/817/2/103.

Mangano, V., E. A. Hoversten, et al. (Jan. 2010). In: *GRB Coordinates Network* 11296, p. 1.

Marconi, A. et al. (June 2004). In: *MNRAS* 351.1, pp. 169–185. DOI: 10.1111/j.1365-2966.2004.07765.x.

Margalit, B. (July 2021). In: *arXiv e-prints*, arXiv:2107.04048, arXiv:2107.04048.

Margalit, B. and E. Quataert (Dec. 2021). In: *ApJL* 923.1, L14, p. L14. DOI: 10.3847/2041-8213/ac3d97.

Margalit, B., E. Quataert, and A. Y. Q. Ho (Apr. 2022). In: *ApJ* 928.2, 122, p. 122. DOI: 10.3847/1538-4357/ac53b0.

Margutti, R., R. Chornock, et al. (Sept. 2018). In: *ApJ* 864.1, 45, p. 45. DOI: 10.3847/1538-4357/aad2df.

Margutti, R., B. D. Metzger, et al. (Feb. 2019). In: *ApJ* 872.1, 18, p. 18. DOI: 10.3847/1538-4357/aafa01.

Margutti, R., A. M. Soderberg, et al. (Nov. 2013). In: *ApJ* 778.1, 18, p. 18. DOI: 10.1088/0004-637X/778/1/18.

Margutti, R. and R. Chornock (Sept. 2021). In: *ARA&A* 59, pp. 155–202. DOI: 10.1146/annurev-astro-112420-030742.

Marino, R. A. et al. (Nov. 2013). In: *A&A* 559, A114, A114. DOI: 10.1051/0004-6361/201321956.

Markert, T. H. et al. (Sept. 1994). In: *EUV, X-Ray, and Gamma-Ray Instrumentation for Astronomy V*. Ed. by O. H. Siegmund and J. V. Vallerga. Vol. 2280. Society of Photo-Optical Instrumentation Engineers (SPIE) Conference Series, pp. 168–180. DOI: 10.1117/12.186812.

Markwardt, C. B. et al. (Oct. 2009). In: *The Astronomer's Telegram* 2258, p. 1.

Martin, D. C. et al. (Jan. 2005). In: *ApJL* 619.1, pp. L1–L6. DOI: 10.1086/426387.

Masci, F. J. et al. (Jan. 2019). In: *PASP* 131.1, p. 018003. DOI: 10.1088/1538-3873/aae8ac.

Mata Sánchez, D. et al. (Dec. 2015). In: *MNRAS* 454.2, pp. 2199–2204. DOI: 10.1093/mnras/stv2111.

Matsumoto, T. and B. D. Metzger (Jan. 2023). In: *arXiv e-prints*, arXiv:2301.11939, arXiv:2301.11939. DOI: 10.48550/arXiv.2301.11939.

Matsuoka, M. et al. (Oct. 2009). In: *PASJ* 61, p. 999. DOI: 10.1093/pasj/61.5.999.

McClintock, J. E. and R. A. Remillard (2006). In: *Compact stellar X-ray sources*. Vol. 39, pp. 157–213.

McHardy, I. M. et al. (Dec. 2006). In: *Nature* 444.7120, pp. 730–732. DOI: 10.1038/nature05389.

McKinney, J. C., A. Tchekhovskoy, and R. D. Blandford (July 2012). In: *MNRAS* 423.4, pp. 3083–3117. DOI: 10.1111/j.1365-2966.2012.21074.x.

McMullin, J. P. et al. (Oct. 2007). In: *Astronomical Data Analysis Software and Systems XVI*. Ed. by R. A. Shaw, F. Hill, and D. J. Bell. Vol. 376. Astronomical Society of the Pacific Conference Series, p. 127.

Mendel, J. T. et al. (Jan. 2014). In: *ApJS* 210.1, 3, p. 3. DOI: 10.1088/0067-0049/210/1/3.

Mereminskiy, I. et al. (Mar. 2020). In: *The Astronomer's Telegram* 13571, p. 1.

Merloni, A. and S. Heinz (Aug. 2008). In: *MNRAS* 388.3, pp. 1011–1030. DOI: 10.1111/j.1365-2966.2008.13472.x.

Merloni, A., S. Heinz, and T. di Matteo (Nov. 2003). In: *MNRAS* 345.4, pp. 1057–1076. DOI: 10.1046/j.1365-2966.2003.07017.x.

Merritt, D. and L. Ferrarese (Jan. 2001). In: *ApJ* 547.1, pp. 140–145. DOI: 10.1086/318372.

Metzger, B. D. (Sept. 2022a). In: *ApJL* 937.1, L12, p. L12. DOI: 10.3847/2041-8213/ac90ba.

Metzger, B. D. (Mar. 2022b). In: *arXiv e-prints*, arXiv:2203.04331, arXiv:2203.04331.

Metzger, B. D., P. Beniamini, and D. Giannios (Apr. 2018). In: *ApJ* 857.2, 95, p. 95. DOI: 10.3847/1538-4357/aab70c.

Metzger, B. D. and N. C. Stone (Sept. 2016). In: *MNRAS* 461.1, pp. 948–966. DOI: 10.1093/mnras/stw1394.

Meyer-Hofmeister, E. (Aug. 2004). In: *A&A* 423, pp. 321–326. DOI: 10.1051/0004-6361:20040369.

Meza, N. and J. P. Anderson (Sept. 2020). In: *A&A* 641, A177, A177. DOI: 10.1051/0004-6361/201937113.

Middleton, M. J. et al. (Jan. 2013). In: *Nature* 493.7431, pp. 187–190. DOI: 10.1038/nature11697.

Migliari, S. and R. P. Fender (Feb. 2006). In: *MNRAS* 366.1, pp. 79–91. DOI: 10.1111/j.1365-2966.2005.09777.x.

Mihara, T. et al. (Nov. 2011). In: *PASJ* 63, S623–S634. DOI: 10.1093/pasj/63.sp3.S623.

Miller, A. A. and X. J. Hall (May 2021). In: *PASP* 133.1023, 054502, p. 054502. DOI: 10.1088/1538-3873/abf038.

Miller, B., E. Gallo, T. Treu, et al. (Mar. 2012). In: *ApJ* 747.1, 57, p. 57. DOI: 10.1088/0004-637X/747/1/57.

Miller, B. P., E. Gallo, J. E. Greene, et al. (Jan. 2015). In: *ApJ* 799.1, 98, p. 98. DOI: 10.1088/0004-637X/799/1/98.

Miller, J. M., M. T. Reynolds, S. B. Yun, et al. (Jan. 2022). In: *The Astronomer's Telegram* 15179, p. 1.

Miller, J. M., M. T. Reynolds, A. Zoghbi, et al. (Feb. 2022). In: *The Astronomer's Telegram* 15205, p. 1.

Miller, K. A. and J. M. Stone (May 2000). In: *ApJ* 534.1, pp. 398–419. DOI: 10.1086/308736.

Miller, M. C. (May 2015). In: *ApJ* 805.1, 83, p. 83. DOI: 10.1088/0004-637X/805/1/83.

Miller, M. C. and E. J. M. Colbert (Jan. 2004). In: *International Journal of Modern Physics D* 13.1, pp. 1–64. DOI: 10.1142/S0218271804004426.

Million, C. et al. (Dec. 2016). In: *ApJ* 833.2, 292, p. 292. DOI: 10.3847/1538-4357/833/2/292.

Mimica, P. et al. (July 2015). In: *MNRAS* 450.3, pp. 2824–2841. DOI: 10.1093/mnras/stv825.

Miniutti, G. et al. (Sept. 2019). In: *Nature* 573.7774, pp. 381–384. DOI: 10.1038/s41586-019-1556-x.

Minkowski, R. L. and G. O. Abell (1963). In: *Basic Astronomical Data: Stars and Stellar Systems*. Ed. by K. A. Strand, p. 481.

Mitsuda, K. et al. (Jan. 1984). In: *PASJ* 36, pp. 741–759.

Modjaz, M. et al. (Dec. 2016). In: *ApJ* 832.2, 108, p. 108. DOI: 10.3847/0004-637X/832/2/108.

Morales-Rueda, L. and T. R. Marsh (June 2002). In: *MNRAS* 332.4, pp. 814–826. DOI: 10.1046/j.1365-8711.2002.05357.x.

Morihana, K. et al. (Oct. 2013). In: *PASJ* 65, L10, p. L10. DOI: 10.1093/pasj/65.5.L10.

Morii, M. et al. (June 2016). In: *PASJ* 68, S11, S11. DOI: 10.1093/pasj/psw007.

Motta, S. et al. (Dec. 2011). In: *MNRAS* 418.4, pp. 2292–2307. DOI: 10.1111/j.1365-2966.2011.19566.x.

Mróz, P., A. Udalski, and A. Gould (Oct. 2022). In: *ApJL* 937.2, L24, p. L24. DOI: 10.3847/2041-8213/ac90bb.

Mummery, A. and S. A. Balbus (Mar. 2020). In: *MNRAS* 492.4, pp. 5655–5674. DOI: 10.1093/mnras/staa192.

Munoz-Arancibia, A. et al. (Mar. 2021). In: *Transient Name Server Discovery Report* 2021-651, pp. 1–651.

Muñoz-Darias, T., M. Coriat, et al. (June 2013). In: *MNRAS* 432.2, pp. 1330–1337. DOI: 10.1093/mnras/stt546.

Muñoz-Darias, T., R. P. Fender, et al. (Oct. 2014). In: *MNRAS* 443.4, pp. 3270–3283. DOI: 10.1093/mnras/stu1334.

Muñoz-Darias, T., S. Motta, and T. M. Belloni (Jan. 2011). In: *MNRAS* 410.1, pp. 679–684. DOI: 10.1111/j.1365-2966.2010.17476.x.

Nakahira, S. et al. (Oct. 2010). In: *PASJ* 62.5, pp. L27–L32. DOI: 10.1093/pasj/62.5.L27.

Nakar, E. (Nov. 2020). In: *Phys. Rep.* 886, pp. 1–84. DOI: 10.1016/j.physrep.2020.08.008.

Narayan, R., I. V. Igumenshchev, and M. A. Abramowicz (Dec. 2003). In: *PASJ* 55, pp. L69–L72. DOI: 10.1093/pasj/55.6.L69.

Narayan, R. and E. Quataert (Jan. 2005). In: *Science* 307.5706, pp. 77–80. DOI: 10.1126/science.1105746.

Narayan, R. and E. Quataert (Mar. 2023). In: *arXiv e-prints*, arXiv:2303.13229, arXiv:2303.13229. DOI: 10.48550/arXiv.2303.13229.

Narayan, R. and I. Yi (June 1994). In: *ApJL* 428, p. L13. DOI: 10.1086/187381.

Narayan, R. and I. Yi (May 1995a). In: *ApJ* 444, p. 231. DOI: 10.1086/175599.

Narayan, R. and I. Yi (Oct. 1995b). In: *ApJ* 452, p. 710. DOI: 10.1086/176343.

Nayana, A. J. and P. Chandra (May 2021). In: *ApJL* 912.1, L9, p. L9. DOI: 10.3847/2041-8213/abed55.

Negoro, H., M. Nakajima, M. Aoki, et al. (Aug. 2020). In: *The Astronomer's Telegram* 13948, p. 1.

Negoro, H., M. Nakajima, S. Nakahira, et al. (Aug. 2011). In: *The Astronomer's Telegram* 3611, p. 1.

Negoro, H., K. Yamaoka, et al. (Sept. 2010). In: *The Astronomer's Telegram* 2873, p. 1.

Negoro, H., M. Kohama, et al. (June 2016). In: *PASJ* 68, S1, S1. DOI: 10.1093/pasj/psw016.

Neustroev, V. V. et al. (Dec. 2014). In: *MNRAS* 445.3, pp. 2424–2439. DOI: 10.1093/mnras/stu1924.

Nicholl, M., P. K. Blanchard, et al. (Sept. 2019). In: *MNRAS* 488.2, pp. 1878–1893. DOI: 10.1093/mnras/stz1837.

Nicholl, M., P. Short, et al. (Nov. 2019). In: *Transient Name Server Classification Report* 2019-2271, p. 1.

Nicholl, M., T. Wevers, et al. (Nov. 2020). In: *MNRAS* 499.1, pp. 482–504. DOI: 10.1093/mnras/staa2824.

Nicholl, M., E. Berger, et al. (Jan. 2019). In: *ApJ* 871.1, 102, p. 102. DOI: 10.3847/1538-4357/aaf470.

Nicholl, M., D. Lanning, et al. (Oct. 2022). In: *MNRAS* 515.4, pp. 5604–5616. DOI: 10.1093/mnras/stac2206.

Nordin, J. et al. (Nov. 2019). In: *A&A* 631, A147, A147. DOI: 10.1051/0004-6361/201935634.

Ofek, E. O. et al. (May 2013). In: *ApJ* 768.1, 47, p. 47. DOI: 10.1088/0004-637X/768/1/47.

Oganesyan, G. et al. (Aug. 2019). In: *A&A* 628, A59, A59. DOI: 10.1051/0004-6361/201935766.

Ohsuga, K. and S. Mineshige (July 2011). In: *ApJ* 736.1, 2, p. 2. DOI: 10.1088/0004-637X/736/1/2.

Oke, J. B., J. G. Cohen, et al. (Apr. 1995). In: *PASP* 107, p. 375. DOI: 10.1086/133562.

Oke, J. B. and J. E. Gunn (June 1982). In: *PASP* 94, p. 586. DOI: 10.1086/131027.

Onori, F. et al. (Oct. 2019). In: *MNRAS* 489.1, pp. 1463–1480. DOI: 10.1093/mnras/stz2053.

Osaki, Y. (Jan. 1996). In: *PASP* 108, p. 39. DOI: 10.1086/133689.

Palaversa, L. et al. (Mar. 2016). In: *ApJ* 819.2, 151, p. 151. DOI: 10.3847/0004-637X/819/2/151.

Panagiotou, C. et al. (Mar. 2023). In: *arXiv e-prints*, arXiv:2303.02710, arXiv:2303.02710. DOI: 10.48550/arXiv.2303.02710.

Parkinson, E. J. et al. (Mar. 2022). In: *MNRAS* 510.4, pp. 5426–5443. DOI: 10.1093/mnras/stac027.

Pasham, D., K. Gendreau, et al. (Feb. 2022). In: *GRB Coordinates Network* 31601, p. 1.

Pasham, D., Y. Yao, et al. (Feb. 2022). In: *The Astronomer's Telegram* 15232, p. 1.

Pasham, D. R., S. B. Cenko, A. J. Levan, et al. (May 2015). In: *ApJ* 805.1, 68, p. 68. DOI: 10.1088/0004-637X/805/1/68.

Pasham, D. R., S. B. Cenko, A. Sadowski, et al. (Mar. 2017). In: *ApJL* 837.2, L30, p. L30. DOI: 10.3847/2041-8213/aa6003.

Pasham, D. R., W. C. G. Ho, et al. (Dec. 2021). In: *Nature Astronomy* 6, pp. 249–258. DOI: 10.1038/s41550-021-01524-8.

Pasham, D. R., M. Lucchini, et al. (Jan. 2023). In: *Nature Astronomy* 7, pp. 88–104. DOI: 10.1038/s41550-022-01820-x.

Patterson, J. and J. C. Raymond (May 1985). In: *ApJ* 292, pp. 550–558. DOI: 10.1086/163188.

Patterson, M. T., E. C. Bellm, et al. (Jan. 2019). In: *PASP* 131.1, p. 018001. DOI: 10.1088/1538-3873/aae904.

Pavlinsky, M. et al. (June 2021). In: *A&A* 650, A42, A42. DOI: 10.1051/0004-6361/202040265.

Perez-Fournon, I. et al. (Aug. 2020). In: *Transient Name Server Classification Report* 2020-2456, p. 1.

Perley, D. A. (Feb. 2022). In: *GRB Coordinates Network* 31592, p. 1.

Perley, D. A., R. M. Quimby, et al. (Oct. 2016). In: *ApJ* 830.1, 13, p. 13. DOI: 10.3847/0004-637X/830/1/13.

Perley, D. A., K. Taggart, et al. (July 2020). In: *Transient Name Server Classification Report* 2020-2086, p. 1.

Perley, D. A., N. R. Tanvir, et al. (Jan. 2016). In: *ApJ* 817.1, 8, p. 8. DOI: 10.3847/0004-637X/817/1/8.

Perley, D. A. (Aug. 2019). In: *PASP* 131.1002, p. 084503. DOI: 10.1088/1538-3873/ab215d.

Perley, D. A., C. Fremling, et al. (Nov. 2020). In: *ApJ* 904.1, 35, p. 35. DOI: 10.3847/1538-4357/abbd98.

Perley, D. A., A. Y. Q. Ho, et al. (Dec. 2021). In: *MNRAS* 508.4, pp. 5138–5147. DOI: 10.1093/mnras/stab2785.

Perley, D. A., P. A. Mazzali, et al. (Mar. 2019). In: *MNRAS* 484.1, pp. 1031–1049. DOI: 10.1093/mnras/sty3420.

Perley, D. A., J. Sollerman, et al. (Mar. 2022). In: *ApJ* 927.2, 180, p. 180. DOI: 10.3847/1538-4357/ac478e.

Perley, R. A., C. J. Chandler, et al. (Sept. 2011). In: *ApJL* 739.1, L1, p. L1. DOI: 10.1088/2041-8205/739/1/L1.

Pessi, P. J. et al. (Dec. 2020). In: *Transient Name Server Classification Report* 2020-3712, p. 1.

Pettini, M. and B. E. J. Pagel (Mar. 2004). In: *MNRAS* 348.3, pp. L59–L63. DOI: 10.1111/j.1365-2966.2004.07591.x.

Pezzulli, E., R. Valiante, and R. Schneider (May 2016). In: *MNRAS* 458.3, pp. 3047–3059. DOI: 10.1093/mnras/stw505.

Phinney, E. S. (Jan. 1989). In: *The Center of the Galaxy*. Ed. by M. Morris. Vol. 136, p. 543.

Pinkney, J. et al. (Oct. 2003). In: *ApJ* 596.2, pp. 903–929. DOI: 10.1086/378118.

Piran, T. (Oct. 2004). In: *Reviews of Modern Physics* 76.4, pp. 1143–1210. DOI: 10.1103/RevModPhys.76.1143.

Piran, T. et al. (June 2015). In: *ApJ* 806.2, 164, p. 164. DOI: 10.1088/0004-637X/806/2/164.

Piro, A. L., A. Haynie, and Y. Yao (Mar. 2021). In: *ApJ* 909.2, 209, p. 209. DOI: 10.3847/1538-4357/abe2b1.

Piro, A. L. and W. Lu (May 2020). In: *ApJ* 894.1, 2, p. 2. DOI: 10.3847/1538-4357/ab83f6.

Poutanen, J., G. Lipunova, et al. (May 2007). In: *MNRAS* 377.3, pp. 1187–1194. DOI: 10.1111/j.1365-2966.2007.11668.x.

Poutanen, J. and A. Veledina (Sept. 2014). In: *SSRv* 183.1-4, pp. 61–85. DOI: 10.1007/s11214-013-0033-3.

Poznanski, D., J. X. Prochaska, and J. S. Bloom (Oct. 2012). In: *MNRAS* 426.2, pp. 1465–1474. DOI: 10.1111/j.1365-2966.2012.21796.x.

Predehl, P., R. Andritschke, et al. (Mar. 2021). In: *A&A* 647, A1, A1. DOI: 10.1051/0004-6361/202039313.

Predehl, P. and J. H. M. M. Schmitt (Jan. 1995). In: *A&A* 500, pp. 459–475.

Prentice, S. J., C. Ashall, et al. (May 2019). In: *MNRAS* 485.2, pp. 1559–1578. DOI: 10.1093/mnras/sty3399.

Prentice, S. J., K. Maguire, et al. (Sept. 2018). In: *ApJL* 865.1, L3, p. L3. DOI: 10.3847/2041-8213/aadd90.

Prigozhin, G. et al. (July 2016). In: *Space Telescopes and Instrumentation 2016: Ultraviolet to Gamma Ray*. Ed. by J.-W. A. den Herder, T. Takahashi, and M. Bautz. Vol. 9905. Society of Photo-Optical Instrumentation Engineers (SPIE) Conference Series, 99051I, p. 99051I. DOI: 10.1117/12.2231718.

Prochaska, J. X. et al. (2020). In: *Journal of Open Source Software* 5.56, p. 2308. DOI: 10.21105/joss.02308. URL: https://doi.org/10.21105/joss.02308.

Prugniel, P. and C. Soubiran (Apr. 2001). In: *A&A* 369, pp. 1048–1057. DOI: 10.1051/0004-6361:20010163.

Prugniel, P., C. Soubiran, et al. (Mar. 2007). In: *arXiv e-prints*, astro-ph/0703658, astro–ph/0703658.

Pursiainen, M. et al. (Nov. 2018). In: *MNRAS* 481.1, pp. 894–917. DOI: 10.1093/mnras/sty2309.

Quataert, E. and D. Kasen (Jan. 2012). In: *MNRAS* 419.1, pp. L1–L5. DOI: 10.1111/j.1745-3933.2011.01151.x.

Quataert, E., D. Lecoanet, and E. R. Coughlin (May 2019). In: *MNRAS* 485.1, pp. L83–L88. DOI: 10.1093/mnrasl/slz031.

Quimby, R. M. et al. (June 2011). In: *Nature* 474.7352, pp. 487–489. DOI: 10.1038/nature10095.

Raftery, A. E. (1995). In: *Sociological Methodology* 25, pp. 111–163. ISSN: 00811750, 14679531. URL: http://www.jstor.org/stable/271063 (visited on 06/24/2022).

Rahoui, F. et al. (Sept. 2015). In: *ApJ* 810.2, 161, p. 161. DOI: 10.1088/0004-637X/810/2/161.

Ramsden, P. et al. (Sept. 2022). In: *MNRAS* 515.1, pp. 1146–1157. DOI: 10.1093/mnras/stac1810.

Ransom, S. (July 2011). ascl: 1107.017.

Ransom, S. M., S. S. Eikenberry, and J. Middleditch (Sept. 2002). In: *AJ* 124.3, pp. 1788–1809. DOI: 10.1086/342285.

Rao, A. et al. (May 2019). In: *The Astronomer's Telegram* 12821, p. 1.

Ratti, E. M. et al. (July 2012). In: *MNRAS* 423.3, pp. 2656–2667. DOI: 10.1111/j.1365-2966.2012.21071.x.

Rau, A. et al. (Dec. 2009). In: *PASP* 121.886, p. 1334. DOI: 10.1086/605911.

Rees, M. J. (June 1988). In: *Nature* 333.6173, pp. 523–528. DOI: 10.1038/333523a0.

Reeves, J. et al. (Mar. 2008). In: *MNRAS* 385.1, pp. L108–L112. DOI: 10.1111/j.1745-3933.2008.00443.x.

Reid, I. N. et al. (July 1991). In: *PASP* 103, p. 661. DOI: 10.1086/132866.

Reines, A. E. and M. Volonteri (Nov. 2015). In: *ApJ* 813.2, 82, p. 82. DOI: 10.1088/0004-637X/813/2/82.

Reis, R. C. et al. (Aug. 2012). In: *Science* 337.6097, p. 949. DOI: 10.1126/science.1223940.

Remillard, R. A., M. Loewenstein, et al. (Mar. 2022). In: *AJ* 163.3, 130, p. 130. DOI: 10.3847/1538-3881/ac4ae6.

Remillard, R. A. and J. E. McClintock (Sept. 2006). In: *ARA&A* 44.1, pp. 49–92. DOI: 10.1146/annurev.astro.44.051905.092532.

Renzini, A. and Y.-j. Peng (Mar. 2015). In: *ApJL* 801.2, L29, p. L29. DOI: 10.1088/2041-8205/801/2/L29.

Repetto, S. and G. Nelemans (Nov. 2015). In: *MNRAS* 453.3, pp. 3341–3355. DOI: 10.1093/mnras/stv1753.

Reusch, S. et al. (June 2022). In: *Physical Review L* 128.22, 221101, p. 221101. DOI: 10.1103/PhysRevLett.128.221101.

Reynolds, C. S. (Sept. 2021). In: *ARA&A* 59, pp. 117–154. DOI: 10.1146/annurev-astro-112420-035022.

Reynolds, C. S. et al. (Aug. 2012). In: *ApJ* 755.2, 88, p. 88. DOI: 10.1088/0004-637X/755/2/88.

Rhodes, L. et al. (May 2023). In: *MNRAS* 521.1, pp. 389–395. DOI: 10.1093/mnras/stad344.

Ricarte, A. and P. Natarajan (Feb. 2018a). In: *MNRAS* 474.2, pp. 1995–2011. DOI: 10.1093/mnras/stx2851.

Ricarte, A. and P. Natarajan (Dec. 2018b). In: *MNRAS* 481.3, pp. 3278–3292. DOI: 10.1093/mnras/sty2448.

Ricarte, A., F. Pacucci, et al. (Oct. 2019). In: *MNRAS* 489.1, pp. 1006–1022. DOI: 10.1093/mnras/stz1891.

Ricarte, A., M. Tremmel, et al. (June 2021). In: *MNRAS* 503.4, pp. 6098–6111. DOI: 10.1093/mnras/stab866.

Ricci, C. and B. Trakhtenbrot (Nov. 2022). In: *arXiv e-prints*, arXiv:2211.05132, arXiv:2211.05132. DOI: 10.48550/arXiv.2211.05132.

Rigault, M. et al. (July 2019). In: *A&A* 627, A115, A115. DOI: 10.1051/0004-6361/201935344.

Rivera Sandoval, L. E. et al. (Oct. 2018). In: *MNRAS* 480.1, pp. L146–L150. DOI: 10.1093/mnrasl/sly145.

Roberson, M., C. Fremling, and M. Kasliwal (Feb. 2022). In: *The Journal of Open Source Software* 7.70, 3612, p. 3612. DOI: 10.21105/joss.03612.

Roming, P. W. A. et al. (Oct. 2005). In: *SSRv* 120.3-4, pp. 95–142. DOI: 10.1007/s11214-005-5095-4.

Rosswog, S., E. Ramirez-Ruiz, and W. R. Hix (Apr. 2009). In: *ApJ* 695.1, pp. 404–419. DOI: 10.1088/0004-637X/695/1/404.

Roth, N. and D. Kasen (Mar. 2018). In: *ApJ* 855.1, 54, p. 54. DOI: 10.3847/1538-4357/aaaec6.

Roth, N., D. Kasen, et al. (Aug. 2016). In: *ApJ* 827.1, 3, p. 3. DOI: 10.3847/0004-637X/827/1/3.

Roth, N., S. van Velzen, et al. (Apr. 2021). In: *ApJ* 910.2, 93, p. 93. DOI: 10.3847/1538-4357/abdf50.

Ruan, J. J. et al. (Sept. 2019). In: *ApJ* 883.1, 76, p. 76. DOI: 10.3847/1538-4357/ab3c1a.

Russell, D. M., R. P. Fender, et al. (Sept. 2006). In: *MNRAS* 371.3, pp. 1334–1350. DOI: 10.1111/j.1365-2966.2006.10756.x.

Russell, D. M., T. D. Russell, et al. (May 2013). In: *ApJL* 768.2, L35, p. L35. DOI: 10.1088/2041-8205/768/2/L35.

Russell, T. D., R. Soria, et al. (Apr. 2014). In: *MNRAS* 439.2, pp. 1381–1389. DOI: 10.1093/mnras/stt2480.

Sądowski, A. and R. Narayan (Mar. 2016). In: *MNRAS* 456.4, pp. 3929–3947. DOI: 10.1093/mnras/stv2941.

Sánchez-Janssen, R. et al. (June 2019). In: *ApJ* 878.1, 18, p. 18. DOI: 10.3847/1538-4357/aaf4fd.

Sari, R., T. Piran, and R. Narayan (Apr. 1998). In: *ApJL* 497.1, pp. L17–L20. DOI: 10.1086/311269.

Sato, R. et al. (Apr. 2012). In: *The Astronomer's Telegram* 4024, p. 1.

Saxton, R. et al. (July 2020). In: *SSRv* 216.5, 85, p. 85. DOI: 10.1007/s11214-020-00708-4.

Sazonov, S. et al. (Dec. 2021). In: *MNRAS* 508.3, pp. 3820–3847. DOI: 10.1093/mnras/stab2843.

Schawinski, K. et al. (May 2014). In: *MNRAS* 440.1, pp. 889–907. DOI: 10.1093/mnras/stu327.

Schlafly, E. F. and D. P. Finkbeiner (Aug. 2011). In: *ApJ* 737, 103, p. 103. DOI: 10.1088/0004-637X/737/2/103.

Schmidt, M. (Feb. 1968). In: *ApJ* 151, p. 393. DOI: 10.1086/149446.

Schrøder, S. L. et al. (Mar. 2020). In: *ApJ* 892.1, 13, p. 13. DOI: 10.3847/1538-4357/ab7014.

Schulze, S. et al. (Aug. 2021). In: *ApJS* 255.2, 29, p. 29. DOI: 10.3847/1538-4365/abff5e.

Schwarzenberg-Czerny, A. (Mar. 1998). In: *Baltic Astronomy* 7, pp. 43–69. DOI: 10.1515/astro-1998-0109.

Semenov, V., S. Dyadechkin, and B. Punsly (Aug. 2004). In: *Science* 305.5686, pp. 978–980. DOI: 10.1126/science.1100638.

Sfaradi, I. et al. (July 2022). In: *ApJ* 933.2, 176, p. 176. DOI: 10.3847/1538-4357/ac74bc.

Shahbaz, T. and E. Kuulkers (Mar. 1998). In: *MNRAS* 295.1, pp. L1–L5. DOI: 10.1046/j.1365-8711.1998.29511221.x.

Shakura, N. I. and R. A. Sunyaev (Jan. 1973). In: *A&A* 24, pp. 337–355.

Shakura, N. I. and R. A. Sunyaev (June 1976). In: *MNRAS* 175, pp. 613–632. DOI: 10.1093/mnras/175.3.613.

Shankar, F. (Dec. 2013). In: *Classical and Quantum Gravity* 30.24, 244001, p. 244001. DOI: 10.1088/0264-9381/30/24/244001.

Shankar, F., M. Bernardi, et al. (Aug. 2016). In: *MNRAS* 460.3, pp. 3119–3142. DOI: 10.1093/mnras/stw678.

Shankar, F., D. H. Weinberg, and J. Miralda-Escudé (Jan. 2009). In: *ApJ* 690.1, pp. 20–41. DOI: 10.1088/0004-637X/690/1/20.

Shappee, B. J. et al. (June 2014). In: *ApJ* 788.1, 48, p. 48. DOI: 10.1088/0004-637X/788/1/48.

Shaw, A. W., P. A. Charles, A. J. Bird, et al. (July 2013). In: *MNRAS* 433.1, pp. 740–745. DOI: 10.1093/mnras/stt763.

Shaw, A. W., P. A. Charles, J. Casares, et al. (Dec. 2016). In: *MNRAS* 463.2, pp. 1314–1322. DOI: 10.1093/mnras/stw2092.

Shaw, A. W., B. E. Tetarenko, et al. (Jan. 2019). In: *MNRAS* 482.2, pp. 1840–1857. DOI: 10.1093/mnras/sty2787.

She, R., L. C. Ho, and H. Feng (June 2017). In: *ApJ* 842.2, 131, p. 131. DOI: 10.3847/1538-4357/aa7634.

Sheinis, A. I. et al. (Aug. 2002). In: *PASP* 114.798, pp. 851–865. DOI: 10.1086/341706.

Shen, R.-F. and C. D. Matzner (Apr. 2014). In: *ApJ* 784.2, 87, p. 87. DOI: 10.1088/0004-637X/784/2/87.

Shidatsu, M. et al. (Dec. 2013). In: *ApJ* 779.1, 26, p. 26. DOI: 10.1088/0004-637X/779/1/26.

Shimura, T. and F. Takahara (June 1995). In: *ApJ* 445, p. 780. DOI: 10.1086/175740.

Shingles, L. et al. (Jan. 2021). In: *Transient Name Server AstroNote* 7, pp. 1–7.

Shu, X. et al. (Nov. 2020). In: *Nature Communications* 11, 5876, p. 5876. DOI: 10.1038/s41467-020-19675-z.

Sidoli, L. et al. (Aug. 2011). In: *MNRAS* 415.3, pp. 2373–2378. DOI: 10.1111/j.1365-2966.2011.18865.x.

Siebert, M. (May 2020). In: *Transient Name Server Classification Report* 2020-1469, p. 1.

Siegel, J. C. et al. (Sept. 2022). In: *arXiv e-prints*, arXiv:2209.06844, arXiv:2209.06844. DOI: 10.48550/arXiv.2209.06844.

Skrutskie, M. F. et al. (Feb. 2006). In: *AJ* 131.2, pp. 1163–1183. DOI: 10.1086/498708.

Smith, K. W. et al. (Aug. 2020). In: *PASP* 132.1014, 085002, p. 085002. DOI: 10.1088/1538-3873/ab936e.

Smith, N. (2017). In: *Handbook of Supernovae*. Ed. by A. W. Alsabti and P. Murdin, p. 403. DOI: 10.1007/978-3-319-21846-5_38.

SNIascore (June 2021). In: *Transient Name Server Classification Report* 2021-1939, pp. 1–1939.

Soderberg, A. M. et al. (Aug. 2006). In: *Nature* 442.7106, pp. 1014–1017. DOI: 10.1038/nature05087.

Soker, N. (May 2022). In: *Research in Astronomy and Astrophysics* 22.5, 055010, p. 055010. DOI: 10.1088/1674-4527/ac5b40.

Soker, N., A. Grichener, and A. Gilkis (Apr. 2019). In: *MNRAS* 484.4, pp. 4972–4979. DOI: 10.1093/mnras/stz364.

Soleri, P. et al. (Feb. 2013). In: *MNRAS* 429.2, pp. 1244–1257. DOI: 10.1093/mnras/sts405.

Somalwar, J. J. et al. (Apr. 2022). In: *ApJ* 929.2, 184, p. 184. DOI: 10.3847/1538-4357/ac5e29.

Sonbas, E. et al. (June 2020). In: *GRB Coordinates Network* 27915, p. 1.

Soria, R., K. Wu, and R. W. Hunstead (Aug. 2000). In: *ApJ* 539.1, pp. 445–462. DOI: 10.1086/309194.

Soumagnac, M. T. and E. O. Ofek (July 2018). In: *PASP* 130.989, p. 075002. DOI: 10.1088/1538-3873/aac410.

Speagle, J. S. et al. (Oct. 2014). In: *ApJS* 214.2, 15, p. 15. DOI: 10.1088/0067-0049/214/2/15.

Stein, R. et al. (Feb. 2021). In: *Nature Astronomy* 5, pp. 510–518. DOI: 10.1038/s41550-020-01295-8.

Steinberg, E. and N. C. Stone (June 2022). In: *arXiv e-prints*, arXiv:2206.10641, arXiv:2206.10641. DOI: 10.48550/arXiv.2206.10641.

Steiner, J. F., J. A. García, et al. (Feb. 2017). In: *ApJ* 836.1, 119, p. 119. DOI: 10.3847/1538-4357/836/1/119.

Steiner, J. F., R. Narayan, et al. (Nov. 2009). In: *PASP* 121.885, p. 1279. DOI: 10.1086/648535.

Stone, N. C., E. Vasiliev, et al. (Mar. 2020). In: *SSRv* 216.3, 35, p. 35. DOI: 10.1007/s11214-020-00651-4.

Stone, N. C., M. Kesden, et al. (Feb. 2019). In: *General Relativity and Gravitation* 51.2, 30, p. 30. DOI: 10.1007/s10714-019-2510-9.

Stone, N. C. and B. D. Metzger (Jan. 2016). In: *MNRAS* 455.1, pp. 859–883. DOI: 10.1093/mnras/stv2281.

Strauss, M. A. et al. (Sept. 2002). In: *AJ* 124.3, pp. 1810–1824. DOI: 10.1086/342343.

Strubbe, L. E. and E. Quataert (Dec. 2009). In: *MNRAS* 400.4, pp. 2070–2084. DOI: 10.1111/j.1365-2966.2009.15599.x.

Strüder, L. et al. (Jan. 2001). In: *A&A* 365, pp. L18–L26. DOI: 10.1051/0004-6361:20000066.

Sugizaki, M. et al. (Nov. 2011). In: *PASJ* 63, S635–S644. DOI: 10.1093/pasj/63.sp3.S635.

Sun, H., B. Zhang, and Z. Li (Oct. 2015). In: *ApJ* 812.1, 33, p. 33. DOI: 10.1088/0004-637X/812/1/33.

Sunyaev, R., V. Arefiev, et al. (Dec. 2021). In: *A&A* 656, A132, A132. DOI: 10.1051/0004-6361/202141179.

Sunyaev, R. and M. Revnivtsev (June 2000). In: *A&A* 358, pp. 617–623.

Swank, J. H. (Jan. 1999). In: *Nuclear Physics B Proceedings Supplements* 69.1-3, pp. 12–19. DOI: 10.1016/S0920-5632(98)00175-3.

Swarup, G. (Jan. 1991). In: *IAU Colloq. 131: Radio Interferometry. Theory, Techniques, and Applications*. Ed. by T. J. Cornwell and R. A. Perley. Vol. 19. Astronomical Society of the Pacific Conference Series, pp. 376–380.

Tachibana, Y. and A. A. Miller (Dec. 2018). In: *PASP* 130.994, p. 128001. DOI: 10.1088/1538-3873/aae3d9.

Taddia, F. et al. (Feb. 2018). In: *A&A* 609, A136, A136. DOI: 10.1051/0004-6361/201730844.

Taggart, K. and D. A. Perley (May 2021). In: *MNRAS* 503.3, pp. 3931–3952. DOI: 10.1093/mnras/stab174.

Tanaka, Y. and N. Shibazaki (Jan. 1996). In: *ARA&A* 34, pp. 607–644. DOI: 10.1146/annurev.astro.34.1.607.

Tananbaum, H. et al. (Nov. 1979). In: *ApJL* 234, pp. L9–L13. DOI: 10.1086/183100.

Tanvir, N. R. et al. (Feb. 2022). In: *GRB Coordinates Network* 31602, p. 1.

Tchekhovskoy, A., B. D. Metzger, et al. (Jan. 2014). In: *MNRAS* 437.3, pp. 2744–2760. DOI: 10.1093/mnras/stt2085.

Tchekhovskoy, A., R. Narayan, and J. C. McKinney (Mar. 2010). In: *ApJ* 711.1, pp. 50–63. DOI: 10.1088/0004-637X/711/1/50.

Tchekhovskoy, A., R. Narayan, and J. C. McKinney (Nov. 2011). In: *MNRAS* 418.1, pp. L79–L83. DOI: 10.1111/j.1745-3933.2011.01147.x.

Teboul, O., N. C. Stone, and J. P. Ostriker (Nov. 2022). In: *arXiv e-prints*, arXiv:2211.05858, arXiv:2211.05858.

Tetarenko, A. J., G. R. Sivakoff, J. C. A. Miller-Jones, M. Bremer, et al. (Jan. 2019). In: *MNRAS* 482.3, pp. 2950–2972. DOI: 10.1093/mnras/sty2853.

Tetarenko, A. J., G. R. Sivakoff, J. C. A. Miller-Jones, E. W. Rosolowsky, et al. (Aug. 2017). In: *MNRAS* 469.3, pp. 3141–3162. DOI: 10.1093/mnras/stx1048.

Tetarenko, B. E., G. Dubus, J. P. Lasota, et al. (Oct. 2018). In: *MNRAS* 480.1, pp. 2–16. DOI: 10.1093/mnras/sty1798.

Tetarenko, B. E., G. Dubus, G. Marcel, et al. (May 2020). In: *MNRAS* 495.4, pp. 3666–3682. DOI: 10.1093/mnras/staa1367.

Tetarenko, B. E., J. P. Lasota, et al. (Feb. 2018). In: *Nature* 554.7690, pp. 69–72. DOI: 10.1038/nature25159.

Tetarenko, B. E., G. R. Sivakoff, C. O. Heinke, et al. (Feb. 2016). In: *ApJS* 222.2, 15, p. 15. DOI: 10.3847/0067-0049/222/2/15.

Thomsen, L. L., T. M. Kwan, et al. (Oct. 2022). In: *ApJL* 937.2, L28, p. L28. DOI: 10.3847/2041-8213/ac911f.

Thomsen, L. L., L. Dai, et al. (Feb. 2022). In: *ApJ* 925.2, 151, p. 151. DOI: 10.3847/1538-4357/ac3df3.

Thomsen, L. L., J. Lixin Dai, et al. (Oct. 2019). In: *ApJL* 884.1, L21, p. L21. DOI: 10.3847/2041-8213/ab4518.

Tiengo, A. et al. (Sept. 2004). In: *A&A* 423, pp. 861–865. DOI: 10.1051/0004-6361:20041027.

Tonry, J., L. Denneau, A. Heinze, H. Weiland, et al. (Dec. 2019). In: *Transient Name Server Discovery Report* 2019-2553, p. 1.

Tonry, J. L., L. Denneau, A. N. Heinze, B. Stalder, et al. (June 2018). In: *PASP* 130.988, p. 064505. DOI: 10.1088/1538-3873/aabadf.

Torres, M. A. P., P. J. Callanan, et al. (Apr. 2002). In: *ApJ* 569.1, pp. 423–431. DOI: 10.1086/339282.

Torres, M. A. P., D. Steeghs, et al. (Oct. 2009). In: *The Astronomer's Telegram* 2268, p. 1.

Truemper, J. (Jan. 1982). In: *Advances in Space Research* 2.4, pp. 241–249. DOI: 10.1016/0273-1177(82)90070-9.

Tsvetkova, A. et al. (Feb. 2021). In: *ApJ* 908.1, 83, p. 83. DOI: 10.3847/1538-4357/abd569.

Tucci, M. and M. Volonteri (Apr. 2017). In: *A&A* 600, A64, A64. DOI: 10.1051/0004-6361/201628419.

Tuchman, Y., S. Mineshige, and J. C. Wheeler (Aug. 1990). In: *ApJ* 359, p. 164. DOI: 10.1086/169045.

Tucker, M. A. (Feb. 2021). In: *Transient Name Server Classification Report* 2021-433, pp. 1–433.

Tucker, M. A. et al. (Nov. 2018). In: *ApJL* 867.1, L9, p. L9. DOI: 10.3847/2041-8213/aae88a.

Ulmer, A. (Mar. 1999). In: *ApJ* 514.1, pp. 180–187. DOI: 10.1086/306909.

Vacca, W. D., M. C. Cushing, and J. T. Rayner (Mar. 2003). In: *PASP* 115, pp. 389–409. DOI: 10.1086/346193. eprint: astro-ph/0211255.

Valenti, S. et al. (Feb. 2008). In: *MNRAS* 383.4, pp. 1485–1500. DOI: 10.1111/j.1365-2966.2007.12647.x.

Valluri, M. et al. (July 2005). In: *ApJ* 628.1, pp. 137–152. DOI: 10.1086/430752.

van der Klis, M. (Jan. 1988). In: *Timing Neutron Stars*. Vol. 262, pp. 27–70.

van der Klis, M. (2006). In: *Compact stellar X-ray sources*. Vol. 39, pp. 39–112.

van Doesburgh, M., M. van der Klis, and S. M. Morsink (Sept. 2018). In: *MNRAS* 479.1, pp. 426–434. DOI: 10.1093/mnras/sty1404.

van Paradijs, J. (June 1996). In: *ApJL* 464, p. L139. DOI: 10.1086/310100.

van Paradijs, J. and J. E. McClintock (Oct. 1994). In: *A&A* 290, pp. 133–136.

van Velzen, S. (Jan. 2018). In: *ApJ* 852.2, 72, p. 72. DOI: 10.3847/1538-4357/aa998e.

van Velzen, S., G. R. Farrar, et al. (Nov. 2011). In: *ApJ* 741.2, 73, p. 73. DOI: 10.1088/0004-637X/741/2/73.

van Velzen, S., S. Gezari, S. B. Cenko, et al. (Feb. 2019). In: *ApJ* 872.2, 198, p. 198. DOI: 10.3847/1538-4357/aafe0c.

van Velzen, S., S. Gezari, E. Hammerstein, et al. (Feb. 2021). In: *ApJ* 908.1, 4, p. 4. DOI: 10.3847/1538-4357/abc258.

van Velzen, S., T. W. S. Holoien, et al. (Oct. 2020). In: *SSRv* 216.8, 124, p. 124. DOI: 10.1007/s11214-020-00753-z.

van Velzen, S., R. Stein, et al. (Nov. 2021). In: *arXiv e-prints*, arXiv:2111.09391, arXiv:2111.09391.

VanderPlas, J. T. (May 2018). In: *ApJS* 236.1, 16, p. 16. DOI: 10.3847/1538-4365/aab766.

Vergani, S. D. et al. (Sept. 2015). In: *A&A* 581, A102, A102. DOI: 10.1051/0004-6361/201425013.

Verner, D. A. et al. (July 1996). In: *ApJ* 465, p. 487. DOI: 10.1086/177435.

Vika, M. et al. (Dec. 2009). In: *MNRAS* 400.3, pp. 1451–1460. DOI: 10.1111/j.1365-2966.2009.15544.x.

Voges, W. et al. (Sept. 1999). In: *A&A* 349, pp. 389–405.

Voggel, K. T. et al. (Feb. 2019). In: *ApJ* 871.2, 159, p. 159. DOI: 10.3847/1538-4357/aaf735.

Vurm, I. and B. D. Metzger (Aug. 2021). In: *ApJ* 917.2, 77, p. 77. DOI: 10.3847/1538-4357/ac0826.

Walton, D. J., W. N. Alston, et al. (Nov. 2020). In: *MNRAS* 499.1, pp. 1480–1498. DOI: 10.1093/mnras/staa2961.

Walton, D. J., E. Nardini, et al. (Feb. 2013). In: *MNRAS* 428.4, pp. 2901–2920. DOI: 10.1093/mnras/sts227.

Walton, D. J., R. C. Reis, et al. (May 2012). In: *MNRAS* 422.3, pp. 2510–2531. DOI: 10.1111/j.1365-2966.2012.20809.x.

Wang, J. and D. Merritt (Jan. 2004). In: *ApJ* 600.1, pp. 149–161. DOI: 10.1086/379767.

Wang-Ji, J. et al. (Mar. 2018). In: *ApJ* 855.1, 61, p. 61. DOI: 10.3847/1538-4357/aaa974.

Warner, B. (1995). Cambridge Astrophysics. Cambridge University Press. DOI: 10.1017/CBO9780511586491.

Waters, C. Z. et al. (Nov. 2020). In: *ApJS* 251.1, 4, p. 4. DOI: 10.3847/1538-4365/abb82b.

Waxman, E. and B. Katz (2017). In: *Handbook of Supernovae*. Ed. by A. W. Alsabti and P. Murdin, p. 967. DOI: 10.1007/978-3-319-21846-5_33.

Wevers, T., D. R. Pasham, S. van Velzen, G. Leloudas, et al. (Oct. 2019). In: *MNRAS* 488.4, pp. 4816–4830. DOI: 10.1093/mnras/stz1976.

Wevers, T. (Sept. 2020). In: *MNRAS* 497.1, pp. L1–L6. DOI: 10.1093/mnrasl/slaa097.

Wevers, T., D. R. Pasham, S. van Velzen, J. C. A. Miller-Jones, et al. (Jan. 2021). In: *arXiv e-prints*, arXiv:2101.04692, arXiv:2101.04692.

Wevers, T., N. C. Stone, et al. (Aug. 2019). In: *MNRAS* 487.3, pp. 4136–4152. DOI: 10.1093/mnras/stz1602.

Wevers, T., S. van Velzen, et al. (Oct. 2017). In: *MNRAS* 471.2, pp. 1694–1708. DOI: 10.1093/mnras/stx1703.

Whitesides, L. et al. (Dec. 2017). In: *ApJ* 851.2, 107, p. 107. DOI: 10.3847/1538-4357/aa99de.

Wijnands, R. et al. (Dec. 2015). In: *MNRAS* 454.2, pp. 1371–1386. DOI: 10.1093/mnras/stv1974.

Wilkes, B. and W. Tucker, eds. (2019). 2514-3433. IOP Publishing. ISBN: 978-0-7503-2163-1. DOI: 10.1088/2514-3433/ab43dc. URL: http://dx.doi.org/10.1088/2514-3433/ab43dc.

Williams, P. K. G. et al. (Apr. 2017). Astrophysics Source Code Library, record ascl:1704.001. ascl: 1704.001.

Willingale, R. et al. (May 2013). In: *MNRAS* 431, pp. 394–404. DOI: 10.1093/mnras/stt175.

Wilms, J., A. Allen, and R. McCray (Oct. 2000). In: *ApJ* 542.2, pp. 914–924. DOI: 10.1086/317016.

Winkler, C. et al. (Nov. 2003). In: *A&A* 411, pp. L1–L6. DOI: 10.1051/0004-6361:20031288.

Wiseman, P. et al. (Oct. 2020). In: *MNRAS* 498.2, pp. 2575–2593. DOI: 10.1093/mnras/staa2474.

Woods, T. E. et al. (Aug. 2019). In: *PASA* 36, e027, e027. DOI: 10.1017/pasa.2019.14.

Woosley, S. E., A. Heger, and T. A. Weaver (Nov. 2002). In: *Reviews of Modern Physics* 74.4, pp. 1015–1071. DOI: 10.1103/RevModPhys.74.1015.

Wright, A. H., A. S. G. Robotham, N. Bourne, et al. (July 2016). In: *MNRAS* 460, p. 765. DOI: 10.1093/mnras/stw832.

Wright, A. H., A. S. G. Robotham, S. P. Driver, et al. (Sept. 2017). In: *MNRAS* 470.1, pp. 283–302. DOI: 10.1093/mnras/stx1149.

Wu, Y. X. et al. (Aug. 2010). In: *ApJ* 718.2, pp. 620–631. DOI: 10.1088/0004-637X/718/2/620.

Xiang, D. et al. (Mar. 2021). In: *ApJ* 910.1, 42, p. 42. DOI: 10.3847/1538-4357/abdeba.

Yadlapalli, N. et al. (Mar. 2021). In: *ApJL* 909.2, L27, p. L27. DOI: 10.3847/2041-8213/abea19.

Yan, L. et al. (Dec. 2020). In: *Transient Name Server Classification Report* 2020-3640, p. 1.

Yao, Y. (July 2021a). In: *Transient Name Server Classification Report* 2021-2295, pp. 1–2295.

Yao, Y. (Oct. 2021b). In: *Transient Name Server Classification Report* 2021-3411, pp. 1–3411.

Yao, Y. (Oct. 2022). In: *Transient Name Server Classification Report* 2022-2915, p. 1.

Yao, Y., M. Brightman, et al. (July 2021). In: *Transient Name Server AstroNote* 183, pp. 1–183.

Yao, Y., M. Chu, et al. (Oct. 2021). In: *Transient Name Server Classification Report* 2021-3611, pp. 1–3611.

Yao, Y., K. De, et al. (Sept. 2020). In: *ApJ* 900.1, 46, p. 46. DOI: 10.3847/1538-4357/abaa3d.

Yao, Y., T. Enoto, et al. (Aug. 2020). In: *The Astronomer's Telegram* 13932, p. 1.

Yao, Y. and H. Feng (Oct. 2019). In: *ApJL* 884.1, L3, p. L3. DOI: 10.3847/2041-8213/ab44c7.

Yao, Y., J. Garcia, et al. (Aug. 2020). In: *The Astronomer's Telegram* 13957, p. 1.

Yao, Y., S. Gezari, et al. (June 2021). In: *Transient Name Server Classification Report* 2021-2155, pp. 1–2155.

Yao, Y., E. Hammerstein, et al. (July 2021). In: *Transient Name Server Classification Report* 2021-2535, pp. 1–2535.

Yao, Y., A. Y. Q. Ho, et al. (Aug. 2022). In: *ApJ* 934.2, 104, p. 104. DOI: 10.3847/1538-4357/ac7a41.

Yao, Y., S. R. Kulkarni, K. B. Burdge, et al. (Oct. 2021). In: *ApJ* 920.2, 120, p. 120. DOI: 10.3847/1538-4357/ac15f9.

Yao, Y., S. R. Kulkarni, K. C. Gendreau, et al. (Oct. 2021). In: *ApJ* 920.2, 121, p. 121. DOI: 10.3847/1538-4357/ac15f8.

Yao, Y., W. Lu, et al. (Sept. 2022). In: *ApJ* 937.1, 8, p. 8. DOI: 10.3847/1538-4357/ac898a.

Yao, Y., A. A. Miller, et al. (Dec. 2019). In: *ApJ* 886.2, 152, p. 152. DOI: 10.3847/1538-4357/ab4cf5.

Yao, Y., D. R. Pasham, and K. C. Gendreau (Feb. 2022). In: *The Astronomer's Telegram* 15230, p. 1.

Yao, Y., D. R. Pasham, K. C. Gendreau, et al. (Feb. 2022). In: *The Astronomer's Telegram* 15217, p. 1.

Yao, Y., V. Ravi, et al. (Mar. 2023). In: *arXiv e-prints*, arXiv:2303.06523, arXiv:2303.06523. DOI: 10.48550/arXiv.2303.06523.

Yao, Y., S. van Velzen, et al. (May 2021). In: *Transient Name Server Classification Report* 2021-1632, pp. 1–1632.

Yaron, O. and A. Gal-Yam (July 2012). In: *PASP* 124.917, p. 668. DOI: 10.1086/666656.

Yu, Q. and Y. Lu (Dec. 2008). In: *ApJ* 689.2, pp. 732–754. DOI: 10.1086/592770.

Yu, Z., C. S. Kochanek, et al. (Oct. 2022). In: *MNRAS* 515.4, pp. 5198–5210. DOI: 10.1093/mnras/stac2073.

Yuan, F., W. Cui, and R. Narayan (Feb. 2005). In: *ApJ* 620.2, pp. 905–914. DOI: 10.1086/427206.

Yuan, F., Z. Gan, et al. (May 2015). In: *ApJ* 804.2, 101, p. 101. DOI: 10.1088/0004-637X/804/2/101.

Yuan, F. and R. Narayan (Aug. 2014). In: *ARA&A* 52, pp. 529–588. DOI: 10.1146/annurev-astro-082812-141003.

Yuan, H. B. and X. W. Liu (Sept. 2012). In: *MNRAS* 425.3, pp. 1763–1771. DOI: 10.1111/j.1365-2966.2012.21674.x.

Yuan, W., C. Zhang, et al. (July 2018). In: *Space Telescopes and Instrumentation 2018: Ultraviolet to Gamma Ray*. Ed. by J.-W. A. den Herder, S. Nikzad, and K. Nakazawa. Vol. 10699. Society of Photo-Optical Instrumentation Engineers (SPIE) Conference Series, 1069925, p. 1069925. DOI: 10.1117/12.2313358.

Zapartas, E. et al. (May 2017). In: *A&A* 601, A29, A29. DOI: 10.1051/0004-6361/201629685.

Zauderer, B. A., E. Berger, R. Margutti, et al. (Apr. 2013). In: *ApJ* 767.2, 152, p. 152. DOI: 10.1088/0004-637X/767/2/152.

Zauderer, B. A., E. Berger, A. M. Soderberg, et al. (Aug. 2011). In: *Nature* 476.7361, pp. 425–428. DOI: 10.1038/nature10366.

Zhang, B. (2018). DOI: 10.1017/9781139226530.

Zhang, G. B., F. Bernardini, et al. (May 2019). In: *ApJ* 876.1, 5, p. 5. DOI: 10.3847/1538-4357/ab12dd.

Zhang, L., D. Altamirano, et al. (Sept. 2020). In: *MNRAS* 499.1, pp. 851–861. DOI: 10.1093/mnras/staa2842.

Zhang, S.-N. (Dec. 2013). In: *Frontiers of Physics* 8.6, pp. 630–660. DOI: 10.1007/s11467-013-0306-z.

Zhang, S.-N., T. Li, et al. (Feb. 2020). In: *Science China Physics, Mechanics, and Astronomy* 63.4, 249502, p. 249502. DOI: 10.1007/s11433-019-1432-6.

Zhang, W., S. E. Woosley, and A. Heger (May 2008). In: *ApJ* 679.1, pp. 639–654. DOI: 10.1086/526404.

Zurita, C., M. Durant, et al. (July 2008). In: *ApJ* 681.2, pp. 1458–1463. DOI: 10.1086/588721.

Zurita, C., C. Sánchez-Fernández, et al. (Aug. 2002). In: *MNRAS* 334.4, pp. 999–1008. DOI: 10.1046/j.1365-8711.2002.05588.x.